Principles of self-organization and self-assembly in biologically inspired non-equilibrium systems

A conceptual approach

Isabella Graf

A dissertation
submitted to the Faculty of Physics
at the Ludwig–Maximilians–Universität München
for the degree of
DOCTOR RERUM NATURALIUM

München 2019

Principles of self-organization and self-assembly in biologically inspired non-equilibrium systems

A conceptual approach

Dissertation
an der Fakultät für Physik
der Ludwig–Maximilians–Universität München

vorgelegt von
Isabella Ruth Graf
aus Tübingen

München, den 16. Dezember 2019

Erstgutachter: Prof. Erwin Frey
Zweitgutachter: Prof. Joachim Krug
Tag der mündlichen Prüfung: 14. Februar 2020

Zusammenfassung (Summary in German)

Man soll die Dinge so einfach machen wie möglich – aber nicht einfacher.
(Albert Einstein)

Wodurch zeichnen sich lebende Systeme aus? Das ist eine der Fragen, die Erwin Schrödinger in seinem berühmten Buch „Was ist Leben?“ aufwirft. Seine Antwort ist überraschend prägnant: Lebende Systeme halten sich vom Gleichgewicht fern und schaffen Ordnung aus Unordnung. Diese bemerkenswerten Fähigkeiten von Organismen, sich selbst in vielschichtige Muster zu organisieren und große Strukturen aufzubauen, steht auch im Mittelpunkt meiner Arbeit. Ziel ist es, generische Prinzipien der Selbstorganisation und Strukturbildung mit Hilfe von theoretischen Studien aufzuzeigen. Zu diesem Zweck wurden mehrere konzeptionelle Modelle untersucht, die durch unterschiedliche biologische Gegebenheiten motiviert sind. Alle diese Modelle umfassen Nichtgleichgewichtsprozesse, die für die Zwecke des jeweiligen biologischen Systems maßgeblich sind. Diese Arbeit ist gemäß den beiden Kernthemen Selbstorganisation und Strukturbildung in zwei Teile gegliedert.

1. **Zytoskelettfilamente und molekulare Motoren**
In Zusammenarbeit mit Mareike Bojer, Moritz Striebel und Erwin Frey
Der erste Teil meiner Dissertation beinhaltet drei Projekte und beschäftigt sich mit der Selbstorganisation im Kontext des Zellzytoskeletts. Diese Struktur ist entscheidend für verschiedene Charakteristika lebender Organismen, die vom intrazellulären Transport bis hin zur Chromosomentrennung reichen, und beruht auf den Wechselwirkungen zwischen Motorproteinen und Zytoskelettfilamenten. Beispielsweise bewegen sich Motorproteine nicht nur zufällig innerhalb der Zellen, sondern werden auch gezielt entlang der Filamente transportiert. In den ersten beiden Projekten haben wir uns die Frage gestellt, welche Rolle das Zusammenspiel dieses gerichteten Transports mit der Diffusion für die Musterbildung und Längenregulierung von Filamenten spielen könnte. Anhand von konzeptionellen Modellen haben wir festgestellt, dass gerichteter Transport – wenngleich er als Nichtgleichgewichtsprozess für die Bildung von Mustern erforderlich sein kann – in begrenzten Geometrien als Transportmittel potentiell ineffizient ist. Dies ist auf die Bildung von „Staus“ zurückzuführen, die starke Korrelationen zwischen den Teilchen hervorrufen und zu sehr langsamer Bewegung führen. Eine endliche Diffusionsgeschwindigkeit hingegen kann eine wichtige Komponente für das Auftreten von selbstorganisierten Oszillationen in der Filamentlänge darstellen. Der Grund dafür ist, dass die Diffusion auf der Zeitskala anderer intrinsischer Prozesse (wie der Wachstumsdynamik von Filamenten) zu langsam ist, um ein Gleichgewicht im System herzustellen, und stattdessen zu Zeitverzögerungen zwischen den verschiedenen Dynamiken führt. Die Ergebnisse dieser Projekte wurden in zwei Publikationen veröffentlicht, die in den Kapiteln 2.5 und 3.5 abgedruckt sind. Ich habe als einzige Erstautorin an der ersten Veröffentlichung mitgewirkt. Für die zweite Veröffentlichung teile ich mir die Erstautorenschaft mit Mareike Bojer.
Das dritte Projekt beschäftigt sich mit der kollektiven Dynamik in Filamentnetzwerken, die

durch Motorproteine verknüpft sind. Durch diese Vernetzung werden nicht nur Motoren entlang von Filamenten transportiert, sondern umgekehrt werden auch Filamente durch Motorproteine, die Kräfte auf die Filamente ausüben, in Bewegung gesetzt. Was sind die wichtigsten Einflussfaktoren auf die entstehende Filamentdynamik im Netzwerk? Um diese Frage zu beantworten, haben wir ein mesoskopisches Modell für nematische Filamentnetzwerke entwickelt. Unsere Analyse dieses Modells legt den folgenden Mechanismus für die Kraftausbreitung durch die Motoren nahe: Aufgrund der Vernetzung durch Motoren pflanzen sich die erzeugten Kräfte über eine charakteristische Reichweite im Netzwerk fort. Diese Reichweite ist groß, wenn die Filamentwechselwirkungen im Vergleich zur Dissipation in der umgebenden Flüssigkeit stark sind. Dann interagieren alle Filamente effektiv miteinander und die lokalen Filamentgeschwindigkeiten werden durch globale Netzwerkeigenschaften bestimmt. Im Gegensatz dazu wird die lokale Filamentgeschwindigkeit bei hoher Dissipation im Fluid stark von den lokal erzeugten Kräften beeinflusst. Dieser Kraftausbreitungsmechanismus eröffnet eine mechanistische Perspektive auf die Selbstorganisation von Filamentnetzwerken. Ein Manuskript, das diese Ergebnisse umfasst, wurde veröffentlicht und ist in Kapitel 4.5 abgedruckt. Moritz Striebel und ich teilen uns die Erstautorenschaft.

2. **Stochastische Effekte bei der Bildung heterogener Strukturen**
In Zusammenarbeit mit Florian Gartner, Patrick Wilke, Philipp Geiger und Erwin Frey
Der zweite Teil meiner Arbeit beschäftigt sich mit der Bildung heterogener Strukturen. Dieser Prozess ist nicht nur für Zellen wichtig, sondern auch für die künstliche Herstellung komplexer Nanostrukturen. Im ersten Projekt haben wir die Bedingungen untersucht, die erfüllt sein müssen, damit solche Prozesse robust und zuverlässig funktionieren. Zu diesem Zweck haben wir ein konzeptionelles Modell für die Assemblierung von Ringen entwickelt, deren Heterogenität durch einen Parameter bestimmt wird. Wir haben festgestellt, dass der Aufbau heterogener Strukturen starken stochastischen Effekten unterworfen ist. Tatsächlich kann es passieren, dass in stochastischen Simulationen keinerlei Strukturen fertiggestellt werden, obwohl eine Beschreibung unter Vernachlässigung von Korrelationen eine perfekte Ausbeute vorhersagt. Diese „stochastische Ertragskatastrophe“ tritt auch in Systemen mit relativ hohen Teilchenzahlen auf.
Wie können Schwankungen in diesen makroskopischen Systemen einen so starken Einfluss haben? Und welche Strategien gibt es, um einen robusten Aufbau heterogener Strukturen zu erreichen? Diese Fragen werden im zweiten Projekt behandelt, in dem wir eine effektive Theorie für das Auftreten stochastischer Effekte in unserem konzeptionellen Modell formuliert haben. Es basiert auf der Intuition, dass Schwankungen in der relativen Verfügbarkeit der verschiedenen Ringbausteine zur Nukleation von zu vielen Strukturen führen können. Wenn die Ressourcen endlich sind, können diese Strukturen nicht vervollständigt werden und die Ausbeute ist gering. Die Verringerung des Ungleichgewichts zwischen den verschiedenen Bausteinen erscheint daher als eine vielversprechende Strategie zur Verbesserung des Strukturbildungsprozesses und wir diskutieren konkrete Wege, wie dieses Prinzip in der Praxis umgesetzt werden könnte. Ein Manuskript zu den Ergebnissen des ersten Projekts wurde veröffentlicht und ist in Kapitel 7.5 abgedruckt. Für dieses Projekt teile ich mir die Erstautorenschaft mit Florian Gartner und Patrick Wilke. Ein Manuskript zu den Ergebnissen des zweiten Projekts ist derzeit in Vorbereitung. Florian Gartner und ich wirken beide als Erstautoren mit. Der Manuskriptentwurf ist in Kapitel 8.5 abgedruckt.

Synopsis

Everything must be made as simple as possible – but not simpler.
(Albert Einstein)

What are the characteristic properties of living systems? This is one of the questions Erwin Schrödinger raises in his famous book "What is life?". His answer is surprisingly concise: Living systems keep themselves out of equilibrium, creating order from disorder. This remarkable ability of organisms to self-organize into complex patterns and to assemble large structures also lies at the heart of my thesis. The goal is to elucidate generic principles of self-organization and self-assembly by means of theoretical modeling. For this purpose, several conceptual models which are inspired by different biological settings were studied. All of these models comprise non-equilibrium processes which are crucial for the purpose of the respective biological system. This thesis is organized into two parts, in accordance with the two main themes of self-organization and self-assembly.

1. **Cytoskeletal filaments and molecular motors**
In collaboration with Mareike Bojer, Moritz Striebel and Erwin Frey
The first part of my thesis contains three projects and is concerned with self-organization in the context of the cell cytoskeleton. This structure is crucial for various features of living organisms ranging from intracellular transport to chromosome segregation, and relies on the interactions between motor proteins and cytoskeletal filaments. For instance, motor proteins do not only diffuse within cells but are also transported in a directed fashion along the filaments.
In the first two projects, we asked what role the interplay of this directed transport with diffusion could have for pattern formation and length regulation of filaments. By means of conceptual modeling, we found that - although directed transport as a non-equilibrium process may be necessary for patterns to form - in confined geometries it can be inefficient as a means of transport. This is due to the formation of "traffic jams" that introduce strong correlations between particles and lead to very slow motion. A finite diffusion speed, on the other hand, can provide an important factor for the occurrence of self-organized filament-length oscillations. The underlying reason is that on the time scale of other intrinsic processes (such as the growth dynamics of filaments), diffusion is too slow to equilibrate the system and instead leads to time delays between the different dynamics. The results of these projects are published in two publications which are reprinted in sections 2.5 and 3.5. I contribute as single first author to the first publication. For the second publication I share co-first authorship with Mareike Bojer.
The third project is concerned with collective dynamics in networks of filaments which are crosslinked by motor proteins. Due to this crosslinking, not only motors are transported along filaments but also, conversely, filaments are set into motion by motor proteins that exert forces on them. What are the main determinants for the emerging filament dynamics

in the network? To address this question, we set up a mesoscopic model for nematic filament networks. Our analysis of this model suggests a mechanism for force propagation by motor crosslinking: Any force generated at one position is propagated through the network over a characteristic range. This range is large if filament interactions are strong compared to the dissipation in the surrounding fluid. Then all filaments effectively interact with each other and the local filament velocities are determined by global network features. In contrast, if dissipation in the fluid is high, the local filament velocity correlates strongly with the locally generated forces. This force propagation mechanism offers a mechanistic perspective on the self-organization of cytoskeletal networks. A manuscript incorporating these findings has been published and is reprinted in section 4.5. Moritz Striebel and I share co-first authorship.

2. **Stochastic effects in heterogeneous self-assembly**
In collaboration with Florian Gartner, Patrick Wilke, Philipp Geiger and Erwin Frey
The second part of my thesis deals with the self-assembly of heterogeneous structures. This process is important not only for cells but also for the artificial fabrication of complex nanostructures. In the first project, we examined conditions that must be met for such processes to function in a robust and resilient way. To this end, we considered a conceptual toy model for the assembly of rings, whose heterogeneity is set by one parameter. We found that the assembly of heterogeneous structures is subject to strong stochastic effects. Indeed, yield can be zero in stochastic simulations although a deterministic mean-field description predicts perfect yield. This "stochastic yield catastrophe" occurs even in systems with relatively high particle numbers.
How can fluctuations in these macroscopic systems have such a strong, detrimental effect? And which strategies exist to guide robust assembly of heterogeneous structures? These questions are addressed in the second project where we formulated an effective theory for the occurrence of stochastic effects in our conceptual model. It is based on the intuition that fluctuations in the relative availability of the different constituents can lead to the nucleation of too many structures. If the resources are finite, these structures then cannot be completed and the yield is low. Decreasing the imbalance between species thus appears as a promising strategy to improve assembly efficiency and we discuss tangible ways for its practical implementation. A manuscript about the results of the first project has been published and is reprinted in section 7.5. For this project I share co-first authorship with Florian Gartner and Patrick Wilke. The results of the second project are currently in preparation for submission with Florian Gartner and me as shared co-first authors. The manuscript draft is reprinted in section 8.5.

Contents

List of publications

Publications directly relevant to this thesis

1. Graf, I. R., & Frey, E. (2017). *Generic Transport Mechanisms for Molecular Traffic in Cellular Protrusions.* **Physical Review Letters**, 118(12), 128101. DOI: 10.1103/PhysRevLett.118.128101. [1]
2. Bojer*, M., Graf*, I. R., & Frey, E. (2018). *Self-organized system-size oscillation of a stochastic lattice-gas model.* **Physical Review E**, 98(1), 012410. DOI: 10.1103/PhysRevE.98.012410. [2]
3. Striebel*, M., Graf*, I. R., & Frey, E. (2020). *A mechanistic view of collective filament motion in active nematic networks.* **Biophysical Journal**, 118(2), 313-324. DOI: 10.1016/j.bpj.2019.11.3387. [3]
4. Gartner*, F. M., Graf*, I. R., Wilke*, P., Geiger, P. M., & Frey, E. (2020). *Stochastic yield catastrophes and robustness in self-assembly.* **eLife**, 9(e51020), 1-37. DOI: 10.7554/eLife.51020. [4]
5. Graf*, I. R., Gartner*, F. M., & Frey, E. (2020). *Understanding and guiding robust self-assembly of heterogeneous structures.* In preparation. [5]

Other publications

6. Bauer, M., Graf, I. R., Ngampruetikorn, V., Stephens, G. J., & Frey, E. (2017). *Exploiting ecology in drug pulse sequences in favour of population reduction.* **PLoS Computational Biology**, 13(9): e1005747. DOI: 10.1371/journal.pcbi.1005747. [6]
7. Gartner, F. M., Graf, I. R., & Frey, E. (2020). *Controlling fidelity and time-efficiency in self-assembly.* In preparation. [7]
8. Träuble, F., Gartner, F. M., Graf, I. R., & Frey, E. (2020). *Topological properties of self-assembly reaction networks determine robustness to stochastic effects.* In preparation. [8]

Abstracts of the projects

Living systems are characterized by their abilities to continuously evolve and self-replicate and to generate patterns and structures. These abilities rely on a constant dissipation of energy that keeps living systems far from equilibrium [9, 10]. While universal properties of, in principal, arbitrarily complex systems in equilibrium have been formulated with the help of Statistical Physics, the systematic study of non-equilibrium systems is still in its infancy. An important role of physics for the research of biological systems is therefore the formulation and investigation of generic principles. The hope is that – in analogy to other fields of physics – these principles apply in different contexts, help to develop predictive theories and do not depend on details of the system. One particular example is the idea that living systems have evolved towards some sort of "optimum". This optimality principle has been successfully related to different aspects of life, ranging from the genetic code (e.g. [11]) and flow in transport networks (e.g. [12, 13]) to information transmission in gene networks (e.g. [14, 15]) and more generally in biological systems (e.g. [16]).

In a similar spirit, this thesis aims at elucidating principles underlying self-organization and self-assembly processes in different non-equilibrium systems. The approach adopted is in terms of conceptual, theoretical modeling: Our aim is not to describe a specific biological system in detail but to identify generic mechanisms that may serve as core principles in more elaborate models. In a bottom-up way, we thus try to reduce the respective system to its essential parts[1], providing a platform with which we can understand the particular mechanism in detail. The main focus of my doctoral studies has been on two topics.
The first one is concerned with the interactions of motor proteins and cytoskeletal filaments in several biological contexts. In particular, our aim was to elucidate general principles for the motion of molecular motors along filaments in a confined geometry (chapter 2), for the potential role of active transport and diffusion for filament length regulation (chapter 3) and for filament dynamics in networks crosslinked by molecular motors (chapter 4). In all these different contexts, interactions between individual elements (filaments or motor proteins) lead to intriguing, and in parts counterintuitive, collective behavior and self-organized patterns. The most important take-home messages can be formulated as follows: 1) In confinement, directed transport of motors which are subject to excluded volume effects can be surprisingly inefficient due to strong nearest-neighbor correlations (chapter 2). 2) Diffusion-limited transport can lead to the occurrence of self-organized length oscillations if the timescale for equilibration by diffusion is long compared to the growth and shrinkage dynamics (chapter 3). 3) Local forces exerted by motor proteins between neighboring filaments in networks are propagated over a characteristic length, which is determined by the ratio of motor forces to the drag in the surrounding fluid (chapter 4).
It would be very enlightening to experimentally test these ideas using for instance microfluidics technology [17–19] or reconstituted *in vitro* systems of purified components [20–23].

[1] with "essential" referring to the specific question asked

The second topic deals with the self-assembly of heterogeneous structures. Based on a conceptual model, we investigated which role stochasticity and finite resources play for assembly efficiency. While perfect yield can always be achieved in a deterministic description of the process, which is valid in the limit of infinite particle numbers, finite systems are susceptible to fluctuations. Intriguingly, even systems with large numbers of particles can be subject to strong stochastic effects that completely suppress yield (chapter 7). Heuristically, this "stochastic yield catastrophe" is due to stochastic variations in the availability of the different constituents for binding. These fluctuations lead to undesirable nucleation events and ultimately to low assembly yield. We quantified this heuristic picture by an effective theory that allowed us to disentangle the various sources of stochasticity in terms of their relevance to assembly efficiency. Focusing on the most detrimental source of fluctuations, we proposed and implemented different supply control strategies to improve the assembly yield (chapter 8). These strategies might prove useful for the design of artificial self-assembly systems [24–28] and might be reflected in assembly principles of macromolecular structures such as the ribosome [29, 30] or the flagellar motor [31, 32] in cells.

1. Transport mechanisms in a confined geometry

With Erwin Frey

Summary

In this project, we investigated a conceptual stochastic model that is motivated biologically by the interplay of active transport of motor proteins along cytoskeletal filaments and of diffusive motion in the cytoplasm. The model was studied both in terms of stochastic simulations with Gillespie's algorithm [33] and by analytical calculations based on the theory of stochastic processes. We found that correlations between motor proteins, induced by excluded volume interactions, can markedly affect the active transport properties in a confined geometry. In particular, while active transport is very efficient for single motor proteins, collective effects can lead to the formation of "traffic jams" that slow down the motor flux considerably. We quantified this correlation effect by deriving an exact identity which relates the nearest-neighbor correlations to the motor densities and allows to analytically predict the densities and currents. In a biological context, these findings suggest that diffusion might play an important role for protein transport in confinement.

Background

While diffusion can be an efficient means of transport on short length or large timescales, transport of material against a concentration gradient or over long distances requires active processes that keep the system out of equilibrium. One way to achieve active motion in cells is via so-called molecular motors that "walk" in a directed fashion along quasi one-dimensional cytoskeletal filaments (for recent reviews see for instance [34–36]). These motors consume chemical energy and transport cargo, which can then accumulate at specific places. For instance, it has been observed experimentally that due to motor transport along actin filaments different proteins accumulate at the tips of filopodia or stereocilia [37–40]. The geometry of these cellular protrusions is rather distinct: While filopodia and stereocilia are connected to the cell body (or a reservoir) at one end, their other end extends into the

surrounding environment [41–43]. Due to the enclosure by the membrane, mass is conserved at this outer end. This mass conservation and the resulting no-flux boundary condition at the tip may lead to interesting phenomena when coupled to the directed transport of motors towards the periphery: If active currents along the filaments arise, these currents need to be counterbalanced by opposing diffusive fluxes. This requirement already hints to the fact that a finite diffusion speed may influence transport in confinement.

Research questions

Which physical principles govern the interplay between active transport, an intrinsically non-equilibrium process, and diffusion in a confined geometry? What role do collective effects play for transport efficiency?

Results

To approach these questions, we considered a simplified, conceptual model. This model builds on the totally asymmetric simple exclusion process (TASEP) [44–46] as a model for active, directed transport and extends it by a second lane mimicking the diffusion in the cytoplasm. The geometry is taken to be half-closed with particle exchange with a reservoir at the base and mass conservation at the tip, as it is the case for cellular protrusions.

The steady-state density profile is characterized by a localized domain wall.

In contrast to a single-lane TASEP, which exhibits three different phases [47–49], there is only one generic steady-state density profile in our model. It is characterized by a localized domain wall [50–53] that separates a low-density region towards the base from a high-density region towards the tip. In the limit where the high-density region shrinks to a few lattice sites, the model exhibits tip localization of motor proteins, which is reminiscent of experimental findings for several motors in filopodia or stereocilia [37–40].

Diffusion is important for tip localization and motor transport.

Our analysis suggests that tip localization is markedly affected by the diffusion in the cytoplasm and by microscopic properties at the tip such as the unbinding rate from the filament. Furthermore, we identified a task sharing mechanism between the active transport and the diffusive motion. While the activity of motors is crucial for generation and maintenance of gradients (which could not be achieved by diffusion alone), diffusion is essential for transport of proteins to the tip. This is surprising because *a priori* active, directed motion would appear to be much more efficient for motor transport as compared to diffusion.

Correlations due to volume exclusion strongly reduce active transport efficiency.

The importance of diffusion for motor transport is due to strong correlations between motors on the TASEP lane, induced by excluded volume effects. These correlations greatly reduce the active current as compared to a mean-field prediction. As a result, collective active transport becomes rather inefficient in contrast to active transport of single motors. By deriving an exact moment identity we quantified this effect analytically.

Relevance and outlook

Our results might prove useful in two regards. From a theoretical point of view, the moment identity, which relates the neighbor correlations to the densities in the system, can in principle be generalized to other systems where a TASEP lane is coupled to another lattice. In this way,

it might contribute to the quantification of correlations and the prediction of active currents also in more elaborate models for motor transport in confined geometries.
On a broader perspective, our results may be beneficial for the conceptual understanding of collective phenomena in systems where active, non-equilibrium and passive, diffusive transport are combined. The interplay of these intrinsically different types of transport is relevant in different contexts ranging from cell migration to cell polarization [54–56].

Publication and contribution
This project builds on and extends work performed during my Master thesis [57] and has been published in *Physical Review Letters*.
I contributed as single first author to this publication. Erwin Frey and I designed the project and wrote the paper. I conceived the theory and performed the entire analysis. Erwin Frey supervised the research.
The publication is reprinted in section 2.5.

2. Coupling filament length regulation to motor transport

With Mareike Bojer and Erwin Frey

Summary
In this project, we investigated what role the interplay of active transport and diffusion might have for length regulation of filaments in a confined geometry. To this end, we extended the model of the previous project by stochastic growth and shrinkage of the system size. Motor proteins that reach the end of the TASEP lane shrink the system (TASEP and diffusion lane) by one lattice site, corresponding to motors that depolymerize the filament at the end, e.g. kinesin-8 [58–62]. Conversely, the system grows spontaneously by addition of lattice sites to the end, corresponding to spontaneous attachment of tubulin dimers [63, 64]. Intriguingly, the combination of motor-induced shrinking, spontaneous growth and diffusion leads to self-organized oscillations if equilibration by diffusion is slow compared to the length changing dynamics. These effects are due to cumulative crowding of motors in the tip region, which occurs since the equilibration of the motor density with the reservoir is time-delayed with respect to the growth and shrinkage dynamics. Such time delays, introduced by slow diffusion, also seem to be important for other protein systems such as the Par or Pom system [65, 66].

Background
Cytoskeletal filaments such as microtubules and actin filaments are not static structures as we implicitly assumed in the first project but can be highly dynamic. Unless stabilized by drugs, they constantly grow and shrink by addition or removal of subunits to or from the ends. Microtubules mostly grow and shrink at one end. Interestingly, their steady-state behavior is not characterized by a roughly constant length with fluctuations around the mean but instead by extended phases of growth and fast shrinkage ("dynamic instability"; [63, 67]). In contrast, actin filaments typically grow at one end and shrink at the other end, leading to so-called treadmilling (e.g. [68]). The process of attachment and detachment of subunits can, however, not be entirely random. If this were the case, filaments would not exhibit

a preferred length but instead the length dynamics would follow a random walk. For this reason, there needs to be some sort of length control mechanism (for a recent review see [69]). Intriguingly, typical lengths of filaments are of the order of micrometers whereas the individual subunits (tubulin or actin) are nanometer scaled [68, 70–72]. So, although length control mechanisms operate on far smaller scales than those of the filaments, the mechanisms require some type of feedback between the length of the large-scale structure and the attachment and detachment dynamics of the small subunits. Several scenarios for how such feedback might be realized have been discussed theoretically and suggested by experimental findings (for recent reviews see [69, 73–75]): A very straightforward way would be to have only a finite number of subunits and, correspondingly, a hard upper bound on the filament length. Such a limiting pool mechanism has been suggested, for instance, for cilia length control [76]. Alternatively, the length dynamics may be coupled to active transport along filaments. Examples include intraflagellar transport where tubulin monomers are transported by kinesins to the tips of cilia or flagella [69, 73, 77–79] and active transport of length-regulator proteins by myosins [41, 42, 80] or kinesins [59, 60, 62, 81, 82].

Research questions

What influence does a finite diffusion speed have on length regulation in confinement? Could it, in combination with active transport, change the underlying self-organization process qualitatively?

Results

To make a step forward in answering these questions, we considered a stochastic lattice-gas model with dynamically changing system size. It is based on the model investigated in the previous project and couples active transport to a length (system-size) regulation mechanism. While the system size extends spontaneously, shrinkage happens due to motors that effectively act as depolymerases once they have walked to the tip of the filament (TASEP lane). In the model, this system-size dynamics also affects the surrounding cytoplasm that extends and shrinks simultaneously with the filament. As a result, there is an intricate coupling between active transport, diffusion and length (system-size) regulation.

For fast growth dynamics, the system exhibits robust periodic changes in length.

For small growth rates, the length dynamics behaves stochastically with a well-defined average length. Surprisingly, however, for large spontaneous growth rates the system size exhibits robust temporal patterns. More specifically, the size periodically displays extended phases of growth and shrinkage.

The self-organized length oscillations are due to slow diffusion and cumulative crowding of motors in the tip region.

If the growth rate is fast compared to diffusion, the changes in length happen on a timescale on which the motor densities in the cytoplasm cannot be equilibrated by diffusion. This separation of timescales results in continuous accumulation of motors in the tip region and in a time delay between the growth and shrinkage dynamics. Due to this time delay, extended phases of growth and shrinkage emerge and instead of relaxing towards a stable fixed point, the system shows robust temporal patterns.

Relevance and outlook
The observed oscillations in the system size are at first sight qualitatively similar to the dynamic instability of microtubules [63, 67]. However, while the dynamic instability of microtubules is characterized by extended phases of rather slow growth and short phases of rapid shrinkage, the oscillations observed in our model are rather symmetric with respect to growth and shrinkage. One reason for this symmetry is that we did not include any non-linear effects into the growth or shrinkage dynamics. Including such nonlinearities could be an interesting question for future research.
On a broader perspective, our model suggests that slow diffusion can be an important factor for the occurrence of self-organized oscillations. The underlying reason is that - while diffusion tends to equilibrate systems on long timescales - equilibration may not take place on the timescale of other intrinsic processes (such as the growth dynamics in our case). This can lead to time delays between different dynamics of the system and, correspondingly, to oscillatory behavior. Similar diffusion-induced time delays and periodic temporal patterns have been observed in other protein systems [65, 66] as well.

Publication and contribution
This project was partially based on Mareike Bojer's Master thesis [83], which I supervised together with Erwin Frey. It has been published in *Physical Review E*.
Mareike Bojer and I contributed equally to this publication. Erwin Frey and I designed the project. Mareike Bojer performed the numerical analysis and conceived and executed the mathematical analysis for the adiabatic limit. I conceived and executed the mathematical analysis for the effective theory. Mareike Bojer, Erwin Frey and I wrote the paper. Erwin Frey supervised the research.
The publication is reprinted in section 2.5.

3. Collective filament dynamics in nematic filament networks

With Moritz Striebel and Erwin Frey

Summary
The goal of this project was to examine the collective dynamics of filaments in cytoskeletal networks crosslinked by motor proteins. For this purpose, we set up an effectively one-dimensional, agent-based model, which focuses on known mechanistic interactions between two microtubules crosslinked by a single kinesin motor [84–87] but coarse-grains other microscopic details such as motor densities. The mechanistic interactions between the filaments are implemented in terms of forces between pairs of filaments that depend on the relative velocities of the filaments and their spatial overlap. By deriving a continuum theory for this mesoscopic agent-based model, we identified a mechanism for force propagation through the network: Due to the crosslinking between filaments, any force that is generated locally between two filaments is propagated through the network over a characteristic lengthscale. This characteristic lengthscale is set by the antagonism between the motor forces and the drag in the fluid and is a control parameter of the dynamics. For biologically realistic parameters, local forces are translated over long distances and the local filament dynamics is essentially determined by the collective action of all motors. This insight provides an explanation as to

why the filament velocities in recent experiments [88] and in the spindle apparatus [89–91] depend only weakly on the local network features. To test our model predictions, we propose a feasible *in vitro* experiment.

Background

The cytoskeleton is crucial for diverse tasks ranging from force and motion generation to chromosome segregation [92, 93]. Its ability to perform these tasks is largely based on the interactions between cytoskeletal filaments and motor proteins: Molecular motors such as kinesin-5 crosslink pairs of microtubules [94] and thereby arrange the microtubules in large networks. These networks are not static structures. Quite the contrary, the crosslinking motor proteins constantly exert forces on the filaments and move them around [23, 35, 64, 95]. The forces depend on the relative orientation of the microtubules [94]: A single motor with two binding domains that crosslinks and walks on two antiparallel filaments slides these filaments past one another. In contrast, two crosslinked parallel microtubules remain static. This behavior suggests that the velocity of a microtubule should strongly depend on the ratio of parallel to antiparallel interaction partners, i.e. the local polarity in the network [96–98]. In particular, no motion is expected in regions with only parallel microtubules. This intuition, however, is in conflict with experimental findings for metaphase spindles in Xenopus egg extracts [89–91]. While the local polarity of the microtubule network varies notably along the spindle axis, the velocity of microtubules is fairly constant, in particular if dynein, a minus-end clustering motor [99, 100], is inhibited. At first sight, one might be tempted to argue that this may well be due to the fact that the spindle is a complex machinery with many other proteins involved. However, the same behavior has also been observed in recent *in vitro* experiments with purified components consisting of kinesin-14 XCTK2 and microtubules only [88].

Research questions

How do the local forces between the filaments manifest in terms of collective filament motion? What is the underlying mechanism determining the relation between the local network polarity and the local filament velocities? How does such a mechanism relate to the experimental findings of polarity-independent filament velocities?

Results

To develop a mechanistic understanding with regard to these questions, we considered a mesoscopic model for the dynamical rearrangement of microtubules in nematic networks. The microtubules are modeled as hard rods and the force generation by crosslinking motors is incorporated by effective interactions between filaments that depend on the relative orientation and motion of the microtubules and on their spatial overlap. By deriving a non-local continuum theory from these mesoscopic interactions, we identified a mechanism for collective filament motion.

Owing to the crosslinking of filaments by motor proteins, locally generated forces are propagated through the network over a characteristic length.

The local force exerted by a motor protein does not only influence the directly crosslinked filaments but is propagated by subsequent crosslinking motors to all filaments that are part of one network patch. As a result, the local microtubule velocity does not solely depend on the

local polarity but rather on an averaged polarity in an effective interaction range ("ambient polarity"). More concretely, the local microtubule speed is determined by the convolution of the polarity profile with an interaction kernel that decays exponentially with the distance measured in units of a characteristic propagation length. This characteristic propagation length depends on the efficiency of force propagation through the network and thus on the relative strength of the motor forces compared to the filament drag in the fluid.

For large drag in the fluid (high dissipation), any force only has a local effect.

If the fluid drag is high or motor forces are weak, local forces exerted on the filaments are dissipated quickly and the effective interaction range is small. As a result, only the interactions with the nearest-neighbor filaments are decisive for filament motion and the filament velocities strongly depend on the local polarity.

For heavily crosslinked filaments, the local filament dynamics depends on the global polarity in the network.

If the dissipation in the fluid is very small or the crosslinking between filaments is very strong, local forces between the microtubules are translated through the entire network and the effective interaction range (the characteristic length) is very large. Consequently, all microtubules in the network experience the same ambient polarity, irrespective of their location or the local polarity. The local filament velocity is then independent of the local polarity, in agreement with experimental findings in the spindle apparatus [89–91] and in reconstituted *in vitro* systems [88]. Interestingly, for biologically plausible parameter values, the characteristic propagation length is of the same order as the spindle size. This suggests that the spindle is indeed in the regime where the filament velocities are approximately independent of the local polarities according to our theoretical framework.

Our model predicts that the velocity distribution of filaments depends on the characteristic length.

In *in vitro* experiments with filament gels, the local polarity in the filament is not constant but exhibits spatial fluctuations [88]. If the characteristic propagation length is large, filament velocities, however, should not strongly depend on the local polarities and the distribution of filament velocities should be narrow. In contrast, if the interaction range is small, the filament velocities will reflect the spatial fluctuations of the polarity profile and the distribution of filament velocities should be broad. Thus, our theory predicts that the velocity distribution strongly depends on the characteristic propagation length. We propose a specific *in vitro* experiment to test this prediction, and we substantiate our suggestion by conducting an *in silico* study which is intended to mimic the experimental setup.

Relevance and outlook

The results of our study offer a new mechanistic perspective on the emergence of collective motion in nematic filament networks. This perspective provides a common explanation for two seemingly conflicting findings: While in dilute systems there is a strong correlation between the local filament dynamics and the local network polarity [96–98], experiments with metaphase spindles in egg extract [89–91, 101] or with reconstituted systems [88] suggest polarity-independent filament velocities. Our theory indicates that these findings can be understood in terms of an intrinsic lengthscale of the system which determines the effective interaction range of filaments and scales with the ratio of motor forces to drag in the surrounding fluid. For dilute systems, this characteristic length is small and the filament dynamics is determined by local network properties. For heavily crosslinked networks, on the other hand,

it can be comparable to the system size and effectively all microtubules interact with each other. The filament dynamics then depends on the global polarity only.
On a broader perspective, we believe that our work can contribute towards the establishment of a concise theoretical framework for the self-organization in filament networks. Indeed, we extended our analytical calculations also to systems with several types of crosslinking motors, ranging from passive crosslinkers to motors with one passive and one active head. For these more complicated systems, the mechanism of force propagation remains unchanged. Our mesoscopic model could be extended in additional interesting ways. For instance, it remains a question for future research how the force propagation mechanism generalizes to three-dimensional networks where filaments are not necessarily aligned in a nematic order. Finally, it would be enlightening to combine a recently established hydrodynamic framework for filament gels [88] with our finding of an exponential interaction kernel with characteristic decay length. Such a combination could provide valuable insight into whether hydrodynamic interactions are important for force propagation and collective filament dynamics in networks.

Publication and contribution
The results of this project are reported in a manuscript, which – at the time of the original submission of this thesis – had been in press in *Biophysical Journal*. While preparing the final version of this work, the manuscript has been published there.
Moritz Striebel and I contributed equally to this publication that will also be part of Moritz Striebel's thesis. Moritz Striebel, Erwin Frey and I designed the project. Moritz Striebel performed the numerical analysis, I conceived and executed the mathematical analysis for the *in silico* study. All other investigations were done by Moritz Striebel and me in cooperation. Moritz Striebel, Erwin Frey and I wrote the paper. Erwin Frey supervised the research.
A publication preprint is reprinted in section 4.5.

4. Stochastic yield catastrophes for heterogeneous structures

With Florian Gartner, Patrick Wilke, Philipp Geiger and Erwin Frey

Summary
The goal of this project was to elucidate principles for robust and efficient self-assembly. One well-known principle in the field is that in order to produce high yield, nucleation of new structures must be slow compared to the growth of existing structures ("slow-nucleation principle"; [102–109]). It is widely accepted that this principle applies both to the assembly of virus capsids [110, 111] as well as for the assembly of DNA origami [112–114] or so-called information-rich structures [115, 116]. While virus capsids can be made from only a few different building blocks, DNA origami and information-rich structures consist of a large number of different constituents. So, what role does the heterogeneity of a structure play for the assembly process? To address this question, we considered a conceptual toy model for the assembly of ring structures whose heterogeneity is set by one parameter. In the deterministic limit of many particles per species, there are two scenarios to robustly achieve high yield, irrespective of the heterogeneity of the target structure. In accordance with the slow-nucleation principle, these scenarios correspond either to an implementation of a small dimerization rate or to a slow provision of constituents. In the case of reduced resources,

however, these two possibilities are not equivalent any more for heterogeneous structures. While slow dimerization reliably leads to high yield, slow provision of constituents is subject to strong stochastic effects. These findings highlight the role of fluctuations in self-assembly and suggest that cells use sophisticated control strategies to avoid stochastic effects.

Background

One of the fascinating characteristics of cells is their ability to self-assemble complex, biomolecular structures such as the ribosome [29, 30], microtubules [117–119] or the flagellar motor [31, 32, 120] from elementary building blocks. Similarly, also viruses constantly face the challenge to assemble their outer shell ("virus capsid") from small proteins [110, 111]. While some viruses form highly complex shells with many different building blocks, others assemble capsids from only a few different subunits. From a theoretical point of view, the assembly of the latter more homogeneous virus capsids has been understood very well [102, 110, 111, 121–123]. For instance, it has been found that for high assembly yield, nucleation of new structures should be slow compared to the growth of larger structures [102–104]. In this way, once a structure has nucleated, it is very likely to grow into the final target structure before other structures nucleate. This sequential production of structures is beneficial because it circumvents kinetic traps [102, 121, 123, 124] which may otherwise arise due to competition for resources. Interestingly, this slow-nucleation principle does not only apply to the assembly of homogeneous structures but has also been found for the assembly of heterogeneous structures [109] or so-called "structures with addressable complexity" [108] made, for instance, from DNA bricks [105, 107] or single-stranded DNA tiles [106]. This observation raises the question whether, more generally, the same principles apply for the self-assembly of both homogeneous and heterogeneous structures.

Research questions

Does the heterogeneity of the target structure qualitatively change the assembly process? Under what conditions can irreversible self-assembly processes proceed efficiently and robustly?

Results

To tackle these questions, we set up a conceptual model for the self-assembly of ring structures with a well-defined size made from different species of particles. In order to interpolate between homogeneous and heterogeneous structures, the size of the target structure and the number of species can be different. For only one species in the system, the target structures are homogeneous, whereas for larger numbers of species (and fixed target size) the heterogeneity is larger as well. There is a fixed number of particles per species and the particles of each species are provided ("activated") stochastically at a fixed rate. Once active, monomers can dimerize or attach to polymers. Correspondingly, polymers grow by monomer attachment until they have reached the target size. The efficiency of the assembly process is characterized in terms of the assembly yield which is proportional to the number of target structures.

In the deterministic limit, assembly yield does not depend on the heterogeneity of the target structure.

If the number of particles in the system is very high ("deterministic limit"), there are two ways to achieve high assembly yield in accordance with the slow-nucleation principle: either

by decreasing the dimerization rate or by decreasing the activation rate. In the first scenario, nucleation of new structures (dimer formation) is suppressed directly by control on the molecular level. In contrast, in the second case, nucleation is slowed down indirectly due to supply control. The efficacy of both scenarios is independent of the heterogeneity of the structure. Indeed, using symmetry arguments we showed analytically that systems with distinct heterogeneity of the target structure behave deterministically equivalently.

Self-assembling heterogeneous systems are generally subject to stochastic effects.

This equivalency, however, breaks down if the resources are reduced. While the assembly of homogeneous structures proceeds as expected deterministically, for heterogeneous target structures, stochastic simulations show that the yield saturates at an imperfect value for small activation rates. This saturation value is the smaller, the smaller the number of particles in the system, and is zero below a threshold value of the number of particles, which depends on the target structure size. These findings are in stark contrast to the deterministic description in terms of mean-field rate equations, which always predicts perfect yield in the limit of slow particle supply, irrespective of the number of particles and the heterogeneity of the target structure. Thus, fluctuations can markedly affect the assembly of heterogeneous structures ("stochastic yield catastrophe").

For heterogeneous structures assembly yield can be a non-monotonic function of the deterministic nucleation speed.

The same stochastic effects lead to another, counterintuitive behavior for heterogeneous structures. When slow activation and slow dimerization occur together, the assembly yield can be a non-monotonic function of the activation rate. Deterministically, a slower activation rate always corresponds to a slower nucleation probability and thus to higher yield. This is not true any more for reduced resources due to the occurrence of stochastic effects. Then, fluctuations in the relative activation levels of the different species lead to transient unavailability of species for binding, which ultimately leads to an effective enhancement of nucleation compared to growth (for details see project 5).

Relevance and outlook

It is important to note that the results of our model do not contradict the slow-nucleation principle. Irrespective of the effect of fluctuations or the heterogeneity of the target structure, favoring nucleation compared to growth leads to low assembly yield. However, while in the deterministic limit, there exist various equivalent ways to limit nucleation, this is more subtle in the case of reduced resources. For instance, reducing the activation rate of monomers is deterministically a promising strategy to slow down nucleation. If fluctuations are present, though, the nucleation of new structures might be reinforced instead. As a result, our results indicate that the slow-nucleation principle has to be interpreted in terms of the corresponding stochastic framework.

Our conceptual model certainly describes an idealized self-assembly process. To begin with, all species are present precisely in their relative stoichiometric concentrations. Furthermore, defect binding is not accounted for. Relaxing either of these two assumptions is expected to lead to additional stochastic effects (compare also [125]). Indeed, in a follow-up project [7] we considered an extension of the model which additionally allows for defect binding. The stochastic effects get even more pronounced in this case since fluctuations do not only enhance nucleation but also defect formation. By isolating the stochasticity in the original model from these additional stochastic effects, we demonstrated that fluctuations in the availability of

particles can themselves lead to a significant decrease of assembly efficiency in an otherwise ideally constructed system.
To test the robustness of our results, we also considered some modifications of the original model. These modifications include choosing a different geometry of the target structure, which does not require a linear assembly path and is non-periodic, and allowing for additional polymer-polymer binding. In both cases, we observed the same stochastic effects, albeit weakened.
Finally, it would be very interesting to test our model predictions with the help of DNA origami [112–114]. One approach may be to generalize the method presented in Ref. [126] to the case of heterogeneous ring structures.

Publication and contribution
The results of this project are reported in a manuscript, which – at the time of the original submission of this thesis – had been *under review* for publication. While preparing the final version of this work, the manuscript has been accepted and published in *eLife*.
Florian Gartner, Patrick Wilke and I contributed equally to this publication, which will also be part of Patrick Wilke's, Florian Gartner's and Philipp Geiger's theses. Florian Gartner, Patrick Wilke, Philipp Geiger, Erwin Frey and I designed the project. Florian Gartner and Patrick Wilke performed the numerical analysis. Florian Gartner and I performed the mathematical analysis. Philipp Geiger designed the illustrations. Florian Gartner, Patrick Wilke, Philipp Geiger, Erwin Frey and I wrote the paper. Erwin Frey supervised the research.
A publication preprint is reprinted in section 7.5

5. Understanding and guiding the assembly of heterogeneous structures
With Florian Gartner and Erwin Frey

Summary
Motivated by the findings of the stochastic yield catastrophe in the previous project, the goal of this project was to gain a more quantitative understanding of the effect of fluctuations on the assembly dynamics of heterogeneous structures. In particular, while it is intuitive that stochasticity might play some role in the assembly process, the strength of the stochastic effects is surprising. Furthermore, *a priori* it is not clear how the different sources of stochasticity (demographic noise due to the stochastic supply/activation of particles vs. reaction noise due to the randomness in binding) contribute to the occurrence of the stochastic yield catastrophe. To address these questions, we formulated an effective theory for the conceptual model introduced in the previous project. It relies on our intuitive perception that the main contribution to the stochastic effects comes from fluctuations in the relative availability of the different species for binding. Consequently, the focus of the effective theory lies on a characterization of the demographic noise which is introduced by these fluctuations in the activation of particles. In return, reaction noise is neglected. Although the predictions of this effective theory are not in perfect agreement with the results of the full stochastic model, the qualitative phenomenology is captured well. This suggests that demographic noise is indeed the main cause of the stochastic yield catastrophes. Based on this insight, we proposed and investigated two strategies to improve the assembly yield by reducing the variability be-

tween species. Instead of favoring a specific assembly path [7, 109], these strategies lead to more "uniform" growth behavior. On a broader perspective, reducing the variability between species may turn out to be a beneficial assembly strategy for living systems and nanotechnological applications.

Background

In order for structures to be multi-functional and to exhibit predefined morphologies, it is beneficial to be composed of many distinct components that can fulfil specific tasks or bind to specific locations [27, 115, 116, 127]. Understanding the principles underlying the assembly dynamics of such heterogeneous structures is thus expected to not only provide insights into the assembly processes in living organisms but also to be important for nanotechnological applications. In the previous project, we discussed one such aspect of the assembly of heterogeneous structures: The assembly process can be subject to strong stochastic effects which completely suppress the yield ("stochastic yield catastrophe"), in particular if the supply of the different species (elementary building blocks) occurs stochastically. Intuitively, this stochastic yield catastrophe is due to fluctuations in the availability of the different species for binding. In light of recent work [109], this seems surprising at first. In this work, it was shown that the assembly yield can be improved considerably by using non-stoichiometric concentrations for the different building blocks. Effectively, this means that the variability between species is increased since some species are present in excess compared to the other ones. How can these findings be reconciled with our intuitive understanding of the stochastic yield catastrophe, namely that the suppression of the yield is due to large fluctuations in the availability of the different species? There are two crucial differences. First, in Ref. [109], the variability between species is increased in a very controlled and coordinated fashion: All species in a small segment of the target structure (and only these) are supplied in excess. This strategy favors a very specific assembly path where nucleation happens in the small "excess segment" and structures then grow from these specific initial seeds. In contrast, in our model the fluctuations in the relative availability of the species are distributed irregularly in the ring structure. This leads to many different nucleation seeds and, correspondingly, to competing assembly pathways. The second difference is that the dynamics in Ref. [109] follows the deterministic chemical Master equations. As a result, the stochastic effects we described in the previous project should not be relevant there. Still, the same idea of favoring a very specific assembly pathway can also be used to control these stochastic effects: In another project (that will not be part of my thesis) we implemented a "just-in-sequence" supply control strategy [7]. This strategy is based on feedback between the subsequent building blocks in the favored assembly pathway. Generally speaking, supply of one species of building blocks only starts once the previous species (in the desired assembly path) has been fully supplied. Consequently, the building blocks can attach one after the other to the growing structures and the assembly efficiency is very high. With respect to our results, this raises the question whether assembly yield can also be improved by a complementary strategy, namely by decreasing the variability between species. To answer this question, a quantitative understanding of the occurrence of the stochastic yield catastrophe is necessary.

Research questions

Why is the self-assembly of heterogeneous structures subject to such strong stochastic effects?

What role do the different sources of stochasticity play for the assembly process? What are possible strategies to control stochastic effects and to kinetically guide the assembly dynamics?

Results

To answer these questions, we developed an effective theory for the conceptual model presented in the previous project. It is based on the intuition that the stochastic yield catastrophe is mainly due to demographic noise in the supply, which entails fluctuations in the availability of the different species for binding. The basic idea behind this intuition is the following: A temporary unavailability of species for binding (for instance due to low activation of the species) blocks those structures from growing that would otherwise bind to a monomer of an unavailable species. As a result, nucleation of new structures is effectively favored compared to growth. In accordance with the slow-nucleation principle, yield is thus low since too many structures compete for the same resources. To quantify this intuition, we employed a "fluctuation-corrected" mean-field ansatz and extended the deterministic mean-field dynamics for the time evolution of the polymer size distribution by a second state. In short, instead of only considering one state per structure size as it can be done in the deterministic limit [4], we derived an effective dynamics for two polymer states: One state describes polymers that can grow by currently available species whereas the other one corresponds to polymers that are blocked due to the unavailability of the neighboring species. We used methods from the theory of stochastic processes and a quasi-stationary approximation to estimate the effective transitions between the different states.

Demographic noise appears to be crucial for the occurrence of the stochastic yield catastrophe.

As expected from the many simplifications which we made to establish the effective theory, there are quantitative deviations between its predictions and the results from stochastic simulations. However, the effective theory captures the different phenomena of the stochastic simulations qualitatively correctly (see also project 4 for a description of these phenomena). Yield saturates at an imperfect value for small activation rates and this saturation value is smaller for smaller numbers of particles in the system. Furthermore, yield can become a non-monotonic function of the deterministic nucleation speed if slow activation and slow dimerization occur simultaneously. This qualitative agreement suggests that indeed demographic noise (and not the reaction noise, which we neglect) contributes substantially to the strong stochastic effects.

Decreasing the fluctuations in the relative availability of the different species improves the assembly yield.

We used this insight to propose and implement two control strategies to improve the efficiency of the self-assembly of heterogeneous structures. The first strategy relies on providing the particles in so-called bursts (or batches). In this case, not all the particles of all species are activated simultaneously but instead the particles are "presorted" in smaller batches which are supplied one after the other. If the number of particles per batch is the same for all species (or at least only exhibits "small" fluctuations), such a procedure effectively aligns the supply levels of all species. Thus, it reduces the variability between species. The second strategy relies on self-inhibitory feedback. It is implemented in a way that the free monomers of each species inhibit further activation of the species. As a result, species that have been activated more (and correspondingly have more free monomers) suppress their own activation and the supply levels are again effectively aligned. Both strategies considerably increase the assembly yield. Furthermore, a strong negative correlation between inter-species variability

and assembly yield can be observed. Taken together, our results suggest that decreasing the inter-species variability, for instance via supply control, may be a profitable strategy to enhance assembly efficiency.

Relevance and outlook

As indicated above, our effective theory is strongly based on the intuition we developed over time but has not been derived from first principles. As a result, it would be very interesting to investigate whether more rigorous approaches could be employed to formulate a stochastic theory. Furthermore, it is a question for future research to derive scaling laws from such a stochastic theory or our effective theory. These could include the dependency of the threshold number of particles (above which yield sets in) on the target structure size, or the scaling of the threshold activation rate (below which stochastic effects occur) with the number of particles or the size of the target structure. We expect such or similar scaling laws to be relevant for nanotechnological applications because they could give estimates on the feasibility of different assembly schemes. Related to this point, it would be exciting to test the suggested supply control strategies in experiments and to investigate whether the underlying principles could be relevant for intracellular self-assembly.

Contribution

The results of this project are reported in a manuscript that is currently *in preparation*.
Florian Gartner and I contributed equally to this project, which will also be part of Florian Gartner's thesis. Florian Gartner, Erwin Frey, and I designed the project. Florian Gartner and I performed the numerical analysis. I conceived and executed the mathematical analysis. Florian Gartner, Erwin Frey and I wrote the paper. Erwin Frey supervised the research.
The manuscript preprint is reprinted in section 8.5.

Part I

Cytoskeletal filaments and molecular motors

1 Introduction: The role of the cytoskeleton in living systems

Living systems exhibit an astonishing complexity and variety of functions and abilities: Cells replicate and divide, change and maintain their shapes, move in free space and through narrow constrictions and generate sophisticated patterns, both intracellular and in the collective with other cells. These capabilities rely on a robust and at the same time dynamic spatio-temporal organization of their "elementary building blocks" like proteins, lipids or DNA. How can a robust and dynamic organization emerge from interactions of a large number of constituents that are themselves highly dynamic?

To address such questions, it has proven very useful to combine insights from biology (such as the identification of protein interactions), with experimental and theoretical methods of physics. Experimental methods include for instance optical tweezers [128, 129] (for recent reviews see e.g. [130, 131]) and fluorescence techniques [132–135] (for recent reviews see also [136–138]). On the theoretical side, the techniques range from the theory of stochastic processes and non-equilibrium systems to nonlinear dynamics. We will mention some specific models and approaches in section 1.2.

One archetypical class of structures that is highly organized and is simultaneously composed of very dynamic structural elements is the cell cytoskeleton (for reviews see e.g. [92, 93, 139]). It corresponds to a network of cytoskeletal filaments which are crosslinked by proteins, and provides mechanical stability to cells. At the same time the cell cytoskeleton is also crucial for dynamic processes such as cell motion, shape changes or cell division. A prominent example is the mitotic spindle which is necessary for chromosome segregation during cell division and is based on the microtubule cytoskeleton (for recent reviews see [140–143]). To establish and coordinate its internal organization and to regulate its dynamics, interactions between the microtubules and associated motor proteins are central. For instance, by consuming chemical energy, motor proteins can "walk" on the filaments in a directed fashion (for reviews see e.g. [34–36, 95, 144]). This non-equilibrium process can be coupled to transport of cargo which then accumulates at specific places. Alternatively, so-called crosslinking motor proteins link two filaments and can thereby generate forces on these filaments. This force generation due to crosslinking is particularly important for the mitotic spindle where it is thought to contribute to polarity sorting [89, 99, 142, 143, 145, 146].

The goal of this introductory chapter is to discuss these properties and the underlying interactions between the cytoskeletal filaments and motor proteins in more detail; section 1.1. Furthermore, a short summary of some theoretical approaches to describe the different levels of the cytoskeleton will be given in section 1.2.

1.1 Biological background: Cytoskeletal filaments and motor proteins

In this section, we give a summary of some of the biological aspects of cytoskeletal filaments and molecular motors. We put some emphasis on the properties that are conceptually relevant to the projects discussed in this first part of the thesis. As we will see later, throughout these projects, we will model cytoskeletal filaments as single, hard rods on which molecular motors walk in a directed fashion, and, correspondingly, we will neglect many of the other properties. Nonetheless, to give a more complete picture about filaments and motors, we also include other aspects in this summary.

1.1.1 From microtubules to actin filaments

There are three main types of cytoskeletal filaments: microtubules, actin filaments and intermediate filaments (see for instance [92, 93, 139] for reviews). All of these filaments assemble into larger networks and interact with molecular motors. While microtubules and actin filaments are polar structures and serve as tracks for molecular motors, intermediate filaments are transported as cargo by the different motor proteins.
Since this first part of the thesis will be mostly concerned with the theoretical description of phenomena that rely on the directional movement of motors along microtubules or actin filaments, we will focus on these two types of filaments.

Microtubules

Microtubules are long and stiff polymer filaments made from tubulin dimers (e.g. [72, 118, 147]). These tubulin dimers contain two distinct subunits (α and β) which provide a directionality to the dimer. Upon polymerization, the tubulin dimers bind to each other in a head-to-tail fashion and thereby form long protofilaments. Typically, 13 protofilaments assemble laterally into a cylindrical form, the microtubule. Due to the directionality of the dimers, microtubules are polar structures with one so-called plus and one minus end. This polarity is crucial for the directional movement of motor proteins along the microtubule (see also below).
These properties of microtubules are reflected in our models as follows:

1. Microtubules are modeled as (infinitely) stiff rods with only one protofilament.
2. Microtubules are considered as polar objects on which motors move in a directed fashion (see also below).
3. While we do not explicitly include the different subunits of the protofilaments, we model the discrete nature of the microtubules: Motors do not slide continuously along the filaments but they make discrete steps (see also below).

Apart from these properties, microtubules also exhibit interesting growth behavior (e.g. [23, 63, 67, 72, 148–150]): Due to the polarity of microtubules, it vastly differs between both ends. While growth and shrinkage (polymerization and depolymerization) are fast at the plus end, the minus end is rather static. If the microtubules are not stabilized by microtubule-associated

proteins, the dynamics at the plus end shows quite peculiar behavior: Instead of stochastic fluctuations around a mean microtubule length, microtubules exhibit a so-called "dynamic instability" [63, 67]. This dynamic instability is characterized by stochastic switches between phases of fast shrinkage ("catastrophes") and prolonged phases of slower growth ("rescues"). In the second project (chapter 3), we are also concerned with length regulation of filaments by motor proteins (see also below). While exhibiting some similarities with this dynamic instability of microtubules, our motivation was not to study a particular biological system but to conceptually understand which role active transport and diffusion may have for length regulation in confinement.

On a broader perspective, microtubules are essential elements of a number of cellular structures, ranging from the mitotic spindle to cilia and flagella (see e.g. [72]). In all these cases, the interactions between the microtubules and its associated motor proteins are crucial.
We will come back to different types of motor-microtubule interactions below.

Actin filaments

On a coarse-grained scale, actin filaments are quite similar to microtubules: They are polar structures which are made from smaller, discrete subunits and serve as tracks for molecular motors [42, 68, 71, 93, 139, 151].
In our models we will thus not explicitly distinguish between actin filaments and microtubules when considering collective transport properties along filaments (chapter 2) and a conceptual model for length regulation in confinement (chapter 3).

For completeness, however, we want to mention some difference which might be relevant for more detailed studies:
Instead of being composed of tubulin, actin filaments are made from F-actin, which arranges in a double-helix form. These double-helices are much thinner as compared to microtubules (roughly 7nm in diameter compared to roughly 25nm for microtubules [93]) and, correspondingly, individual actin filaments are approximately 100 times more flexible than microtubules. When crosslinked into bundles and networks, their persistence length increases considerably (e.g. [92, 152]). Thereby, they can generate strong forces, for instance, for the elongation of filopodia or cell migration (see for instance [43, 153] for reviews). This force generation is also closely related to the polymerization and depolymerization dynamics of actin filaments. Similarly to microtubules, the two ends of the actin filament show very distinct growth dynamics [43, 68, 71, 153]. However, in this case growth and shrinkage do not occur preferentially at the same end but at opposite ends. While the so-called pointed end preferentially depolymerizes (if not stabilized), the so-called barbed end tends to polymerize. As a result, actin filaments show treadmilling behavior where the filaments are constantly turned over [68].

1.1.2 Motor proteins and their interactions with filaments

Motor proteins are responsible for a variety of tasks in cells that largely rely on energy consumption (see e.g. [35, 144, 154, 155]). By ATP hydrolysis motor proteins transform chemical energy into mechanical energy and motion along filaments. Thereby they can not

only transport material in a directed fashion through the cell but, for instance by crosslinking several filaments and walking on them, they also generate forces (chapter 4). Indeed, one has to apply forces on the order of several pN to prevent motors from walking along the filaments ("stall force"; e.g. [86, 156]). This order of magnitude is similar for the different types of motors that move along microtubules and actin filaments, respectively.
Overall, there are three main families of motor proteins: kinesins, dyneins and myosins (see e.g. [157–159], respectively). While myosins interact with and walk on actin filaments, kinesins and dyneins interact with microtubules.
We will briefly discuss the interactions between motors and cytoskeletal filaments which are directly relevant to this thesis next.

Directed transport of motor proteins along cytoskeletal filaments

One of the major roles of motor proteins is to transport cargo to specific parts of the cell. This is achieved by the directed motion of motor proteins along cytoskeletal filaments [34, 151]. Kinesins such as kinesin-8 [58, 59] or kinesin-5 [94] usually walk towards the plus end of the microtubule [160]. In contrast, dyneins are minus-end-directed motors [158, 161]. Both kinesins as well as dyneins are rather processive motors, meaning that they walk along the microtubules over long distances before detaching from the filament [144, 155, 157, 161–163]. While most myosins are non-processive [144, 155, 163], there are also several myosin motors which are crucial for transport of cargo to the distal tips of cellular protrusions and which, hence, walk over long distances as well: Myosin-5, which occurs in homodimeric form in microvilli [39, 154, 161, 164, 165], myosin-10, which is a high-duty-ratio motor in filopodia and spends most of its time tightly bound to actin [39, 40, 43], and myosin-3a [39, 165–167] and myosin-15a [38, 39, 168], which transport regulating proteins to the tips of stereocilia.
The conceptual models we considered for the interplay between directed motor transport and diffusion in a confined geometry (chapters 2 and 3) are motivated by this processive, directed motion along filaments. We will, thus, always assume that the rate of motor detachment from the filament is very small compared to the stepping rate along the filaments.

Instead of transporting cargo along the filaments, motors are also crucial for the formation of filament networks. Since chapter 4 deals with such filament networks, we describe this crosslinking interaction between motors and filaments next.

Crosslinking motor proteins

The organization of cytoskeletal filaments into higher-order structures relies on the crosslinking action of several motor proteins [92]. Due to the flexibility of actin filaments, crosslinking of actin filaments into actin bundles or networks is particularly important for providing stability and rigidity [42, 43, 92, 153]. While the formation of networks of microtubules relies on crosslinking proteins as well, the effects of these proteins are also strongly associated with filament motion. This is an aspect that we explore in more detail in chapter 4.
The basic idea is as follows: Motors with two binding domains can link two filaments and walk along both of them simultaneously [143, 153]. As a result, they exert forces on the filaments and - depending on the relative orientation of the filaments - cause relative or uniform

motion (see also Fig. 1.1 for an illustration): Antiparallel microtubules (i.e. with opposite polarity) are slid apart whereas parallel microtubules stay put (see e.g. Ref. [94] for kinesin-5 and Refs. [169, 170] for kinesin-14). In addition to motors that slide microtubules apart, there are also kinesins [171] and dyneins [95, 145] that focus microtubules into poles [23].
In chapter 4, we will not focus on this pole formation but instead on a conceptual description of the orientation-dependent motion generation by crosslinking motor proteins in filament networks. One of the questions we address is how the behaviour of filament pairs affects the movement of filaments in large networks. Our conceptual model suggests that crosslinking of motor proteins is not only crucial for force generation but also for force propagation through the network.

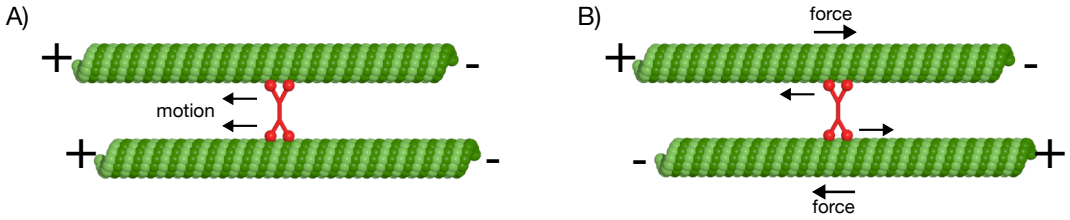

Figure 1.1 | Illustration of the effect of motor crosslinking on the filament dynamics (adapted from [3]). Microtubules (green) are crosslinked by a motor protein (red) that walks with its two heads on both filaments simultaneously. A) A motor that crosslinks two parallel microtubules does not exert any net force on the filaments. It walks with both heads in the same direction (here: towards the plus end of the microtubule; left) and does not get stretched. B) In contrast, a motor that crosslinks two antiparallel microtubules gets stretched due to the directed motion along the filaments. It thus exerts a restoring force in the opposite direction (the motor that walks to the plus end of the upper microtubule at the left exerts a force on the microtubule to the right and vice versa). The microtubules are pushed towards their minus ends.

The final interaction between motors and filaments that we want to mention concerns length regulation of filaments by motor proteins. This interaction conceptually underlies the project discussed in chapter 3.

Length regulation of filaments

As mentioned before cytoskeletal filaments can be highly dynamic [23, 43, 63, 67, 68, 71, 72, 148–150, 153]. They steadily grow and shrink by polymerization and depolymerization at their ends, unless stabilized by drugs. If these processes were entirely random, however, the filament length would perform a (biased) random walk with reflecting boundary at length zero [69]. The resulting length distribution would be exponential (if the growth rate is smaller than the shrinkage rate; otherwise the average length diverges). While such a length distribution would not *per se* be in disagreement with possible length distributions one could obtain from a stochastic dynamics similar to the dynamic instability of microtubules [63, 67], the dynamics would be completely different. Typically, there would be no extended phases of growth and no phases of rapid shrinkage. Furthermore, tightly controlled and peaked length distributions of filaments, which are, for instance, necessary for the staircase patterns of stereocilia in hair cells [41, 42], would not occur. As a result, some sort of length control mechanism is expected to take place (for recent reviews on length and size control see [69, 73, 79]). One possibility is

by coupling the length dynamics to directed transport along filaments. For instance, tubulin is transported by kinesins to the tips of flagella or cilia [77, 78]. This process relies on so-called intraflagellar transport. Alternatively, length control also occurs via active transport of regulator proteins by myosins [41, 42, 80] or via directed motion by kinesins [59, 60, 62, 81, 82]. In the case of microtubules, it is known, for instance, that kinesin-8, a plus-end directed motor, also acts as depolymerase once it has reached the end of the microtubule [59, 172]. Since the motor density at the tip increases with increasing length (cf. antenna profile in Ref. [82]), depolymerization is faster for larger lengths, thus providing a negative feedback mechanism.
For the conceptual model of length regulation in confinement discussed in chapter 3, we took inspiration from this length regulation mechanism by kinesin. More concretely, the specific choice of length dynamics was motivated by experimental studies of microtubules where motor-induced depolymerization [58–62] was observed.

Taken together, all these phenomena highlight the intricate relationship between filaments and motor proteins and illustrate their broad interaction scheme.

1.2 Theoretical approaches

In this section, we give a very brief summary of some theoretical approaches to describe certain parts and properties of the cell cytoskeleton.
In general, there is a large variety of models with very different emphases. Correspondingly, the level of description varies considerably. First, there is a line of research that focuses on the collective transport of motor proteins along single cytoskeletal filaments in terms of the totally asymmetric simple exclusion process (TASEP [44–46]; see also below). In these studies, filaments are typically modeled as one-dimensional rigid objects along which the motor proteins move. Furthermore, to account for the discrete nature of the filaments (in terms of tubulin dimers or F-actin; see section 1.1) and the corresponding discrete stepping behavior of the motor proteins, the filaments are represented as lattices with individual sites instead of continuous objects. Finally, bending properties or lateral interactions between several filaments are ignored.
In contrast, if the goal is to identify rheological properties of the cytoskeleton, the focus lies more on a description of, for instance, the viscoelastic behavior (see e.g. [173, 174]). Such descriptions are often in terms of hydrodynamic theories or so-called active gels ([174–176]; see also below). These theories rely on the identification of slow variables and symmetries and constitute coarse-grained descriptions on sufficiently large length- and timescales.
In the following, we will discuss some approaches that are directly relevant to this thesis in more detail.

1.2.1 Transport along rigid filaments: Totally asymmetric simple exclusion process

The first model that is directly relevant for the conceptual models discussed in chapters 2 and 3 is the totally asymmetric simple exclusion process (TASEP). The TASEP was initially

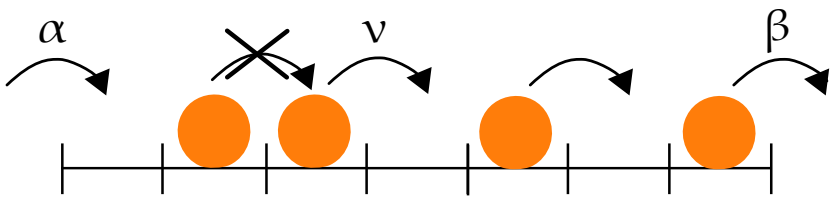

Figure 1.2 | Illustration of the totally asymmetric simple exclusion process (TASEP) with open boundaries (adapted from [2]). Particles are injected at one end at rate α and jump forward one site at a time towards the other end. A jump occurs at rate ν provided that the site in front of the particle is empty (exclusion). At the other end, particles leave the lattice at rate β.

introduced in Refs. [44, 45] as a model to describe ribosome movement and interacting Markov processes, respectively, and has become a paradigmatic model for non-equilibrium dynamics since then [46]. It exhibits rich phase behavior and, in particular, boundary-driven phase transitions [47] – despite its simplicity: Particles jump unidirectionally along a one-dimensional lattice (see also Fig.1.2 for an illustration). A jump occurs at rate $\nu \equiv 1$ but only if the site in front of the particle is empty (exclusion). Furthermore, in the case of open boundaries, particles are injected at one end at rate α, provided that the first site of the lattice is free. Finally, particles leave the system at rate β at the other end.

This TASEP dynamics with open boundary conditions has been solved exactly by either employing a matrix-product ansatz [177] or by solving the recursion relation [48, 49]. These exact solutions have confirmed the phase diagram as obtained through mean-field arguments [47]. In the following, we motivate this phase diagram in a very phenomenological (and incomplete) way. The essential steps follow the analyses presented in Refs. [51, 52, 178, 179]. We start from the mean-field approximation, then present the resulting continuity equation and finally a phenomenological approach to determine the phase diagram.

In a mean-field approximation, the correlations between different states are neglected and higher-order moments are replaced by averaged quantities. In the case of the TASEP, one assumes that the following equality for the densities at subsequent sites i and $i+1$, ρ_i and ρ_{i+1}, holds:

$$\langle \rho_i \rho_{i+1} \rangle = \langle \rho_i \rangle \langle \rho_{i+1} \rangle \quad \forall i.$$

That is, correlations between the neighboring lattices sites are assumed to be negligible. In order to determine the time evolution of the densities, we will combine this mean-field description with a continuum approximation in which the densities at the single lattice sites ρ_i are replaced by a continuous density $\rho(x), x \in [0, L]$ where L denotes the length of the lattice. This continuum limit makes sense if the lattice spacing $a \equiv 1$ is small compared to the lattice length L, i.e. if there are many lattice sites in the lattice. Since there is no in- or outflux of particles along the lattice, the mass in the bulk of the system is conserved. The density $\rho(x)$ thus satisfies a continuum equation with a flux J:

$$\partial_t \rho(x,t) = -\partial_x J(x,t).$$

In order to motivate this flux J, we will look at the flux J_n for non-interacting particles moving along the lattice, first. Since the flux describes the number of particles crossing a

certain position in the lattice per time, J_n is proportional to the number of particles in the lattice and, thus, to the density ρ. However, due to the interactions between particles, the collective flux J does not equal the flux J_n but decreases for increasing density due to the exclusion. For a fully occupied lattice, $\rho \equiv 1$, no flux is possible and, correspondingly, the flux should be zero, $J = 0$. Conversely, an almost empty lattice should not influence the single-particle flux J_n considerably and in the limit of small ρ the fluxes J and J_n should agree. Combining these phenomenological arguments motivates why the flux is given by

$$J = \rho(1 - \rho). \tag{1.1}$$

As a result, we have

$$\partial_t \rho = -\partial_x J = -\partial_x \left(\rho\,(1 - \rho)\right) = (2\rho - 1)\partial_x \rho.$$

This equation implies that in steady-state (where $\partial_t \rho(x, t) = 0$) the density has to be constant: $\rho \equiv \text{const}$.

In general, however, a constant density violates the boundary conditions. At the left end, $x = 0$, influx happens at rate α and, correspondingly, the density is given by $\rho(0) = \alpha$ in steady-state. In contrast, at the other end, $x = L$, particles leave the system at rate β, leading to a steady-state density $\rho(L) = 1 - \beta$ there. So, unless $\alpha = 1 - \beta$ and $\rho(0) = \rho(L)$, the density profile cannot be constant everywhere. Indeed, it is insightful to describe the density profiles with the help of shocks or so-called domain walls that connect two different (constant) densities on the left and right [51, 53, 180]. These shocks are *per se* not static but can move through the system at a velocity V. Due to mass conservation, the relative flux difference between the right- and left-hand side of the shock front $J_+ - J_-$ must correspond to the accumulation rate of mass due to the moving front, $V(\rho_+ - \rho_-)$:

$$V(\rho_+ - \rho_-) = J_+ - J_-,$$

where $\rho_\pm$ and $J_\pm$ denote the densities and fluxes at the right-, $+$, and left-hand, $-$, side of the shock front, respectively. As a result,

$$V = \frac{J_+ - J_-}{\rho_+ - \rho_-} = \tag{1.2}$$

$$= \frac{\rho_+(1 - \rho_+) - \rho_-(1 - \rho_-)}{\rho_+ - \rho_-} = 1 - \rho_+ - \rho_-. \tag{1.3}$$

What does this equation imply for a shock wave that connects densities $\rho_- = \alpha$ and $\rho_+ = 1-\beta$, corresponding to the reservoir densities at both ends? Phenomenologically, we can argue as follows: According to Eq. 1.3, a shock wave which connects densities α and $1 - \beta$ exhibits a shock velocity $V = \beta - \alpha$. For $\beta > \alpha$, the domain wall thus moves to the right of the system ($V > 0$), whereas for $\beta < \alpha$ it moves to the left ($V < 0$). Correspondingly, for $\beta > \alpha$, the region with density $\rho_- = \alpha$ extends until it almost reaches the right boundary – a so-called boundary layer forms. In this case, the bulk of the system is thus determined by the left boundary condition α. In contrast, for $\beta < \alpha$, the density in the bulk is $\rho_+ = 1 - \beta$ and is controlled by the right boundary.

Indeed, this is not the full story because there also exists a special bulk density $\rho_m = 1/2$ ("maximal current" phase; [47–49, 177]) which maximizes the current $J(\rho)$ in the system.

Applying Eq. 1.3 to a domain wall connecting a density of α at the left to a density of $\rho_m = 1/2$ at the right yields the following domain velocity:

$$V = \frac{\frac{1}{4} - \alpha(1-\alpha)}{\frac{1}{2} - \alpha}.$$

This velocity is positive (negative) if $\alpha < 1/2$ ($\alpha > 1/2$). As a result, phenomenologically, if $\alpha < 1/2$ the domain wall moves to the right and the density α dominates. In contrast, if $\alpha > 1/2$ the domain wall moves to the left and the maximal current density ρ_m is established in the bulk.

Using an analogous argument for a domain wall between the maximal current density ρ_m and the density ρ_+ at the right boundary and considering all possible combinations of domain walls yields the following phase diagram for the TASEP (see also [47–49, 177]):

- If $\beta > \alpha$ and $\alpha < 1/2$ the bulk density ρ_b is determined by the left boundary and is given by $\rho_b = \alpha$ (low density (LD) phase).
- If $\beta < \alpha$ and $\beta < 1/2$ the bulk density ρ_b is determined by the right boundary and is given by $\rho_b = 1 - \beta$ (high density (HD) phase).
- If $\alpha, \beta > 1/2$ the bulk density is given by the maximal current density $\rho_b = \rho_m$ (maximal current (MC) phase).

As we will see in chapter 2, our conceptual model for active transport in a confined geometry, which is also based on the TASEP, only exhibits one generic steady-state density profile: a *localized* domain wall connecting a low density at one side to a high density at the other side, similar to models with so-called Langmuir kinetics [53, 181]; see below. Furthermore, in this system, the current is not captured well by the mean-field prediction $J = \rho(1-\rho)$, Eq. 1.1, due to strong correlations between particles. To determine the (fluctuation-corrected) domain wall profile and the actual current, we used an exact moment identity and the domain wall approach given in Eq. 1.2 with the exact expressions for the currents.

Extensions of the TASEP

Apart from being a model for the study of non-equilibrium systems, the TASEP has also been applied to describe several biological processes including transport along filaments (for reviews see for instance [46, 163]). For this purpose, it has been extended in various ways. Here, we will only shortly mention those extensions that are closely related to this thesis. There are, however, many other interesting aspects that have been taken into account such as interactions between multiple types of motors with different stepping behavior [182].
First, to account for motor attachment and detachment along the filament, the so-called TASEP-LK (TASEP with Langmuir kinetics) has been introduced [53, 181]. In this case, motors do not only enter the lattice at the first site but can attach anywhere at a fixed rate. Conversely, the motors do not only exit the lattice at the last site but can in principle detach anywhere. This additional dynamics can lead to phase coexistence and localized domain walls if there is competition between the Langmuir and the TASEP dynamics.
In the TASEP-LK model, attachment of motors along the filaments occurs at a constant rate,

corresponding to the coupling to a reservoir with constant density. However, in particular in crowded environments, diffusion may be slow on the timescale of the motor dynamics and, correspondingly, the reservoir (cytosol) may not be spatially uniform. Several studies took this non-uniform density into account and examined models where the TASEP is coupled to a second lattice with diffusive motion [181, 183–187]. This aspect of coupling directed transport to diffusive motion also underlies the project discussed in chapter 2.
Finally, a different line of research is concerned with possible length regulation mechanisms. To this end, dynamic lattices (e.g. [81, 82, 188–192]) and systems with finite resources (motors and/or filament subunits; e.g. [193–195]) have been studied. Recent work of our group shows, for instance, that coupling of motor-induced depolymerization and finite tubulin and motor resources can lead to bistability [195].
The conceptual model discussed in chapter 3 combines a similar length regulation mechanism with a finite diffusion in the cytosol.

1.2.2 Mechanical properties of filament networks: Hydrodynamic theories and active gels

To conclude this chapter, we briefly mention some complementary approaches for the study of the cell cytoskeleton. While the TASEP and variants thereof have a strong focus on collective transport properties of molecular motors, there is also great interest in understanding collective properties of large biopolymer networks. For instance, cell motility strongly depends on the contractility of the actin network (see e.g. [196]). To understand such mechanical properties it has proven useful to turn to hydrodynamic theories or so-called active (polar) gels (for reviews on this topic see e.g. [173–176, 196–198]). These theories rely on symmetries, local conservation laws and force balances. Thereby, they constitute coarse-grained descriptions which are valid on large length- and timescales, corresponding to the slow modes of the conservation laws. This level of characterization in terms of a few macroscopic variables is convenient because it does not require a detailed knowledge of the microscopic interactions. Conversely, the resulting theories are often phenomenological and it is not always straightforward how to connect the macroscopic parameters to microscopic interactions. It is in principle possible to circumvent this limitation by explicitly deriving coarse-grained descriptions from microscopic interactions (e.g. [199–201]). In general, this derivation is, however, difficult and usually involves some approximation techniques [175, 196].
The project described in chapter 4 is conceptually similar: Starting from mesoscopic interactions between filaments due to motor crosslinking, our goal was to derive a relationship between the network polarity and the local microtubule velocities. To this end, we first established a non-local continuum theory for coarse-grained variables. From this theory we then deduced an analytic expression relating the local microtubule velocity to the network polarity. Note, though, that such a procedure was possible also due to the relative simplicity of the conceptual model which is effectively one-dimensional.

2 Transport mechanisms in a confined geometry

Except in mathematics, the shortest distance between point A and point B is seldom a straight line.
(Albert Einstein)

The goal of this chapter is to summarize the most important findings of our project on the interplay of directed transport and diffusion in confined geometries. The corresponding manuscript has been published in *Physical Review Letters* **118**, 128101 (2017). This chapter is based on and uses parts of this publication [1], which is also reprinted in section 2.5.

2.1 Motivation

This project is motivated by the directed and processive motion of motor proteins along actin filaments in cellular protrusions such as stereocilia and filopodia (as briefly described in section 1.1). These protrusions have a characteristic half-closed geometry (see also Fig. 2.1 (A) for an illustration). At the base (left end) they are connected to the cell body whereas everywhere else they are enclosed by a membrane. As a result, there is mass conservation everywhere except at the base. Furthermore, motors that move along the filament may detach from it and then diffuse in the cytosol. Conversely, motors in the cytosol can attach to the filament and then perform directed motion.

While the motivation for the conceptual model presented in the next section 2.2 originates from these aspects of the motor dynamics in cellular protrusions, the model is not intended to describe this biological setting accurately. For this purpose, one would have had to incorporate many others factors such as treadmilling or aggregation in filament bundles (see section 1.1 and e.g. [39, 41, 153]).

Instead, also from a purely theoretical point of view, the coupling of a non-equilibrium process (active, directed transport) to an equilibrium process (diffusion) in a confined geometry seems interesting to study: At steady-state, the closure at the tip enforces a no-flux boundary condition which opposes the direct motion along the filaments. The fluxes along the filament, thus, need to be balanced by opposite diffusive fluxes. This argument already insinuates that diffusion may play an important role in this system. We will see in section 2.3 that this is indeed the case.

Correspondingly, as mentioned in the abstract of the project, the driving questions are:
Which physical principles govern the interplay between active transport, an intrinsically non-

equilibrium process, and diffusion in a confined geometry? What role do collective effects play for transport efficiency?

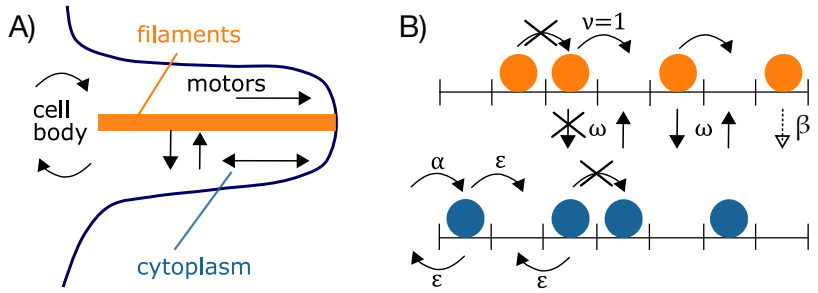

Figure 2.1 | A) Illustration of motor transport and diffusion in cellular protrusions with half-closed geometry (taken from [2]). At the left end, the protrusion is connected to the cell body which acts as a motor reservoir: Motors are exchanged between the protrusion and the cell body. In the protrusion, motors either diffuse in the cytoplasm or move in a directed fashion along the filaments towards the tip of the protrusion. Diffusing motors in the cytoplasm may attach to the filament and then move in a directed fashion. Conversely, motors on the filament may detach from it and then start to diffuse. B) Conceptual model (adapted from [2]). Directed transport along filaments is modeled as a TASEP (see also section 1.2.1) with hopping rate $\nu = 1$ and the diffusion as a SSEP (symmetric simple exclusion process) with hopping rate ϵ. Both lanes are coupled via attachment and detachment kinetics at rate ω each. The system is closed at the tip (right), so there is no out- and influx there. In contrast, motors are injected at rate α from the reservoir at the base (left) into the SSEP lane. Outflux occurs at the same rate as for diffusion, ϵ. For the tip dynamics, we consider two variants: In model A, there is only detachment from the TASEP lane at rate β but no attachment. In model B, the tip dynamics is the same as in the bulk. All processes respect the exclusion of particles.

2.2 Model

Inspired by these questions, we consider a conceptual two-lane lattice-gas model (see also Fig. 2.1 B for an illustration). Both lattices have the same length $l \equiv 1$ with sites $i \in \{0, \dots, L\}$, $L \gg 1$ and lattice spacing $a = 1/L$. One lane models the motor dynamics in the cytosol (diffusion) and the other one the directed motion along the filaments. As motivated in section 1.2.1, this directed motion is described by the totally asymmetric simple exclusion process (TASEP) with hopping rate $\nu = 1$ towards the right end (tip of the protrusion). Diffusion, on the other hand, is represented by the so-called symmetric simple exclusion process (SSEP). As in the TASEP, there is exclusion between particles, so there can be at most one motor per lattice site[1]. Instead of performing directional motion along the lattice as in the TASEP, motors jump either one site to the left or one to the right, at equal rate ϵ each, corresponding to unbiased motion. Motivated by the geometry depicted in Fig. 2.1 A

[1]The exclusion on the TASEP lane is motivated by the discrete nature of cytoskeletal filaments in terms of tubulin dimers or F-actin subunits (see also section 1.1) and hard-core interactions between motors. On the SSEP lane, the motivation was to have an upper bound on the number of particles in the narrow protrusion. Indeed, we show in the Supplementary Material of the publication [1] that in the steady state, up to rescaling of rates, the system with strict particle exclusion ("carrying capacity" of one particle) is equivalent to a system with finite carrying capacity N_{diff}.

the system is closed at the tip, i.e. there is no outflux of motors there and mass is conserved. At the base (left end), motors leave the system via the SSEP lane (cytosol) at the same rate as for the diffusive motion, ϵ. This is supposed to correspond to diffusion of motors out of the protrusion. Conversely, motors also enter the SSEP lane (cytosol) at the left end at rate α. There is no direct influx of motors from the reservoir into the TASEP lane but motors can transition from the SSEP lane to the neighboring site on the TASEP at rate ω, provided that the site on the TASEP is empty. This effectively corresponds to attachment of motors to the filament. Conversely, motors on the TASEP lane can "detach" from it and transition to the neighboring site on the SSEP lane, again respecting the exclusion between motors. For convenience, this happens at the same rate as the attachment, ω. The rate ω is taken to be small, $\omega \equiv \Omega/L \ll \nu = 1$, effectively leading to processive motion along the filaments (see also section 1.1) and introducing competition between the attachment/detachment kinetics along the entire lattice and the transport dynamics (see also the TASEP-LK [53, 181]). Finally, in one version of the model ("model A"), the attachment and detachment dynamics at the right end (tip) is different from the one in the bulk: Motors detach at rate $\beta \gg \omega$ from the TASEP to the SSEP lane (and there is no attachment). This might be the realistic scenario if the detachment rate at the end is strongly enhanced due to the tendency of motors to "continue walking" on the filament. If this is not the case, "model B" might be the more realistic description: There, the dynamics at the tip is the same as in bulk.

2.3 Results

What is the characteristic behavior of this system in the steady-state? To answer this question, we consider the dynamics in the bulk of the system, first. The number of particles n_i^{T} at site i of the TASEP lane changes either by jumps along the TASEP lane, i.e. from sites $i-1$ to site i or from site i to site $i+1$, or by detachment or attachment kinetics from site i of the TASEP lane to the SSEP lane or vice versa. In case of a jump along the TASEP lane from site $i-1$ to site i the occupancy at site i increases by 1 whereas for a jump out of site i to site $i+1$, it decreases. On average, these events happen at rates $\langle n_{i-1}^{\mathrm{T}}(1-n_i^{\mathrm{T}})\rangle$ and $\langle n_i^{\mathrm{T}}(1-n_{i+1}^{\mathrm{T}})\rangle$, respectively. Here, $\langle \ldots \rangle$ denotes the (ensemble) average and the terms in the brackets $(\ldots)$ are due to the exclusion. Similarly, the rates for the attachment and detachment are $\omega\langle n_i^{\mathrm{S}}(1-n_i^{\mathrm{T}})\rangle$ and $\omega\langle n_i^{\mathrm{T}}(1-n_i^{\mathrm{S}})\rangle$ where n_i^{S} denotes the number of particles at site i of the SSEP lane. Combining these terms and using a similar argument for the dynamics of the SSEP lane yields the following dynamics:

$$\partial_t \rho_i^{\mathrm{T}} = \rho_{i-1}^{\mathrm{T}} - f_{i-1} - \rho_i^{\mathrm{T}} + f_i + \omega\left(\rho_i^{\mathrm{S}} - \rho_i^{\mathrm{T}}\right), \tag{2.1}$$

$$\partial_t \rho_i^{\mathrm{S}} = \epsilon\left(\rho_{i+1}^{\mathrm{S}} + \rho_{i-1}^{\mathrm{S}} - 2\rho_i^{\mathrm{S}}\right) + \omega\left(\rho_i^{\mathrm{T}} - \rho_i^{\mathrm{S}}\right), \tag{2.2}$$

where $\rho_i^{\mathrm{T/S}} = \langle n_i^{\mathrm{T/S}}\rangle$ is the average density of particles on the TASEP or SSEP lane. Furthermore, $f_i = \langle n_i^{\mathrm{T}} n_{i+1}^{\mathrm{T}}\rangle$ is the correlator between the occupancies of two neighboring sites on the TASEP lane.

Adding those two equations results in

$$\partial_t(\rho_i^{\mathrm{T}} + \rho_i^{\mathrm{S}}) = \rho_{i-1}^{\mathrm{T}} - f_{i-1} - \rho_i^{\mathrm{T}} + f_i + \epsilon\left(\rho_{i+1}^{\mathrm{S}} + \rho_{i-1}^{\mathrm{S}} - 2\rho_i^{\mathrm{S}}\right) \tag{2.3}$$

for the time evolution of the combined density $\rho_i^{\mathrm{T}} + \rho_i^{\mathrm{S}}$ in the bulk. By introducing the local currents J_i^{T} and J_i^{S} on the TASEP and SSEP lane

$$J_i^{\mathrm{T}} = \rho_i^{\mathrm{T}} - f_i \tag{2.4}$$

and

$$J_i^{\mathrm{S}} = \epsilon \left(\rho_i^{\mathrm{S}} - \rho_{i+1}^{\mathrm{S}}\right) \tag{2.5}$$

for $i = 0, \ldots, L-1$, the equations for the time evolution, Eqs. 2.1 and 2.2, are simplified to

$$\partial_t(\rho_i^{\mathrm{T}} + \rho_i^{\mathrm{S}}) = J_{i-1}^{\mathrm{T}} + J_{i-1}^{\mathrm{S}} - J_i^{\mathrm{T}} - J_i^{\mathrm{S}}. \tag{2.6}$$

In the steady-state $\partial_t(\rho_i^{\mathrm{T}} + \rho_i^{\mathrm{S}}) = 0$, it thus follows:

$$J_{i-1}^{\mathrm{T}} + J_{i-1}^{\mathrm{S}} = J_i^{\mathrm{T}} + J_i^{\mathrm{S}} = \mathrm{const} = 0, \tag{2.7}$$

where the last equality follows from the no-flux boundary condition at the tip: $J_L^{\mathrm{T}} = J_L^{\mathrm{S}} = 0$. Indeed, there is also an effective no-flux boundary condition at the base: There is no influx into the TASEP lane and the overall mass in the system has to be conserved in steady-state. Thus, the in- and out-flux into the SSEP lane have to balance exactly and there can be no overall (combined TASEP and SSEP) flux through the system.

Performing a continuum limit with lattice size $a \to 0$ and using the scaling of $\omega = \Omega/L$, it can be shown (see [1] or the publication reprint in section 2.5) that to lowest order in a, the TASEP density is given by a domain wall connecting a density of 0 on the left to a density of 1 on the right (see also Fig. 2 in the publication):

$$\rho^{\mathrm{T}}(x) = \begin{cases} 0 & \text{for} \quad x \in [0, z[\\ 1 & \text{for} \quad x \in]z, 1], \end{cases} \tag{2.8}$$

where $z \in]0, 1[$ denotes the position of the domain wall. Indeed, this domain-wall profile is the generic steady-state profile of the system and, in particular, there is no maximal current phase. The reason is that diffusion is too slow to exhibit a current of the order of the maximal current $J = 1/4$ (at least not if the rate for diffusion ϵ is of the order of the jump rate ν and not considerably larger).

Intuitively, the domain wall profile comes from the fact that the system is closed at the tip. Due to the closure, motors that move towards the tip accumulate there and form a "traffic jam" with a very high density at the tip. Furthermore, since transport along the empty part of the filament is fast, all particles that attach to the filament quickly catch up with the end of the traffic jam. As there is no direct influx from the left onto the filament, the density close to the base is thus small.

To determine the domain wall position, it is enlightening to go back to Eq. 2.1. In the steady state it reduces to

$$f_i - f_{i-1} = \rho_i^{\mathrm{T}} - \rho_{i-1}^{\mathrm{T}} + \omega \left(\rho_i^{\mathrm{T}} - \rho_i^{\mathrm{S}}\right). \tag{2.9}$$

Due to the simple recursive form, it is straightforward to derive the following moment identity from it:

$$f_i = \rho_i^{\mathrm{T}} + \omega \sum_{j=0}^{i} \left(\rho_j^{\mathrm{T}} - \rho_j^{\mathrm{S}}\right). \tag{2.10}$$

where $f_i = \langle n_i^{\mathrm{T}} n_{i+1}^{\mathrm{T}} \rangle$ as before. It will turn out that this is a crucial equation to go beyond mean-field theory and to predict the active current in the system (see below). The reason is that it relates the nearest-neighbor correlations to the densities in the system.

First, however, considering $i = L - 1$ and the boundary conditions at the tip (see [1] or the publication reprint in section 2.5), yields

$$\text{model A}: \qquad \omega \sum_{i=0}^{L-1} \left(\rho_i^{\mathrm{T}} - \rho_i^{\mathrm{S}}\right) = -\beta \left(\rho_L^{\mathrm{T}} - \left\langle n_L^{\mathrm{T}} n_L^{\mathrm{S}} \right\rangle\right) \tag{2.11}$$

$$\text{model B}: \qquad \omega \sum_{i=0}^{L} \left(\rho_i^{\mathrm{T}} - \rho_i^{\mathrm{S}}\right) = 0. \tag{2.12}$$

In essence, these equations constitute mass-balance equations which quantify that in the steady state the total flux from the SSEP to the TASEP lane needs to equal the flux in the opposite direction: In model A, there is only detachment at the last site (see also section 2.2), so the exchange of particles in the bulk of the system (sites $i \in \{0, \ldots, L-1\}$) needs to be balanced by the detachment at the tip, $-\beta \left(\rho_L^{\mathrm{T}} - \left\langle n_L^{\mathrm{T}} n_L^{\mathrm{S}} \right\rangle\right)$. In contrast, in model B, the rules for attachment and detachment are the same everywhere and, correspondingly, the exchange at the tip is given by $-\omega \langle n_L^{\mathrm{T}}(1 - n_L^{\mathrm{T}}) - n_L^{\mathrm{S}}(1 - n_L^{\mathrm{T}}) \rangle = -\omega \left(\rho_L^{\mathrm{T}} - \rho_L^{\mathrm{S}}\right)$.

Equations 2.11 and 2.12 can be used to determine the position of the domain wall z (see [1] or the publication reprint in section 2.5):

$$\text{model A}: \qquad z = 1 - l \cosh^{-1}\left(\sigma \cosh\left(\frac{1}{l}\right)\right) \tag{2.13}$$

$$\text{model B}: \qquad z = 1 - l \sinh^{-1}\left(\sigma \sinh\left(\frac{1}{l}\right)\right). \tag{2.14}$$

where $l := \sqrt{D/\omega} = \sqrt{\epsilon a^2/\omega}$ can be understood as the typical dwell length for motors in the cytoplasm before attaching to the filament ($D := \epsilon a^2$ is the diffusion constant in the cytoplasm). $\sigma := \frac{\alpha}{\alpha+\epsilon}$ corresponds to the reservoir density in the cell body.

The interesting point about these equations is that they predict a very different dependency of the domain wall position z on the dwell length (see also Fig. 3 in the publication), in particular with regard to a value of "$z = 1$". This situation corresponds to a domain wall located at the tip of the system and, thus, to a system in which the TASEP lane is basically empty, except for the tip region (tip localization). While for model A, $z = 1$ can occur for finite dwell length l, for model B tip localization is only attained in the limit where the reservoir density $\sigma \to 0$. The crucial point is that due to the symmetry of the attachment and detachment kinetics in model B, the total density on the TASEP lane needs to equal the total density on the SSEP lane (compare also Eq. 2.12). Thus, unless the density on the SSEP lane is small (corresponding to small reservoir density σ), the total density on the TASEP is not small either. In contrast, for model A there is fast detachment from the tip of the TASEP lane if diffusion is sufficiently fast (large l) and the motors do not accumulate considerably in the tip region of the SSEP lane. As a result, the jamming on the TASEP lane is reduced and tip localization (in the absence of large traffic jams) is possible.
This deviation between both models highlights the importance of boundary conditions for TASEP-based systems.

To conclude this chapter, we shortly mention another interesting feature of this model, namely that the mean-field prediction for the current-density relation in the original TASEP $J = \rho^T(1-\rho^T)$, Eq. 1.1, does not capture the current along the TASEP lane even approximately. Indeed, if one compares the mean-field prediction for the current along the TASEP lane, obtained from the density profile in a stochastic simulation, to the actual current in the simulation (see Fig. S2 in [1] or the publication reprint in section 2.5), they can differ by orders of magnitude[2]. The reason is that on the TASEP lane, there are strong nearest-neighbor correlations that suppress the current considerably. These are due to the traffic jams that form and are particularly pronounced in the domain wall region (at the left end of the traffic jam).

These correlations can be captured analytically due to the exact moment identity, Eq. 2.10. In short, one can use the exact formula for the TASEP current, Eq. 2.4, to employ a domain wall ansatz [51, 53, 180] (see also section 1.2.1) with site-dependent hopping rates (see [1] or the publication reprint in section 2.5)

$$w_{l,i} = \frac{J_{\mathrm{LD},i}}{\rho^{\mathrm{T}}_{\mathrm{HD},i} - \rho^{\mathrm{T}}_{\mathrm{LD},i}} \qquad w_{r,i} = \frac{J_{\mathrm{HD},i}}{\rho^{\mathrm{T}}_{\mathrm{HD},i} - \rho^{\mathrm{T}}_{\mathrm{LD},i}} \tag{2.15}$$

to the left and right from site i, respectively. Here, $J_{\mathrm{LD},i}$ and $J_{\mathrm{HD},i}$ are the TASEP currents at site i on the left ("low-density"; LD) and right ("high density"; HD) of the domain wall, respectively. $\rho^{\mathrm{T}}_{\mathrm{LD},i}$ and $\rho^{\mathrm{T}}_{\mathrm{HD},i}$ denote the corresponding TASEP densities in the low- and high-density phase. In this way, one obtains a fluctuation-corrected density profile on the TASEP lane

$$\rho^{\mathrm{T}}(x) \approx \frac{\mathrm{erf}\left((x-z)/W(z)\right) + \mathrm{erf}\left(z/W(z)\right)}{\mathrm{erf}\left((1-z)/W(z)\right) + \mathrm{erf}\left(z/W(z)\right)}\,, \tag{2.16}$$

where $W(z) = \sqrt{2\sigma a l \sinh\left(z/l\right)}$ corresponds to the width of the domain wall (which depends on the average position of the domain wall z). Thus, in contrast to the lowest-order domain wall profile given in Eq. 2.8, the domain wall indeed exhibits a finite width, in quantitative agreement with the density profile on the TASEP lane as obtained from stochastic simulations (see Fig. 2 in [1] or in the publication reprint in section 2.5). It turns out that this correct capturing of the width of the domain wall is crucial to obtain the exact current from the moment identity, Eq. 2.10. Indeed, if one uses a refined mean-field approach to determine the density profile on the TASEP lane, the width of the domain wall and the resulting prediction for the covariances are underestimated (see Fig. 2 in the publication). As a result, the current is strongly overestimated. This strong suppression of the current along the TASEP lane suggests an important role of diffusion for motor transport in confined geometries.

2.4 Key points

From my point of view, there are four take-home messages:

- Due to the confined geometry (the mass conservation at the tip), there is only one generic density profile, namely a domain wall that connects a very low density towards the base to a very high density towards the tip.

[2] The deviation scales with Ω and is particularly strong in the figure due to the small value of Ω.

- Due to the formation of these "traffic jams", there are strong nearest-neighbor correlations on the TASEP lane. These suppress the current on the TASEP lane considerably as compared to the mean-field prediction, Eq. 1.1.
- This suppression of the TASEP current suggests that diffusion can have an important role for transport in confined geometries – at least if particles are subject to excluded volume interactions.
- From the recursive structure of the TASEP dynamics, Eq. 2.9, an exact moment identity, Eq. 2.10, can be derived. It relates the nearest-neighbor correlations to the densities in the system and allows to analytically calculate a fluctuation-corrected density profile and the currents in the TASEP and SSEP lanes.

In the spirit of the quote at the beginning of the chapter, one could figuratively say that the fastest way (shortest distance) to reach a target is not always by directed transport (in a straight line).

2.5 Publication: Generic Transport Mechanisms for Molecular Traffic in Cellular Protrusions, PRL 118, 128101 (2017)

This section is a publication reprint of the following manuscript published in **Physical Review Letters** 118, 128101 (2017).

Generic Transport Mechanisms for Molecular Traffic in Cellular Protrusions

by

Isabella R. Graf and Erwin Frey
Arnold-Sommerfeld-Center for Theoretical Physics and Center for NanoScience, Department of Physics, Ludwig-Maximilians-Universität München

DOI: 10.1103/PhysRevLett.118.128101

Generic Transport Mechanisms for Molecular Traffic in Cellular Protrusions

Isabella R. Graf and Erwin Frey*
Arnold-Sommerfeld-Center for Theoretical Physics and Center for NanoScience, Department of Physics, Ludwig-Maximilians-Universität München, D–80333 Munich, Germany
(Received 11 August 2016; published 21 March 2017)

Transport of molecular motors along protein filaments in a half-closed geometry is a common feature of biologically relevant processes in cellular protrusions. Using a lattice-gas model we study how the interplay between active and diffusive transport and mass conservation leads to localized domain walls and tip localization of the motors. We identify a mechanism for task sharing between the active motors (maintaining a gradient) and the diffusive motion (transport to the tip), which ensures that energy consumption is low and motor exchange mostly happens at the tip. These features are attributed to strong nearest-neighbor correlations that lead to a strong reduction of active currents, which we calculate analytically using an exact moment identity, and might prove useful for the understanding of correlations and active transport also in more elaborate systems.

DOI: 10.1103/PhysRevLett.118.128101

Linear protrusions of cells, such as, for instance, filopodia or stereocilia, perform multiple tasks in living organisms, ranging from cell migration and signal transduction to wound healing. They contain actin filaments cross-linked into bundles by actin-binding proteins [1–4], and molecular motors of the myosin family which interact with actin filaments and walk on them in a persistent, unidirectional fashion towards the tip of the protrusion [3–9]. These motors play an important role in the biological function of protrusions [1,4,5]. In particular, they are known to localize to the tips of filopodia and stereocilia, and are (jointly) responsible for length control [2–12].

Motivated by these observations, various models have been investigated. Some are detailed mathematical models addressing specific biological issues. These include the role of motor transport in shaping the concentration profile of G-actin at the base of protrusions [13], the localization of different proteins along stereocilia [14], and the effect of myosin X on filopodial growth [15]. Complementary, simplified conceptual models have been studied asking how the interplay between active and diffusive transport in open systems may lead to nonequilibrium phase transitions and ensuing steady states with interesting correlations and nontrivial density profiles [16–20]. The latter are based on the totally asymmetric simple exclusion process (TASEP) [21,22], a lattice-gas model which, despite its simple structure, has become a paradigm for nonequilibrium dynamics [23,24].

Here we present and analyze a conceptual model capturing two basic properties of the motion of persistent, plus-end directed motors inside narrow, elongated cellular protrusions. First, there is an interplay between two genuinely different types of dynamics: directed (active) transport with steric hindrance along actin filaments, and diffusive motion in the cytoplasm. These are coupled by particle exchange between the filament and the cytoplasm. Second, the half-closed geometry of cellular protrusions is special: At one end, the protrusions are connected to the cell body and thus to a reservoir, whereas everywhere else protein diffusion is confined by the cell membrane, so that mass conservation and resource limitation play an important role there. The combination of mass conservation (closure) on the one hand and the interplay of equilibrium (diffusion) and nonequilibrium (active transport) processes on the other hand is intrinsically interesting to study as closure in a system entails no-flux boundary conditions that oppose currents from active transport. Here, we want to examine the interplay of these mechanisms with the help of an abstract model that is motivated biologically but has a level of description that makes it possible to understand all the processes accounted for. We identify generic mechanisms based on correlations and nonequilibrium physics that could be of importance for biological systems as cellular protrusions but, inevitably, predictions for biological systems are qualitative.

Specifically, we consider a two-lane lattice-gas model in a half-closed geometry [Fig. 1] in steady state, similar to Ref. [25]. One lane represents the actin filament and the second lane the cytoplasm. While there is a rich literature on the nonequilibrium dynamics of two-lane systems [20,25–43], very few of these studies address how the physics of nonequilibrium steady states is affected by a half-closed geometry [25,42]. We are interested in the limit where the actin filament and the cytoplasm are coupled weakly by attachment and detachment processes, while

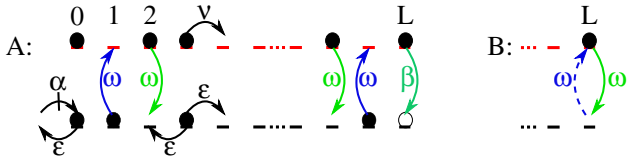

FIG. 1. Illustration of the two-lane lattice-gas model comprised of a TASEP and a SSEP with hopping rates ν and ϵ, respectively. The lanes are coupled via a symmetric attachment and detachment rate $\omega \ll \nu$. In model A, detachment from the last site is given by $\beta \gg \omega$, while in model B exchange between the lanes is fully symmetric. At the tip of the systems mass conservation holds, and at the base particles can enter the SSEP lane at rate α and exit at rate ϵ.

Ref. [25] focuses on the strong coupling limit. Our analyses show that, due to the closure of the system at the tip, there is only one type of density profile, namely, domain walls (DW) separating a high- and a low-density region. The limit where the width of the high-density region becomes microscopically small (of the order of a few lattice sites) corresponds to tip localization. Furthermore, correlations in such systems have not received much attention, and we want to investigate nearest-neighbor (NN) correlations on the filament. In a biological context, this is related to efficient transport on actin filaments and to the significance of steric hindrance of motors there. We find that those correlations reach high values close to the DW, and the transport current along the filament is strongly reduced compared to its mean-field (MF) prediction. This suggests an important role for the cytoplasm, namely, to transport the proteins to the tip. Conversely, active transport effectively sets up and maintains a gradient of motor proteins.

Our model consists of two coupled sublattices [Fig. 1], namely, a TASEP and a SSEP (symmetric simple exclusion process) lane of $L+1$ sites $\in \{0,1,\ldots,L\}$. The dynamics on lane 1 (TASEP) are governed by a rate ν at which particles jump forward one site towards the right (tip) provided that the site in front of them is empty (exclusion). This corresponds to the directional motion of the motors on the filament that is oriented towards the tip. By convention, we measure time in units of ν (i.e., set $\nu = 1$) and length in units of the system size (i.e., the lattice spacing is $a = 1/L$ and the total length $La = 1$). In lane 2 (SSEP) particles jump nondirectionally between neighboring sites, at rate ϵ again respecting exclusion. This represents the diffusive motion in the cytoplasm that is taken to be effectively one-dimensional in the thin cylinderlike protrusions (the steady-state behavior of a system with several lanes for diffusion arranged on a cylinder around the TASEP can be reduced to the steady-state behavior of this model [44]). Particles enter or exit the system only at site 0 of lane 2 (base) but not at site 0 of lane 1. At rate α a particle is injected provided the site is empty and at rate ϵ a particle leaves the system. This reflects the exchange of motors between the protrusion base and the cell body. In the bulk both lanes are coupled via a rate ω at which particles jump from site $i \in \{0,1,\ldots,L-1\}$ of lane 1 to site i of lane 2 or vice versa (each respecting exclusion). Since the biochemistry at the tip is only poorly understood, at site L we consider two extreme cases: In model A, particles jump from site L of lane 1 to site L of lane 2 at rate $\beta \gg \omega$ (respecting exclusion) but not in the opposite direction. This describes a scenario where motors at the tip detach mainly due to the lack of a filament subunit in front of them. In model B, the exchange rates between the lanes at sites L are the same as in the bulk. The comparison of both models stresses that seemingly minor changes in a nonequilibrium system may have a strong influence on the dynamics [45], and highlights the relevance of the biochemistry at the filament tip for the motor density profile. In the following, when considering the continuum limit $a \to 0$, we focus on the mesoscopic limit for ω [18,19]; i.e., we keep $\Omega = \omega/a$ fixed, thus ensuring the number of jumps between lanes is of the same order as that of entry or exit events (persistent motors) and implementing weak coupling between the diffusive and the directed motion. For simplicity, we take the attachment and detachment rates to be equal. However, the qualitative results do not change for different attachment and detachment rates $\omega_A \neq \omega_D$ as long as both are still taken in the mesoscopic limit (not shown here).

A single TASEP exhibits three phases, namely, a maximal current (MC), a low- (LD) and a high-density (HD) phase [16]. Moreover, on the phase boundary between the LD and HD phase the steady-state profile is given by a DW that performs a random walk. Because of the closure at the tip, we do not find a MC phase in our system [44], but instead observe *localized* DWs [17,18]. That is, the generic steady-state TASEP profile $\rho^T(x)$ for both models is given by a localized DW separating low density at the base from high density at the tip [Fig. 2]. For generic parameters, the filament current is thus comparatively small, and restricted to a small part of the system. This might be beneficial from a biological point of view,

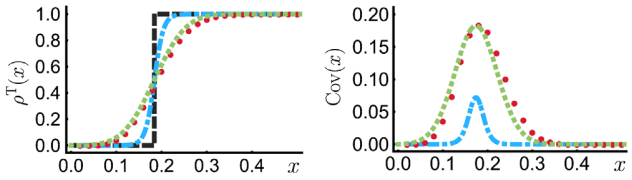

FIG. 2. Representative steady-state DW profile $\rho^T(x)$ (left) with covariances Cov(x) (right) on the TASEP lane are shown exemplarily for model A with $L = 50$, $\beta = 0.2$, $\Omega = 0.001$, $\alpha = 0.1$, and $\epsilon = 0.025$. The covariances are nonzero only in the vicinity of the DW. Using the fluctuation-corrected profile from DW theory, our predictions (dotted green curves) fit the simulation result (filled red circles) very well. If we use the refined MF profile (dot-dashed blue) instead of a step function (dashed black curve), the width of the DW and the strength of the covariances are strongly underestimated [44].

since every motor step on the filament consumes ATP. The position of the DW depends on the model parameters, and is shifted towards the tip (base) for smaller (higher) values of $\sigma := \alpha/(\alpha+\epsilon)$ [44]. This ratio can be thought of as the motor density in the cell body, and thus the value for the cytoplasmic density at the protrusion base. The width of the DW decreases with increasing L and with increasing distance from the tip [44]. Generically, when describing the DW as a random walker (see below), we observe that its motion is mainly confined to a small part of the system. Hence, we assume for the moment that the DW is fully localized and adopt a step-function ansatz for $\rho^T(x)$ that holds to lowest order in a: $\rho^T(x) = 0$ for $x \in [0, z[$, and $\rho^T(x) = 1$ for $x \in]z, 1]$. First, we determine the position z of the DW to find out whether tip localization (i.e., $z \approx 1$) occurs for certain parameter ranges or not. For this purpose we derive a mass-balance equation relating the total average occupancies of the TASEP (T) and the SSEP (S). We denote by n_i^μ the occupation number on site $i \in \{0, \ldots, L\}$ of lane $\mu \in \{T, S\}$; i.e., we write $n_i^\mu = 0$ if site i of lane μ is empty and $n_i^\mu = 1$ if it is occupied. Since $n_i^\mu \in \{0, 1\}$, we have $\langle n_i^\mu \rangle = \mathrm{Prob}\{n_i^\mu = 1\}$; ensemble averages are denoted by $\langle\rangle$. The steady-state condition in the bulk corresponds to a flux balance [44]: $(\rho_{i-1}^T - f_{i-1}) - (\rho_i^T - f_i) = \omega(\rho_i^T - \rho_i^S)$ with the correlator $f_i = \langle n_i^T n_{i+1}^T \rangle$ and the average occupancy $\rho_i^\mu = \langle n_i^\mu \rangle$. The difference of the TASEP currents, from site $i-1$ to site i and from site i to site $i+1$, (left-hand side) must equal the current between sites i of the TASEP and SSEP, $\omega(\langle n_i^T(1-n_i^S)\rangle - \langle n_i^S(1-n_i^T)\rangle)$, (right-hand side). It follows that $f_i = f_0 + \rho_i^T - \rho_0^T + \omega\sum_{j=1}^{i}(\rho_j^T - \rho_j^S)$. At the base, there is no direct flux from the cell body into the filament; so the boundary condition is $f_0 = \rho_0^T + \omega(\rho_0^T - \rho_0^S)$ and we find the following exact *moment identity*,

$$f_i = \rho_i^T + \omega \sum_{j=0}^{i} (\rho_j^T - \rho_j^S). \tag{1}$$

The systems are both closed at the tip but, due to the different attachment and detachment behavior, the boundary conditions read $f_{L-1} = \rho_{L-1}^T - \beta\langle n_L^T(1-n_L^S)\rangle$, and $f_{L-1} = \rho_{L-1}^T + \omega(\rho_L^S - \rho_L^T)$ for models A and B, respectively. Combining these with Eq. (1), the following exact *mass-balance equations* can be derived for model A,

$$\omega \sum_{j=0}^{L-1} (\rho_j^T - \rho_j^S) = -\beta(\rho_L^T - \langle n_L^T n_L^S \rangle), \tag{2}$$

and similarly for model B, $\omega\sum_{j=0}^{L}(\rho_j^T - \rho_j^S) = 0$. These equations relate the average occupancy on the two lanes in such a way that the total influx into the TASEP lane equals the total outflux from it [46]. Interestingly, these equations reveal that a global detailed balance holds for the total exchange between the two lanes, rather than local detailed balance for any pair of sites (cf. adsorption equilibrium in Ref. [25]). The moment identity and the mass-balance equations are useful in two ways: (i) By using the DW ansatz, we are able to find an analytic formula for the DW position; (ii) the moment identity enables us to express covariances with respect to NNs on the TASEP lane in terms of densities.

To address the first issue, we determine the average density $\rho^S(x)$ on the SSEP lane corresponding to the fully localized DW ansatz by solving the bulk equation for the SSEP. For that, we implement the continuum limit and, for model A, assume $\langle n_L^T n_L^S \rangle \approx \rho_L^T \rho_L^S$ [44]. Note, that we only need this MF approximation for the tip densities of model A. This is due to the otherwise symmetric attachment and detachment rates and the diffusive motion in the cytoplasm, for both of which the correlations drop out in the dynamical equation. With the resulting equation for $\rho^S(x)$ we can then conclude $z = 1 - l\cosh^{-1}[\sigma\cosh(1/l)]$ and $z = 1 - l\sinh^{-1}[\sigma\sinh(1/l)]$ for models A and B, respectively, where $l := \sqrt{D/\omega}$ with $D := \epsilon a^2$ being the diffusion constant in the cytoplasm [44]; l can be understood as the typical dwell length for motors in the cytoplasm before attaching to the filament. Comparing these expressions with our stochastic simulation results [47] we find excellent agreement [Fig. 3].

The phase diagrams for the two models are qualitatively different. For model A, one can switch between the DW phase ($z \ll 1$) and the tip-localization phase ($z \approx 1$) by only slightly increasing the dwell length l. In contrast, for model B, tip localization is attained only as $\sigma \to 0$, even for large l

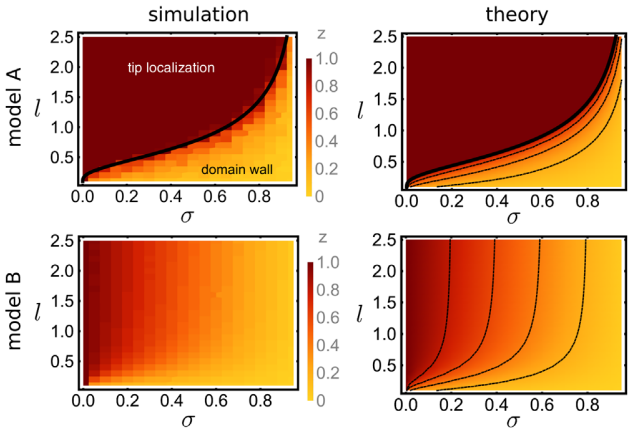

FIG. 3. Phase diagrams for the DW position z (color-coded) for $L = 50$ and $\Omega = 0.001$ for model A (upper panel, $\beta = 0.2$) and model B (lower panel) as a function of the typical dwell length l in the cytoplasm and the cytoplasmic density at the protrusion base σ: the simulation results are shown on the left, the theoretical predictions for the DW position are shown on the right. The black thick lines in the diagrams for model A show the phase boundary $z = 1$ as obtained from theory. The dashed black lines in the diagrams obtained from theory are, from right to left respectively, contour lines of constant $z = 0.2$, 0.4, 0.6, and additionally, $z = 0.8$ for model B.

[44]. This can be understood from the symmetry between the attachment and detachment processes in model B, which should also be reflected in a symmetry in occupancy between the filament and the cytoplasm. For large l, the cytoplasm becomes well-mixed with constant density σ. So, the average density on the filament is σ as well, which is realized for a DW position $z = 1 - \sigma$. For model A, fast diffusion in the cytoplasm leads to rapid diffusion of the motors away from the tip. Therefore, the exit rate at the tip is high and motors quickly leave the tip of the filament, thus enabling tip localization but reducing large jamming. For small but finite σ, there is tip localization also if the typical dwell length is smaller than the system size, $l \leq 1$. That is, even if the motors have a relatively small D, tip localization can occur if the tip has an enhanced detachment rate (model A). For model B, even by increasing l well beyond the system size, tip localization occurs only for very low motor density σ at the base.

These features may have interesting biological implications: A higher detachment rate at the actin filament's end would promote tip localization, but simultaneously avoid jamming. As a result, motor exchange between filament and cytoplasm occurs primarily near the tip (where the DW is located) and the motors at the tip can be continuously replenished by new ones delivered through the cytoplasm. Furthermore, energy consumption (ATP hydrolysis) is low, as the filament current is kept small and mainly restricted to the tip area. Transport to the tip is facilitated mainly by diffusion in the cytoplasm, which does not consume chemical energy. In summary, energy from ATP hydrolysis could efficiently be used to localize motors to the filament tip, while material transport is facilitated by diffusion in the cytoplasm [44].

In this regard, the model is also interesting from a theoretical point of view, as it allows for the calculation of the filament current $J_i^T = \rho_i^T - f_i$ that depends on NN correlations or, equivalently, the NN covariances

$$\mathrm{Cov}_i := \langle n_i^T n_{i+1}^T \rangle - \rho_i^T \rho_{i+1}^T = f_i - \rho_i^T \rho_{i+1}^T \qquad (3)$$

on the TASEP lane. To go beyond MF, we use Eq. (1), which relates f_i to the average densities, and find $\mathrm{Cov}_i = \rho_i^T(1 - \rho_{i+1}^T) + \omega \sum_{j=0}^{i} (\rho_j^T - \rho_j^S)$, which, in the continuum limit, translates to

$$\mathrm{Cov}(x) = \rho^T(x)[1 - \rho^T(x+a)] + \Omega \int_0^x dy(\rho^T - \rho^S). \qquad (4)$$

The value of the first term in Eq. (4) depends sensitively on the width and shape of the DW (the density profile $\rho^T(x)$ is increasing with x, so that $\rho^T(x)[1 - \rho^T(x+a)]$ is maximal if both $\rho^T(x)$ and $\rho^T(x+a)$ are close to 0.5). Therefore, one needs to refine the fully localized DW ansatz, by taking into account the stochastic dynamics of the DW position. Following Refs. [48,49] we consider the DW as a random walker with (site-dependent) hopping rates depending on currents and densities in the low- and high-density regions. For small a we find

$$\rho^T(x) \approx \frac{\mathrm{erf}[(x-z)/W(z)] + \mathrm{erf}[z/W(z)]}{\mathrm{erf}[(1-z)/W(z)] + \mathrm{erf}[z/W(z)]}, \qquad (5)$$

where $W(z) = \sqrt{2\sigma a l \sinh(z/l)}$ [44]. This fluctuation-corrected DW profile, as well as the covariance obtained from it, agree very well with our simulation data [Fig. 2]. If one uses a refined MF method instead, accounting for second-order spatial derivatives, the DW width and the strength of the correlations are both markedly underestimated [44].

In general, covariances are nonzero only close to the DW, but there they can reach quite high values of around 0.2. We have $\mathrm{Cov}_i = \rho_i^T(1 - \rho_{i+1}^T) - J_i^T$, where the first term corresponding to the MF current dominates. Therefore, the actual current $J_i^T = \omega \sum_{j=0}^{i} (\rho_j^S - \rho_j^T)$ can be orders of magnitude smaller than the MF current, and scales with the particle exchange rate ω [44]. That is, density correlations dominate in such a way that they suppress the TASEP current substantially. This demonstrates that, even if basic properties of the single TASEP are captured well by MF theory, correlation effects in TASEP-based systems should be studied more closely and might lead to unanticipated features [50–52].

The covariances are non-negative everywhere, $\mathrm{Cov}_i \geq 0$, so the conditional probabilities obey the inequalities $\mathrm{Prob}\{n_i^T = 1 | n_{i+1}^T = 1\} \geq \mathrm{Prob}\{n_i^T = 1\}$ and $\mathrm{Prob}\{n_{i+1}^T = 1 | n_i^T = 1\} \geq \mathrm{Prob}\{n_{i+1}^T = 1\}$ at any site, implying that particles typically form clusters. As a result, from the DW region onwards (where the covariances are highest), the mean time a particle spends at a certain site is increased considerably compared to freely moving motors. This is due to the effective jump rate on the filament, which is decreased by excluded-volume effects. Thus, in the case of tip localization, particles spend more time near the tip than in the main part of the filament. This prolongation of the residence time is further enhanced by the exclusion in the cytoplasm that prevents motors from detaching if the cytoplasmic tip density is high. This is especially important for model A, where the cytoplasmic tip density takes a value of ≈ 1, which is much higher than in the bulk [44]. Biologically, the extended residence time at the tip might facilitate the tasks of the motors or their cargo at the tip.

Our results all essentially rely on the exact moment identity and the exact mass-balance equations. The derivation of both depends on the TASEP dynamics and the coupling between the two lanes, but not at all on the dynamics of the second (here SSEP) lane. Hence, those equations do not change if this dynamics on the second lane is modified, and we expect them to be useful for other model systems in which a TASEP lane is coupled to another lattice via attachment and detachment kinetics. To our best knowledge, the moment identity has not been

mentioned before. We believe that it might open doors in the understanding of correlations and the prediction of active currents also in more elaborate models. Furthermore, both equations could easily be generalized to the case of different attachment and detachment rates.

Our models could also be varied in other interesting ways. One could account for the three-dimensional geometry or for polymerization and depolymerization of the filament and the accompanying changes in length. Nevertheless, we expect that some of the phenomena seen here should be robust against such modifications. Tip localization, which is mostly based on mass conservation at the tip, should still be present. Second, the TASEP current might still be suppressed, and the roles of the TASEP and the diffusive lane in being responsible for tip localization and motor transport, respectively, should remain untouched. This seems to be supported by more elaborate models in a related context [13,15].

We thank Matthias Rank, Louis Reese, and Emanuel Reithmann for critical reading of this manuscript and for helpful discussions. This research was supported by the German Excellence Initiative via the program "NanoSystems Initiative Munich" (NIM) and by the Deutsche Forschungsgemeinschaft (DFG) through the Graduate School of Quantitative Biosciences Munich (QBM).

*To whom all correspondence should be addressed.
frey@lmu.de.

[1] C. Revenu, R. Athman, S. Robine, and D. Louvard, Nat. Rev. Mol. Cell Biol. **5**, 635 (2004).
[2] P. K. Mattila and P. Lappalainen, Nat. Rev. Mol. Cell Biol. **9**, 446 (2008).
[3] F. Les Erickson, A. C. Corsa, A. C. Dosé, and B. Burnside, Mol. Biol. Cell **14**, 4173 (2003).
[4] R. Nambiar, R. E. McConnell, and M. J. Tyska, Cell Mol. Life Sci. **67**, 1239 (2010).
[5] F. T. Salles, R. C. Merritt, U. Manor, G. W. Dougherty, A. D. Sousa, J. E. Moore, C. M. Yengo, A. C. Dosé, and B. Kachar, Nat. Cell Biol. **11**, 443 (2009).
[6] M. A. Hartman and J. A. Spudich, J. Cell Sci. **125**, 1627 (2012).
[7] M. L. Kerber and R. E. Cheney, J. Cell Sci. **124**, 3733 (2011).
[8] T. Kambara, S. Komaba, and M. Ikebe, J. Biol. Chem. **281**, 37291 (2006).
[9] J. E. Bird, Y. Takagi, N. Billington, M.-P. Strub, J. R. Sellers, and T. B. Friedman, Proc. Natl. Acad. Sci. U.S.A. **111**, 12390 (2014).
[10] A. K. Rzadzinska, M. E. Schneider, C. Davies, G. P. Riordan, and B. Kachar, J. Cell Biol. **164**, 887 (2004).
[11] U. Manor, A. Disanza, M. Grati, L. Andrade, H. Lin, P. P. Di Fiore, G. Scita, and B. Kachar, Curr. Biol. **21**, 167 (2011).
[12] I. A. Belyantseva, E. T. Boger, and T. B. Friedman, Proc. Natl. Acad. Sci. U.S.A. **100**, 13958 (2003).
[13] P. Zhuravlev, Y. Lan, M. Minakova, and G. Papoian, Proc. Natl. Acad. Sci. U.S.A. **109**, 10849 (2012).
[14] M. Naoz, U. Manor, H. Sakaguchi, B. Kachar, and N. S. Gov, Biophys. J. **95**, 5706 (2008).
[15] K. Wolff, C. Barrett-Freeman, M. R. Evans, A. B. Goryachev, and D. Marenduzzo, Phys. Biol. **11**, 016005 (2014).
[16] J. Krug, Phys. Rev. Lett. **67**, 1882 (1991).
[17] R. Lipowsky, S. Klumpp, and T. M. Nieuwenhuizen, Phys. Rev. Lett. **87**, 108101 (2001).
[18] A. Parmeggiani, T. Franosch, and E. Frey, Phys. Rev. Lett. **90**, 086601 (2003).
[19] A. Parmeggiani, T. Franosch, and E. Frey, Phys. Rev. E **70**, 046101 (2004).
[20] M. Evans, Y. Kafri, K. Sugden, and J. Tailleur, J. Stat. Mech. (2011) P06009.
[21] C. T. MacDonald, J. H. Gibbs, and A. C. Pipkin, Biopolymers **6**, 1 (1968).
[22] F. Spitzer, Adv. Math. **5**, 246 (1970).
[23] R. A. Blythe and M. R. Evans, J. Phys. A **40**, R333 (2007).
[24] T. Chou, K. Mallick, and R. K. P. Zia, Rep. Prog. Phys. **74**, 116601 (2011).
[25] M. Müller, S. Klumpp, and R. Lipowsky, J. Phys. Condens. Matter **17**, S3839 (2005).
[26] S. Klumpp and R. Lipowsky, J. Stat. Phys. **113**, 233 (2003).
[27] V. Popkov and G. M. Schütz, J. Stat. Phys. **112**, 523 (2003).
[28] E. Pronina and A. B. Kolomeisky, J. Phys. A **37**, 9907 (2004).
[29] B. Schmittmann, J. Krometis, and R. K. P. Zia, Europhys. Lett. **70**, 299 (2005).
[30] E. Pronina and A. B. Kolomeisky, Physica A (Amsterdam) **372A**, 12 (2006).
[31] T. Reichenbach, E. Frey, and T. Franosch, New J. Phys. **9**, 159 (2007).
[32] E. Pronina and A. B. Kolomeisky, J. Phys. A **40**, 2275 (2007).
[33] R. Jiang, R. Wang, and Q.-S. Wu, Physica A (Amsterdam) **375**, 247 (2007).
[34] T. Reichenbach, T. Franosch, and E. Frey, Eur. Phys. J. E **27**, 47 (2008).
[35] R. Wang, M. Liu, and R. Jiang, Physica A (Amsterdam) **387**, 457 (2008).
[36] M. R. Evans, P. A. Ferrari, and K. Mallick, J. Stat. Phys. **135**, 217 (2009).
[37] C. Schiffmann, C. Appert-Rolland, and L. Santen, J. Stat. Mech. (2010) P06002.
[38] A. Melbinger, T. Reichenbach, T. Franosch, and E. Frey, Phys. Rev. E **83**, 031923 (2011).
[39] B. Saha and S. Mukherji, J. Stat. Mech. (2013) P09004.
[40] A. K. Gupta and I. Dhiman, Phys. Rev. E **89**, 022131 (2014).
[41] D. Johann, D. Goswami, and K. Kruse, Phys. Rev. E **89**, 042713 (2014).
[42] I. Pinkoviezky and N. S. Gov, Phys. Rev. E **89**, 052703 (2014).
[43] A. I. Curatolo, M. R. Evans, Y. Kafri, and J. Tailleur, J. Phys. A **49**, 095601 (2016).
[44] See Supplemental Material at http://link.aps.org/supplemental/10.1103/PhysRevLett.118.128101 for a detailed mathematical analysis (including domain wall theory), details on the different currents and a generalization of our model in cylinderlike geometry.

[45] L. Reese, A. Melbinger, and E. Frey, Interface Focus **4** (2014).
[46] S. Klumpp, M. J. I. Müller, and R. Lipowsky, *Traffic and Granular Flow '05* (Springer, Berlin, 2007), pp. 251–261.
[47] D. T. Gillespie, J. Comput. Phys. **22**, 403 (1976).
[48] B. Derrida, M. R. Evans, and K. Mallick, J. Stat. Phys. **79**, 833 (1995).
[49] A. B. Kolomeisky, G. M. Schütz, E. B. Kolomeisky, and J. P. Straley, J. Phys. A **31**, 6911 (1998).
[50] V. Popkov, A. Rákos, R. D. Willmann, A. B. Kolomeisky, and G. M. Schütz, Phys. Rev. E **67**, 066117 (2003).
[51] K. Tsekouras and A. B. Kolomeisky, J. Phys. A **41**, 095002 (2008).
[52] E. Reithmann, L. Reese, and E. Frey, Phys. Rev. Lett. **117**, 078102 (2016).

Supplemental Material: Generic transport mechanisms for molecular traffic in cellular protrusions

This Supplemental Material gives details on the mathematical analysis of the lattice gas model. We will explain more thoroughly why the generic steady-state TASEP density profile is given by a domain wall and why there is no maximal current phase. Furthermore, the calculation of the density profiles both for TASEP and SSEP are shown explicitly and the analytic expressions for the position of the domain wall are derived. It is demonstrated how domain wall theory is used concretely to improve on the mean-field TASEP density profiles, and on the prediction for the covariances. Those are relevant to see how the actual TASEP current differs from the expected mean-field current. We also display a comparison of the different currents (on the TASEP, on the SSEP and those for attachment and detachment) for a parameter set of model A where tip localisation occurs. Finally, we show that the steady-state behaviour of a geometry with several lanes for diffusion arranged on a cylinder around the TASEP lane can be reduced to the steady-state behaviour of our model by scaling the parameters for diffusion and attachment/detachment with the number of lanes for diffusion. The same holds true for a model where instead of exclusion on the lane for diffusion a finite carrying capacity $N_{\max} > 1$ is used.

CALCULATION OF THE DENSITY PROFILES

To set the stage, let us denote by n_i^μ the occupation number on site $i \in \{0, \dots, L\}$ of lane $\mu \in \{\mathrm{T}, \mathrm{S}\}$, i.e. we will write $n_i^\mu = 0$ if site i of lane μ is empty and $n_i^\mu = 1$ if it is occupied (T: TASEP, S: SSEP). The common bulk master equations of the Markov processes, corresponding to model A and B as shown in Fig. 1, are given by

$$\begin{aligned}
\frac{\mathrm{dProb}\{n_i^\mathrm{T}\}}{\mathrm{d}t} &= \mathrm{Prob}\{n_{i-1}^\mathrm{T}, \overline{n_i^\mathrm{T}}\} - \mathrm{Prob}\{n_i^\mathrm{T}, \overline{n_{i+1}^\mathrm{T}}\} + \omega \left(\mathrm{Prob}\{n_i^\mathrm{S}, \overline{n_i^\mathrm{T}}\} - \mathrm{Prob}\{n_i^\mathrm{T}, \overline{n_i^\mathrm{S}}\}\right), \\
\frac{\mathrm{dProb}\{n_i^\mathrm{S}\}}{\mathrm{d}t} &= \epsilon \left(\mathrm{Prob}\{n_{i-1}^\mathrm{S}, \overline{n_i^\mathrm{S}}\} + \mathrm{Prob}\{n_{i+1}^\mathrm{S}, \overline{n_i^\mathrm{S}}\} - \mathrm{Prob}\{n_i^\mathrm{S}, \overline{n_{i+1}^\mathrm{S}}\} - \mathrm{Prob}\{n_i^\mathrm{S}, \overline{n_{i-1}^\mathrm{S}}\}\right) + \\
&\quad + \omega \left(\mathrm{Prob}\{n_i^\mathrm{T}, \overline{n_i^\mathrm{S}}\} - \mathrm{Prob}\{n_i^\mathrm{S}, \overline{n_i^\mathrm{T}}\}\right),
\end{aligned}$$

where $\mathrm{Prob}\{n_i^\mu\}$ denotes the probability that $n_i^\mu = 1$ and $\mathrm{Prob}\{n_i^\mu, \overline{n_j^\nu}\}$ the one that $n_i^\mu = 1$ and $n_j^\nu = 0$. The term $\mathrm{Prob}\{n_{i-1}^\mathrm{T}, \overline{n_i^\mathrm{T}}\} - \mathrm{Prob}\{n_i^\mathrm{T}, \overline{n_{i+1}^\mathrm{T}}\}$ is due to the jump process on the TASEP lane that respects the exclusion property and occurs at bare rate $\nu = 1$. The terms proportional to ω describe the exchange between the lanes, again respecting the exclusion. And finally, the term proportional to ϵ describes the diffusion on the SSEP lane. Note that we assume exclusion not only on the filament but also in the cytoplasm. This is based on the idea that, due to the finite size of particles, there should be a maximal number inside any finite volume element, introducing a carrying capacity $N_{\max}$. If we assume that the *maximal* effective attachment and detachment rate stay the same, i.e. if we assume that attachment happens at rate $\omega\left(n^\mathrm{S}\left(1 - n^\mathrm{T}\right)\right)$ and detachment at rate $\omega\left(n^\mathrm{T}\left(N_{\max} - n^\mathrm{S}\right)\right)$ where $n^\mathrm{S} \in \{0, 1, \dots, N_{\max}\}$, the case $N_{\max}$ finite but arbitrary can be reduced to $N_{\max} = 1$ by redefinition of the parameters, and in the following we will focus only on the case $N_{\max} = 1$. We will, however, come back to this case again in the last paragraph of the Supplemental Material when we discuss the case of several lanes for diffusion.

The bulk master equations can be rewritten in terms of averages over the occupation numbers by using that $\langle n_i^\mu \rangle = \mathrm{Prob}\left(n_i^\mu = 1\right) = \mathrm{Prob}\{n_i^\mu\}$ and $\langle n_i^\mu \left(1 - n_i^\nu\right)\rangle = \mathrm{Prob}\{n_i^\mu, \overline{n_i^\nu}\}$ hold, as each site can be either empty or occupied by one particle/motor:

$$\partial_t \rho_i^\mathrm{T} = \rho_{i-1}^\mathrm{T} - f_{i-1} - \rho_i^\mathrm{T} + f_i + \omega\left(\rho_i^\mathrm{S} - \rho_i^\mathrm{T}\right), \tag{S1}$$

$$\partial_t \rho_i^\mathrm{S} = \epsilon\left(\rho_{i+1}^\mathrm{S} + \rho_{i-1}^\mathrm{S} - 2\rho_i^\mathrm{S}\right) + \omega\left(\rho_i^\mathrm{T} - \rho_i^\mathrm{S}\right), \tag{S2}$$

where $f_i = \left\langle n_i^\mathrm{T} n_{i+1}^\mathrm{T} \right\rangle$ is the nearest-neighbour correlator for the TASEP. Summing both equations we find

$$\partial_t(\rho_i^\mathrm{T} + \rho_i^\mathrm{S}) = \rho_{i-1}^\mathrm{T} - f_{i-1} - \rho_i^\mathrm{T} + f_i + \epsilon\left(\rho_{i+1}^\mathrm{S} + \rho_{i-1}^\mathrm{S} - 2\rho_i^\mathrm{S}\right) \tag{S3}$$

for the time evolution of the combined density $\rho_i^\mathrm{T} + \rho_i^\mathrm{S}$ in the bulk. At the left boundary (base) we find

$$\begin{aligned}
\partial_t \rho_0^\mathrm{T} &= -\rho_0^\mathrm{T} + f_0 + \omega\left(\rho_0^\mathrm{S} - \rho_0^\mathrm{T}\right) \\
\partial_t \rho_0^\mathrm{S} &= \alpha(1 - \rho_0^\mathrm{S}) - \epsilon\rho_0^\mathrm{S} + \epsilon\left(\rho_1^\mathrm{S} - \rho_0^\mathrm{S}\right) + \omega\left(\rho_0^\mathrm{T} - \rho_0^\mathrm{S}\right)
\end{aligned} \tag{S4}$$

for both models. For the TASEP lane there is only outflux from site 0 to site 1 or exchange with site 0 of the SSEP lane. On the SSEP lane, there is influx at rate α (respecting the exclusion at site 0 of the SSEP), outflux with the diffusion rate ϵ, diffusion between site 0 and site 1 and exchange with site 0 of the TASEP. The behaviour at the right boundary (tip) differs between the models and is given by

$$\begin{aligned}\partial_t \rho_L^{\mathrm{T}} &= \rho_{L-1}^{\mathrm{T}} - f_{L-1} - \beta\left(\rho_L^{\mathrm{T}} - \langle n_L^{\mathrm{T}} n_L^{\mathrm{S}}\rangle\right) \\ \partial_t \rho_L^{\mathrm{S}} &= \epsilon\left(\rho_{L-1}^{\mathrm{S}} - \rho_L^{\mathrm{S}}\right) + \beta\left(\rho_L^{\mathrm{T}} - \langle n_L^{\mathrm{T}} n_L^{\mathrm{S}}\rangle\right)\end{aligned} \tag{S5}$$

for model A, and by

$$\begin{aligned}\partial_t \rho_L^{\mathrm{T}} &= \rho_{L-1}^{\mathrm{T}} - f_{L-1} + \omega\left(\rho_L^{\mathrm{S}} - \rho_L^{\mathrm{T}}\right) \\ \partial_t \rho_L^{\mathrm{S}} &= \epsilon\left(\rho_{L-1}^{\mathrm{S}} - \rho_L^{\mathrm{S}}\right) + \omega\left(\rho_L^{\mathrm{T}} - \rho_L^{\mathrm{S}}\right)\end{aligned} \tag{S6}$$

for model B. For model A, at site L of the TASEP lane there is influx from the neighbouring site $L-1$ and outflux to site L of the SSEP lane at bare rate β respecting the exclusion. For site L of the SSEP lane there is diffusion between sites $L-1$ and L of the SSEP lane and influx from site L of the TASEP lane. For model B, we have the same behaviour except that the asymmetric exchange between sites L of the TASEP and SSEP lane is replaced by the symmetric exchange $\omega\left(\rho_L^{\mathrm{T}} - \rho_L^{\mathrm{S}}\right)$. Since the exchange terms drop out when considering the time derivative of $\rho_L^{\mathrm{T}} + \rho_L^{\mathrm{S}}$, at the tip of both models it holds

$$\partial_t(\rho_L^{\mathrm{T}} + \rho_L^{\mathrm{S}}) = \rho_{L-1}^{\mathrm{T}} - f_{L-1} + \epsilon\left(\rho_{L-1}^{\mathrm{S}} - \rho_L^{\mathrm{S}}\right) = J_{L-1}^{\mathrm{T}} + J_{L-1}^{\mathrm{S}}, \tag{S7}$$

and at the base

$$\partial_t(\rho_0^{\mathrm{T}} + \rho_0^{\mathrm{S}}) = -\rho_0^{\mathrm{T}} + f_0 + \alpha(1-\rho_0^{\mathrm{S}}) - \epsilon\rho_0^{\mathrm{S}} + \epsilon\left(\rho_1^{\mathrm{S}} - \rho_0^{\mathrm{S}}\right) = -J_0^{\mathrm{T}} + \alpha(1-\rho_0^{\mathrm{S}}) - \epsilon\rho_0^{\mathrm{S}} - J_0^{\mathrm{S}} \tag{S8}$$

where we introduced the local currents

$$J_i^{\mathrm{T}} = \rho_i^{\mathrm{T}} - f_i \tag{S9}$$

and

$$J_i^{\mathrm{S}} = \epsilon\left(\rho_i^{\mathrm{S}} - \rho_{i+1}^{\mathrm{S}}\right) \tag{S10}$$

for $i = 0, \ldots, L-1$ on the filament and in the cytoplasm, respectively. With that Eq. (S3) translates to

$$\partial_t(\rho_i^{\mathrm{T}} + \rho_i^{\mathrm{S}}) = J_{i-1}^{\mathrm{T}} + J_{i-1}^{\mathrm{S}} - J_i^{\mathrm{T}} - J_i^{\mathrm{S}}. \tag{S11}$$

Note that we can introduce currents $J_{-1}^{\mathrm{T/S}}$ and $J_L^{\mathrm{T/S}}$ as well. However, as the system is closed at the tip $J_L^{\mathrm{T/S}} \equiv 0$, and since there is no direct influx from the left into the TASEP $J_{-1}^{\mathrm{T}} = 0$. In order to be consistent with the structure of Eq. (S11) where the currents appear as $J_{i-1} - J_i$, we define

$$J_{-1}^{\mathrm{S}} = \alpha(1-\rho_0^{\mathrm{S}}) - \epsilon\rho_0^{\mathrm{S}} \tag{S12}$$

so that

$$\partial_t(\rho_0^{\mathrm{T}} + \rho_0^{\mathrm{S}}) = -J_0^{\mathrm{T}} + J_{-1}^{\mathrm{S}} - J_0^{\mathrm{S}}$$

holds.

As mentioned above, we are interested in the steady-state behaviour of the system and therefore set $\partial_t \rho_i^{T/S} \equiv 0$ for all i. In particular, we have

$$0 = \partial_t \sum_{i=0}^{L} (\rho_i^{\mathrm{T}} + \rho_i^{\mathrm{S}}) = J_{-1}^{\mathrm{S}}$$

where we used Eqs. (S7), (S8), (S11). As a result,

$$\rho_0^{\mathrm{S}} = \frac{\alpha}{\alpha+\epsilon} := \sigma, \tag{S13}$$

and the parameter σ as used for the phase diagrams in Fig. 3 can be identified as the motor density in the cell body.

To proceed, let us now use the continuum limit where $a = \frac{1}{L} \to 0$. That is, we will replace the discrete lattice by the continuous space $[0, 1]$ and the average occupation numbers are replaced by a continuous density

$$\rho_i^\mu \to \rho^\mu (x = x_i) \quad \text{where} \quad x_i = ia.$$

With that, we can substitute $\rho^\mu(x_i) \pm a\partial_x\rho^\mu(x_i) + \frac{1}{2}a^2\partial_x^2\rho^\mu(x_i) + \mathcal{O}(a^3)$ for $\rho^\mu_{i\pm1}$ and the currents are

$$\begin{aligned} J^{\mathrm{T}}(x) &= \rho^{\mathrm{T}}(x) - f(x) \\ J^{\mathrm{S}}(x) &= -a\epsilon\partial_x\rho^{\mathrm{S}}(x) - \frac{1}{2}a^2\epsilon\partial_x^2\rho^{\mathrm{S}}(x) + \mathcal{O}(a^3) \end{aligned}$$

where $f(x)$ is the continuous version of f_i. In the steady-state Eq. (S11) translates to

$$\begin{aligned} 0 = -a\partial_x(J^{\mathrm{T}} + J^{\mathrm{S}}) + \frac{1}{2}a^2\partial_x^2(J^{\mathrm{T}} + J^{\mathrm{S}}) + \mathcal{O}(a^3) = \\ = -a\partial_x(\rho^{\mathrm{T}}(x) - f(x)) + \mathcal{O}(a^2) \end{aligned}$$

to first order in a and thus, we have $\rho^{\mathrm{T}}(x) - f(x) = const$ to lowest order in a. Using Eq. (S7) or (S8) we conclude that $const = 0$ or that the combined current $J_i^{\mathrm{T}} + J_i^{\mathrm{S}}$ must be constant and zero everywhere. This corresponds to the fact that the system is closed at the tip so that in steady state on average there is no influx into the system from the base. Therefore,

$$\rho^{\mathrm{T}}(x) \equiv f(x)$$

or, equivalently,

$$\mathrm{Prob}\{n_i^{\mathrm{T}}\} = \rho_i^{\mathrm{T}} = f_i = \langle n_i^{\mathrm{T}} n_{i+1}^{\mathrm{T}} \rangle = \mathrm{Prob}\{n_i^{\mathrm{T}}, n_{i+1}^{\mathrm{T}}\} = \mathrm{Prob}\{n_{i+1}^{\mathrm{T}} | n_i^{\mathrm{T}}\}\mathrm{Prob}\{n_i^{\mathrm{T}}\}$$

holds to lowest order in a where we defined $\mathrm{Prob}\{n_i^{\mathrm{T}}, n_{i+1}^{\mathrm{T}}\} = \mathrm{Prob}\left(n_i^{\mathrm{T}} = 1, n_{i+1}^{\mathrm{T}} = 1\right)$ and $\mathrm{Prob}\{n_{i+1}^{\mathrm{T}} | n_i^{\mathrm{T}}\} = \mathrm{Prob}\left(n_{i+1}^{\mathrm{T}} = 1 | n_i^{\mathrm{T}} = 1\right)$ analogously to before. This implies that either

$$\rho_i^{\mathrm{T}} = \mathrm{Prob}\{n_i^{\mathrm{T}}\} = 0 \tag{S14}$$

or

$$\mathrm{Prob}\{n_{i+1}^{\mathrm{T}} | n_i^{\mathrm{T}}\} = 1.$$

The latter implies that, whenever site i is occupied, site $i + 1$ is occupied with probability 1 as well. Hence, if there is some site j occupied at some time, any site $i > j$ is occupied at that time as well. It follows that to lowest order in a the density suddenly jumps from zero (S14) to maximal density

$$\rho_i^{\mathrm{T}} = 1. \tag{S15}$$

This means that to lowest order the steady-state TASEP profile is given by a step function separating a region of 0 density on the left (towards the base) from a region of density 1 on the right (towards the tip) and, in particular, there is no maximal current phase as it occurs for TASEP alone. Instead, the generic TASEP profile is given by a domain wall and we make the following fully-localised-DW ansatz:

$$\rho^{\mathrm{T}}(x) = \begin{cases} 0 & \text{for} \quad x \in [0, z[\\ 1 & \text{for} \quad x \in]z, 1] \end{cases} \tag{S16}$$

where $z \in [0, 1]$ is the position of the domain wall (step) that we will determine later.

We will now use this ansatz to determine the steady-state density profile for the SSEP lane depending on z. For this purpose, let us go back to Eq. (S2) that is given by

$$0 = \epsilon a^2\partial_x^2\rho^{\mathrm{S}}(x) + \Omega a(\rho^{\mathrm{T}}(x) - \rho^{\mathrm{S}}(x))$$

in the continuum limit in the steady state. This equation can be solved in the two regions $x < z$ and $x > z$ as

$$\rho^{\mathrm{S}}(x) = \begin{cases} A_1 \cosh\left(\sqrt{\frac{\Omega}{\epsilon a}}x\right) + A_2 \sinh\left(\sqrt{\frac{\Omega}{\epsilon a}}x\right) & \text{for} \quad x \in [0, z[\\ 1 + B_1 \cosh\left(\sqrt{\frac{\Omega}{\epsilon a}}x\right) + B_2 \sinh\left(\sqrt{\frac{\Omega}{\epsilon a}}x\right) & \text{for} \quad x \in]z, 1]. \end{cases}$$

The constants A_1, A_2, B_1 and B_2 can be determined from the boundary conditions: Eq. (S5) yields $\beta\left(\rho_L^{\mathrm{T}} - \left\langle n_L^{\mathrm{T}} n_L^{\mathrm{S}} \right\rangle\right) = 0$ to lowest order in a for model A, and assuming that n_L^{T} and n_L^{S} are uncorrelated (mean-field assumption that is supported by the simulations) we conclude that

$$\rho_L^{\mathrm{S}} = 1$$

for model A, unless $\rho_L^{\mathrm{T}} = 0$ and so $z = 1$. For model B, we can use Eq. (S6) and find

$$\partial_x \rho^{\mathrm{S}}(1) = \frac{\Omega}{\epsilon}\left(1 - \rho^{\mathrm{S}}(1)\right),$$

again unless $z = 1$. This latter case needs to be treated separately. This can be done for instance by regarding the "domain wall" as a boundary layer with slope $(\rho^{\mathrm{S}}(1)_{\mathrm{right}} - \rho^{\mathrm{S}}(1)_{\mathrm{left}})/a$ where $\rho^{\mathrm{S}}(1)_{\mathrm{right}}$ is the density at the very last site L and $\rho^{\mathrm{S}}(1)_{\mathrm{left}}$ is the limit $x \to 1$ of the low-density phase. Basically, this case can be understood as the limit where the domain wall is shifted to the right out of the system. As long as $\epsilon \in \mathcal{O}(a^0)$, the generic density profile is given by a domain wall separating density 0 on the left from density 1 on the right, that is $\rho^{\mathrm{T}} \in \{0, 1\}$ holds to lowest order in a. In the limiting cases $\rho^{\mathrm{T}} \equiv 1$ the density reaches the value of 1 in only a few lattice sites from the base, whereas in the case $\rho^{\mathrm{T}} \equiv 0$ the density has a very small spike (boundary layer) only at the tip. The details of this calculation are, however, out of the scope of this letter and we will carry on with the treatment of the case $z \neq 1$.

For both models we have Eq. (S13) for the boundary condition at the base. Requiring that both the diffusive steady-state density profile and the derivative thereof is continuous (it can be seen from Eq. (S2) that $\left(\rho_{i+1}^{\mathrm{S}} - \rho_i^{\mathrm{S}}\right) - \left(\rho_i^{\mathrm{S}} - \rho_{i-1}^{\mathrm{S}}\right) = \mathcal{O}(a)$ holds), the following expression for the SSEP profiles can be derived:

$$\rho^{\mathrm{S}}(x) = \begin{cases} \sigma \cosh\left(\frac{x}{l}\right) + \left(\coth\left(\frac{1}{l}\right)\left(\cosh\left(\frac{z}{l}\right) - \sigma\right) - \sinh\left(\frac{z}{l}\right)\right)\sinh\left(\frac{x}{l}\right) & \text{for} \quad x \in [0, z[\\ 1 - \left(\cosh\left(\frac{z}{l}\right) - \sigma\right)\left(\cosh\left(\frac{x}{l}\right) - \coth\left(\frac{1}{l}\right)\sinh\left(\frac{x}{l}\right)\right) & \text{for} \quad x \in]z, 1] \end{cases} \tag{S17}$$

for model A and

$$\rho^{\mathrm{S}}(x) = \begin{cases} \sigma \cosh\left(\frac{x}{l}\right) + \left(\gamma\left(\cosh\left(\frac{z}{l}\right) - \sigma\right) - \sinh\left(\frac{z}{l}\right)\right)\sinh\left(\frac{x}{l}\right) & \text{for} \quad x \in [0, z[\\ 1 - \left(\cosh\left(\frac{z}{l}\right) - \sigma\right)\left(\cosh\left(\frac{x}{l}\right) - \gamma\sinh\left(\frac{x}{l}\right)\right) & \text{for} \quad x \in]z, 1] \end{cases} \tag{S18}$$

for model B where

$$l = \sqrt{\frac{\epsilon a}{\Omega}} = \sqrt{\frac{\epsilon a^2}{\omega}} = \sqrt{\frac{D}{\omega}}$$

with the diffusion constant $D = \epsilon a^2$ and

$$\gamma = \frac{\sinh\left(\frac{1}{l}\right) + \frac{a}{l}\cosh\left(\frac{1}{l}\right)}{\cosh\left(\frac{1}{l}\right) + \frac{a}{l}\sinh\left(\frac{1}{l}\right)} \approx \tanh\left(\frac{1}{l}\right).$$

To illustrate the differences between the two models, Fig. S1 shows typical density profiles on the SSEP lane for both cases. As one can see, the density profiles differ significantly between the two models. For model A, the density generically increases considerably from the protrusion base with density σ towards the tip with density 1 (unless $z = 1$). In contrast, the density for model B at the tip reaches a value that is only slightly larger than the value at the base. The fact that for model A the cytoplasmic density at the tip reaches a value very close to 1 is also the reason why for model A, the exclusion in the cytoplasm has a much higher influence on the residence time at the tip compared to model B where the cytoplasm is occupied quite homogeneously and where exclusion at the tip is not more important than in the bulk.

Using Eqs. (S17) and (S18) we now have expressions for the steady-state density profiles that only depend on one quantity, namely z, the position of the domain wall. Using the mass-balance equations [Eq. (2) and the corresponding one for model B], this enables us to find an analytic formula for z.

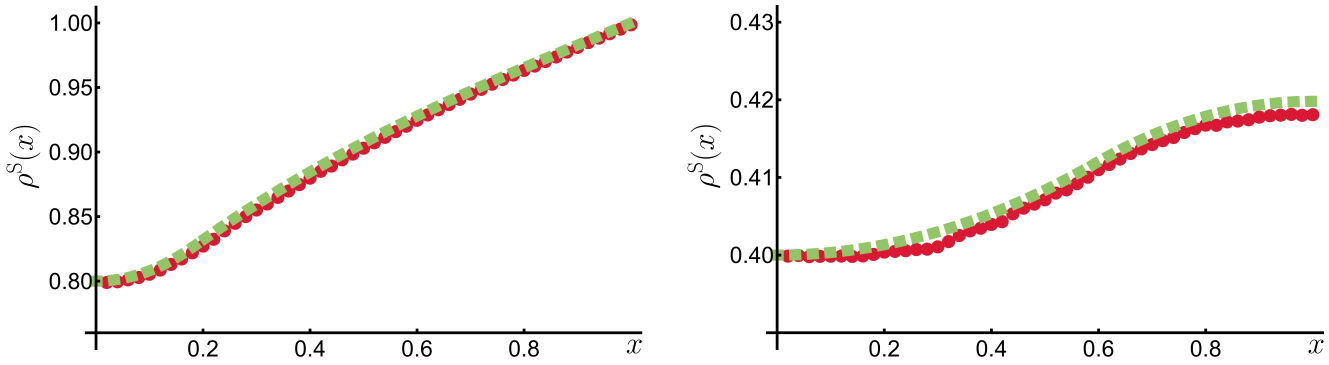

FIG. S1. Steady-state SSEP density profiles are shown examplarily for model A (left panel) with $L=50$, $\beta=0.2$, $\Omega=0.001$, $\alpha=0.1$ and $\epsilon=0.025$ and for model B (right panel) with $L=50$, $\Omega=0.001$, $\alpha=0.2$ and $\epsilon=0.3$. The simulation results (filled red circles) agree well with the theoretical prediction (dotted green curve) according to Eq. (S17) and (S18), respectively. For model A, the density is increasing towards the tip where it has a high slope and reaches a value of 1. For model B, the density is more homogeneous and has a small slope at the tip.

POSITION OF THE DOMAIN WALL

In order to determine the position of the domain wall, we go back to Eq. (S1). In the steady state this reduces to

$$f_i - f_{i-1} = \rho_i^{\mathrm{T}} - \rho_{i-1}^{\mathrm{T}} + \omega\left(\rho_i^{\mathrm{T}} - \rho_i^{\mathrm{S}}\right).$$

Hence, we can write

$$f_i = f_0 + \sum_{j=1}^{i}\left(f_j - f_{j-1}\right) = f_0 + \sum_{j=1}^{i}\left(\rho_j^{\mathrm{T}} - \rho_{j-1}^{\mathrm{T}} + \omega\left(\rho_j^{\mathrm{T}} - \rho_j^{\mathrm{S}}\right)\right) = f_0 + \rho_i^{\mathrm{T}} - \rho_0^{\mathrm{T}} + \omega\sum_{j=1}^{i}\left(\rho_j^{\mathrm{T}} - \rho_j^{\mathrm{S}}\right).$$

Using Eq. (S4) we can rewrite $f_0 = \rho^{\mathrm{T}} + \omega\left(\rho_0^{\mathrm{T}} - \rho_0^{\mathrm{S}}\right)$ and, thus,

$$f_i = \rho_i^{\mathrm{T}} + \omega\sum_{j=0}^{i}\left(\rho_j^{\mathrm{T}} - \rho_j^{\mathrm{S}}\right). \tag{S19}$$

This is the moment-identity [Eq. (1)]. It is an important result for us as it gives an exact relation between the nearest-neighbour correlator $f_i = \langle n_i^{\mathrm{T}} n_{i+1}^{\mathrm{T}}\rangle$ and the average densities. We will use it later to predict the covariances and the TASEP current in the system. This will allow us to make a sharp distinction between the actual TASEP current J_i^{T} and the mean-field current $J_{\mathrm{MF},i}^{\mathrm{T}} = \rho_i^{\mathrm{T}}\left(1-\rho_{i+1}^{\mathrm{T}}\right)$.

From the moment-identity, Eq. (S19), we can also easily deduce the mass-balance equations [Eq. (2) and the corresponding one for model B] by using the boundary conditions at the tip [Eq. (S5) for model A and (S6) for model B] and the moment-identity for $i = L-1$:

$$\text{model A}: \quad \omega\sum_{i=0}^{L-1}\left(\rho_i^{\mathrm{T}} - \rho_i^{\mathrm{S}}\right) = -\beta\left(\rho_L^{\mathrm{T}} - \langle n_L^{\mathrm{T}} n_L^{\mathrm{S}}\rangle\right)$$

$$\text{model B}: \quad \omega\sum_{i=0}^{L}\left(\rho_i^{\mathrm{T}} - \rho_i^{\mathrm{S}}\right) = 0.$$

In order to determine z we will now insert the domain wall ansatz, Eq. (S16), for the TASEP together with the respective SSEP profile into the respective mass-balance equation. For this purpose, we need to write the mass-balance equations in the continuum limit: Using that $\int_0^1 \mathrm{d}x\ \rho^{\mathrm{T}}(x) = 1-z$ and that $\sum_{i=0}^{L}\rho_i^{\mu} \approx \int_0^L \mathrm{d}i\ \rho^{\mu}(ia) = \frac{1}{a}\int_0^1 \mathrm{d}x\ \rho^{\mu}(x)$ we find to lowest order in a:

$$\text{model A}: \quad \Omega\left(1 - z - \int_0^1 \mathrm{d}x\ \rho^{\mathrm{S}}(x)\right) = -\beta\left(\rho^{\mathrm{T}}(1)\left(1-\rho^{\mathrm{S}}(1)\right)\right) = -\epsilon a\partial_x\rho^{\mathrm{S}}(1)$$

$$\text{model B}: \quad 1 - z - \int_0^1 \mathrm{d}x\ \rho^{\mathrm{S}}(x) = 0$$

where for model A the mean-field assumption $\langle n_L^{\mathrm{T}} n_L^{\mathrm{S}} \rangle \approx \rho_L^{\mathrm{T}} \rho_L^{\mathrm{S}}$ was used again, together with Eq. (S5). Inserting the explicit densities (S17) or (S18) into these expressions, integrating and cancelling common factors results in

$$\text{model A}: \qquad \sigma \cosh\left(\frac{1}{l}\right) = \cosh\left(\frac{1-z}{l}\right) \tag{S20}$$

$$\text{model B}: \qquad \sigma \sinh\left(\frac{1}{l}\right) = \sinh\left(\frac{1-z}{l}\right). \tag{S21}$$

Those directly lead to the expressions for the domain wall given in the main text:

$$\text{model A}: \qquad z = 1 - l \cosh^{-1}\left(\sigma \cosh\left(\frac{1}{l}\right)\right) \tag{S22}$$

$$\text{model B}: \qquad z = 1 - l \sinh^{-1}\left(\sigma \sinh\left(\frac{1}{l}\right)\right). \tag{S23}$$

We see that z is shifted towards the tip (base) for smaller (higher) values of $\sigma := \frac{\alpha}{\alpha+\epsilon}$. It is interesting to note that for model A the limit $z \nearrow 1$ is reached for finite values of the parameters σ, ω and ϵ when $\sigma \cosh\left(\frac{1}{l}\right) = 1$ or $l = 1/\cosh^{-1}(1/\sigma)$, whereas for model B, $z \nearrow 1$ is only possible in the limit $\sigma \to 0$. This is also reflected in the fact that $\sigma \cosh\left(\frac{1}{l}\right) = \cosh\left(\frac{1-z}{l}\right)$ lacks a real solution for z if $\sigma \cosh\left(\frac{1}{l}\right) < 1$. That is, for model A there are parameter regimes where there is no domain wall and where to lowest order the density is zero everywhere. For model B, this case only occurs in the limit where the cytoplasmic density at the base is zero. Even for large l we have $z = 1 - l \sinh^{-1}\left(\sigma \sinh\left(\frac{1}{l}\right)\right) \approx 1 - l \sinh^{-1}\left(\frac{\sigma}{l}\right) \approx 1 - \sigma$ and thus, $z < 1$ unless $\sigma = 0$.

REFINED MEAN-FIELD TASEP DENSITY PROFILE

Certainly, the TASEP profile is not just given by a plain step function but has a smooth form that separates the two density regions via an intermediate region where the density increases strongly but whose width is finite. This is due to fluctuations in the stochastic system that soften this transition. Our first approach to resolve this finite width relies on an idea similar to the method used in [39], namely to split the system into a part around the domain wall and the parts further away from it. By this, only parts of the terms contribute, respectively, and assuming a steep domain wall for the TASEP one can neglect the terms stemming from the exchange with the diffusive lane in this narrow region: Reconsidering equation (S1) we realize that in the steady state it can be approximated as

$$0 = a\partial_x\left(\rho^{\mathrm{T}}\left(\rho^{\mathrm{T}} - 1\right)\right) + \frac{1}{2}a^2\partial_x^2\rho^{\mathrm{T}} + \Omega a\left(\rho^{\mathrm{S}} - \rho^{\mathrm{T}}\right)$$

where we used the continuum limit and a mean-field assumption for the nearest-neighbours on the TASEP: $f_i = \langle n_i^{\mathrm{T}} n_{i+1}^{\mathrm{T}} \rangle \approx \rho_i^{\mathrm{T}} \rho_{i+1}^{\mathrm{T}}$. If we want to investigate the vicinity of the domain wall $x \approx z$ this can be done by considering $\tilde{x} := (x - z)/a$ that is very large away from the domain wall. Using this coordinate system the above equation looks like follows:

$$0 = \partial_{\tilde{x}}\left(\rho^{\mathrm{T}}(\tilde{x})\left(\rho^{\mathrm{T}}(\tilde{x}) - 1\right)\right) + \frac{1}{2}\partial_{\tilde{x}}^2\rho^{\mathrm{T}}(\tilde{x}) + \Omega a\left(\rho^{\mathrm{S}}(\tilde{x}) - \rho^{\mathrm{T}}(\tilde{x})\right).$$

Dropping the term of order $\mathcal{O}(a)$, we end up with

$$\rho^{\mathrm{T}}(\tilde{x})\left(\rho^{\mathrm{T}}(\tilde{x}) - 1\right) + \frac{1}{2}\partial_{\tilde{x}}\rho^{\mathrm{T}}(\tilde{x}) = const$$

where *const* can be estimated from the boundary conditions for $\tilde{x} \to \pm\infty$: we have $\rho^{\mathrm{T}}(x = 0) = 1 - \rho^{\mathrm{T}}(x = 1) = 0$ and $\partial_x\rho^{\mathrm{T}}(x)\big|_{x=0/1} \approx 0$, and hence, using $\tilde{x} \to \pm\infty$ we find that $const \approx 0$. As a result, after integrating $\rho^{\mathrm{T}}(\tilde{x})\left(\rho^{\mathrm{T}}(\tilde{x}) - 1\right) + \frac{1}{2}\partial_{\tilde{x}}\rho^{\mathrm{T}}(\tilde{x}) = 0$ with respect to $\tilde{x}$, using that $\rho^{\mathrm{T}}(z) = \frac{1}{2}$, and rescaling we find

$$\rho^{\mathrm{T}}(x) \approx \frac{1}{2}\left[1 + \tanh\left(\frac{x-z}{a}\right)\right]$$

for the refined mean-field TASEP density profile. Contrary to the step profile, Eq. (S16), it exhibits a finite width that scales like a or inversely proportionally to L. But as one can infer from Fig. 2 it still underestimates the actual width due to fluctuations that are ignored by the mean-field assumption for the nearest-neighbours on the TASEP.

DOMAIN WALL THEORY

This is why we also pursue another approach to refine our prediction for the domain wall, namely by going beyond mean-field theory and treating the domain wall as a random walker that moves in a non-uniform potential with reflecting boundaries. This technique has been introduced in Ref. [48] for the TASEP and, more generally, for shock waves in Ref. [49]. It has been applied to TASEP-LK in Refs. [18, 19] using non-uniform hopping rates. We follow their ideas and describe the domain wall by site-dependent hopping rates

$$w_{l,i} = \frac{J_{\mathrm{LD},i}}{\rho^{\mathrm{T}}_{\mathrm{HD},i} - \rho^{\mathrm{T}}_{\mathrm{LD},i}} \qquad w_{r,i} = \frac{J_{\mathrm{HD},i}}{\rho^{\mathrm{T}}_{\mathrm{HD},i} - \rho^{\mathrm{T}}_{\mathrm{LD},i}} \tag{S24}$$

to the left and right from site i, respectively. Here, $J_{\mathrm{LD},i}$ ($J_{\mathrm{HD},i}$) denotes the steady-state TASEP current at site i under the assumption that site i is in the low-density (high-density) phase, i.e. on the left (right) of the domain wall. $\rho^{\mathrm{T}}_{\mathrm{LD},i}$ and $\rho^{\mathrm{T}}_{\mathrm{HD},i}$ are the respective TASEP densities in the low- and high-density phase. The heuristic reason why the hopping rates have the above form, Eq. (S24), is that the low-density current $J_{\mathrm{LD},i}$ should just correspond to the current arriving at the left of the domain wall and causing the domain wall to move one step to the left. Thereby, at site i the density increases by $\rho^{\mathrm{T}}_{\mathrm{HD},i} - \rho^{\mathrm{T}}_{\mathrm{LD},i}$ at rate $w_{l,i}$. Similarly, the high-density current $J_{\mathrm{HD},i}$ should correspond to the current leaving the region at the right of the domain wall, and causing the domain wall to move one step to the left. This happens at rate $w_{r,i}$ and the density decreases by $\rho^{\mathrm{T}}_{\mathrm{HD},i} - \rho^{\mathrm{T}}_{\mathrm{LD},i}$.

From the detailed balance condition $p_{s,i} w_{r,i} = p_{s,i+1} w_{l,i+1}$ it is easy to see that the stationary distribution of the shock position $p_{s,i}$ satisfies

$$p_{s,i} \propto \frac{1}{w_{l,i}} \exp\left[-\sum_{j=1}^{i-1} \ln\left(\frac{w_{l,j}}{w_{r,j}} \right) \right]. \tag{S25}$$

We will show next that $w_{l,i_z} = w_{r,i_z}$ holds for i_z being the discrete domain wall position ($i_z = z/a$): From Eq. (S1) as well as from the definition of the local TASEP current, Eq. (S9), we know that $J^{\mathrm{T}}_i = J^{\mathrm{T}}_{i-1} + \omega\left(\rho^{\mathrm{S}}_i - \rho^{\mathrm{T}}_i\right)$. Hence, we have

$$J^{\mathrm{T}}_i = J^{\mathrm{T}}_0 + \omega \sum_{j=1}^{i} \left(\rho^{\mathrm{S}}_j - \rho^{\mathrm{T}}_j\right), \qquad \text{or}$$

$$J^{\mathrm{T}}_i = J^{\mathrm{T}}_{L-1} - \omega \sum_{j=i+1}^{L-1} \left(\rho^{\mathrm{S}}_j - \rho^{\mathrm{T}}_j\right).$$

As mentioned after introducing $J_{\mathrm{LD/HD},i}$ in Eq. (S24), $J_{\mathrm{LD/HD},i}$ denotes the TASEP current at site i assuming that this site is in the low-density (high-density) region. That is, we can calculate $J_{\mathrm{LD},i}$ ($J_{\mathrm{HD},i}$) by using the above iterations starting from $i = 0$ ($i = L-1$) and assuming that between site 0 (site $L-1$) and site i the densities are given in the low-density (high-density) phase:

$$J_{\mathrm{LD},i} = J_{\mathrm{LD},0} + \omega \sum_{j=1}^{i} \left(\rho^{\mathrm{S}}_{\mathrm{LD},j} - \rho^{\mathrm{T}}_{\mathrm{LD},j}\right), \qquad \text{or} \tag{S26}$$

$$J_{\mathrm{HD},i} = J_{\mathrm{HD},L-1} - \omega \sum_{j=i+1}^{L-1} \left(\rho^{\mathrm{S}}_{\mathrm{HD},j} - \rho^{\mathrm{T}}_{\mathrm{HD},j}\right). \tag{S27}$$

We want to compare those two currents right at the domain wall $i = i_z$. For this purpose, we use that $J_{\mathrm{LD},j} = J^{\mathrm{T}}_j$ for $j < i_z$ and $J_{\mathrm{HD},j} = J^{\mathrm{T}}_j$ for $j > i_z$ since we chose z in such a way that the densities to the left (right) of the fixed domain wall i_z are in the low-density (high-density) phase. As a result,

$$J_{\mathrm{HD},i_z} - J_{\mathrm{LD},i_z} = J_{\mathrm{HD},L-1} - \omega \sum_{j=i_z+1}^{L-1} \left(\rho^{\mathrm{S}}_{\mathrm{HD},j} - \rho^{\mathrm{T}}_{\mathrm{HD},j}\right) - J^{\mathrm{T}}_0 - \omega \sum_{j=1}^{i_z} \left(\rho^{\mathrm{S}}_j - \rho^{\mathrm{T}}_j\right) = J^{\mathrm{T}}_{L-1} - \omega \sum_{j=0}^{L-1} \left(\rho^{\mathrm{S}}_j - \rho^{\mathrm{T}}_j\right) = 0$$

for both models: $J^{\mathrm{T}}_{L-1} = \beta\left(\rho^{\mathrm{T}}_L - \left\langle n^{\mathrm{T}}_L n^{\mathrm{S}}_L \right\rangle\right)$ for model A and $J^{\mathrm{T}}_{L-1} = \omega\left(\rho^{\mathrm{T}}_L - \rho^{\mathrm{S}}_L\right)$ for model B and, hence, the above holds due to the respective mass-balance equation. It follows that

$$w_{l,i_z} = w_{r,i_z} \tag{S28}$$

and, thus, $\ln\left(\frac{w_{l,i_z}}{w_{r,i_z}}\right)=0$. Similarly, we have $\ln\left(\frac{w_{l,j}}{w_{r,j}}\right)<0$ for $j<i_z$ and $\ln\left(\frac{w_{l,j}}{w_{r,j}}\right)>0$ for $j>i_z$ such that the domain wall preferably walks towards the (fixed) domain wall position i_z than away from it. Therefore, the exponential in Eq. (S25) has a maximum at $i=i_z$ and taking the continuous version of this equation

$$p_s(x)\propto\frac{1}{w_l(x)}\exp\left[-\frac{1}{a}\int_0^x \mathrm{d}x'\ln\left(\frac{w_l(x')}{w_r(x')}\right)\right] \tag{S29}$$

we can use the method of steepest descent to approximate

$$\frac{1}{w_l(x)}\exp\left[-\frac{1}{a}\int_0^x \mathrm{d}x'\ln\left(\frac{w_l(x')}{w_r(x')}\right)\right]\approx\frac{1}{w_l(z)}\exp\left[-\frac{1}{a}\int_0^z \mathrm{d}x'\ln\left(\frac{w_l(x')}{w_r(x')}\right)\right]\exp\left[-\frac{1}{2a}(x-z)^2\partial_x\ln\left(\frac{w_l(x)}{w_r(x)}\right)\Big|_{x=z}\right]$$

where $w_l(x)$ and $w_r(x)$ is the continuous version of $w_{l,i}$ and $w_{r,i}$, respectively. Since $\frac{w_l(x)}{w_r(x)}=\frac{J_{\mathrm{LD}}(x)}{J_{\mathrm{HD}}(x)}$, we conclude

$$\begin{aligned}p_s(x)&\propto\exp\left[-\frac{1}{2a}(x-z)^2\frac{J'_{\mathrm{LD}}(z)J_{\mathrm{HD}}(z)-J'_{\mathrm{HD}}(z)J_{\mathrm{LD}}(z)}{J_{\mathrm{LD}}(z)J_{\mathrm{HD}}(z)}\right]=\exp\left[-\frac{1}{2a}(x-z)^2\frac{J'_{\mathrm{LD}}(z)-J'_{\mathrm{HD}}(z)}{J_{\mathrm{LD}}(z)}\right]= \\ &=\exp\left[-\frac{(x-z)^2}{W(z)^2}\right]\end{aligned} \tag{S30}$$

where we used that $J_{\mathrm{LD}}(z)=J_{\mathrm{HD}}(z)$ [Eq. (S28)] and defined the width $W(z)$ by

$$W^{-2}(z)=\frac{J'_{\mathrm{LD}}(z)-J'_{\mathrm{HD}}(z)}{2aJ_{\mathrm{LD}}(z)}.$$

To find a formula for $\rho^{\mathrm{T}}(x)$ we realize that

$$\rho^{\mathrm{T}}(x)=\rho^{\mathrm{T}}_{\mathrm{HD}}(x)\int_0^x \mathrm{d}\tilde{x}\ p_s(\tilde{x})+\rho^{\mathrm{T}}_{\mathrm{LD}}(x)\int_x^1 \mathrm{d}\tilde{x}\ p_s(\tilde{x})\approx\int_0^x \mathrm{d}\tilde{x}\ p_s(\tilde{x})$$

since as along as the shock position is left (right) of x there is a high-density (low-density) region at x and since we can approximate $\rho^{\mathrm{T}}_{\mathrm{HD}}(x)\approx 1$ and $\rho^{\mathrm{T}}_{\mathrm{LD}}(x)\approx 0$ to lowest order. Using Eq. (S30) we can determine $\rho^{\mathrm{T}}(x)$ as

$$\rho^{\mathrm{T}}(x)\approx\frac{\int_0^x \mathrm{d}\tilde{x}\ \exp\left(-\frac{(\tilde{x}-z)^2}{W(z)^2}\right)}{\int_0^1 \mathrm{d}\tilde{x}\ \mathrm{e}\left(-\frac{(\tilde{x}-z)^2}{W(z)^2}\right)}=\frac{\mathrm{erf}\left(\frac{x-z}{W(z)}\right)+\mathrm{erf}\left(\frac{z}{W(z)}\right)}{\mathrm{erf}\left(\frac{1-z}{W(z)}\right)+\mathrm{erf}\left(\frac{z}{W(z)}\right)} \tag{S31}$$

where erf is the error function. Here, we used that we need to normalize $p_s(x)$ such that $\int_0^1 \mathrm{d}\tilde{x}\ p_s(\tilde{x})=1$.

In order to use this formula we still need to determine the width $W(z)$ more concretely. For this purpose, we must make some assumption on how we treat the diffusive (SSEP) lane when considering the low- and high-density currents. We are not aware of previous attempts that apply domain wall theory in case where a TASEP is coupled to another lattice that is occupied stochastically as well. Then the attachment and detachment rates for the TASEP not only depend on the TASEP occupancy but also on the occupancy on the other lattice. The difficulty with this situation is that it is a priori not clear if one should assume that the occupancy on the coupled lattice is fixed, that is, does not change very much if the domain wall is shifted towards the left or right, or if one should look at the momentary steady-state density corresponding to a certain position of the domain wall. For simplicity, we chose the first ansatz that seems to be working well. That means, we use Eqs. (S17) and (S18) for the SSEP density profile with the calculated fixed position of the domain wall z given by Eqs. (S20) and (S21) and we assume that this SSEP density does not change considerably when the domain wall is shifted shortly to some other position $\neq z$, i.e. $\rho^{\mathrm{S}}_{\mathrm{LD}}(x)=\rho^{\mathrm{S}}_{\mathrm{HD}}(x)=\rho^{\mathrm{S}}(x)$.

With that in mind, using Eqs. (S26) and (S27), we find that

$$J_{\mathrm{LD}}(x)=\Omega\int_0^x \mathrm{d}\tilde{x}\ \rho^{\mathrm{S}}(\tilde{x})$$

and obtain

$$\begin{aligned}&\text{model A}: \qquad J_{\mathrm{HD}}(x)=-\Omega\int_x^1 \mathrm{d}\tilde{x}\ \left(\rho^{\mathrm{S}}(\tilde{x})-1\right)-\epsilon a\partial_x\rho^{\mathrm{S}}(1)\\ &\text{model B}: \qquad J_{\mathrm{HD}}(x)=-\Omega\int_x^1 \mathrm{d}\tilde{x}\ \left(\rho^{\mathrm{S}}(\tilde{x})-1\right)\end{aligned}$$

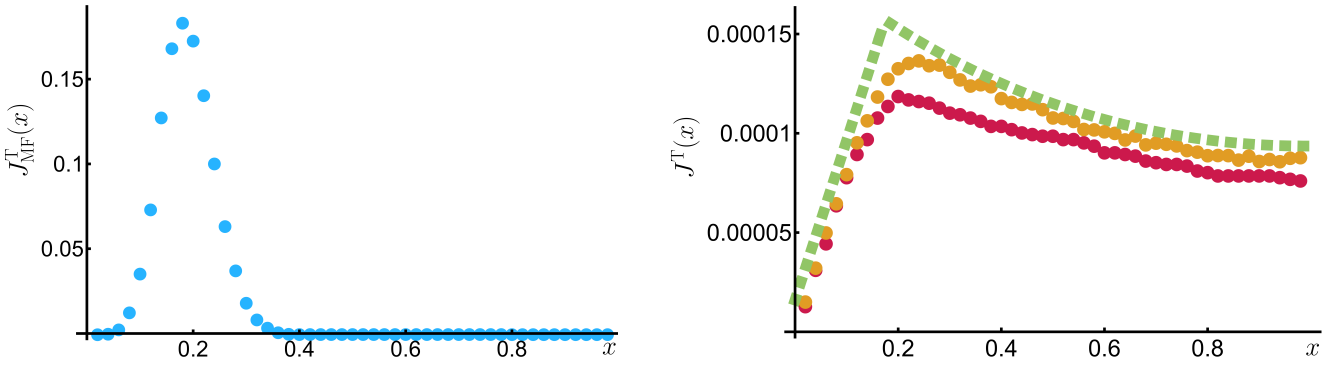

FIG. S2. Comparison between the mean-field current (left panel) and the actual current (right panel) for model A with $L = 50$, $\beta = 0.2$, $\Omega = 0.001$, $\alpha = 0.1$ and $\epsilon = 0.025$. The mean-field current (filled blue (grey) circles) is obtained from the average densities in a simulation. On the right, we show the actual currents as measured directly in a simulation (filled red (dark grey) circles), as obtained from the average densities and the nearest neighbour correlations in the simulation using $J_i^{\mathrm{T}} = \rho_i^{\mathrm{T}} - f_i$ (filled orange (grey) circles) and as predicted by the theory from Eq. (S32) (dotted green (light grey) curve).

where we used that $\rho^{\mathrm{T}}_{\mathrm{LD}}(x) \approx 0$ and $\rho^{\mathrm{T}}_{\mathrm{HD}}(x) \approx 1$. As a result, $J'_{\mathrm{LD}}(x) = \Omega\rho^{\mathrm{S}}(x)$ and $J'_{\mathrm{HD}}(x) = \Omega\left(\rho^{\mathrm{S}}(x) - 1\right)$ so that

$$W(z) = \sqrt{2a\int_0^z \mathrm{d}\tilde{x}\ \rho^{\mathrm{S}}(\tilde{x})} = \sqrt{2\sigma a l \sinh\left(\frac{z}{l}\right)}$$

where the last equality results from integrating ρ^{S} and then using the defining equation for z. Interestingly, the result in this form agrees for both models.

We observe that the width $W(z)$ increases with increasing z or decreasing distance from the tip. Furthermore, in the limit $a \to 0$ it holds that $l \to 0$ (if we keep ϵ constant) so that we can approximate $\operatorname{arccosh}\left(\sigma\cosh\left(\frac{1}{l}\right)\right) \approx \frac{1}{l} + \ln(\sigma)$ and, similarly, $\operatorname{arcsinh}\left(\sigma\sinh\left(\frac{1}{l}\right)\right) \approx \frac{1}{l} + \ln(\sigma)$. Thus, $z \approx -l\ln(\sigma)$ for both models in the limit $a \to 0$ [Eqs. (S22), (S23)]. With that we find

$$W(z) \approx \frac{a^{\frac{3}{4}}\epsilon^{\frac{1}{4}}}{\Omega^{\frac{1}{4}}}\left(1-\sigma^2\right)^{\frac{1}{2}}$$

in the limit $a \to 0$ and so the width of the domain wall decreases with decreasing a or increasing number of sites L.

Note that in order to calculate the position of the domain wall z by the mass-balance equation, we can use the step function instead of the refined profiles. This is due to the fact that there the errors more or less cancel since only the sum $\sum_{i=0}^{L}\rho_i^{\mathrm{T}}$ over the densities on the left and on the right of the domain wall enters. However, this approximation gets worse the closer the calculated z is to 0 or 1 since then, the errors are not symmetric anymore. As a result, also the approximation, Eq. (S31), deteriorates. Certainly, if there is no solution for z, e.g. for some parameters in model A, we can not use this ansatz either. Furthermore, if ϵ is too large, we expect our approximation that $\rho^{\mathrm{S}}(x)$ does not change when the domain wall is shifted to deteriorate as well.

COVARIANCES AND CURRENTS

Another point we want to emphasize is that in the system the nearest-neighbour correlations of the TASEP significantly modify the TASEP current in the sense that the mean-field prediction for it overestimates the current by orders of magnitude. The reason lies in the covariances that reach very high values of around 0.2 in the region of the domain wall (see for example Fig. 2). As we have shown above in Eq. (S19) the nearest-neighbour correlator $f_i = \langle n_i^{\mathrm{T}} n_{i+1}^{\mathrm{T}}\rangle$ is given by $f_i = \rho_i^{\mathrm{T}} + \omega\sum_{j=0}^{i}\left(\rho_j^{\mathrm{T}} - \rho_j^{\mathrm{S}}\right)$. Therefore, the covariances are given by

$$\mathrm{Cov}_i = \rho_i^{\mathrm{T}}(1-\rho_{i+1}^{\mathrm{T}}) + \omega\sum_{j=0}^{i}(\rho_j^{\mathrm{T}} - \rho_j^{\mathrm{S}}) = J^{\mathrm{T}}_{\mathrm{MF},i} + \omega\sum_{j=0}^{i}(\rho_j^{\mathrm{T}} - \rho_j^{\mathrm{S}}).$$

Due to the first term, the mean-field current, which is large (≈ 0.2) in the region of the domain wall, also the covariances are non-zero and large there. However, since the mean-field current gives the main contribution to the

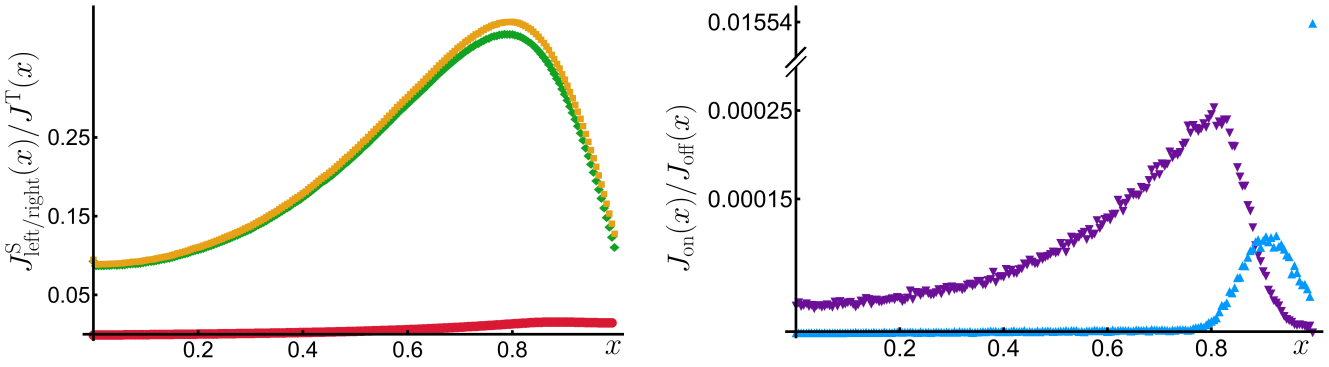

FIG. S3. Illustration of the different currents in model A with $L = 200$, $\beta = 0.2$, $\Omega = 0.1$, $\alpha = 0.1$ and $\epsilon = 1.55$. This choice of parameters corresponds to a domain wall position of $z \approx 0.88$ so that the TASEP occupancy is concentrated on a small region around the tip. The left panel shows a comparison of the current $J^{\mathrm{T}}(x)$ on the TASEP (filled red (dark grey) circles) and the currents $J^{\mathrm{S}}_{\mathrm{left}}(x)$ on the SSEP towards the base (left) (filled orange (light grey) squares) and $J^{\mathrm{S}}_{\mathrm{right}}(x)$ towards the tip (right) (filled green (grey) diamonds). The TASEP current corresponds to the net SSEP current towards the base, that is the difference between the SSEP current towards the base and towards the tip. Both SSEP currents, however, are much larger than the TASEP current suggesting that the motors are mainly transported by the cytoplasm (SSEP) rather than by the filament (TASEP). The right panel shows both the attachment current $J_{\mathrm{on}}(x)$ (filled purple (dark grey) downward facing triangles) and the detachment current $J_{\mathrm{off}}(x)$ (light blue (light grey) upward facing triangles). Both currents are enhanced considerably towards the tip region. As a result, motor exchange happens primarily around the tip region. Furthermore, the maximum of the attachment current is located a little further away from the tip than the maximum of the detachment current so that typically motors attach to the filament, walk a short distance on the filament, detach near the tip and can then diffuse in the cytoplasm back to the cell body or reattach again. Note that the detachment current is particularly high at the last site due to the higher detachment rate at the tip. All currents are measured directly from the simulation that is counting the number of jumps per time.

covariances, this implies that the actual current

$$J_i^{\mathrm{T}} = \rho_i^{\mathrm{T}} - f_i = \omega \sum_{j=0}^{i} \left(\rho_j^{\mathrm{S}} - \rho_j^{\mathrm{T}}\right) = J^{\mathrm{T}}_{\mathrm{MF},i} - \mathrm{Cov}_i \tag{S32}$$

is much smaller than predicted from a mean-field theory. To illustrate this further, in Fig. S2 we show a comparison of the mean-field current on the left as obtained from simulations using the average densities, and of the actual current on the right as obtained directly from the simulation (filled red (dark grey) circles), from the average densities and nearest-neighbour correlations in the simulation (filled orange (grey) circles) and from Eq. (S32) (dotted green (light grey) curve). Certainly, this discrepancy scales with Ω (and the other parameters) and the case shown here is extreme as $\Omega = 0.001$ was chosen. However, the fact that both currents differ by orders of magnitude is robust and also occurs for Ω being of the order of the other jump rates [Fig. S3]. This shows that a mean-field description fails to capture essential properties of our model system.

Furthermore, from the fact that the covariances are non-zero everywhere $\mathrm{Cov}_i \geq 0$ and that we can rewrite

$$\begin{aligned}\mathrm{Cov}_i &= \langle n_i^{\mathrm{T}} n_{i+1}^{\mathrm{T}} \rangle - \rho_i^{\mathrm{T}} \rho_{i+1}^{\mathrm{T}} = \mathrm{Prob}\{n_i^{\mathrm{T}}, n_{i+1}^{\mathrm{T}}\} - \mathrm{Prob}\{n_i^{\mathrm{T}}\}\mathrm{Prob}\{n_{i+1}^{\mathrm{T}}\} = \\ &= \mathrm{Prob}\{n_i^{\mathrm{T}}|n_{i+1}^{\mathrm{T}}\}\mathrm{Prob}\{n_{i+1}^{\mathrm{T}}\} - \mathrm{Prob}\{n_i^{\mathrm{T}}\}\mathrm{Prob}\{n_{i+1}^{\mathrm{T}}\}\end{aligned}$$

we can conclude that $\mathrm{Prob}\{n_i^{\mathrm{T}}|n_{i+1}^{\mathrm{T}}\} \geq \mathrm{Prob}\{n_i^{\mathrm{T}}\}$. And from using a similar argument and only interchanging the roles of i and $i+1$ we find $\mathrm{Prob}\{n_{i+1}^{\mathrm{T}}|n_i^{\mathrm{T}}\} \geq \mathrm{Prob}\{n_{i+1}^{\mathrm{T}}\}$. This tells us that, in particular from the domain wall region onwards where covariances are high, the motors preferentially cluster and hinder each other effectively so that the mean time a particle spends at a certain site is increased considerably with respect to freely moving motors. Eventually, this leads to the substantial difference between the actual current and the mean-field current.

Potentially, those results are also important from a biological point of view. In case of an enhanced detachment rate at the filament's tip (model A), tip localisation is facilitated [Fig. 3] and large traffic jams can be avoided. In this case there is only high filament density in a small region around the tip so that motors spend more time in the tip region than in the other part of the filament, a feature that might be favoured biologically as then the motors or their cargo might have more time to perform the necessary tasks at the tip. Furthermore, transport to the tip might be strongly promoted by diffusion in the cytoplasm (SSEP) whose currents in both the direction of the tip

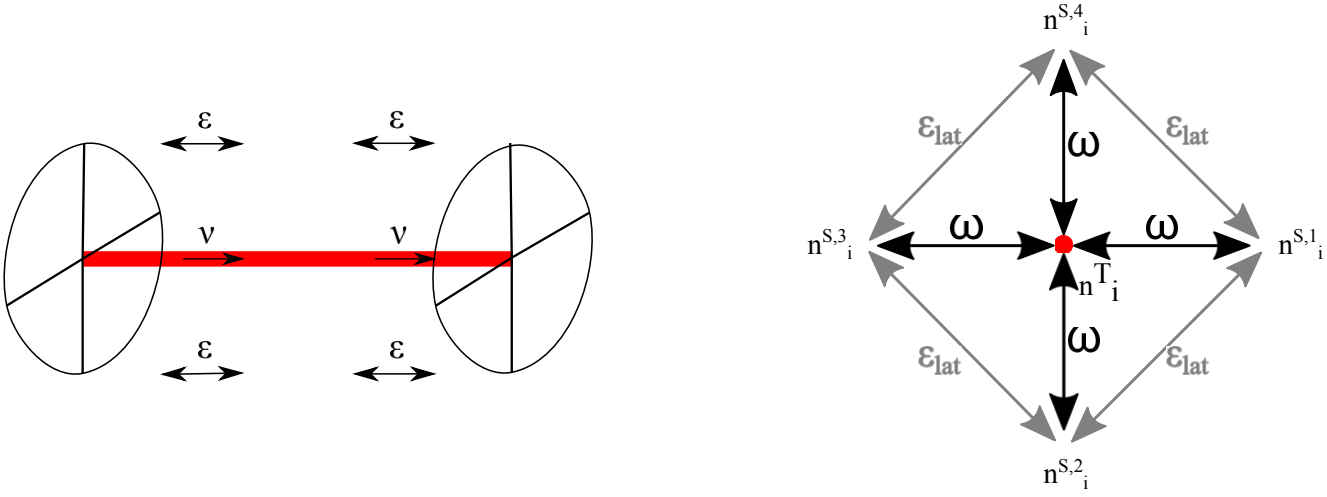

FIG. S4. Illustration of the generalised model with several (here: 4) lanes for diffusion: the three-dimensional view is shown on the left-hand side, the profile is illustrated on the right-hand side. As before the dynamics on the filament (red) are given by a TASEP with jump rate $\nu = 1$ but now the dynamics in the cytoplasm is modelled by several lanes for diffusion (blue), each with diffusive rate ϵ and respecting the exclusion. The lanes for diffusion are arranged in a cylinder-like fashion around the TASEP and each can interact with the TASEP by attachment/detachment processes at rate ω respecting the exclusion. Apart from the diffusion along the cylinder axis there is also lateral diffusion between neighbouring lanes of diffusion. This diffusion happens at rate $\epsilon_{\rm lat}$ and again respects the exclusion. At the base (not shown) there is influx at rate α into every lane for diffusion and outflux at the diffusive rate ϵ.

and of the base significantly exceed the filament (TASEP) current [Fig. S3]. Certainly, in case of our original model where exclusion in the cytoplasm occurs at occupancy 1, the motors cannot really bypass each other, so that the motors do not circulate very often. This, however, should be greatly enhanced in the generalised model with carrying capacity $N_{\rm max} > 1$ (see next chapter) or in a real biological system where the motors can overtake each other in the cytoplasm. The fact that the filament current is strongly suppressed by excluded volume effects might also be beneficial from a biological point of view as every motor step on the filament consumes ATP contrary to diffusion in the cytoplasm. Thus, transport of motors by the cytoplasm rather than by the filament might be advantageous energetically. Moreover, both the attachment and detachment current $J_{\rm on}$ and $J_{\rm off}$ are mainly restricted to the tip area [Fig. S3] so that motor exchange between the filament and the cytoplasm occurs primarily near the tip where the cargo is used. Taken together, tip localisation and the suppression of the filament current might be beneficial from a biological point of view as then energy consumption is low and motors could be efficiently transported to the tip by the cytoplasm. Near the tip they attach to the filament, have an enhanced residence time on the filament due to steric hindrance between the motors and then detach at the tip back into the cytoplasm.

CYLINDRICAL GEOMETRY WITH SEVERAL LANES FOR DIFFUSION

Finally, we want to deal with a generalisation of our model where instead of one lane for diffusion we have several lanes for diffusion arranged on a cylinder around the filament. For an illustration of the case with $N_{\rm diff} = 4$ lanes for diffusion please refer to Fig. S4. The three-dimensional view is shown on the left-hand side, the profile is illustrated on the right-hand side. As before the dynamics on the filament (red) are given by a TASEP lane with jump rate $\nu = 1$ but now the dynamics in the cytoplasm is modelled by several lanes for diffusion (blue), each with diffusive rate ϵ and respecting the exclusion. The lanes for diffusion are arranged in a cylinder-like fashion around the TASEP lane, and each can interact with the TASEP lane by attachment/detachment processes at rate ω respecting the exclusion. Apart from the diffusion along the cylinder axis there is also lateral diffusion between neighbouring lanes of diffusion. This diffusion happens at rate $\epsilon_{\mathbf{lat}}$ and again respects the exclusion. At the base (not shown) there is influx at rate α into every lane for diffusion and outflux at the diffusive rate ϵ.

In the following, we will show that we can reduce the steady-state behaviour of this more elaborate model to the steady-state behaviour of our model by scaling the parameters for diffusion and attachment/detachment by the number of lanes for diffusion $N_{\rm diff}$: $\omega \to \omega N_{\rm diff}$, $\epsilon \to \epsilon N_{\rm diff}$. Here, we only consider the case where we have the same attachment and detachment kinetics at the tip than in the bulk (model B), but an analogous generalisation

and argument can be done for model A or different rates for attachment and detachment. Let us denote by n_i^{T} the occupancy at site i of the TASEP (as before) and by $n_i^{\mathrm{S},m}$ the occupancy at site i of the $m = 1, \ldots, N_{\mathrm{diff}}$-th lane for diffusion. We start by $m = 1$ at an arbitrary lane for diffusion and then consecutively number the lanes for diffusion in clockwise order. Since the lanes are arranged on a cylinder we have periodic boundary conditions and identify $n_i^{\mathrm{S},N_{\mathrm{diff}}+1} \equiv n_i^{\mathrm{S},1}$. With this convention we have the following bulk master equations, written straight away in terms of the averages over occupancies $\rho_i^{\mu,m} = \langle n_i^{\mu,m} \rangle$ and $f_i = \langle n_i^{\mathrm{T}} n_{i+1}^{\mathrm{T}} \rangle$:

$$\begin{aligned}
\partial_t \rho_i^{\mathrm{T}} &= \rho_{i-1}^{\mathrm{T}} - f_{i-1} - \rho_i^{\mathrm{T}} + f_i + \sum_{m=1}^{N_{\mathrm{diff}}} \omega \left(\langle n_i^{\mathrm{S},m}(1 - n_i^{\mathrm{T}}) \rangle - \langle n_i^{\mathrm{T}}(1 - n_i^{\mathrm{S},m}) \rangle \right) \\
\partial_t \rho_i^{\mathrm{S},m} &= \epsilon \left(\rho_{i+1}^{\mathrm{S},m} + \rho_{i-1}^{\mathrm{S},m} - 2\rho_i^{\mathrm{S},m} \right) + \omega \left(\langle n_i^{\mathrm{T}}(1 - n_i^{\mathrm{S},m}) \rangle - \langle n_i^{\mathrm{S},m}(1 - n_i^{\mathrm{T}}) \rangle \right) + \epsilon_{\mathrm{lat}} \left(\rho_i^{\mathrm{S},m+1} + \rho_i^{\mathrm{S},m-1} - 2\rho_i^{\mathrm{S},m} \right).
\end{aligned} \tag{S33}$$

At the base we find

$$\begin{aligned}
\partial_t \rho_0^{\mathrm{T}} &= -\rho_0^{\mathrm{T}} + f_0 + \sum_{m=1}^{N_{\mathrm{diff}}} \omega \left(\langle n_0^{\mathrm{S},m}(1 - n_0^{\mathrm{T}}) \rangle - \langle n_0^{\mathrm{T}}(1 - n_0^{\mathrm{S},m}) \rangle \right) \\
\partial_t \rho_0^{\mathrm{S},m} &= \alpha - (\alpha + \epsilon)\rho_0^{\mathrm{S},m} + \epsilon \left(\rho_1^{\mathrm{S},m} - \rho_0^{\mathrm{S},m} \right) + \omega \left(\langle n_0^{\mathrm{T}}(1 - n_0^{\mathrm{S},m}) \rangle - \langle n_0^{\mathrm{S},m}(1 - n_0^{\mathrm{T}}) \rangle \right) + \epsilon_{\mathrm{lat}} \left(\rho_0^{\mathrm{S},m+1} + \rho_0^{\mathrm{S},m-1} - 2\rho_0^{\mathrm{S},m} \right)
\end{aligned} \tag{S34}$$

and at the tip

$$\begin{aligned}
\partial_t \rho_L^{\mathrm{T}} &= \rho_{L-1}^{\mathrm{T}} - f_{L-1} + \sum_{m=1}^{N_{\mathrm{diff}}} \omega \left(\langle n_L^{\mathrm{S},m}(1 - n_L^{\mathrm{T}}) \rangle - \langle n_L^{\mathrm{T}}(1 - n_L^{\mathrm{S},m}) \rangle \right) \\
\partial_t \rho_L^{\mathrm{S},m} &= \epsilon \left(\rho_{L-1}^{\mathrm{S},m} - \rho_L^{\mathrm{S},m} \right) + \omega \left(\langle n_L^{\mathrm{T}}(1 - n_L^{\mathrm{S},m}) \rangle - \langle n_L^{\mathrm{S},m}(1 - n_L^{\mathrm{T}}) \rangle \right) + \epsilon_{\mathrm{lat}} \left(\rho_L^{\mathrm{S},m+1} + \rho_L^{\mathrm{S},m-1} - 2\rho_L^{\mathrm{S},m} \right).
\end{aligned} \tag{S35}$$

Due to the exclusion property on both the TASEP as well as on the lanes for diffusion the state space of the system is finite. Furthermore, it is an irreducible continuous-time Markov process so there exists a unique steady-state. This is important since then the cylindrical symmetry of the system must be reflected in this steady-state. This is why we can assume that in the steady-state $\left\langle n_i^{\mathrm{S},m} \right\rangle = \left\langle n_i^{\mathrm{S},n} \right\rangle$ and $\langle n_i^{\mathrm{S},m} n_i^{\mathrm{T}} \rangle = \langle n_i^{\mathrm{S},n} n_i^{\mathrm{T}} \rangle$ holds for all m, n. As a result, the terms proportional to ϵ_{lat} drop out in Eqs. (S33)-(S35) and we can define the total occupancy at site i in the cytoplasm

$$n_i^{\mathrm{S}} \equiv \sum_{m=1}^{N_{\mathrm{diff}}} n_i^{\mathrm{S},m}$$

and the corresponding average ρ_i^{S} as the sum of the (average) occupancies at sites i of all the lanes for diffusion taken together. Using this quantity we can rewrite Eqs. (S33)-(S35) in steady-state as follows:

$$\begin{aligned}
0 &= \rho_{i-1}^{\mathrm{T}} - f_{i-1} - \rho_i^{\mathrm{T}} + f_i + \omega \left(\langle n_i^{\mathrm{S}}(1 - n_i^{\mathrm{T}}) \rangle - \langle n_i^{\mathrm{T}}(N_{\mathrm{diff}} - n_i^{\mathrm{S}}) \rangle \right) \\
0 &= \epsilon \left(\rho_{i+1}^{\mathrm{S}} + \rho_{i-1}^{\mathrm{S}} - 2\rho_i^{\mathrm{S}} \right) + \omega \left(\langle n_i^{\mathrm{T}}(N_{\mathrm{diff}} - n_i^{\mathrm{S}}) \rangle - \langle n_i^{\mathrm{S}}(1 - n_i^{\mathrm{T}}) \rangle \right)
\end{aligned} \tag{S36}$$

for the bulk master equation,

$$\begin{aligned}
0 &= -\rho_0^{\mathrm{T}} + f_0 + \omega \left(\langle n_0^{\mathrm{S}}(1 - n_0^{\mathrm{T}}) \rangle - \langle n_0^{\mathrm{T}}(N_{\mathrm{diff}} - n_0^{\mathrm{S}}) \rangle \right) \\
0 &= \alpha N_{\mathrm{diff}} - (\alpha + \epsilon)\rho_0^{\mathrm{S}} + \epsilon \left(\rho_1^{\mathrm{S}} - \rho_0^{\mathrm{S}} \right) + \omega \left(\langle n_0^{\mathrm{T}}(N_{\mathrm{diff}} - n_0^{\mathrm{S}}) \rangle - \langle n_0^{\mathrm{S}}(1 - n_0^{\mathrm{T}}) \rangle \right)
\end{aligned} \tag{S37}$$

for the base and

$$\begin{aligned}
0 &= \rho_{L-1}^{\mathrm{T}} - f_{L-1} + \omega \left(\langle n_L^{\mathrm{S}}(1 - n_L^{\mathrm{T}}) \rangle - \langle n_L^{\mathrm{T}}(N_{\mathrm{diff}} - n_L^{\mathrm{S}}) \rangle \right) \\
0 &= \epsilon \left(\rho_{L-1}^{\mathrm{S}} - \rho_L^{\mathrm{S}} \right) + \omega \left(\langle n_L^{\mathrm{T}}(N_{\mathrm{diff}} - n_L^{\mathrm{S}}) \rangle - \langle n_L^{\mathrm{S}}(1 - n_L^{\mathrm{T}}) \rangle \right)
\end{aligned} \tag{S38}$$

for the tip. From these equations it becomes apparent that the cylindrical system with N_{diff} lanes for diffusion is equivalent to the above mentioned generalisation of our model where exclusion on the filament does not happen at occupancy of 1 but at a maximal occupancy or carrying capacity of $N_{\max} = N_{\mathrm{diff}}$ that is reflected in the term $N_{\mathrm{diff}} - n_i^{\mathrm{S}}$. To show that the steady-state behaviour of those two generalisations of our model are cast by the steady-state behaviour of our model, we next introduce the quantity

$$\tilde{n}_i^{\mathrm{S}} = \frac{1}{N_{\mathrm{diff}}} n_i^{\mathrm{S}} = \frac{1}{N_{\mathrm{diff}}} \sum_{m=1}^{N_{\mathrm{diff}}} n_i^{\mathrm{S},m}$$

and the corresponding average occupancy $\tilde{\rho}_i^{\mathrm{S}}$ at site i of one lane for diffusion. In terms of $\tilde{n}_i^{\mathrm{S}}$ we find

$$\begin{aligned} 0 &= \rho_{i-1}^{\mathrm{T}} - f_{i-1} - \rho_i^{\mathrm{T}} + f_i + \omega N_{\mathrm{diff}} \left(\tilde{\rho}_i^{\mathrm{S}} - \rho_i^{\mathrm{T}}\right) \\ 0 &= \epsilon N_{\mathrm{diff}} \left(\tilde{\rho}_{i+1}^{\mathrm{S}} + \tilde{\rho}_{i-1}^{\mathrm{S}} - 2\tilde{\rho}_i^{\mathrm{S}}\right) + \omega N_{\mathrm{diff}} \left(\rho_i^{\mathrm{T}} - \tilde{\rho}_i^{\mathrm{S}}\right) \end{aligned} \tag{S39}$$

for the bulk and

$$0 = -\rho_0^{\mathrm{T}} + f_0 + \omega N_{\mathrm{diff}} \left(\tilde{\rho}_0^{\mathrm{S}} - \rho_0^{\mathrm{T}}\right) \tag{S40}$$

$$0 = \alpha N_{\mathrm{diff}} - (\alpha + \epsilon) N_{\mathrm{diff}} \tilde{\rho}_0^{\mathrm{S}} + \epsilon N_{\mathrm{diff}} \left(\tilde{\rho}_1^{\mathrm{S}} - \tilde{\rho}_0^{\mathrm{S}}\right) + \omega N_{\mathrm{diff}} \left(\rho_0^{\mathrm{T}} - \tilde{\rho}_0^{\mathrm{S}}\right)$$

$$0 = \rho_{L-1}^{\mathrm{T}} - f_{L-1} + \omega N_{\mathrm{diff}} \left(\tilde{\rho}_L^{\mathrm{S}} - \rho_L^{\mathrm{T}}\right) \tag{S41}$$

$$0 = \epsilon N_{\mathrm{diff}} \left(\tilde{\rho}_{L-1}^{\mathrm{S}} - \tilde{\rho}_L^{\mathrm{S}}\right) + \omega N_{\mathrm{diff}} \left(\rho_L^{\mathrm{T}} - \tilde{\rho}_L^{\mathrm{S}}\right)$$

for the base and the tip where we used that $\langle \tilde{n}_i^{\mathrm{S}} (1 - n_i^{\mathrm{T}}) \rangle - \langle n_i^{\mathrm{T}} (1 - \tilde{n}_i^{\mathrm{S}}) \rangle = \tilde{\rho}_i^{\mathrm{S}} - \rho_i^{\mathrm{T}}$.
In summary, if we replace $\omega \to \omega N_{\mathrm{diff}}$, $\epsilon \to \epsilon N_{\mathrm{diff}}$ and $\alpha \to \alpha N_{\mathrm{diff}}$ in our model we can deduce from the steady-state behaviour of our model the steady-state behaviour of these generalised models. Certainly, to stay within the scope of our considerations, this implies that we need ωN_{diff} to be much smaller than 1 (order a) and $\epsilon N_{\mathrm{diff}}$ to be of the order of 1 implying that the "total attachment/detachment rate" ΩN_{diff} and the "total diffusion rate" $\epsilon N_{\mathrm{diff}}$ should be of the order of the hopping constant $\nu = 1$.

3 Coupling filament length regulation to motor transport

Living matter evades the decay to equilibrium.
(Erwin Schrödinger)

The goal of this chapter is to summarize the most important findings of our project on the influence of directed transport and diffusion on length regulation in confined geometries. The corresponding manuscript has been published in *Physical Review E* **98**, 012410 (2018). This chapter is based on and uses parts of this publication [2], which is also reprinted in section 3.5.

3.1 Motivation

Motivated by the finding of the previous project that diffusion may play an important role for transport in confined geometries, the goal of this project was to examine whether diffusion might also be important for length regulation of filaments in confined geometries. To this end, we extended the model of the previous project by additionally accounting for a length dynamics of the lattices. In particular, we took inspiration from experiments where motor-induced depolymerization at the tip of microtubules was observed [58–62] (see also section 1.1).

While this choice reflects particular biological findings, our goal was not to quantitatively model a specific system – similar as in the case of the previous project. Instead, the model presented in the following section 3.2 allows us to study the role of diffusion and active transport for length regulation in confinement. It should be understood as an exemplary model that identifies certain principles that may be important also for more elaborate models or biological systems.

As mentioned in the abstract of the project, the driving questions are:
What influence does a finite diffusion speed have on length regulation in confinement? Could it, in combination with active transport, change the underlying self-organization process qualitatively?

3.2 Model

We consider the two-lane lattice-gas model as illustrated in Fig. 3.1. As in the model discussed in the previous chapter (Fig. 2.1), directed transport is modeled by a TASEP (see also section 1.2.1) and this TASEP lane is coupled to a second lane for diffusion (diffusion lane; DL). In contrast to the previous model, however, diffusion is not subject to exclusion. This

is partially in order to avoid ambiguity that might arise from the additional length dynamics of the lattices (see below). On the DL motors thus hop at equal rate ϵ to the left and right, irrespective of the number of motors at the target site. Similarly, detachment from the TASEP lane to the DL occurs always at rate ω, independent of the occupancy on the DL. Attachment from the DL to the TASEP lane at rate ω is subject to exclusion as in the previous model. The crucial additional element of this model is that both lattices shrink and grow. While growth (polymerization) occurs spontaneously at rate γ, shrinkage (depolymerization) is motor-dependent. If a motor reaches the right end of the TASEP lane, it depolymerizes the TASEP lane and simultaneously the DL by one lattice site. At the same time, all motors that have been on the last site of the TASEP lane or DL before the shrinkage event, including the one responsible for the depolymerization, are shifted to the new DL tip site. This ensures that there is mass conservation at the tip. If there were exclusion on the DL an implementation of the mass conservation would not be as straightforward. One could, for instance, implement a rule that somehow shifts all particles on the DL towards the base in order to make space for the depolymerizing (and detaching) motor at the tip of the TASEP lane. Alternatively, the depolymerizing motor could be put to the closest empty site on the DL. In both cases, however, one would introduce a somewhat artificial flux.

For the analysis of the model and its dynamics, we focused on the dependence on the spontaneous polymerization rate γ and rescaled time in a way that $\nu \equiv 1$. The other parameters were fixed as follows: As in the previous model, attachment and detachment are supposed to be slow compared to the dynamics along the TASEP, corresponding to the processivity of the molecular motors (see also section 1.1). So, we chose $\omega = 1/L_0$ where $L_0 = 100$ is the initial length of the system[1]. To obtain a diffusion constant that is of the order of molecular motor diffusion in the cytosol, we chose $\epsilon = 5.0$. The influx rate $\alpha = 0.1$ is chosen so that the reservoir density is rather small. Finally, the depolymerization rate is $\delta = 1.0$.

3.3 Results

Based on previous studies where motor-induced shrinkage is coupled to spontaneous growth, we would have expected to observe a length dynamics with a well-defined, self-controlled average length and stochastic fluctuations around this average value (e.g. [82] or see [69] for a review on different length regulation mechanisms). While this is indeed the case for small growth rates γ (see Fig. 5(a) in [2] or in the publication reprint in section 3.5), a qualitatively different behavior is observed for large growth rates[2]. In this case, the system exhibits extended phases of growth and shrinkage (see Fig. 5(b) in [2] or in the publication reprint in section 3.5). On closer inspection, one realizes that this temporal dynamics is dominated by an

[1] Note that since we focus on the steady-state behavior, the initial length L_0 (for fixed $\omega = \Omega/L_0$) does not modify the dynamics in any way.

[2] "Large growth" rates should always be understood as intermediate growth rates $\gamma \lessapprox 0.2$. Indeed Ref. [82] suggests that length regulation is not possible for much larger growth rates. Intuitively, for $\gamma > 1$, there can be no length regulation because then growth is so fast that the motors can not catch up with the growing tip.

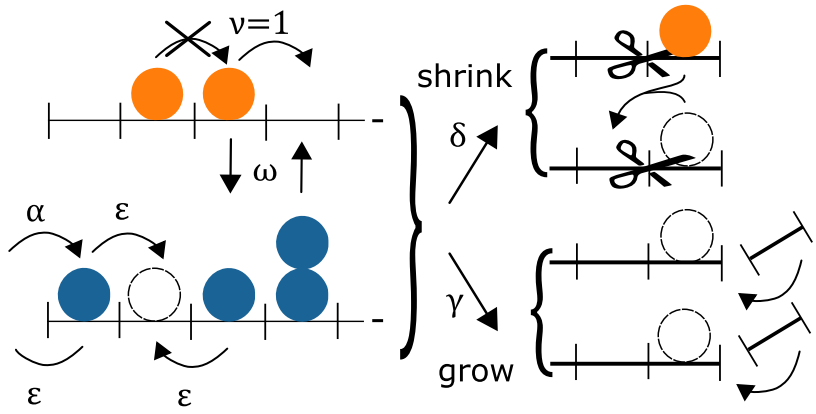

Figure 3.1 | Illustration of the conceptual model (taken from [2]). The lattice-gas model is composed of two lanes which model directed transport (TASEP; see also section 1.2.1) and diffusion (diffusion lane; DL), respectively. Motion on the TASEP lane is subject to exclusion whereas motion on the DL is not. Correspondingly, a motor on the DL hops to its left or right neighboring site at rate ϵ each, irrespective of the occupancy there. Attachment of motors from the DL to the TASEP lane at rate ω only occur if the site on the TASEP lane is empty whereas detachment from the TASEP lane to the DL occurs always at this rate ω. Furthermore, as compared to the model discussed in the previous chapter (Fig. 2.1), the lattices can also grow and shrink. Growth (polymerization) occurs spontaneously at rate γ whereas shrinkage (depolymerization) is motor-induced. If a motor reaches the tip of the TASEP lane, at rate δ it shrinks the TASEP and the diffusion lane by one lattice site and detaches from the TASEP to the DL. Simultaneously, all motors that were at the tip (of either the TASEP or the DL) before the shortening event, including the one responsible for it, are shifted to the new DL tip site. As in the previous model (Fig. 2.1), there is influx from the reservoir on the left into the DL at rate α and outflux at rate ϵ.

underlying quasi-periodic length-changing pattern[3]. To quantify this pattern, we considered the following ensemble autocorrelation function $C(t)$:

$$C(t) := \langle \mathrm{Cov}\left(L\left(\tau\right), L\left(\tau + t\right)\right)\rangle / \sigma^2 \,, \tag{3.1}$$

where $L(\tau)$ and $L(t+\tau)$ denote the lengths at times τ and $t+\tau$, respectively, and σ is the standard deviation of the length. Furthermore, $\mathrm{Cov}(X, Y)$ is the covariance between random variables X and Y and $\langle \ldots \rangle$ denotes the ensemble average. As shown in Fig. 4 in [2] or in the publication reprint in section 3.5, for small growth rates γ this autocorrelation function decays exponentially with time. This corresponds to a typical situation where there is an internal relaxation time over which a perturbation in the steady-state dynamics decays. In contrast, for larger growth rates, the autocorrelation function shows oscillatory behavior with a smaller oscillation frequency for larger growth rates. Note that due to the stochasticity in the dynamics, the autocorrelation is still enveloped by an exponential decay. Taken together, this suggests that the length dynamics for large growth rates corresponds to quasi-periodic oscillations.

Where do these self-organized oscillations come from? To better understand this observation, it is insightful to consider the oscillatory behavior in more details. Fig. 5 (c) in [2] or in the

[3]Here, "quasi-periodic" refers to the fact that the system is stochastic and does not exhibit a perfect periodic behavior but that concomitantly the pattern is characterized by a typical oscillation frequency (see below).

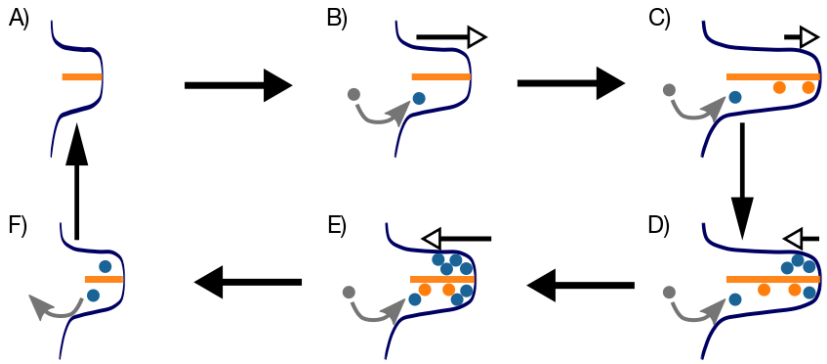

Figure 3.2 | Illustration of the intuitive idea for the occurrence of length oscillations (taken from [2]). If the system is short and empty (A), there will be influx of particles from the reservoir and the lattices will grow spontaneously (B). The injected particles get transported along the TASEP lane towards the tip while the system still grows and new particles enters (C). At some point, the particles "catch up" with the tip and start to accumulate there. As a result, motor-induced shrinkage starts to dominate and turns the growth phase into a shrinkage phase (D). Due to the shrinkage, the crowding of motors in the tip region continuously increases while there is still influx from the reservoir since the density at the left end of the system is still low (if diffusion is slow to equilibrate the density on the DL; E). Once the system is very short, the accumulated motors quickly leave the system (F) and the whole process starts over (A).

publication reprint in section 3.5 shows a zoom in on one oscillation period. Strikingly, while the length dynamics (gray) exhibits (more or less) symmetric phases of growth and shrinkage, the dynamics of the total number of particles in the system (red) shows a sawtooth-shaped pattern. Initially, for increasing length, the number of particles increases, as expected. If the system grows the average density in the system decreases and there should be an influx of particles from the reservoir. However, when the length already starts to shrink, the total number of particles in the system still increases. Only when the system is very short, the total occupancy suddenly drops to a much smaller value. Thus, the dynamics of the total particle number is time-delayed with respect to the length dynamics, suggesting that the density on the DL does not equilibrate on the timescale of the length changes. If this were the case, the instantaneous length would be immediately reflected by the density on the DL and the in- and outflux would instantly adapt to the length dynamics. This limit corresponds to the model discussed in Ref. [82] where length control and a peaked length distribution were observed. In our model, the time delay between the length and particle dynamics manifests itself in terms of strong motor crowding in the tip region of the DL (see also Fig. 5 (c) in [2] or in the publication reprint in section 3.5 where the dynamics of the number of particles in a tip region of 20 sites from the tip is compared to the number of particles in the rest of the lattice). Due to the rather slow diffusion this crowding at the tip is, however, not "communicated" to the base (left end) of the system which is connected to the reservoir. As a result, there is still influx of particles (and consequently further accumulation of motors in the tip region) even if the length already decreases.

Taken together, these findings suggest the following intuition for the occurrence of the length oscillations (see also Fig. 3.2 for an illustration): Consider an empty system. Then the only processes that occur are growth (which is spontaneous) and influx of particles. These particles

are subsequently transported towards the tip. Since growth is always slower than the hopping of particles on the TASEP (as otherwise there could not be any length control and the system would increase indefinitely), the injected particles catch up with the tip at some point. As a result, as they cannot exit the system in the tip region and since diffusion is too slow to transport them back, they start to accumulate there. Eventually, this accumulation will be so large that the motor-induced depolymerization outperforms spontaneous growth and the system starts to shrink. This provides a positive feedback mechanism for the shrinking dynamics as the shortening itself enhances crowding which, in turn, augments shrinking. The system thus shrinks until after a certain time delay the system is so short that the particles at the tip actually diffuse fast enough to leave the system by moving back into the reservoir on the left. The system empties and the whole process starts again. In sum, the periodic behaviour intuitively comes from a positive feedback mechanism with time delay which crucially depends on the *finite* diffusion speed in the cytosol (on the DL).

To check the validity of this intuitive argument, we formulated an effective model for which we can make (partially) analytic predictions and compared them to the results from simulations. The basic idea is to qualitatively divide the system into four regions (see Fig. 7 in [2] or in the publication reprint in section 3.5). This division is based on the intuitive picture and is supposed to reflect that different parts of the system are dominated by different dynamics (influx, growth/shrinkage, accumulation of particles). For details, please refer to chapter IV in [2] or in the publication reprint in section 3.5. Intriguingly, despite many simplifications, this effective model is in quite good quantitative agreement with the full stochastic model. In particular, it recovers the correct shape of the temporal pattern: While the length dynamics is symmetric with respect to growth and shrinkage, the dynamics of the tip density exhibits a saw-tooth shape (see Fig. 8 in the publication).

Furthermore, in agreement with the stochastic simulations, the average maximal length of the system is larger for larger growth rates whereas the average minimal length is slightly smaller for larger growth rates (see Fig. 9 in the publication). The latter finding is, at first sight, rather unintuitive. Why should the minimal length decrease if the growth rate increases? The underlying reason is that for larger growth rates, more particles accumulate at the tip before the system switches from the growth to the shrinkage phase. As a result, not only the growth speed is larger but also the shrinkage speed. Consequently, the system shrinks to a smaller value before diffusion is fast enough to equilibrate the system and to turn the shrinkage back into a growth phase. Nonetheless, as can be seen from Fig. 9 in the publication, this effect is rather weak. Indeed, the analytic expression of the minimal length $l_{\min}$ for the effective model (see chapter IV in [2] or the publication reprint in section 3.5) provides some quantitative insight:

$$l_{\min} \approx \lambda \ln\left[\frac{2\lambda F}{\gamma \Delta \ln(2)}\right], \tag{3.2}$$

where λ is the intrinsic length scale of the system:

$$\lambda \equiv \sqrt{\frac{\epsilon}{\omega}}. \tag{3.3}$$

It can be interpreted as the typical dwell length in the cytosol and so the average distance covered by a particle by diffusion before it attaches to the TASEP lane. Furthermore, $\Delta =$

$1/\omega + \lambda$ corresponds to the typical "cycling time" of motors in the tip region, i.e. the typical time it takes a motor that has just depolymerized the lattice at the tip to diffusive a bit, reattach to the TASEP lane and walk back to the tip. Finally, $F = 2\lambda^3/\left(1 + 2\lambda + 2\lambda^2 + \lambda^3\right)$. Eq. 3.2 suggests that the minimal length is mostly determined by the dwell length λ on the diffusion lane. If the system size is much smaller than this length, motors that depolymerized the system at the tip are very likely to leave the system back into the reservoir. In contrast, if the system is much larger than the dwell length, the motors in the tip region "cycle" in the tip region and depolymerize the TASEP lane over and over again.
The growth rate γ only enters logarithmically.

Finally, the effective model correctly reflects the fact that the oscillation frequency is larger for smaller growth rates γ (see Fig. 10 in [2] or in the publication reprint in section 3.5). This behavior is not obvious from the intuitive picture alone. There are two possible, competing mechanisms: On the one hand, for larger growth rates, the amplitude of the oscillation increases and, thus, the oscillation frequency could decrease. On the other hand, a larger growth rate corresponds to faster growth and shrinkage dynamics. As a result, a larger growth rate could also entail a larger oscillation frequency. It seems that these two opposing effects are correctly balanced in the effective model.

In conclusion, the effective model seems to capture the most important aspects of the self-organized oscillations observed in stochastic simulations. This indicates that the intuitive picture constitutes an – at least to some degree – correct description of the temporal patterning mechanism. Nonetheless, in my opinion, the effective model has its own value because it identifies important control parameters of the dynamics, such as the dwell length on the diffusion lane. Overall, these results allow the conclusion that a *finite* diffusion speed can be an important factor for the occurrence of (self-organized) oscillations. If diffusion is too slow, densities in the system do not equilibrate on other relevant timescales of the system (such as the length dynamics in this case). As a result, time delays can arise that ultimately lead to periodic behavior. Such diffusion-induced time delays have been associated with oscillatory behavior in other protein systems as well [65, 66], suggesting that this phenomenon might also be relevant for more elaborate systems.

3.4 Key points

From my point of view, there are two take-home messages:

- Length regulation in confinement can lead to self-reinforcing crowding of particles.
- Diffusion can play an important role for the occurrence of self-organized oscillations if the timescale for equilibration due to diffusion is large compared to other intrinsic timescales. This is due to time delays that build up as a result of this timescale separation.

Metaphorically speaking, in case of slow diffusion, systems might indeed "evade the decay to equilibrium", as suggested by the quote at the beginning of the chapter.

3.5 Publication: Self-organized system-size oscillation of a stochastic lattice-gas model, PRE 98, 012410 (2018)

This section is a publication reprint of the following manuscript published in **Physical Review E** 98, 012410 (2018).

Self-organized system-size oscillation of a stochastic lattice-gas model

by

Mareike Bojer,[1,2,*] Isabella R. Graf,[1,*] and Erwin Frey[1]
[1] *Arnold-Sommerfeld-Center for Theoretical Physics and Center for NanoScience, Department of Physics, Ludwig-Maximilians-Universität München*
[2] *Department of Physics, Technische Universität München*
[*] *These authors contributed equally to this work.*

DOI: 10.1103/PhysRevE.98.012410

Self-organized system-size oscillation of a stochastic lattice-gas model

Mareike Bojer,[1,2,*] Isabella R. Graf,[1,*] and Erwin Frey[1,†]

[1]*Arnold Sommerfeld Center for Theoretical Physics and Center for NanoScience, Department of Physics, Ludwig-Maximilians-Universität München, Theresienstrasse 37, D-80333 München, Germany*

[2]*Department of Physics, Technische Universität München, D-85748 Garching, Germany*

(Received 29 March 2018; published 17 July 2018)

The totally asymmetric simple exclusion process (TASEP) is a paradigmatic stochastic model for nonequilibrium physics, and has been successfully applied to describe active transport of molecular motors along cytoskeletal filaments. Building on this simple model, we consider a two-lane lattice-gas model that couples directed transport (TASEP) to diffusive motion in a semiclosed geometry, and simultaneously accounts for spontaneous growth and particle-induced shrinkage of the system's size. This particular extension of the TASEP is motivated by the question of how active transport and diffusion might influence length regulation in confined systems. Surprisingly, we find that the size of our intrinsically stochastic system exhibits robust temporal patterns over a broad range of growth rates. More specifically, when particle diffusion is slow relative to the shrinkage dynamics, we observe quasiperiodic changes in length. We provide an intuitive explanation for the occurrence of these self-organized temporal patterns, which is based on the imbalance between the diffusion and shrinkage speed in the confined geometry. Finally, we formulate an effective theory for the oscillatory regime, which explains the origin of the oscillations and correctly predicts the dependence of key quantities, such as the oscillation frequency, on the growth rate.

DOI: 10.1103/PhysRevE.98.012410

I. INTRODUCTION

Understanding collective transport phenomena is an important challenge in theoretical physics, with possible implications for biology and materials science. One-dimensional, asymmetric simple exclusion processes form a prominent class of idealized theoretical models that are amenable to detailed mathematical analyses; see for instance Ref. [1] for a review. Interestingly, these models appeared simultaneously in the mathematical literature as conceptual models with which to study interacting Markov processes [2] and in the biological literature as idealized models for ribosomes moving along mRNA during translation [3]; for recent reviews see Refs. [4,5].

The simplest version of such a model is the *totally asymmetric simple exclusion process* (TASEP). In this one-dimensional stochastic lattice-gas model, particles move stepwise and unidirectionally from lattice site to lattice site at a constant (hopping) rate, provided that the next site is vacant. Models of this class have been used to study the collective, directed transport of molecular motors along microtubules. In that context, the TASEP has been extended to include the exchange of particles between the lattice (microtubules) and the surrounding environment (cytosol) in terms of Langmuir kinetics [6–9]. The traffic jams predicted by these models have recently been observed experimentally [10,11], suggesting that these idealized lattice gases are indeed suitable for describing the collective dynamics of molecular motors.

In a further interesting line of research, extensions of the TASEP to dynamic lattices have been developed [12–28]. On the one hand, motivated by the transport of vesicles along microtubules that facilitate growth of fungal hyphae, or by growth of flagellar filaments, TASEP models have been considered in which a particle that reaches the end of the lattice may extend it by a single site [12,14,15,17,22]. On the other hand, in efforts to quantify experimental observations of motor-mediated microtubule depolymerization *in vitro*, dynamic lattice-gas models have proven useful for probing the regulation of microtubule length by motors that show unidirectional [16,18,29,30] or diffusive motion [31–33]. Recently, these models for depolymerizing molecular motors have been extended towards dynamic microtubules, in order to study the interplay between lattice growth and shrinkage [19–21,23,24,26], and to understand the basic principles underlying cellular length control mechanisms [34,35].

There are many possible extensions of these models, which are both interesting in their own right and can help us to understand important biological processes. Examples include large networks of biofilaments [36–38], limited protein resources [6,39–45], the fact that proteins in the cytosol do not form a spatially uniform reservoir because their dynamics is limited by diffusion [6,46–51], and that proteins may be spatially confined, as they are in fungal hyphae or filopodia [6,9,46,51,52].

In this paper our goal is to study the interplay between diffusive motion and directed transport as a possible mechanism for length regulation under confinement [Fig. 1(a)]. This relationship is of great interest because, in contrast to diffusion, directed transport is an intrinsically nonequilibrium process. It leads to currents of motors directed towards the growing or

*These authors contributed equally to this work.
†Corresponding author: frey@lmu.de

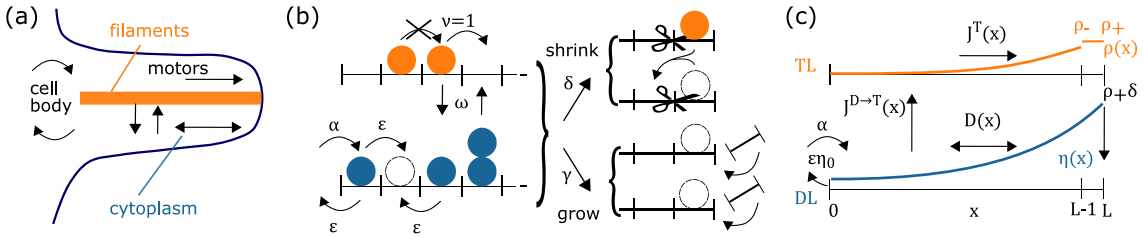

FIG. 1. (a) Illustration of the dynamics in cellular protrusions. Movements of molecular motors are indicated by black arrows, and are restricted to the cell body and the protrusion by the cell membrane. On the filament the motors move unidirectionally towards the protrusion tip, while their motion in the surrounding cytoplasm is diffusive. (b) Illustration of the two-lane lattice-gas model. We consider a two-lane lattice-gas model consisting of a TASEP or transport lane [TL, upper lane, occupied by orange (light gray) particles] and a diffusive lane [DL, lower lane, occupied by blue (dark gray) particles] with hopping rates $\nu \equiv 1$ and ϵ, respectively. The lanes are coupled by attachment and detachment kinetics at rate ω, respecting exclusion for transfer from the DL to TL. Entry and exit occurs via the first DL site only, at rates α and ϵ, respectively. The system spontaneously grows by simultaneously appending a site to the TL and DL tip at rate γ, while both lanes shrink by a site, at rate δ, if the TL tip is occupied by a particle. In the latter case, particle conservation is ensured by shifting all particles of the previous TL and DL tip site to the new DL tip site. (c) Illustration of the particle currents and density profiles. The density profile on the TL (DL), $\rho(x)$ [$\eta(x)$], is displayed in orange (light gray) in the upper panel [blue (dark gray) in the lower panel]. The density $\rho(x)$ is discontinuous at the last TL site, with ρ_- referring to the left and ρ_+ to the right limit. The currents (black arrows) come from entry α, exit $\epsilon\eta_0$, diffusion D, attachment and detachment $J^{D\to T}$, directed movement J^T, and detachment due to depolymerization $\rho_+\delta$.

shrinking end (tip) and so to a strong interaction between the motors and the growing or shrinking end. The combination of transport with diffusion in a semiclosed geometry has recently been studied with a conceptual model [51]. This model assumes a fixed length for the system and suggests an important role for diffusion in the transport of motors to the tip. While biologically motivated exclusion in this model, and also more generally, can change the dynamics qualitatively, here we here focus on the low-density regime where exclusion only has a minor quantitative influence. Instead we extend the previous model by including length regulation. This is motivated by polymerization and depolymerization of filaments in highly dynamic cellular protrusions. For the particular choice of the growth and shrinkage dynamics, we draw our inspiration from experimental studies of microtubules, in which motor-induced depolymerization [29,30,53–55] and growth by attachment of tubulin heterodimers [56,57] were found. Other choices such as the "opposite" scenario where polymerization is motor-dependent and depolymerization is spontaneous, or a system with two types of motors, namely polymerizing and depolymerizing ones, are also expected to give rise to interesting phenomena but are out of the scope of the present paper.

While our motivation originates from specific biological processes, we do not want to study a particular biological system. Rather our lattice-gas model (Fig. 1) provides us with an exemplary model to examine the combined role of diffusion and active transport for length regulation under a confined geometry. Unexpectedly, we find that the size of our intrinsically stochastic system shows periodic behavior when diffusion is slow compared with the growth and shrinkage dynamics. This indicates that diffusion-limited transport can be an important ingredient for the occurrence of (self-organized) oscillations.

This paper is organized as follows. In Sec. II we explain the processes incorporated into the stochastic lattice-gas model and show analytical calculations for the simplest possible scenario, the stationary state, to gain a basic understanding. To check these results and explore a broader parameter regime, we continue in Sec. III with numerical simulations. We determine the dependence of the stationary length on the growth rate and find a parameter regime in which length oscillations occur. For this oscillatory behavior we then develop an intuitive explanation. Finally, in Sec. IV we derive an effective theory from this intuitive explanation, and compare its predictions to the results from stochastic simulations. We conclude with a summary and discussion in Sec. V. Readers who are primarily interested in the phenomenology may want to skip the more technical part of Sec. II B. It aims at giving a mathematical intuition about the processes constituting the presented model.

II. MODEL DEFINITION AND MATHEMATICAL ANALYSIS

A. Stochastic lattice-gas model

As outlined in the Introduction, we consider a two-lane lattice-gas model in a semiclosed geometry [Fig. 1(b)], and extend previous work [51] by combining it with a length-regulation mechanism. One lane, the TASEP or transport lane, TL, emulates the directed transport along filaments in cellular protrusions in terms of a totally asymmetric simple exclusion process (TASEP) [3,58,59]. It is characterized by a rate ν at which particles hop unidirectionally along the lattice, from the base towards the growing or shrinking end (tip). Particles exclude each other; i.e., there can be at most one particle at any lattice site and, consequently, particles can only hop forward if the site ahead of them is empty. Later we will see that exclusion is not essential for the qualitative findings discussed in this paper. We measure all rates in units of ν and thus set $\nu \equiv 1$.

The second lane, the diffusion lane, DL, mimics diffusive transport of motors in the cytosol [Fig. 1(b)], and describes it as effectively one-dimensional: Particles perform a symmetric random walk with hopping rate ϵ to the left and right. As the density of motor proteins in the cytosol is small, we assume no particle exclusion on the DL. Hence the hopping probability is not influenced by the occupancy of the neighboring sites.

Moreover, molecular motors constantly cycle between the filaments and the surrounding cytosol by attaching to the filaments and detaching into the cytosol. This motion is

represented as follows: At a rate ω, a particle from the DL can attach to the corresponding TL site, if it is vacant, and a particle from the TL can always attach to the corresponding DL site.

Particles can enter the system only from a reservoir via the first DL site, corresponding to motors entering the protrusion from the cell body, and similarly can only leave the system via that same site. Entry occurs at rate α, and particles diffuse out at a rate equal to the hopping rate ϵ. We do not model the dynamics in the cell body explicitly, as diffusion in the cell body is three-dimensional and we expect that, as a result, entry and exit events should be roughly uncorrelated. We thus approximate the cell body as an infinite reservoir.

The lanes grow by the spontaneous addition of a TL site to the TL tip at rate γ, accompanied by the simultaneous extension of the DL by one site. Motor-induced depolymerization is realized by cutting off the TL tip site at rate δ. The cytoskeletal filament is considered to span the protrusion, meaning that with shrinking filament the length of the cytosolic volume shrinks as well. So, when the TL shrinks by one site the DL is simultaneously reduced by one site and all leftover particles, including the one responsible for the shortening event, are shifted to the new DL tip site. Thus, the DL tip site can be easily populated by several particles at once. Since the motors can neither penetrate the membrane nor leave the system at the tip, they remain in the cytosol at the tip even when the system shrinks.

In summary, a typical particle journey would start by the particle's entry into the system at the first DL site, followed by diffusion on this lane until it attaches to the TL and begins to hop towards the tip. Once there, it eventually cuts off the site it is occupying and joins the other particles from the previously "lost" DL site on the new DL tip site. Each of these particles then diffuses on the DL until it reattaches to the TL or leaves the system at the DL's first site.

B. Mathematical analysis: Adiabatic limit

To gain a better quantitative understanding of the system, we analyzed the stochastic dynamics of the lattice-gas model in terms of a set of master equations, and employed a mean-field approximation to derive a set of rate equations for the density of motors on the TL and DL. The analysis follows Refs. [51] and [19], and is discussed in detail in Appendix A. Here, we will discuss the main results and their interpretation, focusing on the low-density limit and the limit of slow length change compared with particle movement, i.e., $\nu \equiv 1 \gg \gamma$.

To begin with, let us introduce a set of random variables to describe the state of the system: $L(t)$ denotes the lattice length at time t; configurations on the TL are indicated by a tuple of random variables $(n_i)_{i=0}^{l}$, with n_i describing the occupancy of lattice site i. Each lattice site occupancy can assume the value $n_i = 1$ (occupied) or $n_i = 0$ (empty) due to mutual exclusion. We use l to denote the actual value of $L(t)$ at a specific time. The random variables $(m_i)_{i=0}^{l}$ representing the DL occupancy can take values in $\mathbb{N}_0$ (no exclusion).

The dynamics of the two-lane model is a difficult stochastic many-body problem, in which the bulk dynamics and the size of the system are mutually coupled. In the limit where the bulk dynamics is much faster than the length changes, we may however assume that on the timescale over which the length of the lattice changes, the distribution of particles on the lattice is stationary (*adiabatic assumption*). Thus we can decouple the equations for the length change and particle movement, which simplifies the mathematical analysis considerably. Using a mean-field approximation (see Appendix A) one obtains occupancy densities. We denote these as $\rho_i = \langle n_i \rangle$ and $\eta_i = \langle m_i \rangle$, where averages are ensemble averages.

In the adiabatic limit, the stochastic dynamics of the lattice length is a simple birth-death (polymerization-depolymerization) process. Thus the system length changes as

$$\partial_t L(t) = \gamma - \delta \rho_+(L), \tag{1}$$

with the TL tip density denoted by ρ_+. Spontaneous polymerization occurs at rate γ and motor-induced depolymerization at rate δ. L now refers to the average length and is no longer a stochastic variable. In the following, we will only consider the stationary case (and denote the stationary length by L). Thus the length change equation (1) yields a condition on the TL tip density:

$$\rho_+ = \frac{\gamma}{\delta}. \tag{2}$$

In the remaining part of this section we will formulate the current-balance equations for both lanes to derive a length-dependent expression for the particle density at the tip. Solving for the length L yields the main result of this section, Eq. (13). From the analysis it becomes apparent that the relevant length scale, denoted by λ [Eq. (7)], corresponds to the average distance a particle diffuses on the DL, before it attaches to the TL. Furthermore, apart from the *adiabatic assumption*, meaning that the particle occupancy equilibrates fast in comparison to the length dynamics, we make use of three more approximations: first, a *mean-field approximation* neglecting correlations between the occupancies at different lattice sites, justified by the low-density regime, second, the *continuum limit* requiring that the number of lattice sites is large, and third, a *mesoscopic limit* implying that the total attachment and detachment rates over the entire lattice are comparable to the hopping rate on the TL. A reader not interested in the mathematical details of the dynamics may want to skip the remaining part of this section.

The density profiles on the TL and DL bulk, ρ_i and η_i for $i = 1, \ldots, L$, are determined by the current balance for each lane and site [see also Fig. 1(c)],

$$\text{(TL)} \quad 0 = +J_i^{D\to T} + \left(J_i^T - J_{i+1}^T\right), \tag{3a}$$

$$\text{(DL)} \quad 0 = -J_i^{D\to T} + D_i, \tag{3b}$$

where we have defined the transport current on TL as $J_i^T := \rho_{i-1}(1-\rho_i)$, and the exchange current between TL and DL as $J_i^{D\to T} := \omega(1-\rho_i)\eta_i - \omega\rho_i$. Moreover, diffusion on the DL is described by $D_i := \epsilon(\eta_{i+1} - \eta_i) - \epsilon(\eta_i - \eta_{i-1})$.

At the left boundary (base of the protrusion) which is coupled to the reservoir one finds

$$0 = +J_0^{D\to T} - J_1^T, \tag{4a}$$

$$0 = -J_0^{D\to T} + \epsilon(\eta_1 - \eta_0) - \epsilon\eta_0 + \alpha. \tag{4b}$$

The density current onto the TL's first site is due to particle transfer from the first site of the DL, $J^{D\to T}$, and the transport current on the TL, J^T. For the first site of the DL there is the diffusive current onto the neighboring DL site as well as the exchange with the first site of the TL. Furthermore, at rate α particles enter the first site of the DL from the reservoir. This gives the corresponding influx current α. At diffusion rate ϵ particles also exit the system from the first site of the DL, which leads to a current of $-\epsilon\eta_0$ out of the system.

To solve these equations, we employ a continuum approximation, assuming that the lattice spacing is smaller by far than the lattice length. In other words, we perform a Taylor expansion in the ratio of lattice spacing $a \equiv 1$ to system size, and only keep terms up to second order. In this way, we obtain the following continuous currents with $x \in [0, L]$,

$$J^T(x) = [\rho(x) - \partial_x\rho(x)][1 - \rho(x)], \tag{5a}$$

$$J^{D\to T}(x) = \omega[1 - \rho(x)]\eta(x) - \omega\rho(x), \tag{5b}$$

$$D(x) = \epsilon\partial_x^2\eta(x), \tag{5c}$$

and rewrite the flux balances accordingly. From the flux balances for the first sites $\eta(0)$, $\partial_x\eta(0)$, and $\rho(0)$ are determined to be

$$\eta(0) = \frac{\alpha}{\epsilon}, \tag{6a}$$

$$\partial_x\eta(0) = \lambda^{-2}\,\eta(0), \tag{6b}$$

$$\rho(0) = \omega\,\eta(0), \tag{6c}$$

having defined the length scale

$$\lambda \equiv \sqrt{\frac{\epsilon}{\omega}}. \tag{7}$$

Thus the motor density at the first DL site, $\eta(0)$, equals the ratio of the particle influx rate to the particle outflux rate. $\rho(0)$ is given by the DL density at the first site from which transfer to the first TL site occurs. The length scale λ can be interpreted as the average distance (in units of the lattice spacing) covered by a particle on the DL by diffusion before it attaches to the TL, and it is closely related to the root mean square displacement $\propto \sqrt{\epsilon t}$ after the typical attachment timescale $t = 1/\omega$. It will turn out that λ is the intrinsic length scale of the system and most distances on the lattice will be measured with respect to this quantity. The three boundary conditions [Eq. (6)] will now be used as initial conditions for the bulk equations.

First, in the low-density limit, $\rho \ll 1$, $\rho \ll \eta$, we decouple the two equations [Eq. (3)]. Note that $\rho \ll 1$ implies that $(1 - \rho) \approx 1$, which is equivalent to lifting the particle exclusion. With the two initial conditions, Eqs. (6a) and (6b), we solve the resulting second-order differential equation, $\partial_x^2\eta(x) = \eta(x)/\lambda^2$, to give

$$\eta(x) = \eta(0)\left[\frac{1}{\lambda}\sinh\left(\frac{x}{\lambda}\right) + \cosh\left(\frac{x}{\lambda}\right)\right]. \tag{8}$$

Sorting the bulk current balance on the TL by orders of $1/L$ implies that the TL density is the integral of the DL density that has attached to the TL, $\omega\int_0^x \eta(y)dy = \rho(x) - \rho(0)$, yielding

$$\rho(x) = \rho(0) + \frac{\alpha}{\lambda}\left[\frac{1}{\lambda}\cosh\left(\frac{x}{\lambda}\right) + \sinh\left(\frac{x}{\lambda}\right) - \frac{1}{\lambda}\right]. \tag{9}$$

The resulting density profile for the low-density phase has a functional form similar to the density profile found in Ref. [51] although a static lattice was considered in that case. In particular, the exponential density increase toward the tip can be reproduced.

Regarding the last site, we expect a discontinuity in the density profile, as the hopping rules change discontinuously to accommodate growth and shrinkage. The left limit ρ_- [see also Fig. 1(c)] is determined by the bulk density, while the right limit ρ_+ is fixed by the stationarity condition on the length, i.e., $\rho_+ = \gamma/\delta$, Eq. (2). The system is closed everywhere except at the first site, and consequently, the flux to the last site has to equal the flux out of the TL onto the DL, which is $\rho_+\delta$ to first order,

$$J^T(L) = \rho_+\delta. \tag{10}$$

This equality gives us an implicit condition on the system length L.

The equations for the tip dynamics become more transparent when formulated in the comoving reference frame, as otherwise the last site is not necessarily L. In this frame two additional currents add to the bulk current in the previously used reference frame, the currents from relabeling due to a growth or a shrinkage event:

$$J^T(x) = \rho(x)[1 - \rho(x)] - \gamma\rho(x) + \delta\rho_+\rho(x). \tag{11}$$

Solving the flux balance (10) yields

$$\rho(L) = \tfrac{1}{2}(1 - \sqrt{1 - 4\gamma}) \equiv \rho_-, \tag{12}$$

where ρ_- can be interpreted as the left limit of the density at the last site. Approximating the hyperbolic functions as exponential functions with positive argument ($1 \ll \lambda \ll L$), we obtain

$$L = \lambda\ln\left[2\frac{\lambda}{\alpha}[\rho_- - \rho(0)]\right]. \tag{13}$$

The higher the particle density on the TL, the faster the system depolymerizes. Hence, a smaller value of λ results in a smaller steady-state length. This reasoning not only applies for the prefactor but also for the numerator of the argument in the logarithm. Here the influx into the diffusive lane (α) is weighted by $1/\lambda$. ρ_- corresponds to the critical density that depolymerizes the system at exactly the speed that is necessary in order for polymerization and depolymerization to be balanced on average. The bigger the critical density, the higher the stationary particle density on the TL and the longer it takes to fill the system. Thus the system has more time to grow.

III. NUMERICAL ANALYSIS

So far, we derived analytical expressions for the limit of slow length change with respect to particle density equilibration. Now we want to explore the full regime, which informs us about the phenomenology of the model beyond the adiabatic regime. We therefore perform stochastic simulations of the lattice-gas model defined in Sec. II A employing Gillespie's algorithm [60]. The numerical results will also be used to check

the approximate analytical description for the adiabatic case, which was obtained by using a mean-field analysis.

A. Choice of parameter space and numerical method

For the numerical analysis of the system we focus on the dependence on the growth rate γ, while keeping the other parameters fixed. The variation of γ causes a qualitative change in the dynamics: For small γ, the adiabatic assumption should be valid, and we expect a well-defined length, whereas for large γ Ref. [19] suggests that length regulation is no longer possible [61]. We want to focus the analysis on what happens in an intermediate regime of γ: The initial length L_0 was set to $L_0 = 100$. We fix as attachment and detachment rate $\omega = 1/L_0$, as influx rate $\alpha = 0.1$, as diffusion rate $\epsilon = 5.0$ [62], and as depolymerization rate $\delta = 1.0$; in each case these parameters are expressed in terms of the hopping rate on the TL $\nu \equiv 1$. The choice of $\Omega = \omega L_0 \equiv 1$ to be of the order of the other rates is motivated by the processivity of the molecular motors, which can walk over long distances along the cytoskeletal filament before detaching [63]. It is also the theoretically interesting case as it guarantees that the number of attachment and detachment events over the length of the system competes with the other rates [7,8]. For simplicity, we choose the same rate for attachment and detachment. However, we do not expect the qualitative results to change for different attachment and detachment rates as long as both are still taken to be small. Moreover, α and ϵ together are chosen such that the density at the first site of the DL is rather small. As shown in Ref. [19], length control in their system, that is, the system neither shrinks to zero size nor grows without bound, is only feasible in the low-density parameter regime. Lastly, δ is chosen to be equal to the hopping rate.

We only took into account simulations where the system did not shrink to zero length but a stationary state was reached. Accordingly, we also chose the interval for the growth rate in such a way that most simulations fulfilled this criterion. The choice of L_0 (for fixed $\omega = \Omega/L_0$) did not influence the results in any way, as we discarded the initial behavior before the stationary state.

B. Stochastic simulations and model phenomenology

1. Mean length

We tested the analytical insights described in Sec. II B by comparing them to the results of stochastic simulations. To begin with, we determined the mean length of the system as a function of the growth rate γ, as shown in Fig. 2. For small growth rates, the length increases sublinearly with the growth rate, up to an inflection point from which it then increases superlinearly. As expected, the numerical result agrees nicely with the analytical results in the adiabatic limit as the growth rate tends to zero: $\gamma \to 0$ (i.e., when the growth and shrinkage dynamics are slow relative to the particle dynamics). However, the simulation results deviate strongly from the predictions for larger growth rates γ. As the adiabatic assumption was the only critical assumption in the theoretical analysis [64], the numerical simulations tell us that this approximation cannot be valid for larger growth rates. On the contrary, with increasing growth rates, the particle configuration on the lattice no longer

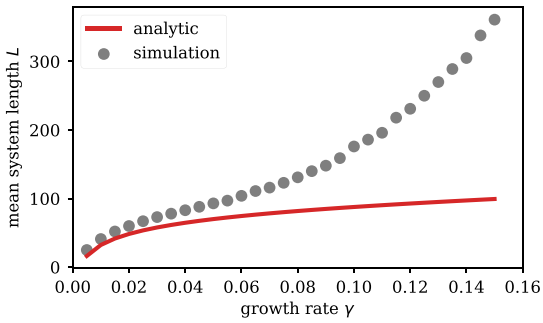

FIG. 2. Mean system length. Mean length of the system is plotted as a function of the growth rate γ. The analytical result (red, solid line) agrees well with the results from stochastic simulations (gray, filled circles) for small growth rates, $\gamma \ll 1$, where the adiabatic assumption is expected to hold. For increasing growth rates the numerical data show an inflection point at which they begin to deviate strongly from the results in the adiabatic limit. This indicates that the dynamics shows qualitatively new behavior for large growth rates.

equilibrates on the timescale of the length changes. As a result, there must be a time lag between the length change and the equilibration of the motor configuration, and this could possibly lead to interesting dynamics. To explore this further, we next study the length distribution.

2. Length distribution

Figure 3 shows the length histograms for different values of the growth rate γ. In the inset, we also show the minimal and maximal lengths in comparison to the average length and the standard deviation of the length. We observe that for larger growth rates the length distributions become broader, while all are right-skewed. This right-skewness implies that we cannot approximate them as Gaussian distributions as it was done in Ref. [19], and so it is not feasible to use a van Kampen

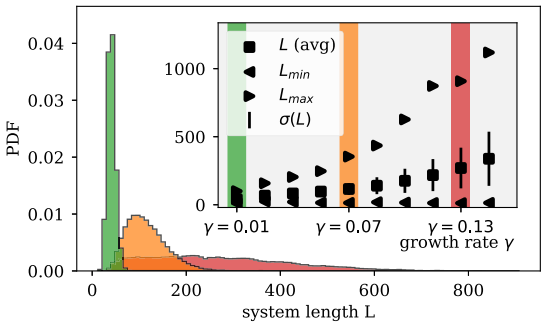

FIG. 3. Length histograms for different growth rates γ and a simulation time of 10^7. The larger the growth rate, the longer the average length and the broader the length distribution. The distributions are right-skewed in contrast to a Gaussian. *Inset:* The average length (squares), the standard deviation (bars) of the average length, and the maximum length reached (right-pointing triangles) increase nonlinearly with larger growth rates, while the minimum length attained (left-pointing triangles) remains essentially constant. The shaded areas [green (gray), orange (light gray), and red (dark gray)] correspond to the value of the growth rate γ in the corresponding length histograms.

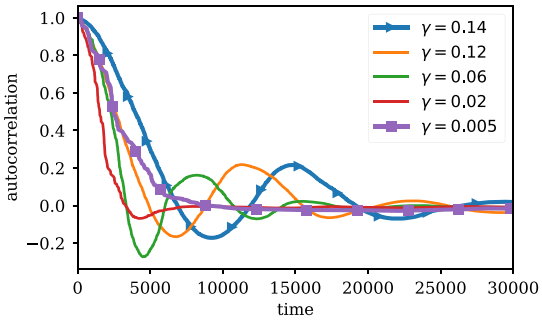

FIG. 4. Autocorrelation function. The autocorrelation functions, each of an ensemble of 1000 runs, for several growth rates γ are compared. The autocorrelation function for the smallest growth rate $\gamma = 0.005$ (purple line with squares) almost immediately decays to zero, while the autocorrelation of $\gamma = 0.14$ (blue line with triangles) oscillates with a frequency comparable to the observed length oscillations.

system-size expansion to obtain higher moments of the length distribution analytically.

From the analysis of the numerical results, we make the following observations: The standard deviation of the length increases with the growth rate. Moreover, the maximum length attained also increases with growth rate, namely faster than linearly. In contrast, the minimum length reached remains rather constant. This is surprising as, intuitively, a larger growth rate should also lead to a larger minimal length. Might this be connected with the suspected time lag between the length change and the equilibration of the motor configuration? To answer this question, we looked at a simple temporal quantity first, namely the autocorrelation function.

3. Autocorrelation

Figure 4 shows the ensemble autocorrelation function for different values of the growth rate γ. It can be stated in terms of the covariance between lengths at times τ and $t + \tau$, $\mathrm{Cov}(L(\tau), L(\tau + t))$, as follows:

$$C(t) := \langle \mathrm{Cov}(L(\tau), L(\tau + t)) \rangle / \sigma^2, \tag{14}$$

where $\langle \ldots \rangle$ denotes the ensemble average and σ is the standard deviation of the length.

In general, we would expect the autocorrelation function $C(t)$ to decay exponentially with time, yielding an autocorrelation time that is equal to the typical internal relaxation time, i.e., the timescale on which a perturbation in length influences the length dynamics. This is indeed the case for a small growth rate ($\gamma = 0.005$ in Fig. 4). However, for larger growth rates, while still being enveloped by an exponential decay, the autocorrelation function oscillates with an oscillation period that increases with the growth rate. This indicates that for large growth rates the length is oscillating and that there might be two qualitatively different limits for the length-changing dynamics, namely for small and large growth rates, respectively. To study this issue further, we looked at individual time traces of the system length for small and large growth rates.

4. Time traces

Visual inspection of the time traces (Fig. 5) confirms the impression gained from the autocorrelation function that for small growth rates the length of the system fluctuates stochastically. In contrast, for large growth rates, the fluctuations in length are very small with respect to a dominant underlying quasiperiodic length-changing pattern, which shows roughly the same oscillation frequency as the corresponding autocorrelation function. This is striking, as one would not automatically assume that enhancing the *spontaneous growth rate* could lead to a quasiperiodic pattern.

What might account for such behavior? The first question that comes to mind is whether the system is actually in a stationary state and, if that were the case, how could it be reconciled with an oscillatory behavior. In this respect, the most obvious quantity to look at is the total number of particles that are either on the TL or on the DL. Is this quantity noisy or does it also show oscillatory behavior for large growth rate γ? For small γ, the total particle number behaves highly stochastically, as expected [Fig. 5(a)]. For large polymerization rates γ, we observe that not only the length but also the total particle number shows oscillatory behavior. Surprisingly, however, the time trace of the total particle number looks very different from the time trace of the system length: Instead of being rather symmetric within one period, the time trace for the total particle number has a sawtooth-like shape; i.e., the total particle number increases steadily almost during the whole period before abruptly and drastically decreasing [Fig. 5(b)]. Hence, the influx of particles dominates the outflux for most of the time and, in addition, the total particle number does not change synchronously with the length. Rather, the dynamics of the total particle number is time-delayed with respect to the length dynamics—contrary to what one would expect if the density on the DL were more or less equilibrated.

This suggests that the DL occupancy is far from homogeneous and that there is an intricate interaction between the motors and the length dynamics: From the equation of motion for the length L (here considered as a stochastic variable), $\partial_t L = \gamma - \delta n_+$ with n_+ being the particle number at the TL tip, one expects that the instantaneous value of n_+ should be a key quantity for the length dynamics. It is determined by the currents along the TL and from the DL tip back to the TL tip or to the base. To garner information about these currents, we determined not only the total number of motors but also the number of motors located in the immediate vicinity of the tip on both the TL and DL; for specificity we chose the size of the "tip neighborhood" to be 20 sites. We refer to the number of motors in the tip neighborhood and in the remaining part of the lane as "tip occupancy" ("tip occ."), and "bulk occupancy" ("bulk occ."), respectively. These quantities are shown in Fig. 5(c) for one oscillation period.

Based on the numerical results we can make several observations. First, since there are typically more particles in the DL tip region of only 20 sites than on the remaining part of the DL, the DL tip density is far higher than the DL bulk density, indicating a considerable crowding of particles at the tip. Second, the DL tip occupancy in particular increases over almost the whole oscillation period before drastically decreasing only at the very end (similarly to the total particle

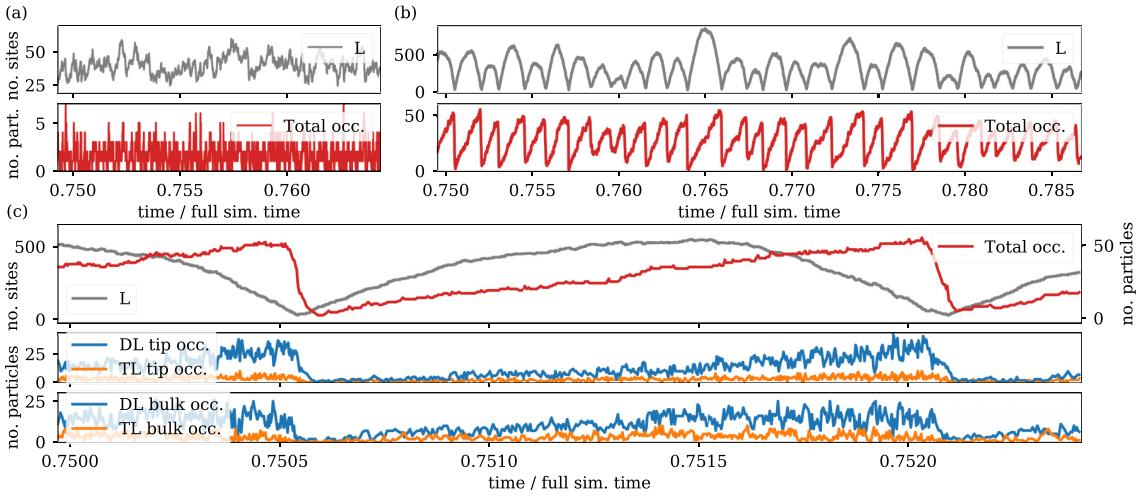

FIG. 5. Time traces for filament length, total particle number, DL occupancy, and TL occupancy for a full simulation time of 10^7. (a) System length (gray) and total particle number [red (dark gray)] dynamics for a long time interval and small growth rate $\gamma = 0.01$. Both the length and the total particle number change stochastically. (b) System length (gray) and total particle number [red (dark gray)] dynamics for a large growth rate $\gamma = 0.14$. We observe length oscillations and a sawtooth-shaped behavior of the total particle number. (c) Zoom-in for large $\gamma = 0.14$. Upper panel: System length (gray) and total particle number [red (dark gray)] dynamics. Middle panel: Occupancy of the TL [orange (light gray), lower line] and DL [blue (dark gray), upper line] tip neighborhood, which is chosen to consist of 20 sites from the tip. Lower panel: Occupancy of the TL [orange (light gray), lower line] and DL [blue (dark gray), upper line] bulk, which corresponds to the whole lane except the tip neighborhood. We observe that the tip neighborhood is densely occupied compared with the bulk.

number). Hence, although the system is already shrinking, the DL tip density continues to increase. This suggests that there is no communication between the DL tip density and the reservoir throughout most of the shrinkage phase: as diffusion is finite, there is no instantaneous equilibration between the (higher) density at the tip and the reservoir density. Only when the system is already very short, the cluster at the tip is released into the reservoir.

This suggests the following mechanism (see Fig. 6): Diffusion of the particles is slow relative to shrinkage, so that as shrinkage proceeds the particles cluster more and more at the tip and do not come into contact with the reservoir at the left end [Fig. 6(e)]. Hence, they cannot leave the system as long as its length is not yet sufficiently short for diffusion to be competitive. Only when the length of the system falls below a critical value [Fig. 6(f)] can the motors diffuse fast enough to reach the first site of the DL and get out of the system. This then happens quickly, as the reservoir particle density is very low and many motors have accumulated at the DL tip that all exit the system at around the same time, equilibrating the DL tip density with the reservoir density. Following this reasoning, this critical length should then depend on the diffusion rate ϵ together with the effective shrinkage speed, as these two parameters determine the typical length that the particles can move away from the tip before the system further shrinks. If the system then becomes depleted of particles [Fig. 6(a)], there are no more particles at the TL tip and, as shrinkage is assumed to be particle-induced, the system can only grow. Since even for "large" growth rates γ, growth is considerably slower than the TL hopping rate, $\gamma \ll 1$, particles begin to move toward the tip as the system grows [Fig. 6(b)] and finally reach the tip and accumulate there [Fig. 6(c)], turning the growth phase into a shrinkage phase (particles "catch up" with the TL tip) [Fig. 6(d)].

Notably, this mechanism, which is based on the particle accumulation at the DL tip, heavily relies on the particle conservation, since particles can leave the tip region only via the diffusive lane. If this were not the case, particles could simply leave the tip region via an exit rate, effectively reducing the clustering at the tip and so shortening the extended shrinkage phase.

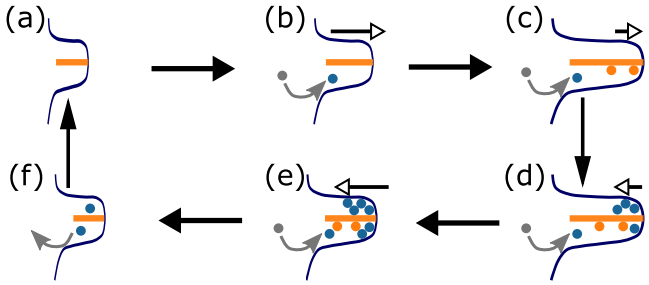

FIG. 6. Intuitive picture for the occurrence of length oscillations. Starting from a short and empty system (a), the only two processes possible are growth and influx of particles from the reservoir into the system (b). Once attached to the TL particles start walking towards the tip, away from the reservoir, and the system grows while new particles enter (c). Since growth is slow compared with transport of particles on the TL, the particles on the TL "catch up" with the tip. Furthermore, due to the finite diffusion and the closure at the tip, the particles then begin crowding at the tip, turning the growth phase into a shrinkage phase (d). During the shrinkage phase more and more particles accumulate at the tip as new particles still enter from the reservoir on the left while the system shrinks from the right (e). Only when the system has become very short is diffusion of particles fast enough that particles which accumulate at the tip can leave the system by exiting into the reservoir (f), leaving behind a short and empty system (a), from which the next oscillation cycle can begin anew.

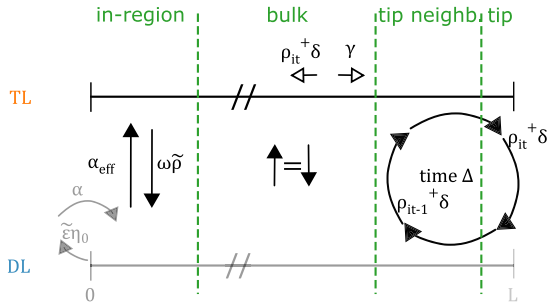

FIG. 7. Schematic of the effective model. We split the system into four regions, and use an effective description of the DL, restricting our analysis to the TL. In the in-region we have attachment at an effective in-rate α_{eff} and detachment at rate ω. The bulk region links the in-region to the tip neighborhood and we assume that in the bulk attachment and detachment balance. For the tip neighborhood we assume that particles which have detached at the tip a time $1/\omega$ earlier reattach to the TL in the tip neighborhood and need another time $\Delta - 1/\omega$ to reach the TL tip again, yielding a recursion relation for the tip density ρ_{it}^{+}. Finally, at the tip we have detachment at rate $\delta\rho^{+}$, and the corresponding shrinkage of the system, and spontaneous growth. The tip and the tip neighborhood are described in the comoving frame.

IV. EFFECTIVE THEORY FOR THE OSCILLATORY REGIME

So far, we have built up a heuristic mechanism from an analysis of the numerical data. To examine the validity of the suggested heuristic mechanism, and to gain a more quantitative understanding of the oscillations in the parameter regime considered, we now construct an effective, semiphenomenological theory. The effective theory incorporates the main ideas of the heuristic picture, and we will check how closely its predictions fit the numerical results.

The theory is based on an effective description of the diffusion lane, and on the idea that, depending on where particles detach from the TL, they either reattach to it after an average time $1/\omega$ (which is the inverse of the attachment rate), or leave the system. We first divide our system qualitatively into four regions (see Fig. 7). From base to tip, these are the "in-region", the "bulk", the "tip neighborhood", and the "tip":

(1) The in-region is close to the base: Here, newly entered particles attach to the TL (via DL), and detach from the TL at rate ω.

(2) The tip: The last site on the TL at which growth and shrinkage (together with detachment of the triggering particle) occur.

(3) The tip neighborhood: Here, particles that have previously detached from the tip reattach to the TL. We neglect detachment and further reattachment, as we assume that particles which detach in the tip neighborhood reattach in the same region, balancing each other out.

(4) The bulk: This merely serves as a linker region between the "in-region" close to the base and the "tip neighborhood" close to the tip. Here, we assume that attachment and detachment of particles balance each other out (particles that detach there also reattach there).

In summary, we assume that particles that enter the system, and do not immediately leave it again, attach to the TL in the in-region. They then either detach there again and return to the reservoir, or they walk on the TL towards the tip. Furthermore, particles that detach at the tip reattach to the TL in the tip neighborhood after an average time $1/\omega$. Moreover, growth and shrinkage occur at the tip.

Note that the division of the system into those regions is motivated by key components of the system dynamics such as the coupling to the reservoir at the base, the particle dynamics on and between the lanes, and the length-changing dynamics at the tip. It is however a theoretical construct and instead of fixed boundaries there will be continuous transitions between the different regimes in the real system.

As we have seen in Sec. III B, the total number of particles in the system increases almost throughout the oscillation period, including the greater part of the shrinkage phase. As a first step, we determine the effective rate at which particles enter the system, and then attach to the TL. This rate will not equal the "bare" in-rate α, as particles can also leave the system again before attaching.

What is the probability, Prob(leaving), that a particle that has just entered leaves the system again before attaching to the TL? To answer this question we assume that the length of the system is considerably larger than the length of a typical journey of a particle on the DL before it attaches to the TL, and discuss the influence of a short length separately below. By carefully keeping track of all possible exit paths we determine Prob(leaving) as

$$\text{Prob(leaving)} = 1 - \frac{\sqrt{\omega\epsilon}}{\tilde{\epsilon}} + O(\omega)$$

(see Appendix C 1), where we allow the exit rate from the system, $\tilde{\epsilon}$, to be different from the diffusion rate ϵ. As a result, the effective on-rate onto the TL is given by

$$\alpha_{\text{eff}} \approx \frac{\alpha}{\tilde{\epsilon}}\sqrt{\omega\epsilon} \tag{15}$$

to lowest order in ω. It is proportional to the ratio of particle influx α to particle outflux $\tilde{\epsilon}$ from and back into the reservoir itself, which can be interpreted as the density in the reservoir. Furthermore, the effective on-rate onto the TL increases with the attachment rate ω, as expected, and with the diffusion rate ϵ, since for a higher diffusion rate (compared with the exit rate $\tilde{\epsilon}$) particles diffuse further into the system. Using this effective entrance rate we now proceed to our effective TASEP model.

First, we estimate the length of the in-region l_I, since—due to attachment and detachment here—its length influences the density. To do so we model a typical particle on the DL (which does not leave the system immediately) until it attaches to the TL, as a symmetric random walker with reflecting boundary at $x = 0$. Attachment to the TL follows a Poisson process at rate ω. Assuming that the particle starts at $x = 0$, and diffuses with diffusion constant ϵ (lattice spacing 1), we find that the average lattice site until which the particle has diffused when attaching to the TL is given by $\langle x\rangle \pm \sigma(x) = \sqrt{\epsilon/\omega}(1 \pm \sqrt{2 - 4/\pi}) = \lambda(1 \pm 0.85)$ (see Appendix C 2). Here $\lambda = \sqrt{\epsilon/\omega}$ is a characteristic length scale of the system (see Sec. II B).

Since we assume the in-region to extend from the base into the system, we will approximate it as the region $[0,2\lambda]$ on symmetry grounds. The left (right) boundary corresponds to the average distance a particle travels before attaching to the

TL (λ) minus (plus) the standard deviation (also λ). The length of the in-region is determined by the characteristic length scale λ:

$$l_I \approx 2\lambda. \tag{16}$$

With this, we now determine the density profile in the in-region, which we assume to equilibrate quickly on the timescale of the oscillations. Furthermore, we assume that attachment is evenly distributed over the whole in-region, yielding an attachment rate of α_{eff}/l_I per site. In the low-density and continuum limit, together with the hopping transport on the TASEP and detachment of particles at rate ω, this yields a density profile in the in-region $\tilde{\rho}(x) = \alpha_{\text{eff}}[1 - e^{-\omega x}]/(l_I\omega)$, $x \in [0, l_I]$ (see Appendix C 2). In particular, the density at the right end of the in-region is given by

$$\tilde{\rho}(l_I) = \frac{\alpha}{2\tilde{\epsilon}}[1 - e^{-2\sqrt{\epsilon\omega}}]. \tag{17}$$

It increases with the density in the reservoir, $\alpha/\tilde{\epsilon}$, and also with both the diffusion rate ϵ and the attachment and detachment rate ω. Note that we measure time in units of the hopping rate $\nu \equiv 1$ on the TASEP, and length in units of the lattice spacing $a \equiv 1$.

We introduced the bulk region in order to interpolate between the densities in the in-region and in the tip neighborhood. Since the bulk region is sufficiently far from the reservoir and from the tip (at least when the length of the system $L \geqslant 4\lambda$) we assume that attachment and detachment approximately balance, and so the density is approximately constant and equal to $\tilde{\rho}(l_I)$ [Eq. (17)].

For the analysis of the dynamics in the tip neighborhood and at the tip, we switch to a different reference frame, namely starting at the tip and reaching into the tip neighborhood, comoving with the tip. The tip neighborhood represents that part of the system within which particles that have detached from the TL tip typically diffuse on the DL before reattaching to the TL. Thus, we assume that the tip neighborhood has the same length as the in-region $l_T = l_I = 2\lambda$ as for both the average distance traversed before attaching to the TL is essential. We will now substantiate the idea that particles that have detached from the tip reattach back to the TL: We suppose that particles that detach at the tip reattach to the TL on average after time $1/\omega$. Furthermore, they then walk to the tip during an additional average time $l_T/2 = \lambda$, since on average they attach to the TL at a distance $l_T/2$ away from the tip and take one directed step during time $1/\nu = 1$. So, the tip density at time t, $\rho^+(t)$, influences the tip density at time $t + 1/\omega + \lambda \equiv t + \Delta$, $\rho^+(t + \Delta)$. We determine $\rho^+(t + \Delta)$ as the steady state of the dynamics in the tip neighborhood and at the tip that results from the usual TASEP dynamics in the low-density and continuum limit combined with growth and shrinkage, and attachment at rate $\delta\rho^+(t)/l_T$ per site in the tip neighborhood (see Appendix C 3).

In summary, we imagine that particles that enter the tip region start "cycling" there: They detach at the tip, diffuse in the tip neighborhood, reattach to the TL, walk back to the tip, detach again and so on (Fig. 7). As long as $\epsilon < 1/\omega$, the average distance λ to the tip after reattaching to the TL is less than the average walking distance $1/\omega$ on the TL, so most particles that reattach to the TL reach the tip.

This procedure yields a recursion relation for the tip densities ρ^+_{it} at times $t_{\text{it}} = \text{it} \times \Delta$ (see Appendix C 3 for an explicit formula) that could, in principle, be used to determine the time evolution of the tip density. So far, however, we have implicitly assumed that the length of the system, l, is infinitely long, $l \gg \lambda$, and we have not considered how the physics changes for comparatively short system lengths. In particular, we ignored the fact that the shorter the system, the less likely particles that have previously detached from the tip are to reattach to the TL, as they may now leave the system beforehand. So, there will be some minimal length at which the majority of particles that had previously been in the tip region has left the system. From about this point the system starts growing again.

To estimate this minimal length, we consider a 1D system with injection of particles (=detachment) at rate r at site l (tip), symmetric diffusion at rate ϵ within the system, outflux (=reattachment) of particles at rate ω everywhere, and an additional outflux of particles at rate $\tilde{\epsilon}$ at site 0. In the steady state and with a continuum approximation, the reattachment probability of a particle detaching at the tip at length l can be approximated as

$$p_{\text{reattach}}(l) \approx 1 - F \exp\left(-\frac{l}{\lambda}\right) \tag{18}$$

for $l \gg \lambda$ (see Appendix C 4), where

$$F = \frac{2\lambda^3}{\varphi + 2\varphi\lambda + (1 + \varphi)\lambda^2 + \lambda^3}. \tag{19}$$

Here, $\varphi = \epsilon/\tilde{\epsilon}$ is the ratio between the diffusion rate and the exit rate. As expected, the reattachment probability decreases with decreasing length l, and has the characteristic length scale λ. Furthermore, F increases with decreasing φ, and so the reattachment probability decreases with decreasing φ. As a result, for a larger exit rate compared with the diffusion rate (small φ), the reattachment probability is small.

We have chosen the time interval Δ in such a way that during time Δ a given particle that has detached at the tip diffuses in the DL, reattaches, and walks back on the TL to the tip. So, in order for a particle to remain in the system, it needs to reattach to the TL each time it has detached and so, it needs to reattach back for all lengths l_{it} the system attains at times $t_{\text{it}} = \text{it} \times \Delta$. We have $p_{\text{survival}}(\{l_{\text{it}}\}_{\text{it}=1,\ldots,n}) = \prod_{\text{it}=1}^{n} p_{\text{reattach}}(l_{\text{it}})$ after a series of lengths $\{l_{\text{it}}\}_{\text{it}=1,\ldots,n}$. We further define the minimal length as the length where approximately 50% of the particles that were in the system at maximal length have left it. Making the rough assumption that the system shrinks at a constant velocity $v \approx \gamma/2$, which is half the maximal growth speed, we find

$$l_{\min} \approx \lambda \ln\left[\frac{2\lambda F}{\gamma\Delta \ln(2)}\right], \tag{20}$$

with F as defined before, Eq. (19) (see Appendix C 4). This means that, to leading order, the minimal length is determined by the typical length scale λ. The weak logarithmic dependency on the inverse growth rate $1/\gamma$ arises from the fact that the growth (and shrinkage) speed scales with γ.

Taking these considerations together, we find the following recursion relation for the tip densities ρ^+_{it} and the lengths l_{it} at

times $t_{\mathrm{it}} = \mathrm{it} \times \Delta$:

$$\rho^+_{\mathrm{it}} = \left\{ \left[\rho^+_{\mathrm{it}-1} \delta^2 \, \mathbb{1}(l_{\mathrm{it}-1} - l_{\min}) - A \right] + \sqrt{\left[\rho^+_{\mathrm{it}-1} \delta^2 \, \mathbb{1}(l_{\mathrm{it}-1} - l_{\min}) - A \right]^2 + 2B \left[\rho^+_{\mathrm{it}-1} \delta \, \mathbb{1}(l_{\mathrm{it}-1} - l_{\min}) + C \right]} \right\} / B, \tag{21a}$$

$$l_{\mathrm{it}} = l_{\mathrm{it}-1} + \gamma \Delta - \rho^+_{\mathrm{it}-1} \delta \Delta, \tag{21b}$$

with initial condition $\rho^+_0 = 0$ and $l_0 = 0$ (which, however, does not influence the long-term behavior, as in the case of the stochastic simulation). Furthermore,

$$A = \delta(1-\gamma) + \gamma(1-\gamma) - \delta\tilde{\rho}(l_I)(2-\gamma), \tag{22}$$

$$B = 2\delta[\delta(1-\tilde{\rho}(l_I)) + \gamma], \tag{23}$$

$$C = (1-\gamma)\tilde{\rho}(l_I), \tag{24}$$

where we use $\tilde{\rho}(l_I)$, $l_{\min}$, and Δ as defined before. Equation (21b) derives from the growth and shrinkage dynamics (constant growth at rate γ and motor-induced shrinkage at rate $\delta\rho^+$) during the time interval Δ, and $\mathbb{1}$ denotes the Heaviside step function.

Solving this recursion relation numerically, we now compare the predictions of our effective theory to the outcomes of simulations. To begin with, let us look at the result of the recursion relation, Eq. (21), itself, which is shown in Fig. 8. In line with the stochastic simulations [Fig. 5(c)], the length changes periodically with relatively symmetrical growth and shrinkage phases, while oscillations of the tip density, in contrast, follow a sawtooth pattern.

For a more quantitative comparison, we have numerically determined several quantities from the recursion relation and compared them to the results from simulations. In accordance with the stochastic simulation, we find that the minimal length is largely independent of the growth rate γ (Fig. 9) with a tiny decrease in minimal length for increasing growth rate in both stochastic simulations and the analytic prediction. This is what we would expect, as the turning point from shrinkage to growth should mainly be determined by the point at which diffusion (rate ϵ) is fast enough relative to the shrinkage dynamics to enable the tip cluster to equilibrate with the reservoir, and thus the system to quickly deplete.

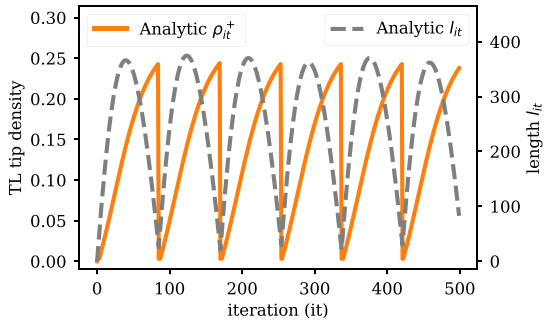

FIG. 8. Solution of the recursion relation for the tip density (orange, solid line) and the length (gray, dashed line) as a function of the iteration step, for $\gamma = 0.14$. Both show periodic behavior, but while the growth and shrinkage phases are rather symmetric for the length dynamics, the tip density exhibits a sawtooth shape.

Second, not only the turning points from shrinkage to growth, but also the inflection points from growth to shrinkage are important. In numerical simulations, not only the maximally reached length during the full simulation (see again Fig. 3 for more details) but also the average maximal length of the system per oscillation period increases faster than linearly with the growth rate (Fig. 9). This behavior is reproduced by our effective theory insofar as it also exhibits a faster than linear increase in the maximal length per oscillation period with the growth rate γ over the parameter range considered. Comparing the prediction of the effective theory with the average maximal length per period from simulations, we find quite good quantitative agreement.

Apart from its amplitude (difference between maximal and minimal length), the oscillation is also characterized by its frequency. Only with the suggested intuitive mechanism in mind, it is not clear *a priori* how the frequency should depend on the growth rate γ: There are two possible, opposing mechanisms. On the one hand, growth (and shrinkage [65]) increase with larger growth rate γ, so the oscillation period (frequency) should decrease (increase) with growth rate γ. On the other hand, for larger growth rate, the amplitude increases as well, namely faster than linearly, and so, the oscillation period (frequency) should increase (decrease). Furthermore, it is not clear how fluctuations in length influence the oscillation frequency. In summary, it is difficult to predict from the

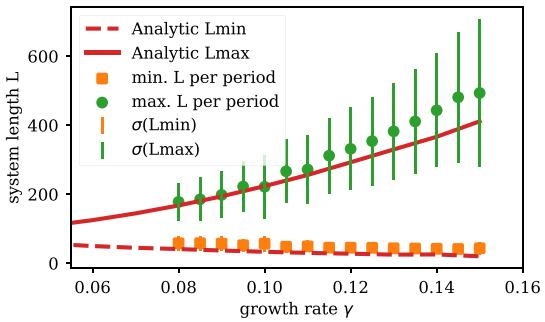

FIG. 9. Minimal and maximal length. The average minimal (maximal) length per oscillation period from stochastic simulations is compared with the prediction from the effective theory. From the stochastic simulations we determined the minimal and maximal length for each oscillation period, and the average minimal (maximal) length is depicted with orange squares (green circles), with error bars representing the corresponding standard deviation. Note that the average minimal length is approximately independent of the growth rate, in contrast to the average maximal length. The prediction from the effective theory is shown with red lines. As in the stochastic simulations the maximal length (solid line) increases with the growth rate γ, whereas the minimal length (dashed line) is only weakly dependent on the growth rate, decreasing slightly with increasing growth rate.

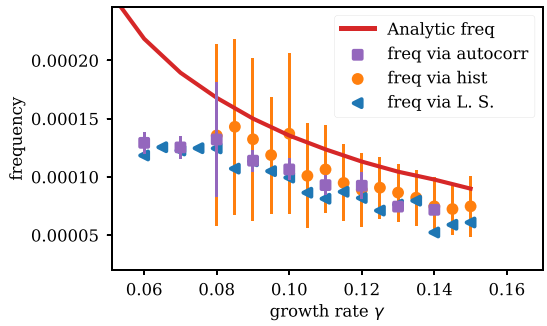

FIG. 10. Oscillation frequency. The oscillation frequency from stochastic simulations is compared with the prediction from the effective theory. We determined the length oscillation frequency from the stochastic simulations, first, by determining the autocorrelation oscillation frequency (freq via autocorr, purple squares), second, by evaluating the distribution of duration between two adjacent minima (freq via hist, orange circles), and third, by performing a Lomb-Scargle analysis comprising a sine fit (freq via L. S., blue left-pointing triangles). For the distribution approach, where a bound on the maximal frequency is used as explained in Appendix B, the distribution average and standard deviation (error bars) are depicted. For the Lomb-Scargle analysis the most probable frequency is shown. Clearly, for all methods the oscillation frequency decreases with larger growth rates. For very small rates noise masks the oscillation, such that the methods employed cannot determine the frequency correctly. Thus, results from the stochastic simulations are only shown for growth rates $\geqslant 0.06$. The predicted oscillation frequency from the effective theory is shown as a solid red line. It displays the same qualitative behavior as the result from stochastic simulations.

intuitive picture alone how the oscillation frequency depends on the growth rate.

We can, however, use our effective theory and the recursion relation to numerically determine the "analytical" oscillation frequency. We find that the analytical oscillation frequency decreases with increasing growth rate γ (Fig. 10). As mentioned above, visual inspection of the autocorrelation functions already suggests that the same is true for the stochastic simulations, and this is confirmed by different methods to determine the oscillation frequency from the stochastic simulations (Fig. 10): In both the simulation results and the analytical prediction, the oscillation frequency at $\gamma = 0.14$ is around half of its value at $\gamma = 0.08$. Note that for smaller growth rate γ it is very hard to determine an oscillation frequency from the stochastic simulations as the oscillation is largely obscured by stochastic noise.

All in all, in the parameter regime considered, our effective theory agrees nicely with the results from stochastic simulations (Sec. III), supporting the intuitive picture on which the effective theory is built.

V. SUMMARY AND DISCUSSION

In summary, we have studied a semiclosed system consisting of two coupled lanes, a TASEP lane and a diffusive lane which, at the tip, spontaneously grow, and shrink when a particle reaches the tip of the TASEP lane. We find two qualitatively different regimes for small and large growth rates, respectively, which differ in the dynamics of length change: For small growth rates, length change is mainly stochastic, while for large growth rates oscillatory patterns dominate.

The occurrence of those oscillatory patterns relies on the accumulation (crowding) of particles at the dynamic tip during the shrinkage phase [Fig. 6(d)]. This crowding leads to a positive feedback mechanism for shrinking [Fig. 6(e)], as each particle that reaches the TASEP lane tip further shrinks the system. The crowding is resolved only after a time delay, namely when the system size becomes comparable to the finite diffusion length. Then exchange of particles can occur between the tip region and the reservoir at the base, and the tip density equilibrates with the reservoir density [Fig. 6(f)], finally turning the shrinkage phase into a growth phase [Fig. 6(a)]. As transport on the TASEP lane is fast compared with the growth of the system, particles entering the system from the reservoir [Fig. 6(b)] "catch up" with the growing tip, and start accumulating there [Fig. 6(c)]. As soon as the crowding reaches a critical value, the whole process begins over again.

We provide a deeper quantitative understanding of the length oscillations by formulating an effective theory. It relies on the intuitive explanation we propose for the occurrence of the oscillations, namely cumulative crowding of motors at the tip due to finite diffusion, and correctly predicts the dependence of the oscillation frequency and amplitude on the growth rate, validating our intuitive picture.

From this intuitive picture it is evident that the emergence of the periodic behavior crucially depends on the finite diffusion speed, which—together with particle confinement—enables crowding of particles. To our knowledge, oscillatory patterns have not been observed in any similar lattice-gas model. We attribute this to the fact that in those models diffusion had not been taken into account explicitly, or only in terms of a homogeneous reservoir, corresponding to infinitely fast diffusion.

In our system, in the limit of infinitely fast diffusion, the equilibration between the DL tip and the reservoir takes place infinitely fast, and the density on the DL is homogeneous. So, in this limit our model reduces to the model discussed in Ref. [19].

On a broader perspective, the time delay due to a finite diffusion speed in a confined geometry also seems to be crucial for the occurrence of oscillatory behavior in other systems, such as in recent models for the Par or Pom protein systems [66,67] and for mass-conserving reaction-diffusion systems [68]. In general, delay times have been associated with periodic behavior in well-mixed systems as well [69,70]. Based on our analysis, we believe that it would be interesting to further explore how time delays can emerge intrinsically in a spatially extended nonequilibrium system, and under what conditions this leads to robust oscillations.

ACKNOWLEDGMENTS

We thank Silke Bergeler, Matthias Rank, Emanuel Reithmann, and Patrick Wilke for critical reading of the manuscript and for helpful comments. This research was supported by the German Excellence Initiative via the program "NanoSystems Initiative Munich" (NIM), and the Deutsche Forschungsgemeinschaft (DFG) via project B02 within the Collaborative Research Center (SFB 863) "Forces in Biomolecular Systems".

M.B. and I.R.G. are supported by a DFG fellowship through the Graduate School of Quantitative Biosciences Munich (QBM).

APPENDIX A: ANALYTIC APPROACH

In the following we perform in detail the calculations leading to the steady-state density profiles as sketched in Sec. II B. In particular, we will elaborate on the used approximations, i.e., the adiabatic assumption, the mean-field approximation, the continuum limit, and the mesoscopic limit. We start with some comments on the used notation.

We denote the first, i.e., the leftmost, site by "0" and the last site by "L". Indices will be used to denote site numbers. Moreover, the results below are stated in terms of $\rho_{j(t)}(t)$, i.e., using the index at time t, not $t+dt$. This is necessary to clarify as site indices change due to length changes. Occupancy numbers n will be approximated by occupancy densities ρ (η) on the TL (DL). Often we simply denote $\langle L\rangle$ by "L". "$\langle\,\rangle$" represents the ensemble average.

We begin with the adiabatic assumption which allows us to decouple length change and particle dynamics. We perform the argument exemplarily for the TL. The first step is to write down the probability for a certain lattice site to be occupied.

Any tuple of length l with entries zero (=empty) or one (=occupied) describes a possible state of the TL with length l, e.g., $(n_0=1,n_1=0,n_2=\ldots,\ldots,n_l=1)$. Let us denote the complete set of such tuples as $\Omega(l)$, and the number of elements it contains by $|\Omega(l)|$. $(n_i)^l_{i=0,j}$ describes the jth element of this set. In this notation the probability of a site i to be occupied with one particle at time $t+dt$ can be written as

$$\mathrm{P}(n_{i(t+dt)}(t+dt)=1)=\sum_{l=0}^{\infty}\sum_{j=1}^{|\Omega(l)|}\mathrm{P}[n_{i(t+dt)}(t+dt)=1\mid(n_i)^l_{i=0,j}(t),L(t)=l]\mathrm{P}[(n_i)^l_{i=0,j}(t)\mid L(t)=l]\mathrm{P}[L(t)=l]. \quad \text{(A1)}$$

The first factor is the probability that site i is occupied at time $t+dt$ under the condition that the system was l sites long at time t and its state was $(n_i)^l_{i=0,j}$. The second factor gives the probability that the system was in state $(n_i)^l_{i=0,j}$ at time t under the condition that its length was l and the last term corresponds to the probability that the system was l sites long. Every possible state at fixed length and any length could contribute, hence the sums. The difficulty is that the length distribution $\mathrm{P}(L(t)=l)$ itself again depends on the occupancy numbers $\{n_i\}$, in particular on the TL tip occupancy n^T_l:

$$\begin{aligned}\partial_t\mathrm{P}(L=l)=&\,\delta n^T_{l+1}\mathrm{P}(L=l+1)+\gamma\mathrm{P}(L=l-1)\\&-\left(\delta n^T_l+\gamma\right)\mathrm{P}(L=l),\end{aligned} \quad \text{(A2)}$$

where the first two terms describe the probability gain due to a shrinkage or growth event of a longer or shorter length, respectively, while the last term represents the corresponding probability loss.

To tackle this problem analytically, we assume that the length changing dynamics happens at a far longer timescale than the particle hopping. Thus both dynamics can be decoupled. We refer to this simplification as *adiabatic assumption*. It is untenable for large growth rates, as confirmed in the simulations, but suitable for small growth rates. In this regime the assumption implies that we can take the particle densities to adapt instantaneously to the current length and correspondingly that we can replace the (changing) length by a constant length when describing the particle occupancy dynamics. Thus, for the occupancy number dynamics, Eq. (A1), we choose the, by this assumption constant, length to equal the average lattice length. Mathematically this can be expressed by setting $\mathrm{P}(L(t)=l)\propto\delta(l,\langle L\rangle)$ where $\delta(i,j)$ is the Kronecker delta. On the other hand, in Eq. (A2) for the length changing dynamics the actual occupancy n^T_l can be replaced by its time average. The time average is equivalent to the ensemble average, ρ_l at length l, that is, the average tip occupancy at length l (in contrast to the average occupancy at site l for arbitrary length or the one for average length $\langle L\rangle$). We find

$$\mathrm{P}(n_{i(t+dt)}(t+dt)=1)=\sum_{j=1}^{|\Omega(\langle L\rangle)|}\mathrm{P}\big[n_{i(t+dt)}(t+dt)=1\mid(n_i)^{\langle L\rangle}_{i=0,j}(t)\big]\mathrm{P}\big[(n_i)^{\langle L\rangle}_{i=0,j}(t)\big] \quad \text{(A3)}$$

and

$$\begin{aligned}\partial_t\mathrm{P}(L=l)=&\,\delta\rho_{l+1}\mathrm{P}(L=l+1)+\gamma\mathrm{P}(L=l-1)\\&-(\delta\rho_l+\gamma)\mathrm{P}(L=l).\end{aligned} \quad \text{(A4)}$$

So, applying the adiabatic assumption, we can decouple the occupancy number and length dynamics and proceed.

From now on, we will furthermore restrict ourselves to the *stationary state* of the system,

$$\partial_t\langle n_i\rangle\stackrel{!}{=}0$$

and $L\equiv\langle L\rangle$. The next approximation to solve the coupled set of occupancy equations is to eliminate the correlations between occupancies at different sites by using the *mean-field approximation*

$$\langle n_i n_j\rangle\approx\langle n_i\rangle\langle n_j\rangle\equiv\rho_i\rho_j.$$

The equations for the occupancy dynamics at any site are then given by

$$\begin{aligned}0=\partial_t\rho_0=&-\nu\rho_0(1-\rho_1)-\omega(\rho_0-\eta_0+\rho_0\eta_0),\\0=\partial_t\rho_i=&\,\nu[\rho_{i-1}(1-\rho_i)-\rho_i(1-\rho_{i+1})]\\&-\omega(\rho_i-\eta_i+\rho_i\eta_i),\end{aligned}$$

$$0 = \partial_t \rho_L = -\gamma \rho_L + \delta \rho_L(\rho_{L-1} - 1) + \nu \rho_{L-1}(1 - \rho_L),$$
$$0 = \partial_t \eta_0 = \alpha - \epsilon(2\eta_0 - \eta_1) + \omega(\rho_0 + \rho_0 \eta_0 - \eta_0),$$
$$0 = \partial_t \eta_i = \epsilon(\eta_{i+1} + \eta_{i-1} - 2\eta_i) + \omega(\rho_i + \rho_i \eta_i - \eta_i),$$
$$0 = \partial_t \eta_L = -\gamma \eta_L + \delta \rho_L(1 + \eta_{L-1}) + \epsilon(\eta_{L-1} - \eta_L),$$

with i denoting any bulk site. The corresponding flux balances are

$$\text{(TL)} \quad 0 = +J_0^{D\to T} - J_1^T, \tag{A5}$$
$$\text{(DL)} \quad 0 = -J_0^{D\to T} + \epsilon(\eta_1 - \eta_0) - \epsilon\eta_0 + \alpha, \tag{A6}$$
$$\text{(TL)} \quad 0 = +J_i^{D\to T} + \left(J_i^T - J_{i+1}^T\right), \tag{A7}$$
$$\text{(DL)} \quad 0 = -J_i^{D\to T} + D_i, \tag{A8}$$

for the first site and the bulk, respectively.

Moreover, although the lattice is growing and shrinking, its length L is typically 100 up to 1000 times larger than the remaining parameters and densities. Thus it is justified to consider the limit where the lattice spacing ξ tends to zero when the total length of the system is rescaled to 1.

The second step is thus to apply the *continuum limit* by replacing the lattice by a smooth interval $[0,1]$. Note that this is different from the choice in Sec. II B, where the interval is set to $[0,L]$ in order to keep the notation cleaner. Here we want to clearly see the orders of the following Taylor expansion. We further define the occupancy density (also named ρ) to be the smooth function satisfying $\rho(\xi i/L) = \rho_i$ with $i = 1,\ldots,L-1$ denoting the lattice site index. We set $\xi = 1$ in order to rescale the system size to 1. ρ can then be Taylor-expanded in the limit $1/L \to 0$:

$$\rho\left(x \pm \frac{1}{L}\right) = \rho(x) \pm \frac{1}{L}\partial_x \rho(x) + \frac{1}{2L^2}\partial_x^2 \rho(x) + O\left(\frac{1}{L^3}\right).$$

For the currents this expansion gives

$$J^T(x) = \left[\rho(x) - \frac{\partial_x}{L}\rho(x)\right][1 - \rho(x)], \tag{A9}$$
$$J^{D\to T}(x) = \omega[1 - \rho(x)]\eta(x) - \omega\rho(x), \tag{A10}$$
$$D(x) = \epsilon\frac{\partial_x^2}{L^2}\eta(x). \tag{A11}$$

Moreover, we focus on the *mesoscopic limit* [7,8] of ω. This implies that $\omega = \Omega/L_0$, with L_0 denoting the initial length, is treated as order $1/L$. Consequently, $J^{D\to T}(x)$ has no 0th order contribution.

As the DL is the only source of particles on the TL, we will at first solve the equation for the diffusive lane and use it to obtain the TL density profile. We begin at the left boundary.

$$\text{(DL)} \quad 0 = -\epsilon\eta(0) + \alpha - J^{D\to T}(0) + \epsilon\frac{\partial_x}{L}\eta(0); \tag{A12}$$

thus, to 0th order in the lattice spacing we are left with $0 = -\epsilon\eta(0) + \alpha$, concluding

$$\eta(0) = \frac{\alpha}{\epsilon}. \tag{A13}$$

For the TL we have

$$0 = \omega[1 - \rho(0)]\eta(0) - \omega\rho(0) - \rho(0)\left[1 - \rho(0) - \frac{\partial_x}{L}\rho(0)\right], \tag{A14}$$

implying $0 = -\rho(0)[1 - \rho(0)] + O(1/L)$. This equation has two solutions, either the first site is always occupied or always empty. To lowest order, as we only treat the low-density limit, the site has to be empty, i.e., $\rho(0) = 0$. To first order, we obtain $0 = \omega\eta(0) - \rho(0)$, thus

$$\rho(0) = \omega\eta(0). \tag{A15}$$

The first order equation for the DL is

$$\omega\{[1 - \rho(0)]\eta(0) - \rho(0)\} = \epsilon\frac{1}{L}\partial_x\eta(0). \tag{A16}$$

With $\rho(0) = 0$ to 0th order, we obtain

$$\frac{\partial_x}{L}\eta(0) = \lambda^{-2}\eta(0), \tag{A17}$$

with

$$\lambda \equiv \sqrt{\frac{\epsilon}{\omega}}. \tag{A18}$$

Having solved the boundary equations, we apply these results to solve the bulk equations. By adding the DL bulk dynamics equation corresponding to Eq. (A8)

$$\text{(DL)} \quad 0 = -J^{D\to T} + \epsilon\frac{\partial_x^2}{L^2}\eta(x) \tag{A19}$$

to the TL bulk dynamics equation derived from Eq. (A7)

$$\text{(TL)} \quad 0 = J^{D\to T}(x) + \frac{\partial_x}{L}\rho(x)[2\rho(x) - 1], \tag{A20}$$

we obtain the first order TASEP bulk equation $0 = \partial_x\rho(x)[2\rho(x) - 1]$. As we are in the low-density limit, the solution $\rho(x) = 1/2$, corresponding to the maximal current solution, can be ruled out, thus $\partial_x\rho(x) = 0$. Using our results from the left boundary as initial values, we conclude that the constant density equals $\rho(x) = \rho(0) = 0$ to first order. We conclude that the occupancy is constant and thus equals the occupancy at the first site. To first order, it has been determined to equal zero [Eq. (A15)], thus $\rho(x) = \rho(0) = 0$. Inserting this result to the second order DL equation gives

$$\epsilon\frac{\partial_x^2}{L^2}\eta(x) = \omega\eta(x), \tag{A21}$$

which is solved by

$$\eta(x) = A\sinh\frac{xL}{\lambda} + B\cosh\frac{xL}{\lambda}. \tag{A22}$$

Using our boundary conditions, $\eta(0) = \alpha/\epsilon$ [Eq. (A13)] and $(\partial_x/L)\eta(0) = \lambda^{-2}\eta(0)$ [Eq. (A17)], gives

$$\eta(x) = \eta(0)\left(\frac{1}{\lambda}\sinh\frac{xL}{\lambda} + \cosh\frac{xL}{\lambda}\right). \tag{A23}$$

We continue with the second order equations of the TL bulk,

$$0 = \omega[1 - \rho(x)]\eta(x) - \omega\rho(x) + \frac{\partial_x}{L}\rho(x)[2\rho(x) - 1]. \tag{A24}$$

Upon employing that the first order value of ρ is zero [Eq. (A15)], we are left with

$$0 = \omega\eta(x) - \frac{\partial_x}{L}\rho(x), \tag{A25}$$

which is solved by

$$\rho(x) = \rho(0) + \frac{\alpha}{\lambda}\left(\frac{1}{\lambda}\cosh\frac{xL}{\lambda} + \sinh\frac{xL}{\lambda} - \frac{1}{\lambda}\right). \tag{A26}$$

In summary, we have found analytic expressions for the steady-state TL and DL occupancy densities in the adiabatic limit.

APPENDIX B: OSCILLATORY BEHAVIOR

In Sec. III we have learned about the existence of a parameter regime where the length change exhibits oscillatory behavior. Following up on these investigations, we want to further discuss the methods used. Moreover we want to examine the occupancy densities at the system tip when the system switches from growth to shrinkage.

As the time intervals between two events in the simulation are not uniformly spaced, we performed a Lomb-Scargle analysis instead of a Fourier analysis [71] to determine the average oscillation frequency (see Fig. 10). The algorithm essentially fits a sine function to the data and checks which frequency matches the data best. We deduced the frequency with the smallest false alarm probability as well as the second and third best choice. For larger γ values, the frequency decreases with increasing growth rate and reassuringly, the three best frequencies agree quite well. For small growth rates, the results should not be taken seriously, as there are also no visible oscillations in the time traces.

Moreover, we determined the minima and maxima of a time series of the length. This was done by cutting off the data of length for lengths larger than the initial length L_0 (which is 2–3 times larger than the minimum average length and smaller than the average length). Within each of the remaining intervals we determined the minimal length, while sorting out all minima that occurred very quickly after each other, i.e., in less time than a threshold ΔT. This threshold excludes small fluctuations around $L = L_0$ and is chosen in a way to minimize artifacts of chopping off the length at L_0. We used $\Delta T = 800$. Note that our choice of ΔT does influence the frequency results as it restricts the maximal frequency. Between each two minima, we then determined the maxima. The respective averages and standard deviations for the maximally and minimally obtained system length during an oscillation period are plotted in Fig. 9. The maxima clearly increase with larger growth rates, whereas the minima remain rather constant. The latter further supports our intuition of a particle cluster at the DL tip, which equilibrates with the reservoir only when the system length is small enough for diffusion to be comparable to shrinkage. From the temporal distance of the minima, the oscillation frequency was deduced (see Fig. 10). The values agree with the result of the Lomb-Scargle analysis mentioned before. As a third method to determine the oscillation frequency we extracted the frequency from the autocorrelation function [Eq. (14)]. We searched for the first 2–4 maxima and minima of the autocorrelation function and averaged their distance. For smaller grow rates we had to reduce the number of maxima and minima, as the number of oscillations reduced from >4, to 2 and even 1 in the case of $\gamma = 0.005$. The extracted frequencies are also shown in Fig. 10.

Figure 11 shows the TASEP tip neighborhood (i.e., 20 tip sites) occupancy at the oscillation maxima corresponding to the turning point between a phase of growth and a phase of shrinkage. The blue upper line represents the mean of the TASEP tip neighborhood occupancy (red squares). The results vary strongly; thus we checked related observables. But also the maximal tip neighborhood occupancy (gray left-pointing triangles) within ten time steps—five before the maximum is reached and five thereafter—and the average (yellow right-pointing triangles) fluctuate. Nevertheless we see that nearly all measurements of the maximal tip neighborhood occupancy (gray left-pointing triangles) lie above the critical density (purple lower line), being γ times the tip neighborhood size (here 20 sites) as the length change is given by $\partial_t L = \gamma - \delta\rho_+$ (as $\delta = 1$). When we compare the critical density to the mean density for a time interval covering more than one oscillation period, and not just at the time points where the amplitude is maximal, the values coincide. It can further be noted that none of the observables of the turning point tip occupancy increases for larger amplitudes, i.e., system lengths (for a fixed growth rate). These observations further support our intuition that the length grows until a critical occupancy density at the tip (depending solely on the growth rate) has been reached, triggering the switch to the shrinking phase. As shown in the time trace plot, Fig. 5, in Sec. III, the total occupancy density follows a sawtooth-like trajectory. This is due to a constant influx from the reservoir during the growth phase and most of the shrinkage phase. Only at the end of the shrinkage phase the cluster at the tip communicates with the reservoir and is quickly emptied.

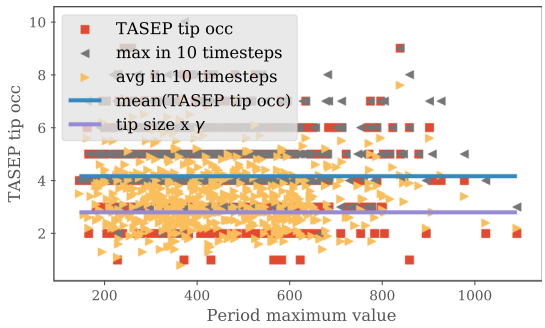

FIG. 11. Occupancies of the TASEP lane tip neighborhood, i.e., here the 20 last sites, at the time point or time interval when the length reaches its maximum during one oscillation period. They have been measured for several periods and are shown for a growth rate of 0.14. The occupancy at these time points (red squares) and their average (upper blue line) as well as the occupancy average (yellow right-pointing triangles) and maximum (gray left-pointing triangles) over a time period of ten events—five before and five after the maximum—is depicted. Moreover, the critical density for switching from growth to shrinkage (lower purple line) is shown.

APPENDIX C: DETAILED CALCULATIONS FOR THE EFFECTIVE THEORY

In this section we elaborate on the mathematical details for the effective theory. First, in Appendix C 1 we determine the effective in-rate from the reservoir onto the TL. In order to estimate the density in the bulk, we infer the length of the in-region; see Appendix C 2. Finally, we deduce the recursion relation for the tip density in Appendix C 3, and the minimal length in Appendix C 4.

1. Effective in-rate α_{eff}

In this subsection, we comment on how we determine the effective rate at which particles enter the system and then attach to the TL. This rate will not equal the "bare" in-rate α as particles can also leave the system before attaching. What is the probability that a particle that enters from the reservoir leaves the system again, before attaching to the TL? To answer this question, let us consider a situation where the length of the system is considerably larger than the length of a typical journey of a particle on the DL before attaching to the TL, the latter of which we estimate as $\lambda \pm \lambda$ (see later). Here, $\lambda = \sqrt{\epsilon/\omega}$ is the characteristic length scale of the system. In this case of large length, the probability that a given particle that enters the DL leaves back into the reservoir before attaching to the TL, Prob(leaving), is given by

$$\text{Prob(leaving)} = \sum_{j=0}^{\infty} p q^j A^j, \tag{C1}$$

where $p = \tilde{\epsilon}/(\tilde{\epsilon} + \epsilon + \omega)$ is the probability that a particle exits from the first DL site back into the reservoir [72]. The quantity $q = \epsilon/(\tilde{\epsilon} + \epsilon + \omega)$ is the probability that a particle proceeds to diffuse into the protrusion and A is the probability that a particle that starts at the first site of the DL returns to the first site of the DL without attaching to the TL in between. Since returning to the first site of the DL without attaching to the TL in between can only happen after an even number of steps on the DL, this probability A comprises the probabilities that the particle diffuses back to the first site of the DL in exactly $2j$ steps, $j \in \mathbb{N}$, without attaching to the TL. The latter are given by the product of the probability that a symmetric random walker returns back to its starting point after exactly $2j$ steps and the probability that the particle stays on the DL in each step. Taken together we determine A as follows:

$$\begin{aligned} A &= \text{Prob(return to site 1 without attaching to TL)} = \sum_{j=1}^{\infty} \text{Prob(return to site 1 in exactly } 2j \text{ steps without attaching to TL)} \\ &= \sum_{j=1}^{\infty} \text{Prob(return to site 1 in exactly } 2j \text{ steps} \mid \text{not attaching to TL during the } 2j \text{ steps)} \\ &\quad \times \text{ Prob(not attaching to TL during the } 2j \text{ steps)} \\ &= \sum_{j=1}^{\infty} f_{2j} \left(\frac{2\epsilon}{2\epsilon+\omega}\right)^{2j-1} = \frac{2\epsilon+\omega}{2\epsilon}\left(1 - \frac{\sqrt{\omega(4\epsilon+\omega)}}{2\epsilon+\omega}\right), \end{aligned}$$

where $f_{2j} = \binom{2j}{j}/[(2j-1)2^{2j}]$ is the probability that a symmetric 1D random walker returns to its starting point for the first time in exactly $2j$ steps. Note that the probability that the particle does not attach during the $2j$ steps only has $2j-1$ terms $2\epsilon/(2\epsilon+\omega)$ as the first step into the protrusion is already accounted for by the probability q in Prob(leaving), Eq. (C1). Combining the result for A with the explicit formulas for p and q we find

$$\text{Prob(leaving)} = 1 - \frac{\omega + \sqrt{\omega(4\epsilon+\omega)}}{\omega + \sqrt{\omega(4\epsilon+\omega)} + 2\tilde{\epsilon}}.$$

We approximate this formula for small ω by Taylor expanding up to first order in ω:

$$\text{Prob(leaving)} = 1 - \frac{\sqrt{\omega\epsilon}}{\tilde{\epsilon}} + \frac{2\epsilon - \tilde{\epsilon}}{2\tilde{\epsilon}^2}\omega + O(\omega^{3/2}).$$

The effective in-rate is given by the "bare" in-rate α weighted by the probability that a particle that enters from the reservoir attaches to the TL. The latter probability is just 1 − Prob(leaving). This implies that the effective in-rate is given by

$$\alpha_{\text{eff}} = \alpha \, \frac{\omega + \sqrt{\omega(4\epsilon+\omega)}}{\omega + \sqrt{\omega(4\epsilon+\omega)} + 2\tilde{\epsilon}} \approx \frac{\alpha}{\tilde{\epsilon}}\sqrt{\omega\epsilon} \tag{C2}$$

to lowest order in ω.

2. Length of the in-region and density in the bulk

To continue we now estimate the length of the "in-region" l_I since—due to the attachment and detachment—the density at the end of the in-region depends on the length. For this, we look at a symmetric random walk with reflecting boundary at $x = 0$ as we want to find out the typical journey of a particle on the DL that is eventually attaching to the TL (and thus not leaving the system again). Using the initial condition $p(x,t=0) = \delta(x)$, the probability distribution of such a process is given by $p(x,t) = e^{-x^2/(4\epsilon t)}/\sqrt{\pi\epsilon t}$ for $x \geqslant 0$ where ϵ is the diffusion constant (lattice spacing 1). To determine the average distance a particle travels on the DL before attaching to the TL, $\langle x \rangle_{\text{attach}}$, and its standard deviation, σ_{attach}, we need to take two processes into account. First, we need to find out how the time at which the particle attaches to the TL is distributed

and, second, how far a particle travels until a certain time point. Using that the attachment process is a Poisson process of rate ω, where the time until an attachment event happens has the probability distribution $f(t) = \mathrm{Prob}(T = t) = \omega e^{-\omega t}$, we calculate the mean and variance as $\langle x\rangle_{\mathrm{attach}} = \int_0^\infty dt\, f(t)\langle x(t)\rangle$ and $\sigma^2_{\mathrm{attach}} = \int_0^\infty dt\, f(t)[\langle x^2(t)\rangle - \langle x(t)\rangle^2]$. Here, $\langle x(t)\rangle$ and $\langle x^2(t)\rangle - \langle x(t)\rangle^2$ are the mean and variance of the traveled distance of the symmetric random walk until time t. For those quantities we find $\langle x(t)\rangle = 2\sqrt{\epsilon t/\pi}$ and $\langle x(t)^2\rangle = 2\epsilon t$ from the above probability distribution $p(x,t)$. As a result, $\langle x\rangle_{\mathrm{attach}} = \sqrt{\epsilon/\omega} = \lambda$ and $\sigma_{\mathrm{attach}} = \lambda\sqrt{2-4/\pi} \approx \lambda = \langle x\rangle_{\mathrm{attach}}$. Therefore, $\langle x\rangle_{\mathrm{attach}} \pm \sigma_{\mathrm{attach}} \approx \lambda \pm \lambda$, which means that the standard deviation is approximately the same as the mean. We will thus approximate the length of the in-region as twice the average distance a particle travels before attaching to the TL:

$$l_I \approx 2\lambda. \tag{C3}$$

With this relation, we now determine the density profile in the in-region which we assume to equilibrate quickly on the timescale of the oscillations. Let us denote by $\tilde{\rho}_i$ the density at site i from the base. Then, we approximate the time evolution of the density at site $i = 1, \ldots, L_I$ as

$$0 = \partial_t \tilde{\rho}_i \approx \tilde{\rho}_{i-1} - \tilde{\rho}_i + \frac{\alpha_{\mathrm{eff}}}{L_I} - \omega\tilde{\rho}_i$$

in the low-density limit with the boundary condition $\tilde{\rho}_0 \approx 0$. Here, $L_I = \mathrm{Round}(l_I)$ is the integer length of the in-region within which we assume homogeneous attachment (at rate $\alpha_{\mathrm{eff}}/L_I$ per site). Performing a continuum limit $i \to x$, $x \in [0,l_I]$, and considering only the first derivative with respect to x, we have

$$0 = -\partial_x\tilde{\rho}(x) + \frac{\alpha_{\mathrm{eff}}}{l_I} - \omega\tilde{\rho}(x)$$

with the solution $\tilde{\rho}(x) = \alpha_{\mathrm{eff}}(1 - e^{-\omega x})/(l_I\omega)$. So, in particular, we obtain for the particle density at the end of the in-region

$$\tilde{\rho}(l_I) = \frac{\alpha}{2\tilde{\epsilon}}(1 - e^{-2\sqrt{\epsilon\omega}}),$$

where we combined all the above results.

3. Recursion relation for the tip density

As mentioned in Sec. IV, for the analysis of the tip neighborhood and the tip, we go to a different reference frame, namely starting at the tip and reaching into the tip neighborhood, comoving with the tip. By $\rho_0 \equiv \rho^+$ we denote the density at the tip and by ρ_i the density at the ith site from the tip. Since we defined the tip neighborhood to be the region where motors that have previously detached at the tip reattach to the TL, we assume that the tip neighborhood has the same length as the in-region $l_T = l_I = 2\lambda$ as for both the average distance before attaching to the TASEP becomes essential.

Note that we ignore the influence of the growth and shrinkage dynamics on the average distance before attaching. This, however, should be legitimate in our parameter regime: Assume that we look at a symmetric random walk on a lattice with one reflecting boundary at the left end where also new particles are injected. At each site, the particles can leave the system at rate ω, and the reflecting boundary moves at rate $v > 0$ to the right (or, in the case of $v < 0$, at rate $-v$ to the left). Then, in the comoving frame (moving with the reflecting boundary), the steady-state profile is proportional to $e^{-x/\bar{\lambda}}$ with the length scale $\bar{\lambda} = 2\epsilon/(v + \sqrt{v^2 + 4\epsilon\omega})$ which corresponds to the average traveled distance before leaving the system via ω. In our case, the velocity is not constant but if we assume that the velocity is homogeneously distributed in $[-\gamma,\gamma]$, we get an average length scale which is very close to λ for our choice of parameters.

Let us now go back to the densities in the tip neighborhood and right at the tip. By taking into account the reattachment of motors that have detached at the tip an (average) time $1/\omega$ before, the growth and shrinkage dynamics, and the usual hopping, we find, for the time evolution of the density ρ_i in the low-density limit,

$$\partial_t\rho_i = \rho_{i+1} - \rho_i + \frac{\delta\rho^+_{\mathrm{before}}}{l_T} + \gamma(\rho_{i-1} - \rho_i) + \delta\rho^+(\rho_{i+1} - \rho_i), \tag{C4}$$

and for the tip density $\rho_0 = \rho^+$,

$$\partial_t\rho^+ = \rho_1 - \gamma\rho^+ - \delta\rho^+(1-\rho_1). \tag{C5}$$

Note, however, that in the last equation for the tip density we take exclusion into account explicitly by assuming that the occupancy at the tip is exactly 1 in the case of a shrinkage event (last term). If exclusion was lifted, there could be more than one particle at the tip and several particles would then be simultaneously released into the cytosol in the case of a shrinkage event.

For the time evolution of ρ_i, Eq. (C4), we assume that the particles that have previously detached at the tip (at rate $\delta\rho^+_{\mathrm{before}}$, corresponding to a previous tip density ρ^+_{before}) homogeneously reattach to the TL in the tip neighborhood. To proceed we now make the following ansatz: We assume that for a tip density ρ^+_{before} at time t we can determine the tip density at time $t' = t + 1/\omega + \lambda = t + \Delta$ by solving Eqs. (C4) and (C5) for ρ^+ in the steady state. The idea behind this is that a particle that has detached at the tip needs on average $1/\omega$ to reattach to the TL, and then has to walk on average λ sites to get back to the tip (we measure time in units of $v \equiv 1$, and length in units of the lattice spacing $a \equiv 1$). Using the continuum approximation in Eq. (C4) and considering only zero- and first-order terms, we find for the density in the tip neighborhood

$$\rho(x) = \tilde{\rho}(l_I) + \frac{\delta\rho^+_{\mathrm{before}}}{l_T}\frac{1}{1 + \delta\rho^+ - \gamma}(l_T + 1 - x),$$

where we used the boundary condition $\rho(l_T + 1) = \tilde{\rho}(l_I)$. As a result, the density at the site next to the tip is given by

$$\rho_1 = \rho(1) = \tilde{\rho}(l_I) + \frac{\delta\rho^+_{\mathrm{before}}}{1 + \delta\rho^+ - \gamma}. \tag{C6}$$

Combining this with Eq. (C5) we solve for ρ_1 and find an equation for the tip density ρ^+ in terms of the previous tip density ρ^+_{before}:

$$(\delta + \gamma)\rho^+(1 - \gamma + \delta\rho^+) = (1 + \delta\rho^+)[(1 - \gamma + \delta\rho^+)\tilde{\rho}(l_I) + \delta\rho^+_{\mathrm{before}}].$$

Bearing in mind that the tip density should be positive, this equation is solved by

$$\rho^+ = \big[\delta^2\rho^+_{\text{before}} - A + \sqrt{(\delta^2\rho^+_{\text{before}} - A)^2 + 2B\big(\delta\rho^+_{\text{before}} + C\big)}\big]/B,$$

where $\tilde{\rho}(l_I) = \alpha(1 - e^{-2\sqrt{\epsilon\omega}})/(2\tilde{\epsilon})$ (see above) and

$$A = \delta(1-\gamma) + \gamma(1-\gamma) - \delta\tilde{\rho}(l_I)(2-\gamma),$$
$$B = 2\delta[\delta(1-\tilde{\rho}(l_I)) + \gamma],$$
$$C = (1-\gamma)\tilde{\rho}(l_I).$$

So, this equation relates the previous tip density ρ^+_{before} at time t to the tip density ρ^+ at time $t+\Delta$. Iterating this procedure, we find a recursion relation for the tip densities ρ^+_{it} at times $t_{\text{it}} = \text{it} \times \Delta$:

$$\rho^+_{\text{it}} = \big[\delta^2\rho^+_{\text{it}-1} - A + \sqrt{(\delta^2\rho^+_{\text{it}-1} - A)^2 + 2B\big(\delta\rho^+_{\text{it}-1} + C\big)}\big]/B. \tag{C7}$$

4. Minimal length

So far, we have considered the situation where the length of the system is much longer than the average distance a particle typically travels on the DL. However—if the system is too small—the particles do not reattach to the TL as they leave the system too quickly. As a result, most of the particles will have left the system before the system is shrunk to zero, and the system will regrow from a minimal length larger than zero. To estimate this minimal length, let us consider a 1D system of length l with injection of particles at rate r at site l, symmetric diffusion at rate ϵ within the system, outflux of particles at rate ω everywhere, and an additional outflux of particles at rate $\tilde{\epsilon}$ at site 0. In the steady state and with a continuum approximation we thus have

$$0 = \partial_t p(x,t) = \epsilon\partial_x^2 p(x,t) - \omega p(x,t),$$
$$0 = \partial_t p(0,t) = \epsilon\partial_x p(0,t) - (\omega+\tilde{\epsilon})p(0,t),$$
$$0 = \partial_t p(l,t) = -\epsilon\partial_x p(l,t) - \omega p(l,t) + r.$$

Those equations are solved by

$$p(x) = \frac{re^{\frac{(l-x)}{\lambda}}}{\omega} \times \frac{\varphi\lambda(1+e^{\frac{2x}{\lambda}}) + (\varphi+\lambda^2)(-1+e^{\frac{2x}{\lambda}})}{\lambda(2\varphi+\lambda^2)(1+e^{\frac{2l}{\lambda}}) + [\varphi+(\varphi+1)\lambda^2](-1+e^{\frac{2l}{\lambda}})},$$

where $\varphi = \epsilon/\tilde{\epsilon}$ is the ratio between the diffusion and the exit rate. So, we determine the (steady-state) probability that a particle that enters the system at site l (the tip) exits it via the rate $\tilde{\epsilon}$ (back into the reservoir) and not via ω (attaching to the TL) as $p_{\text{exit}} = p(0)\tilde{\epsilon}/r$, which yields

$$p_{\text{exit}} = \frac{2\lambda^3 e^{\frac{l}{\lambda}}}{\lambda(2\varphi+\lambda^2)(1+e^{\frac{2l}{\lambda}}) + [\varphi+(\varphi+1)\lambda^2](e^{\frac{2l}{\lambda}}-1)}.$$

As a result, the reattachment probability for a particle detaching at the tip at length l is approximated as

$$p_{\text{reattach}}(l) \approx 1 - Fe^{-\frac{l}{\lambda}} \tag{C8}$$

for $l \gg \lambda$. Here, $F = 2\lambda^3/[\varphi + 2\varphi\lambda + (\varphi+1)\lambda^2 + \lambda^3]$. This means that the probability that a particle has not yet left the system after a series of lengths $\{l_{\text{it}}\}_{\text{it}=1,\ldots,n}$ is given by

$$p_{\text{survival}}(\{l_{\text{it}}\}_{\text{it}=1,\ldots,n}) = \prod_{\text{it}=1}^{n} p_{\text{reattach}}(l_{\text{it}})$$

or, equivalently,

$$\ln[p_{\text{survival}}(\{l_{\text{it}}\}_{\text{it}=1,\ldots,n})] = \sum_{\text{it}=1}^{n} \ln[p_{\text{reattach}}(l_{\text{it}})].$$

Assuming that the system shrinks at constant velocity v: $l(t) = l_0 - vt$, and taking into account that in our effective system each length is realized for time Δ (during this time a particle that has detached potentially reattaches and walks back to the tip), we identify the length dynamics until time t with $\{l_0, l_0 - v\Delta, \ldots, l_0 - v\Delta(t/\Delta)\}$. Approximating the sum as an integral, we then deduce the "survival" probability until time t as

$$\begin{aligned}
\ln[p_{\text{survival}}(t)] &\approx \sum_{k=0}^{\frac{t}{\Delta}} \ln[p_{\text{reattach}}(l_0 - v\Delta k)] \\
&\approx \int_0^{\frac{t}{\Delta}} dk\ \ln[p_{\text{reattach}}(l_0 - v\Delta k)] \\
&= \frac{1}{\Delta}\int_0^{t} dt'\ \ln[p_{\text{reattach}}(l(t'))] \\
&= \frac{1}{v\Delta}\int_{l(t)}^{l_0} dl\ \ln[p_{\text{reattach}}(l)] \\
&\approx \frac{1}{v\Delta}\int_{l(t)}^{\infty} dl\ \ln[p_{\text{reattach}}(l)],
\end{aligned} \tag{C9}$$

where we used the coordinate transformations $t' = k\Delta, l(t') = l_0 - vt'$, and approximated the maximal length of the system l_0 by ∞ as for maximal length the reattachment probability should be close to 1. Approximating the logarithm as $\ln[p_{\text{reattach}}(l)] \approx -1 + p_{\text{reattach}}$ for $p_{\text{reattach}} \geqslant 0.9$ we thus find

$$\ln[p_{\text{survival}}(t)] \approx -\frac{1}{v\Delta}\int_{l(t)}^{\infty} dl\,[1 - p_{\text{reattach}}(l)].$$

Finally, using Eq. (C8) for $1 - p_{\text{reattach}}(l)$ for $l \gg \lambda$ we get

$$\ln[p_{\text{survival}}(t)] \approx -\frac{\lambda F}{v\Delta}e^{-\frac{l(t)}{\lambda}}.$$

Defining the average minimal length as the length where the probability that a particle that was in the system at maximal length has left the system is just 0.5 we find $l_{\min} \approx \lambda\ln\{\lambda F/[v\Delta\ln(2)]\}$. For the (constant) velocity we make a very crude approximation, namely $v \approx \gamma/2$, and we have

$$l_{\min} \approx \lambda\ln\left[\frac{2\lambda F}{\gamma\Delta\ln(2)}\right].$$

[1] R. A. Blythe and M. R. Evans, Nonequilibrium steady states of matrix-product form: A solver's guide, J. Phys. A **40**, R333 (2007).

[2] F. Spitzer, Interaction of Markov processes, Adv. Math. **5**, 246 (1970).

[3] C. T. MacDonald, J. H. Gibbs, and A. C. Pipkin, Kinetics of biopolymerization on nucleic acid templates, Biopolymers **6**, 1 (1968).

[4] T. Chou, K. Mallick, and R. K. P. Zia, Non-equilibrium statistical mechanics: From a paradigmatic model to biological transport, Rep. Prog. Phys. **74**, 116601 (2011).

[5] C. Appert-Rolland, M. Ebbinghaus, and L. Santen, Intracellular transport driven by cytoskeletal motors: General mechanisms and defects, Phys. Rep. **593**, 1 (2015).

[6] R. Lipowsky, S. Klumpp, and T. M. Nieuwenhuizen, Random Walks of Cytoskeletal Motors in Open and Closed Compartments, Phys. Rev. Lett. **87**, 108101 (2001).

[7] A. Parmeggiani, T. Franosch, and E. Frey, Phase Coexistence in Driven One-Dimensional Transport, Phys. Rev. Lett. **90**, 086601 (2003).

[8] A. Parmeggiani, T. Franosch, and E. Frey, Totally asymmetric simple exclusion process with Langmuir kinetics, Phys. Rev. E **70**, 046101 (2004).

[9] S. Klumpp and R. Lipowsky, Traffic of molecular motors through tube-like compartments, J. Stat. Phys. **113**, 233 (2003).

[10] C. Leduc, K. Padberg-Gehle, V. Varga, D. Helbing, S. Diez, and J. Howard, Molecular crowding creates traffic jams of kinesin motors on microtubules, Proc. Natl. Acad. Sci. USA **109**, 6100 (2012).

[11] R. Subramanian, S.-C. Ti, L. Tan, S. A. Darst, and T. M. Kapoor, Marking and measuring single microtubules by PRC1 and kinesin-4, Cell **154**, 377 (2013).

[12] M. R. Evans and K. E. P. Sugden, An exclusion process for modelling hyphal growth, Phys. A (Amsterdam, Neth.) **384**, 53 (2007).

[13] S. A. Nowak, P.-W. Fok, and T. Chou, Dynamic boundaries in asymmetric exclusion processes, Phys. Rev. E **76**, 031135 (2007).

[14] K. E. P. Sugden, M. R. Evans, W. C. K. Poon, and N. D. Read, Model of hyphal tip growth involving microtubule-based transport, Phys. Rev. E **75**, 031909 (2007).

[15] K. E. P. Sugden and M. R. Evans, A dynamically extending exclusion process, J. Stat. Mech.: Theory Exp. (2007) P11013.

[16] L. E. Hough, A. Schwabe, M. A. Glaser, J. R. McIntosh, and M. D. Betterton, Microtubule depolymerization by the kinesin-8 motor Kip3p: A mathematical model, Biophys. J. **96**, 3050 (2009).

[17] M. Schmitt and H. Stark, Modelling bacterial flagellar growth, EPL **96**, 28001 (2011).

[18] L. Reese, A. Melbinger, and E. Frey, Crowding of molecular motors determines microtubule depolymerization, Biophys. J. **101**, 2190 (2011).

[19] A. Melbinger, L. Reese, and E. Frey, Microtubule Length Regulation by Molecular Motors, Phys. Rev. Lett. **108**, 258104 (2012).

[20] D. Johann, C. Erlenkämper, and K. Kruse, Length Regulation of Active Biopolymers by Molecular Motors, Phys. Rev. Lett. **108**, 258103 (2012).

[21] C. Erlenkämper, D. Johann, and K. Kruse, Impact of motor molecules on the dynamics of treadmilling filaments, Phys. Rev. E **86**, 051906 (2012).

[22] S. Muhuri, Scale-invariant density profiles of a dynamically extending TASEP, EPL **101**, 38001 (2013).

[23] H.-S. Kuan and M. D. Betterton, Biophysics of filament length regulation by molecular motors, Phys. Biol. **10**, 036004 (2013).

[24] L. Reese, A. Melbinger, and E. Frey, Molecular mechanisms for microtubule length regulation by kinesin-8 and XMAP215 proteins, Interface Focus **4**, 20140031 (2014).

[25] J. De Gier and C. Finn, Exclusion in a priority queue, J. Stat. Mech.: Theory Exp. (2014) P07014.

[26] C. Arita, A. Lück, and L. Santen, Length regulation of microtubules by molecular motors: Exact solution and density profiles, J. Stat. Mech.: Theory Exp. (2015) P06027.

[27] C. Schultens, A. Schadschneider, and C. Arita, Effective ergodicity breaking in an exclusion process with varying system length, Phys. A (Amsterdam, Neth.) **433**, 100 (2015).

[28] M. Sahoo, J. Dong, and S. Klumpp, Dynamic blockage in an exclusion process, J. Phys. A: Math. Theor. **48**, 015007 (2015).

[29] V. Varga, J. Helenius, K. Tanaka, A. A. Hyman, T. U. Tanaka, and J. Howard, Yeast kinesin-8 depolymerizes microtubules in a length-dependent manner, Nat. Cell Biol. **8**, 957 (2006).

[30] V. Varga, C. Leduc, V. Bormuth, S. Diez, and J. Howard, Kinesin-8 motors act cooperatively to mediate length-dependent microtubule depolymerization, Cell **138**, 1174 (2009).

[31] G. Klein, K. Kruse, G. Cuniberti, and F. Jülicher, Filament Depolymerization by Motor Molecules, Phys. Rev. Lett. **94**, 108102 (2005).

[32] J. Helenius, G. J. Brouhard, Y. Kalaidzidis, S. Diez, and J. Howard, The depolymerizing kinesin MCAK uses lattice diffusion to rapidly target microtubule ends, Nature (London) **441**, 115 (2006).

[33] E. Reithmann, L. Reese, and E. Frey, Nonequilibrium Diffusion and Capture Mechanism Ensures Tip Localization of Regulating Proteins on Dynamic Filaments, Phys. Rev. Lett. **117**, 078102 (2016).

[34] W. F. Marshall, Cellular length control systems, Annu. Rev. Cell Dev. Biol. **20**, 677 (2004).

[35] L. Mohapatra, B. L. Goode, P. Jelenkovic, R. Phillips, and J. Kondev, Design principles of length control of cytoskeletal structures, Annu. Rev. Biophys. **45**, 85 (2016).

[36] I. Neri, N. Kern, and A. Parmeggiani, Totally Asymmetric Simple Exclusion Process on Networks, Phys. Rev. Lett. **107**, 068702 (2011).

[37] I. Neri, N. Kern, and A. Parmeggiani, Modeling Cytoskeletal Traffic: An Interplay between Passive Diffusion and Active Transport, Phys. Rev. Lett. **110**, 098102 (2013).

[38] I. Neri, N. Kern, and A. Parmeggiani, Exclusion processes on networks as models for cytoskeletal transport, New J. Phys. **15**, 085005 (2013).

[39] D. A. Adams, B. Schmittmann, and R. K. P. Zia, Far-from-equilibrium transport with constrained resources, J. Stat. Mech.: Theory Exp. (2008) P06009.

[40] L. J. Cook and R. K. P. Zia, Feedback and fluctuations in a totally asymmetric simple exclusion process with finite resources, J. Stat. Mech.: Theory Exp. (2009) P02012.

[41] L. J. Cook, R. K. P. Zia, and B. Schmittmann, Competition between multiple totally asymmetric simple exclusion processes for a finite pool of resources, Phys. Rev. E **80**, 031142 (2009).

[42] C. A. Brackley, L. Ciandrini, and M. C. Romano, Multiple phase transitions in a system of exclusion processes with limited reservoirs of particles and fuel carriers, J. Stat. Mech.: Theory Exp. (2012) P03002.

[43] P. Greulich, L. Ciandrini, R. J. Allen, and M. C. Romano, Mixed population of competing totally asymmetric simple exclusion processes with a shared reservoir of particles, Phys. Rev. E **85**, 011142 (2012).

[44] L. Ciandrini, I. Neri, J. C. Walter, O. Dauloudet, and A. Parmeggiani, Motor protein traffic regulation by supply-demand balance of resources, Phys. Biol. **11**, 056006 (2014).

[45] M. Rank, A. Mitra, L. Reese, S. Diez, and E. Frey, Limited Resources Induce Bistability in Microtubule Length Regulation, Phys. Rev. Lett. **120**, 148101 (2018).

[46] M. J. I. Müller, S. Klumpp, and R. Lipowsky, Molecular motor traffic in a half-open tube, J. Phys.: Condens. Matter **17**, S3839 (2005).

[47] K. Tsekouras and A. B. Kolomeisky, Parallel coupling of symmetric and asymmetric exclusion processes, J. Phys. A: Math. Theor. **41**, 465001 (2008).

[48] J. Tailleur, M. R. Evans, and Y. Kafri, Nonequilibrium Phase Transitions in the Extraction of Membrane Tubes by Molecular Motors, Phys. Rev. Lett. **102**, 118109 (2009).

[49] M. R. Evans, Y. Kafri, K. E. P. Sugden, and J. Tailleur, Phase diagrams of two-lane driven diffusive systems, J. Stat. Mech.: Theory Exp. (2011) P06009.

[50] B. Saha and S. Mukherji, Coupling driven exclusion and diffusion processes on parallel lanes: Boundary induced phase transitions and boundary layers, J. Stat. Mech.: Theory Exp. (2013) P09004.

[51] I. R. Graf and E. Frey, Generic Transport Mechanisms for Molecular Traffic in Cellular Protrusions, Phys. Rev. Lett. **118**, 128101 (2017).

[52] I. Pinkoviezky and N. S. Gov, Traffic jams and shocks of molecular motors inside cellular protrusions, Phys. Rev. E **89**, 052703 (2014).

[53] M. L. Gupta, P. Carvalho, D. M. Roof, and D. Pellman, Plus end-specific depolymerase activity of Kip3, a kinesin-8 protein, explains its role in positioning the yeast mitotic spindle, Nat. Cell Biol. **8**, 913 (2006).

[54] P. M. Grissom, T. Fiedler, E. L. Grishchuk, D. Nicastro, R. R. West, and J. R. McIntosh, Kinesin-8 from fission yeast: A heterodimeric, plus-end-directed motor that can couple microtubule depolymerization to cargo movement, Mol. Biol. Cell **20**, 963 (2009).

[55] X. Su, R. Ohi, and D. Pellman, Move in for the kill: Motile microtubule regulators, Trends Cell Biol. **22**, 567 (2012).

[56] T. Mitchison and M. Kirschner, Dynamic instability of microtubule growth, Nature (London) **312**, 237 (1984).

[57] J. Howard and A. A. Hyman, Growth, fluctuation and switching at microtubule plus ends, Nat. Rev. Mol. Cell Biol. **10**, 569 (2009).

[58] J. Krug, Boundary-Induced Phase Transitions in Driven Diffusive Systems, Phys. Rev. Lett. **67**, 1882 (1991).

[59] B. Derrida, An exactly soluble non-equilibrium system: The asymmetric simple exclusion process, Phys. Rep. **301**, 65 (1998).

[60] D. T. Gillespie, A general method for numerically simulating the stochastic time evolution of coupled chemical reactions, J. Comput. Phys. **22**, 403 (1976).

[61] For $\gamma > 1$ the system grows indefinitely as then transport on the TL is too slow to keep up with the growth dynamics.

[62] The value of ϵ corresponds to a diffusion constant that is of the order of molecular motor diffusion in cytosol.

[63] S. M. Block, L. S. B. Goldstein, and B. J. Schnapp, Bead movement by single kinesin molecules studied with optical tweezers, Nature (London) **348**, 348 (1990).

[64] Since we focus on the low-density limit for the TL and since there is no exclusion on the DL the mean-field approximation should be valid.

[65] The critical density given by Eq. (2) increases linearly with the growth rate, so for larger γ the shrinkage speed should increase as well.

[66] J.-C. Walter, J. Dorignac, V. Lorman, J. Rech, J.-Y. Bouet, M. Nollmann, J. Palmeri, A. Parmeggiani, and F. Geniet, Surfing on Protein Waves: Proteophoresis as a Mechanism for Bacterial Genome Partitioning, Phys. Rev. Lett. **119**, 028101 (2017).

[67] S. Bergeler and E. Frey, Regulation of Pom cluster dynamics in Myxococcus xanthus, arXiv:1801.06133.

[68] J. Halatek and E. Frey, Rethinking pattern formation in reaction-diffusion systems, Nat. Phys. **14**, 507 (2018).

[69] A. Vilfan and E. Frey, Oscillations in molecular motor assemblies, J. Phys.: Condens. Matter **17**, S3901 (2005).

[70] B. Novák and J. J. Tyson, Design principles of biochemical oscillators, Nat. Rev. Mol. Cell Biol. **9**, 981 (2008).

[71] W. H. Press, *Numerical Recipes in C: The Art of Scientific Computing* (Cambridge University Press, 1992), p. 994.

[72] We allow here that the rate at which a particle leaves into the reservoir, $\tilde{\epsilon}$, can be distinct from the usual diffusion rate ϵ.

4 Collective filament dynamics in nematic filament networks

The whole is more than the sum of its parts.
(Aristoteles)

The goal of this chapter is to summarize the most important findings of our project on the collective filament motion in filament networks crosslinked by motor proteins. The corresponding manuscript has been published[1] in *Biophysical Journal*. This chapter is based on and uses parts of this publication [3], which is also reprinted in section 4.5.

4.1 Motivation

The goal of this project was to understand how collective filament dynamics in filament networks emerges from interactions between individual filaments and motor proteins. This questions was motivated by the mitotic spindle which is responsible for chromosome segregation during cell division (for recent reviews see e.g. [99, 140–143]). The spindle is composed, amongst other things, of microtubules and motor proteins and has a characteristic oval shape with two poles. It has been observed that the interaction between motor proteins and microtubules leads to a flux of microtubules towards these poles [101, 202–205]. The idea is that by crosslinking two microtubules with opposite polarity ("antiparallel microtubules") and walking on them in a directed fashion, kinesin-5 motors drive the sliding of these microtubules past each other (see also section 1.1 and Fig. 1.1). In contrast, if kinesin-5 crosslinks two individual parallel microtubules, they remain static [94]. Transferring these interactions between a single motor and a pair of filaments to filament networks, one would intuitively expect that the local sliding velocity of microtubules should strongly depend on the local polarity in the network, that is, the proportion of antiparallel to parallel interaction partners.

However, this intuition not only contradicts findings in mitotic spindles in Xenopus egg extract [89–91] but also recent experiments with heavily crosslinked filament gels *in vitro* [88]: In the mitotic spindle the polarity along the microtubule axis was measured to vary greatly from one pole to the other [91] whereas simultaneously the flux of microtubules is rather constant, especially if dynein, a minus-end clustering motor, is inhibited [89, 90]. The same phenomenon of a polarity-independent filament velocity was also recently observed in a kinesin-microtubule gel made of purified components and described in terms of a hydrodynamic theory [88]. With the help of photo-bleaching, local velocities of microtubules and network polarities were measured at different positions in the heavily crosslinked filament gel. Intriguingly, it was found that the local microtubule velocity is largely independent of the local network polarity. Where

[1] At the time of the original submission of this thesis, the manuscript had been in press in *Biophysical Journal*.

does this polarity-independent velocity come from? This question lies at the heart of this project. Starting from mesoscopic interactions between microtubules due to crosslinking motors, our goal was to elucidate a biophysical mechanism that determines the relation between the local filament velocities and the local network polarity.

As mentioned in the abstract of the project, the driving questions are:
How do the local forces between the filaments manifest in terms of collective filament motion? What is the underlying mechanism determining the relation between the local network polarity and the local filament velocities? How does such a mechanism relate to the experimental findings of polarity-independent filament velocities?

4.2 Model

We consider the conceptual model as illustrated in Fig. 4.1. The system of size S is effectively one-dimensional and microtubules are modeled as hard rods of fixed length $L \ll S$ that can be either oriented to the left (+) or to the right (−). The microtubules are randomly distributed in the system and are randomly oriented. Microtubules effectively interact with each other due to crosslinking by motor proteins (which are not modeled explicitly) and are thereby set into motion. The velocity of microtubule i oriented to the left/right is denoted by $v_i^{(\pm)}$, respectively.

A motor crosslinking two parallel microtubules favors uniform motion of both microtubules whereas a motor crosslinking to antiparallel microtubules favors a relative velocity $2V_m$ of twice the motor velocity V_m between the microtubules (see Fig. 4.1 A for an illustration). These interactions are motivated by the experimental findings on kinesin-5 described in sections 1.1 and 4.1 where two parallel filaments crosslinked by a motor protein remained static, whereas two crosslinked antiparallel microtubules were slid apart by twice the motor velocity. Assuming a linear force-velocity relation (see e.g. [84–87]), the forces between two parallel ($^{++}_{--}$) and antiparallel ($^{+-}_{-+}$) microtubules crosslinked by a single motor are taken to be

$$F_{ij}^{(^{++}_{--})} = F_\mathrm{m}\left(\frac{v_j^{(\pm)} - v_i^{(\pm)}}{2\,V_\mathrm{m}}\right), \qquad F_{ij}^{(+-)} = -F_{ji}^{(-+)} = F_\mathrm{m}\left(1 + \frac{v_j^{(-)} - v_i^{(+)}}{2\,V_\mathrm{m}}\right). \tag{4.1}$$

Here F_m corresponds to the motor force and F_{ij} denotes the force that filament j exerts on filament i. The force between two parallel microtubules, $F_{ij}^{(^{++}_{--})}$, is zero if their relative velocity is zero, $v_j^{(\pm)} - v_i^{(\pm)} = 0$. In contrast, the force between two antiparallel microtubules, $F_{ij}^{(^{+-}_{-+})}$, is zero if their relative velocity is twice the motor velocity, $v_i^{(+)} - v_j^{(-)} = 2V_m$. If the two microtubules do not move relative to each other $v_i^{(+)} - v_j^{(-)} = 0$, the motor acts with a force of $\pm F_m$ on them.

In principle, each microtubule can interact (be crosslinked) with all microtubules that share an overlap with it (see Fig. 4.1 C for an illustration). To effectively account for the dimensional reduction of nematic networks in three dimensions to only one dimension in the model, we introduce a parameter N which denotes the average number of interaction partners per microtubule. These interaction partners per microtubule are drawn randomly from all possible interaction partners. Furthermore, we assume that the density of motors is constant

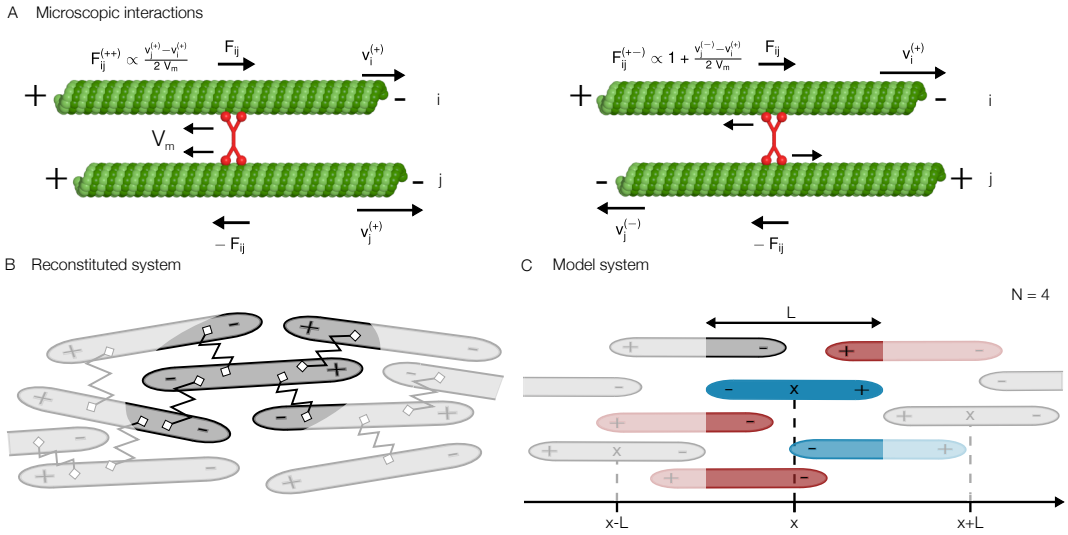

Figure 4.1 | Illustration of motor crosslinking of microtubules and of the conceptual model (taken from [3]) A) Interactions between two microtubules (green) due to crosslinking by a motor protein (red). If the microtubules are oriented in the same direction (left), the motor resists relative motion of the microtubules because it gets stretched otherwise. In contrast, if the microtubules are oriented in the opposite direction (right), the motor is not stretched if the relative velocity between the microtubules equals twice the motor velocity V_m. B) Sketch of a reconstituted system of motors (springs) and microtubules (elongated ellipses) in a nematic arrangement where all microtubules are more or less oriented along one axis. C) Sketch of the quasi-one-dimensional model. Microtubules are modeled as hard rods which are either oriented to the left (+) or to the right (−). Each microtubule has on average N interaction partners that are drawn randomly from all microtubules that share an overlap with the respective microtubule. For instance, the microtubule in the center of the highlighted region (dark blue) could, in principle, interact with all microtubules in the highlighted region. From all these microtubules with some overlap, the colored ones were drawn randomly to interact with the microtubule in the center (parallel interaction partners are in light blue and antiparallel interaction partners in light red). Two interacting microtubules exert forces on each other that depend on their relative orientation and relative velocity. The explicit force-velocity relations are given in A.

and that each microtubule is on average crosslinked by N_m motor proteins. Since we do not model the motors explicitly, the constant density and the average number of crosslinkers per microtubule are incorporated by a weighting factor for each interaction, $N_\mathrm{m}/N/L \cdot L_\mathrm{ov}$, which is proportional to the overlap L_ov between the microtubules. The first term, $N_\mathrm{m}/N/L$, corresponds to the average number of motors per interaction partner per microtubule length and the second one weights the overlap between two microtubules.

The velocity $v_i^{(\pm)}$ of a specific microtubule i in the network is then determined by the force balance equation

$$\gamma v_i^{(\pm)} = \sum_j n_{ij}\, F_{ij}^{(\pm\pm)} + \sum_k n_{ik}\, F_{ik}^{(\pm\mp)}\,, \tag{4.2}$$

where γ denotes the fluid drag coefficient and n_{ij} the (effective) number of motors crosslinking microtubules i and j. The sums run over all parallel and antiparallel interaction partners of microtubule i, respectively.

The local network polarity at position x, $P(x)$, is defined by $P(x) = \varphi^{(+)}(x) - \varphi^{(-)}(x)$ where $\varphi^{(\pm)}(x)$ denotes the fraction of all filaments that pass through position x and are oriented in $(\pm)$ direction, respectively.

4.3 Results

We first examined the system numerically to check whether it captures the most important findings of the experimental *in vitro* system [88]. For this purpose, we solved Eq. 4.2 numerically and measured the local filament velocities and the corresponding local polarities in the network (see Fig. 2 in [3] or in the publication preprint in section 4.5). For biologically reasonable parameter values (for details see section 3.2 in [3] or in the publication preprint in section 4.5) and randomly generated networks, we found good agreement with the experimental findings (compare Fig. 2 in our publication and Fig. 2 in Ref. [88]). In particular, the average filament speed (filled black circles in Fig. 2 in our publication) is independent of the local polarity. While this suggests that our model can indeed capture the most important aspects of the filament dynamics in the *in vitro* microtubule-motor network, it clearly contradicts the intuition given in section 4.1. It, thus, remained elusive why the velocity of the microtubules is polarity-independent.

To gain a better understanding, we developed a non-local continuum theory which explicitly takes the finite length of microtubules L into account (see also section 3.2 in [3] or in the publication preprint in section 4.5). To this end, we applied a continuum limit to the local balance equation, Eq. 4.2:

$$\gamma\, v^{(\pm)}(x) = \frac{1}{L}\int_{x-L}^{x+L} \mathrm{d}y\, \left\{ f^{(\pm\pm)}_{\text{parallel}}(x,y) + f^{(\pm\mp)}_{\text{antiparallel}}(x,y) \right\} , \tag{4.3}$$

with local forces

$$f^{(\pm\pm)}_{\text{parallel}}(x,y) = \hat{N}_{\text{m}}(x,y) \cdot N\, \varphi^{(\pm)}(y) \cdot F^{(\pm\pm)}(x,y) , \tag{4.4a}$$

$$f^{(\pm\mp)}_{\text{antiparallel}}(x,y) = \hat{N}_{\text{m}}(x,y) \cdot N\, \varphi^{(\mp)}(y) \cdot F^{(\pm\mp)}(x,y) . \tag{4.4b}$$

Here, $F^{(\pm\pm)}(x,y)$ and $F^{(\pm\mp)}(x,y)$ correspond to the continuum versions of Eq. 4.1, e.g. $F^{(\pm\pm)}(x,y) = F_{\text{m}}\,[v^{(\pm)}(y) - v^{(\pm)}(x)]/(2\ V_{\text{m}})$. They denote the forces that a microtubule at position y exerts on a microtubule at position x (depending on the relative orientations). $\hat{N}_{\text{m}}(x,y)$ represents the average number of motors that crosslink a pair of filaments located at positions x and y. As mentioned in section 4.2, this number is given by $\hat{N}_{\text{m}}(x,y) = N_{\text{m}}/N \cdot L_{\text{ov}}/L$: Since there are on average N_{m} motors per filament and N interaction partners, on average $N_{\text{m}}/N/L$ motors crosslink a pair of filaments per length of the microtubule. Furthermore, the number of crosslinking motors scales with the size of the overlapping region, $L_{\text{ov}} = L - |x-y|$. Finally, $N\,\varphi^{(\pm)}(y)$ corresponds to the average number of parallel/antiparallel interaction partners at position y under the assumption that the network is dense enough and that there are at least N interaction partners available everywhere: It corresponds to the total number N of interaction partners weighted by the fraction of parallel/antiparallel interaction partners, $\varphi^{(\pm)}(y)$, respectively. In terms of the filament densities this fraction is given by $\varphi^{(\pm)} = \rho^{(\pm)}/(\rho^{(+)} + \rho^{(-)})$.

The coupled integral equations for the force balance in the form of Eq. 4.3 do not reveal much insight, yet. To proceed, we restricted our analysis to systems whose size S is large compared to the filament length L and compared to other intrinsic length scales of the system (see below). For this case, it was possible to derive an explicit (non-local) force-balance equation from the coupled integral equations – against all first expectations. For this purpose, we first decoupled the integral equations and then represented the resulting equation in Fourier space. Finally, we made us of complex calculus to perform the Fourier back transform (see the Supplementary Material of Ref. [3] or of the publication preprint in section 4.5 for details). In the end, this procedure yields an astonishingly simple (approximate) velocity-polarity relation:

$$v^{(\pm)}(x) = \pm V_\mathrm{m}\,(1-\alpha)\,\big(1 \mp \Pi(x)\big)\,, \tag{4.5a}$$

$$\Pi(x) = \frac{1}{2\,l_c}\int_{-\infty}^{\infty} \mathrm{d}y\; \mathrm{e}^{-|x-y|/l_c}\,P(y)\,. \tag{4.5b}$$

where $1/\alpha := 1 + 12\,(l_c/L)^2$ and $\alpha \ll 1$ for biologically reasonable parameters. Furthermore,

$$l_c = L\,\sqrt{\frac{F_\mathrm{m}\,N_\mathrm{m}}{24\,\gamma\,V_\mathrm{m}}}\,. \tag{4.6}$$

This velocity-polarity relation reveals that the velocity of ($\pm$) microtubules at position x, $v^{(\pm)}(x)$, does not directly depend on the local polarity $P(x)$ but instead on the so-called "ambient polarity", $\Pi(x)$. This ambient polarity corresponds to an average of the local polarity with a weight (interaction kernel) that decays exponentially with the distance from the local position x. Depending on the characteristic length of the exponential (the interaction range), l_c, the average is thus effectively taken with respect to a larger or smaller spatial range. Fig. 3 in [3] or in the publication preprint in section 4.5 illustrates this idea. If the interaction range l_c is large compared to the typical lengthscale of fluctuations in the polarity (A), the ambient polarity is effectively constant because all fluctuations are averaged out by the large spatial average. In contrast, for very small l_c, the interaction kernel effectively corresponds to a delta-peak (B) and the ambient polarity profile exhibits the same fluctuations as the local polarity profile.

As can be seen from Eq. 4.6, the characteristic length depends on the ratio of motor forces $F_\mathrm{m}\,N_\mathrm{m}$ to the drag in the fluid $\gamma\,V_\mathrm{m}$. For large drag in the fluid or small motor forces, l_c is small and, thus, the local velocity is mostly determined by the local polarity. In contrast, for very small drag in the fluid or very large motor forces, l_c is very large and the local velocity gets more or less independent of the position since it then only depends on the average polarity of the entire system.

This diverging behavior can be interpreted in terms of a common force propagation mechanism: Locally generated forces are propagated through the network over a characteristic length (l_c). For high drag in the fluid (high dissipation) or weak links between the filaments, the propagation is not very efficient and the local microtubules are mostly influenced by their direct neighbors. Correspondingly, the local velocity strongly depends on the local polarity, as expected from the intuitive argument presented in section 4.1. On the contrary, if the fluid drag (the dissipation) is very small or the network is heavily crosslinked, a force that is locally applied is translated by the crosslinking motors through the entire network and equally

affects all microtubules in the network. Intriguingly, for biologically reasonable parameter values (see section 3.2 in [3] or in the publication preprint in section 4.5), the characteristic length is considerably larger than the filament length L. In this case we are thus exactly in the limit of small fluid drag where the local filament velocities get independent of the local polarity, in agreement with the experimental finding of Ref. [88]. In conclusion, this perspective offers a solution to the seemingly contradictory behavior of heavily crosslinked networks (which exhibit a polarity-independent velocity) and the first intuition we gained from a purely local point of view (according to which the filament velocity should strongly depend on the local polarity).

Furthermore, we used the velocity-polarity relation, Eqs. 4.5a and 4.5b, to make experimentally testable predictions. To this end, we considered an (idealized) experimental setup where a nematically ordered network with periodic boundary conditions is generated by randomly placing and orienting microtubules in the system. Despite the random orientation, the polarity at different positions is not independent since the microtubules have a finite length: One microtubule not only influences the polarity at its midpoint position but everywhere along its length. The polarities at distances less than one microtubule length L apart are thus positively correlated. As a result, the polarity profile is not completely random but correlated on lengths smaller than the microtubule length L (for a typical profile please refer to the Supplementary Material of our publication [3] or of the publication preprint in section 4.5). We quantified this correlation structure in terms of a set of conveniently chosen independent random variables. This representation enabled us to derive an analytic expression which relates the distribution of the local velocities to the distribution of the local polarities:

$$\frac{\mathrm{Var}[v/V_m]}{\mathrm{Var}[P]} = (1-\alpha)^2 \left[1 - \frac{3l_c}{2L}\left(1 - \mathrm{e}^{-L/l_c}\right) + \frac{1}{2}\,\mathrm{e}^{-L/l_c}\right] , \tag{4.7}$$

where $\mathrm{Var}[P] = \mathrm{Var}[P(x)] = \langle P(x)^2\rangle - \langle P(x)\rangle^2$ is the variance of the local polarity and $\mathrm{Var}[v/V_m] = \mathrm{Var}[v(x)/V_m]$ is the variance of the (normalized) velocity v/V_m measured in units of the motor velocity. This analytic expression thus relates the width of the velocity distribution to the width of the polarity distribution. Intriguingly, the ratio of the two widths only depends on the characteristic length l_c but not on other factors such as the density of microtubules. The functional dependence of the ratio of the standard deviations is shown in Fig. 5B of our publication [3] and in the publication preprint in section 4.5. It is the smaller, the larger the characteristic length l_c. Intuitively, if the characteristic length is large, the local velocities are determined by an average over a large spatial region and are, thus, less dependent on local fluctuations. As a result, the distribution of local velocities is narrower. In contrast, if the characteristic length is small, the distribution of the local velocities reflects the variance in the local polarities.

It would be very enlightening to test this prediction in *in vitro* experiments of purified components, similar to the one performed in Ref. [88]. While it might be difficult to modify the characteristic length l_c, Eq. 4.6, by adjusting the motor parameters, it could be feasible to change the drag in the fluid. Thereby, l_c could be changed without affecting other properties of the system and one could test whether the distribution of local velocities changes accordingly. We believe that the type of data required for such experiments is, in principle, already available. However, it might prove challenging to record enough statistics to accurately determine the standard deviations (or distributions).

Taken together, our conceptual model reveals a mechanism for force propagation which suggests that locally generated forces are propagated over a characteristic length through the network. The value of this characteristic length (which corresponds to the efficiency of propagation) depends on the ratio between crosslinking forces in the network and the drag in the surrounding fluid. In fact, an extension of this analysis to different types of crosslinking motors such as passive or oppositely moving ones (see Supplementary Material of our publication [3] or of the publication preprint in section 4.5), provides a more precise interpretation of the characteristic length l_c: While the directionality and magnitude of the filament velocities result from a competition between the different active motor contributions, all motors contribute cooperatively to the effective friction between microtubules and thus to the force propagation. Consequently, the characteristic length is determined by the ratio of the overall internal friction between microtubules (which increases with the number of motors irrespective of whether they are active or not) as compared to the drag in the fluid. In terms of this characteristic length, the mechanistic perspective on collective filament motion presented here constitutes a solution to the seemingly contradictory behavior of heavily crosslinked networks [88–91] as compared to dilute systems [96–98], which behave according to our initial intuition.

4.4 Key points

From my point of view, there are three take-home messages:

- Our analysis suggests a mechanism for force propagation through filament networks: Owing to the crosslinking of microtubules by motor proteins, locally generated, active forces are propagated over a characteristic length through the network.
- The characteristic length (or interaction range) is given by the ratio of the internal friction between microtubules due to crosslinking and the dissipation (drag) in the fluid.
- For heavily crosslinked filament gels, the motor forces between the filaments are very high and all microtubules in the network effectively interact with each other. As a result, the local velocity is largely independent of the locally generated forces and rather depends on global network properties.

In the spirit of the quote by Aristoteles at the beginning of the chapter, the force propagation mechanism can be seen as a truly collective and non-local effect which highlights again that the “whole is more than the sum of its parts”.

4.5 Publication: A mechanistic view of collective filament motion in active nematic networks, Biophysical Journal 118, 2 (2020)

This section is a publication preprint of the following manuscript published[2] in **Biophysical Journal** 118, 2 (2020).

A mechanistic view of collective filament motion in active nematic networks

by

Moritz Striebel,[1,*] Isabella R. Graf,[1,*] and Erwin Frey[1]
[1] *Arnold-Sommerfeld-Center for Theoretical Physics and Center for NanoScience, Department of Physics, Ludwig-Maximilians-Universität München*
[*] *These authors contributed equally to this work.*

DOI: 10.1016/j.bpj.2019.11.3387

[2] At the time of the original submission of this thesis, the manuscript had been in press in *Biophysical Journal*.

A mechanistic view of collective filament motion in active nematic networks

Moritz Striebel[1⋆], Isabella R. Graf[1⋆], Erwin Frey[1†]

[1] Arnold Sommerfeld Center for Theoretical Physics (ASC) and Center for NanoScience (CeNS), Department of Physics, Ludwig-Maximilians-Universität München, Theresienstraße 37, 80333 München, Germany

⋆M.S. and I.R.G. contributed equally to this work.

†Corresponding author: frey@lmu.de.

ABSTRACT

Protein filament networks are structures crucial for force generation and cell shape. A central open question is how collective filament dynamics emerges from interactions between individual network constituents. To address this question we study a minimal but generic model for a nematic network where filament sliding is driven by the action of motor proteins. Our theoretical analysis shows how the interplay between viscous drag on filaments and motor-induced forces governs force propagation through such interconnected filament networks. We find that the ratio between these antagonistic forces establishes the range of filament interaction, which determines how the local filament velocity depends on the polarity of the surrounding network. This force propagation mechanism implies that the polarity-independent sliding observed in Xenopus egg extracts, and *in vitro* experiments with purified components, is a consequence of a large force propagation length. We suggest how our predictions can be tested by tangible *in vitro* experiments whose feasibility is assessed with the help of simulations and an accompanying theoretical analysis.

SIGNIFICANCE

Cells perform a variety of vital tasks ranging from cell division to motion and force generation. These abilities are intrinsically dynamic and rely on active network structures consisting of cytoskeletal filaments and crosslinking motor proteins. How does collective dynamics at the macroscopic level emerge from interactions of individual filaments and motor proteins? We address this open question through a conceptual model for motor-induced motion in networks of interconnected filaments. A prominent representative of this class of structures is the mitotic spindle where motor-driven filament flux is essential to maintain shape and functionality. Through theoretical and numerical analysis, we identify a mechanism which qualitatively accounts for experimental observations of both the spindle and of systems with purified components.

1 Introduction

Living cells have the remarkable ability to actively change their shape, and to generate forces and motion. A key component enabling cells to exhibit these stunning mechanical properties is the cytoskeleton. This structure is built out of various proteins and forms diverse functional networks consisting of polymer filaments such as actin and microtubules, motor proteins, and associated proteins [1, 2]. The motor proteins expend chemical energy to generate forces that act on the cytosceletal filaments [3–5]. In particular, motors that have two binding domains, e.g. kinesin-5, can walk along two filaments at once, causing filaments of opposite polarity to slide past one another [6].

To understand the non-equilibrium physics underlying the dynamics of motor–filament systems, it has proven fruitful to study reconstituted systems of purified components *in vitro* [7–10]. Despite their reduced complexity, these systems still self-organize into intricate patterns and structures reminiscent of those found in living cells. But how is their collective behavior at the macroscopic level linked to the interactions between individual filaments and motors? What are the underlying mechanisms? To provide an answer, we focus here on a generic class of systems in which filaments exhibit nematic order and motors drive relative sliding of filaments. A prominent representative of this class is the poleward flux of microtubules in Xenopus mitotic spindles [11–13]. This process has been attributed to antiparallel, motor-driven interactions between filaments, especially if the motor protein dynein is inhibited [11, 14, 15]. A quite puzzling observation made in these systems was the correlation — or rather, the lack of correlation — between filament speed and network polarity, i.e. the ratio of parallel to antiparallel filaments. Although filament motion is induced by sliding antiparallel filaments past each other, polarity was observed to have barely any influence on the filament speed [14, 16, 17]. This surprising behavior was recently replicated in a system of purified components composed of the kinesin-14 XCTK2 and microtubules, and interpreted in terms of a hydrodynamic theory for heavily crosslinked filament networks [18]. These observations are at variance with previous predictions for dilute filament networks, where filament motion depends linearly on the local polarity [19–21]. How can these conflicting results be reconciled? What are the biophysical mechanisms determining the relation between filament speed and network polarity?

To gain insight into these important questions we study a minimal but generic model consisting of nematically ordered cytoskeletal filaments (like microtubules) and molecular motors (like kinesin-5) that are capable of crosslinking and sliding antiparallel filaments apart. Our mathematical analysis of this theoretical model shows that the interplay between motor-induced forces and viscous drag acting on the filaments determines the relation between filament velocity and the polarity of filaments. Depending on the relative strengths of these forces, we find that the velocity–polarity relation varies continuously between a local and a global law. Our theory reveals the mechanism that underlies this relation between filament velocity and network polarity: For high motor-induced forces and small fluid drag, local forces on the filaments propagate through the strongly interconnected network without dissipation and thereby influence the overall network dynamics. In contrast, for small motor–induced forces or high fluid drag, local forces are quickly damped and only influence the local dynamics. This mechanism provides a deeper understanding of the link between collective filament dynamics and molecular interactions. Moreover, it reconciles previously conflicting results for the velocity-polarity relation in the limit of dilute [19, 20, 20] and heavily crosslinked systems [14, 18, 22]. Strikingly, our theoretical analysis shows that the insensitivity of filament velocities to changes in the network polarity, which was reported for the spindle [14, 16] and *in vitro* systems [18], occurs in a biologically relevant parameter range. In addition our theory predicts how the ratio between the spectrum of measured polarities and filament speeds depends on the ratio of drag to motor-induced forces in the system. We suggest an *in-vitro* experiment to validate those predictions. The feasibility of this experiment is assessed with the help of computer simulations and an accompanying theory.

2 Methods

Biophysical agent-based model of motor-induced filament movement

We are interested in understanding how the interplay between viscous drag and molecular forces between cytoskeletal filaments, mediated by molecular motors, drives the internal dynamics of filament networks. Specifically, we focus on reconstituted *in vitro* systems consisting of microtubules and motors capable of crosslinking neighboring filaments and sliding them apart, c.f. Fig. 1 A, B. Such motor proteins can walk on both filaments simultaneously, so that the forces generated between filaments depend on their relative orientation (Fig. 1 A). *In vitro* such microtubule-motor mixtures were observed to self-organize into a nematic network, where neighboring filaments may be disposed approximately parallel or antiparallel [18].

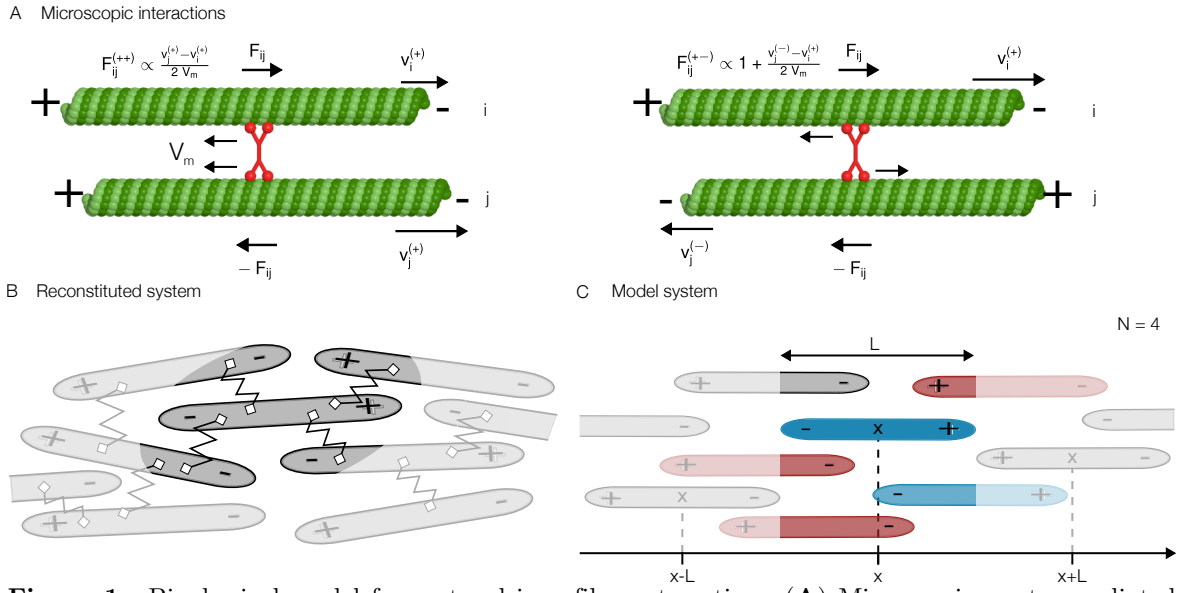

Figure 1. Biophysical model for motor-driven filament motion. (**A**) Microscopic, motor-mediated interactions between microtubules. Neighboring microtubules are connected by motors (red) which walk towards the microtubule's (green) plus end with velocity V_m. A motor exerts zero force if filament motion is such that the motor is not stretched. (**A -left**) A motor connecting two parallel microtubules counteracts relative motion between the filaments. (**A -right**) In contrast, two antiparallel microtubules connected by a motor are slid apart. The force falls to zero once their relative velocity equals twice the motor velocity ($-2\,V_\mathrm{m}$). (**B**) Sketch of a microtubule-motor mixture in a nematically aligned state. The springs denote motors crosslinking neighboring filaments. The highlighted region includes all interactions of the center microtubule. (**C**) The one-dimensional model system. Possible interaction partners of the microtubule in the center (dark blue) are in the highlighted region. To account for the reduced number of interaction partners in the experimental filament network, we draw on average N out of all possible partners to interact (interaction partners are highlighted in color, parallel interaction partners in light blue and antiparallel interaction partners in light red).

Motivated by the nematic order of these filament networks, we set up a biophysical agent-based model, which is effectively one-dimensional. We consider a system of size S where the filaments (microtubules) are assumed to be rigid polar rods of fixed length L, oriented with their plus end either to the left (+) or right (−); see Fig. 1 C. Hence, the dynamics of each polar filament i is determined (solely) by its velocity $v_i^{(\pm)}$. Relative motion between filaments is caused by molecular motors that walk on these crosslinked filaments and thereby exert forces. In-vitro assays involving pairs of isolated microtubules cross-linked by kinesin-5 motors reveal that: (a) Kinesin-5 has the ability to walk simultaneously on both microtubules

with approximately the zero-load velocity V_m, (b) antiparallel microtubules are pushed apart with a relative velocity of $\sim 2V_\mathrm{m}$, and (c) parallel microtubules remain static [6]. Integrating this information with experiments showing a linear force-velocity relation for kinesin motors [23–26], we assume that the forces between two crosslinked parallel ($^{+\,+}_{-\,-}$) and antiparallel ($^{+\,-}_{-\,+}$) filaments per motor are given by

$$F_{ij}^{(^{+\,+}_{-\,-})} = F_\mathrm{m}\left(\frac{v_j^{(\pm)} - v_i^{(\pm)}}{2\,V_\mathrm{m}}\right)\,, \qquad F_{ij}^{(+-)} = -F_{ji}^{(-+)} = F_\mathrm{m}\left(1 + \frac{v_j^{(-)} - v_i^{(+)}}{2\,V_\mathrm{m}}\right)\,. \tag{1}$$

Here F_{ij} denotes the force that filament j exerts on filament i, with F_m signifying the motor stall force; due to force balance $F_{ij} = -F_{ji}$. These forces vanish if the relative motion of the filaments does not induce strain in the crosslinking motors. While for parallel filaments this is the case if the filaments move at the same speed, a motor walking on antiparallel filaments is not strained if these slide apart with relative velocity $2V_\mathrm{m}$, i.e. $v_i^{(+)} - v_j^{(-)} = 2V_\mathrm{m}$. On the other hand, the maximal force between two filaments corresponds to the stall force, F_m, which is defined as the force between two antiparallel filaments fixed at their relative position ($v_i^{(-)} = v_j^{(+)}$). In that case the motor heads move apart until the motor stalls and exerts its maximal force on the filaments. An analogous situation occurs if a motor is attached to two parallel filaments which move with a relative speed $v_j^{(\pm)} - v_i^{(\pm)} = 2\,V_\mathrm{m}$. So the corresponding force is also F_m.

The velocity $v_i^{(\pm)}$ of a specific microtubule i in the network is determined by the force balance equation

$$\gamma v_i^{(\pm)} = \sum_j n_{ij}\, F_{ij}^{(\pm\pm)} + \sum_k n_{ik}\, F_{ik}^{(\pm\mp)}\,, \tag{2}$$

where γ denotes the fluid drag coefficient and n_{ij} the number of motors crosslinking microtubule i and j. The sums run over all parallel and antiparallel interaction partners of microtubule i, respectively. In general, the number of interaction partners as well as the strength of their interaction can depend on a variety of factors. For example, the interactions are influenced by the density of motors in the cytosolic volume as well as along the filament, or the local structure of the filament network. Inclusion of all these factors would lead to a microscopic description with many unknown parameters. Focusing on the mechanistic basis of filament motion here, we make the following assumptions (c.f. Fig. 1 C): First, we consider a homogeneous motor density in the cytosolic volume and along the microtubules. Thus, we describe motors effectively by a constant density, with on average N_m motors per filament. Second, we assume that all filaments have on average N interaction partners that are drawn randomly. This on average accounts for the limited number of neighbors in the three-dimensional network structure. Finally, note that we neglect hydrodynamic interactions between the filaments. A priori, it is not clear whether such interactions would not change the dynamics. However, in a recent study on a motor-filament system, it turned out that the experimental results are well described by a theory neglecting hydrodynamic interactions [27]. Presumably, this is due to "hydrodynamic screening" in dense systems [28].

3 Results

3.1 A local mean-field approximation predicts strong velocity-polarity sensitivity

To gain initial insight into the dynamics of microtubules, we simplify the system even further using a local, continuum mean-field approximation that neglects any lateral displacement between crosslinked filaments. In the continuum description, each microtubule i is identified by its midpoint position x_i. As a crude simplification, we assume that all crosslinked, equally oriented filaments passing through position x move at (roughly) the same velocity $v^{(\pm)}(x)$. This entails that the forces between all parallel filaments, $F^{(^{+\,+}_{-\,-})}(x)$, vanish. Denoting the fraction of filaments at position x oriented in $(\pm)$ direction by $\varphi^{(\pm)}(x)$,

Eq. 2 then simplifies to $\gamma v^{(+)}(x) = N_{\mathrm{m}}\varphi^{(-)}(x)F^{(+-)}(x)$ and $\gamma v^{-}(x) = N_{\mathrm{m}}\varphi^{(+)}(x)F^{(-+)}(x)$ with N_{m} denoting the number of motors per filament as above. Inserting the force velocity equation, Eq. 1, and solving for the velocity yields $v^{(+)}(x) \propto 1 - P(x)$ and $v^{(-)}(x) \propto 1 + P(x)$, where we defined $P(x) = \varphi^{(+)}(x) - \varphi^{(-)}(x)$ as the local network polarity at position x. Hence, the central result of this local mean-field analysis, which will ultimately turn out to be oversimplified, is a linear dependence of the local velocities on the local polarity. This result corresponds to the intuition that forces between filaments — and their relative motions — strongly depends on their relative orientation. In particular, while antiparallel interactions between two filaments introduce motion of both filaments, parallel filaments remain static. As a consequence, filaments with a higher number of antiparallel interactions are expected to exhibit an enhanced speed. However, as we will see next, this intuition is in conflict with numerical simulations (in the biologically relevant parameter regime) as well as with experimental findings for heavily crosslinked filament gels [18].

3.2 The agent-based model can describe the weak velocity-polarity sensitivity

To test whether our model is capable of describing the observations in heavily crosslinked filament networks, we solved the full set of coupled linear equations (Eq. 2) for a one-dimensional network numerically. In order to compare our results to experimental data, we assessed the model parameters as follows: First, we determined the mean number of interaction partners per filament. The typical maximal distance between two microtubules connected by a sliding motor is estimated to be of the order of the tail length of kinesin-5, $\sim 0.1 \mu m$, [5] plus two times the microtubule radius, $\sim 0.024\,\mu m$, [29]. Together with the typical microtubule length, estimated to be $\sim 6 - 7\,\mu m$, these values yield an interaction volume of approximately $1/3\,\mu m^3$. Fürthauer and collaborators argue that the number density of filaments in their experimental setup is approximately $17/\mu m^3$ [18]. So, all in all, we estimate that there are $N \approx 5.5$ interaction partners per filament. In an analogous manner, we assessed the number of microtubules in our one-dimensional representation of the experimental chamber of length $400\,\mu m$ to be ~ 400. Those filaments are placed randomly as described below (*In silico* study: Random polarity field) and experience a drag coefficient of $\gamma = 0.5\,pN\,s/\mu m$ [30–32]. As motor parameters we use $V_{\mathrm{m}} = 20\,nm/s$ [6], $F_{\mathrm{m}} \sim 1\,pN$ [5] and $N_{\mathrm{m}} = 25$ as the average number of motors per filament [18].

Using these parameters we performed numerical simulations, and found good agreement with experimental results (compare Fig. 2 and Fig. 2 in Ref. [18]). In particular, the average filament speed (filled black circles in Fig. 2) is found to be independent of the local polarity. This clearly contradicts the local mean-field theory as discussed above (see section "A local mean-field approximation predicts strong velocity-polarity sensitivity"). To assess why this simplified local view is misleading, we next give a comprehensive mathematical analysis of the full agent-based model.

3.3 Non-local continuum theory

It is evident that in the simplified local mean-field analysis discussed above we neglected the finite extension of filaments. Actually, two filaments which pass through the same location do not necessarily have the same midpoint position. While they share some overlap, they will interact with different neighbors at different positions. If all filaments have the same length L, a filament with midpoint at position x can interact with filaments whose midpoints lie in the interval $[x - L, x + L]$ (cf. Fig 1 C). In this way, the velocities of filaments located at different spatial positions are coupled, leading to non-local correlation effects that could explain the weak dependence of filament speed on local polarity.

Motivated by this heuristic argument, we set out to formulate a continuum theory that quantifies the non-local coupling between the filament velocities ($v^{\pm}(x)$) and densities ($\rho^{(\pm)}(x)$). To this end, we rewrote the local balance equation, Eq. 2, assuming a continuum limit.

$$\gamma\, v^{(\pm)}(x) = \frac{1}{L}\int_{x-L}^{x+L} \mathrm{d}y\, \left\{ f^{(++)}_{\mathrm{parallel}}(x,y) + f^{(+-)}_{\mathrm{antiparallel}}(x,y) \right\}, \tag{3}$$

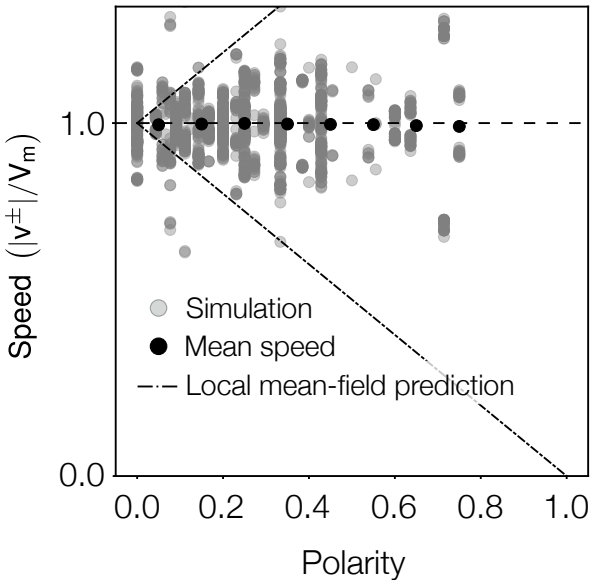

Figure 2. Local microtubule speed vs. local polarity obtained by numerically solving the full set of coupled linear equations (Eq. 2) for a one-dimensional microtubule network. The microtubule network is generated as described in section *In silico* study: Random polarity field. Gray dots represent individual measurements, black dots show the average speed binned for local polarities (bin size $\Delta P = 0.1$). In contrast to the oversimplified discussion (dashed - dotted lines), the velocity does not depend linearly on the local polarity. Instead, the average speed is mostly independent of the local polarity. Note that the vertical stripes are artefacts arising from the discrete nature of the agent-based simulation: Due to the finite number of filaments in an interval $[x, x + \Delta x]$ the polarity can only take on discrete values.

where the local forces are given by

$$f^{(\pm\pm)}_{\text{parallel}}(x,y) = \hat{N}_{\text{m}}(x,y) \cdot N\, \varphi^{(\pm)}(y) \cdot F^{(\pm\pm)}(x,y)\ , \tag{4a}$$

$$f^{(\pm\mp)}_{\text{antiparallel}}(x,y) = \hat{N}_{\text{m}}(x,y) \cdot N\, \varphi^{(\mp)}(y) \cdot F^{(\pm\mp)}(x,y)\ . \tag{4b}$$

Here, the force a motor exerts on the filaments it crosslinks is simply given by the continuum version of Eq. 1, e.g. $F^{(\pm\pm)}(x,y) = F_{\text{m}}\,[v^{(\pm)}(y) - v^{(\pm)}(x)]/(2\,V_{\text{m}})$. The second factor in Eq. 4 accounts for the expected number of interaction partners at position y, given by the number fraction of filaments with the respective polarity $\varphi^{(\pm)}(y)$ multiplied by the average number N of interaction partners: $N\,\varphi^{(\pm)}(y)$. For this functional form to apply, we implicitly assumed that the filament network is not sparse, i.e., that there is always a sufficient number of interaction partners, namely more than N, available. The number fraction can be written in terms of the filament densities as $\varphi^{(\pm)} = \rho^{(\pm)}/(\rho^{(+)} + \rho^{(-)})$. The first factor in Eq. 4, $\hat{N}_{\text{m}}(x,y)$, specifies the average number of motor proteins mediating the interaction between a pair of filaments located at positions x and y. This number is determined by the size of the overlapping region, $L_{\text{ov}} = L - |x - y|$, and the number of motors per filament, N_{m}. Since all the available motors on a filament have to be shared among all of its N interaction partners, only N_{m}/N are available for the interaction with any specific filament. Hence, assuming a uniform motor distribution along each microtubule, the effective number of motors crosslinking a filament pair is on average given by $\hat{N}_{\text{m}}(x,y) = N_{\text{m}}/N \cdot L_{\text{ov}}/L$.

Based on this non-local continuum representation of our agent-based model, we seek a quantitative understanding of how the opposing forces in the filament network give rise to collective (uniform) motion. Ultimately, our goal is to provide an explicit expression relating the polarity and velocity fields.

3.4 Analytic solution for motor-induced filament movement

In this section, we present an analytic solution to our non-local continuum description (Eq. 3). We restrict our analysis to the limit where the system size is large compared to the filament length L and to all other intrinsic length scales of the system we might encounter in the course of the mathematical analysis. Making use of complex calculus, in this limit it is possible to find an explicit expression for the velocity field $v^{(\pm)}(x)$ in terms of the polarity field $P(x)$. This expression, thus, constitutes a velocity-polarity relation which quantifies how the polarity field affects the velocities.

In an experimentally reasonable parameter regime one finds an approximate expression which reads (for a detailed analysis see SI):

$$v^{(\pm)}(x) = \pm V_\mathrm{m}\,(1-\alpha)\,\big(1 \mp \Pi(x)\big)\,, \tag{5a}$$

$$\Pi(x) = \frac{1}{2\,l_c}\int_{-\infty}^{\infty} \mathrm{d}y\; \mathrm{e}^{-|x-y|/l_c}\,P(y)\,. \tag{5b}$$

where $1/\alpha := 1 + 12\,(l_c/L)^2$; for biologically plausible parameter values one has $\alpha \ll 1$. Importantly, Eq. 5a shows that the motion of filaments is neither solely dependent on the local polarity nor fully independent of the polarity field. Instead, the local filament velocities, $v^{(\pm)}(x)$, now depend in a non-local way on the polarity, $P(y)$, as specified by the convolution integral (weighted average), $\Pi(x)$, with an exponential kernel (weight) $\sim \mathrm{e}^{-|x-y|/l_c}$. To emphasize this non-local dependence of the velocities on the polarity, we refer to $\Pi(x)$ as the *ambient polarity* in the following. The characteristic interaction range l_c, over which the polarity field is averaged, is given by

$$l_c = L\,\sqrt{\frac{F_\mathrm{m}\,N_\mathrm{m}}{24\,\gamma\,V_\mathrm{m}}}\,. \tag{6}$$

It is set by the ratio of the total force exerted by motors between microtubules, $F_\mathrm{m}\,N_\mathrm{m}$, to the drag imposed on the microtubule by the surrounding fluid, $\gamma\,V_\mathrm{m}$. Furthermore, it can be interpreted as the length scale over which motion generated by antiparallel filament sliding is propagated by parallel and antiparallel filament interactions through the network. As a result, the interaction range l_c reflects the antagonism between motion-propagating forces (parallel and antiparallel interactions) and the attenuation of force propagation in the filament network mediated by viscous drag. [1] This antagonism is captured by the spatial average of the polarity field which effectively corresponds to a low-pass filter. Due to averaging over local polarities, high-frequency fluctuations in the spatial polarity profile are filtered out and, hence, do not contribute to the velocity. Explicitly, by Fourier transforming Eq. 5b we find a Lorentzian Fourier weight

$$\Pi_k = P_k\,\frac{1}{1+(kl_c)^2}\,, \tag{7}$$

where k denotes the wave number. Hence, the characteristic frequency of the low-pass filter is proportional to the reciprocal of the characteristic length, $1/l_c$, implying that the larger l_c the stronger the filter and the less relevant local fluctuations in the polarity. To put it another way, the speed of a filament at position x depends only on the local "view" of the polarity field within a range defined by l_c (Fig. 3).

To gain an impression of how the interplay between the different forces in the network leads to the non-local effects, it is helpful to consider the limiting cases of large and small l_c, respectively. For large l_c, motor forces dominate viscous drag ($F_\mathrm{m}N_\mathrm{m} \gg \gamma V_\mathrm{m}$). Then, either due to weak dissipation or strong motor-mediated filament coupling, parallel and antiparallel crosslinked filaments translate the motion, generated by interactions between antiparallel filaments, over long distances ($\sim l_c$). As a result, motion

[1] An insightful intuitive explanation for the characteristic length l_c can be found in section "Extension of the analysis to systems with several different types of crosslinking motors" in the SI. It relies on an analysis of systems with several types of motors which proposes a clear separation of the forces acting on microtubules: Active forces which determine the magnitude of the filament speed and passive friction forces between microtubules that determine the force propagation in the network.

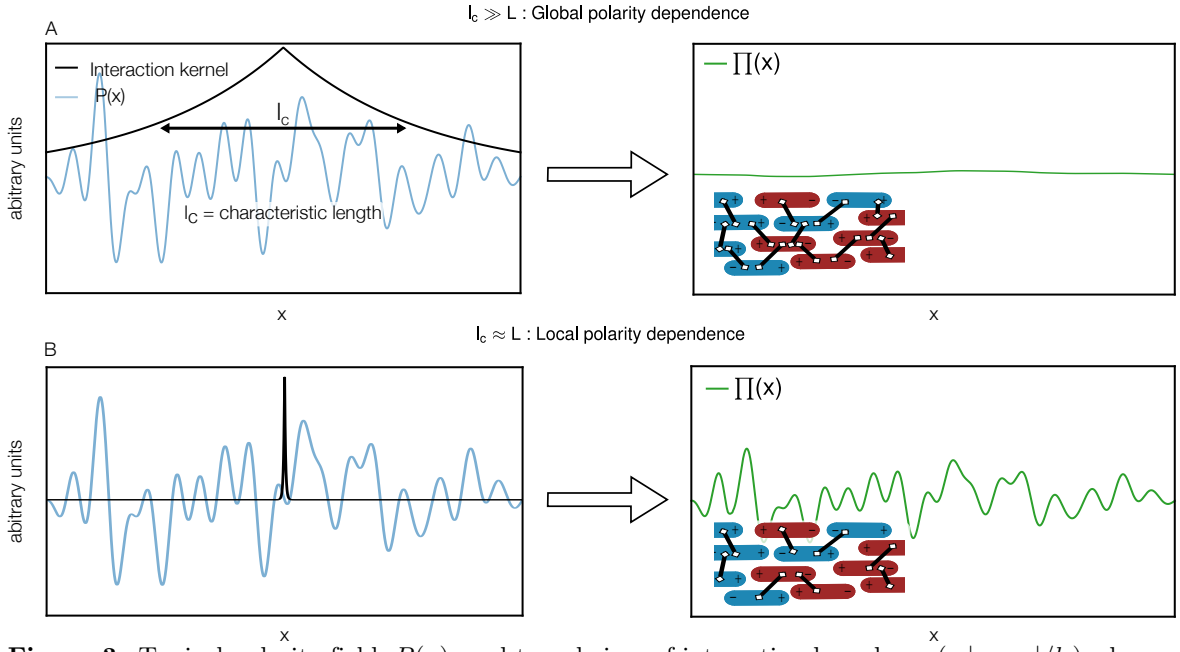

Figure 3. Typical polarity field, $P(x)$, and two choices of interaction kernel, $\exp(-|x-y|/l_c)$, characterizing global and local polarity dependence, respectively. Filaments positioned in a range of l_c around x contribute to the motion of microtubules at x. Depending on the ratio of average motor force exerted on a microtubule to attenuation (drag of microtubules in the fluid), the characteristic propagation length l_c takes different values. (**A**) For large l_c and polarity fields that vary randomly on length scales smaller than l_c, this averaging yields a roughly constant ambient polarity profile, $\Pi(x)$, and hence a roughly constant velocity profile. On a microscopic level, this corresponds to a heavily crosslinked filament network (inset). (**B**) In the limit of small l_c only the local environment, i.e., the direct interaction partners, has an influence on the microtubule motion. The ambient polarity field (velocity field) varies as the polarity field varies.

generated at one position in the network propagates through the entire network. In the asymptotic limit $l_c \to \infty$, the velocity-polarity relation (Eq. 5a) reduces to $v^{(\pm)} = \pm {V_m}^2$, confirming recently published findings for a heavily crosslinked network [18]. In contrast, for small l_c ($F_\mathrm{m} N_\mathrm{m} \ll \gamma V_\mathrm{m}$) force generated at a certain position in the network has only a local effect. Forces generated by antiparallel interactions cannot propagate through the network either due to strong dissipation or a lack of filament interactions. In this limit, the velocity-polarity relation reduces to the result obtained with the local mean-field theory discussed in A local mean-field approximation predicts strong velocity-polarity sensitivity. This relation agrees with the velocity-polarity relation found for dilute filament networks where only local bundles of filaments are considered [20, 21] [3].

3.5 Interpretation of the velocity-polarity relation

With regard to previous results, our considerations offer a solution to the seemingly contradictory behavior of dilute and heavily crosslinked networks. More specifically, our results identify a common mechanism for collective filament dynamics: Due to the finite extension of the microtubules, one microtubule can be crosslinked with several others whose center positions are spread over a region up to twice the microtubule length (Fig. 1C). As a result, although microtubules at different positions might in

[2] for zero overall polarity

[3] Care has to be taken when comparing our result to the dilute limit: We restricted our discussion to the case of sufficient number of interaction partners, whereas usually for dilute systems disconnected patches of filaments are considered. For a more comprehensive discussion on how our results are related to results for dilute systems we refer the reader to the SI.

fact not be directly linked by a motor, an interaction between them can be mediated by successive crosslinks through a chain of microtubules. In this way, the velocity of microtubules at one position influences the velocity at a different position and information on the local polarities propagates through the system. How far this information propagates (l_c) depends on how "effectively" movement at one position is translated into movement at a different position. The greater the efficiency, the smaller the ratio between the passive drag on microtubules in the fluid (and thus the attenuation) and the average maximal force exerted on one microtubule by all motors linking it to other microtubules.

Taken together, our results shed light on the question of what determines the local speed of microtubules in a nematic network: Generally, it is neither the local polarity, $P(x)$, that determines the velocity of microtubules at a certain position nor the overall polarity in the system, P_{glob}. Instead the ambient polarity, $\Pi(x)$, is informative. The ambient polarity corresponds to an average of the polarity with a weight that decays exponentially with the distance from the position of interest (see Eq. 5b). The characteristic decay length, l_c, is proportional to the filament length L, and increases with the ratio of the motor-force on a microtubule, $F_m N_m$, to the fluid drag, γV_m. In general, for a finite decay length and a spatially varying polarity profile, the ambient polarity also varies in space. As can be inferred from Eq. 5b, for larger values of l_c, a larger region of space contributes to the ambient polarity (see also Fig. 3). Accordingly, the ambient polarity then corresponds to an average of the local polarity over more positions. As a result, for a fixed spatial polarity profile, the range of values of the ambient polarity decreases with increasing characteristic propagation length l_c. Due to the linear relationship between the velocities and the ambient polarity, Eq. 5a, the same holds true for the range of velocities.

In the following, we illustrate these predictions with the help of two examples. First, we consider a spatially linear polarity profile. Besides being an instructive case, this polarity profile is of biological relevance. It resembles the measured, approximately linear polarity profiles in the mitotic spindle (see Discussion and Conclusion). As a complement, the setup of the second example is designed to mimic typical *in vitro* experiments. In order to make testable predictions we analyze the suggested (idealized) experiment in detail and focus on quantities which we believe to be accessible in experiments.

3.6 A simple example: The linear polarity profile

Our theory predicts that the range of velocities decreases with increasing characteristic propagation length, l_c. To demonstrate this correlation, we consider a linear polarity profile $P(x) = a\ (x - S/2)$ in a finite interval $x \in [0, S]$ (for details see SI). As motivated above, we describe the local polarity profile in terms of its Fourier coefficients $\hat{P}_k$. The wave numbers are now discrete, $k \in \mathbb{N}$, as the system is finite. The Fourier coefficients of the ambient polarity, $\hat{\Pi}_k$, are given by the Fourier coefficient of the local polarity, $\hat{P}_k$, times a k-dependent weighting factor: $\hat{\Pi}_k = \hat{P}_k / \left[1 + (2\pi k l_c/S)^2\right]$ (see SI). Correspondingly, the ratio between the range of the local polarity $2P_{\max} = aS$ and the range of the ambient polarity $2\Pi_{\max}$ can be approximated as (see SI)

$$\frac{\Pi_{\max}}{P_{\max}} \approx \frac{1}{1 + (\pi l_c/S)^2}. \tag{8}$$

This finding confirms the intuitive expectation that with increasing characteristic length l_c the ambient polarity range $2\Pi_{\max}$ (or analogously the velocity range $2\Pi_{\max} V_m(1-\alpha)$), should decrease relative to the local polarity range, $2P_{\max}$, and the spatial profile gets "squeezed" (Fig. 4). From the approximate expression, Eq. 8, we infer that for characteristic lengths of the same order as the system size, $l_c/S \sim \mathcal{O}(1)$, the range of the ambient polarity $2\Pi_{\max}$ is only a tenth of the range of the local polarity $2P_{\max}$. Due to the linear relationship between the velocity and ambient polarity, Eq. 5a, this small range of ambient polarities implies that also the velocity range for equally oriented microtubules is small. As a result, for $l_c \geq S$, all equally oriented microtubules move as a collective with approximately uniform velocity. In particular, there is also movement in regions where locally the polarity is $P(x) = \pm 1$, corresponding to stretches populated only by parallel microtubules.

For *in vitro* experiments with filament gels or reconstituted systems, it might not be feasible to get information on the entire spatial polarity and velocity fields. Instead, in typical experiments the local

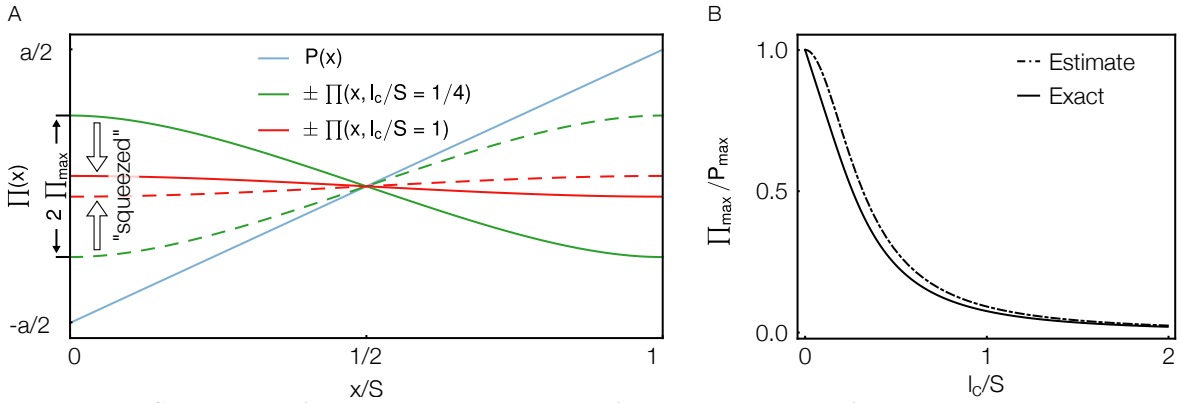

Figure 4. "Squeezing" of the ambient polarity in a finite system with reflecting boundary conditions. (**A**) Sketch of the linear spatial polarity profile, $P(x) = a\ (x - S/2)$, $x \in [0, S]$, together with the ambient polarity profile, $\Pi(x, l_c)$, for two different values of the characteristic length l_c/S (normalized by the system size S). The solid and dashed lines indicate the solutions relevant for $(+)$ and $(-)$ filaments, respectively. For larger l_c, the range of the ambient polarity, $2\Pi_{\max}$, becomes more restricted. (**B**) Ratio between the range of the ambient polarity $2\Pi_{\max}$ and the range of the local polarity $2P_{\max} = aS$ plotted against l_c/S. The curve is well approximated by a Lorentzian decay $1/(1 + (\pi l_c/S)^2)$ (estimate). For the exact expression, please refer to the SI. For larger l_c/S, the range of the ambient polarity relative to that of the local polarity falls off rapidly.

polarity and velocity are recorded only at single points in the filament gel [17, 18, 33]. Data obtained in this way is similar to that shown in Fig. 2 where one data point corresponds to a polarity-velocity pair measured at one location in the gel. In the next section, we thus perform an *in silico* study where we make single velocity and polarity measurements only and do not measure the entire spatial fields. Nevertheless, the key idea motivating the setup of the *in silico* study is the expectation that the spectrum of measured velocities is squeezed compared to the spectrum of local polarities: Due to the filtering of short-wavelength modes, extreme values of the local polarity are averaged out and the velocity profile is smoother than the local polarity profile. In the following, we thus focus on deriving a relation between the measured distribution of local polarities and velocities.

3.7 *In silico* study: Random polarity field

The goal of this section is to suggest an experimental setup that should permit the antagonism between the different forces in the system due to drag and motor-mediated interactions to be explored. To this end, we performed an *in silico* study intended to closely emulate the situation in experiments with *in vitro* filament gels. Photo-bleaching experiments have proven to be a feasible option to simultaneously determine sliding velocities and local gel polarity in filament gels [17, 18, 33]. In these experiments, the fluorescently labelled microtubules in the gel are photo-bleached along a line by laser light. Due to the motion of the filaments in the gel, the bleached line splits into two lines that move to the right (left) and correspond to left-oriented (right-oriented) microtubules, respectively. From the motion of the two lines, the local velocity and the local polarity can be inferred simultaneously: The local velocity of the left-oriented (right-oriented) microtubules is directly obtained from the velocity of the respective line. Furthermore, the local polarity is determined from the ratio of the bleach intensities of the two lines. The data so obtained only contains local information about the velocity and polarity but no spatially resolved information. In order to make experimentally testable predictions, our goal is, therefore, to derive a relationship between the distribution of measured local polarities and the distribution of measured velocities for which spatial resolution is not necessary.

Setup of the *in silico* study To illustrate how a given polarity distribution affects the velocity distribution, we consider a specific example, namely a polarity "environment" resulting from random filament assemblies; for details please refer to the SI. We assume that the filament network is nematically ordered and filaments are randomly oriented to the left or to the right, and therefore neglect the possibility that in the experimental system the spontaneous self-organization into the nematic state might involve some polarity sorting. More specifically, filaments are randomly placed in a chamber of size $S \gg L$ with periodic boundary conditions. Since for random filament assemblies there is no reason why the average number of left- and right-pointing filaments should differ, we choose the number density for both left- and right-pointing microtubules to be identical: $\mu^{(+)} = \mu^{(-)} = \mu$. Importantly, due to the finite extension of the microtubules, the polarity at different positions is not independent. Instead, one finds a positive covariance for the polarities at distances less than one microtubule length L apart (see SI). As a result, the polarity profile is not completely random but correlated on lengths smaller than the microtubule length L (for a typical profile please refer to the SI).

Signature of the ambient polarity in the velocity distribution Based on our theoretical understanding, we expect that, depending on the characteristic length l_c, the distribution of velocities is squeezed compared to the polarity distribution. This is because, depending on the ratio of the antagonistic forces, filament motion arises from averaging the polarity over longer (large l_c) or shorter (small l_c) distances. As we expect the degree of averaging to be reflected in the distribution of velocities, the standard deviation of the microtubule velocities should be an interesting quantity to look at in experiments.

In order to predict the variance of the velocities (ambient polarities) analytically, we describe the local polarity field resulting from the random placement and orientation of filaments in the "experimental" chamber by a set of correlated random variables (see SI). Using their correlation structure, we average the local polarity according to the expression for the ambient polarity (Eq. 5b) and find (see SI)

$$\frac{\mathrm{Var}[v/V_m]}{\mathrm{Var}[P]} = (1-\alpha)^2 \left[1 - \frac{3l_c}{2L}\left(1 - \mathrm{e}^{-L/l_c}\right) + \frac{1}{2}\,\mathrm{e}^{-L/l_c}\right] . \tag{9}$$

Here, $\mathrm{Var}[P] = \mathrm{Var}[P(x)] = \langle P(x)^2\rangle - \langle P(x)\rangle^2$ denotes the variance of the local polarity, and $\mathrm{Var}[v/V_m] = \mathrm{Var}[v(x)/V_m]$ the variance of the (normalized) velocity v/V_m measured in units of the motor velocity. The above equation implies that the variance of the normalized velocity can be considerably smaller than the variance of the spatial polarity profile; see Fig. 5B. The ratio between the two only depends on the characteristic length l_c/L and quickly decays with respect to it. For larger l_c/L, the ambient polarity corresponds to an average over a larger region in space. Therefore, its variance decreases. Due to the linear relationship between the velocity and the ambient polarity, the variance of the velocity decreases to an equal extent.

In order to compare our results to *in vitro* experiments we assessed the values for both the one-dimensional number density of filaments 2μ and the characteristic length l_c. From recent experimental data [18], we estimated $2\mu = 6$ and $l_c/L \approx 10$; see also Section The agent-based model can describe the weak velocity-polarity sensitivity. Given these estimates, our theory yields a standard deviation of the polarity distribution $\sigma[P] = \sqrt{\mathrm{Var}[P]} \approx 0.46$, corresponding to a broad range of observable polarities similar to what is seen in experiments. Using our theoretical results we predict the ratio between the standard deviations of the local polarity and the normalized velocity to be approximately $\sigma[P]/\sigma[v/V_m] = \sqrt{\mathrm{Var}[P]/\mathrm{Var}[v/V_m]} \approx 6.3$. Thus, we expect the mismatch between the widths of the two distributions to be clearly visible in experiments.

Polarity and velocity distribution in the *in silico* study Figure 5A shows a comparison of the distribution of the local polarity and velocity, as measured in the *in silico* study (density plot and histograms) and as predicted analytically (black lines). The density plot shows the measured probability distribution for all combinations of local polarity and velocity. The histograms for both quantities were obtained as projections of the density plot onto the respective axis. While the local polarity takes values

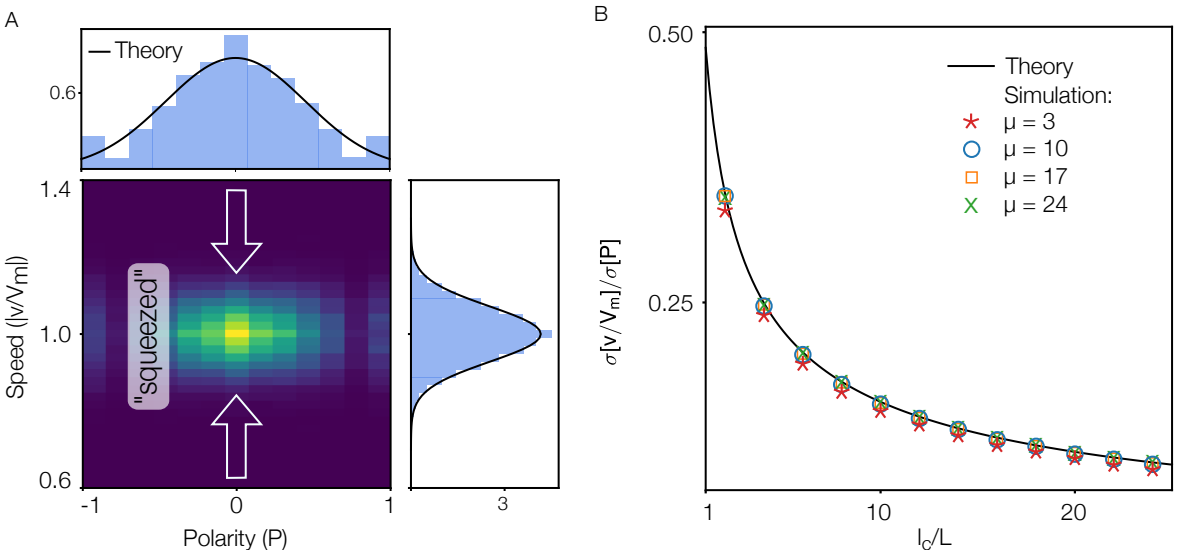

Figure 5. Results for the *in silico* study. (**A**) Density plot displaying the probability distribution for all combinations of local polarity, $P(x)$, and speed, $|v(x)/V_m|$, as measured in the *in silico* study described in section *In silico* study: Random polarity field. The histograms at the top and on the right are projections of the density plot on the respective axis. In both cases, the solid line is the corresponding analytic prediction that was obtained by approximating the distributions by a normal distribution with the respective predicted mean and variance. In comparison to the local polarity (top), the velocity distribution (right) is less broad, i.e., it exhibits a smaller but non-zero standard deviation. The parameters are chosen to match the stochastic agent-based simulation described in section The agent-based model can describe the weak velocity-polarity sensitivity, namely $\mu = 3$ and $l_c/L = 10$. (**B**) Ratio between the standard deviations of the normalized velocity, $\sigma[v/V_m]$, and of the local polarity, $\sigma[P]$, plotted against normalized characteristic length, l_c/L. The results of the numerical solution of the continuum equation, Eq. 5b (symbols) for $\mu = \{3, 10, 17, 24\}$ (red stars, blue circles, yellow squares, green crosses) collapse onto one master curve. The solid line corresponds to the analytic prediction of the master curve. For larger characteristic length, the standard deviation of the velocity decreases relative to the standard deviation of the local polarity. Note that for small $\mu = 3$, there is a slight deviation from the master curve. In this case, the variance of the local polarity is so high that the corresponding, approximate normal distribution has not decayed to zero at $P = \pm 1$ (see histogram at top of A).

in a broad range between ± 1 (histogram at top of Fig. 5A), the distribution of the velocity is squeezed to values of approximately $(1 \pm 0.2)V_m$ (histogram at right of Fig. 5A).

The disparity between the two distributions nicely illustrates the filtering of high-frequency modes discussed in the section Analytic solution for motor-induced filament movement. This filtering is due to long-range interactions induced by the averaging of the polarity field over a length l_c. Since the filtering strongly depends on the characteristic length l_c, the ratio between the standard deviations of the local polarity and velocity distributions, $\sigma[P]/\sigma[v/V_m]$, decreases as l_c increases (Fig. 5B). It would be interesting to test this prediction experimentally by changing, for instance, the concentration of the molecular motors, or the drag in the fluid.

Figure 5B shows how the standard deviation of the velocity distribution, normalized to the standard deviation of the local polarity distribution, depends on the characteristic length l_c. For small $l_c \sim L$, the effective interaction range of microtubules l_c is small and the microtubule dynamics is predominantly determined by the local polarity at their respective position. Conversely, in the limit of large l_c, the dynamics of all microtubules is determined by the same average global polarity. Consequently, all microtubules then exhibit the same velocity and the standard deviation of the velocity $\sigma[v/V_m]$ decays to zero. Notably, the normalized curves for different values of the microtubule density, μ, collapse onto one

master curve when plotted against l_c/L (see SI). Thus, in our thought experiment, where we make a certain assumption with regard to the spatial polarity profile, knowledge of the microtubule density is not necessary.

Experimental relevance In an experimental filament gel other factors also influence filament dynamics. For instance, as molecular motors randomly attach and detach from microtubules, even microtubules at the same position can interact with a different set of microtubules and thus experience different environments. As a result, different microtubules at the same position might actually have a (slightly) different velocity. Correspondingly, for two experimental realizations with an identical polarity profile, the respective average filament speeds at one position x might indeed differ. This effect is not captured by our continuum description, which assumes deterministic velocity profiles $v^{(\pm)}(x)$. Thus, we expect a broader distribution of velocities for *in vitro* measurements compared to our theoretical prediction. To gauge the strength of this effect, we compared our theoretical predictions with the results from stochastic agent-based simulations of the system (for details see SI). We find that the specific value of the width of the velocity distribution depends on details of the velocity measurement in the experiments. Nevertheless, irrespective of these details, the velocity distribution is significantly smaller than the width of the polarity distribution. Similarly, we expect that fluctuations in the concentration of motors lead to a slight broadening of the velocity distribution but will not change the behavior qualitatively.

The *in silico* study considered here clearly simulates an idealized system insofar as we have assumed that there is no overall spatial structure. The analysis can be readily extended to a broader class of systems, in which knowledge of the covariance structure of the polarity field ($\mathrm{Cov}[P](x,y)$) is sufficient to predict the covariance structure of the velocity field ($\mathrm{Cov}[v/V_m](x,y)$) (see SI). Since this signature of our results is strongly dependent on the characteristic length, l_c, we expect such measurements to provide insight into network parameters. Actually, even low-resolution information on the spatial variation of the polarity field could be helpful to test our predictions. As we have seen above, the Fourier coefficients are suppressed by $1/(1+(2\pi l_c k/S)^2)$, $k \in \mathbb{Z}$, in a finite system of size S (or, equivalently, by $1/(1+(l_c k)^2)$, $k \in \mathbb{R}$, in the infinite system). So, for large l_c, the velocity modes with wave vector $k \geq 1/l_c$ should not be visible in experiments.

4 Discussion and Conclusion

In this work, we have considered a mesoscopic model for microtubule dynamics in a nematic, motor-crosslinked network. So far, research has focused on either the dilute or heavily crosslinked limit. Strikingly, the observed behavior in these two cases is qualitatively different: While in the dilute case the microtubule velocities strongly depend on the local network polarity [20, 21], in the heavily crosslinked case the velocity has been found to be independent of the polarity [14, 16, 18]). These distinct phenomenologies are puzzling, as the underlying microscopic motor-mediated microtubule interactions are presumably the same in both cases. Starting from these filament interactions, we have shown how the interplay between movement resulting from motor-crosslinking and the countervailing effects of fluid drag determines the sensitivity of the local filament dynamics to the network polarity. Thereby we provide a better understanding of the essential physical principles that lead to such diverse dynamics.

To this end, we derived a non-local mean-field theory of our system from the microscopic interactions. This theory enabled us to obtain an explicit analytic expression relating the local microtubule velocity to the spatial polarity profile. Our key result is that the local velocity depends on the local *ambient polarity*, which is given by the averaged polarity a microtubule senses in its environment. More specifically, the local velocity is given by the convolution of the polarity and an exponentially decaying interaction kernel with *characteristic propagation length*, l_c. Hence, it is not the local polarity at the position of a microtubule that determines its motion but rather the entire polarity profile in an environment of length l_c. This finding implies that a one-to-one mapping between the local velocities of microtubules and the local polarity as shown in Fig. 2 is not the whole story. Instead, in order to predict

the velocity at a specific location, knowledge of the spatially varying polarity profile in the entire vicinity is needed. In general, such detailed spatial information appears to be inaccessible with current experimental techniques. Fortunately, in order to infer the distribution of velocities from the distribution of local polarities, such detailed information is not essential. For example, in a gel where microtubules are randomly placed in an experimental chamber and stochastically oriented, our theory predicts how the variances of the local polarity and of the velocity are related.

The relationship between the velocity and polarity distributions strongly depends on the characteristic propagation length l_c, which is an important emerging length scale in the system. It can be interpreted as a non-local interaction range of filaments, and is determined by the ratio between the average motor-driven force on a microtubule and the microtubule's drag in the fluid. Thus, this intrinsic length reflects how effectively motion generated at one position is propagated through the interconnected network of filaments. It strongly depends on the network properties.

We have identified a common mechanism explaining the microscopic origin of both uniform filament motion in percolated nematic networks and the strong polarity dependence of microtubule motion in dilute systems: Due to their finite extension, microtubules directly interact with several parallel and antiparallel neighbors within a spatial ranges equal to twice their filament length. Motors between parallel microtubules induce a resistance against relative motion and thus promote uniform motion of crosslinked microtubules. Thereby, motion generated by antiparallel interactions translates through the percolated network of microtubules even into regions with only parallel and no antiparallel interactions where *a priori* no motion is expected. The degree of efficiency of this propagation of motion is quantified by the characteristic propagation length l_c. Hence, it is influenced by the average number of motors per interaction and the drag of filaments in the fluid, among other factors. Filaments at distances larger than l_c apart can be considered to be part of disconnected patches. That is, for small l_c only motor-crosslinks between nearest neighbor filaments are relevant for filament motion, as in the dilute limit. For this case, we recover the linear relationship between local polarity and filament velocity [19–21]. On the other hand, in the limit of large l_c, which corresponds to systems where the patch size exceeds the system size, we find a dependence of the velocity on the global polarity only. Here, the velocity for equally oriented microtubules is the same everywhere in space. In particular, our results explain the weak sensitivity of the filament velocities to the local polarity observed in recent experiments [18] and in the spindle apparatus [11, 14, 16].

In particular we predict a strong dependency of the velocity distribution on the characteristic propagation length. In order to test this prediction, we suggest a practicable *in vitro* experiment whose feasibility we assessed with the help of an *in silico* study intended to mimic the suggested *in vitro* experiment. Intriguingly, it is not necessary to determine the entire spatial polarity and velocity profile to check the validity of our theory. Instead, it suffices to determine the polarity and velocity distributions by measuring the local velocity and polarity at random positions in the filament gel. When plotting the ratio of the standard deviations of the polarity and velocity distribution against the characteristic length l_c, we expect the data to collapse onto a master curve, irrespective of the explicit number of filaments in the experimental chamber (Fig. 5). Furthermore, the ratio of the standard deviations of the polarity and velocity distributions for a specific experimental setup could be used to identify the characteristic propagation length l_c and, allow one to draw conclusions regarding network features (Eq. 6).

Microtubule motion in mitotic spindles formed in Xenopus egg extract is a prominent example for polarity-independent sliding. The polarity profile in these spindles is approximately linear, ranging from zero polarity in the center to highly polar regions at the spindle poles [17]. Nonetheless, microtubules drift with roughly constant velocity towards the spindle poles, especially if dynein is inhibited. Our theory can account for this behavior. In particular, the individual velocities deviate only slightly from the mean velocity if motor-crosslinking is strong, i.e. if the characteristic length exceeds the system size (see Sec. A simple example: The linear polarity profile). Interestingly, for biologically plausible parameters the interaction range is of the same order as the length of the spindles formed in Xenopus egg extracts, $l_c \propto 30 - 80\ \mu m$. Correspondingly, as seen in Fig. 4(A), the velocity of the poleward moving microtubules is expected to be slightly smaller close to the pole than in the center of the spindle.

This variation is due to the dependence of the velocity on the ambient polarity (the local polarity environment). Taken together, our results suggest that, depending on the value of the characteristic length compared to the spindle size, the spatial polarity profile and, in particular, the fact that the poles are highly polar, could be significant for the velocity profile as well. To examine this behavior experimentally, it would be instructive to investigate the velocity distribution of microtubules in a dynein-depleted, unfocused spindle as a function of the distance from the spindle boundary.

More generally, there is not only one type of motor present *in vivo*. Instead several types of motors can, in principle, crosslink and exert forces on filaments. Extending our analysis to a broader class of crosslinking proteins does not change our results qualitatively (see SI). The velocity still depends on the ambient polarity with a characteristic length that is determined by the ratio between the absolute "friction" between microtubules and the drag in the fluid.

From a broader perspective, it would be interesting to extend our work on nematic networks to a more general description of filament gels. To this end, it could be promising to start from recent work on heavily crosslinked filament gels, where a sophisticated hydrodynamic framework has been established from microscopic properties [18]. This theoretical framework assumes an infinitely large characteristic length l_c, so that motion generated at one position propagates through the whole network without loss. Our results suggest that incorporating an exponential interaction kernel into this framework can provide a more comprehensive description of filament motion in crosslinked gels. Such a description would also offer the chance to understand the transition from heavily crosslinked to weakly coupled gels.

Author Contributions

M.S., I.R.G., and E.F. designed research, performed research, and wrote the article.

Acknowledgments

We thank Silke Bergeler, Philipp Geiger, Emanuel Reithmann and Patrick Wilke for helpful feedback on the manuscript.

This research was supported by the German Excellence Initiative via the program "NanoSystems Initiative Munich" (NIM). I.R.G. is supported by a Deutsche Forschungsgemeinschaft fellowship through the Graduate School of Quantitative Biosciences Munich (QBM). We also gratefully acknowledge funding by the Deutsche Forschungsgemeinschaft (DFG, German Research Foundation) – Project-ID 111166240 – Collaborative Research Center (SFB) 863 – Project B2.

References

1. D. A. Fletcher and R. D. Mullins, "Cell mechanics and the cytoskeleton," *Nature*, vol. 463, no. 7280, pp. 485–492, 2010.

2. B. Alberts, *Molecular biology of the cell*. Garland Science, 6 ed., 2015.

3. J. Howard, "Molecular motors: Structural adaptations to cellular functions," *Nature*, vol. 389, no. 6651, pp. 561–567, 1997.

4. J. Howard, "Mechanical Signaling in Networks of Motor and Cytoskeletal Proteins," *Annual Review of Biophysics*, vol. 38, no. 1, pp. 217–234, 2009.

5. R. A. Cross and A. McAinsh, "Prime movers: The mechanochemistry of mitotic kinesins," *Nature Reviews Molecular Cell Biology*, vol. 15, no. 4, pp. 257–271, 2014.

6. L. C. Kapitein, E. J. G. Peterman, B. H. Kwok, J. H. Kim, T. M. Kapoor, and C. F. Schmidt, "The bipolar mitotic kinesin Eg5 moves on both microtubules that it crosslinks," *Nature*, vol. 435, no. 7038, p. 114, 2005.

7. F. J. Nedelec, T. Surrey, A. C. Maggs, and S. Leibler, "Self-organization of microtubules and motors," *Nature*, vol. 389, no. 6648, pp. 305–308, 1997.

8. T. Surrey, A. Laughon, and A. Dev, "Physical Properties Determining Self-Organization of Motors and Microtubules," *Science*, vol. 292, pp. 1167–1172, 2001.

9. T. Sanchez, D. T. Chen, S. J. Decamp, M. Heymann, and Z. Dogic, "Spontaneous motion in hierarchically assembled active matter," *Nature*, vol. 491, no. 7424, pp. 431–434, 2012.

10. J. Roostalu, J. Rickman, C. Thomas, F. Nédélec, and T. Surrey, "Determinants of polar versus nematic organization in networks of dynamic microtubules and mitotic motors," *Cell*, vol. 175, no. 3, pp. 796–808, 2018.

11. D. T. Miyamoto, Z. E. Perlman, K. S. Burbank, A. C. Groen, and T. J. Mitchison, "The kinesin Eg5 drives poleward microtubule flux in Xenopus laevis egg extract spindles," *Journal of Cell Biology*, vol. 167, no. 5, pp. 813–818, 2004.

12. M. Uteng, C. Hentrich, K. Miura, P. Bieling, and T. Surrey, "Poleward transport of Eg5 by dynein-dynactin in Xenopus laevis egg extract spindles," *Journal of Cell Biology*, vol. 182, no. 4, pp. 715–726, 2008.

13. N. P. Ferenz, A. Gable, and P. Wadsworth, "Mitotic functions of kinesin-5," *Seminars in Cell & Developmental Biology*, vol. 21, no. 3, pp. 255 – 259, 2010.

14. K. S. Burbank, T. J. Mitchison, and D. S. Fisher, "Slide-and-Cluster Models for Spindle Assembly," *Current Biology*, vol. 17, no. 16, pp. 1373–1383, 2007.

15. D. Oriola, D. J. Needleman, and J. Brugués, "The Physics of the Metaphase Spindle," *Annual Review of Biophysics*, vol. 47, pp. 655–73, 2018.

16. G. Yang, L. A. Cameron, P. S. Maddox, E. D. Salmon, and G. Danuser, "Regional variation of microtubule flux reveals microtubule organization in the metaphase meiotic spindle," *Journal of Cell Biology*, vol. 182, no. 4, pp. 631–639, 2008.

17. J. Brugués, V. Nuzzo, E. Mazur, and D. J. Needleman, "Nucleation and transport organize microtubules in metaphase spindles," *Cell*, vol. 149, no. 3, pp. 554–564, 2012.

18. S. Fürthauer, B. Lemma, P. J. Foster, S. C. Ems-McClung, C. E. Walczak, Z. Dogic, D. J. Needleman, and M. J. Shelley, "Actively crosslinked microtubule networks: mechanics, dynamics and filament sliding," *arXiv preprint*, p. arXiv:1812.01079, 2018.

19. K. Kruse and F. Jülicher, "Actively contracting bundles of polar filaments," *Physical Review Letters*, vol. 85, no. 8, pp. 1778–1781, 2000.

20. T. Gao, R. Blackwell, M. A. Glaser, M. D. Betterton, and M. J. Shelley, "Multiscale modeling and simulation of microtubule-motor-protein assemblies," *Physical Review E*, vol. 92, no. 6, pp. 1–20, 2015.

21. T. Gao, R. Blackwell, M. A. Glaser, M. D. Betterton, and M. J. Shelley, "Multiscale polar theory of microtubule and motor-protein assemblies," *Physical Review Letters*, vol. 114, no. 4, pp. 1–5, 2015.

22. A. Zemel and A. Mogliner, "Motor-induced sliding of microtubule and actin bundles," *Physical Chemistry Chemical Physics*, vol. 11, no. 24, pp. 4800–4803, 2009.

23. A. J. Hunt, F. Gittes, and J. Howard, "The force exerted by a single kinesin molecule against a viscous load," *Biophysical Journal*, vol. 67, no. 2, pp. 766–781, 1994.

24. K. Svoboda and S. M. Block, "Force and velocity measured for single kinesin molecules," *Cell*, vol. 77, no. 5, pp. 773–784, 1994.

25. K. Visscher, M. J. Schnitzer, and S. M. Block, "Single kinesin molecules studied with a molecular force clamp," *Nature*, vol. 400, pp. 184–189, 1999.

26. M. T. Valentine, P. M. Fordyce, T. C. Krzysiak, S. P. Gilbert, and S. M. Block, "Individual dimers of the mitotic kinesin motor Eg5 step processively and support substantial loads in vitro," *Nat. Cell Biol.*, vol. 8, no. 5, pp. 470–476, 2006.

27. L. Huber, R. Suzuki, T. Krüger, E. Frey, and A. R. Bausch, "Emergence of coexisting ordered states in active matter systems," *Science*, vol. 361, no. 6399, pp. 255–258, 2018.

28. V. Pryamitsyn and V. Ganesan, "Screening of hydrodynamic interactions in Brownian rod suspensions," *Journal of Chemical Physics*, vol. 128, no. 13, 2008.

29. G. M. Cooper, *The Cell*. ASM Press, 5 ed., 2009.

30. K. Tawada and K. Sekimoto, "Protein friction exerted by motor enzymes through a weak-binding interaction," *Journal of theoretical biology*, vol. 150, no. 2, pp. 193–200, 1991.

31. R. Loughlin, R. Heald, and F. Nédélec, "A computational model predicts xenopus meiotic spindle organization," *Journal of Cell Biology*, vol. 191, no. 7, pp. 1239–1249, 2010.

32. G. Letort, A. Z. Politi, H. Ennomani, M. Théry, F. Nedelec, and L. Blanchoin, "Geometrical and mechanical properties control actin filament organization," *PLOS Computational Biology*, vol. 11, pp. 1–21, 05 2015.

33. F. Decker, D. Oriola, B. Dalton, and J. Brugués, "Autocatalytic microtubule nucleation determines the size and mass of spindles," *eLife*, vol. 7, p. e31149, 2018.

Supplementary Material: A mechanistic view of collective filament motion in active nematic networks

M. Striebel[1⋆], I. R. Graf[1⋆], E. Frey

⋆M.S. and I.R.G. contributed equally to this work.

S1 Details of numerical simulation

Agent-based simulation: To simulate the filament gel, we implement an agent-based simulation consisting of M_l left- and M_r right-oriented filaments. As described in detail in section *In silico* study: Random polarity field, we randomly place the filaments in a one-dimensional box with periodic boundary conditions. Next, a vector $\mathbf{I} \in \mathbb{R}^{M_r+M_l}$ consisting of the numbers of overlapping filaments for each filament i is generated. From this vector, a probability vector $\mathbf{p} \in \mathbb{R}^{M_l+M_r}$ is derived so that the average number of interaction partners per filament is given by $N = I_i\, p_i$. Out of the I_i possible interaction partners of filament i, we accept an interaction with probability p_i and reject it with probability $1 - p_i$. Once the interactions are determined, we construct a set of $M_l + M_r$ coupled linear equations on the basis of the force balance equation

$$\gamma\, v_i = \sum_j F_{ij}^{\text{parallel}} + \sum_k F_{ik}^{\text{antiparallel}} \,, \tag{S1}$$

and weigh each interaction by the overlap between the filaments. Here j runs over the parallel interaction partners and k over the antiparallel interaction partners of filament i. The velocities of each filament i are then obtained using matrix inversion.

Continuum simulation: For the continuum simulation, we generate a polarity profile analogous to that in the agent-based simulation. Then we use our theoretical results (Eqs. 5a, 5b) but perform the integration numerically to obtain the velocity field.

S2 A continuum model for motor driven filament motion

Here we derive a solution for our continuum model of filament motion. As a starting point, we use the coupled set of integral equations, Eqs. 3, in the main text which read

$$\gamma\, v^{(+)}(x) = \frac{N}{L}\int_{x-L}^{x+L} \mathrm{d}y\, \frac{\hat{N}_\mathrm{m}(x,y)}{2}\, \{(1+P(y))F^{(++)}(x,y) + (1-P(y))F^{(+-)}(x,y)\} \tag{S2}$$

$$\gamma\, v^{(-)}(x) = \frac{N}{L}\int_{x-L}^{x+L} \mathrm{d}y\, \frac{\hat{N}_\mathrm{m}(x,y)}{2}\, \{(1-P(y))F^{(--)}(x,y) + (1+P(y))F^{(-+)}(x,y)\} \,, \tag{S3}$$

where we used $\varphi^{(\pm)} = 1/2(1 \pm P(y))$.
In general, it is quite challenging to provide an analytic solution to a set of coupled integral equations. Here, however, one can make use of the fact that the difference of the velocities, $v^{(+)} - v^{(-)}$, takes a quite simple form. Namely,

$$\begin{aligned} 2\,\gamma(v^{(+)}(x) - v^{(-)}(x)) = \frac{N}{L}\int_{x-L}^{x+L} \mathrm{d}y\, \hat{N}_\mathrm{m}(x,y)\{&(1+P(y))\,(F^{(++)}(x,y) - F^{(-+)}(x,y)) \\ &+(1-P(y))\,(F^{(+-)}(x,y) - F^{(--)}(x,y))\} \,. \end{aligned} \tag{S4}$$

The difference of the contributing forces reads

$$F^{(++)}(x,y) - F^{(-+)}(x,y) = F^{(+-)}(x,y) - F^{(--)}(x,y) = F_\mathrm{m}\,\left(1 + \frac{v^{(-)}(x) - v^{(+)}(x)}{2V_\mathrm{m}}\right) \,, \tag{S5}$$

and is a function of x only.
Substituting Eq. S5 into Eq. S4 and performing the integration yields

$$v^{(+)}(x) - v^{(-)}(x) = 2\,V_\mathrm{m}\frac{1}{1 + \frac{2\,V_\mathrm{m}\,\gamma}{F_\mathrm{m} N_\mathrm{m}}} \equiv 2\,V_\mathrm{m}(1-\alpha) = \text{const} \,. \tag{S6}$$

As a result, $v^{(-)}$ is expressed in terms of $v^{(+)}$, and we can use this relation to decouple Eq. S2 and Eq. S3.
The resulting integral equation reads

$$\epsilon\, v^{(+)}(x) - V_\mathrm{m}\alpha = \int_{x-L}^{x+L} \frac{\mathrm{d}y}{L^2}\, (L - |x-y|)\left\{v^{(+)}(y) - v^{(+)}(x) - V_\mathrm{m}\alpha\, P(y)\right\} \,, \tag{S7}$$

where we introduced $\epsilon = \frac{2\gamma V_\mathrm{m}}{F_\mathrm{m} N_\mathrm{m}}$.
To proceed further, we rewrite $v(y)$ and $P(y)$ in terms of their full Taylor expansions around x and shift $v^{(+)}$ by $\alpha/\epsilon\ V_\mathrm{m}$, i.e., $v^{(+)} \to v^{(+)} - \alpha/\epsilon\ V_\mathrm{m}$.

Performing the integration yields an ODE coupling the velocity to the polarity field. It reads:

$$\left(\epsilon - \sum_{k=1}^{\infty} \frac{2L^{2k}}{(2+2k)!} \left(\frac{\partial}{\partial x}\right)^{(2k)}\right) v^{(+)}(x) = -V_\mathrm{m}\alpha \sum_{k=0}^{\infty} \frac{2L^{2k}}{(2+2k)!} \left(\frac{\partial}{\partial x}\right)^{(2k)} P(x) \tag{S8}$$

S3 An analytic solution for filament motion in a nematic network

To find a feasible expression relating the velocity and polarity field, we apply the Fourier transformation to Eq. S8. Our system - recast in $v^{(+)}(k)$ and $P(k)$ - becomes

$$v^{(+)}(k) = -2V_\mathrm{m}\alpha \underbrace{\left(\frac{1-\cos(Lk)}{\epsilon(Lk)^2 - 2 + (Lk)^2 + 2\ \cos(Lk)}\right)}_{\equiv \hat{K}(k)}\ P(k) = \mathfrak{F}\{K\} \cdot \mathfrak{F}\{P\}\ . \tag{S9}$$

where $\mathfrak{F}$ denotes the Fourier transformation operator[4]. From the convolution theorem, we directly find that $v^{(+)}(x)$ is given by the convolution of $K(x)$ and $P(x)$. So, in order to tackle our original equations, we are left with finding the Fourier back transformation of $\hat{K}(k)$, i.e., we need to solve

$$K(x) = \frac{1}{2\,\pi} \int_{-\infty}^{\infty} \mathrm{d}k \left(\frac{1-\cos(Lk)}{\epsilon(Lk)^2 - 2 + (Lk)^2 + 2\ \cos(Lk)}\right)\ \exp(ikx)\ . \tag{S10}$$

To proceed further, we assume that the integral can be performed using the residue theorem, i.e.,

$$K(x) = \frac{1}{2\,\pi} \int_{-\infty}^{\infty} \mathrm{d}k \underbrace{\left(\frac{1-\cos(Lk)}{\epsilon(Lk)^2 - 2 + (Lk)^2 + 2\ \cos(Lk)}\right)\ \exp(ikx)}_{f(k)} = i \sum_j \mathrm{Res}_{k_j}\{f(k)\}\ , \tag{S11}$$

with the sum running over all poles in the upper half plane (lower half plane) if $x > 0$ ($x < 0$). In the following, we will restrict the discussion to the case $x > 0$ since the calculations for $x < 0$ are analogous. Note that we exclude the case $x = 0$ explicitly, and assume a smooth solution at $x = 0$. For simplicity, we will use dimensionless variables in the following and recast $k \to kL$ and $x \to x/L$.
To find the potential residues, we search for all solutions of the equation

$$0 \stackrel{!}{=} k^2(1+\epsilon) - 2 + 2\cos(k) = k^2(1+\epsilon) - 4\ \sin^2(k/2)\ . \tag{S12}$$

in the complex plane. In the following, we will use $k = a + ib$ with $a, b \in \mathbb{R}$. Using this notation, the problem of finding possible residues of $f(k)$ has shifted to finding solutions to the equations

$$a\ \sqrt{1+\epsilon} = \pm 2\cosh(b/2)\ \sin(a/2) \tag{S13}$$

$$b\ \sqrt{1+\epsilon} = \pm 2\sinh(b/2)\ \cos(a/2)\ . \tag{S14}$$

We split the discussion into (i) real, (ii) imaginary and (iii) complex solutions of Eq.S12. a^*, b^* will denote solutions of the above equation system.

(i) real solutions ($b^* = 0$) The only real solution of Eq. S12 is given by $a^* = 0$.

(ii) imaginary solutions ($a^* = 0$) Eq. S13 is always fulfilled for $a_0^* = 0$. Moreover, Eq. S14 always has two solutions for $\epsilon > 0$ which can be estimated as $b_0^* = \pm\sqrt{24\sqrt{1+\epsilon} - 24}$ for small ϵ.

[4]It is also possible to derive Eq. S9 by directly inserting the Fourier transforms of $v^{(+)}$ and P into Eq. S7.

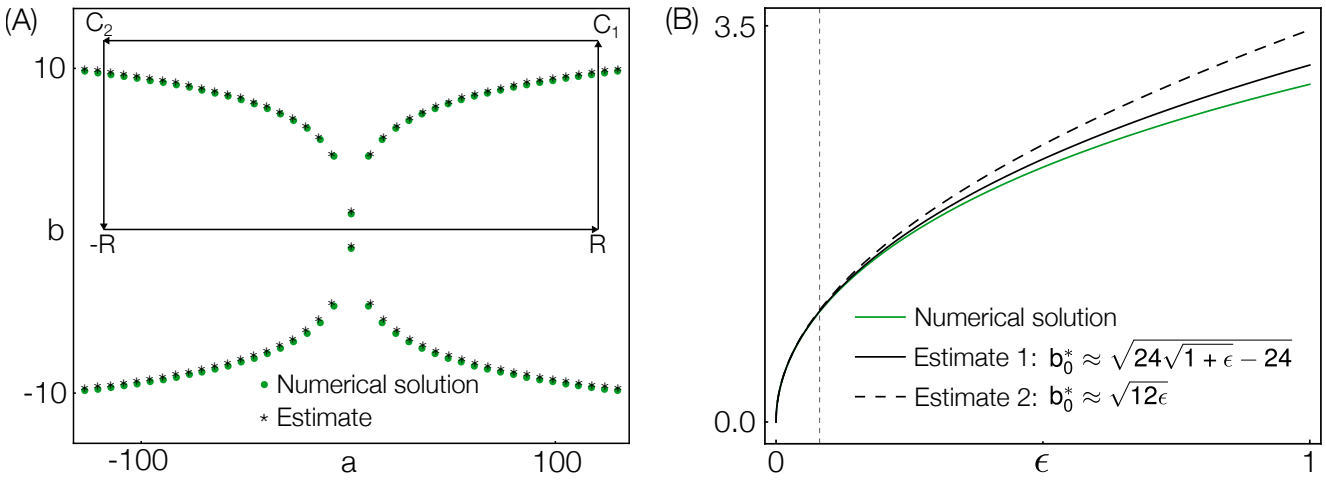

Figure S1: (**A**) Comparison of the estimate of the solutions of the equation system Eq.S13,S14 with the solutions obtained numerically (the results are compared exemplary for $\epsilon = 0.1$). (**B**) Comparison of two estimates for the imaginary pole with the corresponding numerical solutions. The gray dashed line indicates the $\epsilon-$value for which $l_c \approx L$.

(iii) complex solutions ($a^* \neq 0, b^* \neq 0$) The complex solutions are not trivial to find. First, note that the discussion can be split into positive and negative signs of the right-hand side of Eq. S13 and S14.
For a negative sign on the right-hand side, if $a, b > 0$, $\cos(a/2)$ and $\sin(a/2)$ have to be negative for the equation system to be solvable, i.e., we know $a \in (2n\pi, (2n+1)\pi)$ with $n = 1, 3, 5...$.
Investigating Eq. S14 alone, the minimal $b^*(a)$ is found for $a = 2\pi n$ and can be estimated as $b^*_{min}(2n\pi) = \sqrt{24\sqrt{1+\epsilon} - 24}$, i.e.,$b^*_{min}$ is close to 0 for small ϵ. Moreover, one finds that $b^*(a)$ is monotonically increasing in the interval $a \in (2n\pi, (2n+1)\pi)$ and $b^*(a \to (2n+1)\pi) \to \infty$.
Equation S13 implies that $\cosh(b/2)$ has to be sufficiently large if $a \in (2n\pi, (2n+1)\pi)$ with $n = 1, 3, 5...$. Especially for large n this means that a^* has to be close to $(2n+1)\pi$ with $n = 1, 3, 5...$, i.e., $\sin(a^*/2) \approx -1 \Rightarrow b^* \approx 2\text{arcosh}\left(\frac{2\,n+1}{2}\pi\sqrt{1+\epsilon}\right)$.
Taken together, this yields

$$(a^*, b^*) \approx \left((2\,n+1)\pi, 2\text{arcosh}\left(\frac{2\,n+1}{2}\pi\sqrt{1+\epsilon}\right)\right) \quad \text{with } n = 1, 3, 5... \tag{S15}$$

A similar argumentation for a positive sign on the right-hand side of Eq. S13 and Eq. S14 and $a, b > 0$ yields the same result for $n = 2, 4, 5....$ The cases $a > 0, b < 0$, $a < 0, b > 0$ and $a < 0, b < 0$ are analogous.
Taken together, we find the solutions

$$(a^*_n, b^*_n) \approx \left((2\,n+1)\pi, \pm 2\,\text{arcosh}\left(\frac{2\,n+1}{2}\pi\sqrt{1+\epsilon}\right)\right) \tag{S16}$$

$$(a^*_n, b^*_n) \approx \left(-(2\,n+1)\pi, \pm\,2\,\text{arcosh}\left(\frac{2\,n+1}{2}\pi\sqrt{1+\epsilon}\right)\right) \quad \text{with } n = 1, 2, 3... \tag{S17}$$

Figure S3 shows a comparison between the numerically found roots and our approximation for $\epsilon = 0.1$.
Since there is an infinite number of poles with arbitrarily large real part, one can not proceed as usual and use the residue theorem without any additional considerations. So, to make further progress, we continue as follows: First, we show

$$\int_{-\infty}^{\infty} \mathrm{d}k\; f(k) \approx \int_{-R}^{R} \mathrm{d}k\; f(k) \tag{S18}$$

for sufficiently large R.
Second, we compute the integration along the path $\mathcal{C} = \{-R \to R \to C_1 \to C_2 \to -R\}$ according to the residue theorem:

$$\oint_{\mathcal{C}} f(k)\mathrm{d}k = 2\pi\, i \sum_j \text{Res}_{k_j}\{f(k)\}\,. \tag{S19}$$

Third, we show that the path in the complex plane gives a vanishing contribution. Then the real Integral $\int_{-R}^{R} \mathrm{d}k\; f(k)$ can be estimated by

$$\int_{-R}^{R} \mathrm{d}k\ f(k) = 2\pi\ i\ \sum_{n=-M}^{M} \mathrm{Res}_{k_n}\{f(k)\} \tag{S20}$$

where $k_n = k_{-M}...k_M$ denotes the poles in the interior of the integration path sorted by increasing real part. The notation is chosen so that k_0 denotes the purely imaginary pole.

The first step is straightforward since

$$\mathfrak{Re}\left\{\int_R^\infty \mathrm{d}k\ \left(\frac{1-\cos(k)}{(1+\epsilon)k^2-2+2\ \cos(k)}\right)\ \exp\left(ikx\right)\right\} < \int_R^\infty \mathrm{d}k\ \frac{2}{k^2} = \frac{2}{R}\ , \tag{S21}$$

i.e.,

$$\begin{aligned}&\int_{-\infty}^{\infty} \mathrm{d}k\ \left(\frac{1-\cos(k)}{(1+\epsilon)k^2-2+2\ \cos(k)}\right)\ \exp\left(ikx\right)\\ =&\int_{-R}^{R} \mathrm{d}k\ \left(\frac{1-\cos(k)}{(1+\epsilon)k^2-2+2\ \cos(k)}\right)\ \exp\left(ikx\right) + \mathcal{O}(\frac{1}{R})\ .\end{aligned}$$

Next, we aim on showing that there is a path $R \to C_1 \to C_2 \to -R$ so that the integration along that path gives zero contribution in the limit of large R.
Usually, if one deals with functions of the form $g(k)\ \exp(ixk)$ one can make use of Jordan's lemma which states that the integration along the semicircular contour in the upper half plan (lower half plan) for $x > 0$ ($x < 0$) aims to zero for the radius $R \equiv |k| \to \infty$. However, if $f(k)$ is rewritten in the form of $g(k)\ \exp(ixk)$ with $g(k) = (1-\cos(k))/((1+\epsilon)k^2 - 2(1-\cos(k)))$, we face the problem that $g(k)$ does not converge uniformly to zero since $g(k)$ has an infinite number of poles in the upper (and lower) half plane. So, to proceed further we aim on proving that there exists a path so that the contribution of the contour in the complex plane goes to zero for large radius.
First, note that

$$\mathfrak{Re}\{\mathrm{Res}\{f(k)\}|_{k=a+ib}\} = -\mathfrak{Re}\{\mathrm{Res}\{f(k)\}|_{k=-a+ib}\} \tag{S22}$$
$$\mathfrak{Im}\{\mathrm{Res}\{f(k)\}|_{k=a+ib}\} = \mathfrak{Im}\{\mathrm{Res}\{f(k)\}|_{k=-a+ib}\}\ , \tag{S23}$$

i.e., if the integration path is chosen in a way to symmetrically include the poles in the upper left and upper right quarter we know $\mathfrak{Im}\{2\pi i \sum_j \mathrm{Res}_{k_j}\{f(k)\}\} = 0$. Hence, if the contour integral (Eq. S19) is calculated explicitly along such a path, the result has to be real. In the following, we will make use of this fact. To prove that the integration along the contour in the complex plane goes to zero (for large R), we choose an explicit path along a rectangle as shown in Fig.S3. More concretely, the vertices are defined by $R = 2n\pi$, $C_1 = 2n\pi + i2n\pi$ and $C_2 = -2n\pi + i2n\pi$ for $n \in \mathbb{N}$. Since the overall contour integral is real, we only care about terms which can give a real contribution, i.e., we investigate the real (imaginary) parts of the integrand for the integration paths parallel to the real (imaginary) axis:

$$\begin{aligned}\lim_{n\to\infty} \int_0^{2n\pi} \mathrm{d}b\ \mathfrak{Im}\{f(k)|_{k=2n\pi+ib}\}\\ \lim_{n\to\infty} \int_{2n\pi}^{0} \mathrm{d}b\ \mathfrak{Im}\{f(k)|_{k=-2n\pi+ib}\}\\ \lim_{n\to\infty} \int_{2n\pi}^{-2n\ \pi} \mathrm{d}a\ \mathfrak{Re}\{f(k)|_{k=a+2n\pi\ i}\}\ .\end{aligned}$$

To prove that those terms give zero contribution for $n \to \infty$ (and thereby $R \to \infty$), we aim on finding an integrable majorant of the above expressions, and then swap the integration and the limit. It is possible to show that

$$\begin{aligned}\mathfrak{Im}\{f(k)|_{\pm 2n\pi+i\ b}\} < \exp\left(-b\ x\right)\\ \mathfrak{Re}\{f(k)|_{a+2n\pi\ i}\} < \exp\left(-2n\pi\ x\right)\ .\end{aligned}$$

Thus, we found an integrable majorant for both paths. Furthermore, since $\mathfrak{Im}\{f(k)|_{2n\pi+i\ b}\} = -\mathfrak{Im}\{f(k)|_{-2n\pi+i\ b}\}$, the discussion can be restricted to one of the paths $R \to C_1$ or $C_2 \to -R$. Moreover, as we found an integrable majorant for the parts of the contour in the complex plane, we can swap the integral and the limit. Since $\lim_{n\to\infty} |\mathfrak{Im}\{f(k)|_{2n\pi+i\ b}\}| \to 0$, the paths $R \to C_1$ and $C_2 \to -R$ give zero contribution to the contour integral. The same holds true for the integration along

the path $C_1 \to C_2$. Thus, the integration along the contour in the complex plane gives zero contribution for $n \to \infty$ and we can calculate the desired integral by

$$\int_{-\infty}^{\infty} \mathrm{d}k\ f(k) = 2\pi\ i \sum_{j}^{\infty} \mathrm{Res}_{k_j}\{f(k)\} = 2\pi\ \mathfrak{Im}\left\{\left(\mathrm{Res}_{k_0}\{f(k)\} + 2\sum_{j=1}^{M} \mathrm{Res}_{k_j}\{f(k)\}\right)\right\}\ . \tag{S24}$$

In the last step, we made use of Eq.S22. In the following, we will denote the contribution of the k_0 residue to the integral as $f_0(x)$ and the contribution of the sum over all other poles as $f_\infty(x)$ Using the estimated expression for the poles of $f(k)$ and making use of the fact that b_n^* is large, we find an estimate for the imaginary part of the residue which reads

$$\mathfrak{Im}\{\mathrm{Res}_{k_n}\{f(k)\}\} \approx \exp(-b_n x)\cos(a_n x) \tag{S25}$$

for $n = 1...M$. Here, we assumed that $b_n x$ is sufficient large, i.e., we expect deviations for $x \to 0$.
For k_0 we find the residue (for small ϵ)

$$\begin{aligned} f_0(x) &= \mathrm{Res}_{k_0}\{f(k)\} \approx \\ &\approx \frac{2\pi \sinh^2\left(\sqrt{24\sqrt{1+\epsilon}-24}\right)}{\sinh\left(\sqrt{24\sqrt{1+\epsilon}-24}\right) - (1+\epsilon)\sqrt{24\sqrt{1+\epsilon}-24}} \exp\left(-\sqrt{24\sqrt{1+\epsilon}-24}\ x\right)\ . \end{aligned}$$

So, to find a closed form of the integral, we are left with finding an expression for the sum

$$\begin{aligned} f_\infty(x) &= 2\pi \sum_{n=1}^{\infty} \mathrm{Res}_{k_n}\{f(k)\} \\ &= 2\pi \sum_{n=1}^{\infty} \exp\left(-2\ \mathrm{arcosh}\left(\frac{2n+1}{2}\pi\sqrt{1+\epsilon}\right)\ x\right)\ \cos((2n+1)\pi\ x) \\ &\approx 2\pi \left(\frac{1}{\pi^2(1+\epsilon)}\right)^x \sum_{n=1}^{\infty} \frac{\cos((2n+1)\pi\ x)}{(2n+1)^{2x}} \\ &= \pi \left(\frac{1}{4\pi^2(1+\epsilon)}\right)^x \left[\exp\left(-3i\pi\ x\right)\ \phi(\exp(-2i\pi x, 2x, 3/2)) + \exp\left(3i\pi\ x\right)\ \phi(\exp(2i\pi x, 2x, 3/2))\right]\ . \end{aligned} \tag{S26}$$

For the approximation we used $\mathrm{arcosh}(x) \approx \ln(2x)$ for large x. Here, $\phi(z, s, \alpha) = \sum_{n=0}^{\infty} \frac{z^n}{n+\alpha}$ denotes the Lerch zeta function. Fig. S3 (A) shows a comparison between our analytic result and the sum over the first 5000 numerically obtained residues. For a better comparison, we also perform the sum over the approximated residue (Eq.S26) for the first 5000 terms. Moreover, we compute the ratio of f_∞/f_0 to get insight into how much f_∞ contributes to the overall integral.
Taken together, this yields the desired expression for the integral and, thereby, an expression for the interaction kernel in real space which reads

$$\begin{aligned} \int_{-\infty}^{\infty} \mathrm{d}k\ f(k) &= \frac{2\pi \sinh^2\left(\sqrt{24\sqrt{1+\epsilon}-24}\right)}{\sinh\left(\sqrt{24\sqrt{1+\epsilon}-24}\right) - (1+\epsilon)\sqrt{24\sqrt{1+\epsilon}-24}} \exp\left(-\sqrt{24\sqrt{1+\epsilon}-24}\ x\right) \\ &+ \pi \left(\frac{1}{4\pi^2(1+\epsilon)}\right)^x \left[\exp\left(-3i\pi\ x\right)\ \phi\left(\exp(-2i\pi x), 2x, \frac{3}{2}\right) + \exp\left(3i\pi\ x\right)\ \phi\left(\exp(2i\pi x), 2x, \frac{3}{2}\right)\right]\ . \end{aligned} \tag{S27}$$

This expression, however, is not particularly intuitive. Therefore, we seek for a simpler and more meaningful expression.
Fig. S3 (B) indicates that f_∞ is not particularly relevant for the overall integral, i.e., it is promising to use only the $0th$ residue to approximate the integral. Moreover, ϵ is known to be small for biologically meaningful parameters. In hindsight, one can argue that a value of $\epsilon > 1/12$ is not particularly meaningful since for $\epsilon < 1/12$ our result suggests an interaction range $l_c < L$, implying that the microtubules interact only over a distance smaller than one microtubule length. Therefore, it makes sense to consider the limit of small ϵ. Using only the $0th$ residue and considering the lowest order of ϵ yields

$$f(x) \approx \pi \frac{\sqrt{3}}{\sqrt{\epsilon}} \exp\left(-\sqrt{12\epsilon}x\right)\ . \tag{S28}$$

Fig. S3 (B) shows the estimate of the imaginary pole in comparison to the more accurate estimate and the numeric result. Fig. S3 shows a comparison between the numerical solution of the integral, our analytic expression (Eq. S27) and the $0th$ residue approximation for small ϵ (Eq. S28).

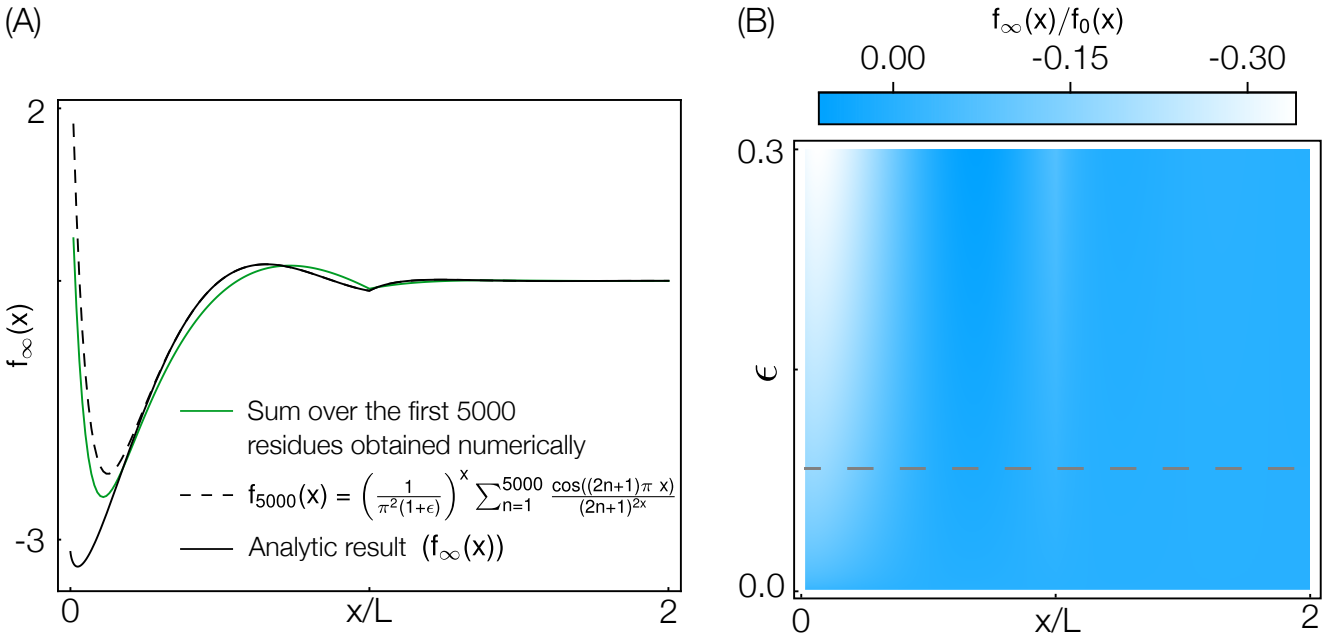

Figure S2: (**A**) Analytic result for the sum over the residues in the complex plane in comparison to the sum over the first 5000 numerically obtained residues. To provide a more accurate comparison, we also compute Eq.S26 for the first 5000 terms. (**B**) To compare the contribution of the k_0 residue and the sum over the other residues to the overall integral, we plot the ratio $f_\infty(x)/f_0(x)$. The dashed line indicates the ϵ value where $l_c \approx L$

Finally, making use of the convolution theorem, Eq. S28 and Eq. S9 yield the desired expression for the filament velocity. Going back to natural variables, i.e., $x \to x\,L$ and $v^{(+)} \to v^{(+)} + \frac{\alpha}{\epsilon} V_\mathrm{m}$ gives the expression used in the main text:

$$v^{(+)}(x) = V_\mathrm{m}(1-\alpha)\left(1 - \frac{1}{2\,l_c}\int_{-\infty}^{\infty} \mathrm{d}y\; P(y) \exp\left(-\frac{|x-y|}{l_c}\right)\right) \tag{S29}$$

where we introduced $l_c = L/\sqrt{12\epsilon}$. The occurrence of the absolute value is due to the fact that an integration over the lower half plane gives an analogous result as compared to the one for the upper half plane.

S4 Extension of the analysis to systems with several different types of crosslinking motors

In the main text, we focus our analysis on the case where there is only one type of motor in the system, namely a crosslinking motor whose two heads are both active and walk to the plus end of the respective microtubule. However, there are also other types of crosslinking motors, for instance motors with only one active head and one passive one that does not move on the microtubule (see Fig. S4 for an illustration). Our analysis can be straightforwardly extended to such other types of crosslinking motors as long as the dominant part of their force generation still happens in the bulk of microtubules and not at the end:[5] More concretely, let us look at a system with five different types of motors (see also Fig. S4 for an illustration):

- one passive crosslinker with two passive heads: P
- two active crosslinkers with two active heads both moving to the $\pm$ end of the microtubule, respectively: $A_\pm$
- two types of crosslinkers ("mixed") with one passive head and one active head that moves to the $\pm$ end of the microtubule, respectively: $M_\pm$.

Furthermore, we again assume a linear force-velocity relation for all motors.

[5]The latter case is true for motors such as dynein which exhibit a much higher residence time at the microtubule minus ends as compared to the bulk (e.g. [14]).

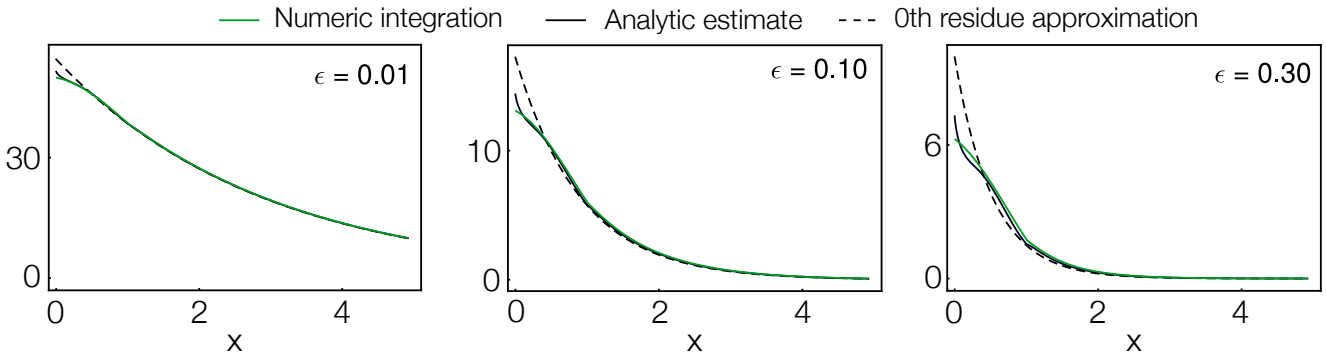

Figure S3: Comparison between numerical integration, analytic approximation and the 0th residue approximation used in the main text. Note that the deviation between the approximations for larger ϵ is manly caused by the wrong estimate of the k_0 residue.

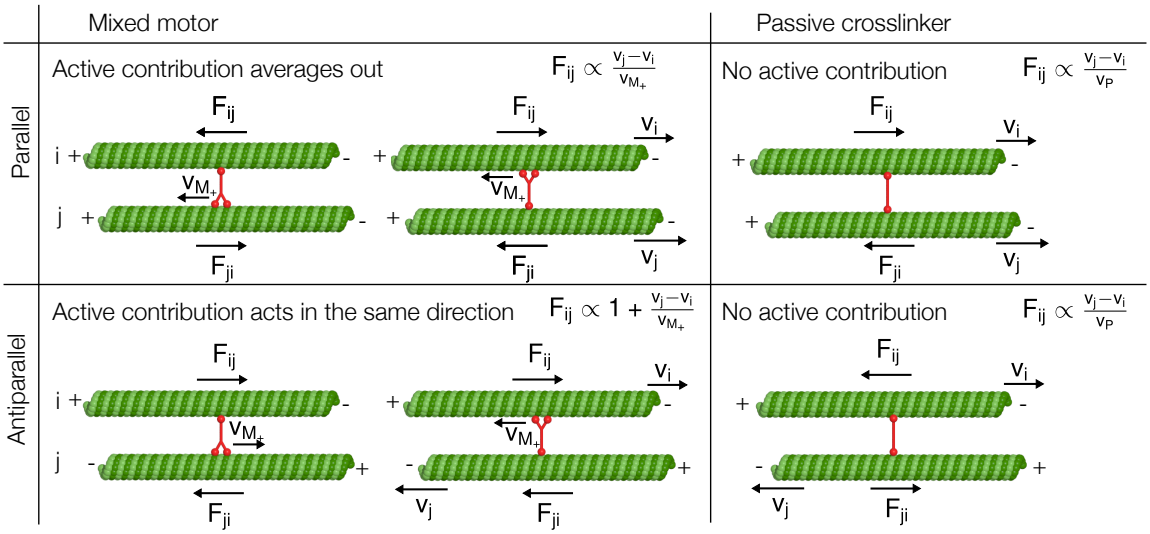

Figure S4: Microscopic, motor-mediated interactions between microtubules for different types of motors. Passive crosslinkers have two passive heads that do not move along the microtubule. "Mixed" motors have one active and one passive head.

The passive crosslinker does not exert any active forces between a pair of microtubules but resists relative motion of the two microtubules, irrespective of their relative orientation:

$$F_P^{(++)}_{(--)}(x,y) = F_P\left(\frac{v^{(\pm)}(y) - v^{(\pm)}(x)}{v_P}\right)$$
$$F_P^{(+-)}_{(-+)}(x,y) = F_P\left(\frac{v^{(\mp)}(y) - v^{(\pm)}(x)}{v_P}\right),$$

where $F_P^{(++)}_{(--)}(x,y)$ is the force a $(\pm)$ microtubule at position y exerts on a parallel $(\pm)$ microtubule at position x. Similarly, $F_P^{(+-)}_{(-+)}(x,y)$ denotes the force a $(\pm)$ microtubule at position y exerts on an antiparallel $(\mp)$ microtubule at position x. F_P denotes the motor force arising for a relative velocity v_P.
The active crosslinker with both heads moving to the $(+)$ end is the one we already described in the main text. It exerts an active force on antiparallel microtubules and resists relative motion of the two crosslinked microtubules, irrespective of the relative orientation:

$$F_{A_+}^{(++)}_{(--)}(x,y) = F_{A_+}\left(\frac{v^{(\pm)}(y) - v^{(\pm)}(x)}{2v_{A_+}}\right)$$
$$F_{A_+}^{(+-)}_{(-+)}(x,y) = F_{A_+}\left(\pm 1 + \frac{v^{(\mp)}(y) - v^{(\pm)}(x)}{2v_{A_+}}\right).$$

Similarly, the active crosslinker with heads moving towards the $(-)$ end exerts the following forces:

$$F_{A_-}^{(++)}(x,y) = F_{A_-}\left(\frac{v^{(\pm)}(y) - v^{(\pm)}(x)}{2v_{A_-}}\right)$$
$$F_{A_-}^{(+-)}(x,y) = F_{A_-}\left(\mp 1 + \frac{v^{(\mp)}(y) - v^{(\pm)}(x)}{2v_{A_-}}\right).$$

$F_{A_\pm}$ denotes the force the motor exerts between two antiparallel microtubules that do not move relative to each other. $v_{A_\pm}$ corresponds to the motor speed of each head along the microtubule.
Finally, the mixed crosslinkers shows "mixed" behavior. For parallel microtubules they behave on average like any other crosslinker (see Fig. S4 for an illustration): Consider a situation where two static $(+)$ microtubules are crosslinked. Then, the mixed crosslinker can be bound either with the active head on microtubule 1 and with the passive one on microtubule 2 or the other way round. In the first case, the $M_\pm$ motor moves microtubule 1 in the $\pm$ direction and microtubule 2 in the $\mp$ direction. In the second case, it is just the opposite: microtubule 1 is pushed in the $\mp$ direction whereas microtubule 2 is pushed in the $\pm$ direction. Since both configurations occur with equal probability, the active contributions does cancel for parallel microtubules. For antiparallel microtubules, on the other hand, the direction of movement of the $(\pm)$ microtubule is always the same, irrespective of which heads is bound to which microtubule. The $M_\pm$ motor moves the $(+)$ microtubule in $\pm$ direction and the $(-)$ microtubule in the $\mp$ direction. For antiparallel microtubules, the active contributions thus do not cancel but are equivalent to the $A_\pm$ motor with two active heads. The passive contribution, steming from relative motion of the microtubules, is always the same: It acts against the direction of motion, irrespective of which head is bound where and how the relative orientation is.
Taken together, the mixed crosslinker with one active and one passive head behaves similarly to any other crosslinker in the case of parallel microtubules and similarly to an active crosslinker in the case of antiparallel microtubules:

$$F_{M_+}^{(++)}(x,y) = F_{M_+}\left(\frac{v^{(\pm)}(y) - v^{(\pm)}(x)}{v_{M_+}}\right)$$
$$F_{M_+}^{(+-)}(x,y) = F_{M_+}\left(\pm 1 + \frac{v^{(\mp)}(y) - v^{(\pm)}(x)}{v_{M_+}}\right),$$

for the mixed motor M_+ with active head moving to the $+$ end, and

$$F_{M_-}^{(++)}(x,y) = F_{M_-}\left(\frac{v^{(\pm)}(y) - v^{(\pm)}(x)}{v_{M_-}}\right)$$
$$F_{M_-}^{(+-)}(x,y) = F_{M_-}\left(\mp 1 + \frac{v^{(\mp)}(y) - v^{(\pm)}(x)}{v_{M_-}}\right),$$

for the mixed motor M_- with active head moving to the $-$ end. $F_{M_\pm}$ denotes the force a $M_\pm$ motor exerts on two static, antiparallel microtubules and $v_{M_\pm}$ is the motor speed of the active head.
Summing all the contributions from all motor types, the total force exerted on a $(+)$ microtubule at position x by parallel $(+)$ microtubules is given by

$$F^{(++)}(x) = \int_{x-L}^{x+L} \frac{\mathrm{d}z}{L}\, \frac{L_{\mathrm{ov}}(x,z)}{L} \varphi^{(+)}(z) \left(\frac{N_P F_P}{v_P} + \frac{N_{A_+} F_{A_+}}{2v_{A_+}} + \frac{N_{A_-} F_{A_-}}{2v_{A_-}} + \frac{N_{M_+} F_{M_+}}{v_{M_+}} + \frac{N_{M_-} F_{M_-}}{v_{M_-}}\right) \left(v^{(+)}(z) - v^{(+)}(x)\right) =$$
$$\equiv \int_{x-L}^{x+L} \frac{\mathrm{d}z}{L}\, \frac{L_{\mathrm{ov}}(x,z)}{L} \varphi^{(+)}(z) C \left(v^{(+)}(z) - v^{(+)}(x)\right),$$

where $L_{\mathrm{ov}}(x,z) = \max(L - |x-z|, 0)$ denotes the overlap between two microtubules at positions x and z as defined in the main text. Furthermore, N_P, $N_{A_\pm}$ and $N_{M_\pm}$ denote the number of passive P, active $A_\pm$ and mixed crosslinkers $M_\pm$ per microtubule, respectively. Furthermore, we defined the sum of the absolute force to velocity ratios

$$C = \frac{N_P F_P}{v_P} + \frac{N_{A_+} F_{A_+}}{2v_{A_+}} + \frac{N_{A_-} F_{A_-}}{2v_{A_-}} + \frac{N_{M_+} F_{M_+}}{v_{M_+}} + \frac{N_{M_-} F_{M_-}}{v_{M_-}}.$$

Similarly, the total force on a $(+)$ microtubule at position x by antiparallel $(-)$ microtubules is given by

$$F^{(+-)}(x) = \int_{x-L}^{x+L} \frac{\mathrm{d}z}{L}\, \frac{L_{\mathrm{ov}}(x,z)}{L} \varphi^{(-)}(z) \left(C \left(v^{(-)}(z) - v^{(+)}(x)\right) + D\right),$$

where we defined D as the sum of the motor forces

$$D = N_{A_+} F_{A_+} + N_{M_+} F_{M_+} - N_{A_-} F_{A_-} - N_{M_-} F_{M_-}.$$

The forces on the $(-)$ microtubules are determined analogously:

$$F^{(--)}(x) = \int_{x-L}^{x+L} \frac{\mathrm{d}z}{L} \, \frac{L_{\mathrm{ov}}(x,z)}{L} \varphi^{(-)}(z) C \left(v^{(-)}(z) - v^{(-)}(x) \right)$$
$$F^{(-+)}(x) = \int_{x-L}^{x+L} \frac{\mathrm{d}z}{L} \, \frac{L_{\mathrm{ov}}(x,z)}{L} \varphi^{(+)}(z) \left(C \left(v^{(+)}(z) - v^{(-)}(x) \right) - D \right).$$

Now, we proceed analogously to the case with only one motor:

$$\gamma v^{(+)}(x) = \int_{x-L}^{x+L} \frac{\mathrm{d}z}{L} \, \frac{L_{\mathrm{ov}}(x,z)}{L} \left(\varphi^{(+)}(z) C \left(v^{(+)}(z) - v^{(+)}(x) \right) + \varphi^{(-)}(z) C \left(v^{(-)}(z) - v^{(+)}(x) \right) + \varphi^{(-)}(z) D \right) \tag{S30}$$
$$\gamma v^{(-)}(x) = \int_{x-L}^{x+L} \frac{\mathrm{d}z}{L} \, \frac{L_{\mathrm{ov}}(x,z)}{L} \left(\varphi^{(-)}(z) C \left(v^{(-)}(z) - v^{(-)}(x) \right) + \varphi^{(+)}(z) C \left(v^{(+)}(z) - v^{(-)}(x) \right) - \varphi^{(+)}(z) D \right). \tag{S31}$$

Subtracting those two equations from one another and performing the integral $\int_{x-L}^{x+L} \frac{\mathrm{d}z}{L} \, \frac{L_{\mathrm{ov}}(x,z)}{L} = 1$, we find

$$\gamma \left(v^{(+)}(x) - v^{(-)} \right) = \int_{x-L}^{x+L} \frac{\mathrm{d}z}{L} \, \frac{L_{\mathrm{ov}}(x,z)}{L} \left(D + C \left(v^{(-)}(x) - v^{(+)}(x) \right) \right) = D + C \left(v^{(-)}(x) - v^{(+)}(x) \right).$$

As a result,

$$v^{(-)}(x) = v^{(+)}(x) - \frac{D}{\gamma + C}, \tag{S32}$$

which is the generalization of Eq. S6.
As for the original case, this result can be plugged into Eq. S30, effectively decoupling the two equations. It follows that

$$\tilde{\epsilon} v^{(+)}(x) - \frac{D}{2C} \frac{\gamma}{\gamma + C} = \int_{x-L}^{x+L} \frac{\mathrm{d}z}{L} \, \frac{L_{\mathrm{ov}}(x,z)}{L} \left(v^{(+)}(z) - v^{(+)}(x) \right) - \frac{D}{2C} \frac{\gamma}{\gamma + C} \int_{x-L}^{x+L} \frac{\mathrm{d}z}{L} \, \frac{L_{\mathrm{ov}}(x,z)}{L} P(z),$$

where we defined $\tilde{\epsilon} = \gamma / C$ and used that we can write the densities in terms of the polarity $\varphi^{(\pm)}(z) = (1 \pm P(z))/2$. Comparing this expression with the analogous result, Eq. S7, we realize that

$$\epsilon = \frac{\gamma}{\frac{F_m N_m}{2 V_m}} \to \tilde{\epsilon} = \frac{\gamma}{C}$$
$$V_m \alpha = V_m \frac{\gamma}{\gamma + \frac{F_m N_m}{2 V_m}} \to \frac{D}{2C} \frac{\gamma}{\gamma + C}$$

Performing the same steps as above, we can thus conclude

$$v^{(+)}(x) = \frac{D}{2(\gamma + C)} \left(1 - \frac{1}{2 l_c} \int_{-\infty}^{\infty} \mathrm{d}y \; P(y) e^{-|x-y|/l_c} \right) \tag{S33}$$
$$v^{(-)}(x) = -\frac{D}{2(\gamma + C)} \left(1 + \frac{1}{2 l_c} \int_{-\infty}^{\infty} \mathrm{d}y \; P(y) e^{-|x-y|/l_c} \right), \tag{S34}$$

with the characteristic length

$$l_c = \frac{L}{\sqrt{12 \tilde{\epsilon}}} = L \frac{C}{12 \gamma} = L \frac{\sqrt{\frac{N_P F_P}{v_P} + \frac{N_{A_+} F_{A_+}}{2 v_{A_+}} + \frac{N_{A_-} F_{A_-}}{2 v_{A_-}} + \frac{N_{M_+} F_{M_+}}{v_{M_+}} + \frac{N_{M_-} F_{M_-}}{v_{M_-}}}}{12 \gamma} = L \sqrt{\sum_{i=P, A_\pm, M_\pm} \frac{N_i F_i}{24 \gamma v_i f_i}} \tag{S35}$$

with the motor forces F_i, number of motors per filament N_i and relevant motor velocities v_i. The factors f_i are 1 for $A_\pm$ and 1/2 for $M_\pm$, corresponding to the fraction of active heads, and 0 for P due to the convention chosen. The prefactor is

$$\frac{D}{2(\gamma + C)} = \frac{N_{A_+} F_{A_+} + N_{M_+} F_{M_+} - N_{A_-} F_{A_-} - N_{M_-} F_{M_-}}{2 \left(\gamma + \sum_{i=P, A_\pm, M_\pm} \frac{N_i F_i}{2 v_i f_i} \right)}. \tag{S36}$$

Thus, the characteristic length is determined by the ratio between the friction in the fluid and the "friction" between all crosslinked microtubules. This friction is determined by the sum of the passive contribution of all motors, irrespective of their direction of motion or whether they are active or not. This passive contribution is independent of the motor properties

as each motor resists relative motion of filaments compared to the favored relative velocity. In contrast, for the maximal speed of the microtubules $D/2/(\gamma + C)$ the direction of the motors is relevant, as expected: D does not correspond to an absolute sum of the different motor types but motors with opposite direction of motion enter with opposite sign, effectively competing against each other.
On a broader perspective, we conclude that systems with different types of motors behave qualitatively similarly as the original system. Their characteristic length only depends on the total passive forces exerted by all motor types and the sign and magnitude of the velocities are determined by the competition between the active motor contributions.
This result provides an insightful intuitive explanation for the characteristic length l_c. The only non-collective length scale in the system is L, the length of microtubules. Hence, by a basic scaling argument, l_c needs to be a linear function of L, multiplied by a dimensionless quantity. The only meaningful combination of the system parameters yielding a dimensionless quantity is the ratio of the different forces in the system: drag in the fluid and forces between microtubules. But, which are the relevant forces between microtubules? Is it the averaged active force on the microtubules or rather the total "friction" between microtubules induced by the motor resistance to relative motion? To obtain an intuitive answer to this question, consider a system with two types of motors whose heads move in the opposite direction. Then, for equal proportion of both types, the average active force on all microtubules is zero, irrespective of the absolute number of motors. The force propagation through the network, however, should depend on the number of links in the network or, equivalently, the absolute number of motors. The same is true for the friction between microtubules that linearly increases with the absolute number of motors. Taken together, this suggests that l_c should depend on the total friction between microtubules rather than on the averaged active forces. Thus, l_c should be proportional to L and a function of the ratio between the drag in the fluid γV_m and the total filament friction $F_m N_m$. Note that it remains unclear from this intuitive argument why the functional dependence is given by a square root.

S5 Fourier representation of the ambient polarity

The ambient polarity is given by the convolution of the local polarity with an exponentially decaying interaction kernel, Eq. 5b. As the Fourier transformation of a convolution of two functions is given by the product of the two Fourier transformations, it is instructive to consider the Fourier representation of the polarities. We distinguish two cases. First, we consider an infinite system where the fields are defined on the entire real axis, and, second, a periodic system with period R.

S5.1 Infinite case

For a polarity, $P(x)$, defined on the real axis, $x \in \mathbb{R}$, we define the Fourier transformation as

$$\hat{P}(k) = \frac{1}{2\pi} \int_{-\infty}^{\infty} \mathrm{d}y \; P(y) e^{iky}, \qquad k \in \mathbb{R},$$

with the corresponding back transformation $P(x) = \int_{-\infty}^{\infty} \mathrm{d}k \; \hat{P}(k) e^{-ikx}$. Similarly, the Fourier transformation of the ambient polarity is

$$\begin{aligned}
\hat{\Pi}(k) &= \frac{1}{2\pi} \int_{-\infty}^{\infty} \mathrm{d}y \; \Pi(y) e^{iky} = \frac{1}{2\pi} \int_{-\infty}^{\infty} \mathrm{d}y \; \frac{1}{2l_c} \int_{-\infty}^{\infty} \mathrm{d}z \; P(z) e^{-|y-z|/l_c} e^{iky} = \\
&= \frac{1}{2\pi} \int_{-\infty}^{\infty} \mathrm{d}z P(z) \frac{1}{2l_c} \int_{-\infty}^{\infty} \mathrm{d}y \; e^{-|y-z|/l_c} e^{iky} = \frac{1}{2\pi} \int_{-\infty}^{\infty} \mathrm{d}z P(z) e^{ikz} \frac{1}{2l_c} \int_{-\infty}^{\infty} \mathrm{d}w \; e^{-|w|/l_c} e^{ikw} = \\
&= \hat{P}(k) \frac{1}{1 + (kl_c)^2} \equiv \hat{P}(k) \hat{K}(k),
\end{aligned} \tag{S37}$$

where we exchanged the integrals and performed the Fourier transformation of the exponentially decaying interaction kernel, $\hat{K}(k) = 1/(1 + (kl_c)^2)$. This result implies that the spatial modes are suppressed according to a Lorentzian. So, faster fluctuations are damped more, and the ambient polarity does not exhibit spatial variations corresponding to large wave vectors $k \gg 1/l_c$ (small wavelength). Intuitively, the lack of fast fluctuations in the ambient polarity is due to the averaging of local polarities in a range of size l_c. As we will see in the following, we get a very similar result in the periodic case.

S5.2 Finite interval with periodic continuation

If the system is periodic with period R, the polarity, $P(x)$, $x \in [0, R]$, is described by a Fourier series, $P(x) = \sum_{n=-\infty}^{\infty} \hat{P}_n e^{-in\frac{2\pi}{R}x}$, with Fourier coefficients

$$\hat{P}_n = \frac{1}{R} \int_0^R \mathrm{d}y \; P(y) e^{in\frac{2\pi}{R}y}, \qquad n \in \mathbb{Z}. \tag{S38}$$

The Fourier coefficients for the ambient polarity, $\hat{\Pi}_n$, $n \in \mathbb{Z}$, are given by

$$\begin{aligned}
\hat{\Pi}_n &= \frac{1}{R}\int_0^R \mathrm{d}y\ \Pi(y) e^{in\frac{2\pi}{R}y} = \frac{1}{R}\int_0^R \mathrm{d}y\ \frac{1}{2l_c}\int_{-\infty}^{\infty} \mathrm{d}z\ P(z) e^{-|y-z|/l_c} e^{in\frac{2\pi}{R}y} = \\
&= \frac{1}{R}\int_{-\infty}^{\infty} \mathrm{d}z\ P(z)\frac{1}{2l_c}\int_0^R \mathrm{d}y\ e^{-|y-z|/l_c} e^{in\frac{2\pi}{R}y} = \frac{1}{R}\sum_{m=-\infty}^{\infty}\int_{mR}^{(m+1)R} \mathrm{d}z\ P(z)\frac{1}{2l_c}\int_0^R \mathrm{d}y\ e^{-|y-z|/l_c} e^{in\frac{2\pi}{R}y} = \\
&= \frac{1}{R}\sum_{m=-\infty}^{\infty}\int_0^R \mathrm{d}w\ P(w+mR) e^{in\frac{2\pi}{R}w}\frac{1}{2l_c}\int_{-mR-w}^{-(m-1)R-w} \mathrm{d}v\ e^{-|v|/l_c} e^{in\frac{2\pi}{R}v} e^{in2\pi m} = \\
&= \frac{1}{R}\int_0^R \mathrm{d}w\ P(w) e^{in\frac{2\pi}{R}w}\frac{1}{2l_c}\int_{-\infty}^{\infty} \mathrm{d}v\ e^{-|v|/l_c} e^{in\frac{2\pi}{R}v} = \\
&= \hat{P}_n \frac{1}{1+(2\pi l_c n/R)^2} \equiv \hat{P}_n \hat{K}(\frac{2\pi n}{R}).
\end{aligned} \tag{S39}$$

In these steps, we exchanged the integrals and used that the infinite integral can be expressed in terms of an infinite sum of integrals over a period R each. Furthermore, we used the substitutions $w = z - mR$ and $v = y - mR - w$ and the periodicity: $P(w + mR) = P(w)$ and $e^{in2\pi m} = 1$ for $m \in \mathbb{Z}$. We could have guessed this result from the result of the infinite case, Eq. S37, as in the periodic case only wave vectors k which are a multiple of $2\pi/R$ are possible: $k = n2\pi/R$ for some $n \in \mathbb{Z}$. So, again, fast fluctuations are strongly suppressed in the ambient polarity.

S5.3 Relevance

Importantly, these results are not restricted to a specific class of polarity profiles but generally capture the relationship between the local and ambient polarity in an infinite (large) system. Hence, the ambient polarity (the velocity) is expected to vary at most on length scales larger than the characteristic length l_c. Related to this, extreme values of the local polarity are averaged out and do not show up in the distribution of velocities. This observation is illustrated by two examples in the main text, namely the pedagogical case with linear polarity profile and the *in silico* study with random polarity profile.

S6 Linear polarity profile

As a first example to illustrate the relationship between the ranges of local and ambient polarity, we consider a linear polarity profile $P(x) = a * (x - S/2)$ on a finite interval $x \in [0, S]$ (where $|a| \leq 2/S$ to ensure that the polarity does not exceed ± 1). This situation is in contrast to the main analysis in the manuscript which focuses on an infinite system. Consequently, we have to specify some boundary conditions.

S6.1 Motivation of boundary conditions

In order to fix the boundary conditions, we start from the premise that even at the boundary, the system is dense and the number of interaction partners of a microtubule is limited by the number of neighbors and not by the overall number of microtubules. In other words, the number of interaction partners per microtubules is the same, irrespective of whether the microtubule is located in the bulk of the system or at the boundary. This implies that microtubules at the left (right) boundary have twice as many crosslinks towards their right (left) as compared to microtubules in the bulk of the system (and none to the left (right) due to the boundary). To approximately account for this effect, we mirror the polarity profile at its boundaries $x = 0$ and $x = S$, so we have $P(-x) = P(x)$ and $P(S - x) = P(S + x)$. By repeated application of this mirroring, the polarity profile is continued to the entire real axis. The resulting continued spatial polarity profile is $2S$ periodic. Thus, we approximate our finite system by a periodically continued spatial polarity field with the same (infinite) interaction kernel $\exp(-|x - y|/l_c)$ as for the infinite system.

S6.2 Fourier coefficients

The local polarity is represented by a Fourier series with Fourier coefficients given in Eq.S38 for $R = 2S$. More concretely, due to the symmetry $P(x) = P(-x)$ the Fourier coefficients are given by

$$\begin{aligned}
\hat{P}_n &= \frac{1}{2S}\int_{-S}^{S} \mathrm{d}y\ P(y) e^{in\frac{\pi}{S}y} = \frac{1}{2S}\int_0^S \mathrm{d}y\ P(y)(e^{in\frac{\pi}{S}y} + e^{-in\frac{\pi}{S}y}) = \\
&= \frac{1}{2S}\int_0^S \mathrm{d}y\ a(y - \frac{S}{2})(e^{in\frac{\pi}{S}y} + e^{-in\frac{\pi}{S}y}) = \begin{cases} -a\frac{2S}{n^2\pi^2} & \text{n odd} \\ 0 & \text{n even.} \end{cases}
\end{aligned}$$

Eq. S39 then implies that the Fourier coefficients of the ambient polarity are given by

$$\hat{\Pi}_n = \begin{cases} -a\frac{2S}{n^2\pi^2(1+(\pi l_c n/S)^2)} & \text{n odd} \\ 0 & \text{n even.} \end{cases}$$

S6.3 Ratio between the ambient and local polarity range

From the Fourier coefficients, we can straightforwardly determine the ratio between the ranges of local and ambient polarity. Due to the monotonicity of the local polarity and the from-the-center decreasing interaction kernel, the maximum (minimum) of the ambient polarity is at the same location as the maximum (minimum) of the local polarity. In order to compute the ratio between the two ranges of values, it is thus sufficient to determine the ambient polarity at $x = S$ where it attains its maximum (due to the symmetry, the minimal value at $x = 0$ corresponds to the inverse of the maximal value):

$$\begin{aligned}\Pi_{\max} = \Pi(x = S) = \sum_{n=-\infty}^{\infty} \hat{\Pi}_n e^{-in\pi} = a \sum_{n=-\infty}^{\infty} \frac{2S}{(2n+1)^2\pi^2(1+(\pi l_c(2n+1)/S)^2)} = \\ = \left(1 - \frac{2l_c}{S}\tanh(\frac{S}{2l_c})\right)\frac{aS}{2} = \left(1 - \frac{2l_c}{S}\tanh(\frac{S}{2l_c})\right)P_{\max},\end{aligned}$$

where we used that $P_{\max} = P(x = S) = aS/2$. A more instructive expression can be obtained by using a large wavelength approximation, describing the local and ambient polarities by their lowest modes $n = \pm 1$, $P(x) \approx 2\hat{P}_1 \cos(\frac{\pi}{S}x)$ and $\Pi(x) \approx 2\hat{\Pi}_1 \cos(\frac{\pi}{S}x)$. Thereby, the ratio of the ranges of the local and ambient polarity is approximately

$$\frac{\Pi_{\max}}{P_{\max}} \approx \frac{\hat{\Pi}_1}{\hat{P}_1} = \frac{1}{1+(\pi l_c/S)^2}.$$

As can be seen in Figure 4, this expression is a fairly good approximation, in particular for large enough l_c/S as expected. It predicts that the range of the ambient polarity is strongly "squeezed" for large characteristic length.

S7 *In silico* study: Random polarity field

In this appendix, we give details on how we construct the random polarity field in the *in silico* study described in section "*In silico* study: Random polarity field". Furthermore, we derive the formula for the ratio between the variances of the local and ambient polarity, Eq. 9.

S7.1 Construction

Our goal is to mimic a realistic polarity profile that arises from spontaneous self-organization of stabilized microtubules and crosslinking motors into nematically aligned filament gels in the experiments. To this end, we construct a network of randomly oriented microtubules with approximately constant density. Explicitly, the network is created in the following way: First, we divide the system of size S ($S \gg L$) into small containers of size Δx. Second, for each container the numbers of microtubules with midpoint in the container and pointing to the left or right, respectively, is drawn independently according to a binomial distribution with mean $\mu\Delta x/L$ for each type of microtubules (left/right). Here, μ can be interpreted as the average 1D number density of left- or right-oriented microtubules, respectively.

S7.2 Distribution of the local polarity

This procedure results in a spatial profile for the number of microtubule midpoints which is rough. However, due to the finite extension of microtubules the corresponding polarity and density profiles, $P(x)$ ($\rho(x)$), are smoothed. The local polarity at a certain position is determined by all the microtubules that cross this position and not only those whose midpoint is located there: Denote by $h^{\pm}_{x,\Delta x}$ the (randomly drawn) number of left- or right-oriented microtubules with midpoint in $[x, x + \Delta x)$ and by $H^{\pm}_x$ the (resulting) number of left- or right-oriented microtubules that cross position x. As all microtubules with midpoints in $[x - L/2, x + L/2]$ pass through x, these quantities are related as follows:[6]

$$H^{\pm}_x = \sum_{k=-\frac{L}{2\Delta x}}^{\frac{L}{2\Delta x}-1} h^{\pm}_{x+k\Delta x,\Delta x}.$$

[6]Note that we ignore sets of measure zero.

Here $h^{\pm}_{x+k\Delta x,\Delta x}$ are independent and identically distributed according to a Binomial distribution with mean $\mu\Delta x/L$. For small enough intervals Δx, we can approximate these Binomial distributions by Poisson distributions:

$$h^{\pm}_{x+k\Delta x,\Delta x} \overset{iid}{\sim} \text{Poisson}(\mu\Delta x/L).$$

As $H^{\pm}_x$ corresponds to the sum over $L/\Delta x$ of these random variables, it is distributed according to a Poisson distribution as well, and the mean is given by the sum of the means:

$$H^{\pm}_x \sim \text{Poisson}(\mu). \tag{S40}$$

Importantly, the finite extension of the microtubules introduces correlations in the number of microtubules crossing different positions x. That is, the quantities H^+_x (H^-_x) for different x are not independent: Their covariance is given by

$$\begin{aligned}\text{Cov}(H^+_x, H^+_y) &= \langle H^+_x H^+_y\rangle - \langle H^+_x\rangle\langle H^+_y\rangle = \langle H^+_x H^+_y\rangle - \mu^2 = \\ &= \sum_{k=-\frac{L}{2\Delta x}}^{\frac{L}{2\Delta x}-1}\sum_{j=-\frac{L}{2\Delta x}}^{\frac{L}{2\Delta x}-1}\left\langle h^+_{x+k\Delta x,\Delta x}h^+_{y+j\Delta x,\Delta x}\right\rangle - \mu^2 = \sum_{k=-\frac{L}{2\Delta x}}^{\frac{L}{2\Delta x}-1}\sum_{j=-\frac{L}{2\Delta x}}^{\frac{L}{2\Delta x}-1}\left(\left(\frac{\mu\Delta x}{L}\right)^2 + \frac{\mu\Delta x}{L}\delta_{x+k\Delta x,y+j\Delta x}\right) - \mu^2,\end{aligned} \tag{S41}$$

where in the last step we used that the random variables $h^+_{z,\Delta x}$ for different z are independent with mean $\mu\Delta x/L$: If $z_1 \neq z_2$ we have $\langle h^+_{z_1,\Delta x}h^+_{z_2,\Delta x}\rangle = \langle h^+_{z_1,\Delta x}\rangle\langle h^+_{z_2,\Delta x}\rangle = (\mu\Delta x/L)^2$. In contrast, the second moment of a Poisson distribution with mean λ is given by $\lambda^2+\lambda$, so $\langle\left(h^+_{z,\Delta x}\right)^2\rangle = (\mu\Delta x/L)^2 + \mu\Delta x/L$. Performing the sum over the constant $\left(\frac{\mu\Delta x}{L}\right)^2$ in Eq. S41, we find the following expression for the covariance:

$$\text{Cov}(H^+_x, H^+_y) = \frac{\mu\Delta x}{L}\sum_{k=-\frac{L}{2\Delta x}}^{\frac{L}{2\Delta x}-1}\sum_{j=-\frac{L}{2\Delta x}}^{\frac{L}{2\Delta x}-1}\delta_{j,k+\frac{x-y}{\Delta x}} = \begin{cases} 0 & \text{if } |x-y| \geq L \\ \mu(1-\frac{|x-y|}{L}) & \text{if } |x-y| < L. \end{cases} \tag{S42}$$

This equation implies that H^+_x and H^+_y are independent if $|x-y| \geq L$ (then their covariance is zero), and that for $|x-y| < L$ their correlation decays linearly with the distance. Taken together,

$$\langle H^+_x H^+_y\rangle = \mu^2 + \mu\left(1-\frac{|x-y|}{L}\right)\Theta\left(1-\frac{|x-y|}{L}\right). \tag{S43}$$

Due to symmetry, the same is true for H^-_x. Furthermore, H^+_x and H^-_y are independent for all x, y.
Equipped with these properties of the number of microtubules passing through the different positions $H^{\pm}_x$, we now consider the local polarity. In terms of $H^{\pm}_x$ it is defined as

$$P(x) = \frac{H^+_x - H^-_x}{H^+_x + H^-_x}.$$

Due to the symmetry between left- and right-oriented microtubules, the average is

$$\langle P(x)\rangle = \sum_{r,l=0}^{\infty} p(r)p(l)\frac{r-l}{r+l} = 0,$$

where we defined $p(r) := \text{Prob}(H^{\pm}_x = r) = (\mu^r/r!)e^{-\mu}$.
The calculation of the other moments is a bit more involved, and we will repeatedly use the following identity for $a \geq 1$ and $i \in \mathbb{N}$

$$\frac{\mu^a}{a^i} = \int_0^{\mu} \mathrm{d}\mu_1 \frac{1}{\mu_1}\int_0^{\mu_1}\mathrm{d}\mu_2\frac{1}{\mu_2}\ldots\int_0^{\mu_{i-1}}\mathrm{d}\mu_i\frac{1}{\mu_i}\mu_i^a\,, \tag{S44}$$

which is straightforwardly proven by induction and explicit integration of the right-hand side. Using this identity S44, the variance of the local polarity is given by

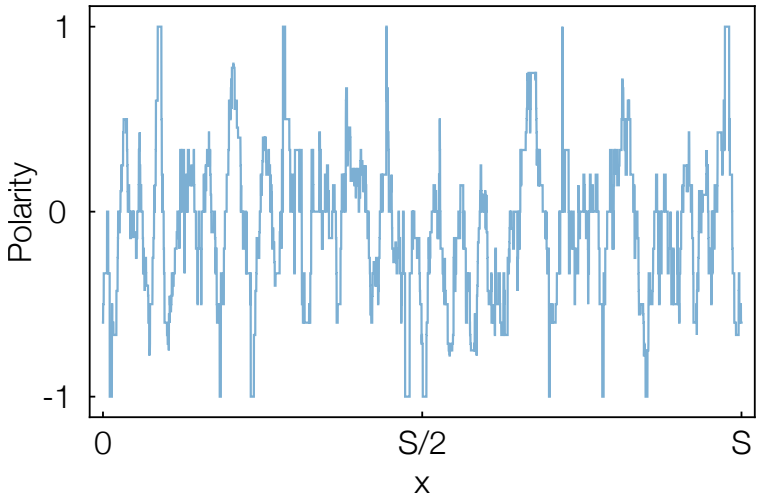

Figure S5: Exemplary polarity profile for a system of size $S = 400\mu m$ with microtubules of length $L = 6\mu m$. The polarity profile is not completely random with independent values in all bins. Instead the polarities at different positions are correlated over a typical distance L (Eq. S42).

$$\begin{aligned}
\mathrm{Var}[P(x)] = \langle P(x)^2\rangle - \langle P(x)\rangle^2 &= \sum_{r,l=0}^{\infty} p(r)p(l)\left(\frac{r-l}{r+l}\right)^2 = \sum_{r,l=0}^{\infty} e^{-2\mu}\frac{(r-l)^2}{r!l!}\frac{\mu^{r+l}}{(r+l)^2} = \\
&= e^{-2\mu}\int_0^{\mu} \mathrm{d}\mu_1 \frac{1}{\mu_1}\int_0^{\mu_1}\mathrm{d}\mu_2\frac{1}{\mu_2}\sum_{r,l=0}^{\infty}\frac{(r-l)^2}{r!l!}\mu_2^{r+l} = \\
&= e^{-2\mu}\int_0^{\mu} \mathrm{d}\mu_1 \frac{1}{\mu_1}\int_0^{\mu_1}\mathrm{d}\mu_2\frac{1}{\mu_2}e^{2\mu_2}\left(2\langle X^2\rangle_{X\sim\mathrm{Poisson}(\mu_2)} - 2\langle X\rangle^2_{X\sim\mathrm{Poisson}(\mu_2)}\right) = \\
&= e^{-2\mu}\int_0^{\mu} \mathrm{d}\mu_1 \frac{1}{\mu_1}\int_0^{\mu_1}\mathrm{d}\mu_2\frac{1}{\mu_2}e^{2\mu_2}\ 2\mu_2 = e^{-2\mu}(\mathrm{Ei}(2\mu) - \log(2\mu) - \Gamma),
\end{aligned}$$

with the exponential integral Ei(x) and the Euler-Mascheroni constant Γ. Furthermore $\langle f(X)\rangle_{X\sim\mathrm{Poisson}(\mu)}$ denotes the average of $f(X)$ where X is distributed according to a Poisson distribution with parameter μ. In this calculation we used that H_x^+ and H_x^- and, thus, the probabilities for r and l, $p(r)$ and $p(l)$, are independent.
In summary, we have

$$\begin{aligned}
\langle P\rangle &= 0 \\
\mathrm{Var}[P] &= e^{-2\mu}(\mathrm{Ei}(2\mu) - \log(2\mu) - \Gamma).
\end{aligned}$$

As expected, since the number of both types of microtubules (to the left and right, respectively) is on average the same everywhere, the mean of the polarity is zero. The variance of the local polarity $\mathrm{Var}[P]$ is monotonically decreasing for $\mu \geq 1$ and decays to 0 for large average densities μ, implying that the distribution of local polarities is less broad for larger values of μ. This result is intuitive as for higher μ more microtubules contribute to the local polarity and so the variance is smaller.

S7.3 Autocorrelation of the local polarity

Although the local polarity is already well characterized by its mean and variance (see Fig. 5A), for the distribution of the ambient polarity, information on the correlation between the local polarities at different positions is necessary. Thus, as a next step, we determine the autocorrelation of the local polarity

$$\langle P(x)P(y)\rangle = \langle\left(\frac{H_x^+ - H_x^-}{H_x^+ + H_x^-}\right)\left(\frac{H_y^+ - H_y^-}{H_y^+ + H_y^-}\right)\rangle = \sum_{r_x,l_x=0}^{\infty}\sum_{r_y,l_y=0}^{\infty} p(r_x,r_y)p(l_x,l_y)\left(\frac{r_x-l_x}{r_x+l_x}\right)\left(\frac{r_y-l_y}{r_y+l_y}\right),$$

where $p(r_x, r_y) = \text{Prob}(H_x^+ = r_x, H_y^+ = r_y)$ is the joint probability that $H_x^+ = r_x$ and $H_y^+ = r_y$. The random variables H_x^+ and H_y^+ are independent only if $|x-y| \geq L$, so the joint probability $p(r_x, r_y)$ can be factorized as $p(r_x)p(r_y)$ only in this case. Then, due to the symmetry between H_x^+ and H_x^- (and analogously for y), we have $\langle P(x)P(y)\rangle = 0$.
If, however, $|x-y| < L$, such a factorization is not possible as $H_x^\pm$ and $H_y^\pm$ are correlated. To circumvent this difficulty, we split the random variables in two parts, namely one that describes the overlap/correlation of both, $H_0^\pm$, and one that captures the independent contributions, $\tilde{H}_x^\pm$ and $\tilde{H}_y^\pm$:

$$H_x^\pm = H_0^\pm + \tilde{H}_x^\pm$$
$$H_y^\pm = H_0^\pm + \tilde{H}_y^\pm.$$

More concretely, we choose

$$H_0^\pm = \sum_{k=-\frac{L}{2\Delta x}}^{\frac{L}{2\Delta x}-1-\frac{y-x}{\Delta x}} h^\pm_{y+k\Delta x,\Delta x} \sim \text{Poisson}\left(\mu_0 \equiv \mu\left(1-\frac{|x-y|}{L}\right)\right)$$
$$\tilde{H}_x^\pm = \sum_{k=-\frac{L}{2\Delta x}}^{\frac{y-x}{\Delta x}-\frac{L}{2\Delta x}-1} h^\pm_{x+k\Delta x,\Delta x} \sim \text{Poisson}\left(\mu_1 \equiv \mu\frac{|x-y|}{L}\right)$$
$$\tilde{H}_y^\pm = \sum_{k=\frac{L}{2\Delta x}-\frac{y-x}{\Delta x}}^{\frac{L}{2\Delta x}-1} h^\pm_{y+k\Delta x,\Delta x} \sim \text{Poisson}\left(\mu_1 \equiv \mu\frac{|x-y|}{L}\right)$$

where we assumed $x < y$ without loss of generality. The advantage of this decomposition is that now all $H_0^\pm$, $\tilde{H}_x^\pm$ and $\tilde{H}_y^\pm$ are independent (due to the independence of $h^\pm_{z,\Delta x}$ for different z).
For $|x-y| < L$, the autocorrelation of the local polarity is thus given by

$$\langle P(x)P(y)\rangle = \langle\left(\frac{H_0^+ + \tilde{H}_x^+ - H_0^- - \tilde{H}_x^-}{H_0^+ + \tilde{H}_x^+ + H_0^- + \tilde{H}_x^-}\right)\left(\frac{H_0^+ + \tilde{H}_y^+ - H_0^- - \tilde{H}_y^-}{H_0^+ + \tilde{H}_y^+ + H_0^- + \tilde{H}_y^-}\right)\rangle =$$
$$= \sum_{l_0,l_x,l_y=0}^{\infty}\sum_{r_0,r_x,r_y=0}^{\infty} \frac{e^{-2\mu_0-4\mu_1}\mu_0^{l_0+r_0}\mu_1^{l_x+l_y+r_x+r_y}}{l_0!l_x!l_y!r_0!r_x!r_y!}\left(\frac{r_0+r_x-l_0-l_x}{r_0+r_x+l_0+l_x}\right)\left(\frac{r_0+r_y-l_0-l_y}{r_0+r_y+l_0+l_y}\right).$$

As we will see, we can make use of identity S44 again. In order to do so, we rewrite this expression in a slightly more complicated form

$$\langle P(x)P(y)\rangle =$$
$$= e^{-2\mu_0-4\mu_1}\sum_{l_0,l_x,l_y=0}^{\infty}\sum_{r_0,r_x,r_y=0}^{\infty} f^{-1}\epsilon^{l_0+r_0}\sigma_1^{r_0+r_x+l_0+l_x}\sigma_2^{r_0+r_y+l_0+l_y}\left(\frac{r_0+r_x-l_0-l_x}{r_0+r_x+l_0+l_x}\right)\left(\frac{r_0+r_y-l_0-l_y}{r_0+r_y+l_0+l_y}\right)\Bigg|_{\substack{\epsilon=\mu_0/\mu_1^2\\ \sigma_1=\sigma_2=\mu_1}},$$

where we defined $f = f(l_i, r_i) = l_0!l_x!l_y!r_0!r_x!r_y!$ as the product of the factorials. Applying now identity S44, we end up with

$$\langle P(x)P(y)\rangle =$$
$$= e^{-2\mu_0-4\mu_1}\int_0^{\sigma_1} \mathrm{d}s_1 \frac{1}{s_1}\int_0^{\sigma_2}\mathrm{d}s_2\frac{1}{s_2}\sum_{\{l_i,r_i\}} f^{-1}\epsilon^{l_0+r_0}s_1^{r_0+r_x+l_0+l_x}s_2^{r_0+r_y+l_0+l_y}\left(r_0+r_x-l_0-l_x\right)\left(r_0+r_y-l_0-l_y\right)\Bigg|_{\mathcal{C}},$$

where the sum is over all l_i, r_i, $i \in \{0, x, y\}$ from 0 to ∞ and $\mathcal{C} \equiv \{\epsilon{=}\mu_0/\mu_1^2, \sigma_1{=}\sigma_2{=}\mu_1\}$. To continue, we rewrite the integrand as follows

$$\sum_{\{l_i,r_i\}} f^{-1}\epsilon^{l_0+r_0}s_1^{r_0+r_x+l_0+l_x}s_2^{r_0+r_y+l_0+l_y}\left(r_0+r_x-l_0-l_x\right)\left(r_0+r_y-l_0-l_y\right) =$$
$$= \sum_{\{l_i,r_i\}}\frac{1}{l_0!l_x!l_y!r_0!r_x!r_y!}(s_1s_2\epsilon)^{l_0+r_0}s_1^{r_x+l_x}s_2^{r_y+l_y}\left(r_0+r_x-l_0-l_x\right)\left(r_0+r_y-l_0-l_y\right) =$$
$$= e^{2s_1+2s_2+2s_1s_2\epsilon}\langle\left(r_0-l_0+r_x-l_x\right)\left(r_0-l_0+r_y-l_y\right)\rangle_{s_1,s_2,s_1s_2\epsilon},$$

where the average $\langle\rangle_{s_1,s_2,s_1s_2\epsilon}$ has to be interpreted with respect to the six independent variables $l_x, r_x \sim \text{Poisson}(s_1)$, $l_y, r_y \sim \text{Poisson}(s_2)$ and $l_0, r_0 \sim \text{Poisson}(s_1 s_2 \epsilon)$. Due to the independence and as $\langle r_x - l_x\rangle = \langle r_x - l_x\rangle = 0$ the average is given by

$$\langle (r_0 - l_0 + r_x - l_x)\,(r_0 - l_0 + r_y - l_y)\rangle_{s_1,s_2,s_1s_2\epsilon} = \langle (r_0 - l_0)^2\rangle_{s_1s_2\epsilon} = \text{Var}_{s_1s_2\epsilon}(r_0) + \text{Var}_{s_1s_2\epsilon}(l_0) = 2s_1s_2\epsilon.$$

Taken together, we determine the autocorrelation of the local polarity to be

$$\langle P(x)P(y)\rangle = e^{-2\mu_0 - 4\mu_1} \int_0^{\sigma_1} \mathrm{d}s_1 \frac{1}{s_1} \int_0^{\sigma_2} \mathrm{d}s_2 \frac{1}{s_2} e^{2s_1 + 2s_2 + 2s_1 s_2 \epsilon} 2 s_1 s_2 \epsilon \Big|_{\mathcal{C}} = \tag{S45}$$

$$= e^{-\frac{2\mu^2}{\mu_0}} \left(\text{Ei}\left(\frac{2\mu_1^2}{\mu_0}\right) - 2\text{Ei}\left(\frac{2\mu_1^2}{\mu_0}\left(1 + \frac{\mu_0}{\mu_1}\right)\right) + \text{Ei}\left(\frac{2\mu_1^2}{\mu_0}\left(1 + \frac{\mu_0}{\mu_1}\right)^2\right)\right), \tag{S46}$$

where we used that $\mu_0 + \mu_1 = \mu$. $\text{Ei}(x)$ denotes the exponential integral as before. When plotting the autocorrelation $\langle P(x)P(y)\rangle$ against the normalized distance $|x-y|/L$ (using that $\mu_0 = \mu(1 - |x-y|/L)$ and $\mu_1 = \mu|x-y|/L$), one realizes that the autocorrelation decays approximately linearly with the distance: $\langle P(x)P(y)\rangle \sim 1 - |x-y|/L$. The origin of the approximately linear decay is that the number of microtubules directly linking two points decreases linearly with the distance as well. The proportionality constant for the linear decay, which corresponds to the limit for $|x-y| \to 0$ ($\mu_0 \to \mu, \mu_1 \to 0$), is calculated to be

$$e^{-2\mu}(\text{Ei}(2\mu) - \log(2\mu) - \Gamma) = \text{Var}[P],$$

where we used that $\text{Ei}(x) \approx \Gamma + \log(x)$ for small x. This is consistent with the result for the variance of the local polarity: $\lim_{|x-y|\to 0}\langle P(x)P(y)\rangle = \text{Var}[P]$.
In summary, we thus find for the autocorrelation of the local polarity

$$\langle P(x)P(y)\rangle \approx \text{Var}[P]\left(1 - \frac{|x-y|}{L}\right)\Theta\left(L - |x-y|\right). \tag{S47}$$

This equality implies that the local polarities at positions less than one microtubule length apart are not independent. Instead, the finite length of microtubules introduces correlations as one microtubules contributes to the polarity at different locations. The strength of the correlations decays approximately linearly with the distance, analogously to the number of microtubules directly connecting the two locations. In the following, we will use this result to determine the distribution of the ambient polarity.

S7.4 Distribution of the ambient polarity

Analogously to the local polarity, we characterize the distribution of the ambient polarity by its average and variance, implicitly assuming that the ambient polarity is reasonably well described by a normal distribution. In the calculations, however we do not explicitly use that the distribution is approximated by a normal distribution and our results are valid irrespective of this assumption.
From the definition of the ambient polarity $\Pi(x) = \int_{-\infty}^{\infty} \mathrm{d}y P(y) e^{-|x-y|/l_c}/(2l_c)$, its average and variance are given by

$$\langle \Pi\rangle = \frac{1}{2l_c}\int_{-\infty}^{\infty} \mathrm{d}y\; e^{-\frac{|y|}{l_c}}\,\langle P(y)\rangle = 0 \tag{S48}$$

$$\text{Var}[\Pi] = \langle \Pi^2\rangle = \frac{1}{4l_c^2}\int_{-\infty}^{\infty}\mathrm{d}y \int_{-\infty}^{\infty}\mathrm{d}z\; e^{-\frac{|y|}{l_c}} e^{-\frac{|z|}{l_c}}\,\langle P(y)P(z)\rangle = \tag{S49}$$

$$= \text{Var}[P]\;\frac{1}{4l_c^2}\int_{-\infty}^{\infty}\mathrm{d}y \int_{y-L}^{y+L}\mathrm{d}z\; e^{-\frac{|y|}{l_c}} e^{-\frac{|z|}{l_c}}\left(1 - \frac{|y-z|}{L}\right) = \tag{S50}$$

$$= \text{Var}[P]\;\left(1 - \frac{3l_c}{2L}\left(1 - e^{-L/l_c}\right) + \frac{1}{2}e^{-L/l_c}\right), \tag{S51}$$

where - due to the translational symmetry - we considered $x = 0$ without loss of generality. From Eq. 5a in the main text, $v^{(\pm)}/V_m = \pm(1-\alpha)(1 \mp \Pi)$, we immediately conclude that the variance of the normalized velocity $v^{(\pm)}/V_m$, $\text{Var}[v/V_m]$, is given by

$$\text{Var}[v/V_m] = \text{Var}[P]\;(1-\alpha)^2\left(1 - \frac{3l_c}{2L}\left(1 - e^{-L/l_c}\right) + \frac{1}{2}e^{-L/l_c}\right). \tag{S52}$$

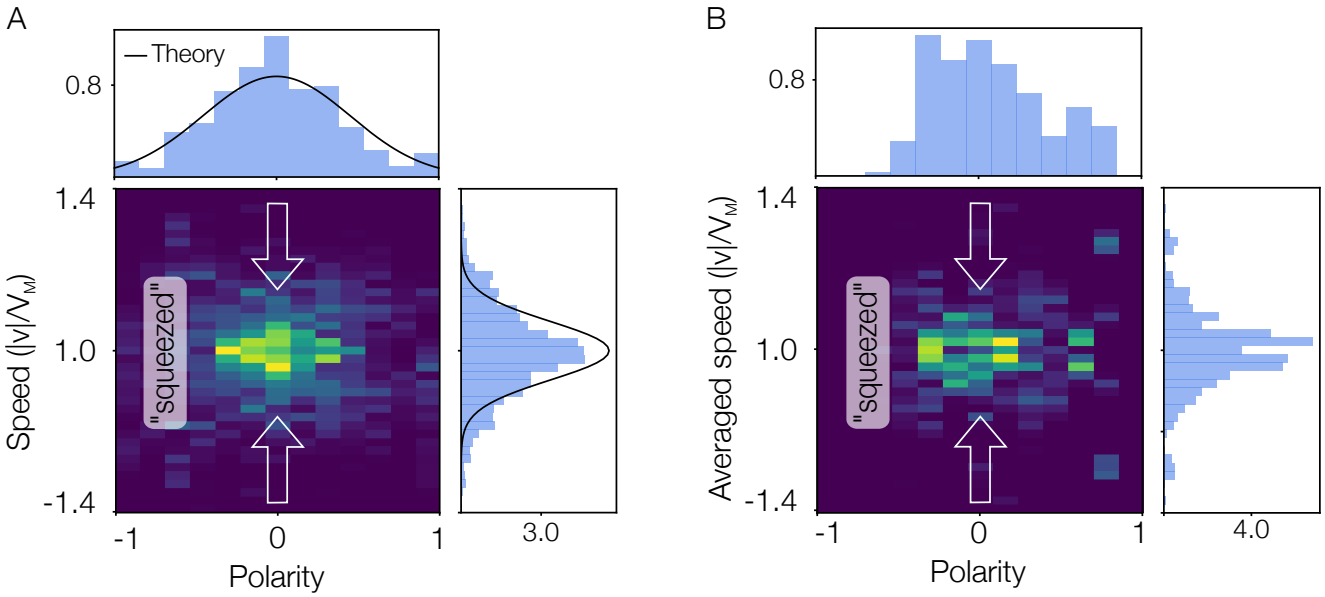

Figure S6: Density plot and histograms for the local polarity and speed analogous to Fig. 5 but measured in the stochastic agent-based simulation. Measurements are taken for 6000 independent filament gels. The parameters are identical to the ones used in the main text. (**A**) The local speed $|v^{(\pm)}|$ is calculated as the average speed of all equally-oriented microtubules passing through the respective position. Compared to the prediction from the nonlocal continuum theory (black lines), the variance of the velocity is slightly larger. (**B**) The local averaged speed $|v^{(\pm)}|$ is calculated as the average speed of all equally-oriented microtubules that are part of a region of $4\mu m$ in the center of the filament gel. Compared to the measurement in (**A**), the variance of both the polarity and the velocity is smaller.

Taking the limit $l_c \to 0$, we find $\mathrm{Var}[\Pi] = \mathrm{Var}[P] = \mathrm{Var}[v/V_m]/(1-\alpha)$, and, conversely, for $l_c \to \infty$, we have $\mathrm{Var}[\Pi], \mathrm{Var}[v/V_m] \to 0$. These limits illustrate our intuition that for small characteristic length only the local polarity matters, whereas for large characteristic length all microtubules feel the same ambient polarity.

S8 Stochastic, agent-based simulation of the *in silico* study

For the *in silico* study in the main text, a random polarity profile was generated as described in Appendix "*In silico* study: Random polarity field". The velocities are then determined from Eqs. 5a, 5b according to the continuum description. In this continuum approximation, all microtubules at one position exhibit exactly the same speed. This assumption will not be satisfied in experimental filament gels where two microtubules at the same location by chance can be connected to a different set of microtubules and thus experience a different environment. As a result, not only microtubules at different locations show a different speed but also the speed of microtubules at the same location can vary, leading to a broader distribution of the microtubule velocities. The goal of this Appendix is to gauge the strength of this effect.
To this end, the *in silico* study is performed again in terms of a stochastic, agent-based simulation for the same parameters as in the main text (Fig. 5): Compared to the *in silico* study in the main text, not only the microtubules are randomly distributed but also the interactions between microtubules are randomly chosen. That is, each microtubule randomly interacts with on average N of its neighbors, and the individual velocities are determined from the force-balance equations 3. Figure S8A shows the measured probability distribution for all combinations of local polarity and velocity, analogously to Fig. 5. As in the main text, the histograms for both quantities were obtained as projections of the density plot to the respective axis. Since in the agent-based simulations not all microtubules at one position x exhibit the same velocity, here, "local velocity" refers to the average velocity of all equally-oriented microtubules passing through position x. As expected, the distribution of the average velocity in the stochastic *in silico* study is broader than the velocity distribution in the main text which agreed very well with the prediction from our theory (black lines). The ratio of both standard deviations is approximately $\sigma[v/V_m]/\sigma[P] = 0.28$, indicating that the stochastic nature of the interactions indeed influences the filament velocities. If the average number of interaction partners is increased the results from the stochastic simulation approach our continuum theory (c.f. Fig S8). This is because fluctuations in the number of interaction partners are less pronounced for large N.
In experiments with filament gels, average velocities at single points x in space usually can not be unravelled. Instead, one measures the average polarity and velocity of regions of the order of several μm. This averaging is expected to lead to a narrower distribution of polarities and velocities as compared to measurements of the polarities and velocities of single points

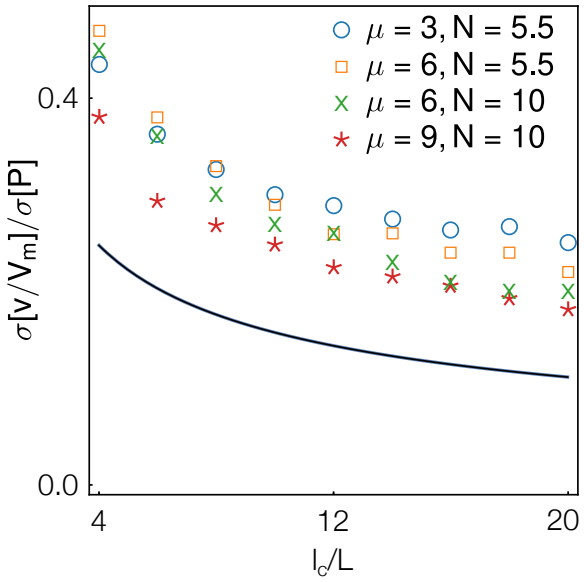

Figure S7: Ratio between the standard deviations of the normalized velocity, $\sigma[v/V_m]$, and of the local polarity, $\sigma[P]$, plotted against the normalized characteristic length, l_c/L, for the stochastic agent-based simulation (symbols), in comparison to the non-local mean field prediction (black line). l_c was varied by varying γ. The stochastic selection of interaction partners counteracts the "squeezing" effect due to averaging of the local polarity. This effect is more pronounced for decreasing μ and N since stochastic effects are more relevant for a small number of interaction partners. The width of the velocity distribution still decreases as l_c/L increases.

in space. To estimate the influence of this averaging procedure, we perform a second measurement in the stochastic *in silico* study. The goal of this second version is to mimic a typical measurement in experiments, so we do not record the average velocities of single points in space. Instead, we measure the average velocity and polarity of all equally oriented microtubules that are part of a region of $4\mu m$ in the center of the filament gel of length $400\mu m$. Performing this measurement for 6000 independent filament gels yields a distribution of polarities and velocities as shown in the density plots and histograms in Fig. S8B. As can be seen from a comparison of Figs. S8A and B, the distributions for the polarity and velocity after averaging over a range of several μm is noticeably smaller. Indeed, the result of the average measurements in the stochastic, agent-based *in silico* study is similar to the one shown in the main text. This finding implies that the expected broadening and narrowing of the velocity distribution due to stochasticity and averaging, respectively, more or less balance. Of course, this depends on choices such as the size of the region the velocity and polarity are averaged over. In the *in silico* study we chose it to be $4\mu m$, similar to the width of the photo-bleached region in *in vitro* filament gels [18]. Generally, the width of the velocity distribution is expected to depend on experimental details but we anticipate that independent of these details the width of the velocity distribution decreases with increasing characteristic length (c.f. Fig S8).

S9 Extension of the *in silico* study to a broader class of systems

The analysis in section "The agent-based model can describe the weak velocity-polarity sensitivity" in the main text, and the corresponding construction of the polarity field in the *in silico* study, Appendix "*In silico* study: Random polarity field", are based on the assumption that the polarity field does not have any spatial structure. That is, the system is translationally invariant and - on average - all positions are equivalent. However, generally, this premise will not be fulfilled. In this appendix, we thus want to extend our previous analysis to a broader class of systems.

S9.1 Class of systems

As we have seen before in Appendix "*In silico* study: Random polarity field", the variance of the ambient polarity, Var[Π], depends on the autocorrelation of the local polarity $\langle P(x)P(y)\rangle$. Thus, in order to make any statements about the distribution of the ambient polarity, we need to make some assumptions on the correlation of the local polarities at different locations. The most obvious property of the system that leads to correlations of the local polarities at different locations is the finite extension of microtubules. As discussed before, due to the finite microtubule length $L > 0$, an excess of microtubules at one position leads to an excess of microtubules at distances maximally L apart. In the following, we will assume that this

contribution to the correlation dominates, and that there are only weak correlation effects, for instance due to filament dynamics or feedback. We believe that in this case it is reasonable to assume that the covariance of the local polarity at different positions (the autocorrelation) decays linearly with distance up to $|x-y| = L$:

$$\mathrm{Cov}[P](x,y) \equiv \langle P(x)P(y)\rangle - \langle P(x)\rangle\langle P(y)\rangle \approx \mathrm{Var}[P]\left(1-\frac{|x-y|}{L}\right)\Theta\left(L-|x-y|\right). \tag{S53}$$

Here we furthermore assumed that the magnitude of the fluctuations in the polarity is similar everywhere: $\mathrm{Var}[P]$ is approximately spatially invariant.
We will restrict our discussion to this class of system as quantitative statements for the general case are difficult to obtain.

S9.2 Prediction

Let us consider systems where Eq. S53 holds. Suppose we measure the spatial profile of the average of the local polarities and of the velocities, $\langle P(x)\rangle$ and $\langle v^{(\pm)}(x)\rangle$, where the average denotes an ensemble average at fixed position x. Moreover, we determine the average variance of the local polarity $\mathrm{Var}[P] = \langle \mathrm{Var}[P(x)]\rangle_x$, where $\mathrm{Var}[P(x)] = \langle P(x)^2\rangle - \langle P(x)\rangle^2$ is the variance of the local polarity at fixed position x and $\langle\rangle_x$ denotes an average over all locations x. Then, our theory predicts that the covariance of the velocity at different positions is

$$\begin{aligned}
\mathrm{Cov}[v^{(+)}](x,y) &\equiv \langle v^{(+)}(x)v^{(+)}(y)\rangle - \langle v^{(+)}(x)\rangle\langle v^{(+)}(y)\rangle = \\
&= V_m^2(1-\alpha)^2\left(\langle(1-\Pi(x))(1-\Pi(y))\rangle - \langle 1-\Pi(x)\rangle\langle 1-\Pi(y)\rangle\right) = \\
&= V_m^2(1-\alpha)^2\left(\langle\Pi(x)\Pi(y)\rangle - \langle\Pi(x)\rangle\langle\Pi(y)\rangle\right) = \\
&= V_m^2(1-\alpha)^2\frac{1}{4l_c^2}\int_{-\infty}^{\infty}\mathrm{d}z_1\int_{-\infty}^{\infty}\mathrm{d}z_2 e^{-\frac{|x-z_1|}{l_c}}e^{-\frac{|y-z_2|}{l_c}}\left(\langle P(z_1)P(z_2)\rangle - \langle P(z_1)\rangle\langle P(z_2)\rangle\right).
\end{aligned}$$

Using assumption S53, this expression becomes

$$\begin{aligned}
&\mathrm{Cov}[v^{(+)}](x,y) = \\
&= V_m^2(1-\alpha)^2\mathrm{Var}[P]\frac{1}{4l_c^2}\int_{-\infty}^{\infty}\mathrm{d}z_1\int_{-\infty}^{\infty}\mathrm{d}z_2 e^{-\frac{|x-z_1|}{l_c}}e^{-\frac{|y-z_2|}{l_c}}\left(1-\frac{|z_1-z_2|}{L}\right)\Theta\left(L-|z_1-z_2|\right),
\end{aligned}$$

which holds for the velocities $v^{(-)}$ as well. For general distance $x-y$, the analytic expression is not very insightful and the expression is best understood graphically.
Fig. S8 shows a comparison between the normalized covariance of the local polarities (the autocorrelation coefficient), $\mathrm{Cov}[P](x,y)/\mathrm{Var}_P$, and of the velocity, $\mathrm{Cov}[v^{(\pm)}](x,y)/\mathrm{Var}[v^{(\pm)}]$, for different l_c. Whereas the correlation of the local polarity quickly decays to zero (after a distance $|x-y| = L$), the correlation of the velocities is much more long-ranged and its correlation length increases with l_c.
The covariance of the velocity for $x = y$, $\mathrm{Cov}[v^{(+)}](x,x)$, which corresponds to the variance of the velocity $\mathrm{Var}[v^{(\pm)}]$, is given as

$$\mathrm{Var}[v^{(+)}] = V_m^2(1-\alpha)^2\mathrm{Var}[P]\left(1-\frac{3l_c}{2L}\left(1-e^{-\frac{L}{l_c}}\right)+\frac{1}{2}e^{-\frac{L}{l_c}}\right),$$

in terms of the variance of the local polarity, $\mathrm{Var}[P]$. Similarly, the variance of the ambient polarity, $\mathrm{Var}[\Pi]$, is given by

$$\mathrm{Var}[\Pi] = \mathrm{Var}[P]\left(1-\frac{3l_c}{2L}\left(1-e^{-\frac{L}{l_c}}\right)+\frac{1}{2}e^{-\frac{L}{l_c}}\right).$$

So, for the broader class of systems considered here we recover exactly the same result as for the *in silico* study, Eq. S51.

S10 Comparison of our results for small characteristic length to the dilute limit

One of the central results of our work is that there is an intrinsic length scale of the system that determines the velocity-polarity relation. This characteristic length l_c captures how far information on the local forces propagates through the

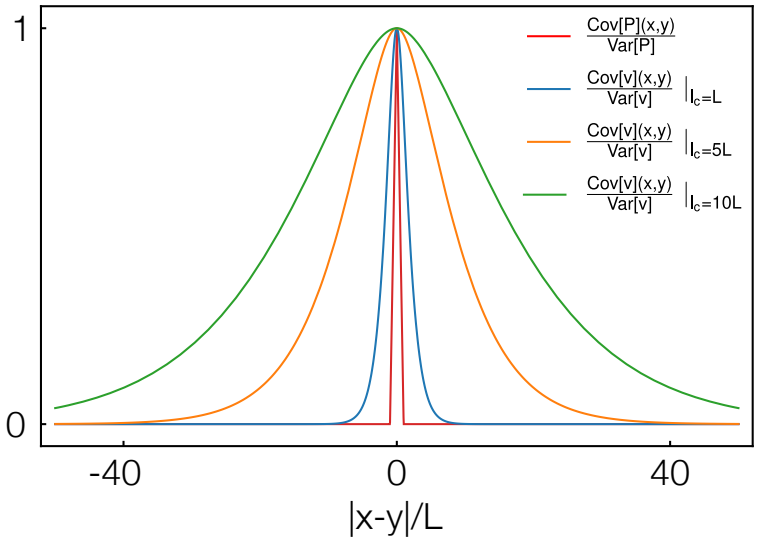

Figure S8: Comparison of the autocorrelation coefficient of the local polarity, $\mathrm{Cov}[P](x,y)/\mathrm{Var}[P]$, and of the velocity, $\mathrm{Cov}[v^{(\pm)}](x,y)/\mathrm{Var}[v^{(\pm)}]$, for different values of the characteristic length l_c. The velocity correlations decay much slower as compared to the correlations in the local polarity. The correlation length of the velocity scales with l_c, that is, for larger l_c, the correlations length is larger as well.

network. Naively, one can argue that for dilute systems l_c is small and, correspondingly, that forces only act locally. This conclusion fits well with the intuitive conception of a dilute limit where filaments are arranged in disconnected patches. Nonetheless, one has to be careful to directly compare our result to the dilute limit. With regard to this limit, there are two main assumptions in our continuum theory.

1. *Single patch:* All microtubules are directly or indirectly (via other microtubules) connected to each other and there are no disconnected patches of microtubules. This assumption corresponds to hypothesizing that the filament network works above the percolation threshold and that the average number of interaction partners N is not too small.

2. *Sufficient interaction partners:* The number of neighbors a microtubule interacts with is limited by the average number of interaction partners N and not by the number of neighbors. This assumption is based on the idea that there is always a sufficient number of neighbors (possible interaction partners) present for each microtubule. Instead of linearly depending on the microtubule densities, the force thus exhibits a dependency on the fraction $\varphi^{(\pm)}$ (Eq. 3).

Both assumptions do not necessarily apply to the dilute limit. We believe that the second assumption regarding a sufficient number of interaction partners can be readily relaxed also within a continuum description. For this purpose, one could, for instance, try to incorporate a phenomenological term $N\rho^{(\pm)}/(N+\rho^{+}+\rho^{-})$ for the number of interactions with $(\pm)$ microtubules. Such a term would converge to $N\varphi^{(\pm)}$ for large total density $\rho \equiv \rho^{+}+\rho^{-} \gg N$, as used in our description. Conversely, for small ρ it captures a linear dependency of the number of $(\pm)$ interactions on the respective density. Taken together, investigating how such an effective term changes the behavior should be instructive for a more quantitative understanding of the dilute limit.
The first assumption is conceptually more difficult to overcome within a continuum description. But indeed, for parameters estimated as in section "The agent-based model can describe the weak velocity-polarity sensitivity", regions with zero density (and thus disconnected patches) occur regularly in our stochastic, agent-based simulation. These empty spaces arise due to the stochastic loss of connections between microtubules and a following drifting apart of different patches. Vice versa, such empty spaces stochastically vanish again if two patches meet. The interplay of these opposing, stochastic processes leads to patch boundaries that are not static but change randomly. We suppose that one could effectively incorporate this behavior into our continuum theory. To this end, one might first consider systems of finite sizes and then try to average their behavior with regard to exponentially distributed system sizes. Intuitively, we would expect that this procedure leads to an enhanced effective attenuation and thus to a lower effective value of the characteristic length l_c but does not change our results qualitatively: Due to the stochastic loss of connections between patches (particularly for systems close to the percolation threshold), there is not only loss of information due to drag but also abruptly at the boundaries of the patches. If these boundaries are fluctuating, the abrupt loss at the boundaries is on average smoothed and should be qualitatively comparable to a continuous loss of information by drag.
Overall, we think that - despite these assumptions of our theory - our results help bridging the gap between previous findings for dilute and heavily crosslinked filament networks.

5 Summary and discussion

In a nutshell, this first part of my thesis has been a conceptual journey through the cytoskeleton in terms of stochastic simulations, numerical solutions of coupled equations and various analytical methods – definitely strongly influenced by my view as a theorist. It started from considering directed motion of motor proteins along cytoskeletal filaments (chapter 2), went on to some ideas about length regulation of filaments through motor transport (chapter 3) and finally ended up at the filament dynamics in networks crosslinked by motor proteins (chapter 4). All these biologically inspired settings rely on microscopic interactions between the elementary building blocks of the cytoskeleton, the motor proteins and filaments – be it through active transport, regulatory activity or crosslinking. However, we found that it is through the collective action of many of these components that qualitatively different and in all cases somewhat counterintuitive behavior arises.
While transport through directed motion is very efficient for single motor proteins, our results suggest that excluded volume effects between motors can lead to the formation of "traffic jams" and can substantially reduce transport efficiency, in particular in confined geometries (chapter 2).
Likewise, any kind of length regulation of filaments relies on feedback mechanisms and interactions between different agents. The self-organized length oscillations that occur in our model if the equilibration due to diffusion is slow compared to the intrinsic timescale of the length dynamics are also inherently collective (chapter 3): The temporal patterns are based on crowding of particles, which leads to a feedback mechanism with time delay.
Finally, only a collective effect can explain how filament motion in filament networks can occur even in regions with no local motion-generating forces (chapter 4). Our theoretical investigations suggest a mechanism of force propagation where locally generated forces are transmitted through the network by the collective action of crosslinking proteins.

From my point of view, there are two promising lines of research that could develop from these projects. Since in all cases the approach employed was in terms of conceptual modeling, it would undoubtedly be very interesting to test our model predictions with the help of minimal experimental systems. The first two projects would certainly require comparably small-scale setups on the order of individual filaments up to filament bundles. Thus, it might prove valuable to engage microfluidics technology [17–19] to put the findings of these projects to the test. For the third project, on the other hand, reconstituted *in vitro* systems of purified components [20–23] may be one way to go. Indeed, we suggest a specific *in vitro* experiment to check our predictions. The type of data required for such a test of our theory is, to our knowledge, already available. However, since our predictions rely on an analysis of velocity and polarity distributions, the challenge might be to record enough statistics to be able to do this diligently.

From a more theoretical point of view, I believe that one could gain new insights by combining several of the particular interactions between motors and filaments studied here. For instance,

it has been observed in the mitotic spindle that motor-microtubule interactions lead to sliding of microtubules towards the poles [101, 202–205]. Simultaneously, microtubules have dynamic lengths and the average microtubule length is not independent of the position within the spindle [91]. Thus, it might be interesting to study how a (spatially and/or temporally) varying microtubule length affects the force propagation through filament networks.
In the context of spatially defined structures such as the mitotic spindle, it would certainly also be enlightening to take the spatial boundaries into account more carefully. In particular, I could imagine that there exists an intricate relationship between the dynamics of the boundary itself and its effect on the dynamics of the whole structure. To address this hypothesis, it may be instructive to study what influence the boundaries of a network have on the proposed force propagation mechanism. Such an insight could then be employed to examine the mutual interaction between the network structure and the long-time dynamics.

Part II

Stochastic effects in heterogeneous self-assembly

6 Introduction: Self-assembly of viruses and of artificial nanostructures

One of the most fascinating properties of living systems is their ability to generate order from disorder. While the first part of this thesis is concerned with principles of self-organization and pattern formation in the context of molecular motors and cytoskeletal filaments, this second part aims to elucidate principles for the self-assembly of macromolecular structures. The notion of "self-assembly" is, generally speaking, not well-defined and various interpretations of this term exist. In the projects discussed in chapters 7 and 8, we focus on non-equilibrium processes which kinetically assemble macroscopic structures from small subunits (see Fig. 6.1 A for an illustration). Importantly, these processes only occur under very limited external guidance and not according to a preset protocol. In particular, there is no external influence on the microscopic level.

This autonomy raises several questions. How can living organisms generate highly heterogeneous and complex structures such as ribosomes [29, 30] or flagellar motors [31, 32] based on (short-range) interactions between the constituents? And why does intracellular self-assembly proceed with such high fidelity and accuracy? Can we use insights gained from living organisms to design artificial self-assembly systems that perform specific tasks or functions? To address these questions it has proven useful to combine experimental methods (such as size-exclusion chromatography; see e.g. [102, 206–208]; and DNA-origami or DNA-brick techniques; for reviews see for instance [112–114]) with theoretical modeling approaches (ranging from rate equation models; e.g. [102, 109, 124]; to particle-based simulations; e.g. [107, 116, 209–216]).

Broadly speaking, there are two main subfields which are concerned either with the assembly of virus capsids (section 6.1; for reviews see e.g. [110, 111, 217–219]) or with so-called "structures with addressable complexity" [108] and generally heterogeneous structures made up from many distinct components (section 6.2; for reviews see e.g. [27, 28, 115, 127]). While virus capsids typically contain several copies of one protein and are highly symmetric, artificially made structures can, in principle, be arbitrarily shaped and composed.
Nonetheless, common principles have developed from the study of both types of structures. In particular, in order for self-assembly to be efficient and to produce high yield, nucleation of new structures should be slow compared to growth of already existing structures (section 6.3; [102–109]). Thereby, competition for resources is minimized and so-called kinetic or depletion traps (e.g. [26, 102, 109, 116, 121, 123, 124, 127, 215, 220]) are circumvented.

To avoid such kinetic traps also another principle has emerged especially in the field of virus capsid assembly, namely that typically weak and reversible interactions between constituents are favorable [25, 116, 213, 221, 222]. In contrast, in the projects discussed in this thesis, we will focus on self-assembly processes that involve irreversible assembly steps (on the relevant timescales). Thus, our emphasis is on kinetic rather than equilibrium properties.

The goal of this chapter is to give a short overview of some aspects of the self-assembly of virus capsids (section 6.1) and of the role of self-assembly in nanotechnological applications like DNA origami (section 6.2). Finally, we briefly explain the "slow-nucleation principle" for efficient self-assembly (section 6.3), which will also be directly relevant for our findings discussed in chapter 7.

6.1 Virus capsid assembly

The assembly of virus capsids has been the subject of many investigations (for reviews on the topic see for instance [110, 111, 217–219]). From these investigations, important principles for efficient self-assembly have been established and different approaches to describe and understand the underlying processes theoretically have been proposed. Since they will also be relevant for our projects, here we briefly summarize some of the most important findings from experiments and some of the theoretical frameworks to understand virus capsid assembly.

Biological background

Viruses are essentially made from a genome that is surrounded by a shell or so-called virus capsid. The structure, size and composition of this capsid can vary greatly ranging from small viruses such as the Human Papilloma Virus made from roughly 70 copies of a single protein [223] up to the Megavirus which consists of more than 1000 proteins [224]. Most virus capsids are, however, highly symmetric and built from many copies of a few proteins. Indeed, it was already realized in the middle of the 20th century that it would not be possible to form a virus capsid made from one polypeptide only [225]. The reason is that the virus genome needs to contain all the information about the capsid while being small enough to fit into it in the end. In this context, it was argued some years later that shell designs with the highest ratio of shell volume to expended genome size should be beneficial economically [226].
Apart from these principles also other assembly characteristics have emerged in experiments over the years. The following paragraph summarizes some of these characteristics based on Refs. [102, 121, 122, 124, 206, 208, 213, 222, 227]: First, assembly yield only sets in after the so-called lag time and has a characteristic sigmoidal shape. The underlying process can be described as a nucleation and growth process for which nucleation has to be slow compared to growth in order for assembly to be efficient (see also section 6.3). Under these efficient/optimal assembly conditions intermediate assembly products are only present transiently. This was demonstrated for instance by employing size-exclusion chromatography experiments where only the free subunits and the final capsids occur in detectable concentrations. Finally, it was found that binding interactions between the subunits are typically weak and, correspondingly, growth is reversible.

All these findings have not only been observed experimentally but were also confirmed in different theoretical studies (see below). We describe some of the theoretical techniques that were used to model virus capsid assembly next. There are at least three different approaches: in terms of thermodynamics, by kinetic rate equations and with the help of particle-based simulations [209–214]. Here, we will focus on the first two and mention important insights gained from them.

Theoretical approaches

A first important insight was gained by a description of capsid assembly as an equilibrium process. Through minimization of the free energy under the constraint that mass is conserved, the so-called law of mass action was derived [228, 229]. It predicts that the concentration of capsids scales like $\sim \phi^L$ where ϕ is the concentration of free subunits and L the size of the capsid. Furthermore, according to the law of mass action, intermediates are only present in very low concentrations for "typical" assembly conditions [121], in agreement with the experimental findings described above. Moreover, a quantitative comparison with experiments suggests weak binding interactions between the constituents [227].
Apart from thermodynamical considerations, also assembly kinetics has been a focus of study. One approach to describe the assembly kinetics is via rate equations that capture the dynamics of the polymer sizes [102, 121, 124]. Conceptually, this approach is very similar to the one Becker and Döring pursued to quantify crystallization phenomena [230] only that in the case of virus assembly the final structures have a fixed, finite size. In these rate equations, capsids grow one subunit at a time with reversible binding and unbinding. Intriguingly, the solution of these equations exhibit many of the features observed experimentally: the lag time which is determined by the mean capsid assembly time (see also [104, 122]), the sigmoidal shape of the temporal evolution of the assembly yield and low concentrations of intermediates under good assembly conditions. And also another important conclusion about virus capsid assembly could be drawn from this approach: Nucleation of structures has to be slow compared to growth since otherwise the free subunits get depleted before assembly sets in and the system ends up in a kinetic trap. We will come back to this point later (section 6.3). Finally, a comparison of an extended kinetic model with short-timescale experiments suggested the existence of a subunit activation step before binding takes place [122]. This may be related to conformational changes or allosteric effects (see also [110, 231]).

6.2 Nanotechnological techniques

Information about living organisms is, to a large extent, encoded in the DNA. This idea to use DNA to store information is also at the core of one of the most promising strategies to assemble heterogeneous and functional nanostructures, namely DNA-based assembly (for reviews and perspectives on this topic see for instance [28, 112–115, 127, 232, 233]). It is believed (and has partially already been demonstrated) that such nanostructures will prove very useful for different purposes ranging from molecular robots (e.g. [234]) and molecular force clamps (e.g. [235]) to biosensors and devices to manipulate light (reviewed in [114]). These versatile properties rely on the fact that the structures are made from many distinct building blocks. Such heterogeneous structures also lie at the heart of our projects in which we examined the role of structure heterogeneity and stochasticity for the assembly dynamics. While the different experimental methods to build these nanostructures are not directly relevant to these projects, they illustrate nicely how structure heterogeneity can be achieved in nanotechnological applications. We will thus shortly review some of these techniques.

DNA origami

The first technique is DNA origami. It has been introduced by Rothemund in 2006 [236] and is partially based on ideas put forward by Seeman in 1982 [237]. Seeman suggested to use the complementarity of DNA base pairs to assemble designed structures with precisely controllable shapes. In DNA origami technology this idea is implemented by a long single-stranded DNA (the so-called scaffold strand) that is then folded due to the interaction with a large number of short staple strands (for reviews see e.g. [112–114]). While double-stranded DNA has a persistence length of several dozens of nanometers, the persistence length of single-stranded DNA is only roughly 1 nanometer, leading to a high flexibility of the scaffold strand [113] and, thus, versatility in use. The basic concept to use a single scaffold strand has been extended in many ways, for instance, by tethering multiple DNA origami structures via junctions based on strand exchange. By using several-arm junctions with different lengths it is possible to control the angles between the different origami subunits [238, 239]. Similarly, while the original geometries were restricted to two dimensions, several studies have realized three-dimensional structures (see e.g. [240–242]), for instance, by connecting planar origami structures at specified angles. Finally, there have been various successful approaches to assemble nanoparticles with the help of DNA origami (e.g. [243]).

DNA-brick based assembly

A partially complementary and more recent approach is DNA-brick based assembly [105, 106]. Instead of using a long scaffold strand, it relies on short, synthetic strands of DNA ("bricks" or "tiles") that interact via local binding rules. This assembly scheme allows for modularity and different subunits can be combined in various ways. Originally, it was expected that assembly via DNA bricks would only be versatile if the stoichiometric concentrations would be perfectly balanced (see e.g. [232, 233]). The idea was that kinetic traps would occur since too many nucleation seeds form. It has been suggested both theoretically and by experimental studies that this effect is (partially) suppressed due to generally slow nucleation compared to growth [105, 107]. However, yields are still not as high as for DNA origami, in particular for larger structures [105, 114, 233].

Colloidal materials [28, 115]

Finally, interactions between DNA base pairs are also used for the assembly of colloidal materials with specified magnetic, electronic or mechanical properties. In order to assemble colloids into non-symmetric structures, specified interactions between the subunits are required. One suggestion to achieve this has been a so-called "lock-and-key" mechanism where shape complementarity leads to specific binding due to entropic depletion forces. For large structures, however, this approach is not expected to be versatile enough. Instead, it was proposed to mediate interactions between colloids through DNA hybridization. This allows for control of the interaction strength by variation of the lengths of the sticky ends that link two colloids.

Theoretical description of heterogeneous structures

To conclude the chapter, we will mention some insights gained from theoretical studies that are related to our findings.
As mentioned above, it is generally expected that non-stoichiometric concentrations of building blocks lead to uncontrolled nucleation events and, thus, to low assembly yield. Recently, however, it has been suggested that exactly the use of non-stoichiometric concentrations may be a way to build large structures made from many different components [109]. The idea is that – instead of having random variability in the concentrations of subunits – one could enrich a specific region of the target structure. As a result, nucleation in this particular region is strongly favored compared to nucleation of other seeds and competition between different assembly paths can be largely eliminated.
While this strategy relies on a control of the supply of subunits, also the influence of microscopic properties has been studied. For instance, it has been suggested that it might be beneficial to choose the strength of the specific interactions between subunits as similar as possible [216]. Based on this principle, the authors suggest a way to improve the fidelity in DNA-brick based assembly schemes.
Finally, there is some debate about whether or not hierarchical assembly may be a good strategy to build heterogeneous or so-called information-rich structures. On the one hand, hierarchical assembly schemes seem to be strongly susceptible to kinetic traps caused by unspecific interactions [215]. If the latter are strong, step-by-step assembly via successive attachment of single subunits can outperform a hierarchical assembly process. On the other hand, if unspecific interactions can be well-controlled, the opposite behavior was found [116]. It thus remains a question for future research whether hierarchical assembly "may be a way to make large information-rich structures" [116].

6.3 Slow-nucleation principle

To conclude this introductory chapter, we want to emphasize the "slow-nucleation principle" again [102–109] because it will be crucial for our results.
As illustrated in Fig. 6.1 the idea is the following: Suppose nucleation of new structures is fast compared to growth (A). Then it is likely that too many nucleation seeds form that all compete for the same resources and, thereby, can not be finished due to resource depletion. As a result, if the resources are finite, the process ends up in a configuration with many half-finished polymer structures that - even if polymer-polymer binding occurs - might not be compatible due to overlapping parts. Correspondingly, the assembly yield is low.
In contrast, if nucleation is very slow, a newly nucleated structure will grow into the target structure before a new nucleation event occurs (B). In this case, the structures are thus assembled one after the other and there is no competition for resources. The assembly yield is high because kinetic traps are circumvented.
As we will see in chapter 7, this principle also underlies our findings.

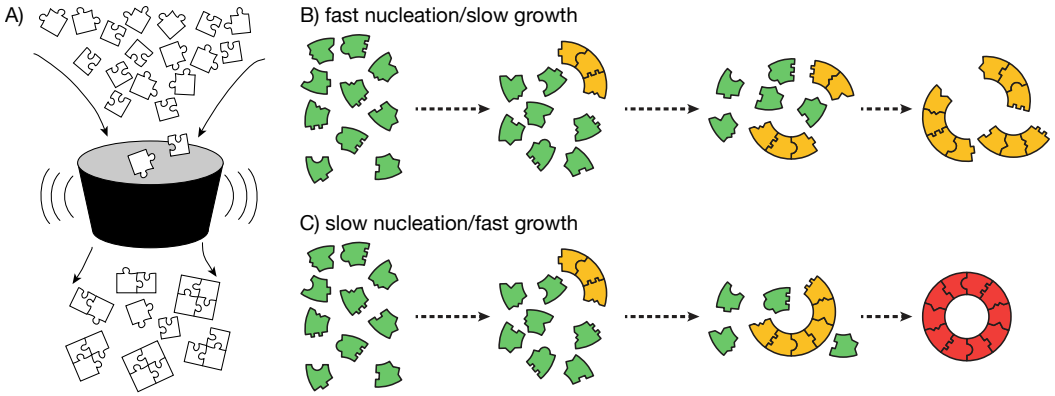

Figure 6.1 | A) Illustration of a self-assembly process (Image credit: Philipp Geiger). The process starts with individual subunits that then – through local interactions – form macroscopic structures. We focus on non-equilibrium self-assembly, meaning that we consider processes where part of the reactions are irreversible (on the timescale of the assembly process) and that we focus on kinetic (instead of equilibrium) properties. B,C) Slow nucleation principle: If nucleation of new structures is fast compared to growth (B), it is likely that many nucleation seeds form before polymers have grown into the target structure. As a result, the system gets kinetically trapped in half-finished polymer structures. In contrast, if growth is favored compared to nucleation (C), a newly nucleated structure is likely to grow into the target structure before new nucleation events occur. There is no competition for resources in this case and assembly is very efficient.

7 Stochastic yield catastrophes for heterogeneous structures

Simplicity is the ultimate sophistication.
(Leonardo da Vinci)

The goal of this chapter is to summarize the most important findings of our project on the self-assembly of heterogeneous structures. The corresponding manuscript has been published[1] in *eLife*. This chapter is based on and uses parts of this publication [4], which is also reprinted in section 7.5.

7.1 Motivation

Self-assembled structures range from very homogeneous virus capsids which are composed of only a single or few different species up to DNA-brick structures with many distinct building blocks. Despite these differences, common principles for the assembly of both types of structures have emerged (see also the introductory chapter 6). For instance, it is a well accepted strategy that nucleation of new structures should be slow compared to growth of structures in order to obtain high assembly yield (see also section 6.3). However, it is an open question whether different ways to accomplish slow nucleation are indeed equivalent and whether the heterogeneity of a target structure plays any role for achieving slow nucleation. The goal of this project was to address these questions with the help of a conceptual model. In particular, we focused on a situation where the assembly process involves irreversible steps and where resources are finite. In such a situation with finite particle numbers stochastic effects may become important and it is *a priori* not clear whether the strength of these stochastic effects may depend on the number of different building blocks that make up the target structure. It turns out that the self-assembly of heterogeneous structures can indeed be subject to strong stochastic effects if there are fluctuations in the availability of the different building blocks for binding. Intriguingly, these stochastic effects can lead to qualitatively different behavior as compared to a description in terms of mean-field equations that neglect this variability between the various constituents. For instance, the assembly yield in systems with fluctuations in the availability of the different building blocks can be a non-monotonic function of the nucleation probability in the corresponding system with well-balanced components.

As mentioned in the abstract of the project, the driving questions for this project are:
Does the heterogeneity of the target structure qualitatively change the assembly process? Under what conditions can irreversible self-assembly processes proceed efficiently and robustly?

[1] At the time of the original submission of this thesis, the manuscript had been under review for publication.

7.2 Model

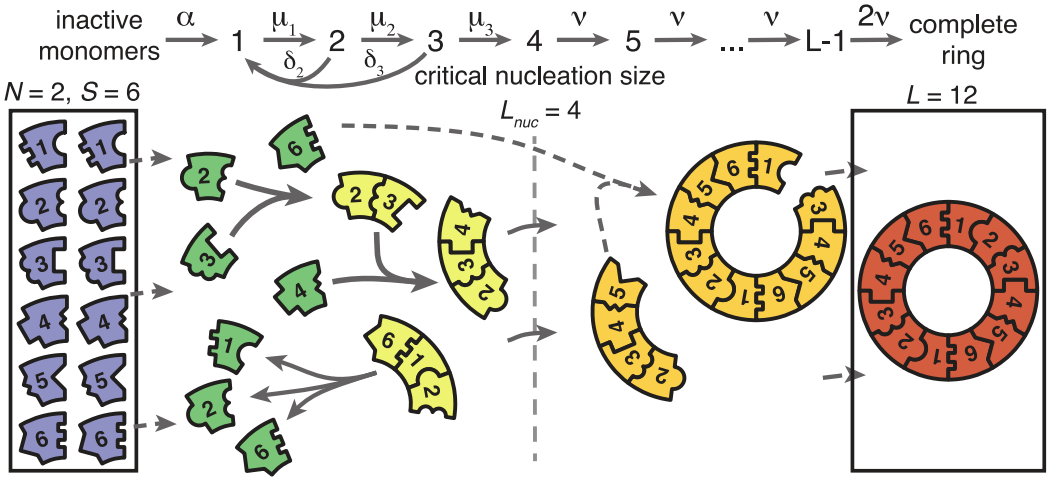

Figure 7.1 | Illustration of the model (slightly adapted from [4]). Ring structures of size L assemble from S different species $\in \{1, 2, \ldots, S\}$. Each species is present N times and all monomers are inactive initially (blue). Monomers get activated at per-capita rate α and, once active (green), can bind to each other. Binding only occurs between periodically consecutive species (e.g. species 1 can only bind to species S from the right and to species 2 from the left) and structures only grow by addition of single monomers. Below a critical nucleation size L_{nuc}, polymers (yellow) are unstable and decay again into monomers. In contrast, above the critical nucleation size, the structures (orange) are stable and grow irreversibly. Once a structure has reached the target structure size L, the ring is finished and does not grow further (red). To avoid ambiguity, we restrict the size of the target structure L to a multiple of the number of species S. Then each species occurs equally often in a ring and all final rings are identical.

To address these questions, we considered the conceptual model as illustrated in Fig. 7.1. Rings of size L are assembled from S different species in a well-mixed system. The species bind to each other in a periodically consecutive way and occur equally often in a final ring (thus, L is an integer multiple of S). That is, species i can only bind to species $(i \pm 1) \text{mod} S$. Monomers first dimerize and then structures grow one-by-one by monomer attachment. Below a critical nucleation size L_{nuc}, structures of size $l < L_{\text{nuc}}$ grow at per-capita rate μ_l and decay again into monomers at rate δ_l. In contrast, above the critical nucleation size, structures of size $l \geq L_{\text{nuc}}$ are stable and grow irreversibly at per-capita rate $\nu \equiv 1$ per binding site until they reach the target structure size L. These different growth regimes are motivated by typical nucleation-and-growth phenomena. In terms of classical nucleation theory, the critical nucleation size L_{nuc} corresponds to the structure size where the free energy barrier is maximal [206, 230, 244, 245]. To account for the effect of finite resources, we assume that there is a finite number N of particles per species in the system. Finally, to explore which effect an additional activation step (as suggested for instance in Refs. [122, 231]; see also section 6.1) has on the self-assembly dynamics, we assume that all particles are initially in an inactive state in which they can not bind to other structures. Activation then occurs at per-capita rate α, independent for all species and particles. Once active, particles bind to each other as described above.

The choice of the particular target structure (namely periodic rings in which all species occur equally often) and the symmetry between the different species is motivated by the fact that it is the simplest possible structure which allows for variable heterogeneity: All species are equivalent and at the same time the heterogeneity of the structure can be tuned by modifying the ratio between the size of the structure L and the number of species S. Furthermore, this perfect arrangement enables us to trace back the origin of the strong stochastic effects we observe in this model: they are due to fluctuations in the availability of the different species. If, for instance, we had allowed for different numbers of particles per species, these stochastic effects might have been overlaid by other stochastic effects similar as in Ref. [125].

For convenience, for the analysis presented in the next chapter 7.3, we will focus on the case of equal sub-nucleation growth rates $\mu_l \equiv \mu \ \forall l$ and equal decay rates $\delta_l \equiv \delta \ \forall l$. A discussion of the general case can be found in the Supplementary Material of the publication preprint in chapter 7.5. Furthermore, if not stated otherwise, we will consider the case where $L_{\mathrm{nuc}} = 2$. Then, all reactions are irreversible and dimerization occurs at per-capita rate μ whereas all growth (elongation) steps take place at per-capita rate $\nu \equiv 1$.

The quality of the assembly process is determined in terms of the yield y. It corresponds to the number of finished rings compared to the maximally possible number, NS/L. Here we only focus on the assembly yield at the end of the process when no further growth is possible since all monomers have been activated and are bound in structures larger or equal to the critical nucleation size L_{nuc}.

7.3 Results

What behavior do we expect from this model? As explained in detail in section 6.3, an important guiding principle for self-assembly is that for efficient assembly nucleation of new structures should be slow compared to growth. Intuitively, in our model, this could be achieved in two ways. First, one can implement a slow sub-nucleation rate $\mu \ll 1$ as compared to the growth rate $\nu = 1$. In this case, nucleation is directly disfavored relative to growth since it is simply more likely that monomers attach to a larger structure as compared to a smaller structure. However, there is also a second, more indirect way, namely by decreasing the activation rate α. For small α the number of active monomers is typically small. As a result, dimerization (which requires two active monomers) is expected to occur much more rarely as compared to growth of larger structures (for which only one monomer is necessary). In both cases of small dimerization rates or small activation rates, there is a high tendency that initiated structures first finish before new structures are nucleated. Assembly thus proceeds consecutively and the assembly yield is high because kinetic traps are avoided. Taken together, we intuitively expect that the assembly yield should be high for slow activation and/or slow dimerization rates.

This is exactly what we observed in the limit where the number N of particles per species is large (see Fig. 2(a,b) in the publication preprint in chapter 7.5). In (a), we consider the so-called "activation scenario" where nucleation is limited by a small activation rate α and the dimerization rate is equal to the growth rate $\mu = \nu = 1$. In (b), nucleation is limited by a small dimerization rate μ and the activation rate is chosen as $\alpha \to \infty$; "dimerization scenario". In both cases, yield is very low for large α or μ. It sharply increases below a threshold value α_{th}

or μ_{th} and reaches a perfect value of 1 in the limit of small α or μ. The threshold values scale as $\alpha_{\text{th}} \sim N/L^3$ and $\mu_{\text{th}} \sim 1/L^2$ (compare Eq. 1 in the publication preprint in chapter 7.5 and the analytical derivation in the Supplementary Material, where we introduced the initial monomer concentration $C = N/V$). While the number N of particles per species is thus not decisive for the dimerization scenario, the transition to perfect yield in the activation scenario scales with N. Intuitively, this comes from the fact that in the dimerization scenario all reactions rely on two-particle interactions. In contrast, activation is a single-particle reaction and, thus, α has to be rescaled by N (or the concentration) in order to obtain equivalent behavior for different values of N. The inset in Fig. 2(a) in the publication preprint in chapter 7.5 shows exactly this behavior: If the activation rate is rescaled by N, all curves for different N collapse onto one master curve. Remarkably, these results are entirely independent of the heterogeneity of the target structure (the number of species S) if the target structure size L and the number of particles N per species are fixed. Furthermore, they do not depend on whether the system was simulated stochastically based on Gillespie's algorithm ([33]; symbols) or whether it was described in terms of the corresponding chemical rate equations which are mean-field equations that neglect fluctuations and correlations between species.

Intriguingly, the qualitative behavior in the activation scenario changes drastically for heterogeneous structures if the number N of particles in the system is reduced (see Fig. 3(a) in the publication preprint in chapter 7.5). While a numerical integration of the chemical rate equations (black line) still predicts a perfect yield of 1 in the limit of small activation rate, the results from stochastic simulations (symbols) show that in this limit yield saturates at an imperfect value $y_{\text{max}} < 1$. This saturation value $y_{\text{max}} < 1$ strongly decreases with the number N of particles per species. Surprisingly, already for $N = 5000$ particles per species, this effect is clearly visible (in the case of $L = S = 60$ in Fig. 3(a)). And indeed for small enough N (in Fig. 3(a), $N = 100$), the maximal yield in stochastic simulations is 0 although the deterministic chemical rate equations would predict a perfect yield of 1. We thus termed this phenomenon "stochastic yield catastrophe".

Where does this stochastic yield catastrophe come from? As we explain more thoroughly in the next chapter 8, it is due to the stochastic activation of particles that introduces fluctuations in the availability of the different species. If there are certain species that are momentarily less available, this unavailability of certain species can block the growth of structures that would otherwise grow by attachment of this species. Since this effect is the more pronounced for larger structures (see chapter 8), growth of structures is effectively disfavored compared to nucleation and, in accordance with the slow-nucleation principle, yield is lower.

The strength of the stochastic effects depends both on the critical nucleation size L_{nuc} and on the number of species S (if the structure size L and the number of maximally possible ring structures NS/L (and not N itself) is fixed; see Fig. 3(d) in the publication preprint in chapter 7.5): While the maximal yield is always perfect for completely homogeneous structures ($S = 1$) where there can be no fluctuations in the availability of the different species, yield decreases for larger number of species S. With regard to the self-assembly of artificial structures or in living organisms, this finding suggests that in order to achieve high assembly yield, it is preferential to build as homogeneous structures as possible. Moreover, for larger critical nucleation size L_{nuc}, the maximal yield is larger. This behavior is intuitive: For larger L_{nuc}, more steps of the assembly process are reversible and it is, thus, more feasible to correct for too many nucleation events.

In the dimerization scenario, all particles are active from the beginning and there are no fluctuations in the availability of the different species. Correspondingly, this scenario is not subject to substantial stochastic effects (see Fig. 3(b) in the publication preprint in chapter 7.5). Yield is always perfect in the limit of small dimerization, irrespective of the number of particles per species.

Counterintuitive behavior arises if both scenarios are combined. Fig. 5(a,b) in the publication preprint in chapter 7.5 shows how the yield depends on the activation rate α for different values of the dimerization rate $\mu \ll \nu = 1$. While the deterministic rate equations (lines) predict monotonic behavior with respect to the activation rate, the yield in the stochastic simulations can be a non-monotonic function of the activation rate (see e.g. the yellow and green lines in (a,b)). If μ is not small enough, yield is low for large α (corresponding to the dimerization scenario). A lower α first improves yield because the fluctuations are not strong, yet, and a slower activation rate yields to a slower nucleation speed. Further decrease of α, though, enhances the fluctuations that, in turn, effectively increase the nucleation probability again (see above). As a result, yield is deterministically suppressed for large α and is suppressed by stochastic effects for small α. Depending on the strength of these effects, yield can be either monotonically increasing, monotonically decreasing or exhibit non-monotonic behavior with respect to α.
In a deterministic description in terms of chemical rate equations, the stochasticity due to the random activation process is not taken into account and all species are equivalent. In this case, a lower value of α always leads to a slower nucleation probability and thus an improved assembly efficiency.

Remarkably, our finding of the stochastic yield catastrophe is robust to model modifications. Both for systems where polymer-polymer binding is additionally considered (Fig. 6 in the publication preprint in chapter 7.5) as well as for systems with a non-periodic geometry (and thus non-equivalent species) and a non-linear assembly path (Fig. 7 in the publication preprint in chapter 7.5), we find the same qualitative behavior: In the activation scenario, yield saturates at an imperfect value that, generally speaking, decreases for smaller numbers of particles in the system.
This suggests that stochastic effects may be an important limitation for the self-assembly of heterogeneous structures.

7.4 Key points

From my point of view, there are three take-home messages:

- The assembly of heterogeneous structures can be subject to strong stochastic effects which suppress the assembly yield considerably (or even completely; “stochastic yield catastrophe”).
- The assembly yield can be a non-monotonic or even an increasing function of the deterministic nucleation speed. The slow-nucleation principle, thus, has to be interpreted in terms of the corresponding stochastic framework.
- Chemical rate equations are, in general, not sufficient to describe the self-assembly of heterogeneous structures.

In the spirit of the quote by Leonardo da Vinci at the beginning of the chapter, I believe that in our case it was indeed the simplicity of the model and the assumption of a principally perfectly functioning and designed system that made it possible to uncover the strong influence of fluctuations in the availability of the different species on the efficiency of the assembly process.

7.5 Publication: Stochastic yield catastrophes and robustness in self-assembly, eLife 9, e51020 (2020)

This section is a publication preprint of the following manuscript published[2] in **eLife** 9, e51020 (2020).

Stochastic yield catastrophes and robustness in self-assembly

by

Florian M. Gartner,[1,*] Isabella R. Graf,[1,*] Patrick Wilke,[1,*] Philipp M. Geiger[1], and Erwin Frey[1]

[1] *Arnold-Sommerfeld-Center for Theoretical Physics and Center for NanoScience, Department of Physics, Ludwig-Maximilians-Universität München*

[*] *These authors contributed equally to this work.*

DOI: 10.7554/eLife.51020

[2] At the time of the original submission of this thesis, the manuscript had been under review for publication.

Stochastic Yield Catastrophes and Robustness in Self-Assembly

Florian M. Gartner[1⋆], Isabella R. Graf[1⋆], Patrick Wilke[1⋆], Philipp M. Geiger[1], Erwin Frey[1†]

[1]Arnold Sommerfeld Center for Theoretical Physics (ASC) and Center for NanoScience (CeNS), Department of Physics, Ludwig-Maximilians-Universität München, Theresienstraße 37, 80333 München, Germany

⋆ F.M.G., I.R.G. and P.W. contributed equally to this work.

†Corresponding author: frey@lmu.de.

ABSTRACT

A guiding principle in self-assembly is that, for high production yield, nucleation of structures must be significantly slower than their growth. However, details of the mechanism that impedes nucleation are broadly considered irrelevant. Here, we analyze self-assembly into finite-sized target structures employing mathematical modeling. We investigate two key scenarios to delay nucleation: (i) by introducing a slow activation step for the assembling constituents and, (ii) by decreasing the dimerization rate. These scenarios have widely different characteristics. While the dimerization scenario exhibits robust behavior, the activation scenario is highly sensitive to demographic fluctuations. These demographic fluctuations ultimately disfavor growth compared to nucleation and can suppress yield completely. The occurrence of this stochastic yield catastrophe does not depend on model details but is generic as soon as number fluctuations between constituents are taken into account. On a broader perspective, our results reveal that stochasticity is an important limiting factor for self-assembly and that the specific implementation of the nucleation process plays a significant role in determining the yield.

1 Introduction

Efficient and accurate assembly of macromolecular structures is vital for living organisms. Not only must resource use be carefully controlled, but malfunctioning aggregates can also pose a substantial threat to the organism itself [8, 22]. Furthermore, artificial self-assembly processes have important applications in a variety of research areas like nanotechnology, biology, and medicine [39, 40, 43]. In these areas, we find a broad range of assembly schemes. For example, while a large number of viruses assemble capsids from identical protein subunits, some others, like the Escherichia virus T4, form highly complex and heterogeneous virions encompassing many different types of constituents [15, 26, 44, 45]. Furthermore, artificially built DNA structures can reach up to Gigadalton sizes and can, in principle, comprise an unlimited number of different subunits [11, 23, 33, 36]. Notwithstanding these differences, a generic self-assembly process always includes three key steps: First, subunits must be made available, e.g. by gene expression, or rendered competent for binding, e.g. by nucleotide exchange [2, 3, 38] ('activation'). Second, the formation of a structure must be initiated by a nucleation event ('nucleation'). Due to cooperative or allosteric effects in binding, there might be a significant nucleation barrier [3, 16, 20, 25, 35]. Third, following nucleation, structures grow via aggregation of substructures ('growth'). To avoid kinetic traps that may occur due to irreversibility or very slow disassembly of substructures [14, 17], structure nucleation must be significantly slower than growth [16, 21, 23, 33, 37, 45]. Physically speaking, there are no irreversible reactions. However, in the biological context, self-assembly describes the (relatively fast)

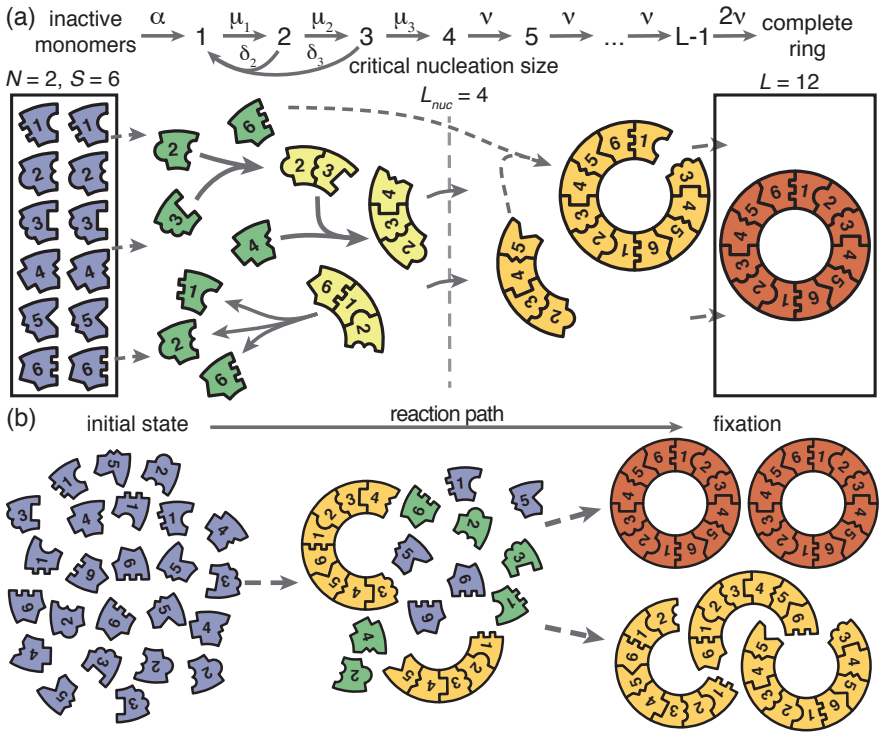

Figure 1. Schematic description of the model. **(a)** Rings of size L are assembled from S different particle species. N monomers of each species are initially in an inactive state (blue) and are activated at the same per-capita rate α. Once active (green), species with periodically consecutive index can bind to each other. Structures grow by attachment of single monomers. Below a critical nucleation size (L_{nuc}), structures of size l (light yellow) grow and decay into monomers at size-dependent rates μ_l and δ_l, respectively. Above the critical size, polymers (dark yellow) are stable and grow at size-independent rate ν until the ring is complete (the absorbing state; red). **(b)** Illustration of depletion traps. If nucleation is slow compared to growth, initiated structures are likely to be completed. Otherwise, many stable nuclei will form that cannot be completed before resources run out.

formation of long-lasting, stable structures. Therefore, at least part of the assembly reactions are often considered to be irreversible on the time scale of the assembly process.

In this manuscript we investigate, for a given target structure, whether the nature of the specific mechanism employed in order to slow down nucleation influences the yield of assembled product. To address this question, we examine a generic model that incorporates the key elements of self-assembly outlined above.

2 Model definition

We model the assembly of a fixed number of well-defined target structures from limited resources. Specifically, we consider a set of S different species of constituents denoted by $1, \ldots, S$ which assemble into rings of size L. The cases $S = 1$ and $1 < S \leq L$ ($S = L$) are denoted as homogeneous and partially (fully) heterogeneous, respectively. The homogeneous model builds on previous work on virus capsid [3, 17], linear protein filament assembly [7, 27, 28] and aggregation and polymerization models [24]. The heterogeneous model in turn links to previous model systems used to study, for example, DNA-brick-based assembly of heterogeneous structures [6, 19, 30]. We emphasize that, even though strikingly similar experimental realizations of our model exist [11, 32, 36], it is not intended to describe any particular system. The ring structure represents a general linear assembly process involving building

blocks with equivalent binding properties and resulting in a target of finite size. The main assumption in the ring model is that the different constituents assemble linearly in a sequential order. In many biological self-assembling systems like bacterial flagellum assembly or biogenesis of the ribosome subunits the assumption of a linear binding sequence appears to be justified [4, 31]. In order to test the validity of our results beyond these constraints we also perform stochastic simulations of generalized self-assembling systems that do not obey a sequential binding order: i) by explicitly allowing for polymer-polymer bindings and ii) by considering the assembly of finite sized squares that grow independently in two dimensions (see Figs. 6 and 7).

The assembly process starts with N inactive monomers of each species. We use $C = N/V$ to denote the initial concentration of each monomer species, where V is the reaction volume. Monomers are activated independently at the same per capita rate α, and, once active, are available for binding. Binding takes place only between constituents of species with periodically consecutive indices, for example 1 and 2 or S and 1 (leading to structures such as $\ldots 1231 \ldots$ for $S = 3$); see Fig. 1. To avoid ambiguity, we restrict ring sizes to integer multiples of the number of species S. Furthermore, we neglect the possibility of incorrect binding, e.g. species 1 binding to 3 or $S-1$. Polymers, i.e., incomplete ring structures, grow via consecutive attachment of monomers. For simplicity, polymer-polymer binding is disregarded at first, as it is typically assumed to be of minor importance [3, 18, 30, 45]. To probe the robustness of the model, later we consider an extended model including polymer-polymer binding for which the results are qualitatively the same (see Fig. 6 and the discussion). Furthermore, it has been observed that nucleation phenomena play a critical role for self-assembly processes [3, 23, 33, 37]. So it is in general necessary to take into account a critical nucleation size, which marks the transition between slow particle nucleation and the faster subsequent structure growth [25, 28–30]. We denote this critical nucleation size by L_{nuc}, which in terms of classical nucleation theory corresponds to the structure size at which the free energy barrier has its maximum. For $l < L_{\mathrm{nuc}}$ attachment of monomers to existing structures and decay of structures (reversible binding) into monomers take place at size-dependent reaction rates μ_l and δ_l, respectively (Fig. 1). Here, we focus on identical rates $\mu_l = \mu$ and $\delta_l = \delta$. A discussion of the general case is given in the Supplemental Material [1]. Above the nucleation size, polymers grow by attachment of monomers with reaction rate $\nu \geq \mu$ per binding site. As we consider successfully nucleated structures to be stable on the observational time scales, monomer detachment from structures above the critical nucelation size is neglected (irreversible binding) [3, 30]. Complete rings neither grow nor decay (absorbing state).

We investigate two scenarios for the control of nucleation speed, first separately and then in combination. For the 'activation scenario' we set $\mu = \nu$ (all binding rates are equal) and control the assembly process by varying the activation rate α. For the 'dimerization scenario' all particles are inherently active ($\alpha \to \infty$) and we control the assembly process by varying the dimerization rate μ (we focus on $L_{\mathrm{nuc}} = 2$). It has been demonstrated previously in [3] and [9, 16, 29] that either a slow activation or a slow dimerization step are suitable in principle to retard nucleation and favour growth of the structures over the initiation of new ones. We quantify the quality of the assembly process in terms of the assembly yield, defined as the number of successfully assembled ring structures relative to the maximal possible number NS/L. Yield is measured when all resources have been used up and the system has reached its final state. We do not discuss the assembly time in this manuscript, however, in the SI we show typical trajectories for the time evolution of the yield in the activation and dimerization scenario. If the assembly product is stable (absorbing state), the yield can only increase with time. Consequently, the final yield constitutes the upper limit for the yield irrespective of additional time constraints. Therefore, the final yield is an informative and unambiguous observable to describe the efficiency of the assembly reaction.

We simulated our system both stochastically via Gillespie's algorithm [12] and deterministically as a set of ordinary differential equations corresponding to chemical rate equations (see Supplemental Material [1]).

3 Results

3.1 Deterministic behavior in the macroscopic limit.

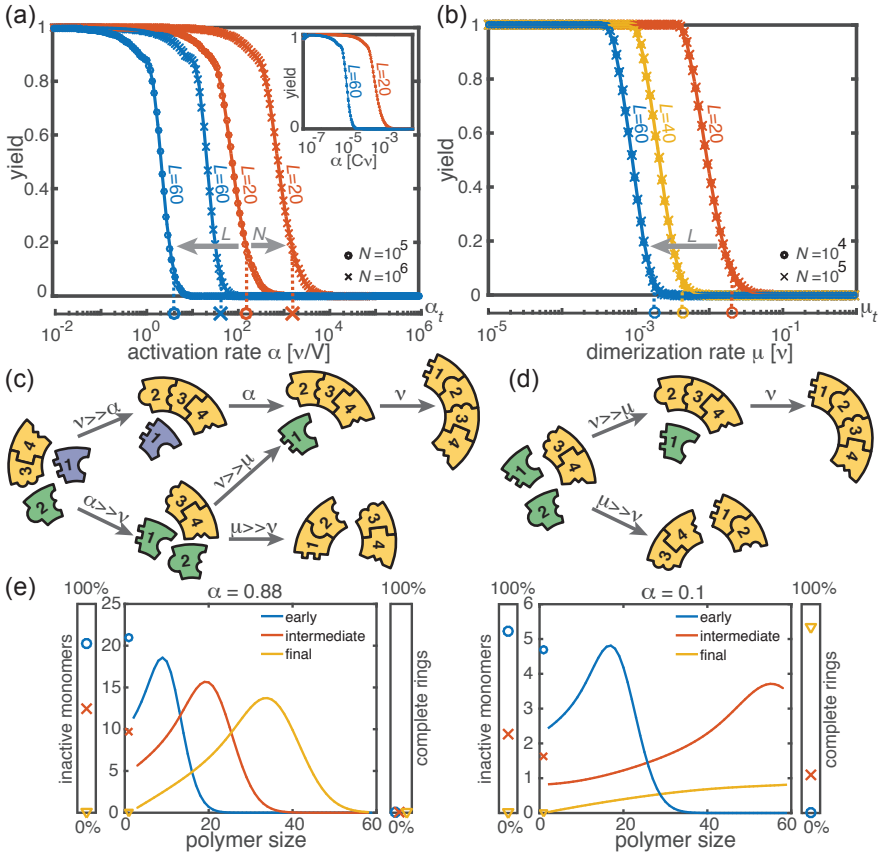

Figure 2. Deterministic behavior in the macroscopic limit $N \gg 1$. **(a, b)** Yield for different particle numbers N (symbols) and ring sizes L (colors) for $L_{\mathrm{nuc}} = 2$. Decreasing either (a) the activation rate ('activation scenario': $\mu = \nu$) or (b) the dimerization rate ('dimerization scenario': $\alpha \to \infty$) achieves perfect yield. The stochastic simulation results (symbols) average over 16 realizations and agree exactly with the integration of the chemical rate equations (lines). The threshold values (Eq. 1) are indicated by the vertical dashed lines. Plotting yield against the dimensionless quantity $\alpha/(\nu C)$ causes the curves for different C to collapse into a single master curve (inset in a). For both scenarios there is no dependency on the number of species S in the deterministic limit. **(c, d)** Illustration showing how depletion traps are avoided by either slow activation (c) or slow dimerization (d). If the activation or the dimerization rate is small (large) compared to the growth rate, assembly paths leading to complete rings are favored (disfavored). The color scheme is the same as in Fig. 1. **(e)** Deterministically, the size distribution of polymers behaves like a wave, and is shown for large and small activation rate for $L = 60$, $L_{\mathrm{nuc}} = 2$, $N = 10000$ and $\mu = \nu = 1$. The distributions are obtained from a numerical integration of the deterministic mean-field dynamics, Eq. 6, and are plotted for early, intermediate and final simulation times. The respective percentage of inactive monomers and complete rings is indicated by the symbols in the scale bar on the left or right.

First, we consider the macroscopic limit, $N \gg 1$, and investigate how assembly yield depends on the activation rate α (activation scenario) and the dimerization rate μ (dimerization scenario) for $L_{\mathrm{nuc}} = 2$. Here, the deterministic description coincides with the stochastic simulations (Fig. 2(a) and (b)). For both high activation and high dimerization rates, yield is very poor. Upon decreasing either the

activation rate (Fig. 2(a)) or the dimerization rate (Fig. 2(b)), however, we find a threshold value, $\alpha_{\rm th}$ or $\mu_{\rm th}$, below which a rapid transition to the perfect yield of 1 is observed both in the deterministic and stochastic simulation. By exploiting the symmetries of the system with respect to relabeling of species, one can show that, in the deterministic limit, the behavior is independent of the number of species S (for fixed L and N, see Supplemental Material [1]). Consequently, all systems behave equivalently to the homogeneous system and yield becomes independent of S in this limit. Note, however, that equivalent systems with differing S have different total numbers of particles SN and hence assemble different total numbers of rings.

Decreasing the activation rate reduces the concentration of active monomers in the system. Hence growth of the polymers is favored over nucleation, because growth depends linearly on the concentration of active monomers while nucleation shows a quadratic dependence. Likewise, lower dimerization rates slow down nucleation relative to growth. Both mechanisms therefore restrict the number of nucleation events, and ensure that initiated structures can be completed before resources become depleted (see Fig. 2(c) and (d)).

Mathematically, the deterministic time evolution of the polymer size distribution $c(l,t)$ is described by an advection-diffusion equation [9, 41] with advection and diffusion coefficients depending on the instantaneous concentration of active monomers (see Supplemental Material [1]). Solving this equation results in the wavefront of the size distribution advancing from small to large polymer sizes (Fig. 2(e)). Yield production sets in as soon as the distance travelled by this wavefront reaches the maximal ring size L. Exploiting this condition, we find that in the deterministic system for $L_{\rm nuc} = 2$, a non-zero yield is obtained if either the activation rate or the dimerization rate remains below a corresponding threshold value, i.e. if $\alpha < \alpha_{\rm th}$ or $\mu < \mu_{\rm th}$, where

$$\alpha_{\rm th} = P_\alpha \frac{\nu}{\mu} \frac{\nu C}{(L-\sqrt{L})^3} \quad \text{and} \quad \mu_{\rm th} = P_\mu \frac{\nu}{(L-\sqrt{L})^2} \tag{1}$$

(see Supplemental Material [1]) with proportionality constants $P_\alpha = [\sqrt{\pi}\Gamma(2/3)/\Gamma(7/6)]^3/3 \approx 5.77$ and $P_\mu = \pi^2/2 \approx 4.93$. These relations generalize previous results [29] to finite activation rates and for heterogeneous systems. A comparison between the threshold values given by Eq. 1 and the simulated yield curves is shown in Fig. 2(a,b). The relations highlight important differences between the two scenarios (where $\alpha \to \infty$ and $\mu = \nu$, respectively): While $\alpha_{\rm th}$ decreases cubically with the ring size L, $\mu_{\rm th}$ does so only quadratically. Furthermore, the threshold activation rate $\alpha_{\rm th}$ increases with the initial monomer concentration C. Consequently, for fixed activation rate, the yield can be optimized by increasing C. In contrast, the threshold dimerization rate is independent of C and the yield curves coincide for $N \gg 1$. Finally, if α is finite and $\mu < \nu$, the interplay between the two slow-nucleation scenarios may lead to enhanced yield. This is reflected by the factor ν/μ in $\alpha_{\rm th}$, and we will come back to this point later when we discuss the stochastic effects.

In summary, for large particle numbers ($N \gg 1$), perfect yield can be achieved in two different ways, independently of the heterogeneity of the system - by decreasing either the activation rate (activation scenario) or the dimerization rate (dimerization scenario) below its respective threshold value.

3.2 Stochastic effects in the case of reduced resources.

Next, we consider the limit where the particle number becomes relevant for the physics of the system. In the activation scenario, we find a markedly different phenomenology if resources are sparse. Figure 3(a) shows the dependence of the average yield on the activation rate for different, low particle numbers in the completely heterogeneous case ($S = L$) [1]. Whereas the deterministic theory predicts perfect yield for small activation rates, in the stochastic simulation yield saturates at an imperfect value $y_{\rm max} < 1$.

[1]Here, we restrict our discussion to the average yield. The error of the mean is negligible due to the large number of simulations used to calculate the average yield. Still, due to the randomness in binding and activation, the yield can differ between simulations. A figure with the average yield and its standard deviation is shown in the Supplemental Material [1]. For very low and very high average yield, the standard deviation has to be small due to the boundedness of the yield. For intermediate values of the average, the standard deviation is highest but still small compared to the average yield. Thus, the average yield is meaningful for the essential understanding of the assembly process.

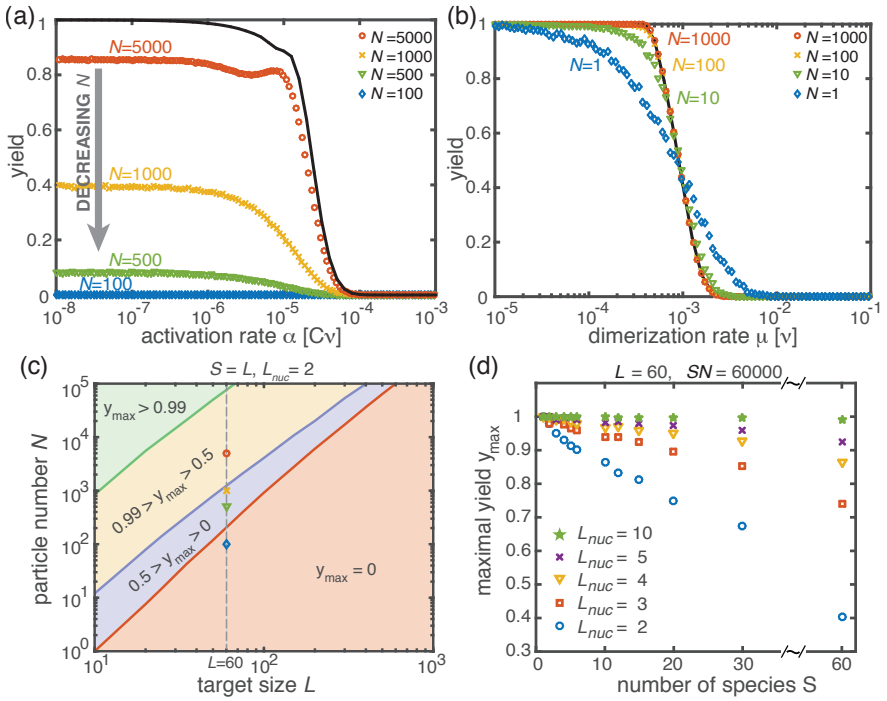

Figure 3. Stochastic effects in the case of reduced resources. **(a, b)** Yield of the fully heterogeneous system ($S = L$) for reduced number of particles (symbols) for $L = 60$ and $L_{\mathrm{nuc}} = 2$ averaged over 1024 ensembles). In the activation scenario, at low activation rates the yield saturates at an imperfect value $y_{\max}$, which decreases with the number of particles (a). This finding disagrees with the deterministic prediction (black line) of perfect yield for $\alpha \to 0$. In contrast, the dimerization scenario robustly exhibits the maximal yield of 1 for small N, in agreement with the deterministic prediction (black line) (b). **(c)** Diagram showing different regimes of $y_{\max}(N, L)$ in dependence of the particle number N and target size L (for the fully heterogeneous system $S = L$) as obtained from stochastic simulations in the limit $\alpha \to 0$. The minimal number of particles necessary to obtain a fixed yield increases in a strongly nonlinear way with the target size. The symbols along the line $L = 60$ represent the saturation values of the yield curves in (a). **(d)** Dependence of $y_{\max}$ on the number of species S for fixed $L = 60$ and fixed number of ring structures NS/L. Symbols indicate different values of the critical nucleation size L_{nuc}. The impact of stochastic effects strongly depends on the number of species under the constraint of a fixed total number of particles NS and fixed target size L. The homogeneous system is not subject to stochastic effects at all. Higher reversibility for larger L_{nuc} also mitigates stochastic effects.

Reducing the particle number N decreases this saturation value $y_{\max}$ until no finished structures are produced ($y_{\max} \to 0$). The magnitude of this effect strongly depends on the size of the target structure L if the system is heterogeneous. Fig. 3(c) shows a diagram characterizing different regimes for the saturation value of the yield, $y_{\max}(N, L)$, in dependence of the particle number N and the size of the target structure L for fully heterogeneous systems ($S = L$). We find that the threshold particle number N_y^{th} necessary to obtain a fixed yield y increases nonlinearly with the target size L. For the depicted range of L, the dependence of the threshold for nonzero yield, $N_{>0}^{th}$, on L can approximately be described by a power-law: $N_{>0}^{th} \sim L^{\xi}$, with exponent $\xi \approx 2.8$ for $L \leq 600$. Consequently, for $L = 600$ already more than 10^5 rings must be assembled in order to obtain a yield larger than zero. In the SI we included two additional plots that show the dependence of $y_{\max}$ on N for fixed L and the dependence on L for fixed N, respectively. The suppression of the yield is caused by fluctuations (see explanation below) and is not captured by a deterministic description. Because these stochastic effects can decrease the yield from a perfect value in a deterministic description to zero (see Fig. 3(a)), we term this effect 'stochastic yield

catastrophe'.

For fixed target size L and fixed maximum number of target structures $\frac{NS}{L}$, $y_{\max}$ increases with decreasing number of species, see Fig. 3(d). In the fully homogeneous case, $S = 1$, a perfect yield of 1 is always achieved for $\alpha \to 0$. The decrease of the maximal yield with the number of species S thus suggests that, in order to obtain high yield, it is beneficial to design structures with as few different species as possible. In large part this effect is due to the constraint $SN = \text{const}$, whereby the more homogeneous systems (small S) require larger numbers of particles per species N and, correspondingly, exhibit less stochasticity. If N is fixed instead of SN, the yield still initially decreases with increasing number of species S but then quickly reaches a stationary plateau and gets independent of S for $S \gg 1$, see Supplemental Material [1]. Moreover, increasing the nucleation size L_{nuc}, and with it the reversibility of binding, also increases $y_{\max}$, see Fig. 3(d). This indicates that, beside heterogeneity of the target structure, irreversibility of binding on the relevant time scale makes the system susceptible to stochastic effects.

The stochastic yield catastrophe is mainly attributable to fluctuations in the number of active monomers. In the deterministic (mean-field) equation the different particle species evolve in balanced stoichiometric concentrations. However, if activation is much slower than binding, the number of active monomers present at any given time is small, and the mean-field assumption of equal concentrations is violated due to fluctuations (for $S > 1$). Activated monomers then might not fit any of the existing larger structures and would instead initiate new structures. Figure 4(a) illustrates this effect and shows how fluctuations in the availability of active particles lead to an enhanced nucleation and, correspondingly, to a decrease in yield. Due to the effective enhancement of the nucleation rate, the resulting polymer size distribution has a higher amplitude than that predicted deterministically (Fig. 4(b)) and the system is prone to depletion traps. A similar broadening of the size distribution has been reported in the context of stochastic coagulation-fragmentation of identical particles [5].

In the dimerization scenario, in contrast, there is no stochastic activation step. All particles are available for binding from the outset. Consequently, stochastic effects do not play an essential role in the dimerization scenario and perfect yield can be reached robustly for all system sizes, regardless of the number of species S (Fig. 3(b)).

3.3 Non-monotonic yield curves for a combination of slow dimerization and activation.

So far, the two implementations of the 'slow nucleation principle' have been investigated separately. Surprisingly, we observe counter-intuitive behavior in a mixed scenario in which both dimerization and activation occur slowly (i.e., $\mu < \nu$, $\alpha < \infty$). Figure 5 shows that, depending on the ratio μ/ν, the yield can become a non-monotonic function of α. In the regime where α is large, nucleation is dimerization-limited; therefore activation is irrelevant and the system behaves as in the dimerization scenario for $\alpha \to \infty$. Upon decreasing α we then encounter a second regime, where activation and dimerization jointly limit nucleation. The yield increases due to synergism between slow dimerization and activation (see μ/ν dependence of α_{th}, Eq. 1), whilst the average number of active monomers is still high and fluctuations are negligible. Finally, a stochastic yield catastrophe occurs if α is further reduced and activation becomes the limiting step. This decline is caused by an increase in nucleation events due to relative fluctuations in the availability of the different species ("fluctuations between species"). This contrasts the deterministic description where nucleation is always slower for smaller activation rate. Depending on the ratio μ/ν, the ring size L and the particle number N, maximal yield is obtained either in the dimerization-limited (red curves, Fig. 5), activation-limited (blue curve, Fig. 5(b)) or intermediate regime (green and orange curves).

3.4 Robustness of the results to model modifications.

In our model, the reason for the stochastic yield catastrophe is that - due to fluctuations between species - the effective nucleation rate is strongly enhanced. Hence, if binding to a larger structure is temporarily impossible, activated monomers tend to initiate new structures, causing an excess of structures that

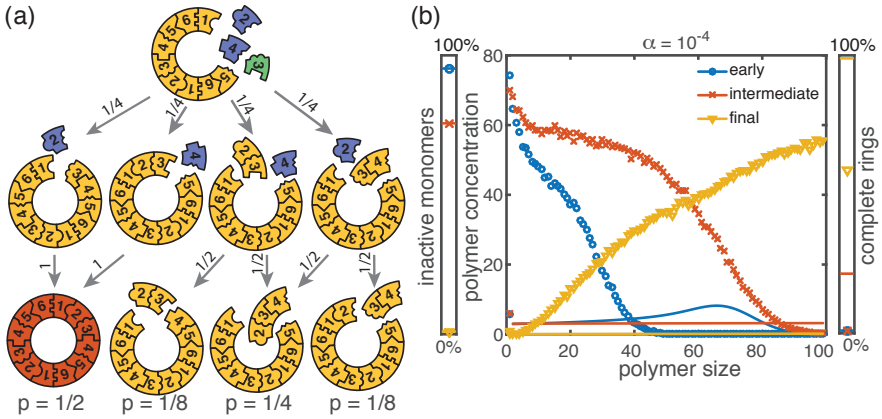

Figure 4. Cause and effect of stochasticity in the activation scenario. **(a)** Illustration of the significance of stochastic effects when resources are sparse. Arrows indicate possible transitions and the probabilities in the depicted situation for sufficiently small activation rate α. For small α, the random order of activation alone determines the availability of monomers and therefore the order of binding. In the depicted situation, the complete structure is assembled only with probability $1/2$. In all other cases, only fragments of the structure are assembled such that the final yield is decreased. **(b)** Polymer size distribution for the activation scenario (symbols) as obtained from stochastic simulations, in comparison with its deterministic prediction (lines) for $S = L = 100$, $N = 1000$ and $L_{\mathrm{nuc}} = 2$. Due to the enhanced number of nucleation events, the stochastic wave encompasses far more structures and moves more slowly. As a result, it does not quite reach the absorbing boundary.

ultimately cannot be completed. Natural questions that arise are whether i) relaxing the constraint that polymers cannot bind other polymers or ii) abandoning the assumption of a linear assembly path, will resolve the stochastic yield catastrophe. To answer these questions, we performed stochastic simulations for extensions of our model system showing that the stochastic yield catastrophe indeed persists.

We start by considering the ring model from the previous section but take polymer-polymer binding into account in addition to growth via monomer attachment (Fig.6). In detail, we assume that two structures of arbitrary size (and with combined length $\leq L$) bind at rate ν if they fit together, i.e. if the left (right) end of the first structure is periodically continued by the right (left) end of the second one. Realistically, the rate of binding between two structures is expected to decrease with the motility and thus the sizes of the structures. In order to assess the effect of polymer-polymer binding, we focus on the worst case where the rate for binding is independent of the size of both structures. If a stochastic yield catastrophe occurs for this choice of parameters, we expect it to be even more pronounced in all the "intermediate cases". Fig. 6 shows the dependence of the yield on the activation rate in the polymer-polymer model. As before, yield increases below a critical activation rate and then saturates at an imperfect value for small activation rates. Decreasing the number of particles per species, decreases this saturation value. Compared to the original model, the stochastic yield catastrophe is mitigated but still significant: For structures of size $S = L = 100$, yield saturates at around 0.87 for $N = 100$ particles per species and at around 0.33 for $N = 10$ particles per species. We thus conclude that polymer-polymer binding indeed alleviates the stochastic yield catastrophe but does not resolve it. Since binding only happens between consecutive species, structures with overlapping parts intrinsically can not bind together and depletion traps continue to occur. Taken together, also in the extended model, fluctuations in the availability of the different species lead to an excess of intermediate-sized structures that get kinetically trapped due to structural mismatches. Note that in the extreme case of $N = 1$, incomplete polymers can always combine into 1 final ring structure so that in this case yield is always 1. Analogously, for high activation rates yield is improved for $N = 10$ compared to $N \geq 50$ (Fig. 6 b).

Kinetic trapping due to structural mismatches can occur in every (partially) irreversible heterogeneous assembly process with finite-sized target structure and limited resources. From our results,

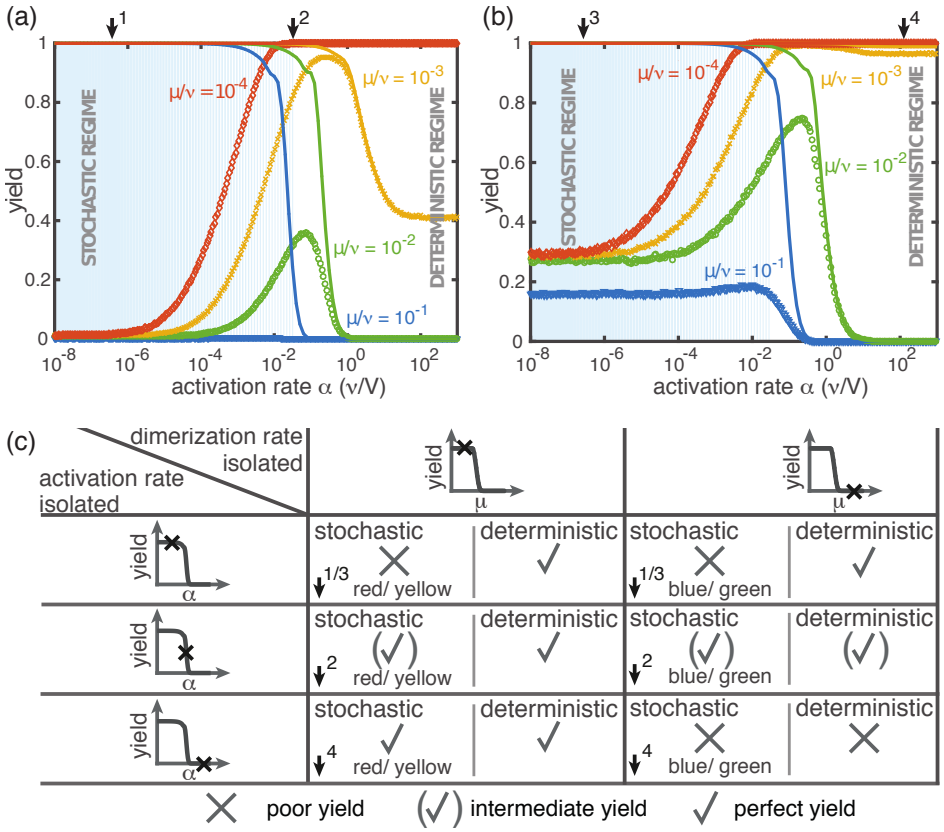

Figure 5. Yield for a combination of slow dimerization and activation. **(a, b)** Dependence of the yield of the fully heterogeneous system on the activation rate α for $N = 100$ and different values of the dimerization rate (colors/symbols) for $L = 60$ (a) and $L = 40$ (b) (averaged over 1024 ensembles). For large activation rates yield behaves deterministically (lines). In contrast, for small activation rates stochastic effects (blue shading) lead to a decrease in yield. Depending on the parameters, the yield maximum is attained in either the deterministic, stochastic or intermediate regime. **(c)** Table summarizing the qualitative behavior of the yield (poor/intermediate/perfect) for a combination of dimerization and activation rates for both the deterministic and the stochastic limit. The columns correspond to low and high values of the dimerization rate, as indicated by the marker in the corresponding deterministic yield curve at the top of the column. Similarly, the rows correspond to low, intermediate and high activation rates. Arrows and colors indicate where and for which curve this behavior can be observed in (a) and (b). Deviations between the deterministic and stochastic limits are most prominent for low activation rates.

we thus expect a stochastic yield catastrophe to be common to such systems. In order to further test this hypothesis, we simulated another variant of our model where finite sized squares assemble via monomer attachment from a pool of initially inactive particles, see Fig 7 . In contrast to the original model, the assembled structures are non-periodic and exhibit a non-linear assembly path where structures can grow independently in two dimensions. While the ring model assumes a sequential order of binding of the monomers, the square allows for a variety of distinct assembly paths that all lead to the same final structure. Note that, because of the absence of periodicity the square model is only well defined for the completely heterogeneous case. Figure 7 depicts the dependence of the yield on the activation rate for a square of size $S = 100$. Also in this case, we find that the yield saturates at an imperfect value for small activation rates. Hence, we showed that the stochastic yield catastrophe is not resolved neither by accounting for polymer-polymer combination nor by considering more general assembly processes with multiple parallel assembly paths. This observation supports the general validity of our findings and

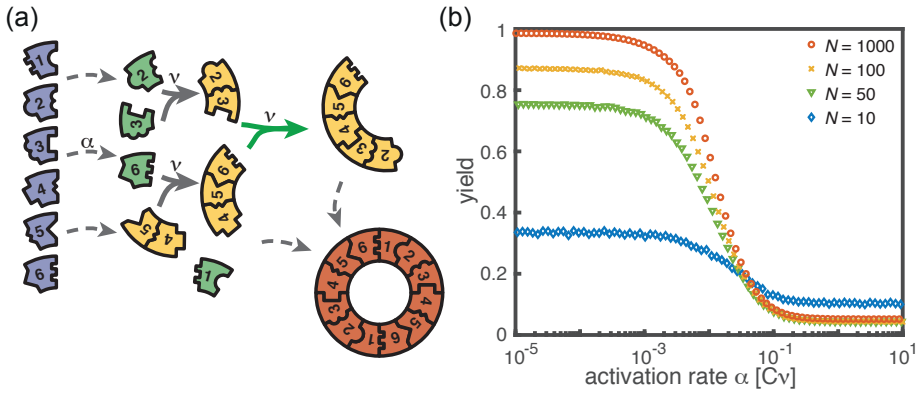

Figure 6. Extended model including polymer-polymer binding. **(a)** In the extended model, structures not only grow by monomer attachment but also by binding with another polymer (colored arrow). As before, binding only happens between periodically consecutive species with rate ν per binding site. So, the reaction rate for two polymers is identical to the one for monomer-polymer binding, ν. Furthermore, only polymers with combined length $\leq L$ can bind. All other processes and rules are the same as in the original model described in Fig. 1. **(b)** The yield of the extended model as obtained from stochastic simulations is shown in dependence of the activation rate α for $S = L = 100$, $\mu = \nu = 1$, $L_{\text{nuc}} = 2$ and different values of the number of particles per species, N averaged over 1024 ensembles). The qualitative behavior is the same as for the original model. In particular, yield saturates (in the stochastic limit) at an imperfect value for slow activation rates. Note that for small particle numbers polymer-polymer binding results in an increase of the minimal yield (here for large activation rates). This is due to the fact that even in the case where a priori too many nucleation events happen, polymers can combine into final structures.

indicates that stochastic yield catastrophes are a general phenomenon of (partially) irreversible and heterogeneous self-assembling systems that occur if particle number fluctuations are non-negligible.

4 Discussion

Our results show that different ways to slow down nucleation are indeed not equivalent, and that the explicit implementation is crucial for assembly efficiency. Susceptibility to stochastic effects is highly dependent on the specific scenario. Whereas systems for which dimerization limits nucleation are robust against stochastic effects, stochastic yield catastrophes can occur in heterogeneous systems when resource supply limits nucleation. The occurrence of stochastic yield catastrophes is not captured by the deterministic rate equations, for which the qualitative behavior of both scenarios is the same. Therefore, a stochastic description of the self-assembly process, which includes fluctuations in the availability of the different species, is required. The interplay between stochastic and deterministic dynamics can lead to a plethora of interesting behaviors. For example, the combination of slow activation and slow nucleation may result in a non-monotonic dependence of the yield on the activation rate. While deterministically, yield is always improved by decreasing the activation rate, stochastic fluctuations between species strongly suppress the yield for small activation rate by effectively enhancing the nucleation speed. This observation clearly demonstrates that a *deterministically* slow nucleation speed is not sufficient in order to obtain good yield in heterogeneous self-assembly. For example, a slow activation step does not necessarily result in few nucleation events although deterministically this behavior is expected. Thus, our results indicate that the slow nucleation principle has to be interpreted in terms of the stochastic framework and have important implications for yield optimization.

We showed that demographic noise can cause stochastic yield catastrophes in heterogeneous self-assembly. However, other types of noise, such as spatiotemporal fluctuations induced by diffusion,

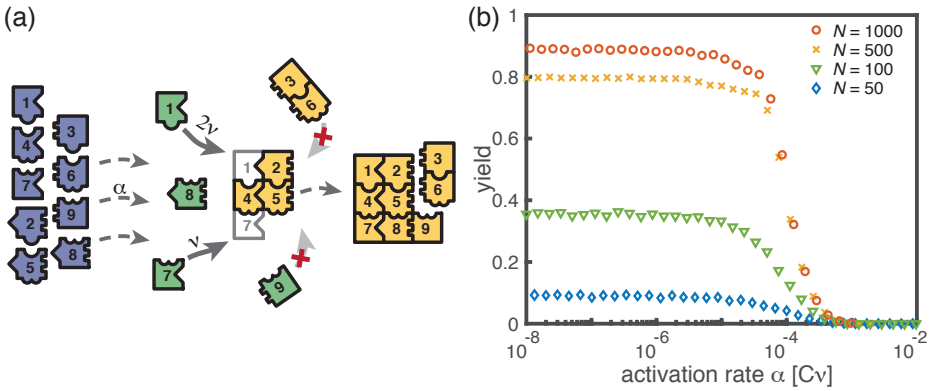

Figure 7. Assembly of squares of size $\sqrt{L} \times \sqrt{L}$ from L different particle species. **(a)** As in the ring models, there are N monomers of each species in the system. All particles are initially in an inactive state (blue) and are activated at the same per-capita rate α. Once active (green), species with neighboring position within the square (left/right, up/down) can bind to each other. Structures grow by attachment of single monomers until the square is complete (absorbing state). Depending on the number b of contacts between the monomer and the structure, the corresponding rate is $b\nu$. For simplicity, all polymers (yellow) are stable ($L_{\mathrm{nuc}} = 2$) and we do not consider polymer-polymer binding. **(b)** The yield of the square model as obtained from stochastic simulations is shown in dependence of the activation rate α for $S = L = 100$, $\mu = \nu = 1$ and different values of the number of particles per species, N (averaged over 256 ensembles). The qualitative behavior is the same as for the previous models: Whereas the yield is poor for large activation rates, it strongly increases below a threshold value and saturates (in the stochastic limit) at an imperfect value < 1 for small activation rates. The saturation value decreases with decreasing number of particles in the system.

are also expected to trigger stochastic yield catastrophes. Hence, our results have broad implications for complex biological and artificial systems, which typically exhibit various sources of noise. We characterize conditions under which stochastic yield catastrophes occur, and demonstrate how they can be mitigated. These insights could usefully inform the design of experiments to circumvent yield catastrophes: In particular, while slow provision of constituents is a feasible strategy for experiments, it is highly susceptible to stochastic effects. On the other hand, irrespective of its robustness to stochastic effects, the experimental realization of the dimerization scenario relies on cooperative or allosteric effects in binding, and may therefore require more sophisticated design of the constituents [34, 42]. Our theoretical analysis shows that stochasticity can be alleviated either by decreasing heterogeneity (presumably lowering realizable complexity) or by increasing reversibility (potentially requiring fine-tuning of bond strengths and reducing the stability of the assembly product). Alternative approaches to control stochasticity include the promotion of specific assembly paths [10, 30] and the control of fluctuations [13]. One possibility to test these ideas and the ensuing control strategies could be via experiments based on DNA origami. Instead of building homogeneous ring structures as in Ref. [36], one would have to design heterogeneous ring structures made from several different types of constituents with specified binding properties. By varying the opening angle of the "wedges" (and thus the preferred number of building blocks in the ring) and/or the number of constituents, both the target structure size L as well as the heterogeneity of the target structure S could be controlled.

Moreover, the ideas presented in this manuscript are relevant for the understanding of intracellular self-assembly. In cells, provision of building blocks is typically a gradual process, as synthesis is either inherently slow or an explicit activation step, such as phosphorylation, is required. In addition, the constituents of the complex structures assembled in cells are usually present in small numbers and subject to diffusion. Hence, stochastic yield catastrophes would be expected to have devastating consequences for self-assembly, unless the relevant cellular processes use elaborate control mechanisms to circumvent stochastic effects. Further exploration of these control mechanisms should enhance the

understanding of self-assembly processes in cells and help improve synthesis of complex nanostructures.

5 Methods and Materials

Here we show the derivation of Eq. 1 in the main text, giving the threshold values for the rate constants below which finite yield is obtained. The details can be found in the SI.

5.1 Master equation and chemical rate equations

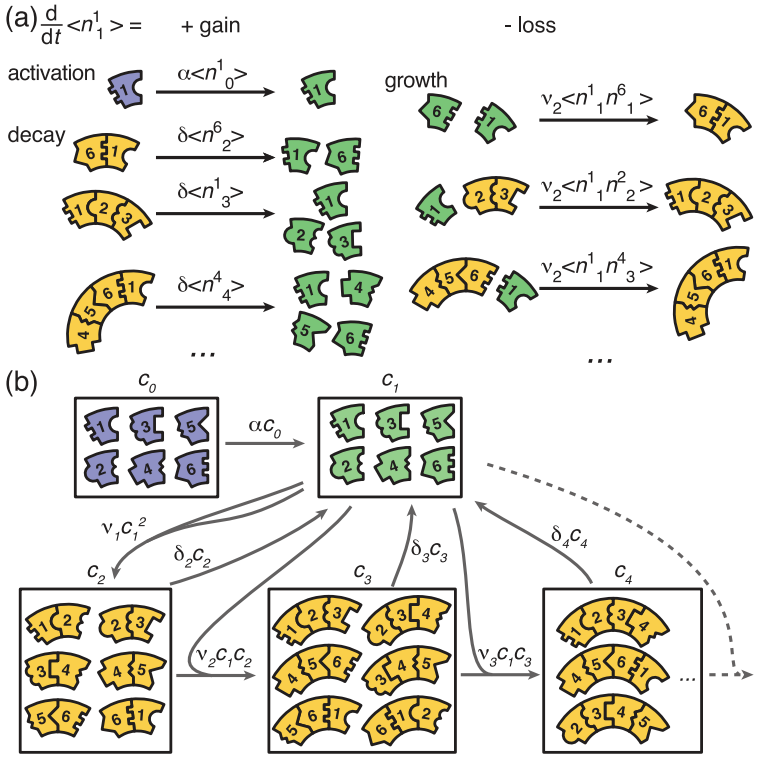

Figure 8. Graphical illustration of Eqs. (2) and (6). **(a)** Visualization of the gain and loss terms in the dynamics of the active monomers in Eq. (2b). Gain of active monomers is due to activation of inactive monomers as well as decay of unstable polymers. Loss of active monomers is due to dimerization and attachment of monomers to larger polymers. **(b)** Visualization of the transitions between clusters of different sizes (without distinction of species). The first and second box represent the active and inactive monomers in the system, the subsequent boxes each represent the ensamble of polymers of a certain size. The arrows between the boxes show possible reactions and transitions with the reaction rates indicated accordingly. Each arrow starting from or leading to a box is associated with a corresponding loss or gain term on the right hand side of Eq. 2 and Eq. 6.

We start with the general Master equation and derive the chemical rate equations (deterministic/mean-field equations) for the heterogeneous self-assembly process. We renounce to show the full Master equation here but instead state the system that describes the evolution of the first moments. To this end, we denote the random variable that describes the number of polymers of size ℓ and species s in the system at time t by $n_\ell^s(t)$ with $2 \leq \ell < L$ and $1 \leq s \leq S$. The species of a polymer is defined by the species of the respective monomer at its left end. Furthermore, n_0^s and n_1^s denote the number of inactive and active monomers of species s, respectively, and n_L the number of complete rings. We signify the reaction rate for binding of a monomer to a polymer of size ℓ by ν_ℓ. α denotes the

activation rate and δ_ℓ the decay rate of a polymer of size ℓ. By $\langle ... \rangle$ we indicate (ensemble) averages. The system governing the evolution of the first moments (the averages) of the $\{n_\ell^s\}$ is then given by:

$$\frac{d}{dt}\langle n_0^s \rangle = -\alpha \langle n_0^s \rangle , \tag{2a}$$

$$\frac{d}{dt}\langle n_1^s \rangle = \alpha \langle n_0^s \rangle - \sum_{\ell=1}^{L-1} \nu_\ell \left(\langle n_1^s n_\ell^{s+1} \rangle + \langle n_1^s n_\ell^{s-\ell} \rangle \right) + \sum_{\ell=2}^{L_{\mathrm{nuc}}-1} \sum_{k=s+1-\ell}^{k=s} \delta_\ell \langle n_\ell^k \rangle , \tag{2b}$$

$$\frac{d}{dt}\langle n_2^s \rangle = \nu_1 \langle n_1^s \, n_1^{s+1} \rangle - \nu_2 \langle n_2^s \, n_1^{s+2} \rangle - \nu_2 \langle n_2^s \, n_1^{s-1} \rangle - \delta_2 \langle n_2^s \rangle \, \mathbf{1}_{\{2<L_{\mathrm{nuc}}\}} , \tag{2c}$$

$$\frac{d}{dt}\langle n_\ell^s \rangle = \nu_{\ell-1} \langle n_{\ell-1}^s \, n_1^{\ell+s-1} \rangle + \nu_{\ell-1} \langle n_{\ell-1}^{s+1} \, n_1^s \rangle - \nu_\ell \langle n_\ell^s \, n_1^{s+\ell} \rangle - \nu_\ell \langle n_\ell^s \, n_1^{s-1} \rangle - \delta \langle n_\ell^s \rangle \, \mathbf{1}_{\{\ell<L_{\mathrm{nuc}}\}} , \tag{2d}$$

$$\frac{d}{dt}\langle n_L^s \rangle = \nu_{L-1} \langle n_{L-1}^s \, n_1^{L+s-1} \rangle + \nu_{L-1} \langle n_{L-1}^{s+1} \, n_1^s \rangle . \tag{2e}$$

The different terms of this equation are illustrated graphically in Figure 8. The first equation describes loss of inactive particles due to activation at rate α. Eq. (2b) gives the temporal change of the number of active monomers that is governed by the following processes: activation of inactive monomers at rate α, binding of active monomers to the left or to the right end of an existing structure of size ℓ at rate ν_ℓ, and decay of below-critical polymers of size ℓ into monomers at rate δ_ℓ (disassembly).

Equations (2c) and (2d) describe the dynamics of dimers and larger polymers of size $3 \leq \ell < L$, respectively. The terms account for reactions of polymers with active monomers (polymerization) as well as decay in the case of below-critical polymers (disassembly). The indicator function $\mathbf{1}_{\{x<L_{\mathrm{nuc}}\}}$ equals 1 if the condition $x < L_{\mathrm{nuc}}$ is satisfied and 0 otherwise. Note that a polymer of size $\ell \geq 3$ can grow by attaching a monomer to its left or to its right end whereas the formation of a dimer of a specific species is only possible via one reaction pathway (dimerization reaction). Finally, polymers of length L – the complete ring structures – form an absorbing state and, therefore, include only the respective gain terms (cf. Eq 2e).

We simulated the Master equation underlying Eq. (2) stochastically using Gillespie's algorithm. For the following deterministic analysis, we neglect correlations between particle numbers $\{n_\ell^s\}$, which is valid assumption for large particle numbers. Then the two-point correlator can be approximated as the product of the corresponding mean values (mean-field approximation)

$$\langle n_i^s n_j^k \rangle = \langle n_i^s \rangle \langle n_j^k \rangle \ \forall s, k \tag{3}$$

Furthermore, for the expectation values it must hold

$$\langle n_\ell^s \rangle = \langle n_\ell^1 \rangle \ \forall s \tag{4}$$

because all species have equivalent properties (there is no distinct species) and hence the system is invariant under relabelling of the upper index. By

$$c_\ell := \frac{\langle n_\ell^s \rangle}{V}, \tag{5}$$

we denote the concentration of any monomer or polymer species of size ℓ, where V is the reaction volume. Due to the symmetry formulated in Eq. (4), the heterogeneous assembly process decouples into a set of S identical and independent homogeneous assembly processes in the deterministic limit. The corresponding homogeneous system then is described by the following set of equations that is obtained

by applying (3), (4) and (5) to (2)

$$\frac{d}{dt}c_0 = -\alpha\, c_0\,, \tag{6a}$$

$$\frac{d}{dt}c_1 = \alpha\, c_0 - 2c_1 \sum_{\ell=1}^{L-1} \nu_\ell\, c_\ell + \sum_{\ell=2}^{L_{\rm nuc}-1} l\, \delta_\ell\, c_\ell\,, \tag{6b}$$

$$\frac{d}{dt}c_2 = \nu_1\, c_1^2 - 2\,\nu_2\, c_1\, c_2 - \delta_2\, c_2\, \mathbf{1}_{\{2<L_{\rm nuc}\}}\,, \tag{6c}$$

$$\frac{d}{dt}c_\ell = 2\,\nu_{\ell-1}\, c_1\, c_{\ell-1} - 2\nu_\ell\, c_1\, c_\ell - \delta_\ell\, c_\ell\, \mathbf{1}_{\{\ell<L_{\rm nuc}\}}\,, \qquad \text{for } 3 \le \ell < L\,, \tag{6d}$$

$$\frac{d}{dt}c_L = 2\,\nu_{L-1}\, c_1\, c_{L-1}\,. \tag{6e}$$

The rate constants ν_ℓ in Eq. (6) and (2) differ by a factor of V. For convenience, we use however the same symbol in both cases. The rate constants ν_ℓ in Eq. (6) can be interpreted in the usual units $[\frac{\text{liter}}{\text{mol sec}}]$. Due to the symmetry, the yield, which is given by the quotient of the number of completely assembled rings and the maximum number of complete rings, becomes independent of the number of species S

$$\text{yield(t)} = \frac{Sc_L(t)V}{SNL^{-1}} = \frac{c_L(t)VL}{N}\,. \tag{7}$$

Hence, it is enough to study the dynamics of the homogeneous system, Eq. (6), to identify the condition under which non zero yield is obtained.

5.2 Effective description by an advection-diffusion equation

The dynamical properties of the evolution of the polymer-size distribution become evident if the set of ODEs (6) is rewritten as a partial differential equation. This approach was previously described in the context of virus capsid assembly [29, 45].

For simplicity, we restrict ourselves to the case $L_{\rm nuc} = 2$ and let $\nu_1 = \mu$ and $\nu_{\ell\ge 2} = \nu$. Then, for the polymers with $\ell > 2$ we have

$$\partial_t c_\ell = 2\nu c_1\, \left[c_{\ell-1} - c_\ell\right]. \tag{8}$$

As a next step, we approximate the index $\ell \in \{2, 3, \ldots, L\}$ indicating the length of the polymer as a continuous variable $x \in [2, L]$ and define $c(x = \ell) := c_\ell$. By $A := c_1$ we denote the concentration of active monomers in the following to emphasize their special role. Formally expanding the right-hand side of Eq. (8) in a Taylor series up to second order

$$c(\ell - 1) = c(\ell) - \partial_x c(\ell) + \frac{1}{2}\partial_x^2 c(\ell)\,, \tag{9}$$

one arrives at the advection-diffusion equation with both advection and diffusion coefficients depending on the concentration of active monomers $A(t)$

$$\partial_t c(x) = -2\nu A\, \partial_x c(x) + \nu A\, \partial_x^2 c(x)\,. \tag{10}$$

Equation (10) can be written in the form of a continuity equation $\partial_t c(x) = -\partial_x J(x)$ with flux $J = 2\nu A\; c - \nu A\; \partial_x c$. The flux at the left boundary $x = 2$ equals the influx of polymers due to dimerization of free monomers $J(2, t) = \mu A^2$. This enforces a Robin boundary condition at $x = 2$

$$2\nu A\; c(2, t) - \nu A\; \partial_x c(2, t) = \mu A^2\,. \tag{11}$$

At $x = L$ we set an absorbing boundary $c(L, t) = 0$ so that completed structures are removed from the system. The time evolution of the concentration of active monomers is given by

$$\partial_t A = \alpha C e^{-\alpha t} - 2\mu A^2 - 2\nu A \int_2^L c(x, t)\, dx\,. \tag{12}$$

The terms on the right-hand side account for activation of inactive particles, dimerization, and binding of active particles to polymers (polymerization).

Qualitatively, Eq. (10) describes a profile that emerges at $x=2$ from the boundary condition Eq. (11) moves to the right with time-dependent velocity $2\nu A(t)$ due to the advection term, and broadens with a time-dependent diffusion coefficient $\nu A(t)$. In the SI we show how the full solution of Eqs. (10) and (11) can be found assuming knowledge of $A(t)$. Here, we focus only on the derivation of the threshold activation rate and threshold dimerization rate that mark the onset of non-zero yield.

Yield production starts as soon as the density wave reaches the absorbing boundary at $x=L$. Therefore, finite yield is obtained if the sum of the advectively travelled distance d_{adv} and the diffusively travelled distance d_{diff} exceeds the system size $L-2$

$$d_{\mathrm{adv}} + d_{\mathrm{diff}} \geq L - 2\,. \tag{13}$$

According to Eq. (10), $d_{\mathrm{adv}} = 2\nu \int_0^\infty A(t)dt$ and $d_{\mathrm{diff}} = \sqrt{2\nu \int_0^\infty A(t)dt}$, giving as condition for the onset of finite yield

$$2\nu \int_0^\infty A(t)dt \stackrel{!}{=} \frac{1}{4}\left(\sqrt{1+4(L-2)}-1\right)^2 \approx L - \sqrt{L}\,, \tag{14}$$

where the last approximation is valid for large L.

In order to obtain $\int_0^\infty A(t)dt$ we derive an effective two-component system that governs the evolution of $A(t)$. To this end, we denote the total number of polymers in Eq. (12) by $B(t) := \int_2^\infty c(x,t)\,dx$ (as long as yield is zero the upper boundary is irrelevant and we can consider $L=\infty$). Eq. (12) then reads

$$\frac{d}{dt}A = \alpha C e^{-\alpha t} - 2\mu A^2 - 2\nu AB\,, \tag{15}$$

and the dynamics of B is determined from the boundary condition, Eq. (11)

$$\frac{d}{dt}B = \int_2^\infty \partial_t c(x,t)\,dx = \int_2^\infty -\partial_x J(x,t)\,dx = -\underbrace{J(\infty,t)}_{=0} + J(2,t) = \mu A(t)^2. \tag{16}$$

Measuring A and B in units of the initial monomer concentration C and time in units of $(\nu C)^{-1}$ the equations are rewritten in dimensionless units as

$$\frac{d}{dt}A = \omega e^{-\omega t} - 2\eta A^2 - 2A\ B\,, \tag{17a}$$

$$\frac{d}{dt}B = \eta A^2\,, \tag{17b}$$

where $\omega = \frac{\alpha}{\nu C}$ and $\eta = \frac{\mu}{\nu}$. Eq. (17) describes a closed two-component system for the concentration of active monomers A and the total concentration of polymers B. It describes the dynamics exactly as long as yield is zero. In order to evaluate the condition (14) we need to determine the integral over $A(t)$ as a function of ω and η

$$\int_0^\infty A_{\omega,\eta}(t)dt := g(\omega,\eta)\,. \tag{18}$$

To that end, we proceed by looking at both scenarios separately. The numerical analysis, confirming our analytic results, is given in the SI.

5.3 Dimerization scenario

The activation rate in the dimerization scenario is $\alpha \to \infty$, and instead of the term $\omega e^{-\omega t}$ in $\mathrm{d}A/\mathrm{d}t$, we set the initial condition $A(0) = 1$ (and $B(0) = 0$). Furthermore, $\eta = \mu/\nu \ll 1$ and we can neglect the term proportional to η in $\mathrm{d}A/\mathrm{d}t$. As a result,

$$\frac{\mathrm{d}A}{\mathrm{d}B} = -\frac{2B}{\eta A}.$$

Solving this equation for A as a function of B using the initial condition $A(B = 0) = 1$, the totally travelled distance of the wave is determined to be

$$2g(\omega, \eta) = 2\frac{\pi}{2\sqrt{2}}\frac{1}{\sqrt{\eta}}, \tag{19}$$

where for the evaluation of the integral we used the substitution $\eta A^2 \mathrm{d}t = \mathrm{d}B$.

5.4 Activation scenario

In the activation scenario, yield sets in only if the activation rate and thus the effective nucleation rate is slow. As a result, in addition to $\omega \ll 1$, we can again neglect the term proportional to η in $\mathrm{d}A/\mathrm{d}t$. This time, however, we have to keep the term $\omega e^{-\omega t}$. As a next step, we assume that $\mathrm{d}A/\mathrm{d}t$ is much smaller than the remaining terms on the right-hand side, $\omega e^{-\omega t}$ and $-2AB$. This assumption might seem crude at first sight but is justified *a posteriori* by the solution of the equation (see SI). Hence, we get the algebraic equation $A(t) = \omega e^{-\omega t}/(2B(t))$. Using it to solve $\mathrm{d}B/\mathrm{d}t = \eta A^2$ for B, and then to determine A, the totally travelled distance of the wave is deduced as

$$2g(\omega, \eta) = 2\frac{3^{2/3}\sqrt{\pi}\Gamma(2/3)}{6\Gamma(7/6)}(\omega\eta)^{-1/3}. \tag{20}$$

Taken together, we therefore obtain two conditions out of which one must be fulfilled in order to obtain finite yield

$$2a(\eta\omega)^{-\frac{1}{3}} \geq L - \sqrt{L} \quad \Rightarrow \quad \alpha < \alpha_{\mathrm{th}} := P_\alpha \frac{\nu}{\mu}\frac{\nu C}{(L - \sqrt{L})^3} \tag{21}$$

$$\text{or} \quad 2b\eta^{-\frac{1}{2}} \geq L - \sqrt{L} \quad \Rightarrow \quad \mu < \mu_{\mathrm{th}} := P_\mu \frac{\nu}{(L - \sqrt{L})^2}\,, \tag{22}$$

where a and b are numerical factors, and $P_\alpha = 8a^3 \approx 5.77$ and $P_\mu = 4b^2 \approx 4.93$. This verifies Eq. (1) in the main text.

6 Acknowledgments

We thank Nigel Goldenfeld for a stimulating discussion, and Raphaela Geßele and Laeschkir Hassan for helpful feedback on the manuscript. This research was supported by the German Excellence Initiative via the program 'NanoSystems Initiative Munich'(NIM) and was funded by the Deutsche Forschungsgemeinschaft (DFG, German Research Foundation) under Germany's Excellence Strategy – EXC-2094 – 390783311. F.M.G. and I.R.G. are supported by a DFG fellowship through the Graduate School of Quantitative Biosciences Munich (QBM). We also gratefully acknowledge financial support by the DFG Research Training Group GRK2062 (Molecular Principles of Synthetic Biology). Finally, E.F. thanks the Aspen Center for Physics, which is supported by National Science Foundation grant PHY-1607611, for their hospitality and inspiring discussions with colleagues.

References

1. See Supplementary Information.

2. Bruce Alberts, Alexander Johnson, Julian Lewis, David Morgan, Martin Raff, Keith Roberts, Peter Walter, John Wilson, and Tim Hunt. *Molecular Biology of the Cell*. Garland Science, 2015.

3. Chao Chen, C Cheng Kao, and Bogdan Dragnea. Self-assembly of brome mosaic virus capsids: insights from shorter time-scale experiments. *The Journal of Physical Chemistry A*, 112(39):9405–9412, 2008.

4. Fabienne FV Chevance and Kelly T Hughes. Coordinating assembly of a bacterial macromolecular machine. *Nature Reviews Microbiology*, 6(6):455, 2008.

5. Maria R D'Orsogna, Qi Lei, and Tom Chou. First assembly times and equilibration in stochastic coagulation-fragmentation. *The Journal of chemical physics*, 143(1):014112, 2015.

6. Maria R D'Orsogna, Bingyu Zhao, Bijan Berenji, and Tom Chou. Combinatoric analysis of heterogeneous stochastic self-assembly. *The Journal of chemical physics*, 139(12):121918, 2013.

7. MR D'Orsogna, Greg Lakatos, and Tom Chou. Stochastic self-assembly of incommensurate clusters. *The Journal of chemical physics*, 136(8):084110, 2012.

8. D Allan Drummond and Claus O Wilke. The evolutionary consequences of erroneous protein synthesis. *Nature Reviews Genetics*, 10(10):715–724, 2009.

9. Dan Endres and Adam Zlotnick. Model-based analysis of assembly kinetics for virus capsids or other spherical polymers. *Biophysical journal*, 83(2):1217–1230, 2002.

10. Florian M Gartner, Isabella R Graf, and Erwin Frey. Controlling fidelity and time efficiency in self-assembly. *in preparation*, 2019.

11. Thomas Gerling, Klaus F Wagenbauer, Andrea M Neuner, and Hendrik Dietz. Dynamic dna devices and assemblies formed by shape-complementary, non–base pairing 3d components. *Science*, 347(6229):1446–1452, 2015.

12. Daniel T Gillespie. Stochastic simulation of chemical kinetics. *Annu. Rev. Phys. Chem.*, 58:35–55, 2007.

13. Isabella R Graf, Florian M Gartner, and Erwin Frey. Understanding and guiding robust self-assembly of heterogeneous structures. *in preparation*, 2019.

14. James Grant, Robert L Jack, and Stephen Whitelam. Analyzing mechanisms and microscopic reversibility of self-assembly. *The Journal of chemical physics*, 135(21):214505, 2011.

15. Michael F Hagan. Modeling viral capsid assembly. *Advances in chemical physics*, 155:1, 2014.

16. Michael F Hagan and Oren M Elrad. Understanding the concentration dependence of viral capsid assembly kinetics - the origin of the lag time and identifying the critical nucleus size. *Biophysical journal*, 98(6):1065–1074, 2010.

17. Michael F Hagan, Oren M Elrad, and Robert L Jack. Mechanisms of kinetic trapping in self-assembly and phase transformation. *The Journal of chemical physics*, 135(10):104115, 2011.

18. Thomas K Haxton and Stephen Whitelam. Do hierarchical structures assemble best via hierarchical pathways? *Soft Matter*, 9(29):6851–6861, 2013.

19. Lester O Hedges, Ranjan V Mannige, and Stephen Whitelam. Growth of equilibrium structures built from a large number of distinct component types. *Soft Matter*, 10(34):6404–6416, 2014.

20. William M Jacobs and Daan Frenkel. Self-assembly protocol design for periodic multicomponent structures. *Soft Matter*, 11(46):8930–8938, 2015.

21. William M Jacobs, Aleks Reinhardt, and Daan Frenkel. Rational design of self-assembly pathways for complex multicomponent structures. *Proceedings of the National Academy of Sciences*, 112(20):6313–6318, 2015.

22. Mathias Jucker and Lary C Walker. Self-propagation of pathogenic protein aggregates in neurodegenerative diseases. *Nature*, 501(7465):45–51, 2013.

23. Yonggang Ke, Luvena L Ong, William M Shih, and Peng Yin. Three-dimensional structures self-assembled from dna bricks. *Science*, 338(6111):1177–1183, 2012.

24. Pavel L Krapivsky, Sidney Redner, and Eli Ben-Naim. *A kinetic view of statistical physics*. Cambridge University Press, 2010.

25. Guillermo R Lazaro and Michael F Hagan. Allosteric control of icosahedral capsid assembly. *The Journal of Physical Chemistry B*, 120(26):6306–6318, 2016.

26. Petr G Leiman, Fumio Arisaka, Mark J Van Raaij, Victor A Kostyuchenko, Anastasia A Aksyuk, Shuji Kanamaru, and Michael G Rossmann. Morphogenesis of the t4 tail and tail fibers. *Virology journal*, 7(1):355, 2010.

27. Thomas CT Michaels, Mathias MJ Bellaiche, Michael F Hagan, and Tuomas PJ Knowles. Kinetic constraints on self-assembly into closed supramolecular structures. *Scientific Reports*, 7(1):12295, 2017.

28. Thomas CT Michaels, Alexander J Dear, Julius B Kirkegaard, Kadi L Saar, David A Weitz, and Tuomas PJ Knowles. Fluctuations in the kinetics of linear protein self-assembly. *Phys. Rev. Lett.*, 116(25):258103, 2016.

29. Alexander Yu Morozov, Robijn F Bruinsma, and Joseph Rudnick. Assembly of viruses and the pseudo-law of mass action. *The Journal of chemical physics*, 131(15):10B607, 2009.

30. Arvind Murugan, James Zou, and Michael P Brenner. Undesired usage and the robust self-assembly of heterogeneous structures. *Nature Communications*, 6:6203, 2015.

31. Cohue Pena, Ed Hurt, and Vikram Govind Panse. Eukaryotic ribosome assembly, transport and quality control. *Nature structural & molecular biology*, 24(9):689, 2017.

32. Florian Praetorius and Hendrik Dietz. Self-assembly of genetically encoded dna-protein hybrid nanoscale shapes. *Science*, 355(6331):eaam5488, 2017.

33. Aleks Reinhardt and Daan Frenkel. Numerical evidence for nucleated self-assembly of dna brick structures. *Phys. Rev. Lett.*, 112(23):238103, 2014.

34. Stefano Sacanna, WTM Irvine, Paul M Chaikin, and David J Pine. Lock and key colloids. *Nature*, 464(7288):575–578, 2010.

35. Richard P Sear. Nucleation: theory and applications to protein solutions and colloidal suspensions. *Journal of Physics: Condensed Matter*, 19(3):033101, 2007.

36. Klaus F Wagenbauer, Christian Sigl, and Hendrik Dietz. Gigadalton-scale shape-programmable dna assemblies. *Nature*, 552(7683):78–83, 2017.

37. Bryan Wei, Mingjie Dai, and Peng Yin. Complex shapes self-assembled from single-stranded dna tiles. *Nature*, 485(7400):623, 2012.

38. Stephen Whitelam. Hierarchical assembly may be a way to make large information-rich structures. *Soft Matter*, 11(42):8225–8235, 2015.

39. George M Whitesides and Bartosz Grzybowski. Self-assembly at all scales. *Science*, 295(5564):2418–2421, 2002.

40. George M Whitesides, John P Mathias, and Christopher T Seto. Molecular self-assembly and nanochemistry: a chemical strategy for the synthesis of nanostructures. *Science*, 254(5036):1312–1319, 1991.

41. Romain Yvinec, Maria R D'Orsogna, and Tom Chou. First passage times in homogeneous nucleation and self-assembly. *The Journal of chemical physics*, 137(24):244107, 2012.

42. Zorana Zeravcic, Vinothan N Manoharan, and Michael P Brenner. Colloquium: Toward living matter with colloidal particles. *Reviews of Modern Physics*, 89(3):031001, 2017.

43. Shuguang Zhang. Fabrication of novel biomaterials through molecular self-assembly. *Nature Biotechnology*, 21(10):1171–1178, 2003.

44. Adam Zlotnick. Are weak protein–protein interactions the general rule in capsid assembly? *Virology*, 315(2):269–274, 2003.

45. Adam Zlotnick, Jennifer M Johnson, Paul W Wingfield, Stephen J Stahl, and Dan Endres. A theoretical model successfully identifies features of hepatitis b virus capsid assembly. *Biochemistry*, 38(44):14644–14652, 1999.

Supplementary Information for

'Stochastic Yield Catastrophes and Robustness in Self-Assembly'

Florian M. Gartner,* Isabella R. Graf,* Patrick Wilke,* Philipp M. Geiger, and Erwin Frey†
Arnold Sommerfeld Center for Theoretical Physics and Center for NanoScience,
Department of Physics, Ludwig-Maximilians-Universität München,
Theresienstraße 37, D-80333 München, Germany

* These authors contributed equally.
† frey@lmu.de

CONTENTS

A. CHEMICAL REACTION EQUATIONS AND THE EQUIVALENCE OF MODELS WITH DIFFERENT NUMBERS OF SPECIES

In this section we derive the chemical rate equations (deterministic equations) for the self-assembly process as described in the main text. Furthermore, we show that for general S in the deterministic limit the model is equivalent to a set of S independent assembly processes with only one species.

Homogeneous structures

First, we consider the homogeneous model ($S=1$). By $c_\ell(t)$ we denote the concentration of complexes of length ℓ ($\ell \geq 2$) at time t, $c_1(t)$ is the concentration of active monomers and $c_0(t)$ the concentration of inactive monomers at time t. In the following we will usually skip the time argument for better readability. We denote the reaction rate for binding of a monomer to a polymer of size ℓ by ν_ℓ. The model from the main text is recovered by setting $\nu_\ell := \mu_\ell$ if $\ell < L_{\text{nuc}}$, and $\nu_\ell := \nu$ otherwise. The ensuing set of ordinary differential equations then reads:

$$\frac{d}{dt}c_0 = -\alpha\, c_0\,, \tag{1a}$$

$$\frac{d}{dt}c_1 = \alpha\, c_0 - 2c_1 \sum_{\ell=1}^{L-1} \nu_\ell\, c_\ell + \sum_{\ell=2}^{L_{\text{nuc}}-1} l\, \delta_\ell\, c_\ell\,, \tag{1b}$$

$$\frac{d}{dt}c_2 = \nu_1\, c_1^2 - 2\,\nu_2\, c_1\, c_2 - \delta_2\, c_2\, \mathbf{1}_{\{2<L_{\text{nuc}}\}}\,, \tag{1c}$$

$$\frac{d}{dt}c_\ell = 2\,\nu_{\ell-1}\, c_1\, c_{\ell-1} - 2\nu_\ell\, c_1\, c_\ell - \delta_\ell\, c_\ell\, \mathbf{1}_{\{\ell<L_{\text{nuc}}\}}\,, \qquad \text{for } 3 \leq \ell < L\,, \tag{1d}$$

$$\frac{d}{dt}c_L = 2\,\nu_{L-1}\, c_1\, c_{L-1}\,. \tag{1e}$$

The indicator function $\mathbf{1}_{\{x<L_{\text{nuc}}\}}$ equals 1 if the condition $x < L_{\text{nuc}}$ is satisfied and 0 otherwise. The first equation describes loss of inactive particles due to activation at rate α. The equation is uncoupled from the remainder of the equations and is solved by $c_0(t) = Ce^{-\alpha t}$, with C denoting the initial concentration of inactive monomers. The temporal change of the active monomers is governed by the following processes (Eq. (1b)): activation of inactive monomers at rate α, binding of active monomers to existing structures at rate ν_ℓ (polymerization), and decay of below-critical polymers into monomers at rate δ_ℓ (disassembly). All binding rates appear with a factor of 2 because a monomer can attach to a polymer on its left or on its right end.

Note that there is a subtlety with the dimerization term "$2\,\nu_1\, c_1^2$": the dimerization term as well bears a factor of 2 because two identical monomers A and B can form a dimer in two possible ways, either as AB or BA. Additionally, there is a stoichiometric factor of 2 for this reaction. However, one factor of 2 is cancelled again because, assuming there

are n monomers, the number of ordered pairs of monomers that describe possible reaction partners is $\frac{1}{2}n(n-1) \approx n^2/2$ (if n is large) rather than n^2 (the number of reaction partners when two different species react). This leaves us with a single factor of 2 like for all the other binding reactions.

Equations (1c) and (1d) describe the dynamics of dimers and larger polymers of size $3 \leq \ell < L$, respectively. The terms account for reactions of polymers with active monomers (polymerization) as well as decay in the case of below-critical polymers (disassembly). The dimerization term in the equation for $\partial_t c_2$ lacks the factor of 2 because the stoichiometric factor is missing as compared with the dimerization term in the line above. Finally, polymers of length L – the complete ring structures – form an absorbing state and therefore only include a reactive gain term (Eq. (1e)).

Heterogeneous structures

Next we consider systems with more than one particle species ($S > 1$). The heterogeneous system can be described by dynamical equations equivalent to the homogeneous system. We show this starting from a full description that distinguishes both monomers and polymers into a set of different species $1, \ldots, S$. In order to formulate the dynamic equations and to see the equivalence to a one-species model, we distinguish both monomers and polymers into a set of different species $1, \ldots, S$. The species of a polymer is defined by the species of the respective monomer at its left end. As polymers assemble in consecutive order of species, a polymer is uniquely determined by its length and species (i.e. species of leftmost monomer). In that sense, c_ℓ^s with $0 \leq \ell < L$ and $1 \leq s \leq S$ denotes the concentration of a polymer of length ℓ and species s (c_0^s and c_1^s again denote inactive and active monomers of species s, respectively). For example, c_4^5 denotes the concentration of polymers [5678] if $S \geq 8$, or of polymers [5612] if $S = 6$. Upper indices are always assumed to be taken modulo S whenever they lie outside the range $[1, S]$. Therefore, the dynamics of the concentrations c_ℓ^s with $3 \leq \ell < L$ is given by

$$\frac{d}{dt}c_\ell^s = \nu_{\ell-1}\, c_{\ell-1}^s\, c_1^{\ell+s-1} + \nu_{\ell-1}\, c_{\ell-1}^{s+1}\, c_1^s - \nu_\ell\, c_\ell^s\, c_1^{s+\ell} - \nu_\ell\, c_\ell^s\, c_1^{s-1} - \delta\, c_\ell^s\, \mathbf{1}_{\{\ell<L_{\mathrm{nuc}}\}}\,. \tag{2}$$

The terms on the right-hand side account for the influx due to binding of the respective polymers of length $\ell - 1$ with a monomer either on the right or on the left (first and second term), and for the outflux due to reactions of a polymer of length ℓ and species s (third and fourth term), as well as for decay into monomers for $\ell < L_{\mathrm{nuc}}$ (last term). For the dynamics of the dimers, however, there is only one gain term arising from dimerization:

$$\frac{d}{dt}c_2^s = \nu_1\, c_1^s\, c_1^{s+1} - \nu_2\, c_2^s\, c_1^{s+2} - \nu_2\, c_2^s\, c_1^{s-1} - \delta_2\, c_2^s\, \mathbf{1}_{\{2<L_{\mathrm{nuc}}\}}\,. \tag{3}$$

Equivalently, for the active monomers we find:

$$\frac{d}{dt}c_1^s = \alpha\, C e^{-\alpha t} - c_1^s \sum_{\ell=1}^{L-1} \nu_\ell \left(c_\ell^{s+1} + c_\ell^{s-\ell}\right) + \sum_{\ell=2}^{L_{\mathrm{nuc}}-1} \sum_{k=s+1-\ell}^{k=s} \delta_\ell c_\ell^k\,. \tag{4}$$

Now we exploit the symmetry of the system with respect to the species index, that is, the upper index in $\{c_\ell^s\}$: Since all species in the system are equivalent, the dynamic equations are invariant under relabelling of the upper indices. Consequently, it must hold that:

$$c_\ell^s(t) = c_\ell^k(t), \qquad \text{for any } s, k \leq S \text{ at any time } t. \tag{5}$$

In other words, the upper index is irrelevant and can also be discarded. The variable c_ℓ then denotes the concentration of *any* one polymer species of length ℓ. Taking advantage of this symmetry for the equations of the heterogeneous system, (Eq. (2), Eq. (3) and Eq. (4)), and collecting equal terms leads to a set of equations fully identical to those for the homogeneous system (Eq. (1)). We show the equivalence to the homogeneous model exemplarily for the dynamics of the polymers with size $\ell \geq 3$ in Eq. (2). Applying $c_\ell^s(t) = c_\ell(t)$ to Eq. (2) yields for the dynamics of the concentration of an arbitrary polymer species of size ℓ:

$$\begin{aligned}\frac{d}{dt}c_\ell &= \nu_{\ell-1}\, c_{\ell-1}\, c_1 + \nu_{\ell-1}\, c_{\ell-1}\, c_1 - \nu_\ell\, c_\ell\, c_1 - \nu_\ell\, c_\ell\, c_1 - \delta\, c_\ell\, \mathbf{1}_{\{\ell<L_{\text{nuc}}\}}\,. \\ &= 2\nu_{\ell-1}\, c_{\ell-1}\, c_1 - 2\nu_\ell\, c_\ell\, c_1 - \delta\, c_\ell\, \mathbf{1}_{\{\ell<L_{\text{nuc}}\}},\end{aligned}$$

which is identical to the respective dynamic equation (1d) for the homogeneous model. The other equations for the heterogeneous system reduce to those for the homogeneous system in an analogous manner.

Summarizing, we have shown that the (deterministic) heterogeneous assembly process decouples into a set of S identical and independent homogeneous processes. In particular, yield, which is given by the quotient of the number of completely assembled rings and the maximal possible number of complete rings, becomes independent of S:

$$\text{yield(t)} = \frac{Sc_L(t)}{SNL^{-1}} = \frac{c_L(t)L}{N}\,. \tag{6}$$

B. EFFECTIVE DESCRIPTION OF THE EVOLUTION OF THE POLYMER SIZE DISTRIBUTION AS AN ADVECTION-DIFFUSION EQUATION

The dynamical properties of the evolution of the polymer size distribution become evident if the set of ODEs (1) is rewritten as a partial differential equation. This approach was previously described in the context of virus capsid assembly[9,45] but we will restate the essential steps here for the convenience of the reader. To this end we interpret the length index of the polymer $\ell \in \{2, 3, \ldots, L\}$ as a continuous variable that we rename $x \in [2, L]$. With such a continuous description in view we write $c(x = \ell) := c_\ell$ to denote the concentration of polymers of size ℓ.

Since the active monomers play a special role, we denote their concentration in the following by A. For simplicity we restrict our discussion to the case $L_{\text{nuc}} = 2$ and let $\nu_1 = \mu$ and $\nu_{\ell\geq 2} = \nu$. Generalizations to $L_{\text{nuc}} > 2$ can be done in a similar way. Then, for the polymers with $\ell \geq 3$ we have:

$$\partial_t c(\ell) = 2\nu A\, \big[c(\ell-1) - c(\ell)\big]\,. \tag{7}$$

Formally, expanding the right-hand side in a Taylor series up to second order

$$c(\ell-1) = c(\ell) - \partial_x c(\ell) + \frac{1}{2}\partial_x^2 c(\ell)\,, \tag{8}$$

we arrive at an advection-diffusion equation with both advection and diffusion coefficients depending on the concentration of active monomers $A(t)$,

$$\partial_t c(x) = -2\nu A\,\partial_x c(x) + \nu A\,\partial_x^2 c(x)\,. \tag{9}$$

Equation (9) can be written in the form of a continuity equation $\partial_t c(x) = -\partial_x J(x)$ with flux $J = 2\nu A\ c - \nu A\ \partial_x c$. The flux at the left boundary, $x = 2$, equals the influx of polymers due to dimerization of free monomers, $J(2,t) = \mu A^2$. This enforces a Robin boundary condition at $x = 2$,

$$2\nu A\ c(2,t) - \nu A\ \partial_x c(2,t) = \mu A^2\,. \tag{10}$$

At $x = L$, we have an absorbing boundary $c(L,t) = 0$ so that completed structures are removed from the system. Furthermore, the time evolution of the concentration of active particles is given by

$$\partial_t A = \alpha C e^{-\alpha t} - 2\mu A^2 - 2\nu A \int_2^L c(x,t)\,dx\,. \tag{11}$$

The terms on the right-hand side account for activation of inactive particles, dimerization, and binding of active particles to polymers (polymerization).

Qualitatively, Eq. (9) describes a profile that emerges at $x = 2$ from the boundary condition, Eq. (10), moves to the right with time dependent velocity $2\nu A(t)$ due to the advection term, and broadens with a time-dependent diffusion coefficient $\nu A(t)$. The concentration of active particles A determines both the influx of dimers at $x = 2$, as well as the speed and diffusion of the wave profile.

Next, we derive an expression that solves Eq. (9), assuming that we know $A(t)$. We start by solving Eq. (9) at the left boundary $c(2,t)$, and then translate the resulting expression to obtain a solution for $c(x,t)$. To obtain $c(2,t)$ in dependence of $a(t)$ we can solve $\frac{d}{dt}c(2,t) = \mu A^2 - \nu A c(2,t)$ (see Eq. (1c)) by 'variation of the constants' as

$$c(2,t) = \int_0^t \mu A(\tilde{t})^2 \exp\left[-\int_{\tilde{t}}^t \nu A(t')dt'\right] d\tilde{t}\,. \tag{12}$$

With help of this expression we find $c(x,t)$: Given $c(2,t)$, the advective part of Eq. (9),

$$\partial_t \tilde{c}(x) = -2\nu A\,\partial_x \tilde{c}(x)\,. \tag{13}$$

is solved by

$$c_{\text{advec}}(x,t) = c(2,\tau(x,t))\,. \tag{14}$$

Here, $\tau(x,t)$ denotes the time that a particle at position x and time t was at $x=2$. In other words, a particle at time t and position x has entered the system at $x=2$ at time $\tau(x,t)$. This ansatz solves the PDE (Eq. (13)) if and only if $\tau(x,t)$ satisfies

$$\tau(x,t) = \tilde{A}^{-1}\left(\tilde{A}(t) - \frac{x-2}{2\nu}\right) \tag{15}$$

with $\tilde{A}$ being an arbitrary integral of A such that $\partial_t \tilde{A}(t) = A(t)$ and $\tilde{A}^{-1}$ denoting its inverse. More easily, we find this form of τ by requiring that the integral over the velocity from time τ to t equals the travelled distance $x-2$:

$$\int_{\tau}^{t} 2\nu\ A(t')dt' = x-2\ . \tag{16}$$

To include the diffusive contribution in Eq. (13), we use the diffusion kernel,

$$k(x,y,t) = \left(4\pi \int_{\tau(y,t)}^{t} D(t)\right)^{-1/2} \exp\left(\frac{-x^2}{4\int_{\tau(y,t)}^{t} D(t)}\right), \tag{17}$$

with the time dependent diffusion constant $D(t) = \nu A(t)$. The kernel $k(x,y,t)$ accounts for the mass that has been diffusively transported from y a distance of x. Because the mass has entered the system at $x=2$ at time $\tau(y,t)$, it diffused for the time $t-\tau(y,t)$. The complete expression for $c(x,t)$ is then obtained as the convolution of $c_{\text{advec}}(x,t)$ (Eq. (14)), that is obtained from Eq. (12) and Eq. (15), and the diffusion kernel $k(x,y,t)$ (Eq. (17)):

$$c(x,t) = \int c_{\text{advec}}(s,t)k(x-s,s,t)ds = \int c(2,\tau(s,t))k(x-s,s,t)ds\ . \tag{18}$$

Interpreting the terms in the equations and the general form of the solution, we are able to understand the qualitative behavior of the system. If both the activation and the dimerization rate are large, the system produces zero yield: both advection and diffusion are driven by the concentration of active monomers A. If activation is fast, the concentration of active monomers A will become large initially since activation is faster than the reaction dynamics. Consequently, provided $\mu \sim \nu$, dimerization dominates over binding because it depends quadratically on A, see Eq. (11). The reservoir of free particles then depletes quickly and cannot sustain the motion of the wave for long enough to reach the absorbing boundary, resulting in a very low yield. Only if either the activation rate is low enough or if $\mu \ll \nu$, the motion of the wave can be sustained until it reaches the absorbing boundary.

C. THRESHOLD VALUES FOR THE ACTIVATION AND DIMERIZATION RATE

Based on the analysis from the previous section, we will now determine the threshold activation rate and threshold dimerization rate which mark the onset of non-zero yield. Yield production starts as soon as the density wave reaches the absorbing boundary at

$x = L$. Therefore, finite yield is obtained if and only if the sum of the advectively travelled distance d_{adv} and the diffusively travelled distance d_{diff} exceeds the system size $L - 2$:

$$d_{\text{adv}} + d_{\text{diff}} \geq L - 2\,. \tag{19}$$

The condition for the onset of non-zero yield is obtained by assuming equality in this relation. The advectively travelled distance is obtained from Eq. (16) by setting the borders of the integral over the velocity to $\tau = 0$ and $t = \infty$:

$$d_{\text{adv}} = \int_0^\infty 2\nu A(t')dt'. \tag{20}$$

The diffusively travelled distance is approximately given by the standard deviation of the Gaussian diffusion kernel, Eq. (17), again with $\tau = 0$ and $t = \infty$,

$$d_{\text{diff}} = \sqrt{2\nu \int_0^\infty A(t)dt}. \tag{21}$$

Taken together, we obtain a condition for the onset of finite yield:

$$2\nu \int_0^\infty A(t)dt + \sqrt{2\nu \int_0^\infty A(t)dt} = L - 2\,. \tag{22}$$

Substituting $y = \sqrt{2\nu \int A}$ and requiring that y is positive, we can solve the quadratic equation and find that Eq. (22) is equivalent to

$$2\nu \int_0^\infty A(t)dt = y^2 = \frac{1}{4}\left(\sqrt{1 + 4(L-2)} - 1\right)^2 \approx L - \sqrt{L}\,, \tag{23}$$

where the last approximation is valid for large L.

We determine the threshold values for the activation rate α and the dimerization rate μ by finding solutions of the dynamical equation for the active particles $A(t)$, Eq. (11), such that the condition, Eq. (23), is fulfilled. Thus, we start by deriving the dependence of $\int_0^\infty A(t)dt$ on α and μ.

The concentration $c(x,t)$ appears in Eq. (11) only in terms of an integral $\int_2^L c(x,t)\,dx$, counting the total number of polymers in the system. As long as yield is zero there is no outflux of polymers at the absorbing boundary $x = L$ and the total number of polymers in the system only increases due to the influx at the left boundary $x = 2$. As long as yield is zero we can therefore equivalently consider the limit $L \to \infty$. We denote the total number of polymers in Eq. (11) by $B(t) := \int c(x,t)\,dx$ for which the dynamics is determined from the boundary condition, Eq. (10):

$$\frac{d}{dt}B = \int_2^\infty \partial_t c(x,t)\,dx = \int_2^\infty -\partial_x J(x,t)\,dx = -\underbrace{J(\infty,t)}_{=0} + J(2,t) = \mu A(t)^2. \tag{24}$$

Hence, as long as yield is zero, the total number of polymers increases with the rate of the dimerization events. The system then simplifies to a set of two coupled ordinary differential equations for A and B:

$$\frac{d}{dt}A = \alpha C e^{-\alpha t} - 2\mu A^2 - 2\nu A\ B\ , \tag{25a}$$

$$\frac{d}{dt}B = \mu A^2\ . \tag{25b}$$

The dynamics of A and B is equivalent to a two-state activator-inhibitor system, where A dimerizes into B at rate μ, and B degrades (inhibits) A at rate 2ν. Note that Eq. (25a) describes the exact dynamics of the active monomers A and total number of polymers B in the deterministic system as long as yield is zero. The system has therefore been greatly reduced from originally $S\,N$ coupled ODEs to now only 2 coupled ODEs.

For the further analysis it is useful to non-dimensionalize Eq. (25a) by measuring A and B in units of the initial concentration of inactive monomers C and time in units of $(\nu C)^{-1}$:

$$\frac{d}{dt}A = \omega e^{-\omega t} - 2\eta A^2 - 2A\ B\,, \tag{26a}$$

$$\frac{d}{dt}B = \eta A^2\,, \tag{26b}$$

with the remaining dimensionless parameters $\omega = \frac{\alpha}{\nu C}$ and $\eta = \frac{\mu}{\nu}$. We are interested in the integral over $A(t)$ as a function of ω and η,

$$\int_0^\infty A_{\omega,\eta}(t)dt := g(\omega,\eta)\,, \tag{27}$$

which relates to the totally travelled distance of the wave. Note that, in case of zero yield, $2g(\omega,\eta)$ is the total advectively travelled distance of the wave (cf. Eq. (20)) and the square of the diffusively travelled distance (cf. Eq. (21)).

Analysis of the dimerization scenario

The dimerization scenario is characterized by fast activation $\alpha \gg C\nu$ and slow dimerization $\mu \ll \nu$. For the dimensionless parameters these assumptions translate to $\eta \ll 1$ and $\eta \ll \omega$. Because for small $\eta \ll 1$ nucleation is much slower than growth we neglect the dimerization term in Eq. (26a) against the growth term. Furthermore, because $\eta \ll \omega$ activation happens on a fast time scale compared with nucleation and we may therefore integrate out the fast time scale assuming that all particles are activated instantaneously at the beginning. The system Eq. (26) then reduces to

$$\frac{d}{dt}A = -2A\ B\,, \tag{28a}$$

$$\frac{d}{dt}B = \eta A^2\,, \tag{28b}$$

with the initial condition $A(0) = 1$ and $B(0) = 0$. We divide the first equation by the second one (formally applying the chain rule and the inverse function theorem) to obtain a single equation for the dynamics of $A(B)$:

$$\frac{dA}{dB} = -\frac{2}{\eta}\frac{B}{A}\,, \tag{29}$$

where $A(B{=}0) = 1$. This first order ODE can be solved by separation of variables and subsequent integration, yielding

$$A(B) = \sqrt{1 - \frac{2}{\eta}B^2}\,. \tag{30}$$

Because the number of active monomers $A(t)$ must vanish for $t \to \infty$, the final value of B is

$$B_\infty := B(t{=}\infty) = \sqrt{\frac{\eta}{2}}\,. \tag{31}$$

Thereby, we calculate the function $g(\eta)$ via variable substitution $dt = \frac{dB}{\eta A^2}$:

$$g(\eta) = \int_0^\infty A(t)dt = \int_0^{B_\infty} A(B)\frac{dB}{\eta A(B)^2} = \frac{1}{\eta}\int_0^{B_\infty} \frac{dB}{\sqrt{1 - \frac{2}{\eta}B^2}} = \frac{\pi}{2\sqrt{2}}\,\eta^{-\frac{1}{2}}\,. \tag{32}$$

So, the dependence of the travelled distance of the wave on η obeys a power law with exponent $-\frac{1}{2}$, confirming the previous result[9]. For the coefficient we find $\frac{\pi}{2\sqrt{2}} \approx 1.1107$.

Additionally, we can determine the time dependent solutions $A(t)$ and $B(t)$. Using the solution for $A(B)$ from Eq. (30) in Eq. (28b) we obtain $B(t)$ as

$$B(t) = \sqrt{\frac{\eta}{2}}\tanh\left(\sqrt{2\eta}t\right)\,. \tag{33}$$

We use this expression for $B(t)$ in Eq. (28a) to obtain $A(t)$. The resulting ODEs can again be solved by separation of variables as

$$A(t) = \frac{1}{\cosh\left(\sqrt{2\eta}t\right)}. \tag{34}$$

Analysis of the activation scenario

In the activation scenario, $\alpha \ll C\nu$, such that $\omega \ll 1$ and $\omega \ll \eta$. As we know already that decreasing ω will slow down nucleation relative to growth we can again neglect the dimerization term in Eq. (26a). In contrast to the dimerization scenario, however, we have to keep the activation term. Transforming time via $\tau := 1 - e^{-\omega t}$ such that $\tau \in [0, 1]$ and writing $a(\tau) = a(1 - e^{-\omega t}) := A(t)$ and $b(\tau) = b(1 - e^{-\omega t}) := B(t)$ the system in Eq. (26) becomes:

$$\frac{d}{d\tau}a = 1 - \frac{2}{\omega(1-\tau)}ab\,, \tag{35a}$$

$$\frac{d}{d\tau}b = \frac{\eta}{\omega(1-\tau)}a^2\,, \tag{35b}$$

with the initial condition $a(0) = b(0) = 0$. The function $g(\omega, \eta)$ transforms as

$$g(\omega, \eta) = \int_0^\infty A(t)dt = \frac{1}{\omega} \int_0^1 \frac{a(\tau)}{1-\tau} d\tau. \tag{36}$$

In the following we derive the asymptotic solution for $a(\tau)$ in the limit of small ω in order to evaluate the integral in Eq. (36). In the limit $\tau \to 1$ ($\Leftrightarrow t \to \infty$) both $a(\tau)$ and $\frac{d}{d\tau}a(\tau)$ will become small whereas $b(\tau)$ increases monotonically. The reaction term in Eq. (35a) is furthermore weighted by a factor $\frac{1}{\omega}$ which will become large if $\omega \ll 1$. We therefore postulate that for sufficiently large τ the derivative $\frac{d}{d\tau}a(\tau)$ is much smaller than the two terms on the right-hand side of Eq. (35a) and hence negligible. This assumption has to be justified *a posteriori* with the obtained solution. Neglecting the derivative term $\frac{d}{d\tau}a$ in (35a) reduces the equation to an algebraic equation and we find

$$a = \frac{\omega(1-\tau)}{2b}. \tag{37}$$

Using this result in Eq. (35b) we can solve for b by separation of variables and subsequent integration:

$$b(\tau) = (\omega\eta)^{\frac{1}{3}} \cdot \left(\frac{3}{4}\tau - \frac{3}{8}\tau^2\right)^{\frac{1}{3}} . \tag{38}$$

From Eq. (37) we immediately obtain $a(\tau)$:

$$a(\tau) = \frac{\omega^{\frac{2}{3}}}{\eta^{\frac{1}{3}}} \cdot \frac{1-\tau}{(6\tau - 3\tau^2)^{\frac{1}{3}}} := \frac{\omega^{\frac{2}{3}}}{\eta^{\frac{1}{3}}} h(\tau) , \tag{39}$$

where by $h(\tau)$ we denote the part of the solution that depends only on τ. Hence, we find that a and hence also $\frac{d}{d\tau}a$ scale like $\sim \omega^{\frac{2}{3}}$, and will thus become small if $\omega \ll 1$ and τ is large enough. Therefore the solution is consistent[1] and justifies the approximation in which we neglected the derivative term in the limit of small ω and sufficiently large τ.

---

[1] Consistency of the solution with the approximation is a sufficient criterion for the validity of the approximation: We can solve the system for A and B in Eq. (35) iteratively by defining

$$\frac{d}{d\tau}a_{i-1} = 1 - \frac{2}{\omega(1-\tau)} a_i b_i ,$$
$$\frac{d}{d\tau}b_i = \frac{\eta}{\omega(1-\tau)} a_i^2 .$$

Assuming that for $i \to \infty$, a_i and b_i converge to the correct solutions $a(\tau)$ and $b(\tau)$ when starting with $a_0 = 0$, we obtain a_1 and b_1 as given by Eq. (39) and Eq. (38) and can iteratively refine the approximation. The next iteration step then reads: $\frac{d}{d\tau}a_1 = 1 - \frac{2}{\omega(1-\tau)} a_2 b_2$. As $a_1 \sim \omega^{\frac{2}{3}}$ we know that the left-hand side will be small and a_1 and b_1 solve the system if the left-hand side equals 0. Writing $a_2 = a_1 + \tilde{a}_2$ and $b_2 = b_1 + \tilde{b}_2$ this gives:

$$\frac{d}{d\tau}a_1 = 1 - \frac{2}{\omega(1-\tau)}(a_1 + \tilde{a}_2)(b_1 + \tilde{b}_2) \approx \frac{2}{\omega(1-\tau)}(a_1\tilde{b}_2 + b_1\tilde{a}_2) . \tag{40}$$

From dimensional analysis it follows that the correction terms $\tilde{a}_2$ and $\tilde{b}_2$ must scale like $\tilde{a}_2 \sim \omega^{\frac{4}{3}}$ and $\tilde{b}_2 \sim \omega$ and are hence much smaller than the first order approximations a_1 and b_1. Higher order corrections will give even smaller contributions showing that if $\frac{d}{d\tau}a_1 \ll 1$, a_1 is indeed a very good approximation.

In the limit $\tau \to 0$, however, the expression for $a(\tau)$ in Eq. (39) diverges and consistency is violated. Hence, the obtained solution is valid only for sufficiently large τ.

We fix some small $\epsilon > 0$ such that the approximation can be assumed to be sufficiently good if $\frac{d}{dt}a < \epsilon$. Furthermore, we define τ_ϵ such that $\frac{d}{d\tau}a < \epsilon$ for all $\tau > \tau_\epsilon$. Using Eq. (39) we can write this as $\frac{d}{d\tau}h < \epsilon\eta^{\frac{1}{3}}/\omega^{\frac{2}{3}}$ for all $\tau > \tau_\epsilon$, where the left-hand side, $\frac{d}{d\tau}h$, depends only on τ. Hence, by decreasing ω we can make τ_ϵ arbitrarily small: $\lim_{\omega\to 0}\tau_\epsilon = 0$. In order to calculate $g(\omega, \eta)$ the integral in Eq. (36) can be separated in a domain where the approximation $a(\tau)$ is accurate and a domain where the correct solution $\tilde{a}(\tau)$ deviates strongly from $a(\tau)$:

$$g(\omega,\eta) = \frac{1}{\omega}\int_0^{\tau_\epsilon} \frac{\tilde{a}(\tau)}{1-\tau}d\tau + \frac{1}{\omega}\int_{\tau_\epsilon}^{1} \frac{a(\tau)}{1-\tau}d\tau. \tag{41}$$

We see from Eq. (35a) that $\frac{d}{d\tau}\tilde{a} = 1$ describes an upper bound to $\tilde{a}$ showing that $\tilde{a}(\tau) \leq \tau$. Therefore we can bound the contribution of the first integral as $\int_0^{\tau_\epsilon}\frac{\tilde{a}(\tau)}{1-\tau}d\tau \leq \int_0^{\tau_\epsilon}\frac{\tau}{1-\tau_\epsilon}d\tau = \frac{1}{2}\frac{\tau_\epsilon^2}{1-\tau_\epsilon}$. Because this upper bound for the integral goes to 0 if ω and hence τ_ϵ become small the first integral will become negligible against the second one. Asymptotically, we therefore only need to consider the second integral with the solution for $a(\tau)$ as given by Eq. (39):

$$\begin{aligned} g(\omega,\eta) &= (\omega\eta)^{-\frac{1}{3}}\int_0^1 (6t-3t^2)^{-\frac{1}{3}}dt = (\omega\eta)^{-\frac{1}{3}}\int_0^3 \frac{dz}{6z^{\frac{1}{3}}\sqrt{1-\frac{z}{3}}} = \\ &= \frac{3^{\frac{2}{3}}\sqrt{\pi}\,\Gamma(\frac{2}{3})}{6\,\Gamma(\frac{7}{6})}(\omega\eta)^{-\frac{1}{3}} \approx 0.8969\cdot(\omega\eta)^{-\frac{1}{3}}\ , \end{aligned} \tag{42}$$

where we used the substitution $t = 1-\sqrt{1-z/3}$ and $\Gamma(x)$ is the (Euler) Gamma function. So, in the limit of small ω, g scales with ω and η with identical exponent $-\frac{1}{3}$. This contrasts the dimerization scenario where g as well as A and B depend only on η and are independent of ω (cf. Eq. (32), (33) and (34)).

Numerical analysis and the threshold values for the rate constants

In order to confirm the results of the last two paragraphs and to see how $g(\omega, \eta)$ behaves in the intermediate regime where ω and η are of the same order of magnitude we also investigate the function $g(\omega, \eta)$ numerically. For that purpose we numerically integrate the ODE-system for $A(t)$ and $B(t)$ in Eq. (26) for different values of ω and η with a semi-implicit method. Subsequently, we integrate the solution $A(t)$ using an adaptive recursive Simpson's rule. Plotting g in dependence of ω for fixed η on a double-logarithmic scale reveals a rather simple bipartite form of g, see Fig. S1a:

$$g(\omega,\eta) = \begin{cases} g_1(\eta)\omega^{-\frac{1}{3}} & \omega \ll 1 \\ g_2(\eta) & \omega \gg 1. \end{cases} \tag{43}$$

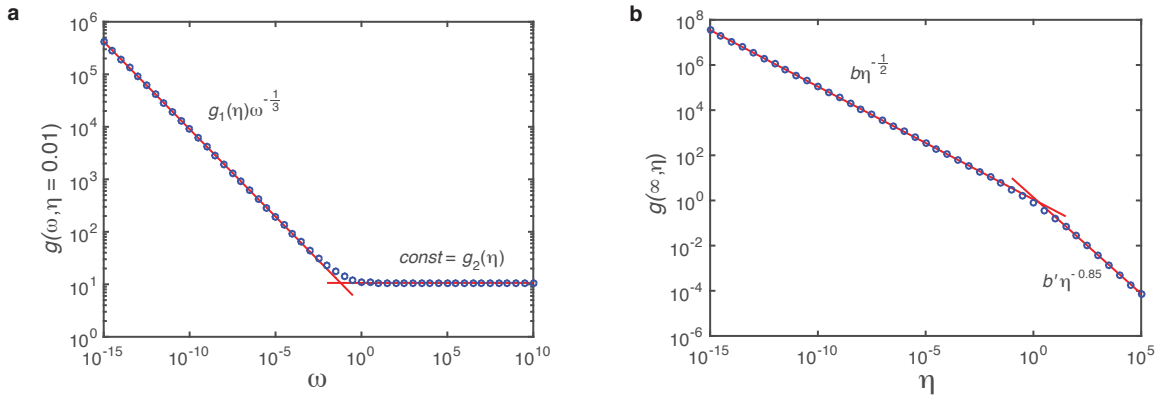

Fig. S 1: **Fit of $g(\omega,\eta)$ on log-log scale**. The function $g(\omega,\eta) = \int_0^\infty A_{\omega,\eta}(t)dt$ describes (half) the travelled distance of the profile of the polymer size distribution in dependence of $\omega = \frac{\alpha}{\nu C}$ and $\eta = \frac{\mu}{\nu}$. Marker points show solutions for $g(\omega,\eta)$ as obtained numerically from integration of Eq.(26). Red lines are linear fits on log-log scale. In **a)** we plot $g(\omega,\eta)$ for fixed η (here exemplarily for $\eta = 0.01$) over 25 orders of magnitude in ω and find a markedly bipartite behavior: For small ω the dependence on ω is perfectly matched by a power law with exponent $-\frac{1}{3}$ and η-dependent coefficient $g_1(\eta)$, whereas for large ω it is a constant $g_2(\eta)$. **b)** Plotting $g_2(\eta) = g(\omega = \infty, \eta)$ in dependence of η reveals again strictly bipartite behavior. Here, however, only the brach for small η is realistically relevant. With the coefficient $g_1(\eta)$ that can be determined in a similar way this leads to the final form of $g(\omega,\eta)$ as given by Eq. (46).

The transition between these two regimes is rather sharp so that g is best described in a piecewise fashion

$$g(\omega,\eta) = \max\left(g_1(\eta)\omega^{-\frac{1}{3}}, g_2(\eta)\right). \tag{44}$$

Next, we plot the coefficients $g_1(\eta)$ and $g_2(\eta)$ against η. Here we find that $g_1(\eta) = a\eta^{-\frac{1}{3}}$ with $a = \text{const} \approx 0.90$ and $g_2(\eta)$ is again bipartite with a sharp kink in between (Fig. S1b):

$$g_2(\eta) = \min\left(b\eta^{-\frac{1}{2}}, b'\eta^{-0.85}\right), \tag{45}$$

where $b \approx 1.11$ and $b' \approx 1.37$. The transition between both regimes is at $\eta \approx 1.82$. The second regime is not relevant for self-assembly since it refers to both large ω and large η, hence the travelled distance $2g$ is too small to give finite yield in this regime. Therefore, we discard the second regime and obtain as final result

$$g(\omega,\eta) = \max\left(a(\eta\omega)^{-\frac{1}{3}}, b\eta^{-\frac{1}{2}}\right), \tag{46}$$

with $a \approx 0.90$ and $b \approx 1.11$. This confirms perfectly the exponents as well as the coefficients found in the last two paragraphs. It is, however, surprising that there is such a sharp

transition between both regimes, which allows to define $g(\omega, \eta)$ in a piecewise fashion. This behavior must be the result of a series of lower oder terms in $g(\omega, \eta)$ which are unimportant in the limits $\omega \ll \eta$ and $\eta \ll \omega$ but cause the sharp transition when ω and η are of the same order of magnitude.

Finally, we return to our original task of finding the threshold values of the activation and dimerization rate for the onset of yield. Using our result for $g(\omega, \eta)$ in Eq. (23) we find as necessary and sufficient condition to obtain finite yield in the deterministic system:

$$2 \max \left(a(\eta\omega)^{-\frac{1}{3}}, b\eta^{-\frac{1}{2}} \right) \geq L - \sqrt{L} \, . \tag{47}$$

Alternatively, we can state this result as two separate conditions out of which at least one must be fulfilled to obtain finite yield:

$$2a(\eta\omega)^{-\frac{1}{3}} \geq L - \sqrt{L} \qquad \Rightarrow \qquad \alpha < \alpha_{\text{th}} := P_\alpha \frac{\nu}{\mu} \frac{\nu C}{(L - \sqrt{L})^3} \tag{48}$$

$$\text{or} \qquad 2b\eta^{-\frac{1}{2}} \geq L - \sqrt{L} \qquad \Rightarrow \qquad \mu < \mu_{\text{th}} := P_\mu \frac{\nu}{(L - \sqrt{L})^2} \tag{49}$$

where $P_\alpha = 8a^3 \approx 5.77$ and $P_\mu = 4b^2 \approx 4.93$. This verifies Eq. (1) in the main text.

D. IMPACT OF THE IMPLEMENTATION OF SUB-NUCLEATION REACTIONS

In the main text we focused our discussion on irreversible binding $L_{nuc} = 2$. In this section we investigate the effect of different implementations of the sub-nucleation reactions.

In general, perfect yield is trivially achieved if the complete ring is the only stable structure. However, yield can be maximal already for smaller nucleation sizes L_{nuc} depending on the explicit decay rate δ. In the deterministic limit without the dimerization and activation mechanisms ($\mu = \nu$, $\alpha \to \infty$) a rapid transition from zero yield to perfect yield occurs in dependence of the critical nucleation size (see Fig. S2). The threshold value in this case is approximately half the ring size and is weakly affected by the decay rate δ. In order to obtain finite yield for small nucleation sizes, an extremely high decay rate would be necessary. Hence, maximizing the yield solely by increasing the nucleation size is not very feasible.

In our model, the subcritical reaction rates μ_i may take different values. Here, we want to restrict our discussion to two scenarios. First, all rates have an identical value $\mu_i = \mu$ and second, the rates increase linearly up to the super-nucleation reaction rate: $\mu_i = \mu + (\nu - \mu) \frac{i-1}{L_{nuc}-1}$.

In the deterministic limit, both implementations show the same qualitative behavior as the dimerization mechanism with $L_{nuc} = 2$ in the main text (see Fig. S3). The only relevant aspect for the final yield is the extend to which nucleation is slowed down in total. In the constant scenario all reaction steps contribute equally. As a results there is a strong dependence on the number of such reaction steps, i.e. on the critical nucleation size. If however, the reaction rates increase linearly with the size of the polymers, the dimerzation rate dominates. Only in the case $\mu \ll \nu$ finite yield is observed at all. In this limit the dimerization rate is much smaller than the subsequent growth rates. The explicit form of the different μ_i is not of major importance for the yield. The total slowdown of nucleation is the central feature. Structure decay does not play any role for intermediate nucleation sizes.

The last question we want to address is how the combination of activation and dimerization mechanism and the corresponding non-monotonic behavior is affected by the nucleation size. Again, we compare constant sub-nucleation growth with a linearly increasing growth rate (see Fig. S4). In the deterministic regime both implementations behave qualitatively similar as the dimerization mechanism discussed in the main text. However, in both cases the stochastic yield catastrophe is less pronounced. For the constant growth rates a saturation of the maximal yield is observed for sufficiently low μ. If the profile is linear this effect is weaker as compared to the constant case and a dependency on the explicit value of μ is still observed. The saturation value is not reached for these reactions rates.

Taking all our results for the sub-nucleation behavior together we draw the following conclusions: First, structure decay by itself it not very efficient in order to maximize yield. Second, the explicit choice of the sub-nucleation rates is of minor importance for the qualitative behavior. The system behaves similarly to the case $L_{nuc} = 2$. Third, larger nucleation sizes mitigate the stochastic yield catastrophe in general.

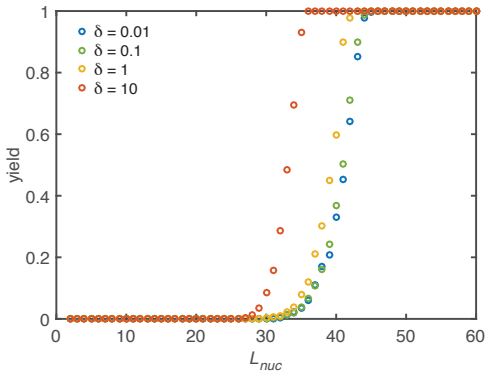

Fig. S 2: **Yield maximization due to increased nucleation size.** Without activation and dimerization mechanism ($\alpha \to \infty, \mu = \nu$) the yield can still be optimized by increasing the critical nucleation size L_{nuc}. However, a significant improvement is only achieved for critical sizes larger than half the ring size. Above, a rapid transition to perfect yield takes place. Below no effect is observed at all. Increasing δ shifts the onset of yield to slightly smaller critical nucleation sizes. Other parameters: $L = 60$, $N = 10000$.

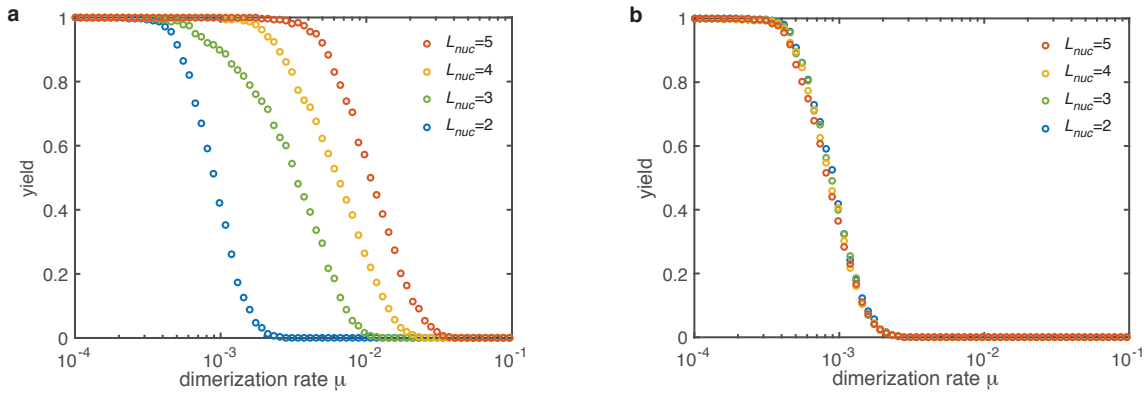

Fig. S 3: **Yield for the dimerization mechanism ($\alpha \to \infty$) with different nucleation sizes (colors). a** If all sub-nucleation growth rates are identical ($\mu_i = \mu$) increasing the nucleation size increases the threshold value μ_{th}. The slow down of nucleation due to the individual sub-nucleation steps in total determines the yield. **b** If the sub-nucleation growth rates increase linear $\left(\mu_i = \mu + (\nu - \mu)\frac{i-1}{L_{nuc}-1}\right)$ no dependence on the nucleation size is observed. The dimerization rate $\mu_1 = \mu$ (which is the most limiting step) dominates entirely. Other parameters: $L = 60$, $N = 10000$, $\delta = 1$.

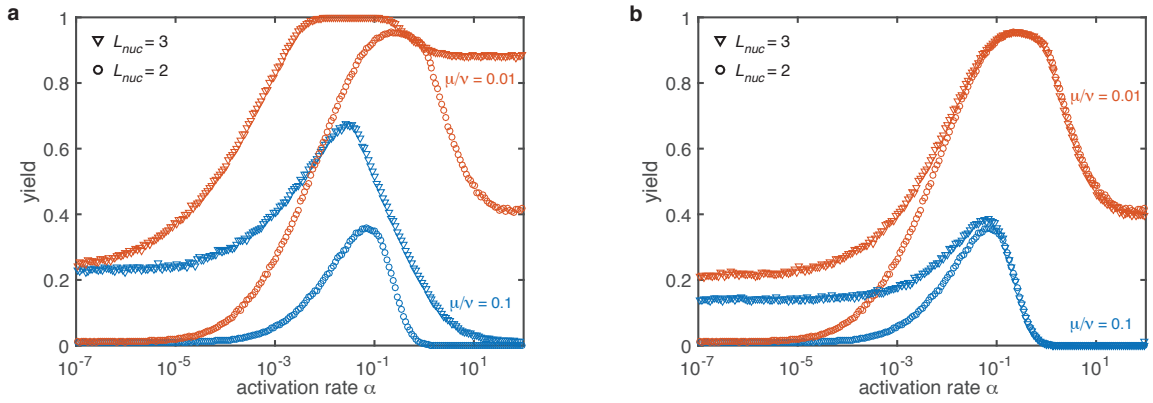

Fig. S 4: **Combined mechanisms for different nucleation sizes (symbols) and dimerization rates (color).** **a** If the sub-nucleation growth rates are identical ($\mu_i = \mu$) The stochastic yield catastrophe is weakened but still has a drastic impact. The qualitative behavior remains unchanged. **b** For a linearly increasing sub-nucleation growth rate $\left(\mu_i = \mu + (\nu - \mu)\frac{i-1}{L_{nuc}-1}\right)$ in the deterministic regime no changes are observed at all. The effect of the stochastic yield catastrophe is less pronounced. This improvement is mainly caused by structure decay which mitigates stochastic fluctuations. However, a slight dependency of the saturation value on the rate μ is observed. Other parameters: $L = 60$, $S = L$, $N = 100$, $\delta = 0.1$.

E. TIME EVOLUTION OF THE YIELD IN THE ACTIVATION AND DIMERIZATION SCENARIO

In the main text we focus on the final yield, which represents the maximal yield that can be obtained in the assembly reaction for $t \to \infty$. Here, we briefly discuss the temporal evolution of the yield in the two scenarios. Figure S5 shows the yield as a function of time for the dimerization scenario (blue) and the activation scenario (red) for the corresponding parameters indicated in the plot. Drawn lines show the evolution of the yield in the stochastic simulation whereas dashed lines represent its deterministic evolution obtained by integrating the corresponding mean-field rate equations (only shown for the activation scenario).
In both scenarios, yield production sets in after a short lag time[16]. The emergence of a lag time can be understood in terms of the interpretation of the assembly process as the progression of a travelling wave (see Sec. B). The travelling wave thereby describes the polymer size distribution and the time that is needed for the wave to reach the absorbing boundary equals the lag time for yield production observed in Fig. S5. After the lag time, the yield increases very abruptly in the dimerization scenario and a bit more continually in the activation scenario. Since monomers are provided gradually in the activation scenario, the emerging wave is flatter and extends over a larger range (in polymer size space) as compared to the dimerization scenario. Consequently, yield production is more gradual in the activation scenario than in the dimerization scenario. For the same reason, the dimerization scenario is generally "faster" or more time efficient than the activation scenario. For a detailed analysis of the time efficiency of these and other self-assembly scenarios we refer the reader to [10].

In all depicted situations, the yield increases monotonically with time. This is, of course, generally true since the completed ring structures define an absorbing state in our system. The final yield, which is indicated in the right bar, therefore represents the upper limit for the yield that can be achieved in the assembly reaction. Figure S5 shows that the temporal yield curves initially are rather steep and quickly reach a value that lies within 10% of the final yield ("quickly" thereby refers to the respective time scale), before the curves flatten and increase more slowly. This underlines that the final yield is a meaningful observable that not only describes the upper limit for the yield but also approximates the typical yield of the assembly reaction under appropriate time constraints that are not too restrictive (on the time scale set by the respective lag time).

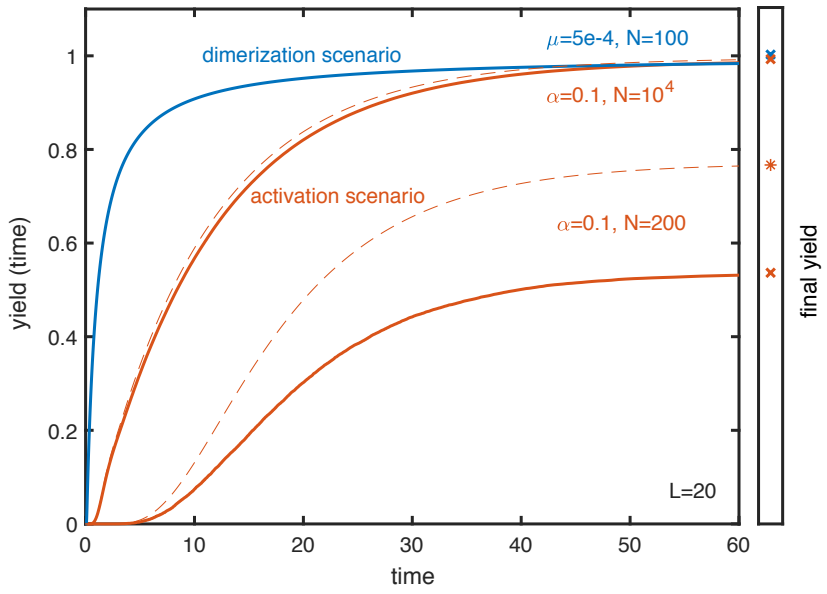

Fig. S 5: **Time evolution of the yield in the activation and dimerization scenario.** The time dependence of the yield is depicted for a dimerization scenario (blue) with $\mu = 5 \times 10^{-4}$ and $N = 100$ and for two activation scenarios (red) with $\alpha = 0.1$ and $N = 10^2$ and $N = 10^4$, respectively, for target structures of size $L = 20$. Drawn lines show the time evolution of the stochastic systems while dashed lines describe the time evolution in the corresponding deterministic systems (where the final yield may be higher in the activation scenario). In all cases the yield increases monotonically with time. The final yield, that is indicated in right bar, represents the upper limit of the yield at any time. Yield production in the activation scenario is generally more gradual than in the dimerization scenario. Therefore, the dimerization scenario is, in general, more time efficient than the activation scenario.

F. STANDARD DEVIATION OF THE YIELD

In the main text, the analysis focuses on the average yield. A priori it is, however, not apparent that this average quantity is informative, in particular due to the strong effect of stochasticity in the system. Here, we thus take a step forward to complement this picture by additionally considering a simple measure for the fluctuations of the yield, its standard deviation. Fig. S6 is an extension of Fig. 3(a) in the main text, showing the dependence of the average yield and its sample standard deviation on the activation rate. Since yield is always positive, the standard deviation of the yield has to be small if the average yield is close to 0 ($N = 500$ in Fig. S6). The same holds true for average yield close to 1 as the yield is bounded by 1 from above ($N = 5000$ in Fig. S6). For intermediate values of the average yield, the standard deviation is highest but still small compared to the average yield ($N = 1000$ in Fig. S6). The average yield is, thus, meaningful. Naturally the ratio of the standard deviation compared to the average yield also depends on the number of particles per species N and on the number of species S. Generally speaking, for higher N and S, this ratio decreases (see Fig. S7 for the dependency on S).

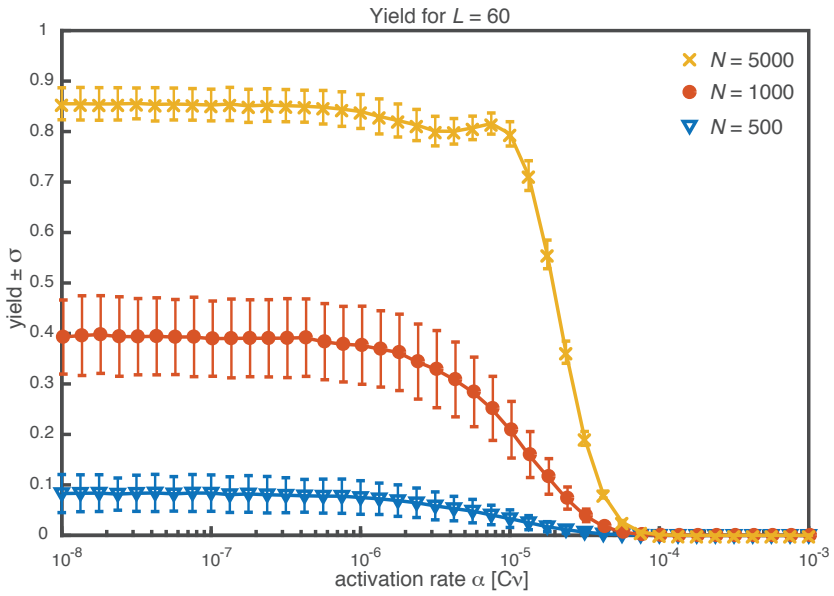

Fig. S 6: **Average yield and its sample standard deviation.** For average yield close to 0 or close to 1, the standard deviation has to be small due to the boundedness of the yield to the interval $[0, 1]$. For intermediate values, the standard deviation is highest. Its value is, however, still considerably smaller than the average yield. The parameters are $L = 60$, $S = L$, $\mu = \nu = 1$ and different particle numbers N (colors/symbols). To obtain the average yield, the yield has been averaged over 1000 simulations. The standard deviation corresponds to the unbiased sample standard deviation.

G. INFLUENCE OF THE HETEROGENEITY OF THE TARGET STRUCTURE FOR FIXED NUMBER OF PARTICLES PER SPECIES

Fig. 3(d) in the main text shows how the maximal yield $y_{\max}$ depends on the number of species S if the ring size L and the number of possible ring structures NS/L is fixed. This comparison for fixed NS is motivated by the question which role the heterogeneity of a structure plays for assembly efficiency if a certain number of structures should be realized. Fig. 3(d) illustrates that a higher number of species S (more heterogeneous structures) leads to a lower maximally possible yield, suggesting that it is beneficial to build structures with as few different species as possible. However, this situation does not correspond to the deterministically equivalent case[2] of fixed number of particles per species N. Instead, for higher number of species S, the number of particles per species $N \propto 1/S$ decreases. How does the heterogeneity of the structures S alter the maximally possible yield if L and N (instead of L and NS) are fixed? Fig. S7 shows how the maximal yield $y_{\max}$ and its standard deviation (obtained as average yield and sample standard deviation for $\alpha = 10^{-8}$ when the yield has well saturated and the dynamics (except for the timescale) get independent of the exact value of the rate-limiting activation rate) depend on the number of species S. For homogeneous structures $S = 1$ yield is always perfect since in this case there can be no fluctuations between species. As a result, the average yield is 1 and the standard deviation is 0. For increasing S, the average yield decreases until it levels off for $S \gg 1$. This behavior indicates that indeed the decreasing number of particles per species N for larger S is essential for the decrease of the maximal yield with S in Fig. 3(d). As mentioned above, the standard deviation is largest for small $S > 1$ and decreases with S.

[2] Note, though, that in the deterministic case the maximally possible yield is always 1, namely for $\alpha \to 0$.

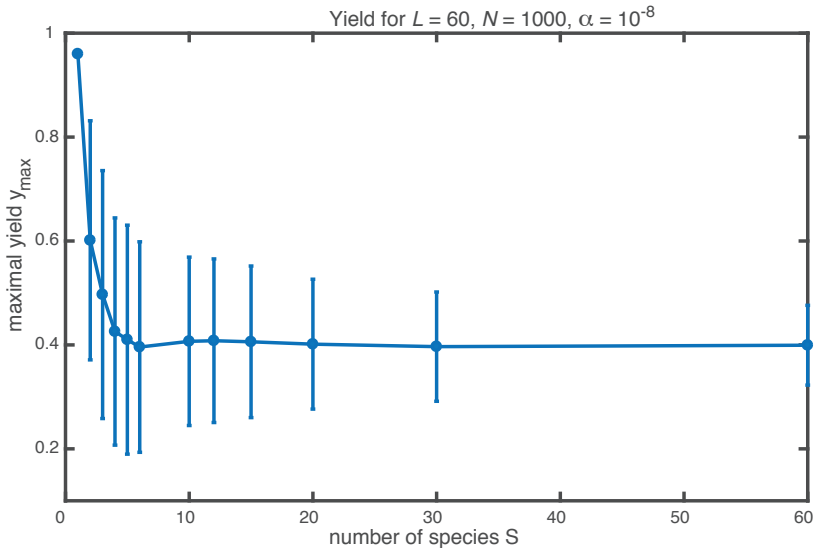

Fig. S 7: **Influence of the heterogeneity of the target structure on the yield for fixed number of particles per species N.** The maximal yield and its standard deviation (obtained as average yield and sample standard deviation for $\alpha = 10^{-8}$) are plotted against the number of species S making up the structure of size $L = 60$. The number of particles per species $N = 1000$ is fixed. Yield drops from a perfect value of 1 for $S = 1$ to a smaller value and levels off for $S \gg 1$. The standard deviation is largest for small S (except for $S = 1$ where the yield is always perfect) and decreases with increasing number of species.

H. DEPENDENCE OF THE MAXIMAL YIELD $y_{\max}$ IN THE ACTIVATION SCENARIO ON N AND L

Fig. 3(c) in the main text characterizes the dependence of the maximal yield $y_{\max}$ in the activation scenario as a "phase diagram" distinguishing different regimes of $y_{\max}$ in dependence of the particle number N and target size L. Supplementing this figure in the main text, Fig. S8 shows the maximum yield that is obtained in the activation scenario in the limit $\alpha \to 0$ for fixed L in dependence of N (Fig. S8a) as well as for fixed N in dependence of L (Fig. S8b). For larger particle number N, the maximal yield exhibits a transition from 0 to 1 over roughly three orders of magnitude. Increasing L shifts the transition to larger N. The threshold particle number where the transition starts is characterised by $N_{\text{th}}^{>0}(L)$ (see main text). Approximately, for $L \leq 600$, we find $N_{\text{th}}^{>0}(L) \sim L^{2.8}$ (cf. main text, Fig. 3(c)). Similarly, decreasing the target size L for fixed N, the maximal yield exhibits a transition from 0 to 1 over roughly one order of magnitude in L. The corresponding threshold value $L_{\text{th}}^{>0}$ as a function of N is obtained as the inverse function of $N_{\text{th}}^{>0}(L)$. Hence, at least for $N \leq 10^5$, approximately it holds $L_{\text{th}}^{>0}(N) \sim N^{0.36}$.
Since $y_{\max}$ is largely independent of the number of species S for fixed N and L (see Sec. G), the maximal yield in the activation scenario (for $L_{\text{nuc}} = 2$) can be fully characterized as a function $y_{\max}(N, L)$ of N and L. Hence, $y_{\max}$ can roughly be expressed in terms of the threshold particle number $N_{\text{th}}^{>0}(L)$ as

$$y_{\max}(N,L) \begin{cases} \approx 1 & \text{if } N > 10^3 N_{\text{th}}^{>0}(L) \\ < 1 & \text{if } N_{\text{th}}^{>0}(L) < N < 10^3 N_{\text{th}}^{>0}(L) \\ = 0 & \text{if } N < N_{\text{th}}^{>0}(L) \end{cases} \tag{50}$$

As can be seen from Fig. 3(c) in the main text, the transition line between zero and nonzero yield slightly flattens with increasing L. Hence, the power law $N_{\text{th}}^{>0}(L) \sim L^{2.8}$ (and similarly for $L_{\text{th}}^{>0}$) only holds approximately and for a restricted range in L and N. The asymptotic behavior of $N_{\text{th}}^{>0}$ in the limit $L \to \infty$ remains elusive.

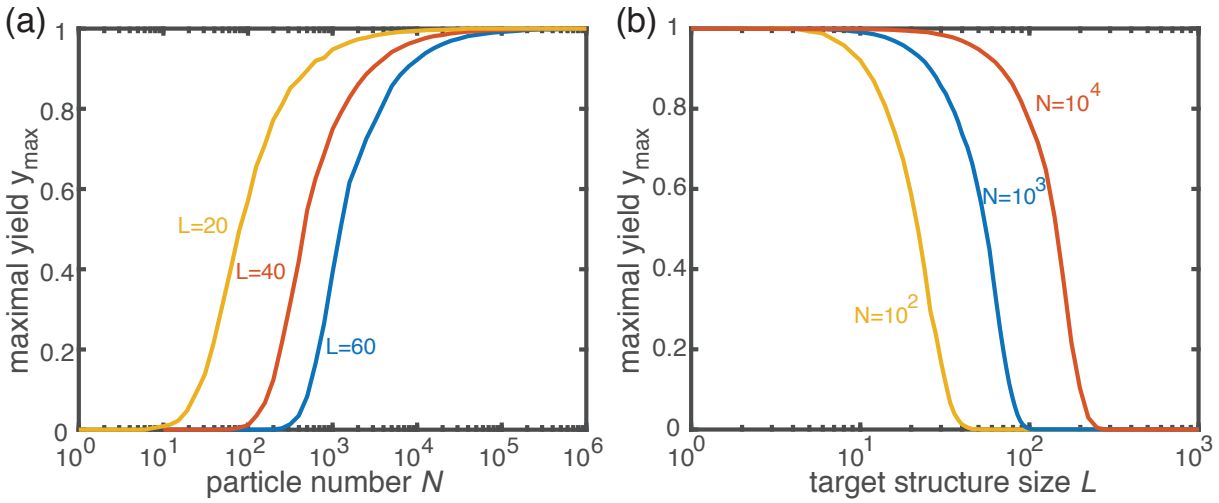

Fig. S 8: **Dependence of the maximal yield $y_{\max}$ in the activation scenario on N and L.** For each data point, $y_{\max}$ was determined as the average yield of 100 independent stochastic simulations of the activation scenario with $\alpha = 10^{-12}$. **a** Variation of the particle number N for different target sizes L. The maximal yield increases from 0 to 1 over roughly three order of magnitude in N. The onset of the transition depends on L. **b** Variation of the target size L for different particle numbers N. Increasing the target size L with N being fixed causes the maximal yield to drop to 0. The transition from 1 to 0 spans roughly one order of magnitude in L and its position is determined by N.

8 Understanding and guiding the assembly of heterogeneous structures

What I cannot create, I do not understand.
(Richard Feynman)

The goal of this chapter is to summarize the most important findings of our project on understanding and guiding robust self-assembly of heterogeneous structures. The corresponding manuscript is currently in preparation for submission. This chapter is based on and uses parts of the manuscript preprint in section 8.5.

8.1 Motivation

This project was directly motivated by the previous project (chapter 7) where – by means of a conceptual model – we found that the self-assembly of heterogeneous structures can be subject to strong stochastic effects that suppress the assembly yield considerably. While we proposed that the origin of these stochastic effects are fluctuations in the relative availability of the different building blocks, a quantitative understanding for their occurrence was still lacking.

In particular, the strength of the stochastic effects is counterintuitive: Even for large particle numbers in the system, stochasticity clearly alters the behavior of the system. Furthermore, there are at least two possible sources of stochasticity: First, there are fluctuations in the activation of species and, consequently, in the availability of species for binding (demographic noise). Second, there is randomness in choosing a binding partner (reaction noise). *A priori* it is not clear how much the different sources of stochasticity contribute to the observed stochastic effects.

The goal of this project was thus to gain a more thorough understanding of the origin of the strong stochastic effects and, building upon it, to propose different control strategies to improve assembly efficiency.

As mentioned in the abstract of the project, the driving questions for this project are:
Why is the self-assembly of heterogeneous structures subject to such strong stochastic effects? What role do the different sources of stochasticity play for the assembly process? What are possible strategies to control stochastic effects and to kinetically guide the assembly dynamics?

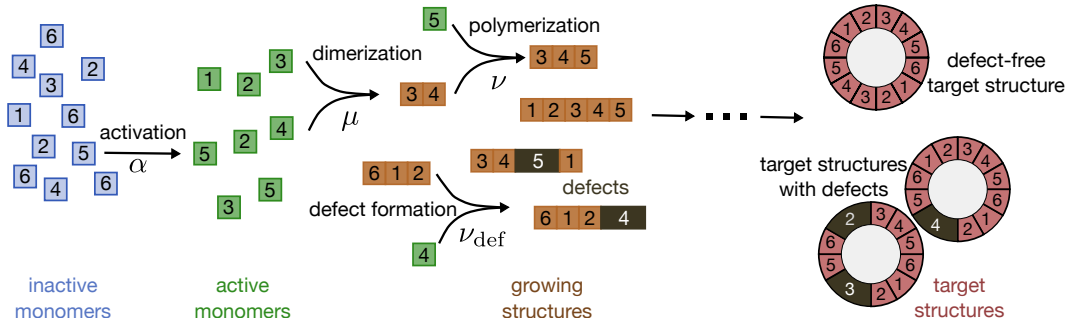

Figure 8.1 | Illustration of the model (taken from the manuscript preprint in section 8.5). The model is based on the model of the previous project (chapter 7) and extends it by additional erroneous binding: A species i can bind to its next-nearest neighboring species $i \pm 2$ at per-capita rate $\nu_{\text{def}} < \nu$, thereby creating a defect in the structure. For simplicity, we restrict our analysis to the case where the critical nucleation size is $L_{\text{nuc}} = 2$ and, thus, all growth processes are irreversible.

8.2 Model

To address these questions, we considered the model as illustrated in Fig. 8.1. It is based on the model studied in the previous project (chapter 7) and extends it by additionally taking into account erroneous binding between next-nearest neighbors i and $i \pm 2$ (as it was done in our other project [7] that is not part of my thesis). More concretely, in addition to correct growth of polymers by monomers of a neighboring species, at rate $\nu_{\text{def}} < \nu$ a monomer of the next-nearest species can attach to a polymer of size $l \geq 2$, thereby creating a defect in the structure. Once the structure has reached the target size L (including the defects; see the final target structures in Fig. 8.1), the ring closes and no further growth of this ring is possible. Furthermore, we restrict our analysis to the case where the critical nucleation size is $L_{\text{nuc}} = 2$. In this case, growth is completely irreversible.

As in the previous project, the quality of the assembly process is measured in terms of the final yield at the end of the process when no more growth is possible:

$$\text{yield} = \frac{L * \#\text{target structures}}{NS}.$$

It is defined as the number of finished target structures compared to the maximally possible number of defect-free target structures, $N/(L/S) = NS/L$. Analogously, the defect-free yield is defined as the number of defect-free target structures compared to NS/L:

$$\text{yield}_{\text{defect-free}} = \frac{L * \#\text{defect-free target structures}}{NS}.$$

In this summary, we will mostly focus on the case of no erroneous binding: $\nu_{\text{def}} = 0$.

8.3 Results

As discussed in detail in the previous chapter 7, this model exhibits rather counterintuitive behavior. In a deterministic description of the system that neglects correlations or fluctuations,

the yield is always perfect in the limit of small dimerization rate μ or small activation rate α, irrespective of the number of species S and of the number of particles N per species. This deterministic prediction is in agreement with an intuitive expectation according to which both small dimerization as well as small activation lead to a slow nucleation and, consequently, to a high yield ("slow nucleation principle"; see also section 6.3). However, it is in stark contrast to results from stochastic simulations, which show that for heterogeneous systems yield saturates at an imperfect value in the limit of small α (if the number N of particles per species is not too large; see Fig. 3(a) in the manuscript preprint in chapter 7.5). Surprisingly, this saturation due to stochastic effects is already considerable for systems with large numbers N of particles per species, for which fluctuations are not expected to play any role. So, where do these strong stochastic effects come from?

The idea of this project was to formulate an effective theory that takes into account the fluctuations in the availability of the different species for binding (demographic noise) but neglects reaction noise due to the randomness in choosing a binding partner. The motivation for this ansatz is illustrated in Fig. 3(a,b) in the manuscript preprint in section 8.5.
In contrast to a deterministic description of the process, which assumes that all species are equivalent, the different species can indeed be differently available for binding. One reason is that activation occurs randomly and, consequently, not all species have been activated equally up to a certain point in time. In the exemplary situation depicted in Fig. 3(a,b) in the manuscript preprint in section 8.5, for instance, all particles of species 1, 4 and 5 are already active. In contrast, species 6 has been activated much less as compared to the average. Correspondingly, there is currently no particle of species 6 available for binding (there is one particle of species 6 already bound in the polymer 5-6-1-2 but this one has already two neighboring particles bound to it); we denote such species as "unavailable" species. Since in the sketch there is also currently no active monomer of species 2 present, the polymer 3-4-5 has no possibility to grow by attachment of a correct binding partner. We denote such polymers as "blocked polymers" because they are blocked from growing by the unavailability of their neighboring species. In the case where erroneous binding is possible, the result may be that species 1 instead of species 6 binds to the polymer and thereby creates a defect in the structure. Alternatively, the unavailability of species may also lead to additional nucleation events, such as for instance due to dimerization of the free monomers of species 4 and 5. Taken together, our intuition was that fluctuations in the availability of the different species may lead to polymer configurations ("blocked polymers") that are prevented from growing due to the unavailability of "unavailable species" and that this may lead to additional nucleation events (or to defect binding).

To quantify this intuition, we proceeded step by step:
First, by employing a "fluctuation-corrected mean-field" ansatz, we approximated the probability of species to be "unavailable" and the resulting number of unavailable species. This number of unavailable species depends, for instance, on the typical fluctuations in the relative availability of species due to the activation process and, correspondingly, is time-dependent: At the beginning (the end) there are no fluctuations because all particles of all species are inactive (active). In contrast, during the assembly process, some species might have been activated more by chance and, thus, there should be variability in the availability of the different species.

Depending on the number of unavailable species, there will be more or less polymers in a blocked configuration. Thus, as a next step, we gauged the probability of a polymer to be in the blocked state, as a function of the number of unavailable species. It turns out that this probability depends on the size of the polymer: the probability of a larger polymer to be blocked as a result of the unavailability of species is higher. The reason is that – if polymers only grow by attachment of available species – each polymer will at some point reach a configuration where it would require unavailable species at both ends to be able to grow. Larger polymers are, thus, more likely to be in this blocked configuration. This finding contrasts the deterministic description (please refer to the Supplementary Material of the manuscript preprint of the previous project in chapter 7.5), in which the size of a polymer does not influence its growth behavior. Furthermore, it gives an idea why fluctuations might suppress the yield: If the probability of structures to grow strongly decreases with the structure size, more smaller structures will form. These then all compete for the same resources and cannot be completed as resources get depleted; the assembly yield is low.

Finally, we used these probabilities for a polymer to be in a blocked state to write down an effective theory in terms of two states per structure size: a "growing state" for polymers that can grow by attachment of available species and a "blocked state" for the other polymers.

Intriguingly, this effective theory, which is based on many simplifications, captures the behavior of the system qualitatively correctly (see Fig. 2 in the manuscript preprint in section 8.5): For instance, it predicts that the yield saturates at an imperfect value in the limit of small activation rates (a) or that the yield can be a non-monotonic function of the activation rate if the dimerization rate μ is smaller than the growth rate ν (b). This suggests that it is indeed the demographic noise due to the activation of particles and not the reaction noise that is mostly responsible for the strong stochastic effects (the stochastic yield catastrophe).

This demographic noise is captured by one crucial quantity of the system: the variance of the number of activated particles of a (randomly chosen) species up to time t. Since all particles are activated independently at per-capita rate α, the survival probability for a single particle is given by $1-e^{-\alpha t}$ and the number of activated particles per species follows a Binomial distribution with sample size N (the number of particles per species) and probability $1-e^{-\alpha t}$. The variance is thus given by

$$\sigma_0^2 = N\,(1 - e^{-\alpha t})\,e^{-\alpha t}\,. \tag{8.1}$$

As expected, it is zero at the beginning ($t = 0$) and at the end ($t \to \infty$) since then all particles are either inactive or all are active. When plotted against the average number of activation events per species, the variance exhibits a symmetric shape with a pronounced peak in the center (see Fig. 3(d) in the manuscript preprint in section 8.5, which shows the behavior of $\sqrt{3}\sigma_0$, which can be interpreted as the variance in the relative availability of one species as compared to its neighbors; thus the additional factor $\sqrt{3}$). So, the demographic noise is highest when just half of all particles have been activated.

Can we use this insight to propose strategies to improve the assembly efficiency? For instance, are there reasonable ways how to suppress the demographic noise in the system and do such systems indeed produce better yield? To answer these questions, we implemented two specific strategies which were designed to reduce the demographic noise in the system:

First, we considered a modification of the original model in which not all particles are added to the system from the start but instead the particles are provided in successive "bursts". Each burst consists of N/b particles per species (where b is the total number of bursts). Only when all particles of one burst have been activated and all binding reactions have taken place, particles of the next burst are put into the system. In this way, the variance of the number of species σ_0^2 is constrained by an external supply control: It is zero in between two successive bursts (see Fig. 5(a) in the manuscript preprint in section 8.5). As a result, the overall variance is the smaller, the more bursts are used to provide the particles. Based on our effective theory, we would thus expect that the assembly yield should improve for larger numbers of bursts. As shown in Fig. 5(b) in the manuscript preprint in section 8.5, this is indeed the case: The saturation value of the yield is larger for larger numbers of bursts and there is a clear negative correlation between the deviation of the number of activated particles between neighboring species over time and the assembly efficiency. Of course, the impact of bursts strongly depends on how "reliable" the bursts are. In the optimized scenario described here, each burst contains exactly N/b particles per species. As we show in the Appendix of the manuscript preprint in section 8.5 more bursts indeed improve assembly efficiency as long as the distribution of particles per burst is "narrow enough": If the number of particles per species is drawn independently from a Binomial distribution, yield increases with the number of bursts if the Fano factor for each burst is below 1. In fact, we prove that if the number of particles per species per burst is drawn randomly from a Poisson distribution with mean N/b (which has a Fano factor of 1), the process is independent of the number of bursts (in the limit where the activation rate is small, $\alpha \to 0$, and only the order of the activation events matters).

The control strategy to provide the particles in bursts relies on external supply control. Is there also a way to decrease the demographic noise by an internal supply control mechanism? To address this question, we considered a second complementary approach, where the different species inhibit their own activation. For this purpose, the activation rate in the original model is modified as follows:

$$\alpha^{(i)} = \alpha_0 e^{q m_i^a} , \tag{8.2}$$

where $\alpha^{(i)}$ is the activation rate of species i, m_i^a is the number of active monomers of species i, α_0 is the bare activation rate and $q \leq 0$ is the inhibition strength. The case $q = 0$ corresponds to the original model. The idea is that species that have been activated more, generally speaking, have more active monomers. Such a species would then tend to inhibit its own activation and, potentially, the activation levels of the different species could align. Indeed, Fig. 5(c) in the manuscript preprint in section 8.5 shows that the standard deviation of the fluctuations in the activation levels between neighboring species decreases for increasing inhibition strength q. This decreased variance again leads to an improved assembly efficiency: Fig. 5(d) in the manuscript preprint in section 8.5 shows how the assembly yield depends on the activation rate α for different values of the inhibition strength q. For higher q, the saturation value increases considerably. As a result, there is again a clear negative correlation between the strength of the demographic noise (c) and the assembly efficiency (d).

Taken together, these findings suggest that demographic noise (and related to it fluctuations in the availability of the different species) plays an important role for assembly efficiency, as suggested by the effective theory. Control strategies that reduce this demographic noise might thus hold promise for increasing the assembly efficiency of heterogeneous structures.

Intriguingly, as mentioned already in the introductory section 6.2, also the opposite approach, namely increasing the variability between species by implementing non-stoichiometric concentrations, has recently been suggested as a means to improve the assembly yield [109]. How do these ideas fit together? The important point is that, in order to increase the yield, the variability between species needs to be augmented in a coordinated way: In Ref. [109] the use of non-stoichiometric concentrations is beneficial because a specific region of the target structure is enriched. This coordinated variability between species favors a very specific assembly path where nucleation starts in the enhanced region and structures then grow from there. As a result, the competition between the different assembly paths is reduced to a minimum and the assembly yield is high.

A similar outcome can also be achieved by implementing non-homogeneous activation rates as illustrated in Fig. 6(a) in the manuscript preprint in section 8.5:

$$\alpha^{(i)} = \begin{cases} \alpha_0\, w^i & \text{for } i \leq S/2 \\ \alpha_0\, w^{S-(i-1)} & \text{for } i > S/2, \end{cases} \tag{8.3}$$

where w determines the strength of the hierarchy of the activation rates and α_0 is the basal activation rate. Two neighboring species, e.g. species $S/2$ and $S/2+1$, are activated fastest, and the activation rates of the other species are exponentially suppressed with the distance to these fastest species. As long as the activation rates are not so high that many species are activated before binding takes place, this arrangement leads to a strongly favored assembly pathway: Nucleation occurs preferentially between the two species which have the highest activation rate and then structures grow symmetrically towards both ends $i = 1$ and $i = S$. This improves yield considerably (see also Fig. 6(b) in the manuscript preprint in section 8.5).

Finally, in our other project [7], which is not part of my thesis, we considered a so-called just-in-sequence mechanism which is based on inhibitory feedback between neighboring species (see Fig. 6(c) in the manuscript preprint in section 8.5 for an illustration). This inhibitory feedback leads to an assembly cascade where all species are supplied in just the right order for binding. As a result, competition between different assembly paths is suppressed and this control strategy exhibits a very high assembly fidelity. In particular, it also controls erroneous binding.

8.4 Key points

From my point of view, there are three take-home messages:

- Fluctuations in the availability of different species (demographic noise) can be a strong limiting factor for the assembly of heterogeneous structures.
- Controlling demographic noise might thus be a promising strategy to improve assembly efficiency. Here, we examined two specific examples which are based on supply regulation by either external control or by self-inhibitory feedback.
- Remarkably, also increasing the variability between species can enhance the assembly yield – provided that it is well-coordinated and favors a specific assembly path.

Richard Feynman's quote at the beginning of the chapter nicely illustrates our approach in this project: Our goal was to build an effective theory in order to better understand the occurrence of the strong stochastic effects we observed in the previous project (chapter 7). I believe we learned a lot from it.

8.5 Manuscript preprint: Understanding and guiding robust self-assembly of heterogeneous structures

This section is a preprint of the following manuscript.

Understanding and guiding robust self-assembly of heterogeneous structures

by

Isabella R. Graf,[1,*] Florian M. Gartner,[1,*] and Erwin Frey[1]
[1] *Arnold-Sommerfeld-Center for Theoretical Physics and Center for NanoScience, Department of Physics, Ludwig-Maximilians-Universität München*
[*] *These authors contributed equally to this work.*

Understanding and guiding robust self-assembly of heterogeneous structures

Isabella R. Graf,[1,*] Florian M. Gartner,[1,*] and Erwin Frey[1,†]

[1] *Arnold Sommerfeld Center for Theoretical Physics and Center for NanoScience, Department of Physics, Ludwig-Maximilians-Universität München, Theresienstrasse 37, D–80333 München, Germany*

Self-assembly is not only crucial for living organisms but also an important component for the technological production of functional nanostructures. For these structures to be versatile, they must be heterogeneous and consist of a number of different modules that are responsible for specific functions or tasks. Recently, however, a conceptual model has demonstrated that the self-assembly of heterogeneous structures can be subject to strong stochastic effects that significantly suppress yield. Given that self-assembly is an essential process in living systems and in nanotechnological applications, this finding raises two immediate questions: How do heterogeneous structures assemble efficiently in living organisms? Which guiding strategies could be implemented into the design of artificial assembly systems in order to achieve high assembly yield? An answer to these questions requires a thorough understanding of the occurrence of the detrimental stochastic effects ("stochastic yield catastrophe"). To make progress, here we formulate an effective theory for the aforementioned conceptual model that enables us to unravel the various sources of stochasticity in terms of their relevance to assembly efficiency. From this effective theory, we identify the fluctuations in the availability of the different constituents for binding as the major cause of the stochastic yield catastrophe. We use this insight to propose and implement two control strategies to improve yield by reducing the variance in the relative availability of constituents. These are based on supply control by providing particles in bursts or by implementing self-inhibitory feedback. Remarkably, also a strong increase in the variance between constituents enhances assembly yield, provided it is coordinated and favors a specific assembly path. We discuss possible limitations and applications of all control strategies and place our findings in a broader perspective.

I. INTRODUCTION

One of the defining features of living systems is their ability to autonomously generate complex structures and macro-molecular machineries. Underlying this ability are self-assembly and self-organization processes. These rely on local interactions between constituents but are generically not driven by external guidance or a global control system [1, 2]: Unlike someone who assembles bricks in the correct order to create a predefined structure, the assembly of cellular structures such as microtubules [3–5], ribosomes [6, 7], flagellar motors [8, 9] or intracellular viruses [10–12] must work without an externally provided construction plan. How do local interactions between constituents suffice to build macroscopic structures? In particular, it is still an open question why assembly yield can be high although the free energy landscape may exhibit many local minima [2, 13–15] in which the dynamics can get kinetically trapped on the relevant timescales. As a result of such kinetic trapping, only fragments of structures might be formed but no complete structures [2, 16, 17].

Elucidating principles for the kinetics of self-assembly processes is expected to be useful not only for the understanding of intracellular self-assembly but also for the design of artificial self-assembly systems [13]. These artificial assembly processes are based on techniques such as DNA nanotechnology, including DNA origami [18, 19], DNA bricks [20], or single-stranded tiles [21], and allow for a rich variety of possible large-scale structures. As a result, artificial self-assembly is believed to be a promising route towards functional nanostructures [2, 22], with proof-of-principle achievements ranging from nanoboxes with programmable lids [23] to micrometer-sized colloids [24].

The problem of kinetic trapping has long been studied in these systems and has been described both in experiments reproducing natural assembly processes of, for example, virus capsids [10, 25, 26], as well as in artificial self-assembly systems based on DNA nanotechnology [27, 28]. It has been pointed out by several studies that reversibility of binding is a possibility to overcome kinetic trapping [29–34]. However, for virus capsids and other functional biological structures it has been shown that at least part of the reactions are not reversible on the time scale of the assembly process [35, 36]. From a biological point of view, this (partial) irreversibility is reasonable since, for instance, virus shells must be stable to protect their cargo in adverse environments, which requires sufficiently strong and stable bonds. Allosteric control has therefore been proposed as a viable mechanism to actively suppress nucleation and thereby avoid kinetic trapping in weakly reversible self-assembly [36–39]. And indeed, it has been demonstrated that allosteric effects play an important role in the self-assembly of viruses, flagellar motors and actin filaments [37, 38, 40–43].

Furthermore, the principle of "slow nucleation but fast growth" has become a guiding rule for self-assembly [10, 16, 20, 44, 45]. It is based on the idea that if nucle-

* These authors contributed equally to this work.
† Please send correspondence to frey@lmu.de.

ation of new structures is slow compared to the growth of existing structures, the structures are formed one after the other and there is no competition for resources. One would expect that such a situation could be induced by allosteric effects, which are assumed to control the nucleation speed. However, a recent study shows that for heterogeneous systems, the way in which allosteric control is implemented plays a critical role [46]. In particular, if fluctuations in the availability of the different kinds of building blocks are relevant, a severe stochastic effect termed 'stochastic yield catastrophe' can cause kinetic trapping in weakly reversible self-assembly. This type of kinetic trapping is special in that it constitutes a genuinely stochastic effect that is not captured by mean-field chemical rate equations.

Since fluctuations in the relative concentrations of particles can arise in multiple different ways ranging from diffusion to stochastic production of the building blocks, stochastic yield catastrophes might represent a major limitation for self-assembly efficiency. Hence, it is crucial to gain a deeper understanding about the underlying causes of stochastic yield catastrophes in order to propose effective strategies to mitigate their detrimental effect. These insights could enhance our understanding of cellular self-assembly processes and usefully inform experiments and nanotechnological implementations. To this end, here we revisit a conceptual model of a linear, heterogeneous assembly process as introduced in Ref. [46] and focus on a quantitative understanding of the role of fluctuations. In line with Einstein's demand on what a proper model should be like [47], we find that this model is conceptually rich enough to show all essential features of self-assembly processes and – at the same time – as simple as possible to allow for an in-depth theoretical analysis. We develop an effective stochastic theory that extends a previously formulated mean-field description [46]. In contrast to this mean-field description, it captures the observed phenomenology, including the stochastic yield catastrophe, qualitatively correctly. Our analysis reveals that the main contribution to the stochastic yield catastrophe is indeed due to demographic noise, rather than inherent reaction noise. Based on this insight, we propose different strategies to suppress the detrimental effect of fluctuations and discuss their possible implementations. Concretely, these strategies prevent stochastic effects either by reducing fluctuations in the availability of the different species or by controlling the supply in a way to favor specific assembly paths. We expect that these strategies could be implemented in systems based on modern nanotechnological devices in rather straightforward ways. Hence, these strategies might constitute viable ways to realize irreversible self-assembly of complex information-rich nanostructures.

II. MODEL DEFINITION AND RESULTS FROM STOCHASTIC SIMULATIONS

A. Stochastic model

We consider a conceptual irreversible self-assembly process with a unique target structure (ring) of finite size L composed of monomers of S different species, as illustrated in Fig. 1, which summarizes the key processes during self-assembly. Specifically, we take into account a stochastic activation step and irreversible binding reactions as introduced in Refs. [46, 48]. All monomers are inactive initially and are activated at a per capita rate α. Once active, monomers of species $i \in \{1, \dots, S\}$ bind other monomers of the (periodically) neighboring species $(i\pm1)\mathrm{mod}S$ to form dimers at rate μ (*dimerization*), e.g. active monomers 3 and 4 in Fig. 1. Furthermore, monomers can also attach to larger structures by binding to a periodically consecutive species (*correct binding*) at rate ν, e.g. active monomer 5 and polymer 3-4. Alternatively, binding may also occur between polymers and monomers of the next-nearest-neighbor species at a reduced rate $\nu_{\mathrm{def}} \ll \nu$, creating a defect in the structure (*defect formation*, e.g. active monomer 4 and polymer 6-1-2, creating a defect at species 3 (or 5). Since polymer-polymer binding is typically assumed to be less relevant as compared to binding between monomers and polymers [10, 17, 49, 50], we assume that structures only grow by the attachment of monomers. Once the structure has reached the target size L (including the defects; see the final target structures in Fig. 1), the ring closes and no further growth of this ring is possible.

A typical assembly pathway proceeds as follows: As soon as some monomers have been activated, monomers dimerize and polymers start to grow by monomer attachment of correct (neighboring) or defect-forming (next-nearest neigbhboring) species. These polymers then all continue to grow until they have either reached the target size or until all monomers are bound in polymers.

The quality of the assembly process (*"yield"*) is measured at exactly this time when no further growth is possible any more as all monomers have been activated and are depleted (bound in larger structures). The yield Y is defined as the number of finished target structures, N_{target}, compared to the maximally possible number of defect-free target structures, N^*_{target}. In a perfect assembly process each species occurs exactly L/S times in each finished structure. Hence, the number of possible defect-free target structures is given by $N^*_{\mathrm{target}} = N/(L/S)$. Hence, the yield is defined as

$$Y = \frac{LN_{\mathrm{target}}}{SN}\,. \tag{1}$$

Analogously, the defect-free yield, $Y^{(0)}$ is defined as the number of defect-free target structures, $N^{(0)}_{\mathrm{target}}$, com-

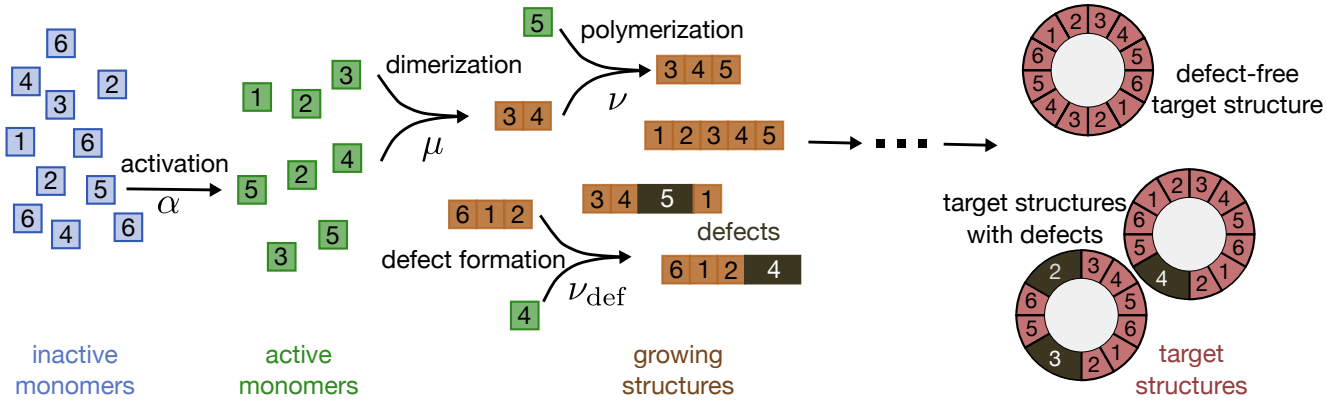

FIG. 1. **Schematic of the conceptual self-assembly model** Rings of target size L are assembled from S different species of particles (here $L = 12$ and $S = 6$). All monomers start in an inactive state (blue) and have to be activated before being able to bind. This activation happens at a per-capita rate α. Structures grow by attachment of active monomers (green). Defect-free binding happens only between nearest-neighbor species (in a periodically consecutive ordering), so species i can bind to $i \pm 1$ (modulo S). Dimerization happens at rate μ whereas monomer binding to larger structures (orange) happens at rate ν. Defect formation occurs at a much lower rate $\nu_{\rm def} \ll \nu$ between next-nearest neighbors, leaving out one species and thereby creating a defect (black). A structure is finished (red) once its size (including the defects) has reached the target size L. There are N particles of each species, so that in total the system could build NS/L defect-free target structures.

pared to $N^*_{\rm target}$:

$$Y^{(0)} = \frac{LN^{(0)}_{\rm target}}{SN}\,. \tag{2}$$

If many structures are completed during the process (irrespective of whether they contain defects or not), the yield is high. In contrast, the defect-free yield is high only if many defect-free structure are produced. It thus quantifies the quality and amount of target structures.

B. Mean-field behavior (abundant resources)

In this section we summarize the most important findings of the previous studies [46, 48] to gain a first intuition about the self-assembly process. We discuss the more intuitive deterministic limit of large system size $N \to \infty$ first and focus on the case of finite resources afterwards.

A well-known principle for efficient self-assembly is the 'slow-nucleation principle' [10, 20, 21, 44–46, 51] which states that the assembly yield is high if nucleation of new structures is slow compared to the growth of structures. In this case, it is very likely that a structure that has been nucleated grows into the target structure before a new structure is nucleated. As a result, structures are assembled one after the other and the assembly yield is high. Conversely, if nucleation of new structures is fast, many structures will be nucleated simultaneously. These polymers then compete for the same resources and resources run out before the structures are completed ('depletion trap').

In the deterministic limit of many particles per species $N \to \infty$, the self-assembly process in our model, Fig. 1, behaves according to the slow-nucleation principle [46]. For high activation rate (large α) and fast dimerization ($\mu \approx \nu$), the number of active monomers is high and nucleation of new structures (dimerization) occurs more frequently than growth of larger structures. Correspondingly, the yield is very low. In agreement with the slow-nucleation principle, the efficiency of the assembly process can be improved by either decreasing the dimerization rate μ or the activation rate α compared to the growth rate $\nu \equiv 1$: Yield is a monotonic function of both α and μ and perfect yield is always achieved in the limit of small α or μ, irrespective of the number of particles $N \gg 1$ or species S [46, 48]. Indeed, for fixed number of particles N per species and fixed target size L yield is independent of the number of species S.
As discussed in the next section II C, stochastic effects do, however, qualitatively alter the self-assembly process.

C. Stochastic effects for finite resources

For reduced resources (smaller N) and heterogeneous structures $S > 1$, fluctuations in the dynamics become relevant and the behavior of the system is qualitatively different from the behavior in the deterministic limit [46, 48]. In this case, stochastic simulations of the system based on Gillespie's algorithm [52] demonstrate that the yield saturates at an imperfect value $Y_{\rm max}$ in the limit of small α if N is not large enough (Fig. 2 (a, d)). Previously, we have shown that below a threshold value of N, which depends on the size of the target structure, this saturation value $Y_{\rm max}$ is in fact zero and the system produces no yield although yield is perfect in the corresponding deterministic description ('stochastic yield catastrophe') [46]. Furthermore, we have shown that yield can be a non-monotonic function of the activation rate both

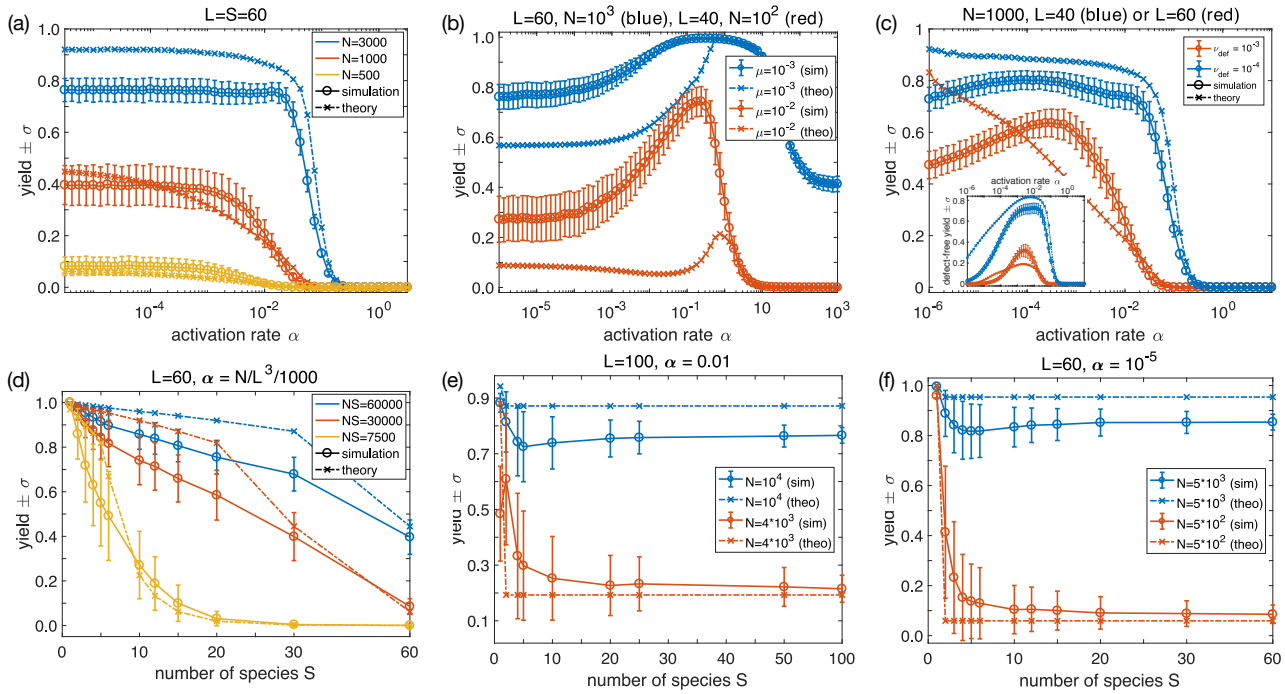

FIG. 2. **Stochastic yield catastrophe as observed in stochastic simulations (circles) and results of the effective theory (crosses).** (a) The average yield and its standard deviation (in stochastic simulations) are plotted against the activation rate α for different numbers of particles per species $N = 3000$ (blue), $N = 1000$ (red) and $N = 500$ (yellow). Yields saturates at an imperfect value for $\alpha \to 0$. The parameters are $L = S = 60$, $\mu = \nu = 1$ and $\nu_{\rm def} = 0$. (b) For small dimerization rate, here $\mu = 10^{-3}$ (blue; $L = S = 60$, $N = 10^3$) or $\mu = 10^{-2}$ (red; $L = S = 40$, $N = 10^2$), the average yield can become a non-monotonic function of the activation rate α. The other parameters are $\nu = 1$ and $\nu_{\rm def} = 0$. (c) For finite defect formation rate, here $\nu_{\rm def} = 10^{-4}$ (blue) or $\nu_{\rm def} = 10^{-3}$ (red), both the defect-free yield (inset), i.e. the yield of all target structures without defects, as well as the total yield (main figure), i.e. the yield of all target structures with and without defects, can be a non-monotonic function of the activation rate α. The other parameters are $N = 1000$, $\mu = \nu = 1$ and $L = S = 60$ (red) or $L = S = 40$ (blue). (d) The average yield and its standard deviation are plotted against the number of species S for fixed total number of particles $NS = 60000$ (blue), $NS = 30000$ (red) and $NS = 7500$ (yellow). In this case, the average yield decreases with increasing heterogeneity of the structure (number of species S that make up the ring). The parameters are $L = 60$, $\alpha = N/L^3/1000$, $\mu = \nu = 1$ and $\nu_{\rm def} = 0$. The activation rate is chosen small enough that the yield has already reached its saturation value $Y_{\rm max}$ for $\alpha \to 0$. (e, f) The average yield and its standard deviation are plotted against the number of species S. In contrast to (d), here the number of particles per species N (and not NS) is fixed. Yield is highest for homogeneous structures $S = 1$ and levels off at an imperfect value for $S \gg 1$ (e) The parameters are $L = 100$, $\alpha = 10^{-2}$, $\mu = \nu = 1$, $\nu_{\rm def} = 0$ and $N = 10^4$ (blue) or $N = 4 * 10^3$ (red) as indicated. (f) The parameters are $L = 60$, $\alpha = 10^{-5}$, $\mu = \nu = 1$, $\nu_{\rm def} = 0$ and $N = 5 * 10^3$ (blue) or $N = 5 * 10^2$ (red) as indicated.

for $\mu < \nu$ or $\nu_{\rm def} > 0$ (Fig. 2 (b,c)), a feature that does not occur in the limit $N \to \infty$. In the case $\nu_{\rm def} > 0$, also the defect-free yield shows non-monotonic behavior with respect to the activation rate α (inset in Fig. 2 (c)). Finally, for fixed number N of particles per species and fixed target structure size L, the yield is not independent of the number of species S (Fig. 2 (e,f)). Instead, the yield is large for $S = 1$ but then drops for $S > 1$ and saturates for $S \gg 1$. It remained, however, elusive why these stochastic effects are so strong and which sources of stochasticity (demographic noise or reaction noise) contribute mostly to the observed phenomenology. One goal of this manuscript is to gain a deeper insight into which physical principles underlie the stochastic yield catastrophe.

D. Fundamental difference between the deterministic and the stochastic limit

What is the fundamental difference between the deterministic limit ($N \to \infty$) and the case of reduced resources? For $N \to \infty$, the randomness of binding and fluctuations in the relative number of the different constituents (demographic noise) are negligible [46, 48]. This is, however, not true for reduced resources. Heuristically, if certain species are temporarily less available than others due to random fluctuations in the activation of particles, the neighboring species will tend to nucleate additional structures or to form defects (Fig. 3 (a, b)). For instance, if a species required for correct growth is temporarily not available as an active monomer (e.g. species

6 in Fig. 3 (a)), a monomer of the next species might form a defect (species 1 in the figure). Similarly, active monomers of this next species might dimerize with a monomer of their other neighboring species instead. As a result, there will be too many nucleation events or too many defective structures, suppressing the (defect-free) yield. While it is intuitive that fluctuations in the availability of the different species may lead to additional nucleation events or defect formation, a quantitative understanding is still lacking. Due to the central limit theorem, demographic fluctuations or shot noise are typically expected to scale as $1/\sqrt{N}$ compared to the mean N. So, why do demographic fluctuations in the relative availability of the different species lead to such strong stochastic effects even in cases when the number of particles per species N is large? To which extent do the different sources of stochasticity (demographic noise, reaction noise due to randomness in binding) contribute to the observed effects? To address these questions, we next formulate an effective theory. This effective description of the self-assembly process focuses on stochasticity introduced by demographic fluctuations in the relative number of active monomers of the different species and neglects reaction noise. It will turn out that effectively putting in this source of stochasticity can indeed qualitatively account for the observed strong deviations from the deterministic description.

III. EFFECTIVE THEORY: IDEA

The goal of this section is to provide a first motivation for the formulation of the effective theory. Since the effective theory will be based on the deterministic description of the system in Ref. [46], we summarize the most important aspects of this deterministic picture first. In addition, this summary is intended to give insights into which additional aspects might be important for a description of the stochastic effects. Building on these insights, we will then argue for our particular approach to extend the deterministic description.

A. Reduction to one-species problem in the deterministic limit

The deterministic description of the process as presented in Ref. [46] is based on the assumption that the number N of particles per species is large. Accordingly, it neglects chemical noise due to randomness in choosing a binding partner and demographic fluctuations in the number of active particles of the different species. Consequently, all species are equivalent and all structures of equal size can be treated on the same footing, irrespective of which species they are composed of. Using symmetry arguments, it is thus possible to characterize the assembly dynamics only in terms of the size l of the different structures (for simplicity, we restrict our discussion to the case without defect formation $\nu_{\mathrm{def}} = 0$). Polymers of all sizes $l \in \{2, \dots, L-1\}$ (except for the target size $l = L$) grow by attachment of monomers at rate ν per monomer at either end. In the time evolution of the number c_l of polymers of size l per species, this process corresponds to a loss term of $-2\nu m^a c_l$ where m^a denotes the number of active monomers per species. The factor of 2 comes from the two configurations in which a monomer can bind to a polymer (namely from the left or right). This loss term appears as a gain term for the number c_{l+1} of structures of size $l+1$ since attachment of a monomer to a structure of size l leads to a structure of size $l+1$. Furthermore, two active monomers dimerize at per capita rate μ. For m^a active monomers per species, this yields a gain term $\mu(m^a)^2$ for the dimers. In contrast to the gain term due to polymer growth, there is no factor of 2 here. This is due to the fact that there is only one possibility to create a dimer from two monomers. Taken together, the time evolution of the number of structures c_l of size $l \geq 2$ per species is thus given by [46]

$$\partial_t c_2 = \mu(m^a)^2 - 2\nu m^a c_2\,, \tag{3a}$$

$$\partial_t c_l = 2\nu m^a (c_{l-1} - c_l)\,, \tag{3b}$$

$$\partial_t c_L = 2\nu m^a c_{L-1}\,. \tag{3c}$$

Initially there are N inactive monomers of each species. All of these are activated at the per-capita rate α. The survival probability up to time t is thus $e^{-\alpha t}$ and the average number of inactive monomers at time t is $Ne^{-\alpha t}$. Hence, the gain term for active monomers at time t (which is given by the total activation rate) is $\alpha N e^{-\alpha t}$. The loss term has two contributions, one from dimerization and one from growth of polymers. Analogously to the corresponding loss/gain terms for the polymers, these are given by $-2\nu m^a c_l$ for $l \in \{2, \dots, L-1\}$ for polymer growth and $-2\mu(m^a)^2$ for dimerization. The additional factor of 2 in the dimerization loss term is a stoichiometric factor (two monomers participate in the dimerization). In summary, the time evolution of the monomers is given by [46]

$$\partial_t m^a = N\alpha e^{-\alpha t} - 2\mu(m^a)^2 - 2\nu m^a \sum_{l=2}^{L-1} c_l\,. \tag{4}$$

Note that here and in the following we always consider the number of structures *per species*. For better readability, we will not explicitly mention this in the following.

As mentioned before, in the deterministic limit, the assembly yield is independent of the number of species S (for fixed N and L). This equivalency is apparent from the time evolution of the structures, Eqs. 3 and 4, into which the number of species S does not enter. It is, however, in conflict with stochastic simulations where heterogeneous systems ($S > 2$) are subject to strong fluctuation effects but the homogeneous system ($S = 1$) is not (Fig. 2 (e,f)). The reason for the equivalency in the deterministic description lies in the assumption that all species behave identically. Extending the deterministic

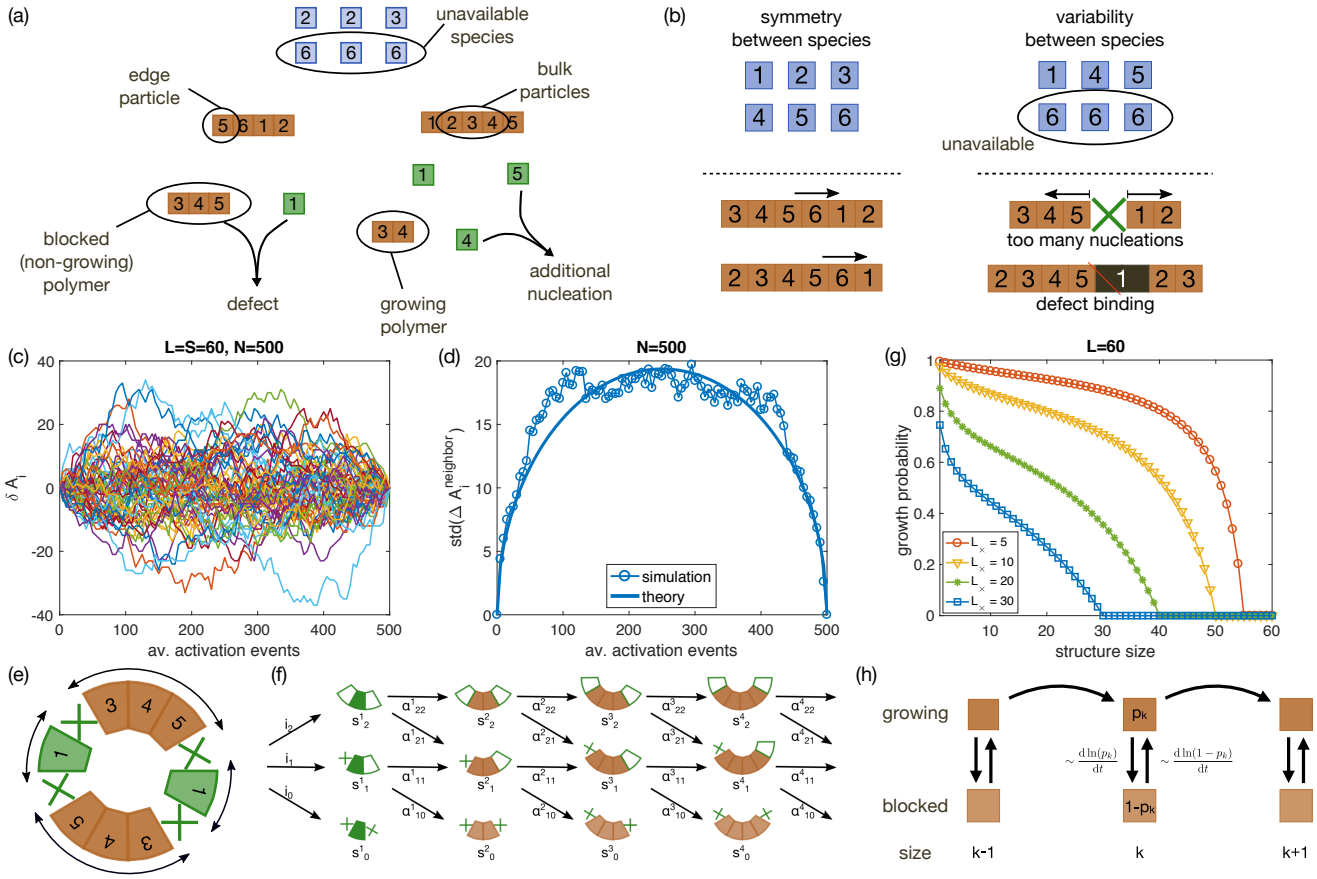

FIG. 3. **Illustration of the effective theory and the terminology.** (a, b) Species which are currently unavailable for binding (in short: "unavailable species") lead to additional nucleation events and defect formation. If a species ("unavailable species"; here e.g. species 6) has been activated much less than its neighbors, these neighbors tend to nucleate new structures (e.g. excess of active monomers of species 4 and 5 in (a) or missing link between polymers 3-4-5 and 1-2 in (b)) or to form defects (e.g. active monomer 1 binds erroneously to polymer 3-4-5 due to a lack of other binding partners, thereby forming a defect). In the deterministic description, which assumes symmetry between the species, all species are equally available and large structures form. (c) The number of activated particles of the different species A_i (different colors) relative to their mean, $\delta A_i = A_i - \bar{A}$, is shown in dependence of the average number of activation events per species $\bar{A}$. The data are shown for one simulation with parameters $L = 60$, $N = 500$, $\nu = \mu = 1$, $\nu_{\rm def} = 0$ and $\alpha = 0.01$. (d) The simulated (symbols) and theoretical values (line) of the standard deviation of the neighbor fluctuations $\sigma = \mathrm{std}(\Delta A_i^{\rm neighbor} = A_{i+1} + A_{i-1} - A_i - \bar{A}) = \sqrt{3\bar{A}(1 - \bar{A}/N)}$, are plotted against the average number of activation events per species, $\bar{A}$, and for the same parameter values as in (a). The standard deviation is calculated with respect to all species i in a single realization of the process. (e) Unavailable species (crosses) act as obstacles for growth. The distribution of segment sizes between unavailable species depends on the probability that species are unavailable. (f) Illustration of the assembly paths into structures with different numbers of "growing ends". If structures grow by attachment of monomers of an available species, the number of growing ends either stays the same or decreases by one. (g) Prediction for the steady-state probability p_l that a structure that grows to size l ends up in a state where it can grow by attachment of monomers of available species. This probability depends on the number $S_\times$ of unavailable species. The relevant parameters are $L = 60$ and $L_\times = (L/S)S_\times = 5$ (red circles), $L_\times = 10$ (yellow triangles), $L_\times = 20$ (green stars) and $L_\times = 20$ (blue squares). (h) In the effective theory, structures can be either in a state where both neighboring species are unavailable ("blocked") or in a state where at least one neighbor is available ("growing"); see also (a). Structures in the blocked state can only grow once an unavailable species is activated, whereas structures in the growing state can also grow by available species. Over time, the number of unavailable species changes. As a result, structures can change from being blocked to being able to grow or vice versa.

picture with the goal to capture the stochastic limit, will thus require to reconsider this assumption. In the next subsection, we will motivate our particular choice for extending the deterministic description.

B. Effective description of the stochastic system as one-species problem

A fully stochastic description of our system would require a high-dimensional master equation, including all

possible structure configurations (lengths and compositions). Such a master equation is not very revealing *per se* since it reflects the complexity of the dynamics one-to-one. However, by finding an (effective) representation in a lower-dimension space, one can hope to get important insights into which features of the full process are crucial for the dynamics and which are not. A typical approach for finding such a lower-dimensional representation are moment-closure techniques [53]. For this purpose, one derives a hierarchy of equations that relates the different moments to each other. For large systems with many interacting elements, this hierarchy is typically extensive and it is necessary to define a closure relation that truncates the hierarchy. In the simplest case, only the first moment (i.e. the average) is taken into account while all correlations are neglected. Implementing this procedure rigorously [46] leads to the deterministic description, Eqs. 3 and 4. We tried to refine this closure relation by considering second-order moments. However, due to the large number of combinatorial possibilities, there is no canonical choice for the closure relation and we did not succeed to define a reasonable one. Is there another possibility to effectively reduce the high-dimensional system to a lower-dimensional space? Potentially yes, at least if one assumes that only demographic fluctuations in the relative number of active monomers between species but not reaction noise are crucial. In this case, it might not be necessary to resolve the exact composition of the structures. Instead one could try to classify structures into two different states per given size of a structure: one for structures which currently cannot grow due to a lack of neighboring particles ("blocked polymers") and one for the structures that can grow by monomer attachment of neighboring species ("growing polymers"); see Fig. 3 (a) for an illustration. In that way, the description is still "close" to the deterministic description in the sense that only an additional state has to be introduced. If this were successful, it would reduce the original set of $(L+1)\times S$ ordinary, stochastic differential equations [54] to a system of $2(L+1)$ ordinary differential equations (see also below for details) compared to L in the deterministic case (Eqs. 3 and 4).

Of course, to formulate such an effective theory it is necessary to define more precisely what we mean by "blocked" and "growing polymers". To do this and to develop a good intuition for the system, in the next section, we will look more closely at the system's properties and, in particular, the variations between species.

C. Origin of stochastic yield catastrophe: Inter-species variability and "unavailable species"

As mentioned above, intuitively, fluctuations in the availability of the different species can lead to undesirable nucleation events or defect formation if the species necessary for correct growth are currently unavailable for binding. So, how distinct is the availability of the different species? Or, more concretely, how much do the numbers of activated particles A_i of the different species vary compared to each other and compared to the mean value $\bar{A}=\sum_i A_i/S$? Fig. 3(a) shows the deviation $\delta A_i = A_i - \bar{A}$ of the number of activated particles for all species (colors) relative to their mean value, as measured in one single stochastic simulation with parameters $L=60$ and $N=100$. The deviation is plotted against the average number of activation events per species $\bar{A}$ (which is a monotonic function of time). As expected, the deviation is zero at the beginning ($\bar{A}=0$) and at the end ($\bar{A}=N$) since then no particles of either species or all particles of all species are activated, respectively. In between these two limits, it attains values of typically 2-3 % of the total number of particles per species N. This value can be understood analytically: There are N particles of each species and NS particles in total. Furthermore, if the average number of activation events per species is $\bar{A}$, in total $S\bar{A}$ activation events have happened. Thus, since activation of particles occurs independently for all particles and species, the number of activated particles of one species A_i is determined by the following random process: Take $S\bar{A}$ random draws without replacement from a population of size SN that contains N "successes" (particles of species i). The distribution corresponding to this random process is called hypergeometric distribution [55] with parameters SN, N and $S\bar{A}$:

$$A_i \sim \mathrm{HypGeo}(SN, N, S\bar{A}). \tag{5}$$

Its variance is given by

$$\mathrm{Var}_0 = \bar{A}\left(1-\frac{1}{S}\right)\left(1-\frac{\bar{A}}{N}\right)\frac{NS}{NS-1} \approx \bar{A}\left(1-\frac{\bar{A}}{N}\right), \tag{6}$$

where the approximation is valid for large S. As a result, the standard deviation is maximal when half of the particles have been activated on average, $\bar{A}=N/2$, with a value of $\sqrt{N}/2$ which is roughly 11 (or 2.2 %) for $N=500$.

Since the average number of particles per species $\bar{A}\propto N$, this scaling of the variance shows that the fluctuations in the relative particle number of the different species are indeed of the order $1/\sqrt{N}$ compared to the total number of particles N per species. As mentioned above, this scaling is expected for demographic noise. But how can these order $1/\sqrt{N}$ fluctuations have such a strong effect even for large N? There are several possible reasons: First, the dynamics of the process triggers a kind of reinforcing effect ("snowball effect") where the effect of fluctuations gets amplified due to the dynamics it causes itself. If fluctuations at the beginning of the dynamics result in too many nucleation events, too many structures form. In the worst case, none of these structures is then completed due to competition for resources. So, a small fluctuation in the beginning has a large effect on the outcome and whether a fluctuation changes the self-assembly process considerably is thus history- and time-dependent. This dependence on time is amplified even more since the population size is non-constant. As a result, it is

not necessarily the standard deviation compared to the total number of particles N that is relevant for the process but rather the standard deviation compared to the mean number of activated particles, $\bar{A}$. So, the quantity to look at is not $\mathrm{Var}_0/N^2 = \bar{A}\,(1-\bar{A}/N)/N^2$ but rather the coefficient of variation,

$$CV^2 = \frac{\mathrm{Var}_0}{\bar{A}^2} = \frac{\bar{A}(1-\bar{A}/N)}{\bar{A}^2} = \frac{1-\bar{A}/N}{\bar{A}}\,. \qquad (7)$$

This coefficient of variation is indeed very large at the beginning (it diverges for $\bar{A} \to 0$ due to the zero mean), suggesting that in particular at the beginning, there can be too many undesirable nucleation events. In conclusion, the effect of fluctuations is strongly time- and history-dependent.

In this section, we tried to motivate our approach to extend the deterministic description of the self-assembly process by its "essential" ingredients. It is based on the idea that it is mainly the demographic noise that is decisive for the dynamics of the assembly process. So, inspired by the species symmetry in the deterministic description, we assume that it is not necessary to keep track of all possible configurations of structures but that it is sufficient to characterize structures only in terms of whether they can grow by monomer attachment or whether they are blocked due to unavailable species. The probabilities to be in either state are expected to depend on the variability between species which is quantified by the distribution of the number of active particles, Eq. 5. We will revisit this distribution when we set up the effective theory in the next section.

IV. EFFECTIVE THEORY: QUANTIFICATION

The goal of this section is to make the effective theory for the model in Fig. 1 explicit. As we formulate the theory, we also try to give an answer to the following questions: How does variability between species influence the dynamics of the assembly process? How does a species that is currently not available for binding alter the self-assembly dynamics?

We will proceed as follows: First, we introduce some terminology (Sec. IV A) that will make the formulation of the effective theory more convenient; see also Fig. 3 (a). Next, we determine the probability of species i to be currently unavailable for binding; for a precise definition see Sec. IV A and Fig. 3 (a). This can be due to low activation of species i itself or due to high activation of the neighboring species $i \pm 1$ and thus a high likelihood for species i to be bound to these neighboring species on both sides already; for instance, species 6 in Fig. 3 (a) has been activated less than average and, at the same time, its neighbors, species 5 and 1, have been activated more than average. From the probability of being unavailable for binding and the corresponding number of "unavailable species" we then determine the probability for a structure to be able to further grow, depending on the length of the structure. Finally, we write down an *effective one-species theory* for the polymer-size distribution that considers two states, one "blocked" and one "growing" state for each polymer size (for a precise definition see Sec. IV A; in Fig. 3 (a) the polymer 3-4-5 is blocked because there is neither an active monomer of species 2 nor one of species 6 whereas 3-4 can grow by attachment of an active monomer of species 5). A reader not interested in the mathematical details is referred to Sec. IV F for a summary.

A. Terminology

To begin with we define some terminology that will be useful in formulating the effective theory; for an illustration see also Fig. 3(a):

- "*Monomers*" denote particles that are not bound to any other particle, yet.
- "*Edge particles*" are defined as particles attached to either end of unfinished polymers, e.g. particles of species 5 and 2 in the polymer 5-6-1-2.
- In contrast, "*bulk particles*" are defined as those particles that are part of a larger polymer but are not edge particles, e.g. particles of species 2, 3 and 4 in the polymer 1-2-3-4-5.
- "*Growing polymers*" in a given system are defined as those polymers that have available binding partners in the pool of active monomers which (upon binding to the polymer) lead to the correct assembly of the structure, without creating a defect, e.g. polymer 3-4 to which active monomer 5 could bind to.
- "*Blocked polymers*", on the other hand, are those polymers in the system that lack correct binding partners in the monomer pool, e.g. polymer 3-4-5 can only grow by attachment of an active monomer which is out-of-sequence and would create a defect (monomer of species 1) since there are no active monomers of species 2 or 6 available.
- Finally, we denote a species as "*unavailable*" if it is currently not available for binding to any structure (monomer or polymer) in the system. For this to be the case two conditions need to be fulfilled: First, there is no active monomer of that species present. Second, there are no edge particles of that species. If there are neither active monomers nor edge particles, all activated particles are bulk particles and, thus, already have binding partners on both sides. Hence, in this case there are currently no processes possible that would lead to further binding of a particle of an unavailable species to another monomer

or polymer. Note that this definition does not necessarily imply that the unavailable species has not been activated, at all, but rather that its activation is small compared to its neighboring species (see also below) and, as a result, it is not available for binding (any more).

B. Probability for the unavailability of species

How do fluctuations in the relative number of particles of the different species translate into species currently not being available for binding? To address this question, we will employ a fluctuation-corrected mean-field argument in the following: Denote by $N_i^{(b)}$ the number of particles of species i a neighboring species can bind to. This number has two contributions, namely the edge particles and active monomers of this species. Deterministically, the number of edge particles per species is given by $2\,u$ where

$$u = \sum_{k=2}^{L-1} c_k \tag{8}$$

is the total number of all unfinished polymers (of size $k \in \{2, \ldots, L-1\}$) per species. The reason is that each unfinished polymer has two ends, implying that there are in total $2\,S\,\sum_{k=2}^{L-1} c_k$ edge particles or on average $2\,\sum_{k=2}^{L-1} c_k$ per species. As a result, deterministically (i.e. in a mean-field description) $N_i^{(b)}$ is given by

$$\bar{N}_i^{(b)} = 2\,u + m^a \tag{9}$$

where m^a is the number of active monomers per species. Due to the species symmetry in the deterministic mean-field description [46], this result is independent of the species index i.

This will not be the whole story in a stochastic description since fluctuations in the activation of the different species are expected to influence the number of active monomers and edge particles of the different species. Heuristically, if species i is activated less (more) than average, there will be less (more) active monomers and/or edge particles, so $N_i^{(b)}$ will be smaller (larger). To quantify this heuristic picture, we apply a fluctuation-corrected mean-field argument which conceptually corresponds to a lowest-order perturbation theory in the fluctuations: We assume that $N_i^{(b)}$ increases (decreases) by 1 for each particle that species i is activated more (less) than average. That is, $N_i^{(b)}$ has an additional term

$$\delta A_i = A_i - \bar{A}, \tag{10}$$

where A_i is the number of activated particles of species i and $\bar{A} = \sum_i A_i/S$ is the average over all species, as above. The idea is that each additionally activated particle is either present as an active monomer or bound to a polymer as an edge particle. Conversely, if one had to remove one particle of one species from a mean-field configuration with the goal to change "as little as possible", one would remove an active monomer or an edge particle. Removing or adding an edge particle also changes the number of edge particles of the neighboring species. Thus, $N_i^{(b)}$ is also affected by the activation levels of the neighboring species $i\pm1$. For simplicity, we assume that each additionally (less) activated particle of one of the neighboring species reduces (augments) the number of edge particles or the number of active monomers of species i by 1 [56]. Thus, from this direct dependency of the number of edge particles of species i on the activation levels of the neighboring species $i \pm 1$, $N_i^{(b)}$ gets reduced by

$$-(\delta A_{i+1} + \delta A_{i-1}). \tag{11}$$

Taken together, we find the following fluctuation-corrected mean-field expression for the number of active monomers and edge particles of species i

$$\begin{aligned} N_i^{(b)} &= 2\,u + m^a + \delta A_i - (\delta A_{i+1} + \delta A_{i-1}) \\ &= 2\,u + m^a + \bar{A} + A_i - (A_{i+1} + A_{i-1})\,. \end{aligned} \tag{12}$$

In principle, this expression can become negative. This is an artefact of the above mentioned procedure which *per se* only makes sense for small fluctuations with respect to the mean-field configuration. We elaborate on this point in the following: In a mean-field configuration, the number of particles of species i a neighboring species can bind to is given by $N_i^{(b)} = \bar{N}_i^{(b)} = 2\,u + m^a$. Decreasing the activation level of species i, A_i, or increasing the levels of $i\pm1$, $A_{i\pm1}$, will effectively remove active monomers and edge particles of species i, thus decreasing $N_i^{(b)}$. Of course, if at all, this procedure only makes sense until there are no more active monomers and edge particles of species i left: $N_i^{(b)} = 0$. Further reduction of A_i or increase $A_{i\pm1}$ will certainly also affect the bulk particles of species i, potentially "breaking up" larger polymers. Then, we formally have $N_i^{(b)} < 0$. Intricately, it is exactly this tail statistics when formally $N_i^{(b)} < 0$ that is presumably most relevant for the strength of the stochastic effects: As soon as fluctuations are large enough to trigger a qualitatively different growth behavior ("breaking up larger polymers"), strong stochastic effects are expected. Since it appears infeasible to us to derive this tail statistics from first principles, we try to gauge its effect through the probability that $N_i^{(b)} \leq 0$. More concretely, we use this "lowest-order perturbation theory procedure" and its prediction of the transition from $N_i^{(b)} > 0$ to $N_i^{(b)} \leq 0$ as a proxy for when a species qualitatively changes the growth behavior of the neighboring species because it is unavailable for binding.

In this picture, the probability of species i to be unavailable ("unavailability probability") is

$$\begin{aligned} p_\times &= \mathrm{Prob}(N_i^{(b)} \leq 0) \\ &= \mathrm{Prob}(A_{i+1} + A_{i-1} - A_i - \bar{A} \geq 2\,u + m^a). \end{aligned} \tag{13}$$

Does this formula for the probability meet the intuitive criteria for when a species should be unavailable? Which characteristics should such a probability of species i to be currently unavailable for binding have intuitively? First, it should increase if species i has been activated less than average because then it is likely that the species is unavailable for binding. Indeed, the smaller A_i, the larger $p_\times$ according to Eq. 13. Moreover, if the neighboring species $i\pm1$ are present in excess, they also effectively reduce the number of active monomers and edge particles of species i by binding to them. Thus, the probability for species i to be unavailable should increase. Also this correlation is reflected in Eq. 13: The larger $A_{i+1}+A_{i-1}$, the larger $p_\times$. Finally, if the average number of unfinished structures and active monomers, $2\,u+m^a$, increases, the probability to be unavailable should decrease. This is because then the deviation from the mean and, thus, the fluctuations must be larger. In fact, for larger $2\,u+m^a$ in Eq. 13, the unavailability probability $p_\times$ decreases. In sum, the effective probability given in Eq. 13 at least captures our intuitive expectations.

In order to find an explicit expression for $p_\times$ from Eq. 13, we next determine the distribution of the number of activated particles, A_i, up to time t. For each particle the survival probability up to time t, i.e. the probability not to become activated until time t, is given by $e^{-\alpha t}$. Thus, since all particles are activated independently, the number of activated particles of species i is binomially distributed with number of trials N and probability $1-e^{-\alpha t}$:

$$A_i \sim \mathrm{Bin}(N, 1-e^{-\alpha t}). \tag{14}$$

The variance of this distribution ("single-species variance") is given by

$$\sigma_0^2 = N\,(1-e^{-\alpha t})\,e^{-\alpha t}\,. \tag{15}$$

Moreover, the number of activated particles of each species is independent for all species, that is, the A_i are independent for all i. As a result, the fluctuations in the relative activation levels between neighboring species $\Delta A_i^{\mathrm{neighbor}} := A_{i+1}+A_{i-1}-A_i-\bar{A}$ exhibit a variance

$$\sigma^2 \approx 3\sigma_0^2. \tag{16}$$

Note that here we assumed $\bar{A}$ to be deterministic: $\bar{A}=N(1-e^{-\alpha t})$ which is a reasonable assumption if $S\gg1$. Interestingly, this predicted standard deviation of $\Delta A_i^{\mathrm{neighbor}}$,

$$\sqrt{3}\sigma_0 = \sqrt{3N(1-e^{-\alpha t})e^{-\alpha t}}\,, \tag{17}$$

already captures the standard deviation in a *single* realization of the stochastic process when averaged over all species i quite well; see Fig. 3(d). This observation indicates that the system is self-averaging, at least for large numbers of species $S\gg1$. Such a self-averaging property of the system is reassuring because this whole idea for the quantification of the effective theory is based on a (fluctuation-corrected) mean-field argument that should ultimately capture the typical behavior of single realizations of the self-assembly process. If there would not be any "internal averaging" in a single realization, there would not be much hope that the fluctuation-corrected mean-field argument for the unavailability probability, Eq. 13, is informative.

Combining all of the above and approximating the distribution of $\Delta A_i^{\mathrm{neighbor}}$ as a Gaussian distribution with mean zero and standard deviation σ, Eq. 16, we find the following expression for the probability of species i to be unavailable:

$$\begin{aligned} p_\times &= \mathrm{Prob}(\Delta A_i^{\mathrm{neighbor}} \geq 2u+m^a) \\ &= \frac{1}{2}\left[1-\mathrm{erf}\left(\frac{2u+m^a}{\sqrt{6}\sigma_0}\right)\right], \end{aligned} \tag{18}$$

where erf is the error function.

This equation makes sense intuitively: If there are on average more active monomers and edge particles per species (larger number of unfinished structures $2u+m^a$), larger fluctuations are required to find a species without active monomers and edge particles. As a consequence, the probability of a species to be unavailable for binding decreases.

So far, we only considered a single species and asked what the probability is that this particular species is unavailable. For the dynamics of the self-assembly process it is, however, relevant to know *how many* species are unavailable, since this determines which fraction of structures can grow. It is a nontrivial problem to determine the overall number of unavailable species from the single-species probability, due to correlations between species. For simplicity, we neglect these correlations and assume that the probability for species to be unavailable is independent for all species [57]. Then, the number of unavailable species scales with the number of species and is given by

$$S_\times = S\,p_\times = \frac{S}{2}\left[1-\mathrm{erf}\left(\frac{2u+m^a}{\sqrt{6}\sigma_0}\right)\right]. \tag{19}$$

If the number of species S does not equal the size of the target structure L ($S<L$) it is useful to also define the number of "unavailable sites" in the full ring structure,

$$L_\times = \frac{L}{S}S_\times = \frac{L}{2}\left[1-\mathrm{erf}\left(\frac{2u+m^a}{\sqrt{6}\sigma_0}\right)\right]. \tag{20}$$

This number does not equal the number of unavailable species if each species occurs repeatedly in the ring, i.e. if $L/S>1$. Each unavailable species, thus, has to be associated with L/S unavailable sites along the ring.

C. Size-dependent probability for a growing polymer to be able to further grow

Suppose there are $S_\times$ unavailable species and, correspondingly, $L_\times$ unavailable sites along the ring. What is

the probability p_l that a structure that has reached size $l \in \{2, \dots, L-1\}$ can further grow by attachment of an available species? To answer this question, let us look at segments of size l (Fig. 3(e-f)). These segments can be in three states: i) available species can bind to both ends (denoted by S_2^l; two "growing" ends), ii) an available species can bind to one end, whereas the other end would require an unavailable species to grow (S_1^l; one "growing" end, one "blocked" end), and iii) both ends require an unavailable species to grow and are, correspondingly, blocked by the unavailability of the neighboring species (S_0^l; two "blocked" ends).

What are the abundances of these states, denoted by s_2^l, s_1^l and s_0^l, respectively? And what do the (relative) abundances tell us about the probability that a structure that has reached size l can grow further by attachment of available species?

We will proceed as follows: First, as illustrated in Fig. 3(f), we define a simplified assembly process that is supposed to reflect the original assembly process in a stationary state in which the number of unavailable sites $L_\times$ is fixed. For this simplified assembly process, we then derive effective transition probabilities and determine the steady-state configuration by considering all possible assembly/growth paths into a structure of size l in state S_j^l, $j = 0, 1, 2$. Finally, this configuration will be used to determine the probabilities p_l that a structure which has grown to size l ends up in state where it has at least one growing end.

1. *Simplified assembly process*

Assuming for simplicity that structures only grow by attachment of available species, in the simplified assembly process, we consider the following transitions between structures of different sizes (see also Fig. 3(f)):

$$S_2^l \xrightarrow{\alpha_{22}^l} S_2^{l+1}\,, \tag{21a}$$

$$S_2^l \xrightarrow{\alpha_{21}^l} S_1^{l+1}\,, \tag{21b}$$

$$S_1^l \xrightarrow{\alpha_{11}^l} S_1^{l+1}\,, \tag{21c}$$

$$S_1^l \xrightarrow{\alpha_{10}^l} S_0^{l+1}\,. \tag{21d}$$

Here, α_{ij}^l denotes the transition rate from a structure of size l and state i to size $l+1$ and state $j = i$ or $j = i-1$. The basic idea to just consider these transitions in the simplified assembly process depicted in Fig. 3(f) is as follows: Available species only bind to so-called "growing" ends of structures. If an available species binds to a growing end of a structure S_2^l or S_1^l of size l, this growing end is replaced by a new end in the structure of size $l+1$, namely the subsequent species. This new end can be either growing (if another available species could subsequently bind) or blocked (if the next required species for growth is an unavailable species). Thus, by binding of an available species, the number of growing ends either stays the same or decreases by 1 but can never increase. As a result, there are only transitions between S_i^l and S_i^{l+1}, S_{i-1}^{l+1} for $i = 1, 2$.

Note that the simplified assembly process assumes that unavailable species are not present at all (instead of being present as bulk particles). Correspondingly, the transition rates α_{ij}^l automatically entail that all structures in the simplified assembly process are made up from available species only. Certainly, this is not satisfied in the original assembly process. Unfortunately, however, we were not successful in incorporating this aspect directly into the simplified assembly process, for instance, by additionally considering the possibility that blocked structures grow at a reduced rate (corresponding to activation events of unavailable species). One reason is that it was not clear to us how one should choose such a reduced rate in comparison to the other transition rates. Furthermore, even with a given reduced rate, we did not manage to derive an analytic expression for the probabilities p_l that a structure that has grown into size l can grow further, which is what we need to formulate the effective theory (see later). This effective theory will then indeed include the aspect that the number of available species changes over time but will be based on the quasi-stationary approximation of a fixed number of unavailable species $L_\times$ in the simplified assembly process. It will turn out that the fact that structures in the simplified assembly process only contain available species leads to a strict length cutoff in the dynamics above which there is no growth at all. We will come back to this point at the end of the section when we compare the predictions of the effective theory to results from stochastic simulations.

2. *Transition rates*

In order to determine the transition rates explicitly, consider a structure of size l with two available species next to both ends (two growing ends). For such a structure, there are $\binom{L-(l+2)}{L_\times}$ possibilities to distribute the $L_\times$ unavailable sites to the $L-(l+2)$ remaining sites on the ring. This number of possibilities decreases to $\binom{L-(l+3)}{L_\times}$ possibilities if the structure grows in a way that after growth there are still two growing ends. As a result, if the unavailable species (and sites [58]) are randomly distributed around the ring, the probability that this happens is $\binom{L-(l+3)}{L_\times}/\binom{L-(l+2)}{L_\times}$. Correspondingly, the probability that the structure grows into a structure with one growing and one blocked end is $1 - \binom{L-(l+3)}{L_\times}/\binom{L-(l+2)}{L_\times}$. Translating this probability into a transition rate yields $2\gamma(1 - \binom{L-(l+3)}{L_\times}/\binom{L-(l+2)}{L_\times})$ where γ corresponds to the total rate of attachment of an active monomer of an available species to one end. The factor of 2 is due to the fact that the rate that a monomer binds to a structure with two growing ends is twice as large as the rate that it binds to a structure with one growing end. Employing an

analogous argument for structures with one growing and one blocked end, we find the following transition rates (see Appendix for details)

$$\alpha_{22}^l = 2\gamma \frac{\binom{L-(l+3)}{L_\times}}{\binom{L-(l+2)}{L_\times}} = 2\gamma\left(1 - \frac{L_\times}{L-(l+2)}\right) = 2\gamma - \alpha_{21}^l, \tag{22a}$$

$$\alpha_{11}^l = \gamma \frac{\binom{L-(l+3)}{L_\times-1}}{\binom{L-(l+2)}{L_\times-1}} = \gamma\left(1 - \frac{L_\times - 1}{L-(l+2)}\right) = \gamma - \alpha_{10}^l. \tag{22b}$$

To determine the steady-state configuration of the simplified assembly process, we do not only need the transition rates between the states in the network but we also have to define a boundary condition which specifies at which rates ("influx rates") active monomers enter the system at the left boundary $l = 1$. For this purpose, we will denote by i_2, i_1 and i_0 the influx of active monomers that can grow at both ends (corresponding to state s_2^1), at only one end (s_1^1) and at no end (s_0^1), respectively. The total influx of active monomers $I = i_2 + i_1 + i_0$ is not crucial for the growth probabilities because it just scales the occupancy in the network and will drop out at the end. What is relevant are the relative influx rates for the different states. Similarly to above, the explicit forms we use come from considering the probabilities for a random monomer of an available species to have two, one or zero available neighbors, respectively: If the monomer has two available neighbors, there are $\binom{L-3}{L_\times}$ possibilities to distribute the remaining unavailable sites along the ring. For one or zero available neighbors, the number of possibilities are $2\binom{L-3}{L_\times-1}$ and $\binom{L-3}{L_\times-2}$, respectively. If the unavailable sites are randomly distributed around the ring, the influx rates have to scale with exactly these numbers of possibilities and we get

$$i_2 = \binom{L-3}{L_\times} I\,, \tag{23a}$$

$$i_1 = 2\binom{L-3}{L_\times-1} I\,, \tag{23b}$$

$$i_0 = \binom{L-3}{L_\times-2} I\,. \tag{23c}$$

3. *Steady-state configuration and growth probabilities*

From the influx rates, Eq. 23, and the transitions rates, Eq. 21, one can determine the steady-state numbers s_j^l of structures of size l with $j = 1, 2$ growing ends (see Appendix B). How is the probability p_l that a structure that grows into size l has at least one growing end expressed in terms of these steady-state numbers? It is given as the ratio of (1) the rate γ_1 at which structures of size $l-1$ grow into structures of size l that are still able to further grow by attachment of an available species compared to (2) the overall rate γ_2 at which structures of size $l-1$ grow into structures of size l:

$$p_l = \frac{\gamma_1}{\gamma_2}. \tag{24}$$

γ_2 has two contributions, namely the rate at which a monomer of an available species attaches to any structure of size $l-1$ with one growing end, $(\alpha_{11}^{l-1}+\alpha_{10}^{l-1})s_1^{l-1}$, and the corresponding one for attachment to a structure with two growing ends $(\alpha_{22}^{l-1}+\alpha_{21}^{l-1})s_2^{l-1}$. According to Eq. 22, $\alpha_{11}^{l-1}+\alpha_{10}^{l-1} = \gamma$ and $\alpha_{22}^{l-1}+\alpha_{21}^{l-1} = 2\gamma$, so we find

$$\gamma_2 = (\alpha_{11}^{l-1} + \alpha_{10}^{l-1})s_1^{l-1} + (\alpha_{22}^{l-1} + \alpha_{21}^{l-1})s_2^{l-1} \tag{25}$$

$$= \gamma(s_1^{l-1} + 2s_2^{l-1}). \tag{26}$$

γ_1 only counts the growth events for which the resulting structure is still able to grow by attachment of an available species (at least at one end). Correspondingly, it has the same contributions as γ_2 except that is does not include the transition $s_1^{l-1} \to s_0^l$ which produces a structure that cannot grow further. Compared to γ_2 the rate is thus reduced by $\alpha_{10}^{l-1}s_1^{l-1}$ and we have

$$\gamma_1 = \alpha_{11}^{l-1}s_1^{l-1} + (\alpha_{22}^{l-1} + \alpha_{21}^{l-1})s_2^{l-1} \tag{27}$$

$$= \alpha_{11}^{l-1}s_1^{l-1} + 2\gamma s_2^{l-1}. \tag{28}$$

It follows that

$$p_l = \frac{\alpha_{11}^{l-1}s_1^{l-1} + 2\gamma s_2^{l-1}}{\gamma s_1^{l-1} + 2\gamma s_2^{l-1}}\,. \tag{29}$$

Combining the above and using $\gamma - \alpha_{11}^{l-1} = \alpha_{10}^{l-1}$ yields the following expression for the probability p_l that a structure that has reached size l can grow further by attachment of available species:

$$p_l = 1 - \frac{\alpha_{10}^{l-1}}{\gamma}\ \frac{s_1^{l-1}}{s_1^{l-1} + 2s_2^{l-1}} \tag{30}$$

Finally, and as explained in detail in Appendix B, considering all possible assembly/growth paths to determine s_j^l gives an explicit expression of p_l

$$p_l = \begin{cases} 1 - \frac{lL_\times(L_\times-1)}{[L-(l+1)]\,[L+(l-1)L_\times-l]}\,, & l < L - L_\times \\ 0 & \text{else,} \end{cases} \tag{31}$$

if $L_\times > 1$. Otherwise, $p_l = 1$ for all l.

Figure 3(g) shows p_l as a function of the structure size l for a ring size $L = 60$ and for different, fixed numbers of unavailable sites $L_\times = 5$, $L_\times = 10$, $L_\times = 20$, and $L_\times = 30$. Intriguingly, p_l decreases for larger structure size l, implying that it becomes increasingly difficult for structures to grow further once they get larger. This suggests that unavailable species foster growth of small structures compared to large ones, which, generally speaking, leads to lower yield.

In closing this section, we would like to critically assess the validity of the simplified assembly process. First,

we assumed that always the same species are unavailable for binding. As can be seen in Fig 3(c) this assumption that always the same species are unavailable describes the right trend: If a species has a very low activation level compared to the mean at one point in time t_0, it is more likely to still have a very low activation level later, as compared to a species with high activation level at t_0. However, it is also evident from the figure that this statement is not strictly true. Indeed, there are species that have an average activation level at first but then over time change to having a low activation level compared to the mean and become unavailable for binding. Related to the first assumption, we furthermore hypothesized that these unavailable species are entirely unavailable, meaning that they are not incorporated in any structure. As a result, only structures of size $l \leq L - L_\times - 1$ can grow and the growth probability is identical to zero for all other structures. This assumption cannot be quite true since unavailable for binding only refers to not being present as active monomer or as edge particles but not to being absent completely. Nonetheless, from comparison of this theory with stochastic simulations it seems that ultimately this is a reasonable approximation for understanding the qualitative behavior (see Sec. V).

D. Two-state ansatz

The probability p_l determined in the last section represents the probability that a *specific* polymer that has *just* reached size l is able to grow further by monomer attachment of available species, i.e. has at least one growing end when it has reached size l. This probability is, however, *not* the same as the fraction of structures of size l that has at least one growing end. The reason is a bit subtle and has to do with what we condition on.

In the way we determined p_l in the previous section (Eq. 31), it corresponds to the probability that a *specific* structure that has *just* grown from size $l-1$ to size l is in a state with at least one growing end, i.e. is (in the terminology of the previous section) in state $S^l_{i=1}$ or $S^l_{i=2}$. We, thus, condition on the fact that the specific structure *just grows* from size to $l-1$ to l. We could also have looked at the fraction $f_l = (S^l_{i=1} + S^l_{i=2})/(S^l_{i=0} + S^l_{i=1} + S^l_{i=2})$ of structures of size l in a state with one or two growing ends, $S^l_{i=1}$ or $S^l_{i=2}$, as compared to a state with two blocked ends, $S^l_{i=0}$. This fraction f_l would describe the probability that a *randomly picked* structure *of size* l can, in principle, grow. Hence, f_l would correspond to conditioning the probability on the fact that the structure *has* a size l (irrespective of when it reached this size).

These two probabilities p_l and f_l are, in general, not the same. The reason is that structures of size l with at least one growing end continue to grow while the structures of size l with no growing end accumulate. As a result, over time the number of structures of size l that cannot grow increases compared to the one of size l that can grow. This can be seen very nicely in the simplified assembly process mentioned in the previous section: Indeed, f_l would be ill-defined there because there is a continuous influx of monomers and the states S^l_0 would get more and more populated. In contrast, the numbers of structures in the states $S^l_{1,2}$ converge to a steady-state value because there is not only influx into these states but also outflux from them (due to the growth of structures).

Taken together, the probabilities p_l determined in Eq. 31 do not correspond to the fraction of structures of size l that can grow.

As a result, if there are now c_l structures of size l, one cannot conclude that a fraction p_l of those grows by monomer attachment and, correspondingly, that there are $p_l \cdot c_l$ structures of size l (per species) available for binding.

One approach to resolve this issue would be to try to determine the momentary fraction f_l of structures of size l that can grow. Since, however, many factor would influence how exactly f_l should change over time (including the growth dynamics itself!), we chose an alternative approach: Instead of treating all structures of a certain size as one "population" – as one does in a mean-field description [46] – we introduce two populations G_l and B_l (for growing and blocked) with corresponding concentrations g_l and b_l (Fig. 3(h)). The first population G_l includes all structures that grow by attachment of monomers of available species (i.e. those with at least one growing end), whereas B_l denotes those that are blocked (meaning they only grow if currently unavailable species get activated).

The respective probabilities of these populations correspond to the growth probabilities p_l determined in Eq. 31 which quantify how likely it is that a structure that has just reached size l can grow further by attachment of an available species. Thus, if a structure of size $l-1$ grows to size l, with probability p_l it ends up in G_l and with probability $1-p_l$ in B_l:

$$G_{l-1} \longrightarrow \begin{cases} G_l & \text{with probability } p_l \\ B_l & \text{with probability } 1-p_l. \end{cases} \tag{32}$$

If now structures in G_l grow, this does not influence the population B_l and there is no need to determine a momentary fraction f_l of structures that can, in principle, grow.

Due to activation and binding events, the number of unavailable species $S_\times$ and thus p_l (Eq. 31) change over time. If the number of unavailable species increases, structures previously in the growing state might get blocked and, vice versa, if the number of unavailable species decreases, structures that were in the blocked state might transition to the growing state. As a result, there has to be an exchange between the populations G_l and B_l if $\mathrm{d}S_\times/\mathrm{d}t \neq 0$. In order to formulate the effective theory, it is necessary to quantify this exchange. For this purpose, we define the flux between the two states B_l and G_l as the number of structures that transition from B_l to G_l per time. How does this flux depend on the derivative of the probability p_l, $\mathrm{d}p_l/\mathrm{d}t$?

Since this dependency is not entirely intuitive, we consider a much simpler system first. In this simpler system, it is straightforward to derive the fluxes and the resulting formulas for the fluxes can then be generalized for our purpose. Consider a system with N particles where each can be in either of two states, with $p(t)$ denoting the fraction in state g at time t: Then we have

$$N_g(t) = Np(t)\,, \text{ and } N_g(t+\Delta t) = Np(t+\Delta t)\,. \quad (33)$$

Consequently,

$$N_g(t+\Delta t) - N_g(t) = N_g(t)\,\frac{p(t+\Delta t) - p(t)}{p(t)}\,, \quad (34)$$

and hence

$$\frac{\mathrm{d}N_g(t)}{\mathrm{d}t} = N_g \frac{\mathrm{d}\ln p(t)}{\mathrm{d}t} = (N_g - N)\,\frac{\mathrm{d}}{\mathrm{d}t}\ln\left(1-p(t)\right), \quad (35)$$

where we used $(N - N_g)/(1 - p) = N - N_g/p$ in the last step. Equation 35 implies that the per-capita rate of exchange between the two states is not equal to the change in probability but rather to the change in the logarithm of the probability. Intuitively, in order for the probability p to change by a fixed value, always the same number of particles has to transition from one state to the other, irrespective of the number of particles in the original state. As a result, if the number of particles was high (low) in the original state, a small (large) fraction of them needs to be exchanged.

In our system, there are not only two states but particles can transition between different states (growing/blocked and different polymer sizes). Nonetheless, the exchange dynamics relative to the number of particles in each state should be the same as in the simple system. Thus, the fluxes between the "growing" G_l and "non-growing/blocked" B_l populations (i.e. the number of structures that transition from B_l to G_l per time) are given by

$$J_l^{B\to G} = -J_l^{G\to B} = \begin{cases} g_l \frac{\mathrm{d}}{\mathrm{d}t}\log p_l & \text{if } \frac{\mathrm{d}p_l}{\mathrm{d}t} < 0 \\ -b_l \frac{\mathrm{d}}{\mathrm{d}t}\log(1-p_l) & \text{if } \frac{\mathrm{d}p_l}{\mathrm{d}t} > 0. \end{cases} \quad (36)$$

These equations imply that if the probability p_l decreases ($\mathrm{d}p_l/\mathrm{d}t < 0$) a part of the structures of size l currently in the growing state will transition to the non-growing (blocked) state: $J_l^{G\to B} > 0$. Conversely, if p_l increases ($\mathrm{d}p_l/\mathrm{d}t < 0$) structures of size l can grow again and will transition from the blocked to the growing state: $J_l^{B\to G} > 0$.

Before we discuss the last aspect of the effective theory, namely the monomer dynamics, we give a short summary of the mathematical analysis so far. Starting from the fluctuations in the relative availability of the different species due to the random activation process, we aimed to quantify how these fluctuations modify the growth dynamics of self-assembling structures. Intuitively, the idea is the following: If certain species are less activated than their neighboring species, these species can become unavailable for binding. This unavailability of some species then blocks the growth of those structures that need the unavailable species for the next step of the assembly process. Assuming a random distribution of these unavailable species along the ring structure, we quantified this blockade effect through the probabilities p_l that a structure that has just reached size l can continue to grow (i.e. is not blocked by unavailable species), Eq. 31. These growth probabilities are large if the number of unavailable species is small, as one would intuitively expect; see also Fig. 3 (g). Importantly, one has to distinguish between the probability (p_l) that a single structure that has *just* reached size l can continue to grow and the probability f_l that a randomly picked structure *of this size* l is able to grow. The reason is that structures that can continue to grow have a different growth dynamics than those that cannot: While structures in the growing state can grow as usual, structures in the non-growing (blocked) state can only grow if a currently unavailable species is activated. As a result of this diverging growth dynamics, there is generally an accumulation of non-growing structures (compared to growing ones). This accumulation entails that the probability f_l that a randomly picked structure of size l cannot grow is much higher than the probability p_l that a single structure that has just reached size l can grow further. To account for this difference, we introduced two distinct states for each structure size, corresponding to the growing and non-growing (blocked) polymers.

What remains to be discussed before we can write down the full dynamics of the self-assembly process is the effective behavior of the monomers. This will be done in the next subsection.

E. Monomer dynamics

So far, we have identified two different states for the polymers, namely blocked (non-growing) and growing ones, depending on whether the species they need for further growth are currently unavailable or not. This separation already implies that there need to be at least two different states of active monomers, namely those monomers belonging to currently unavailable species and those that belong to species that are currently available for binding. Furthermore, in analogy with the polymer states, also a third state is reasonable, namely a "blocked" (non-growing) monomer which would need monomers of unavailable species on both sides to be able to form a dimer. What are the respective probabilities for these states of monomers if there are $S_\times$ unavailable species in the system? We denote them by capital letters P to avoid confusion with the probabilities p_l that a structure that reached size l ended up in the growing state.

The probability of monomers to belong to an unavail-

able species can be approximated by

$$P_\times = \frac{S_\times}{S} = \frac{L_\times}{L}, \tag{37}$$

since there is the same total number N of particles of each species and a randomly chosen monomer thus corresponds with probability $S_\times/S$ to an unavailable species [59]. The probability of a monomer to be blocked is given by

$$P_\mathrm{b} = 1 - p_1 \tag{38}$$

with p_1 determined by Eq. 31, analogously to the probability $1-p_l$ that a polymer of size l is in the blocked (non-growing) state. Finally, the probability of all other monomers ("normal monomers") is given by the remaining probability

$$P_\mathrm{n} = 1 - P_\mathrm{b} - P_\times \,. \tag{39}$$

Since $P_\times$ and P_b increase with the number of unavailable species, the probability of a monomer to be in the "normal" state decreases with increasing $L_\times$ or increasing fluctuations in the relative availability of species. Indeed, one can interpret the normal monomers as the equivalent to the monomers in the deterministic description: If the fluctuations between the species are small and there are no unavailable species, $L_\times = 0$, we have $P_\times = P_\mathrm{b} = 0$ and all monomers are in the normal state: $P_\mathrm{n} = 1$. In fact, we then have $p_l = 1$ for all l implying that also all polymers are in the "growing" state which is the equivalent to the (unique) polymer state in the deterministic description.

When we explored a dynamics with these three states of monomers (combined with the polymer dynamics as stated below), it turned out that these are sufficient to capture the qualitative behavior of the stochastic model. However, in particular for self-assembly processes with a small dimerization rate, $\mu \ll \nu$, where the monomer dynamics plays an important role, the quantitative agreement with the result from stochastic simulations can be improved considerably by the introduction of an additional monomer state. This "unblocked" state comprises all monomers that have been in the blocked state but then got unblocked due to a decrease in the number of unavailable species over time, $\mathrm{d}L_\times/\mathrm{d}t < 0$; see also Fig. 4 for an illustration of the monomer dynamics. Such a decrease in $L_\times$ eventually happens in each system, since after activation of all particles, there is no variability between species and, thus, no species with less activation compared to the other species. The reason why this additional state changes the dynamics is that it can prevent the different monomers that have been blocked before from instantaneously dimerizing with each other once they are unblocked. Such a behavior would not make much sense since the different species in the blocked state either correspond to exactly the same species or are separated by at least one unavailable species. In both cases, they are not supposed to bind to each other. With the introduction of the unblocked state, it is possible to eliminate this binding pattern by not allowing the monomers in the unblocked state to dimerize with each other. If they would just transition back to the normal state instead, such a rule could not be implemented since monomers need to be able to dimerize. In summary, we take into account a forth monomer state that, however, is not directly accessible if monomers are activated but gets populated by the originally blocked monomers. Based on these effective states of monomers and the description of polymers in two different state (non-growing/blocked and growing), we will next formulate the full effective theory.

F. Effective theory

In the last sections, we have discussed several aspects of the effect of stochasticity and the resulting variability between species. First, we have introduced the concept of a currently unavailable species. It is a species that does not have any (already activated) particles with free binding sites on the left or right. Roughly speaking, if a species is considerably less activated than other species it is likely that it becomes an unvailable species. The unavailability of such a species then effectively blocks the growth of structures. Employing a fluctuation-corrected mean-field argument, relating fluctuations in the random activation of the different species to the availability of particles for binding, we have then deduced the probability of a structure to further grow by attachment of monomers of an available species. Importantly, this probability p_l, of being in the "growing state", Eq. 31, depends on the size l of the structure so that larger structures are less likely to grow by attachment of available species. Instead they need to "wait" for a monomer of a currently unavailable species to be activated before they can grow ("blocked state").

To sum up, the picture is as follows: There are two types of species, available and unavailable ones, and each structure can be in either of two states, a growing and a blocked state (see also Fig. 3 (a)). Unavailable species have been activated less compared to their neighboring species and due to their unavailability block the growth of structures. Once they get activated, they bind to all structures because most structures can grow by attachment of a monomer of an unavailable species – at least at one end [60]. In contrast, monomers of available species can principally only bind to structures in the growing state (Fig. 4), i.e. to structures that are not completely blocked by the unavailability of the neighboring species but instead can grow at least at one end by attachment of an available species. If structures of size $l-1$ grow by monomer attachment, with a certain probability $1-p_l$ they end up in the non-growing (blocked) state in which both ends need a monomer of an unavailable species to grow further. This probability $1-p_l$, Eq. 31, increases with increasing number of unavailable species and with increasing size of the structure l. With the inverse probability p_l, structures end up in the growing state. As a result, during the growth process more and more structures

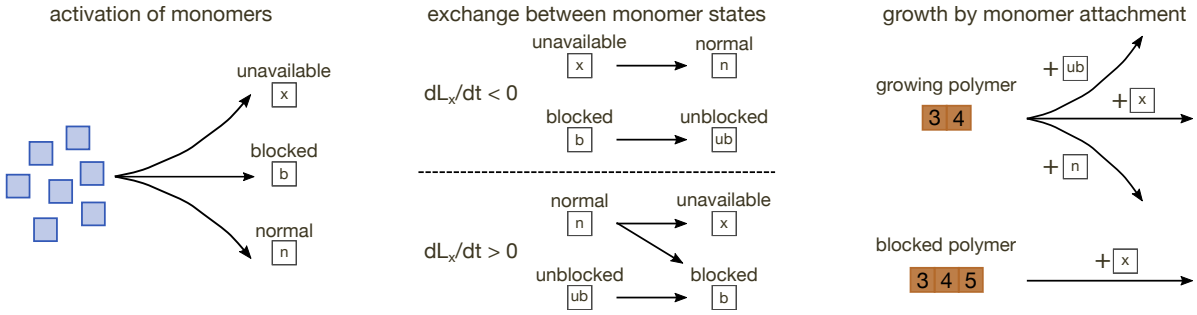

FIG. 4. **Illustration of the monomer dynamics.** There are four monomer states: an unavailable, blocked, unblocked and normal one. Monomers in the unavailable, blocked and normal state are activated at rates $N\alpha e^{-\alpha t}P_\times$, $N\alpha e^{-\alpha t}P_\mathrm{b}$ and $N\alpha e^{-\alpha t}P_\mathrm{n}$, respectively. If the number of unavailable species decreases, monomers in the unavailable state transition to the normal state and monomers in the blocked state transition to the unblocked state. Conversely, if the number of unavailable species increases, monomers in the normal state either transition to the unavailable or to the blocked state. Monomers in the unblocked state transition back to the blocked state. Polymers in the growing state can bind to monomers in the normal, unavailable and unblocked state. In contrast, polymers in the non-growing state can only bind to monomers in the unavailable state.

will transition from the growing to the blocked state in which activation of a monomer of an unavailable species is necessary for further growth.

Taken together, we can now build up the effective growth dynamics of the self-assembly process with no defect formation, $\nu_\mathrm{def}=0$; for an analysis of the more general case, we refer the reader to Appendix C. For better readability, we will explain the different contributions to the dynamics in separate paragraphs: activation of monomers (proportional to α), dimerization between monomers (proportional to μ), growth dynamics of polymers by monomer attachment (terms proportional to ν), and the exchange dynamics between the different states of each structure size (denoted by ρ and ϱ). The full dynamics is shown in Sec. IV F 5. We use the following notation: g_l (b_l) denotes the concentration of polymers of size $l\geq 2$ in the growing (blocked) state. The concentrations m_n, $m_\times$, m_b and m_ub denote the concentration of monomers in the normal, unavailable, blocked and unblocked state, respectively; see also Sec. IV E. All concentrations always refer to one species.

1. *Activation of monomers (see also Fig. 4)*

Each of the N particles for each species is activated at a per-capita rate α. Hence, at time t, on average $Ne^{-\alpha t}$ particles per species are still inactive, and the overall rate of monomer activation per species is thus $\alpha Ne^{-\alpha t}$. As we have discussed in detail in Sec. IV E, there are four different monomers states, one for monomers belonging to unavailable species $m_\times$, one for monomers that are blocked by an unavailable species on each end m_b, one for monomers that had been blocked but were "freed" (unblocked) due to a decrease in the number of unavailable species, m_ub, and the remaining one for normal monomers m_n. At activation, monomers either end up in the normal, unavailable or blocked state with respective probabilities P_n, $P_\times$ and $P_\mathrm{b}=1-P_\mathrm{n}-P_\times$. The corresponding gain terms in the monomer dynamics are, thus, $\alpha Ne^{-\alpha t}P_\mathrm{n}$, $\alpha Ne^{-\alpha t}P_\times$ and $\alpha Ne^{-\alpha t}P_\mathrm{b}$, respectively. There is no gain term for unblocked monomers due to activation because this type of monomer only includes the monomers that have been in the blocked state before and then got unblocked as fluctuations between species (or, equivalently, $L_\times$) decreased.

2. *Dimerization between monomers*

In general, dimerization happens at rate μ. However, not all monomers can dimerize with all other monomers. More concretely, monomers in the blocked state can only dimerize with monomers in the unavailable state (because by definition they are blocked on both sides by an unavailable species). There are $2m_\times m_\mathrm{b}$ different combinations of monomers for such dimerization events where the factor of 2 takes into account that monomer 1 can bind from the left or from the right to monomer 2. Thus, the overall rate for this process is $2\mu m_\mathrm{b}m_\times$ and it occurs as loss terms in the dynamics of both m_b and $m_\times$. In the gain term for the dimers g_2 and b_2, these terms are multiplied by the probabilities p_2 and $1-p_2$, respectively, to account for the fact that a newly formed dimer is with probability p_2 in the growing state and with inverse probability $1-p_2$ in the non-growing (blocked) one. Monomers in the unavailable state not only dimerize with monomers in the blocked state but also with monomers in the normal and unblocked state because monomers of the unavailable species are supposed to be "required" by all other structures. Analogous to the previous case, the corresponding rates are $2\mu m_\mathrm{n}m_\times$ and $2\mu m_\mathrm{ub}m_\times$, respectively, again with additional factors p_2 and $1-p_2$ for the gain terms. Finally, monomers in the unavailable state dimerize among themselves. Due to the indistinguishability between monomers of one state, there are only $m_\times^2$

combinations for two monomers in the unavailable state to dimerize. Since two monomers are lost in the process, the overall loss rate for the monomers is still $2\mu m_\times^2$. The gain term for the dimers is, however, just $\mu m_\times^2$, again weighted with the probabilities p_2 and $1-p_2$. Monomers in the normal state not only dimerize with the monomers in the unavailable state but also with themselves (as is the case in the deterministic description where there are only "normal" monomers) and with the unblocked monomers (which are basically the same as normal monomers only that they have been in the blocked state before). Similarly to above, the corresponding loss terms are $2\mu m_\mathrm{n}^2$ and $2\mu m_\mathrm{n} m_\mathrm{ub}$ and the gain terms are $\mu m_\mathrm{n}^2 p_2$ or $\mu m_\mathrm{n}^2(1-p_2)$ and $2\mu m_\mathrm{n} m_\mathrm{ub} p_2$ or $2\mu m_\mathrm{n} m_\mathrm{ub}(1-p_2)$, respectively. Finally, monomers in the unblocked state behave similarly as the monomers in the normal state only that they do not dimerize among themselves. Thus, there are just the loss terms from dimerization of monomers in the unblocked state with monomers in either the normal or the unavailable state, as described above.

3. *Growth dynamics (see also Fig. 4)*

As mentioned above, monomers of the unavailable type (i.e. monomers of an unavailable species) bind to all polymers. These binding processes are represented by the terms

$$2\nu m_\times g_l p_{l+1} + 2\nu m_\times g_l(1-p_{l+1}) = 2\nu m_\times g_l \tag{40a}$$
$$2\nu m_\times b_l p_{l+1} + 2\nu m_\times b_l(1-p_{l+1}) = 2\nu m_\times b_l\,. \tag{40b}$$

For instance, each monomer of the unavailable type can bind at rate ν to each structure of size l in the growing state. Overall, there are $2m_\times g_l$ possible combinations because the monomer can attach from both sides to the structure. So, the overall binding for a monomer of the unavailable type to a structure of size l in the growing state is $2\nu m_\times g_l$. With probability p_{l+1} the newly formed structure of size $l+1$ is in the growing state and with the inverse probability $1-p_{l+1}$ in the blocked state. As a result, the rate of formation of a structure of size $l+1$ in the growing or blocked state due to binding of a monomer in the unavailable state to a growing structure of size l is given by $2\nu m_\times g_l p_{l+1}$ or $2\nu m_\times g_l(1-p_{l+1})$, respectively. Similarly, the overall binding rate for a monomer in the unavailable state to a structure of size l in the blocked state is $2\nu m_\times b_l$. Again, the thereby formed structures of size $l+1$ are in the growing (non-growing) state with probability p_{l+1} (inverse probability $1-p_{l+1}$) and the respective rates are $2\nu m_\times b_l p_{l+1}$ and $2\nu m_\times b_l(1-p_{l+1})$.

4. *Exchange dynamics*

The strength of stochastic fluctuations and with it the number of unavailable species changes over time. For instance, as shown above in Fig. 3(d), the standard deviation of the availability of different species as compared to their neighbors is maximal when just half the particles have been activated and is zero at the beginning and at the end of the process. As a result, the probability for a structure of size l to be in the growing state, p_l, changes over time. If p_l changes there needs to be an exchange of structures of size l between the corresponding growing (G_l) and blocked state (B_l). A structure in the blocked state that was blocked by the unavailability of its two neighboring species might, for instance, transition to the growing state once one of the originally unavailable neighboring species gets available. As motivated in Sec. IV D, the corresponding fluxes between the states are proportional to the derivative of the logarithm of the respective probability p_l or $1-p_l$ (depending on the direction of the exchange). Thus, we have

$$\rho_l = J_l^{B\to G} = \begin{cases} \frac{g_l}{p_l}\frac{\mathrm{d}p_l}{\mathrm{d}t} & \text{if } \frac{\mathrm{d}p_l}{\mathrm{d}t} < 0 \\ \frac{b_l}{1-p_l}\frac{\mathrm{d}p_l}{\mathrm{d}t} & \text{if } \frac{\mathrm{d}p_l}{\mathrm{d}t} > 0, \end{cases} \tag{41}$$

where we defined ρ_l as the flux from the blocked to the growing state, $J_l^{B\to G}$ (compare also Eq. 36). So, if the probability to be in the growing state p_l increases (decreases), there is positive flow from the blocked (growing) to the growing (blocked) state.

The fluxes between the monomer states are a bit more involved because there are not only two different states but, in principle, four of them. We denote them by a slightly different letter, ϱ, to avoid confusion with the other fluxes. If the number of unavailable species decreases, $\mathrm{d}L_\times/\mathrm{d}t < 0$, the generalization is straightforward: Monomers of the unavailable type transition to the normal state and monomers that had been blocked by unavailable species will become unblocked (see also Fig. 4). Thus, there are only transitions from one state to one other state. As motivated in Sec. IV D, the per-capita transition rates are proportional to the derivative of the logarithm of the probability of the respective state. In the case $\mathrm{d}L_\times/\mathrm{d}t < 0$, we thus have

$$\varrho_\mathrm{n} = -\varrho_\times = -\frac{m_\times}{P_\times}\frac{\mathrm{d}P_\times}{\mathrm{d}t} \tag{42a}$$
$$\varrho_\mathrm{ub} = -\varrho_\mathrm{b} = -\frac{m_\mathrm{b}}{P_\mathrm{b}}\frac{\mathrm{d}P_\mathrm{b}}{\mathrm{d}t}. \tag{42b}$$

Here $\mathrm{d}P_\times/\mathrm{d}t < 0$ and $\mathrm{d}P_\mathrm{b}/\mathrm{d}t < 0$, so that the flux into the normal, ϱ_n, and unblocked state, ϱ_ub, is positive, as expected.

In contrast, if the number of unavailable species increases, both the number of active monomers in the unavailable state as well as the number of active monomers in the blocked state increases. This implies that monomers in the normal state can either transition to the unavailable or to the blocked state (see also Fig. 4). Furthermore, monomers in the unblocked state transition back to the blocked state. As we show in Appendix B 2,

these transitions for $\mathrm{d}L_\times/\mathrm{d}t > 0$ are realized by

$$\varrho_\mathrm{n} = \frac{m_\mathrm{n}}{P_\mathrm{n}}\frac{\mathrm{d}P_\mathrm{n}}{\mathrm{d}t} = -\frac{m_\mathrm{n}}{P_\mathrm{n}}\frac{\mathrm{d}p_\times}{\mathrm{d}t} - \frac{m_\mathrm{n}}{P_\mathrm{n}}\frac{\mathrm{d}P_\mathrm{b}}{\mathrm{d}t} \tag{43a}$$

$$\varrho_\times = \frac{m_\mathrm{n}}{P_\mathrm{n}}\frac{\mathrm{d}P_\times}{\mathrm{d}t} \tag{43b}$$

$$\varrho_\mathrm{ub} = -\frac{m_\mathrm{ub}}{1-P_\mathrm{b}}\frac{\mathrm{d}P_\mathrm{b}}{\mathrm{d}t} \tag{43c}$$

$$\varrho_\mathrm{b} = \frac{m_\mathrm{n}}{P_\mathrm{n}}\frac{\mathrm{d}P_\mathrm{b}}{\mathrm{d}t} + \frac{m_\mathrm{ub}}{1-P_\mathrm{b}}\frac{\mathrm{d}P_\mathrm{b}}{\mathrm{d}t}. \tag{43d}$$

Now, $\mathrm{d}P_\times/\mathrm{d}t > 0$, $\mathrm{d}P_\mathrm{b}/\mathrm{d}t > 0$ and $\mathrm{d}P_\mathrm{n}/\mathrm{d}t < 0$, so that there is indeed flux from the normal to the unavailable and blocked state and from the unblocked to the blocked state. The influx from the normal into the unavailable state $\varrho_\times$ is proportional to the number of monomers in the normal state m_n and to the change in the likelihood of species to be unavailable, $\mathrm{d}P_\times/\mathrm{d}t$. This term appears as a gain term for the monomers of unavailable species, $\varrho_\times$, and as a loss term for monomers in the normal state, ϱ_n. Monomers in the normal state also transition to the blocked state. This flux is again proportional to m_n and to the change in the likelihood of species to be blocked, $\mathrm{d}P_\mathrm{b}/\mathrm{d}t$. This term appears in ϱ_n as loss term and as gain term in ϱ_b. Finally, monomers in the unblocked state transition back to the blocked state. The corresponding flux is proportional to the number of monomers in the unblocked state m_ub, and to the change in the likelihood of species to be unblocked, $\mathrm{d}P_\mathrm{ub}/\mathrm{d}t = \mathrm{d}(1-P_\mathrm{b})/\mathrm{d}t = -\mathrm{d}P_\mathrm{b}/\mathrm{d}t$.

Irrespective of the sign of $\mathrm{d}L_\times/\mathrm{d}t$, we have

$$\varrho_\mathrm{n} + \varrho_\times + \varrho_\mathrm{b} + \varrho_\mathrm{ub} = 0 \tag{44}$$

due to conservation of particles.

5. *Full dynamics*

Combining all of these contributions to the dynamics, the full dynamics reads as follows:
Monomer dynamics (see also Secs. IV F 1, IV F 2, IV F 3 and IV F 4):

$$\partial_t m_\mathrm{n} = \alpha N e^{-\alpha t} P_\mathrm{n} - 2\mu D_\mathrm{n} - 2\nu m_\mathrm{n}\gamma + \varrho_\mathrm{n} \tag{45a}$$

$$\partial_t m_\times = \alpha N e^{-\alpha t} P_\times - 2\mu D_\times - 2\nu m_\times(\gamma+\beta) + \varrho_\times \tag{45b}$$

$$\partial_t m_\mathrm{b} = \alpha N e^{-\alpha t} P_\mathrm{b} - 2\mu D_\mathrm{b} + \varrho_\mathrm{b} \tag{45c}$$

$$\partial_t m_\mathrm{ub} = -2\mu D_\mathrm{ub} - 2\nu m_\mathrm{ub}\gamma + \varrho_\mathrm{ub} \tag{45d}$$

where

$$2D_\mathrm{n} = 2\left(m_\mathrm{n}^2 + m_\mathrm{n}m_\times + m_\mathrm{n}m_\mathrm{ub}\right) \tag{46a}$$

$$2D_\times = 2\left(m_\times^2 + m_\times m_\mathrm{n} + m_\times m_\mathrm{ub} + m_\times m_\mathrm{b}\right) \tag{46b}$$

$$2D_\mathrm{b} = 2m_\mathrm{b}m_\times \tag{46c}$$

$$2D_\mathrm{ub} = 2\left(m_\mathrm{ub}m_\mathrm{n} + m_\mathrm{ub}m_\times\right), \tag{46d}$$

denote the number of ways in which a monomer in the normal, unavailable, blocked or unblocked state can dimerize with another monomer, respectively. Here, m_n, $m_\times$, m_b and m_ub denote the numbers of monomers in the normal, unavailable, blocked and unblocked state (per species), respectively; see also Sec. IV E. Furthermore, $\gamma = \sum_{l=2}^{L-1} g_l$ and $\beta = \sum_{l=2}^{L-1} b_l$ denote the total number of unfinished polymers in the growing and blocked state, respectively. Here, g_l and b_l denote the numbers of polymers of size $l \geq 2$ (per species) in the growing and blocked state, respectively.
Polymer dynamics (see also Secs. IV F 2, IV F 3 and IV F 4):

$$\partial_t g_2 = \mu\left(D_\mathrm{n} + D_\times + D_\mathrm{b} + D_\mathrm{ub}\right)p_2 - 2\nu g_2 M_\mathrm{G} + \rho_2 \tag{47a}$$

$$\partial_t b_2 = \mu\left(D_\mathrm{n} + D_\times + D_\mathrm{b} + D_\mathrm{ub}\right)(1-p_2) - 2\nu b_2 m_\times - \rho_2 \tag{47b}$$

for the dimers and

$$\partial_t g_l = 2\nu\left(g_{l-1}M_\mathrm{G} + b_{l-1}m_\times\right)p_l - 2\nu g_l M_\mathrm{G} + \rho_l \tag{48a}$$

$$\partial_t b_l = 2\nu\left(g_{l-1}M_\mathrm{G} + b_{l-1}m_\times\right)(1-p_l) - 2\nu b_l m_\times - \rho_l \tag{48b}$$

for all polymers with $l \in \{3,\ldots,L-1\}$ where $M_\mathrm{G} = (m_\mathrm{n} + m_\times + m_\mathrm{ub})$ denotes the number of monomers that can bind to structures in the growing state. Finally, for the final target structures there is only one state (since they do not grow further) which we denote by G_L with concentration g_L:

$$\partial_t g_L = 2\nu\left(g_{L-1}M_\mathrm{G} + b_{L-1}m_\times\right). \tag{49}$$

The probabilities $p_{l\geq 2}$ are defined in Eq. 31 and the probabilities for the monomers in Eqs. 37, 38 and 39. The full dynamics (Eqs. 45, 47, 48, 49) is solved numerically using MATLAB.

V. COMPARISON TO STOCHASTIC SIMULATIONS AND DETERMINISTIC THEORY

Does this effective theory capture the strong stochastic effects as observed in stochastic simulations of the system? Figure 2 shows the result of a numerical integration of the effective theory (Eqs. 45, 47, 48, 49), in comparison with the stochastic simulations. While the effective theory does not coincide fully quantitatively with the stochastic simulations, it correctly predicts the qualitative behavior of the system, in contrast to the deterministic theory [46] (not shown). First, the effective theory correctly predicts that the yield saturates at an imperfect value $Y_\mathrm{max} < 1$ in the limit of small activation rate (Fig. 2 (a)). This imperfect value decreases for smaller numbers N of particles per species and for larger target structure sizes L. Furthermore, we recover the non-monotonic behavior of the (defect-free) yield with the activation rate,

if the dimerization rate is small ($\mu \ll \nu$; Fig. 2 (b)) or if defect formation is allowed ($\nu_{\text{def}} > 0$; Fig. 2(c)). Note that in the case of defect formation, we do recover the non-monotonic behavior of the defect-free yield (yield of all defect-free target structures) but not of the total yield (yield of all target structures). This is presumably because in our theory defect formation is always possible and since we do not account for additional fluctuations in the availability of the different species due to defect formation [48]; for details on the effective theory with defect formation, $\nu_{\text{def}} > 0$, please refer to Appendix C. Finally, for fixed target size L and fixed total number of particles NS (or, equivalently, fixed number of rings NS/L if assembly proceeds perfectly), the yield decreases for larger heterogeneity of the target structure (corresponding to the number of species S in the system) (Fig. 2 (d)). In contrast, yield becomes independent of the number of species S for $S \gg 1$ if the number of particles per species N is kept constant (Fig. 2 (e) and (f)). This implies that, as long as the structures are not fully homogeneous and variability between different species exists ($S \gg 1$), for constant N and L the number of species is not decisive for the process. In the effective theory, this can be seen from the fact that only the number of unavailable sites along the ring, $L_\times$, enters but not the number of unavailable species, $S_\times$ itself (at least if we assume that the periodicity of the arrangement does not change the length of segments of available species considerably, see Sec. IV C). As a result, the redundancy L/S of the structure does not influence the assembly process in the effective theory, as long as N and L are constant. In this case of fixed N and L, the average yield can even be a non-monotonic function of the number of species (blue (upper) curves in Figs. 2(e) and (f)). We speculate that this is a consequence of the variance of the yield being dependent on the number of species in the system and of the yield being bounded between 0 and 1: Our effective theory suggests that the single-species fluctuations are one of the decisive factors for the strength of stochastic effects. These fluctuations are quantified by the average variance between neighboring species. This variance, however, is also subject to stochasticity itself: The fewer species there are in the system, the more we expect the average variance between neighboring species (where the average is taken with respect to the different species) to fluctuate between single realizations of the assembly process. As a result, it is intuitive that also the yield fluctuates more if there are less species. Since, furthermore, yield is bounded by 0 and 1, this could imply that for systems with yield "close to" 1, fluctuations might actually decrease the average yield, whereas for yields close to 0, the opposite happens. This suggests that in cases where the yield for $S \gg 1$ is "close to" 0, systems with few species actually exhibit a higher average yield (as they are subject to more fluctuations) (red (lower) curves in Figs. 2(e) and (f)), whereas for the case where the average yield is "close to" 1, the opposite is true, and yield can indeed be a non-monotonic function of the number of species S (blue (upper) curves in Figs. 2(e) and (f)) It would be very interesting to check more rigorously whether this speculation is indeed true.

So far, we have focused on the final yield of the assembly process. In order to check whether the effective theory captures the dynamics of the polymer size distribution qualitatively correctly (and not only the final yield), we compare the temporal evolution of the polymer size distribution as predicted by the effective theory and as measured in stochastic simulations in Appendix A. While there exist obvious differences (such as, for instance, the dynamics of the monomers and the resulting dynamics for the smaller structures), the front of the wave in the stochastic simulations seems to be predicted quite reliably by the effective theory. This front is mainly determined by the probabilities p_l, Eq. 31, that determine which portion of structures of size l ends up in the growing state. These probabilities predict that there is a sharp transition between structures of size $l > L - L_\times - 1$ that do not grow at all and smaller structures $l \leq L - L_\times - 1$ that have a high likelihood to grow (see also Sec. IV C and Fig. 3). As a result of the sharp transition and the fact that large structures do not grow much, the waves produced by the effective theory build up much larger and, correspondingly, move much more slowly through the system (as more structures grow simultaneously), as compared to the waves predicted by the deterministic theory [46]. This higher amplitude and slower speed of the wave predicted by the effective theory is in agreement with the waves from the stochastic simulations, suggesting that the probabilities p_l capture the dynamics reasonably well although they were determined from a much simplified assembly process (see Sec. IV C). Finally, although there are quantitative deviations in the monomer dynamics, in both the stochastic simulations and in the effective theory the number of monomers is high until very late in the process.

Taken together, these results suggest that the effective theory captures the most important aspects of the self-assembly process. In order to suggest ways how to improve yield in the system, it thus seems promising to analyze the integral new aspects of the effective theory as compared to a deterministic description of the system as given in Sec. III A.

VI. REDUCE FLUCTUATIONS IN THE AVAILABILITY OF THE DIFFERENT SPECIES IN ORDER TO IMPROVE YIELD

How can we use the insights gained from the formulation of the effective theory to suggest viable ways to improve the yield in the self-assembly process? Since, deterministically, the yield is always perfect for small enough activation rate, we take a closer look at the difference between the deterministic and effective theory. This difference is in the additional blocked state B_l in the effective theory. This state describes structures that would need a

particle of an unavailable species to grow and thus, generally speaking, tend not to grow due to variability between species. These fluctuations are quantified by the single-species standard deviation σ_0, Eq. 15. Our effective theory thus suggests that reducing the single-species standard deviation should improve the yield in the system. In the following, we will consider two specific ways to achieve this goal.

A. Provision in bursts

As shown in Fig. 3(d), where $\sqrt{3\sigma_0}$ (black) is plotted against the average number of activation events per species, the single-species standard deviation has a pronounced maximum when on average half the particles have been activated. Our effective theory, thus, suggests that in order to improve the assembly yield one could constrain the system in a way that the single-species standard deviation takes on a value of zero from time to time. This can be achieved by providing particles in bursts: Instead of providing all N particles of each species right from the beginning, the particles are put into the system in b bursts, where each burst contains a number of N/b particles per species. This means that at first only N/b particles of each species are put into the system. Only when these particles have been activated and the binding processes have been completed, the next burst of particles is provided - and so on until all N particles per species have been provided. Figure 5(a) shows the resulting single-species standard deviation measured in stochastic simulations when a total number of $N = 500$ particles is provided in 1, 2, 10 or 20 subsequent bursts (the x-axis represents time in units of activation events). The standard deviation decreases for larger numbers of bursts since it is reduced to zero at the end of each burst: After the i-th burst exactly iN/b particles of each species have been activated and there is no variability between species at this point in time. Consequently, the maximum of the single-species standard deviation decreases from $\frac{1}{2}\sqrt{N}$ in the original system to $\frac{1}{2}\sqrt{N/b}$; see Appendix D for more details. According to the effective theory, the yield is expected to increase as a result of the reduced single-species standard deviation. Fig. 5(b) shows the final yield curves in dependence of the activation rate α for the different numbers of bursts. Indeed, it is found that the yield strongly increases with increasing number of bursts. As one can infer upon inspection of Fig. 5(a), this increase in the yield correlates with a smaller standard deviation of the neighbor fluctuations.

In order to improve the yield by providing the particles in bursts it is necessary that the bursts are sufficiently deterministic, i.e. the number of particles per species per burst has to be subject to little fluctuations. Otherwise, the single-species standard deviation cannot be reduced effectively. Indeed, we show in Appendix E that if the number of particles per species per burst is drawn randomly from a Poisson distribution with mean N/b, the process is independent of the number of bursts. There, we also discuss some aspects of bursts for which the number of particles per species per burst is drawn independently from a Gaussian or Binomial distribution, respectively. We find that, for provision of particles in bursts to be effective, the width of the distribution of the particles per species per bursts need not be too large (Fano factor $F < 1$).

B. Self-inhibitory feedback

As indicated by the effective theory, the large single-species variance is detrimental because it favors growth and nucleation of small structures as compared to large structures. The reason is that, when species are unavailable, active monomers of the neighboring species can accumulate as there are no fitting polymers to bind. Subsequently, this accumulation of active particles strongly increases the tendency to form new nuclei. A very direct way to avoid this problem would be to introduce a self-inhibition mechanism that suppresses the accumulation of these active monomers. Explicitly, we will consider a variant of the system ("self-inhibition scenario") where the activation rate of species i is given by

$$\alpha^{(i)} = \alpha_0 \exp\left(q m_i^a\right), \tag{50}$$

where m_i^a is the number of active monomers of species i, α_0 is the bare activation rate and $q \leq 0$ is the inhibition strength. If one species has been activated more (less) than average, it will typically have more (less) active monomers than average. In the self-inhibition scenario with $q < 0$, this implies that the activation of additional monomers is suppressed (enhanced) for over-represented (under-represented) species and so the different levels of activation are expected to converge. Fig. 5(c) shows how for increasing inhibition strength q the standard deviation of the neighbor fluctuations decreases. The effect of the inhibition strength q on reducing the neighbor fluctuations is pronounced already in the early stages of the assembly process where not as many structures and monomers are present. This is particularly useful because fluctuations in the beginning are expected to suppress yield most considerably. We thus anticipate from the effective theory that yield should improve. Indeed, Fig. 5(d) shows that higher inhibition strengths improve yield significantly. Again, we see that there is a clear correlation between higher yield and smaller neighbor fluctuations; compare Figs. 5(c) and (d).

Taken together, decreasing the variance between the species by either directly influencing the single-species variance or by self-adjusting the activation levels of different species due to feedback, can strongly improve yield, as suggested by the effective theory.

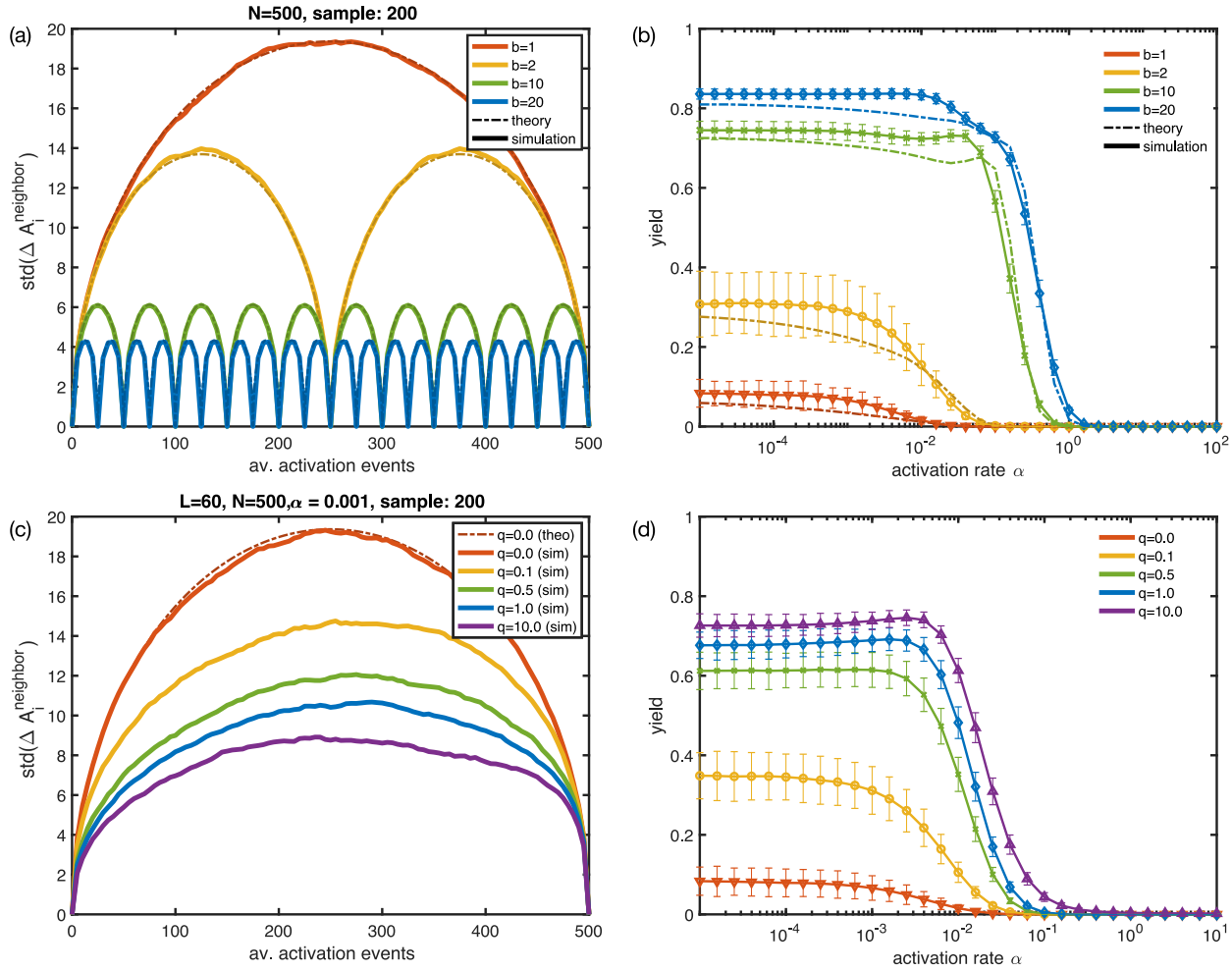

FIG. 5. **Decreasing the variance in the relative number of available particles per species improves yield.** (a) Burst scenario: The standard deviation of the neighbor fluctuations $\mathrm{std}(\Delta A_i^{\mathrm{neighbor}})$ for the original system and for systems with $b = 2$, 10 and 20 bursts, respectively, are plotted against the average number of activation events per species. The theoretical predictions are shown with dotted-dashed lines and the results from stochastic simulations (averaged over 200 samples) with solid lines (and slightly lighter color to ease the comparison). The parameter values are $L = 60$, $N = 500$, $\nu = \mu = 1$, $\nu_{\mathrm{def}} = 0$ and $\alpha = 10^{-4}$. Note that for the stochastic simulations with several bursts, we measured the standard deviation in one burst and concatenated it b times with itself. Since the assembly dynamics does not influence the activation of particles, the standard deviations should statistically be the same in all bursts. (b) Burst scenario: The average assembly yield and its standard deviation obtained from stochastic simulations (1000 samples; solid lines with markers) is shown in dependence of the activation rate for different number of bursts. The theoretical predictions from the effective theory with bursts (see Appendix D) are shown for comparison (dotted-dashed lines). The parameters are $L = 60$, $N = 500$, $\nu = \mu = 1$, $\nu_{\mathrm{def}} = 0$ and number of bursts as indicated in the plot. (c) Self-inhibition scenario: The standard deviation of the neighbor fluctuations $\mathrm{std}(\Delta A_i^{\mathrm{neighbor}})$ as obtained from stochastic simulations (averaged over 200 samples) is shown for different inhibition strengths q (different colors, solid lines). The theoretical prediction for zero inhibition strength is shown as dotted-dashed line in red. The parameters are $L = 60$, $N = 500$, $\nu = \mu = 1$, $\nu_{\mathrm{def}} = 0$, $\alpha_0 = 10^{-3}$ and inhibition strength as indicated in the plot. (d) Self-inhibition scenario: the average assembly yield and its sample standard deviation obtained from stochastic simulations (1000 samples) is plotted as a function of the bare activation rate α_0 for different inhibition strength q (different colors). The other parameters are $L = 60$, $N = 500$, $\nu = \mu = 1$, $\nu_{\mathrm{def}} = 0$.

VII. CONTROLLED VARIABILITY BETWEEN SPECIES

Remarkably, not only decreasing the variance between species but also increasing it in a controlled fashion can improve yield [17, 48]. In this section, we will shortly discuss two suggestions of recent studies [17, 48] as well as a third possibility to increase the yield by increasing the variance between the relative concentrations of the different species. Key to all of these strategies is that

by inducing differences in the concentrations of active monomers specific assembly paths are favored.

A. Non-stoichiometric concentrations: specific assembly path

Recently, it has been shown that one can considerably enhance assembly efficiency by using non-stoichiometric concentrations for the different building blocks [17]. Specifically, it was suggested to provide building blocks of a small region of the target structure in excess compared to the remaining species. In light of our results, this is surprising at first glance: Rather than decreasing the variability between different species, this setup actually increases the inter-species variation. How can the observed increase in efficiency be reconciled with the finding that fluctuations in the relative concentrations of species favor kinetic trapping? The key insight that solves this riddle is that one has to use non-stochiometric concentrations in a highly coordinated fashion. Instead of indiscriminately over-expressing species randomly, one has to specifically select a set of species in a single connected region of the structure [17]. This procedure then favors a specific assembly path by favoring the formation of nucleation seeds in that chosen region. As a result, all structures grow from these more or less identical seeds without competition for resources; the assembly yield is high.

B. Non-homogeneous activation rates

A very similar effect can be achieved by using non-homogeneous activation rates for the different species. For randomly distributed rates along the ring, this would increase fluctuations in the relative availability of species and thus lead to a lower yield; see Appendix F, Figs. 14, 15. If, however, a specific assembly path is favored by specifying a particular order of species activation, yield can be increased. Figure 6(a) illustrates such a choice of activation rates

$$\alpha^{(i)} = \begin{cases} \alpha_0\, w^i & \text{for } i \leq S/2 \\ \alpha_0\, w^{S-(i-1)} & \text{for } i > S/2, \end{cases} \tag{51}$$

where α_0 scales all rates homogeneously and w determines the relative magnitude of the activation rates. The two species with indices $S/2$ and $S/2+1$ have the largest activation rates, their neighbors the second largest and so on. In this way, this specific choice of activation rates favors assembly paths that proceed in the same order by starting with nucleation of species $S/2$ and $S/2+1$ and subsequently grow to larger and smaller indices to the right and to the left. Correspondingly, due to reduced competition for resources, the yield increases [61] if $w > 1$; see Fig. 6(b). Increasing the exponential weight w enhances the tendency of particles to be activated in the chosen order and hence improves the yield. However, once w becomes so large that activation of some species is faster than binding, active monomers of those species would accumulate and form new nuclei. Consequently, the yield decreases again once w exceeds this threshold. The maximal (total) activation rate in the system is the activation rate of species $L/2$ and $L/2+1$ and is given by $\alpha_{\max} \sim N\alpha_0 w^{L/2}$. In contrast, the time scale for binding is νN. Hence, the threshold can be estimated by equating $\alpha_{\max} = \nu N$, resulting in an expected yield drop if $w > w_{\max} := \alpha_0^{-2/L}$. As the maximal activation rate and therefore $w_{\max}$ depend on α_0, the range of values of w for which yield improves increases with decreasing α_0. Therefore, the maximum yield rises if α_0 is reduced, see Fig. 6(b).

C. Just-in-sequence mechanism

The purpose of using non-stoichiometric concentrations or non-homogeneous activation rates is to control the order in which particles become available for binding and thereby to favor specific assembly pathways. We recently presented a mechanism for efficient self-assembly that implements such a 'supply control strategy' in a similar but more effective way, based on inhibitory feedback between neighboring species [48]. To that end, we assume that the inactive (and optionally active) monomers of species $i < L$ inhibit the activation of the subsequent species $i+1$. In this way, species $i+1$ gets activated 'just-in-sequence' after species i has been activated and has, in large part, been assembled already. Only species 1 is not inhibited. The resulting inhibition cascade that ensures that the particles are provided and assembled in the specified sequence is illustrated in Fig. 6. We termed this supply control strategy 'just-in-sequence', or short, JIS mechanism. Similar to Eq. 50, we assume that the activation rate of species $i+1$ with $i < L$ is given by

$$\alpha^{(i+1)} = \alpha_0 e^{q m_i^i}, \tag{52}$$

where α_0 denotes the basal activation rate, $q < 0$ the parameter that controls the strength of inhibition and m_i^i the concentration of inactive monomers of species i. Optionally, one could also account for inhibition by active monomers by replacing m_i^i with $m_i^i + m_i^a$ as this would only have a negligible effect on the assembly process [48]. Figure 6 shows the yield in dependence of the activation rate α for different values of the inhibition strength q and for $S = 60$ and $N = 500$. Interestingly, a small nonzero q reduces the yield compared to the original case with $q = 0$, because weak inhibition amplifies stochastic effects [48]. However, by further increasing the inhibition strength, the yield quickly rises up to the perfect value of 1 in the respective regime of α. Moreover, the threshold activation rate below which the yield rises increases due to a finite inhibition strength. Note that, in comparison with the self-inhibitory mechanism, a much

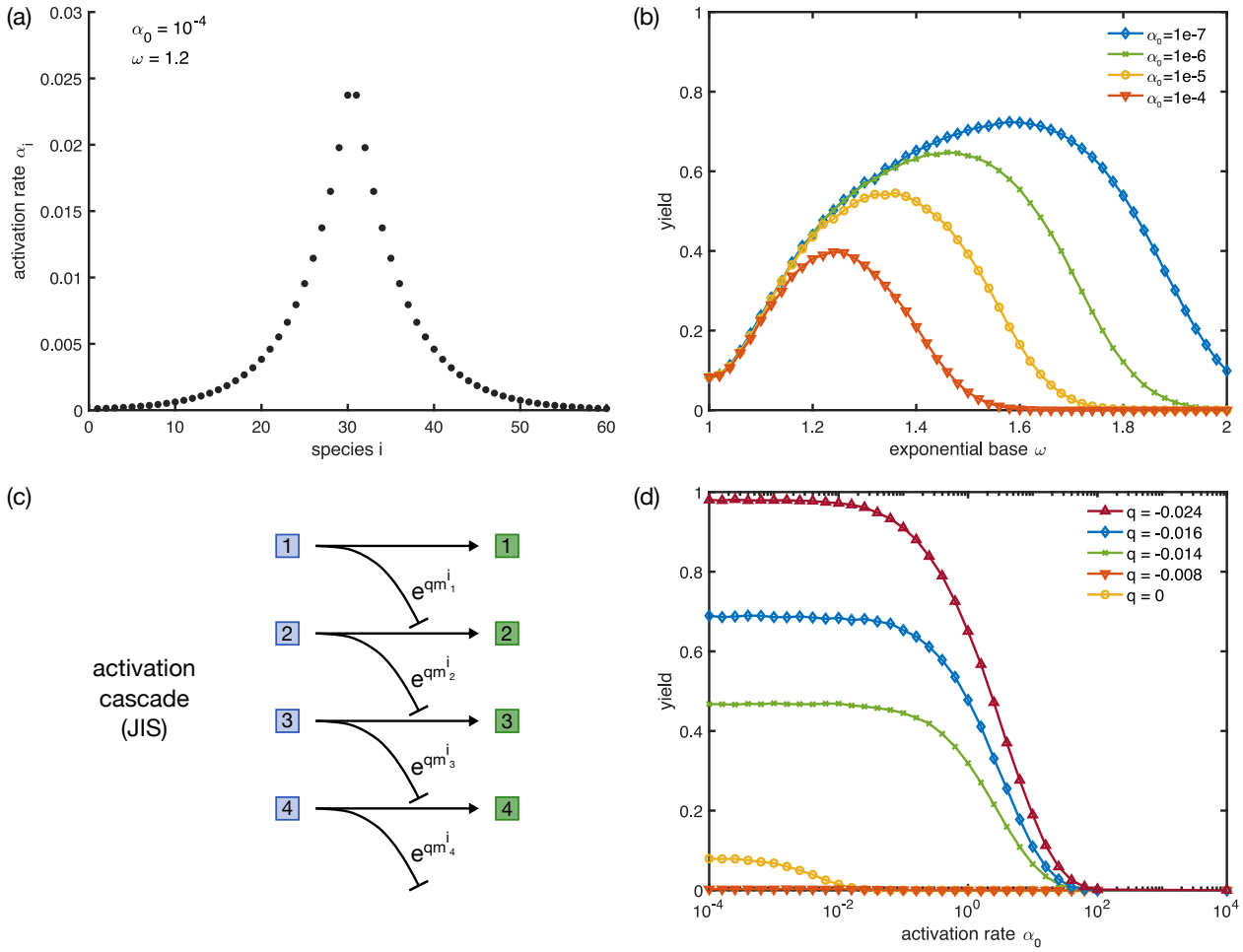

FIG. 6. **Increasing the variance in a coordinated fashion improves yield.** (a,b) Non-homogeneous activation rates. Yield can be improved by choosing the activation rates non-homogeneously. (a) Activation rates plotted against the species index according to Eq. 51 for $\alpha_0 + 10^{-4}$, $\omega = 1.2$ and $L = 60$. The activation rate is highest for the two species in the middle, $i = S/2$ and $i = S/2+1$, and decreases exponentially to the left and to the right. Therefore, assembly pathways that start with the dimerization of species $S/2$ and $S/2+1$ are strongly favored. (b) Yield plotted against the magnitude of the exponential base ω for different basal activation rates α_0 and $S = 60$, $N = 500$. The yield increases with increasing ω and attains a maximum. Then yield drops again because for large ω activation of the species becomes fast compared to the growth dynamics. (c,d) JIS scenario. Just-in-sequence supply can be realized effectively with inhibitory feedback, thereby greatly enhancing the yield. (c) Inhibition cascade. The inactive monomers of each species i inhibit the activation of the subsequent species $i+1$ as described by Eq. 52. Only species 1 is not inhibited and is therefore activated first. This triggers an activation cascade which provides the particles in sequence with the specified assembly pathway. (d) Yield in dependence of α_0 for different inhibition strengths q and $S = 60$, $N = 500$. For small, nonzero values of q the yield decreases due to an amplification of stochastic effects. For larger values of q, however, the yield quickly rises up to the perfect value of 1. For increasing q, the threshold activation rate is shifted towards higher values of α_0.

lower inhibition strength q is required to achieve high yield. This is because in the self-inhibitory mechanism inhibition is effectuated by the active monomers while in the JIS mechanism it is accomplished by the inactive monomers, which are usually present in much larger numbers. Hence, the JIS mechanism is a very effective strategy to increase self-assembly efficiency and to avoid stochastic yield catastrophes.

VIII. CHARACTERIZATION OF THE MITIGATION MECHANISMS

As noted in this and earlier studies [46, 48], there exists a variety of methods how to mitigate the stochastic yield catastrophe in heterogeneous self-assembly systems. Depending on the system, one may have access to manipulate or control different elements of the assembly

process and hence some strategies can be more feasible than others. For instance, if one has direct control over the binding properties of the constituents, it might be most efficient to reduce the ratio between the molecular rates for nucleation and growth by relying on allosteric effects. As long as the availability of constituents is not rate-limiting, stochastic effects then do not severely limit the yield of the assembly process [46, 48]. However, controlling the assembly process via the molecular binding rates might be effortful and not very versatile since the constituents would need to be specially tailored for a specific target structure and the corresponding assembly process. Furthermore, allosteric control might require an elaborate design of the constituents, hard to be realized in a controlled fashion in nanotechnological applications. In these applications, it might be more viable to execute control on a systemic level via supply regulation [48]. Supply regulation exerts control over the assembly process by governing the way, specifically the order and amount, in which particles are provided. Elaborate binding properties enabling e.g. allosteric effects are thereby not required. Furthermore, supply regulation provides a way to realize effective self-assembly even if the binding reactions are not or only weakly reversible on the time scale of the assembly process. This is convenient since not relying on reversibility of binding allows to maximize the bond strengths in order to assemble stable and long-living structures. On the downside, however, stochastic effects can easily jeopardize the assembly efficiency if the availability of binding particles is constrained. In order to overcome the limitation arising from the stochastic yield catastrophe, we have discussed several possibilities to implement efficient supply control strategies. Here we want to briefly mention these different possibilities and discuss their respective advantages and drawbacks. We classify these mechanisms by two main distinguishing features: type of regulation and effect on the inter-species variance; see Fig. 7.

Regarding the type of regulation, we have encountered two principally different strategies: the JIS mechanism [48] and the self-inhibitory feedback mechanism both rely on feedback that returns information about the specific state of the assembly process (specifically how many active and/or inactive monomers there are). This information is used to regulate the supply in a self-organized, autonomous fashion. In contrast, in the burst scenario, no such feedback was implemented. Instead, we assumed that the bursts were provided automatically after long enough time spans so that all particles of the previous burst had enough time to bind. Similarly, in the scenarios with non-homogeneous activation rates or non-stoichiometric concentrations [17], no feedback of information about the state of the system was needed.

A second distinguishing characteristic of the presented supply control strategies is their respective effect on the inter-species variance. Processes like bursts or self-inhibition decrease the variance between the species' concentrations and thereby reduce stochastic effects without favoring specific assembly paths. Conversely, strategies including just-in-sequence supply [48], engineering inhomogeneous activation rates or choosing non-stoichiometric concentrations [17] increase the variance in a coordinated way. In this fashion, certain assembly paths are favored which leads to reduced competition for resources and consequently suppresses stochastic effects. The advantage of using a strategy that decreases the inter-species variance is that such a strategy is expected to be applicable independently of the heterogeneity and design of the target structure: Irrespective of whether certain species occur several times in the target structure, decreasing inter-species fluctuations reduces undesirable nucleation events [62]. Conversely, for those strategies that favor specific assembly paths, supply regulation has to be adapted accordingly if species occur several times in the target structure and hence in the assembly path. Specifically, this would demand a higher degree of regulation as it must be assured then that species are delivered not only in the correct order but also in the correct amount. The specific mechanisms discussed here are not directly suitable for this purpose: there is no control over the portion of each species that is delivered at once (specifically, constituents cannot be activated in fractions of their total numbers). However, more sophisticated supply regulatory mechanisms based

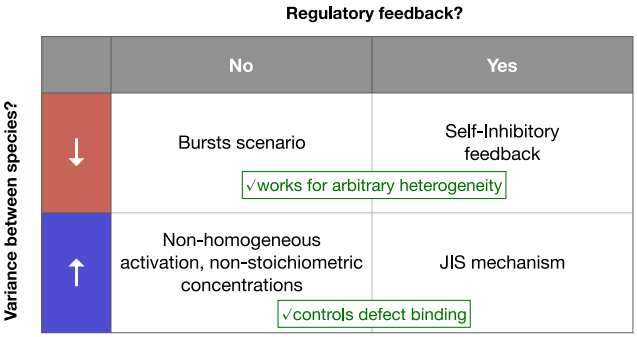

FIG. 7. **Summary of the different control strategies to improve yield and guide the assembly process.** In essence, the control strategies discussed in this manuscript in order to improve yield can be classified into two categories. First, the variance between species is either decreased (burst scenario and self-inhibitory feedback) or increased in a coordinated fashion (non-homogeneous activation rates, non-stoichiometric concentrations [17] and coordinated inhibition of neighboring species (JIS mechanism) [48]). Second, these strategies either rely on regulatory feedback (self-inhibitory feedback and coordinated inhibition of neighboring species (JIS mechanism) [48]) or not (non-homogeneous activation rates, non-stoichiometric concentrations [17] and burst scenario). Increasing the variance in a controlled manner by either non-homogeneous activation rates or in the JIS mechanism not only improves yield but also controls defect formation. In contrast, reducing the variance is generally useful for heterogeneous structures, irrespective of whether species occur several times in one target structure or not.

on feedback might be able to support the self-assembly of structures also with repeated patterns of constituents. A major advantage of providing constituents in a way to favor a specific assembly path lies in the reduction of assembly errors and defects that would result form incorrect binding events [48]. This is plausible because if particles are delivered specifically as they are needed in the assembly process the probability for cross-specific binding reactions is minimized and correct growth fostered.

In conclusion, depending on whether structures are fully heterogeneous or show repeated patterns and whether or not defect control is essential, a coordinated increase or a general decrease of inter-species variability may be beneficial.

IX. SUMMARY AND DISCUSSION

The goal of this manuscript was to understand the role of stochastic effects in heterogeneous self-assembly processes. To this end, we formulated an effective theory for a conceptual model for the assembly of heterogeneous ring structures. Previously it was shown that stochastic effects can be detrimental for the yield of the self-assembly process ("stochastic yield catastrophe") [46, 48]. However, it remained elusive why stochastic fluctuations do have such a strong effect and which role the different sources of stochasticity play for the assembly process. The main insights gained from our analysis are the following: First, we have shown that fluctuations in the relative availability of species are the main cause for the stochastic yield catastrophe. An effective theory incorporating only this source of stochasticity and neglecting other fluctuations such as randomness in binding captures the phenomenology of the full stochastic model. Second, the effective theory allowed us to pinpoint the consequences of inter-species variability on the fidelity of the assembly process: If certain species are activated less than their binding partners, they can become temporarily unavailable for the assembly process. Their unavailability then blocks the growth of neighboring structures. Growth is biased towards small structures, which accumulate in the system. This accumulation is detrimental because a substantial amount will not be completed before resources run out. As a result, the assembly yield is low [10, 20, 21, 44–46, 51]. This effect that may lead to kinetic trapping is not captured in a deterministic description but constitutes a genuine stochastic effects caused by fluctuations in the relative concentrations of the different species.

Importantly, our theoretical analysis also reveals that the strength of the fluctuations in the relative availability of the different species is, to a large extent, set by the single-species variance in the supply. This key insight enabled us to identify different ways to significantly increase assembly efficiency by reducing variability between species. All of these strategies use supply regulation to suppress stochastic effects and avoid kinetic trapping. We distinguished these strategies according to two relevant criteria: whether or not feedback or information about the system is used to regulate the supply (*type of regulation*) and whether the variance between different species is reduced or specific assembly paths are favored (*effect on inter-species variance*). Corresponding to this classification scheme we discussed five different strategies to improve the yield. The first two strategies reduce the inter-species variance with or without the help of feedback:

- Burst scenario: inactive monomers are provided in several bursts, each of which contains a fraction of the total number of monomers in stoichiometric ratios. The time intervals between subsequent bursts are sufficiently long so that all possible binding reactions of the previous burst have taken place before the next burst is provided.

- Self-inhibition scenario: activation is inhibited by active monomers of the same species. The accumulation of active monomers of single species is thereby inhibited.

We found that improving the yield by providing particles in bursts requires the bursts to be sufficiently deterministic, i.e. the number of particles per species per burst must be tightly controlled to obey stoichiometric ratios; see Appendix E. We believe that cells could, in principle, effectuate such a strategy by controlling the composition of bursts via a regulation of several genes by a common promoter. Interesting open questions in the context of whether this would be a realistic possibility for cells concern the dependence of the yield on the exact (deterministic or stochastic) timing between the bursts. Furthermore, it might be enlightening to consider bursts of different size and to ask to what extend the order of bursts of different sizes matters.

Two recent studies demonstrated that also the opposite strategy, namely increasing the variation between species, can increase yield [17, 48]. However, increasing the inter-species variability only leads to an improved assembly process if it occurs in a very coordinated way that favors a specific assembly path (see also Appendix F). Then, competition of different structures for the same resources is reduced to a minimum and the assembly process leads to completed target structures. The following strategies have been proposed to favor specific assembly paths, where only the last one relies on feedback:

- Non-stoichiometric concentrations [17]: certain species are heavily over-represented to trigger nucleation events specifically between these species and to favor assembly paths that emanate from these nuclei.

- Inhomogeneous activation rates: exponentially increasing or decreasing activation rates provide active monomers in sequence with a specific assembly path.

- Just-in-sequence scenario [48]: activation is inhibited by inactive monomers of the neighboring species. The resulting inhibition cascade between the species favors a specific assembly path and delivers active monomers just-in-sequence with this chosen path.

From a theoretical perspective, there are several other interesting aspects about the described stochastic effects in self-assembling systems. Naively, one might ask how fluctuations between the concentrations of species, which are typically of the order of $1/\sqrt{N}$ (compared to the number of particles per species N), can lead to such dramatic effects. To answer this question, two aspects should be considered: First, at early stages of the assembly process, the relevance of stochastic effects must be evaluated with respect to the number of particles that have been activated to that point, rather than the total number of particles. Hence fluctuations at the beginning of the assembly process might not be suppressed as $\sim 1/\sqrt{N}$ but rather as $\sim 1/\sqrt{N_{\text{eff}}}$ where N_{eff} is some effective particle number which can be much smaller than N. Hence at the onset of the assembly process fluctuations are indeed much more substantial even if N is large. Second, it is exactly the first part of the assembly process that is most crucial for the final state. If too many structures nucleate in the beginning, too many structures compete for the same resources and none of them can be finished. This implies that especially fluctuations at the beginning of the assembly process may have a big impact since their influence determines the fate of the system. A similar phenomenology is observed, for instance, in self-reinforcing processes [63].

On a broader perspective, we demonstrate that demographic noise can be an important limiting factor for the self-assembly of heterogeneous structures. In our model, demographic noise is due to an additional activation step that renders particles competent for binding. This can be either interpreted in terms of an actual activation step (such as for instance due to allosteric effects [39, 49, 64]) or in terms of co-translational [65] or co-transcriptional assembly [66]: While the building blocks are still produced, the assembly process already takes place simultaneously. The effects of simultaneous production and assembly of building blocks is expected to be relevant both for self-assembly in living organisms as well as in nanotechnological applications: In particular, it has been suggested that combining *in vivo* transcription with simultaneous RNA-based assembly techniques might be a promising route for the further development of nanotechnology [66–69]. In light of our findings, it will be interesting to see whether such approaches applied to the assembly of large and heterogeneous structures need further regulation mechanisms to circumvent strong stochastic effects. Our proposed control strategies may then provide a first step to improve assembly efficiency.

ACKNOWLEDGMENTS

We thank Philipp Geiger and Patrick Wilke for helpful comments. This research was funded via the Excellence Cluster "ORIGINS" by the Deutsche Forschungsgemeinschaft (DFG, German Research Foundation) under Germany's Excellence Strategy – EXC-2094 – 390783311. IRG and FG were supported by a DFG fellowship through the Graduate School of Quantitative Biosciences Munich (QBM).

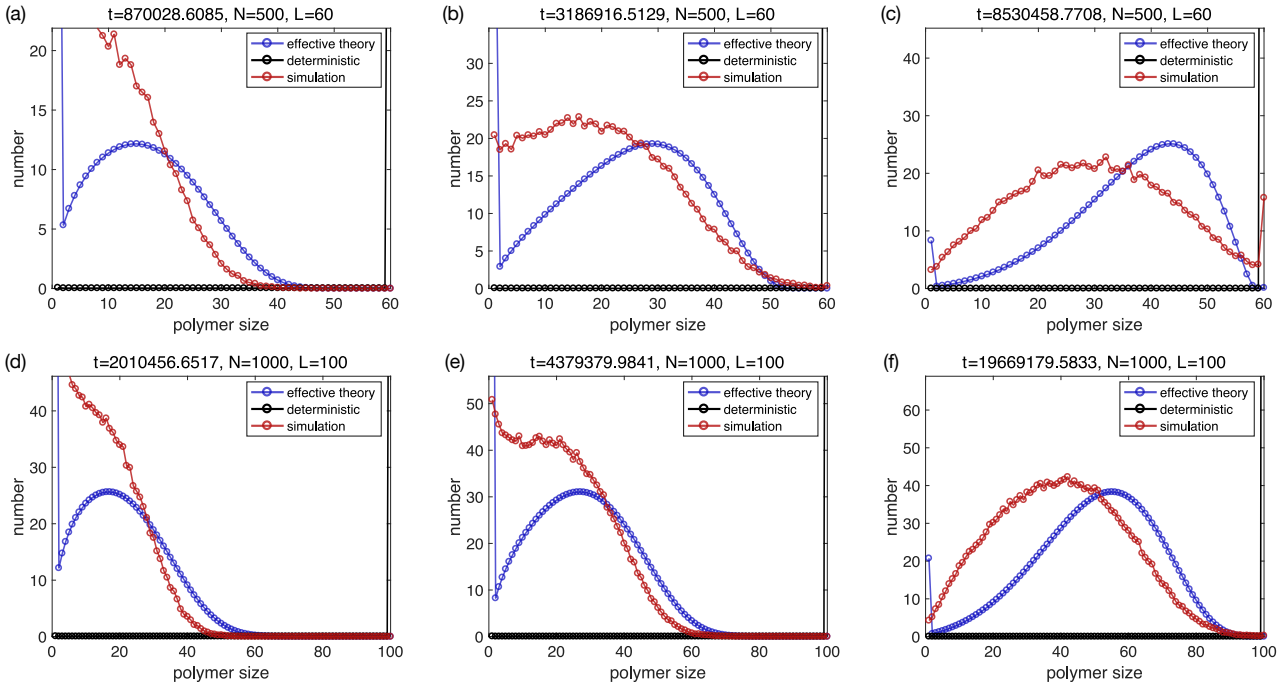

FIG. 8. **Temporal evolution of the polymer size distribution in the limit $\alpha \to 0$.** The polymer size distribution (of all species combined) as measured in stochastic simulations (red; averaged over 100 simulations each) is shown in comparison to the prediction of the effective theory ($Sc_l(t) = S(g_l(t) + b_l(t))$ as obtained by a numerical integration of Eqs. 45, 47, 48, 49; blue) and in comparison to the prediction of the deterministic theory ($Sc_l(t)$ as obtained by a numerical integration of Eqs. 3, 4; see also Ref. [46]; black). For each parameter combination ($L = 60$, $N = 500$ in (a,b,c) and $L = 100$, $N = 1000$ in (d,e,f)) the polymer size distribution is shown for small (a,d), intermediate (b,e) and large time (c,f), respectively. The other parameters are $L = S$, $\mu = \nu = 1$, $\nu_{\mathrm{def}} = 0$ and $\alpha = 10^{-4}N/L^3$. The wave predicted by the deterministic theory has an extremely small amplitude and is therefore not visible.

Appendix A: Temporal evolution of the polymer size distribution

Figs. 8, 9 show the time evolution of the structure size distribution (of all species combined) in the stochastic simulations and in the effective theory (with $c_l(t) = g_l(t) + b_l(t)$ according to Eqs. 45, 47, 48, 49), in comparison to the deterministic prediction (c_l according to Eqs. 3, 4) as presented in Ref. [46]. We make the following observations: On the one hand, the monomer dynamics does not seem to be reproduced very well by the effective theory. Correspondingly, the back of the wave decays more rapidly in the effective theory as compared to the stochastic simulations. In relation to the deterministic wave, however, the waves produced by the effective theory and by the stochastic simulations are quite similar. This is true in particular in the limit $\alpha \to 0$ (Fig. 8) where the deterministic wave is not really visible because it exhibits a very small amplitude. In both the stochastic simulations and in the effective theory the number of monomers is high until very late in the process and the waves move much more slowly as compared to the deterministic wave because many structures compete for the same resources. Furthermore, while the effective theory does not capture the front of the wave perfectly, it does describe the right trend. As a result, the approximations made to determine the probabilities p_l in terms of the simplified assembly process appear to be justifiable in retrospect.

Appendix B: Detailed mathematical analysis

In this section, we will present the details of the parts of the mathematical analysis that have been skipped in the main text.

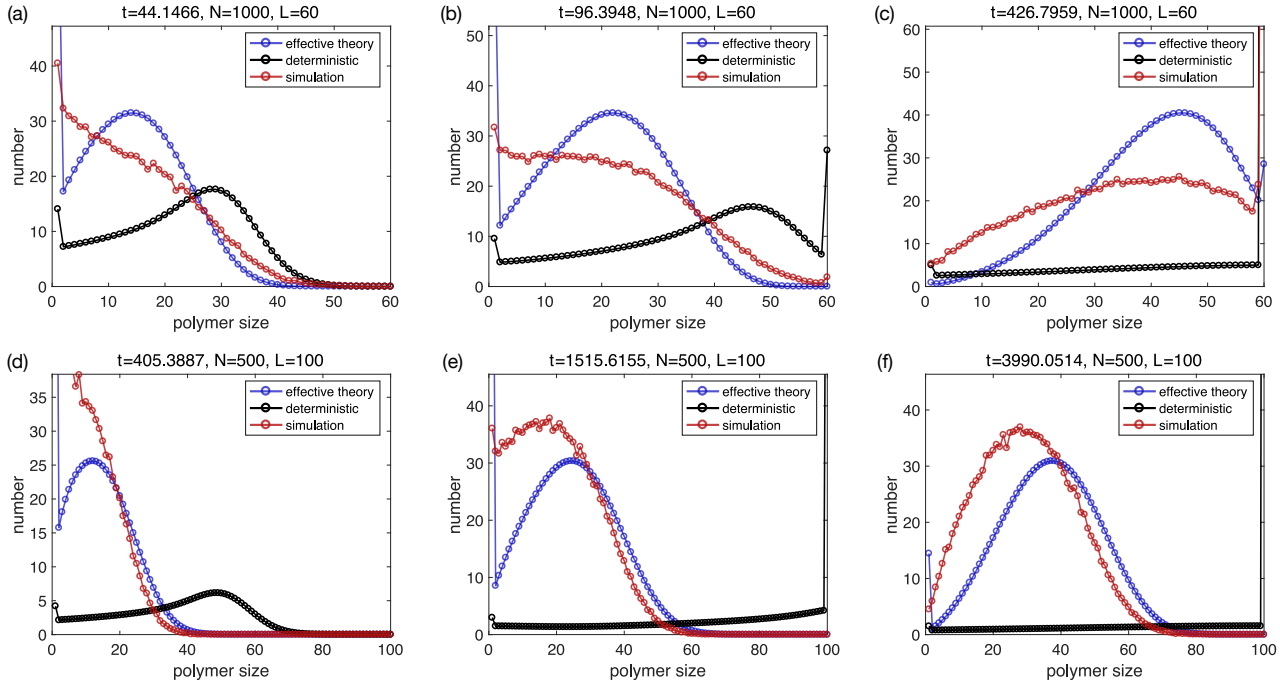

FIG. 9. **Temporal evolution of the polymer size distribution for $\alpha = N/L^3$.** The polymer size distribution (of all species combined) as measured in stochastic simulations (red; averaged over 100 simulations each) is shown in comparison to the prediction of the effective theory ($Sc_l(t) = S(g_l(t) + b_l(t))$ as obtained by a numerical integration of Eqs. 45, 47, 48, 49; blue) and in comparison to the prediction of the deterministic theory ($Sc_l(t)$ as obtained by a numerical integration of Eqs. 3, 4; see also Ref. [46]; black). For each parameter combination ($L = 60$, $N = 1000$ in (a,b,c) and $L = 100$, $N = 500$ in (d,e,f)) the polymer size distribution is shown for small (a,d), intermediate (b,e) and large time (c,f), respectively. The other parameters are $L = S$, $\mu = \nu = 1$, $\nu_{\text{def}} = 0$.

1. Derivation of the growth probabilities p_l

In this subsection, we will explain our choice of transition rates α^l_{jk} more thoroughly. From the resulting formulas (which are also given in the main text, Eq. 22), we derive the steady-state occupancy in the effective assembly network (Eq. 21 and Fig. 3 (f)). This steady-state occupancy will then be used to calculate the growth probabilities p_l, Eq. 31.

a. Transition rates α^l_{jk}

To determine the transition rates between the different states S^l_i of the simplified assembly process described in section IV C and illustrated in Fig. 3(f), we proceed as follows: First, we derive the probability Π^l_{ij} that a structure of size l with $i = 1$ or $i = 2$ growing ends has $j = 0, 1$ or 2 growing ends after attachment of a monomer to one of the original growing ends. Then, we use this probability to calculate the transition rates.

To determine Π^l_{ij}, it is convenient to consider the ways in which a monomer can attach to a structure of size l with $i = 1$ or $i = 2$ growing ends: We begin with a structure that has two growing ends. Then, a monomer can attach either to the left or to the right. In order to calculate the probability that the structure still has two growing ends after the monomer attachment, we consider the probabilities of the following configurations ("embeddings"; see Fig. 10 A for an illustration):

a) The two neigboring sites of the structure of size l with two growing ends both correspond to species that can grow further in the direction away from the structure (left configuration in A). That is, regardless of which end of the structure a monomer attaches to, the new end will also be in a growing state.

b) One neighboring site corresponds to a species that can grow further in the direction away from the structure, whereas the other one does not (middle configurations in A). In this case, the probability that the new end is in the growing state is 1/2 and the probability that the new end is in the blocked state is also 1/2.

c) Both neighboring sites correspond to species that cannot grow further in the direction away from the structure

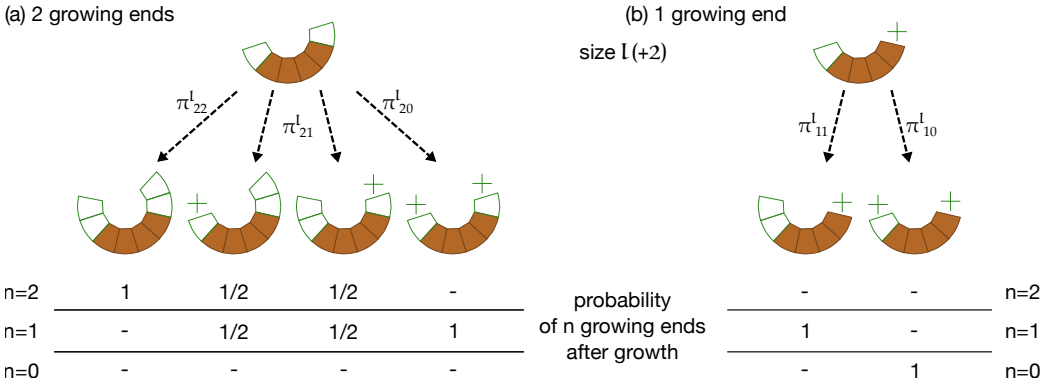

FIG. 10. **Illustration of the probabilities π^l_{ij} that a structure of size l with i growing ends is embedded in configurations with additional growing or blocked ends.** (a) A structure of size l with two growing ends $i = 2$ can be embedded in four different configurations of structures: one structure with an additional growing end at both ends ($j = 2$; left), two structures with one additional growing and one additional blocked end ($j = 1$; middle) and one structure with two additional blocked ends ($j = 0$; right). If the original structure of size l is embedded in the structure on the left ($j = 2$), it will with probability 1 still have two growing ends after growth by one monomer. If it is embedded in one of the middle structures ($j = 1$), after growth by one monomer it will have either one or two growing ends (depending on which monomer attached to it). The probability is 1/2 for both cases. Finally, if the original structure was embedded in the structure on the right ($j = 0$), after growth it will in both cases have one growing and one blocked end. Thus the probability to end up in a configuration with one growing end and one blocked end is 1. (b) A structure of size l with one growing end $i = 1$ can be embedded in two configurations: one structure with an additional growing site next to the original growing end ($j = 1$; left) and one structure with a blocked site next to the growing end ($j = 0$; right). If it is embedded in the structure on the left ($j = 1$), after growth (which can only happen at one end) it will still have one growing end. In contrast, if it is embedded in the structure on the right ($j = 0$), it will be blocked after growth.

(left configurations in A). Then, the probability that the new end is in the blocked state is 1.
What are the probabilities for either of these configuration? If we assume that the unavailable species are distributed randomly along the ring, the number of configurations in which the next-nearest neighbor species at each end of the structure of size l are available (configuration a) is given by

$$X^l_{22} = \binom{L-(l+4)}{L_\times}$$

since the $L_\times$ unavailable species can be distributed to the remaining $L-(l+4)$ sites along the ring (the configuration we consider comprises the original structure of size l, the two neighboring species and the two next-nearest neighboring species). Similarly, the number of configurations in which the next-nearest neighbor species at one end of the structure of size l is available but the next-nearest neighbor at the other end is unavailable (configuration b) is given by

$$X^l_{21} = 2\binom{L-(l+4)}{L_\times - 1}$$

because one of the unavailable species is already part of the complex of size l plus the four surrounding next and next-nearest neighbors. Thus, only $L_\times - 1$ unavailable species are distributed among the remaining $L-(l+4)$ sites along the ring. The factor 2 comes from the fact that there are two equivalent configurations of this type (the available next-nearest species can be on the left or on the right). Finally, the number of configurations in which the next-nearest neighbor species at both ends of the structure of size l are unavailable (configuration c) is given by

$$X^l_{20} = \binom{L-(l+4)}{L_\times - 2}$$

because two of the unavailable species are already part of the complex of size l plus the four surrounding next and next-nearest neighbors.

From the number of configurations we can determine the respective probabilities by normalizing the number of

configurations by the overall number of configurations:

$$\pi_{22}^l = \frac{X_{22}^l}{X_{22}^l + X_{21}^l + X_{20}^l}$$
$$\pi_{21}^l = \frac{X_{21}^l}{X_{22}^l + X_{21}^l + X_{20}^l}$$
$$\pi_{20}^l = \frac{X_{20}^l}{X_{22}^l + X_{21}^l + X_{20}^l}.$$

As mentioned before, in configuration a (π_{22}^l), the probability that after growth by a monomer the structure still has two growing ends is 1. In configuration b (π_{21}^l) it is 1/2 and in configuration c (π_{20}^l) it is zero. The overall probability Π_{22}^l that a structure of size l with two growing ends has still two growing ends after attachment of a monomer to one of the original growing ends is given by

$$\Pi_{22}^l = \pi_{22}^l + \frac{1}{2}\pi_{21}^l = 1 - \frac{L_\times}{L - l - 2}.$$

In the last step, we plugged in the explicit formulas in terms of the binomial coefficients.
Analogously, the overall probability Π_{21}^l that a structure of size l with two growing ends has still one growing end after attachment of a monomer to one of the original growing ends is given by

$$\Pi_{21}^l = \pi_{20}^l + \frac{1}{2}\pi_{21}^l = \frac{L_\times}{L - l - 2}.$$

For structures with only one growing end, the situation is simpler because attachment of a monomer can only occur at one end (see Fig. 10 B for an illustration). Then the only question is whether the next-nearest neighbor at the growing end is available or not. Analogously to above, the number of configurations in which the next-nearest neighboring species at the growing end of the structure of size l is available (left in panel B) is given by

$$X_{11}^l = \binom{L - (l+3)}{L_\times - 1}.$$

In this case, the size of the relevant complex is $l+3$, namely the original size l plus the two nearest neighbors plus the next-nearest neighbor at the growing end. Since one end of the structure is blocked, one of the neighboring species is unavailable and, thus, there remain $L_\times - 1$ unavailable species that can be distributed among $L - (l+3)$ sites along the ring. Similarly, the number of configurations in which the next-nearest neighboring species at the growing end of the structure of size l is unavailable (right in panel B) is given by

$$X_{10}^l = \binom{L - (l+3)}{L_\times - 2}.$$

In this case one of the neighboring species and the next-nearest neighboring species at the growing end are unavailable; there remain $L_\times - 2$ unavailable species that can be distributed among $L - (l+3)$ sites along the ring.

The respective probabilities for these configurations are

$$\pi_{11}^l = \frac{X_{11}^l}{X_{11}^l + X_{10}^l} = 1 - \frac{L_\times - 1}{L - l - 2} = \Pi_{11}^l$$
$$\pi_{10}^l = \frac{X_{10}^l}{X_{11}^l + X_{10}^l} = \frac{L_\times - 1}{L - l - 2} = \Pi_{10}^l,$$

where we plugged in the explicit expressions in terms of the binomial coefficients. Furthermore, due to the way in which the configurations were defined, the overall probabilities Π_{1j}^l that a structure of size l with one growing end has $j = 0$ or 1 growing ends after attachment of a monomer are in this case directly given by the probabilities of the respective configuration (see also the table at the bottom of Fig. 10 B).

How can we use these probabilities Π_{ij}^l to determine the transition rates? Π_{ij}^l denotes the conditional probability that a structure of size l with $i = 1$ or $i = 2$ growing ends has $j = 0, 1, 2$ growing ends after a monomer has attached, if we already know that attachment happens. So, to translate these conditional probabilities, we need to multiply them by the rate at which monomer attachment occurs.
In the main text, we defined γ as the total rate of attachment of a monomer to one growing end. Thus, the overall rate

for attachment of a monomer to a structure with two growing ends is 2γ and the one for attachment to a structure with one growing end is γ. Therefore, the probabilities for structures with two growing ends have to be multiplied by 2γ and the ones for structures with one growing end by γ. The transition rates are thus given by

$$\begin{aligned}
\alpha_{22}^l &= 2\gamma\Pi_{22}^l = 2\gamma\left(1 - \frac{L_\times}{L-l-2}\right)\\
\alpha_{21}^l &= 2\gamma\Pi_{22}^l = 2\gamma\frac{L_\times}{L-l-2}\\
\alpha_{22}^l &= \gamma\Pi_{22}^l = \gamma\left(1 - \frac{L_\times - 1}{L-l-2}\right)\\
\alpha_{22}^l &= \gamma\Pi_{22}^l = \gamma\frac{L_\times - 1}{L-l-2},
\end{aligned}$$

as stated in the main text, Eq. 22.

b. Steady-state occupancy s_j^l in the effective assembly network for fixed number of unavailable sites $L_\times$

In this section, we will determine the steady-state occupancy s_j^l in the simplified assembly network described in section IV C and illustrated in Fig. 3(f).

To this end, we consider the in- and outfluxes into the states S_j^l for $l \geq 2$ and $j = 1, 2$ (l denotes the size of the structure and j the number of growing ends). Since the number of growing ends cannot increase in the simplified assembly network, the influx into state S_2^l is solely from state S_2^{l-1} at rate α_{22}^{l-1}. Outflux occurs at rates α_{22}^l into state S_2^{l+1} and α_{21}^l into state S_1^{l+1}. Thus, the temporal evolution of the number s_2^l of particles in state S_2^l is given by

$$\frac{\mathrm{d}s_2^l}{\mathrm{d}t} = \alpha_{22}^{l-1}s_2^{l-1} - \left(\alpha_{22}^l + \alpha_{21}^l\right)s_2^l = \alpha_{22}^{l-1}s_2^{l-1} - 2\gamma s_2^l.$$

Regarding state S_1^l, there is influx from state S_2^{l-1} at rate α_{21}^{l-1} and from S_1^{l-1} at rate α_{11}^{l-1}. Outflux occurs at rates α_{11}^l into state S_1^{l+1} and α_{10}^l into state S_0^{l+1}. The temporal evolution of the number s_1^l of particles in state S_1^l is thus

$$\frac{\mathrm{d}s_1^l}{\mathrm{d}t} = \alpha_{21}^{l-1}s_2^{l-1} + \alpha_{11}^{l-1}s_1^{l-1} - \left(\alpha_{11}^l + \alpha_{10}^l\right)s_1^l = \alpha_{21}^{l-1}s_2^{l-1} + \alpha_{11}^{l-1}s_1^{l-1} - \gamma s_1^l.$$

In steady-state, $\mathrm{d}s_j^l/\mathrm{d}t = 0$, these equations are rewritten in terms of a recursion relation as

$$\begin{aligned}
s_2^l &= \frac{\alpha_{22}^{l-1}}{2\gamma}s_2^{l-1}\\
s_1^l &= \frac{\alpha_{21}^{l-1}}{\gamma}s_2^{l-1} + \frac{\alpha_{11}^{l-1}}{\gamma}s_1^{l-1}.
\end{aligned}$$

The solution to this recursion relation for $l \geq 3$ is given by

$$s_2^l = \frac{(L-L_\times-3)(L-L_\times-4)\dots(L-L_\times-l)}{(L-3)(L-4)\dots(L-(l+1))}\left(L-L_\times-(l+1)\right)s_2^1 = \tag{B1a}$$

$$= \left(L-L_\times-(l+1)\right)s_2^1\phi_l, \tag{B1b}$$

$$s_1^l = \frac{(L-L_\times-3)(L-L_\times-4)\dots(L-L_\times-l)}{(L-3)(L-4)\dots(L-(l+1))}\left((L-L_\times-2)s_1^1 + 2(l-1)L_\times s_2^1\right) = \tag{B1c}$$

$$= \left((L-L_\times-2)s_1^1 + 2(l-1)L_\times s_2^1\right)\phi_l, \tag{B1d}$$

where we defined

$$\phi_l = \frac{(L-L_\times-3)(L-L_\times-4)\dots(L-L_\times-l)}{(L-3)(L-4)\dots(L-(l+1))}.$$

These expressions depend on the steady-state numbers s_j^1 of monomers with either $j=1$ or $j=2$ growing ends. To make progress, we thus need to determine these steady-state numbers. This can be done by considering the steady-state dynamics of the monomer states. Into state S_2^1 there is an influx i_2 (as defined in the main text in Eq. 23), and the monomers transition to states S_1^2 and S_2^2 at rates α_{21}^1 and α_{22}^1, respectively. As a result,

$$\frac{\mathrm{d}s_2^1}{\mathrm{d}t} = i_2 - \left(\alpha_{22}^1 + \alpha_{21}^1\right) s_2^1 = i_2 - 2\gamma s_2^1.$$

Similarly, we have

$$\frac{\mathrm{d}s_1^1}{\mathrm{d}t} = i_1 - \left(\alpha_{11}^1 + \alpha_{10}^1\right) s_1^1 = i_1 - \gamma s_1^1.$$

In steady-state, these equations reduce to

$$s_2^1 = \frac{i_2}{2\gamma} \tag{B2a}$$

$$s_1^1 = \frac{i_1}{\gamma}. \tag{B2b}$$

c. Growth probabilities p_l

Finally we plug in the expressions, Eqs. B1, B2, for the steady-state number s_j^l of particles in state S_j^l into the equation for the probability p_l, Eq. 30. Using the explicit form of the influx rates i_2 and i_1, Eq. 23, yields after some algebra

$$p_l = \begin{cases} 1 - \frac{lL_\times(L_\times - 1)}{[L-(l+1)]\,[L+(l-1)L_\times - l]}\,, & l < L - L_\times \\ 0 & \text{else,} \end{cases} \tag{B3}$$

as given in the main text, Eq. 31. As it is derived here, it is only valid for $l \geq 4$ (since Eq. B1 is only valid for $l \geq 3$). By explicitly calculating p_l for $l = 1, 2$ and 3 from the recursion relation, one can, however, show that the same formulas also apply in these cases. More generally, if there is less than one species unavailable, $L_\times < 1$, all structures can grow. Then we have $p_l = 1\ \forall l$.

2. Exchange dynamics between the different monomer states

In this subsection, we give details on how we determined the fluxes between the different monomer states if the number of unavailable sites $L_\times$ changes.

For this purpose, it is illustrative to consider a system with three states A, B and C and total number of particles N. We assume that the probability to be in state A at time t is $p_A(t)$ and analogously for B and C the probabilities are $p_B(t)$ and $p_C(t)$ with $p_A(t) + p_B(t) + p_C(t) = 1$. Furthermore, we assume that the total number is conserved: $N = \text{const}$. Then, we have for the numbers of particles N_A, N_B and N_C at time t:

$$N_A(t) = Np_A(t) \qquad N_B(t) = Np_B(t) \qquad N_C(t) = Np_C(t).$$

For the derivatives, we thus find analogously to the main text

$$\frac{\mathrm{d}N_A}{\mathrm{d}t} = N\frac{\mathrm{d}p_A}{\mathrm{d}t} = \frac{N_A}{p_A}\frac{\mathrm{d}p_A}{\mathrm{d}t} = N_A\frac{\mathrm{d}\,\ln(p_A)}{\mathrm{d}t},$$

and similarly for B and C. As a result, for a three-state system we get exactly the same per-capita rates of exchange r_A^{pc} as for the two-state system discussed in the main text in Sec. IV D:

$$r_A^{\mathrm{pc}} = \frac{\mathrm{dln}(p_A)}{\mathrm{d}t}.$$

It is given by the time derivative of the logarithm of the corresponding probability. The only difference now is that it is not clear, yet, which portion of A transforms to B and C, respectively, if $\mathrm{d}p_A/\mathrm{d}t < 0$.

To answer this question, we consider two cases:
For the first case, we assume that $\mathrm{d}p_A/\mathrm{d}t < 0$ and $\mathrm{d}p_B/\mathrm{d}t > 0$ and $\mathrm{d}p_C/\mathrm{d}t > 0$, so there is only outflux from state A into states B and C. In this case, it is useful to rewrite the time derivatives of N_B and N_C as follows:

$$\frac{\mathrm{d}N_B}{\mathrm{d}t} = N\frac{\mathrm{d}p_B}{\mathrm{d}t} = \frac{N_A}{p_A}\frac{\mathrm{d}p_B}{\mathrm{d}t}$$
$$\frac{\mathrm{d}N_C}{\mathrm{d}t} = N\frac{\mathrm{d}p_C}{\mathrm{d}t} = \frac{N_A}{p_A}\frac{\mathrm{d}p_C}{\mathrm{d}t}.$$

Thus, the fractions of particles that transition from state A to the states B and C are proportional to the corresponding changes in the probability, $\mathrm{d}p_B/\mathrm{d}t$ and $\mathrm{d}p_C/\mathrm{d}t$, respectively.
For the second case, we assume that $\mathrm{d}p_A/\mathrm{d}t < 0$ and $\mathrm{d}p_B/\mathrm{d}t < 0$ whereas $\mathrm{d}p_C/\mathrm{d}t > 0$, so there is outflux from states A and B into state C. The time derivative of N_C is then conveniently rewritten as

$$\frac{\mathrm{d}N_C}{\mathrm{d}t} = N\frac{\mathrm{d}p_C}{\mathrm{d}t} = -N\left(\frac{\mathrm{d}p_A}{\mathrm{d}t} + \frac{\mathrm{d}p_B}{\mathrm{d}t}\right) = -\frac{N_A}{p_A}\frac{\mathrm{d}p_A}{\mathrm{d}t} - \frac{N_B}{p_B}\frac{\mathrm{d}p_B}{\mathrm{d}t},$$

where the second equality follows from conservation of probability $p_A + p_B + p_C = 1$. As expected, the flux into state C then just corresponds to the sum of the two outfluxes from states A and B, respectively.

These "rules" can now be applied to the exchange of monomers between the different states:
Consider first the case where the number of unavailable species decreases, $\mathrm{d}L_\times/\mathrm{d}t < 0$. Some monomers of the blocked state will then transition to the unblocked state and some monomers that have been unavailable previously will transition to the normal state. In this case, there are only interactions between two states each and we can immediately conclude that the fluxes between the states are given by

$$\varrho_\times = \frac{m_\times}{P_\times}\frac{\mathrm{d}P_\times}{\mathrm{d}t} \qquad \varrho_\mathrm{n} = -\varrho_\times \tag{B4a}$$
$$\varrho_\mathrm{b} = \frac{m_\mathrm{b}}{P_\mathrm{b}}\frac{\mathrm{d}P_\mathrm{b}}{\mathrm{d}t} \qquad \varrho_\mathrm{ub} = -\varrho_\mathrm{b}, \tag{B4b}$$

as given in the main text, Eq. 42.

In the case where the number of unavailable species increases, $\mathrm{d}L_\times/\mathrm{d}t > 0$, some monomers of the unblocked state transition back to the blocked state and some monomers of the normal state either transition to the unavailable state or also to the blocked state. In this case, we thus have according to the above rules:

$$\varrho_\times = \frac{m_\mathrm{n}}{P_\mathrm{n}}\frac{\mathrm{d}P_\times}{\mathrm{d}t} \tag{B5a}$$
$$\varrho_\mathrm{n} = \frac{m_\mathrm{n}}{P_\mathrm{n}}\frac{\mathrm{d}P_\mathrm{n}}{\mathrm{d}t} \tag{B5b}$$
$$\varrho_\mathrm{b} = \frac{m_\mathrm{n}}{P_\mathrm{n}}\frac{\mathrm{d}P_\mathrm{b}}{\mathrm{d}t} + \frac{m_\mathrm{ub}}{1-P_\mathrm{b}}\frac{\mathrm{d}P_\mathrm{b}}{\mathrm{d}t} \tag{B5c}$$
$$\varrho_\mathrm{ub} = \frac{m_\mathrm{ub}}{P_\mathrm{ub}}\frac{\mathrm{d}P_\mathrm{ub}}{\mathrm{d}t} = -\frac{m_\mathrm{ub}}{1-P_\mathrm{b}}\frac{\mathrm{d}P_\mathrm{b}}{\mathrm{d}t}, \tag{B5d}$$

where we used that the unblocked state effectively corresponds to a probability $1 - P_\mathrm{b}$ because all outflux from the blocked state goes into it (instead of going into the unavailable or the normal state). These equations correspond to Eq. 43 as given in the main text.

Appendix C: Effective theory with defect formation

In the main text, we presented the effective theory for the case of no defect formation $\nu_\mathrm{def} = 0$. Here, we explain our approach to generalize the theory by effectively including erroneous binding. We make several (crude) simplifications:

- Erroneous binding (defect formation) is not subject to stochastic effects. That is, all monomers in states in which they cannot regularly bind to a polymer can bind at rate ν_def to this polymer, thereby creating a defect in the structure. The essential idea is that it is unlikely that a polymer or monomer in the blocked state is blocked

by two unavailable species in a row: Say species i and $j > i$ were unavailable, then a structure $(i{+}1)\ldots(j{-}1)$ is in the blocked state. We assume that it is unlikely that simultaneously also species $i{-}1$ and $j{+}1$ are unavailable, so the structure $(i{+}1)\ldots(j{-}1)$ can grow by erroneous binding by either species $i{-}1$ or $j{+}1$.

- Although structures with defects will effectively include unavailable species (because these species have typically been left out if erroneous binding occurs), we take the probabilities that these structures end up in a growing or blocked state to be the same as for the structures with defects: p_l. This certainly is a simplification because in the "derivation" of p_l on the basis of the simplified assembly process described in section IV C and illustrated in Fig. 3(f), we assumed that all structures only grow by attachment of available species.
  As a result, the further growth dynamics of a polymer does not depend on whether it contains defects or not.

- We do not take into account that erroneous binding can lead to additional stochastic effects (see also [48]).

In order to write down the ensuing dynamics of all the structures, we define the following quantities:

- g_l^D for $l \geq 4$ denotes the concentration of polymers with at least one defect and size l in the growing state. The size l always refers to the number of subunits in the structure plus the number of defects. If, for instance, a polymer of size l grows by erroneous binding (creating a defect in the structure), the size of the resulting polymer is taken to be $l+2$. This convention is convenient because it ensures that it is always the structures of size L that do not grow further. Since we do not keep track of the number of defects in a structure, this would be difficult to achieve otherwise.
  Since erroneous binding only occurs from the dimers onwards (there is no erroneous dimerization), polymers with defects have at least a size $l = 4$.

- Analogously, b_l^D for $l \geq 4$ denotes the concentration of polymers with at least one defect and size l in the blocked state.

- As before, g_l and b_l are defined as the concentration of polymers of size l with no defect in the growing and blocked state, respectively.

How does the dynamics of monomers change due to the defect formation? First, the monomers that could bind regularly to the (defect-free) polymers in either the growing and/or blocked state, can now additionally grow to the corresponding defect-containing polymers in either the growing and/or blocked state because we assume that defect-free structures and defect-containing structures in the growing and or blocked state do not differ in their growth dynamics.
Second, the monomers that previously could not bind to a polymer in a certain state, can now erroneously bind to these polymers at rate ν_{def}, irrespective of whether the polymers in question already contain defects or not. In this case, an (additional) defect is created in the structure.
With these ingredients the monomer dynamics reads as follows:

$$\partial_t m_{\mathrm{n}} = \alpha N e^{-\alpha t} P_{\mathrm{n}} - 2\mu D_{\mathrm{n}} - 2\nu m_{\mathrm{n}}\gamma + \varrho_{\mathrm{n}} - \left[2\nu_{\mathrm{def}} m_{\mathrm{n}} \left(\beta_{\mathrm{def}} + \beta_{\mathrm{def}}^D\right) + 2\nu m_{\mathrm{n}}\gamma^D\right] \tag{C1a}$$

$$\partial_t m_{\times} = \alpha N e^{-\alpha t} P_{\times} - 2\mu D_{\times} - 2\nu m_{\times} \left(\gamma + \beta\right) + \varrho_{\times} - \left[2\nu m_{\times} \left(\gamma^D + \beta^D\right)\right] \tag{C1b}$$

$$\partial_t m_{\mathrm{b}} = \alpha N e^{-\alpha t} P_{\mathrm{b}} - 2\mu D_{\mathrm{b}} + \varrho_{\mathrm{b}} - \left[2\nu_{\mathrm{def}} m_{\mathrm{b}} \left(\beta_{\mathrm{def}} + \beta_{\mathrm{def}}^D + \gamma_{\mathrm{def}} + \gamma_{\mathrm{def}}^D\right)\right] \tag{C1c}$$

$$\partial_t m_{\mathrm{ub}} = -2\mu D_{\mathrm{ub}} - 2\nu m_{\mathrm{ub}}\gamma + \varrho_{\mathrm{ub}} - \left[2\nu_{\mathrm{def}} m_{\mathrm{ub}} \left(\beta_{\mathrm{def}} + \beta_{\mathrm{def}}^D\right) + 2\nu m_{\mathrm{ub}}\gamma^D\right] \tag{C1d}$$

Here, the expressions $[\ldots]$ in the brackets at the end of each line correspond to the new terms with respect to the equations presented in the main text where $\nu_{\mathrm{def}} = 0$ was assumed. Furthermore, we defined

$$\gamma^D = \sum_{l=4}^{L-1} g_l^D \qquad \beta^D = \sum_{l=4}^{L-1} b_l^D \tag{C2a}$$

$$\gamma_{\mathrm{def}} = \sum_{l=2}^{L-2} g_l \qquad \beta_{\mathrm{def}} = \sum_{l=2}^{L-2} b_l \tag{C2b}$$

$$\gamma_{\mathrm{def}}^D = \sum_{l=4}^{L-2} g_l^D \qquad \beta_{\mathrm{def}}^D = \sum_{l=4}^{L-2} b_l^D \tag{C2c}$$

as i) all the unfinished polymers with defects (superscript D) in either the growing (γ^D) or blocked state (β^D)
ii) all unfinished polymers without defects (no superscript) in either the growing (γ_{def}) or blocked state (β_{def}) whose

size is less than or equal to $L-2$ so that they still grow by erroneous binding (subscript "def") without surpassing the target structure size
iii) all unfinished polymers with defects (superscript D) in either the growing (γ^D_{def}) or blocked state (β^D_{def}) whose size is less than or equal to $L-2$ so that they still grow by erroneous binding (subscript "def") without surpassing the target structure size.

Before going to the polymers, we shortly illustrate the above "rules" for m_{n}: Previously, the monomers in the normal state could only bind to unfinished polymers in the growing state γ. So now they additionally bind to the unfinished polymers in the growing state γ^D with defects and erroneously to the polymers in the blocked states with size $l \leq L-2$ (β_{def} and β^D_{def}).

How does the dynamics of the dimers change? Dimers cannot contain defects, so there are no polymers g_2^D or b_2^D and the only new terms in g_2 and b_2 come from erroneous binding of dimers with monomers with which they do not bind correctly:

$$\partial_t g_2 = \mu\left(D_{\mathrm{n}} + D_{\times} + D_{\mathrm{b}} + D_{\mathrm{ub}}\right) p_2 - 2\nu g_2 M_{\mathrm{G}} + \rho_2 - \left[2\nu_{\mathrm{def}} g_2 m_{\mathrm{b}}\right] \tag{C3a}$$
$$\partial_t b_2 = \mu\left(D_{\mathrm{n}} + D_{\times} + D_{\mathrm{b}} + D_{\mathrm{ub}}\right)(1-p_2) - 2\nu b_2 m_{\times} - \rho_2 - \left[2\nu_{\mathrm{def}} b_2 M_D\right], \tag{C3b}$$

where the new terms [...] are again in the brackets. Furthermore, we defined

$$M_D = m_{\mathrm{n}} + m_{\mathrm{ub}} + m_{\mathrm{b}} \tag{C4}$$

as all the monomers that bind erroneously to polymers in the blocked state, thereby creating a defect. These are exactly monomers in the normal, unblocked and blocked state because these cannot bind to polymers in the growing state.

These additional terms for the monomers appear equivalently for all other polymers without defects that are of size $l \leq L-2$ and, thus, are small enough to potentially bind erroneously:

$$\partial_t g_l = 2\nu\left(g_{l-1} M_{\mathrm{G}} + b_{l-1} m_{\times}\right) p_l - 2\nu g_l M_{\mathrm{G}} + \rho_l - \left[2\nu_{\mathrm{def}} g_l m_{\mathrm{b}}\right] \tag{C5a}$$
$$\partial_t b_l = 2\nu\left(g_{l-1} M_{\mathrm{G}} + b_{l-1} m_{\times}\right)(1-p_l) - 2\nu b_l m_{\times} - \rho_l - \left[2\nu_{\mathrm{def}} b_l M_D\right]. \tag{C5b}$$

Finally, the dynamics of the polymers of size $L-1$ and L without defects does not change because only a correct monomer can bind to these structures and they cannot be made by erroneous binding:

$$\partial_t g_{L-1} = 2\nu\left(g_{L-2} M_{\mathrm{G}} + b_{L-2} m_{\times}\right) p_{L-1} - 2\nu g_{L-1} M_{\mathrm{G}} + \rho_{L-1} \tag{C6a}$$
$$\partial_t b_{L-1} = 2\nu\left(g_{L-2} M_{\mathrm{G}} + b_{L-2} m_{\times}\right)(1-p_{L-1}) - 2\nu b_{L-1} m_{\times} - \rho_{L-1}. \tag{C6b}$$
$$\partial_t g_L = 2\nu\left(g_{L-1} M_{\mathrm{G}} + b_{L-1} m_{\times}\right) \tag{C6c}$$

What is the dynamics of the polymers with defects? To address this question, we distinguish several cases for the growth into the structures and for the growth out of them. We begin with the growth into the structures:

- Polymers of size $l = 4$ with defect can only result from erroneous binding of a dimer with a monomer (total size: 2 (from dimer) + 1 (from monomer) + 1 (from defect)).
- Polymers of size $l = 5$ with defect(s) can result from correct growth of a polymer of size $l = 4$ with defect or from erroneous binding of a monomer with a polymer of size $l = 3$ without defects (there are no polymers of size $l = 3$ with defects).
- Polymers of size $6 \leq l \leq L$ with defect(s) can result from correct growth of a polymer of size $l-1$ with defect or from erroneous binding of a monomer with a polymer of size $l-2$ with or without defects.

For the growth out of the structures we have

- Polymers of size $4 \leq l \leq L-2$ can either grow correctly or erroneously by binding of a monomer in the respective state(s) (see also the dynamics of the monomers).
- Polymers of size $l = L-1$ can only grow correctly by binding of a monomer in the respective state(s) because they are too large to incorporate another defect.
- Polymers of size $l = L$ do not grow any more.

Taken together, these aspects yield the following dynamics of polymers with defects: For structures of size $l = 4$:

$$\partial_t g_4^D = 2\nu_{\rm def}\left(g_2 m_{\rm b} + b_2 M_D\right) p_4 - 2\nu g_4^D M_G - 2\nu_{\rm def} g_4^D m_{\rm b} + \tilde{\rho}_4^D \tag{C7a}$$

$$\partial_t b_4^D = 2\nu_{\rm def}\left(g_2 m_{\rm b} + b_2 M_D\right)(1 - p_4) - 2\nu b_4^D m_\times - 2\nu_{\rm def} b_4^D M_D - \tilde{\rho}_4^D, \tag{C7b}$$

where the flux $\tilde{\rho}_4^D$ between the blocked and growing state is defined analogously to the fluxes between the blocked and growing states for the polymers without defects (see below). For structures of size $l = 5$ we have

$$\partial_t g_5^D = \left(2\nu_{\rm def}\left(g_3 m_{\rm b} + b_3 M_D\right) + 2\nu\left(g_4^D M_G + b_4^D m_\times\right)\right) p_5 - 2\nu g_5^D M_G - 2\nu_{\rm def} g_5^D m_{\rm b} + \tilde{\rho}_5^D \tag{C8a}$$

$$\partial_t b_5^D = \left(2\nu_{\rm def}\left(g_3 m_{\rm b} + b_3 M_D\right) + 2\nu\left(g_4^D M_G + b_4^D m_\times\right)\right)(1 - p_5) - 2\nu b_5^D m_\times - 2\nu_{\rm def} b_5^D M_D - \tilde{\rho}_5^D, \tag{C8b}$$

and for all structures with $6 \le l \le L - 2$:

$$\partial_t g_l^D = \left(2\nu_{\rm def}\Big(\left(g_{l-2} + g_{l-2}^D\right) m_{\rm b} + \left(b_{l-2} + b_{l-2}^D\right) M_D\Big) + 2\nu\Big(g_{l-1}^D M_G + b_{l-1}^D m_\times\Big)\right) p_l - \tag{C9a}$$

$$- 2\nu g_l^D M_G - 2\nu_{\rm def} g_l^D m_{\rm b} + \tilde{\rho}_l^D$$

$$\partial_t b_5^D = \left(2\nu_{\rm def}\Big(\left(g_{l-2} + g_{l-2}^D\right) m_{\rm b} + \left(b_{l-2} + b_{l-2}^D\right) M_D\Big) + 2\nu\Big(g_{l-1}^D M_G + b_{l-1}^D m_\times\Big)\right)(1 - p_l) - \tag{C9b}$$

$$- 2\nu b_l^D m_\times - 2\nu_{\rm def} b_l^D M_D - \tilde{\rho}_l^D.$$

Finally, we find for the structures of size $l = L - 1$

$$\partial_t g_{L-1}^D = \left(2\nu_{\rm def}\Big(\left(g_{L-3} + g_{L-3}^D\right) m_{\rm b} + \left(b_{L-3} + b_{L-3}^D\right) M_D\Big) + 2\nu\Big(g_{L-2}^D M_G + b_{L-2}^D m_\times\Big)\right) p_{L-1} - 2\nu g_{L-1}^D M_G + \tilde{\rho}_{L-1}^D$$

$$\partial_t b_{L-1}^D = \left(2\nu_{\rm def}\Big(\left(g_{L-3} + g_{L-3}^D\right) m_{\rm b} + \left(b_{L-3} + b_{L-3}^D\right) M_D\Big) + 2\nu\Big(g_{L-2}^D M_G + b_{L-2}^D m_\times\Big)\right)(1 - p_l) - 2\nu b_{L-1}^D m_\times - \tilde{\rho}_{L-1}^D,$$

and of size $l = L$:

$$\partial_t g_L^D = 2\nu_{\rm def}\Big(\left(g_{L-2} + g_{L-2}^D\right) m_{\rm b} + \left(b_{L-2} + b_{L-2}^D\right) M_D\Big) + 2\nu\Big(g_{L-1}^D M_G + b_{L-1}^D m_\times\Big). \tag{C11}$$

The only thing left to determine is the exchange dynamics between the polymers with defect in the growing and blocked state, respectively. Since we assumed that the dynamics of polymers in the growing and blocked state does not depend on whether the polymers include defects or not, these fluxes for the polymers with defects are entirely analogous to the fluxes for the polymers without defects. We thus have:

$$\tilde{\rho}_l^D = J_l^{B^D \to G^D} = \begin{cases} \frac{g_l^D}{p_l}\frac{{\rm d}p_l}{{\rm d}t} & \text{if } \frac{{\rm d}p_l}{{\rm d}t} < 0 \\ \frac{b_l^D}{1-p_l}\frac{{\rm d}p_l}{{\rm d}t} & \text{if } \frac{{\rm d}p_l}{{\rm d}t} > 0. \end{cases} \tag{C12}$$

As one can observe in Fig 2 (c), a numerical integration of the full dynamics presented in this section in MATLAB captures the non-monotonic behavior of the defect-free yield (inset) but not of the overall yield. This is presumably due to two of the simplifications we made: First, erroneous binding is always possible, irrespective of the state of the polymers (growing/blocked). As a result, if stochastic effects are strong, erroneous binding is very likely and in the limit of small activation $\alpha \to 0$, structures acquire more and more defects, leading to a higher yield. (In principle, the maximal possible yield is $L/(L/2+1) \approx 2$ because from the dimer state onwards all structures might only bind erroneously and then only $2+(L-2)/2 = L/2+1$ (instead of L) particles would make up one final structure.) Second, we did not consider that erroneous binding might itself enhance stochastic effects: If species i is unavailable for a long time, the neighboring species $i \pm 1$ might bind erroneously instead of species i. In the end, however, this means that there will be too many particles of species i available because the defects have already taken the original places of species i.

Appendix D: Effective theory with bursts

The effective theory as given in the main text, Eqs. 45, 47, 48, 49, can be straightforwardly generalized to the burst scenario if the bursts are well-separated as described in the main text: The particles of the i-th burst are provided to

the system only once all binding reactions of the previous $i-1$-th burst have taken place and no more reactions are possible.

For b bursts in total, the dynamics of the i-th burst is then determined by the original dynamics as given in the main text, 45, 47, 48, 49, except for two small modifications.
First, the influx of active particles into the monomer states $\mu \in \{\mathrm{n}, \times, \mathrm{b}\}$ due to the activation process is modified by

$$\alpha N e^{-\alpha t} P_\mu \longrightarrow \alpha \frac{N}{b}\, e^{-\alpha\left(t - t_{i-1}^{\mathrm{final}}\right)} P_\mu \tag{D1}$$

for all $t \in [t_{i-1}^{\mathrm{final}}, t_i^{\mathrm{final}}]$ where t_i^{final} denotes the time after which all reactions after the i-th burst have taken place (and $t_0^{\mathrm{final}} = 0$ by convention). This is just due to the fact that in each burst not N but N/b particles are provided. Furthermore, at $t = t_{i-1}^{\mathrm{final}}$ the number of inactive particles is increased to N again and a new round of activation starts.
Second, one has to rescale the time and the number of particles in σ_0 with respect to the formula Eq. 15 given in the main text:

$$\sigma_0^2 = N\left(1 - e^{-\alpha t}\right) e^{-\alpha t} \longrightarrow \frac{N}{b}\left(1 - e^{-\alpha\left(t - t_{i-1}^{\mathrm{final}}\right)}\right) e^{-\alpha\left(t - t_{i-1}^{\mathrm{final}}\right)}. \tag{D2}$$

Again, this is due to the fact that at $t = t_{i-1}^{\mathrm{final}}$, there is no variability between the species because exactly N/b particles per species per preceding burst have been provided. Furthermore, per burst there are only N/b (instead of N) particles per species, so the Binomial distribution is with respect to N/b (and not N as before). As a result, over time the maximal standard deviation is given by $\sqrt{N/b}/2$ for b bursts instead of $\sqrt{N}/2$ for only one burst (see also Fig. 5(a)).

The full dynamics is then obtained by a piecewise integration of this dynamics where the initial configuration of the i-th burst is given by the final configuration of the $i-1$-th burst (and by convention the initial configuration of the 1st burst corresponds to the original configuration of the system: all particles are inactive).

Appendix E: Random bursts (limit $\alpha \to 0$)

In the main text, we restricted our discussion to the case of deterministic bursts with exactly N/b particles per species per burst (where b denotes the number of bursts). Here, we will touch upon some features of random bursts where the numbers of particles per species per burst are drawn independently from a random distribution. We will focus on three types of distributions: Poisson, Gaussian and Binomial statistics. As in the main text, we will restrict our discussion to the case where the bursts are well-separated in time, meaning that particles of the i-th burst are only provided once all binding reactions between the particles of the previous bursts have taken place. Furthermore, we consider the limit $\alpha \to 0$, i.e. the limit where particles are provided one after the other with all possible binding reactions taking place in between. In this limit, only the ordering of particles matters.

The yield is determined as the number of particles in the target structures relative to the total number N_{tot} of particles (of all species) provided to the system:

$$Y = \frac{L N_{\mathrm{target}}}{N_{\mathrm{tot}}}\,. \tag{E1}$$

In the case of a deterministic number of particles, the total number is $N_{\mathrm{tot}} = NS$ and we recover the definition of the yield as given in the main text.

1. Poisson bursts: no advantage due to several bursts

In this subsection, we illustrate that for bursts for which the particles per species and per burst are drawn independently from a Poisson distribution with parameter (mean) N/b per species per burst, the number of bursts does not have any influence in the limit $\alpha \to 0$.

In Figure 11 the average yield (and its standard deviation) is shown for systems with b bursts for which the number of particles per species per burst is drawn independently from a Poisson distribution with mean N_0/b. We observe that in this case the yield is independent of the number b of bursts, in contrast to the case of deterministic bursts discussed in the main text; Fig. 5(b)).

In more mathematical terms, this can be understood as follows: Suppose there are two species V and W whose numbers of particles are independently Poisson distributed with mean $\bar{V}$ and $\bar{W}$, respectively. Then the distribution

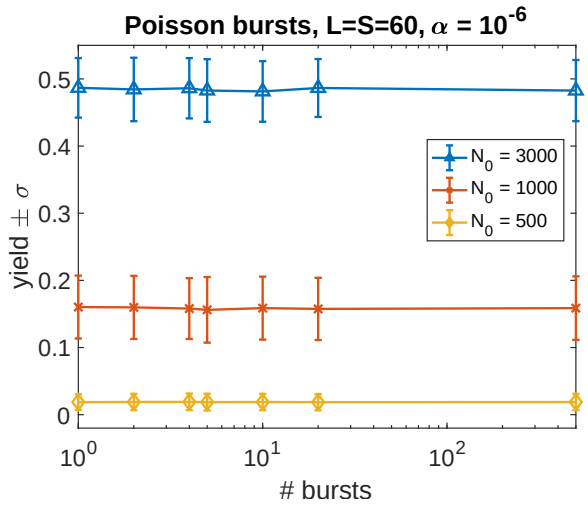

FIG. 11. **Different numbers of bursts with Poisson distributed numbers of particles.** Particles are provided in b bursts for which the number of particles per species per burst is each drawn independently according to a Poisson distribution with mean N_0/b.The average yield and its standard deviation (averaged over 1000 samples each) is plotted against the number of bursts for different values of N_0: $N_0 = 3000$ (blue triangles), $N_0 = 1000$ (red crosses), $N_0 = 3000$ (yellow diamonds). The other parameters are $L = S = 60$, $\mu = \nu = 1$, $\nu_{\text{def}} = 0$ and $\alpha = 10^{-6}$.

of the number v of particles of species V conditioned on the total number of particles of species V and W being $v + w = z$ is given as Binomial distribution with sample size z and probability $\bar{V}/(\bar{V} + \bar{W})$:

$$\text{Prob}(V = v|V + W = z) = \frac{\text{Prob}(V = v, V + W = z)}{\text{Prob}(V + W = z)} = \frac{\text{Prob}(V = v, W = z - v)}{\text{Prob}(V + W = z)} = \frac{\text{Prob}(V = v)\text{Prob}(W = z - v)}{\text{Prob}(V + W = z)} =$$
$$= \frac{\frac{\bar{V}^v}{v!}e^{-\bar{V}}\ \frac{\bar{W}^{z-v}}{(z-v)!}e^{-\bar{W}}}{\frac{(\bar{V}+\bar{W})^z}{z!}e^{-\bar{V}-\bar{W}}} = \binom{z}{v}\left(\frac{\bar{V}}{\bar{V}+\bar{W}}\right)^v\left(\frac{\bar{W}}{\bar{V}+\bar{W}}\right)^{z-v}, \tag{E2}$$

where the third equation is due to the independence of V and W. Furthermore, since the sum of independent Poisson distributions is again a Poisson distribution with the summed average, $V + W$ is Poisson distributed with mean $\bar{V} + \bar{W}$. Equation E2 shows that the distribution of the number v of particles of species V conditioned on the total number of particles of species V and W being $v + w = z$ only depends on the ratio of the averages of the two Poisson distributions but not on their absolute values.

This argument can be transferred to the self-assembly process with Poisson distributed bursts. The total number of particles of each species up to burst i is Poisson distributed since the individual numbers of particles per burst are Poisson distributed as well. For all these Poisson distributions, the ratio between the mean of the number of particles of one species and the mean of the number of particles of all the $S-1$ other species is always $1/(S-1)$ (or in terms of $\bar{V}/(\bar{V} + \bar{W}) = 1/S$), irrespective of how many bursts are used and in which burst the system currently is. So, the single-species variance after $\bar{A}$ activation events (or $S\bar{A}$ total activation events) is given by

$$\sigma^2_{\text{Poisson}} = S\bar{A}\frac{1}{S}\left(1 - \frac{1}{S}\right) \approx \bar{A}, \tag{E3}$$

irrespective of the number of bursts. Taken together, this (non-rigorous) argument underpins that in the case of Poisson bursts, the variances in the relative availabilities of the different species is independent of the number of bursts. Furthermore, Equation E3 suggests that, in contrast to the deterministic case where the number of particles per species (per burst) is fixed, the variance increases linearly with the number of activation events and does not decrease again.

2. Gaussian and Binomial bursts

So far, we have considered two cases: deterministic bursts (with zero variability or zero Fano factor, $F_{\text{d}} = 0$) and Poisson bursts (with Fano factor, $F_{\text{Poisson}} = 1$). This raises the question how the yield depends, more generally, on

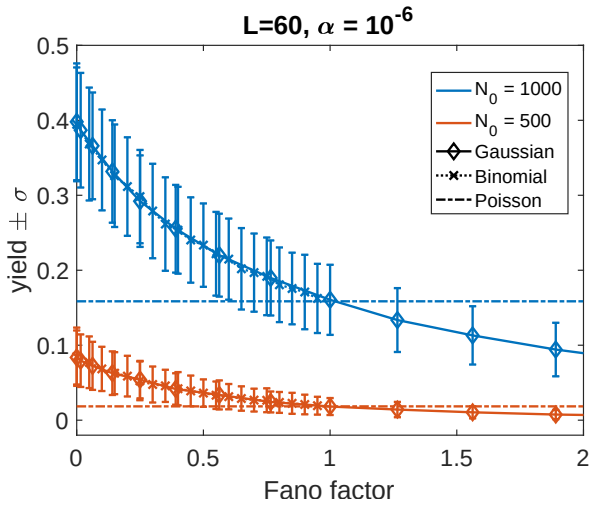

FIG. 12. **Single random burst with different distributions.** The yield and its standard deviation (averaged over 1000 samples each) for systems with one single burst for which the number of particles per species is drawn according to different distributions is plotted against the Fano factor of the respective distribution. In the Gaussian (Binomial) burst, the number of each species is drawn independently according to a Gaussian (Binomial) distribution with mean $N_0 = 1000$ (blue; Gaussian: diamonds; Binomial: crosses) or $N_0 = 500$ (red; Gaussian: diamonds; Binomial: crosses) and Fano factor $F = \sigma^2/N_0$. In the Poisson burst, the number of each species is drawn according to a Poisson distribution with mean N_0. In this case, the Fano factor is always 1. For better comparison, we nonetheless plot the corresponding average value of the yield (dotted-dashed line) as a function of the "Fano factor" although the Fano factor does not change. The other parameters are $L = S = 60$, $\mu = \nu = 1$, $\nu_{\text{def}} = 0$ and $\alpha = 10^{-6}$.

the Fano factor which is defined as the ratio between the variance $\sigma^2(X)$ and the mean $\langle X\rangle$ of a random variable X:

$$F(X) = \frac{\sigma^2(X)}{\langle X\rangle}.$$

Since the Fano factor for a Poisson distribution is always 1, we consider two other distributions to address this question: a Binomial distribution and a Gaussian distribution. More concretely, we performed simulations for well-separated bursts for which the number of particles per species per burst is drawn independently from a Binomial or Gaussian distribution, respectively. In the case of b bursts, the mean is taken to be N_0/b per burst per species. Furthermore, the variance per burst per species is chosen as $\sigma^2 = FN_0/b$, so the Fano factor is F. These expressions for the mean and the variance directly define the Gaussian distribution. For the Binomial distributions, the mean and variance translate into a probability p and a sample size N_S as follows:

$$N_S p \stackrel{!}{=} \frac{N_0}{b} \quad \text{and} \quad N_s p(1-p) \stackrel{!}{=} F\frac{N_0}{b} \implies p = 1 - F \quad \text{and} \quad N_S = \frac{N_0}{b(1-F)}. \tag{E4}$$

Correspondingly, the Binomial distribution can only be defined for a Fano factor $F < 1$.

a. Single random burst

We consider a system with $b = 1$ burst first. Figure 12 shows how the yield depends on the Fano factor F for a single burst for which the number of particles per species is drawn independently from a Gaussian or Binomial distribution with mean N_0 and Fano factor F. For comparison, we also show the average yield of a single Poisson burst with mean N_0. In this case, the Fano factor is always $F = 1$ and we only plot it as a line for better comparison. As expected, the yield is smaller for higher Fano factor or larger variance σ^2. Furthermore, it does not depend on whether the burst is drawn from a Gaussian or Binomial distribution since these two distributions align for large enough sample size: The curves for the two cases lie on top of each other (note, though, that the Binomial distribution is only defined for Fano factors $F < 1$; see Eq. E4). At a Fano factor $F = 1$, these curves cross the average yield for the corresponding Poisson distribution which also exhibits a Fano factor of 1. Taken together, this suggests that even a single burst with "controlled variance" (Fano factor $F < 1$) improves the yield as compared to a system where the particles are provided according to a Poisson process.

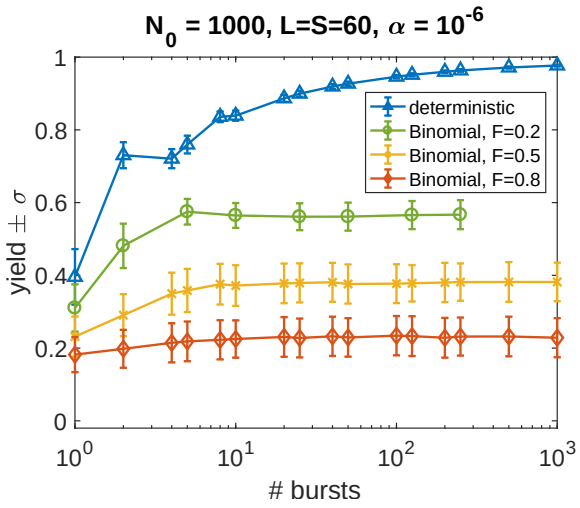

FIG. 13. **Different numbers of bursts with binomially distributed numbers of particles.** The yield and its standard deviation (averaged over 1000 samples each) for systems with b bursts for which the numbers of particles per species per burst are drawn independently from a Binomial distribution with mean $N_0/b = 1000/b$ and Fano factor $F = 0.2$ (green circles), $F = 0.5$ (yellow crosses) and $F = 0.8$ (red diamonds) is plotted against the number of bursts b. For comparison, we also show the yield and its standard deviation (averaged over 1000 samples each) for "deterministic" bursts with exactly N_0/b particles per species per burst. The other parameters are $L = S = 60$, $\mu = \nu = 1$, $\nu_{\text{def}} = 0$ and $\alpha = 10^{-6}$. Note that for a Fano factor $F = 0.2$ the maximal number of bursts that ensures that the sample size N_S of the binomial distribution (see Eq. E4) is an integer value is $b_{\max} = 250$.

b. *Several bursts*

As discussed in the main text, a higher number of bursts improves assembly efficiency if the number of particles per species per burst is deterministic (and equal for all species; compare Fig. 5(a,b)). How does this change if the number of particles per burst is drawn according to a distribution with non-zero variance? To address this question, we considered the case where the number of particles per species is drawn independently according to a Binomial distribution with mean N_0/b per burst (for b bursts) and Fano factor F. We restrict our discussion to the case of the Binomial distribution: For large numbers of bursts the number of particles per species per burst is small and then one has to be careful to use a Gaussian distributions due to two reasons:
First, a Gaussian distribution can, in principle, generate negative values. Second, and more importantly, we would have to convert the continuous Gaussian distribution into a discrete distribution (since the number of particles of each species should be a natural number). For small averages, this conversion would lead to artefacts.

Fig. 13 shows how the yield depends on the number of bursts if the number of particles per species per burst is drawn independently from a Binomial distribution with mean $N_0 = 1000$ and Fano factor as indicated in the legend. In the deterministic case $F = 0$, the yield increases considerably with the number of bursts (apart from the kink). For larger values of the Fano factor, this increase is less pronounced but still present. Note, however, that the Binomial distribution only allows for Fano factors $F < 1$ (see Eq. E4).

Taken together, this suggests that as long as the bursts are "deterministic enough", i.e. exhibit a small Fano factor, yield indeed increases for larger numbers of bursts.

Appendix F: Random non-homogeneous activation rates

As discussed in the main text, non-homogeneous activation rates can considerably increase the yield (compare Fig. 6(a,b)) if they favor a specific assembly path. In this section, we briefly illustrate that a system with non-homogeneous activation rates that are randomly distributed over the species generally strongly decreases the assembly efficiency.

We consider two scenarios.
In the first case, the activation rate of species i is determined by

$$\alpha^{(i)} = \alpha_0(1 + \epsilon U_{[0,1)})$$

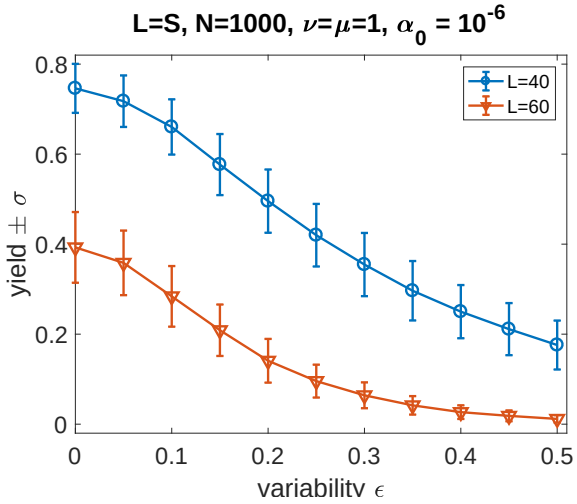

FIG. 14. **Random inhomogeneous activation rates with uniformly distributed variability.** The average yield and its standard deviation (for a sample of size 1000 each) is plotted against the variability ϵ in the activation rate. The activation rate of species i is given by $\alpha^{(i)} = \alpha_0(1 + \epsilon U_{[0,1)})$ where $U_{[0,1)}$ is uniformly distributed between $[0, 1)$ and is chosen independently for all species and all samples. The parameters are $L = 40$ (blue circles) or $L = 60$ (red triangles) and $S = L$, $N = 1000$, $\alpha_0 = 10^{-6}$, $\mu = \nu = 1$

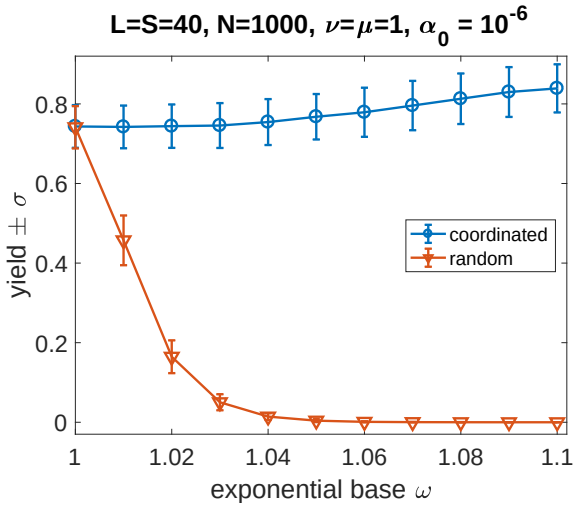

FIG. 15. **Random inhomogeneous activation rates with exponentially faster species.** The average yield and its standard deviation (for a sample of size 1000 each; red triangles) are plotted against the exponential base w. The activation rate of species i is given by $\alpha^{(i)} = \alpha_0 f(\text{perm}(i))$ where perm creates a random permutation of the species $1, 2, \ldots, S$, independently for all samples. f is the scaling function that was also chosen for the case with coordinated inhomogeneous activation rates as described in the main text: $f(i) = w^i$ for $i \leq S/2$ and $f(i) = w^{S-i}$ for $i > S/2$. For comparison, the coordinated case without permutation, perm $\equiv$ identity, is also shown (blue circles). The parameters are $L = S = 40$, $N = 1000$, $\alpha_0 = 10^{-6}$, $\mu = \nu = 1$.

where $U_{[0,1)}$ is uniformly distributed between $[0, 1)$ and is chosen independently for all species and all samples. ϵ controls the typical variability between two species.

Figure 14 shows how the yield depends on the variability ϵ. For larger variability between the species, the average yield decreases. This is expected as higher variability generally leads to larger fluctuations in the availability of the different species and, thus, to stronger stochastic effects that suppress the yield.

In the second case, we taken the same functional form as in the main text (exponential) only that these activation rates are not coordinated among the species to yield a favored assembly path but instead are randomly distributed among the different species. That is, the activation rate of species i is given by

$$\alpha^{(i)} = \alpha_0 f\left(\mathrm{perm}(i)\right)$$

where f is the scaling function that was also chosen for the case with coordinated inhomogeneous activation rates as described in the main text: $f(i) = w^i$ for $i \leq S/2$ and $f(i) = w^{S-i}$ for $i > S/2$. However, in contrast to the situation in the main text, perm now creates a random permutation of the species $1, 2, \ldots, S$, independently for all samples.

Fig. 14 shows how the yield depends on the exponential base w. Since in this case the variability between species is extremely large (due to the exponential functional form of the scaling function f), the yield strongly decreases with w and is zero already for $w \approx 1.05$. For comparison, we show again the dependency of the yield on w if the inhomogeneous activated rates are coordinated as described in the main text: perm $\equiv$ identity. Due to the small range of w shown, the yield only slightly increases.

[1] George M Whitesides and Bartosz Grzybowski, "Self-assembly at all scales," Science **295**, 2418–2421 (2002).
[2] Stephen Whitelam and Robert L Jack, "The statistical mechanics of dynamic pathways to self-assembly," Annual review of physical chemistry **66**, 143–163 (2015).
[3] Marc Kirschner and Tim Mitchison, "Beyond self-assembly: From microtubules to morphogenesis," Cell **45**, 329–342 (1986).
[4] Eva Nogales and Hong Wei Wang, "Structural intermediates in microtubule assembly and disassembly: How and why?" Current Opinion in Cell Biology **18**, 179–184 (2006).
[5] Johanna Roostalu and Thomas Surrey, "Microtubule nucleation: Beyond the template," Nature Reviews Molecular Cell Biology **18**, 702–710 (2017).
[6] Dieter Kressler, Ed Hurt, and Jochen Baßler, "Driving ribosome assembly," Biochimica et Biophysica Acta - Molecular Cell Research **1803**, 673–683 (2010).
[7] Alessandro Fatica and David Tollervey, "Making ribosomes," Current Opinion in Cell Biology **14**, 313–318 (2002).
[8] Howard C. Berg, "The Rotary Motor of Bacterial Flagella," Annual Review of Biochemistry **72**, 19–54 (2003).
[9] Tohru Minamino and Katsumi Imada, "The bacterial flagellar motor and its structural diversity," Trends in Microbiology **23**, 267–274 (2015).
[10] Adam Zlotnick, Jennifer M Johnson, Paul W Wingfield, Stephen J Stahl, and Dan Endres, "A theoretical model successfully identifies features of hepatitis b virus capsid assembly," Biochemistry **38**, 14644–14652 (1999).
[11] Adam Zlotnick, "Are weak protein–protein interactions the general rule in capsid assembly?" Virology **315**, 269–274 (2003).
[12] Michael F Hagan, "Modeling viral capsid assembly," Advances in chemical physics **155**, 1 (2014).
[13] Zorana Zeravcic, Vinothan N Manoharan, and Michael P Brenner, "Colloquium: Toward living matter with colloidal particles," Reviews of Modern Physics **89**, 031001 (2017).
[14] Thomas CT Michaels, Lucie X Liu, Samo Curk, Peter G Bolhuis, Andela Saric, and Tuomas PJ Knowles, "Reaction rate theory for supramolecular kinetics: application to protein aggregation," arXiv preprint arXiv:1803.04851 (2018).
[15] Samuel I.A. Cohen, Risto Cukalevski, Thomas C.T. Michaels, A. Šarić, Mattias Törnquist, Michele Vendruscolo, Christopher M. Dobson, Alexander K. Buell, Tuomas P.J. Knowles, and Sara Linse, "Distinct thermodynamic signatures of oligomer generation in the aggregation of the amyloid-β peptide," Nature Chemistry **10**, 523–531 (2018).
[16] Michael F Hagan, Oren M Elrad, and Robert L Jack, "Mechanisms of kinetic trapping in self-assembly and phase transformation," The Journal of chemical physics **135**, 104115 (2011).
[17] Arvind Murugan, James Zou, and Michael P Brenner, "Undesired usage and the robust self-assembly of heterogeneous structures," Nature Communications **6**, 6203 (2015).
[18] PWK Rothemund, Nature **440**, 297 (2006).
[19] Klaus F Wagenbauer, Christian Sigl, and Hendrik Dietz, "Gigadalton-scale shape-programmable dna assemblies," Nature **552**, 78–83 (2017).
[20] Yonggang Ke, Luvena L Ong, William M Shih, and Peng Yin, "Three-dimensional structures self-assembled from dna bricks," Science **338**, 1177–1183 (2012).
[21] Bryan Wei, Mingjie Dai, and Peng Yin, "Complex shapes self-assembled from single-stranded dna tiles," Nature **485**, 623 (2013).
[22] Shuguang Zhang, "Fabrication of novel biomaterials through molecular self-assembly," Nature Biotechnology **21**, 1171–1178 (2003).
[23] ES Andersen, M Dong, MM Nielsen, K Jahn, R Subramani, and XXX, "Self-assembly of a nanoscale dna box with a controllable lid," Nature **459**, 73–76 (2009).
[24] MP Valignat, O Theodoly, JC Crocker, WB Russel, and PM Chaikin, "Reversible self-assembly and directed assembly of dna-linked micrometer-sized colloids," Proceedings of the National Academy of Sciences **102**, 4225–29 (2005).
[25] Adam Zlotnick, Ryan Aldrich, Jennifer M Johnson, Pablo Ceres, and Mark J Young, "Mechanism of capsid assembly for an icosahedral plant virus," Virology **277**, 450–456 (2000).
[26] Masanori Nakagawa, Shumpei Kai, Tatsuo Kojima, and Shuichi Hiraoka, "Energy-landscape-independent kinetic trap of an incomplete cage in the self-assembly of a pd2l4 cage," Chemistry–A European Journal **24**, 8804–8808 (2018).
[27] Benedict EK Snodin, Flavio Romano, Lorenzo Rovigatti, Thomas E Ouldridge, Ard A Louis, and Jonathan PK Doye, "Direct simulation of the self-assembly of a small dna origami," ACS nano **10**, 1724–1737 (2016).
[28] Hannah K Wayment-Steele, Daan Frenkel, and Aleks Reinhardt, "Investigating the role of boundary bricks in dna brick self-assembly," Soft Matter **13**, 1670–1680 (2017).
[29] George M. Whitesides and Mila Boncheva, "Beyond molecules: Self-assembly of mesoscopic and macroscopic components," Proceedings of the National Academy of Sciences of the United States of America **99**, 4769–4774 (2002).
[30] Michael F. Hagan and David Chandler, "Dynamic pathways for viral capsid assembly," Biophysical Journal **91**, 42–54 (2006), arXiv:0511006 [q-bio].
[31] Adam Zlotnick, "Distinguishing reversible from irreversible virus capsid assembly," Journal of molecular biology **366**, 14–18 (2007).
[32] Robert L. Jack, Michael F. Hagan, and David Chandler, "Fluctuation-dissipation ratios in the dynamics of self-assembly," Physical Review E - Statistical, Nonlinear, and Soft Matter Physics **76**, 1–8 (2007).
[33] Hung D. Nguyen, Vijay S. Reddy, and Charles L. Brooks, "Deciphering the kinetic mechanism of spontaneous self-assembly of icosahedral capsids," Nano Letters **7**, 338–344 (2007).

[34] D. C. Rapaport, "Role of reversibility in viral capsid growth: A paradigm for self-assembly," Physical Review Letters **101**, 1–4 (2008), arXiv:0803.0115.

[35] Sushmita Singh and Adam Zlotnick, "Observed hysteresis of virus capsid disassembly is implicit in kinetic models of assembly," Journal of Biological Chemistry **278**, 18249–18255 (2003).

[36] Alexander Yu Morozov, Robijn F Bruinsma, and Joseph Rudnick, "Assembly of viruses and the pseudo-law of mass action," The Journal of chemical physics **131**, 10B607 (2009).

[37] D. L. Caspar, "Movement and self-control in protein assemblies. Quasi-equivalence revisited," Biophysical Journal **32**, 103–138 (1980).

[38] C. Packianathan, S. P. Katen, C. E. Dann, and A. Zlotnick, "Conformational Changes in the Hepatitis B Virus Core Protein Are Consistent with a Role for Allostery in Virus Assembly," Journal of Virology **84**, 1607–1615 (2010).

[39] Guillermo R Lazaro and Michael F Hagan, "Allosteric control of icosahedral capsid assembly," The Journal of Physical Chemistry B **120**, 6306–6318 (2016).

[40] FRANK Birnbaum and MICHAEL Nassal, "Hepatitis b virus nucleocapsid assembly: primary structure requirements in the core protein." Journal of virology **64**, 3319–3330 (1990).

[41] M. C. Johnson, H. M. Scobie, Y. M. Ma, and V. M. Vogt, "Nucleic Acid-Independent Retrovirus Assembly Can Be Driven by Dimerization," Journal of Virology **76**, 11177–11185 (2002).

[42] Yu May Ma and Volker M Vogt, "Rous sarcoma virus gag protein-oligonucleotide interaction suggests a critical role for protein dimer formation in assembly," Journal of virology **76**, 5452–5462 (2002).

[43] Siddhartha AK Datta, Zhuojun Zhao, Patrick K Clark, Sergey Tarasov, Jerry N Alexandratos, Stephen J Campbell, Mamuka Kvaratskhelia, Jacob Lebowitz, and Alan Rein, "Interactions between hiv-1 gag molecules in solution: an inositol phosphate-mediated switch," Journal of molecular biology **365**, 799–811 (2007).

[44] Aleks Reinhardt and Daan Frenkel, "Numerical evidence for nucleated self-assembly of dna brick structures," Phys. Rev. Lett. **112**, 238103 (2014).

[45] William M Jacobs, Aleks Reinhardt, and Daan Frenkel, "Rational design of self-assembly pathways for complex multicomponent structures," Proceedings of the National Academy of Sciences **112**, 6313–6318 (2015).

[46] Florian M Gartner, Isabella R Graf, Patrick Wilke, Philipp M Geiger, and Erwin Frey, "Stochastic yield catastrophes and robustness in self-assembly," arXiv preprint arXiv:1905.09912 (2019).

[47] "A model should be as simple as it can be but no simpler", *Albert Einstein*.

[48] Florian M. Gartner, Isabella R. Graf, and Erwin Frey, "Controlling fidelity and time-efficiency in self-assembly," (2019).

[49] Chao Chen, C Cheng Kao, and Bogdan Dragnea, "Self-assembly of brome mosaic virus capsids: insights from shorter time-scale experiments," The Journal of Physical Chemistry A **112**, 9405–9412 (2008).

[50] Thomas K Haxton and Stephen Whitelam, "Do hierarchical structures assemble best via hierarchical pathways?" Soft Matter **9**, 6851–6861 (2013).

[51] Michael F Hagan and Oren M Elrad, "Understanding the concentration dependence of viral capsid assembly kinetics?the origin of the lag time and identifying the critical nucleus size," Biophysical journal **98**, 1065–1074 (2010).

[52] Daniel T Gillespie, "A general method for numerically simulating the stochastic time evolution of coupled chemical reactions," Journal of Computational Physics **22**, 403–434 (1976).

[53] Christian Kuehn, "Moment closure—a brief review," in *Control of Self-Organizing Nonlinear Systems*, edited by Eckehard Schöll, Sabine H. L. Klapp, and Philipp Hövel (Springer International Publishing, Cham, 2016) pp. 253–271.

[54] There are $(L+1)\times S$ different types of active and inactive monomers and structures of size $l \in \{2,\dots,L\}$ if $\nu_{def}=0$. If $\nu_{def}>0$ and one only distinguishes between defective and non-defective structures, this number roughly doubles.

[55] John A Rice, *Mathematical statistics and data analysis* (Cengage Learning, 3rd edition, 2006).

[56] Note that one could also argue that each additionally (less) activated particle of each neighboring species $i\pm1$ reduces (augments) this number by $1/2$, splitting its effect between species i and $i\pm2$. The qualitative results are the same in both cases.

[57] Whether different species are unavailable for binding is, of course, not entirely independent. For instance, an excess activation of one species will make it more likely for both neighboring species to be unavailable for binding. Conversely, however, if one species is unavailable, the neighboring species is less likely to be unavailable as well. Taken together, an independence assumption might be reasonable.

[58] Note that in this derivation, we neglect that if $L/S>1$ the segments along the ring are correlated due to the periodic design of the structures.

[59] In this argument, we neglect that the different species are not all equally available at all times. However, as we have seen before, the relative deviation is only of the order $1/\sqrt{N}$ and, thus, not expected to be crucial in this step.

[60] In more technical terms, the probability for structures in the simplified assembly process to have two growing ends (Fig. 3(f)), i.e. two ends to which an available species binds, is quite low for $L_\times \geq 2$ and large structure sizes. So, most larger structures in the growing state actually bind an unavailable species on one end and an available one on the other end; see also Eq. B1 for an expression of the steady-state occupancies of the states with two or one growing end, respectively.

[61] Also $0<w<1$ would improve the yield as it would only reverse the order of activation and the corresponding assembly path compared to $w>1$.

[62] Of course, fluctuations should be minimized with respect to the stoichiometrically given concentration ratios. If a species occurs twice as many times in the final structure, it should also be available twice as many times.

[63] Robin Pemantle, "A survey of random processes with reinforcement," Probability Surveys **4**, 1–79 (2007).

[64] Adam Zlotnick and Suchetana Mukhopadhyay, "Virus assembly, allostery and antivirals," Trends in Microbiology **19**,

14–23 (2011).
[65] Eviatar Natan, Jonathan N. Wells, Sarah A. Teichmann, and Joseph A. Marsh, "Regulation, evolution and consequences of cotranslational protein complex assembly," Current Opinion in Structural Biology **42**, 90–97 (2017).
[66] Jaimie Marie Stewart and Elisa Franco, "Self-assembly of large RNA structures: learning from DNA nanotechnology," DNA and RNA Nanotechnology **2**, 23–35 (2015).
[67] Camille J Delebecque, Ariel B Lindner, Pamela A Silver, and Faisal A Aldaye, "Organization of Intracellular Reactions with Rationally Designed RNA Assemblies," Science **333**, 470–474 (2011).
[68] Florian Praetorius, Benjamin Kick, Karl L. Behler, Maximilian N. Honemann, Dirk Weuster-Botz, and Hendrik Dietz, "Biotechnological mass production of DNA origami," Nature **552**, 84–87 (2017).
[69] Mo Li, Mengxi Zheng, Siyu Wu, Cheng Tian, Di Liu, Yossi Weizmann, Wen Jiang, Guansong Wang, and Chengde Mao, "In vivo production of RNA nanostructures via programmed folding of single-stranded RNAs," Nature Communications **9**, 2196 (2018).

9 Summary and discussion

In summary, the goal of this second part of my thesis was to elucidate what role fluctuations play for the self-assembly of heterogeneous structures made up from different species of particles. For this purpose, we considered a conceptual model for an irreversible self-assembly process into several identical, well-defined target structures. We found that stochastic effects can strongly suppress assembly efficiency if there is demographic noise in the availability of the species. In the model this demographic noise is due to an activation step: Particles need to be activated before they are able to bind to other particles. In a deterministic description of the system in terms of mean-field equations, such an additional activation process is beneficial for the assembly performance and the yield is perfect if activation occurs slow enough. However, in a stochastic system a slow activation step introduces fluctuations in the availability of the different species, which can ultimately lead to a strong decrease of assembly efficiency.

Similar fluctuations might also arise from diffusion of particles in space or from a gradual production of the building blocks through gene expression. As a result, we believe that the occurrence of these stochastic effects has important implications for the self-assembly in living organisms and for artificial self-assembly. In fact, there have been several studies in which DNA- or RNA-based artificial self-assembly processes have been combined with *in vivo* transcription and it has been suggested that co-transcriptional assembly is a promising strategy for the further development of nanotechnology (see e.g. [246–249]). Conceptually, such a co-transcriptional assembly is similar to our model with a (slow) activation step: Assembly already takes place while the building blocks are still produced. Therefore, it will be interesting to see whether such approaches – when applied to the assembly of large, heterogeneous RNA- or DNA-brick structures – will be limited by similar stochastic effects as observed in our model. In this context, it would also be enlightening to test our model predictions by DNA-origami methods (see also chapter 6). For instance, it might be possible to extend the experimental system of Ref. [126], where homogeneous ring structures are build from DNA origami, to heterogeneous rings.

Due to the simplicity of the model we considered, there are of course many aspects of self-assembly systems whose influence on the occurrence of strong stochastic effects could be explored. For instance, in a follow-up project [8], we investigated what role the topology of assembly networks has for assembly efficiency. As also intuitively expected, self-assembly systems with more freedom in the assembly sequence are generally less susceptible to demographic noise because the order in which particles are made available is less important. Furthermore, this study suggests that hierarchical assembly schemes may be a way to avoid stochastic effects. The reason is that in a hierarchical assembly process, the individual assembly hierarchies involve fewer different building blocks and are thus less prone to fluctuations in the availability of different species. This aspect might add another interesting point to the

current discussion of whether or not hierarchical assembly is a promising strategy to increase the assembly efficiency of heterogeneous structures (see also chapter 6).

Conclusion and outlook

Science cannot solve the ultimate mystery of nature. And that is because, in the last analysis, we ourselves are a part of the mystery that we are trying to solve.
(Max Planck)

A friend of mine recently asked me how I was doing and whether or not I would like the process of thesis writing since it may be stressful but it might also be a nice opportunity to reflect on the work that one did during the last years. I think she hit the nail on the head. For me personally, the process of writing this thesis was definitely stressful: The time to write felt too short and there are many things that I would still have liked to improve, check or try out. Nonetheless, it has also been a good opportunity for me to think about how I see myself as a scientist.
In particular, I realized that I have a strange relation to details. On the one hand, I certainly have a cognitive bias towards a conceptual reasoning: I am not naturally drawn to remembering names (of historical figures, proteins, equations) or details (such as people's faces). This is definitely reflected in my thesis. Irrespective of whether our original motivation came from microtubules or actin filaments, they were coarse-grained as straight, hard rods with perfect alignment and without any defects. Similarly, the self-assembly model we considered is – in a sense – as simple as it gets: rings with maximal internal symmetries (or at most squares) and numerically numbered species, sometimes with defects.
On the other hand, what drives me to do science is the curiosity to understand – in as much (technical) detail as possible – why things happen. At least for me, such a detailed understanding is only feasible if I reduce the complex world around me to conceptual questions. Correspondingly, while it is difficult to summarize the different topics covered in this thesis in one single question, they can be united in terms of one framework: All are based on conceptual approaches that focus on one (or maybe few) particular aspects of the problem, and in each case, we tried to elucidate principles that may also be relevant for more elaborate models.

From my point of view this conceptual approach has two advantages: Firstly, it allows us to really understand what is going on. Secondly, the uncovered principles are certainly interesting in their own right and might one day prove relevant for systems of which we could never have thought of.
Then again, it is not always obvious whether the principles are indeed relevant for the intricate living systems or technological applications we aimed to describe in the first place: They might still apply, but they might just not be crucial for the complex system.
In my mind, it is exactly the challenge of theoretical biophysics to ask what the right level of description is for the specific (complex) system and to determine what is important for the question under consideration.

In the end, the way to find this out is to collaborate with experimentalists or, at least, to suggest specific experiments in which the proposed theoretical principles can be tested. If I were to redo my PhD, the one thing I would change was to pursue such collaborations more rigorously. And thanks to the technological advancements in synthetic biology and bottom-up systems, I am sure that the ability to actually do experiments that test our predictions is – at least to a large extent – already present.
I believe the closest we got to this goal is in the project about filament networks (chapter 4), where we implemented a specific *in silico* study which was designed to mimic recent *in vitro* experiments and which makes specific predictions for such experimental systems. But looking back, the other models could, in principle, also be tested experimentally: For the models about motor transport along filaments (chapters 2 and 3), it might be feasible to use microfluidics technology [17–19], and for the projects on self-assembly (chapters 7 and 8), DNA-origami or DNA-brick based methods [28, 112–115, 127, 232, 233] could be applied.
Indeed, I believe experimentalists in both of these fields also show great interest to test conceptual ideas and to pursue proof-of-principle studies.

In conclusion, I would be very happy to see at least some of the principles of self-assembly and self-organization that were formulated in this thesis to be tested in experiments. I am convinced that in order to formulate such principles it is important to start from conceptual models and to extend them step by step. The models and principles presented here may provide a good starting point for more elaborate systems.

Bibliography

[1] IR Graf and E Frey. *Generic Transport Mechanisms for Molecular Traffic in Cellular Protrusions.* In: **Physical Review Letters** 118.12 (2017), p. 128101. DOI: 10.1103/PhysRevLett.118.128101 (cit. on pp. i, 13, 14, 16–18).

[2] M Bojer, IR Graf, and E Frey. *Self-organized system-size oscillation of a stochastic lattice-gas model.* In: **Physical Review E** 98.1 (2018), p. 012410. DOI: 10.1103/PhysRevE.98.012410 (cit. on pp. i, 9, 14, 41–46).

[3] M Striebel, IR Graf, and E Frey. *A mechanistic view of collective filament motion in active nematic networks.* In: **Biophysical Journal** 118.2 (2020), pp. 313–324. DOI: 10.1016/j.bpj.2019.11.3387 (cit. on pp. i, 7, 67, 69–73).

[4] FM Gartner et al. *Stochastic yield catastrophes and robustness in self-assembly.* In: **eLife** 9.e51020 (2020), pp. 1–37. DOI: 10.7554/elife.51020 (cit. on pp. i, xvi, 123, 124).

[5] IR Graf, FM Gartner, and E Frey. *Understanding and guiding robust self-assembly of heterogeneous structures.* In preparation (2020) (cit. on p. i).

[6] M Bauer et al. *Exploiting ecology in drug pulse sequences in favour of population reduction.* In: **PLoS Computational Biology** 13.9 (2017), e1005747. DOI: 10.1371/journal.pcbi.1005747 (cit. on p. i).

[7] FM Gartner, IR Graf, and E Frey. *Controlling fidelity and time-efficiency in self-assembly.* In preparation (2020) (cit. on pp. i, xiii, xv, 174, 178).

[8] F Träuble et al. *Topological properties of self-assembly reaction networks determine robustness to stochastic effects.* In preparation (2020) (cit. on pp. i, 227).

[9] E Schrödinger. *What is life? The physical aspect of the living cell and mind.* Cambridge: Cambridge University Press, 1944 (cit. on p. iii).

[10] FS Gnesotto et al. *Broken detailed balance and non-equilibrium dynamics in living systems: A review.* In: **Reports on Progress in Physics** 81.6 (2018). DOI: 10.1088/1361-6633/aab3ed (cit. on p. iii).

[11] K Vetsigian, C Woese, and N Goldenfeld. *Collective evolution and the genetic code.* In: **Proceedings of the National Academy of Sciences** 103.28 (2006), pp. 10696–701. DOI: 10.1073/pnas.0603780103 (cit. on p. iii).

[12] TF Sherman. *On connecting large vessels to small. The meaning of Murray's law.* In: **Journal of General Physiology** 78.4 (1981), pp. 431–453. DOI: 10.1085/jgp.78.4.431 (cit. on p. iii).

[13] H Ronellenfitsch and E Katifori. *Global Optimization, Local Adaptation, and the Role of Growth in Distribution Networks.* In: **Physical Review Letters** 117.13 (2016), p. 138301. DOI: 10.1103/PhysRevLett.117.138301 (cit. on p. iii).

[14] G Tkačik and A M Walczak. *Information transmission in genetic regulatory networks: A review.* In: **Journal of Physics Condensed Matter** 23.15 (2011). DOI: 10.1088/0953-8984/23/15/153102 (cit. on p. iii).

[15] J O Dubuis et al. *Positional information, in bits.* In: **Proceedings of the National Academy of Sciences** 110.41 (2013), pp. 16301–16308. DOI: 10.1073/pnas.1315642110 (cit. on p. iii).

[16] G Tkačik and W Bialek. *Information Processing in Living Systems.* In: **Annual Review of Condensed Matter Physics** 7.1 (2016), pp. 89–117. DOI: 10.1146/annurev-conmatphys-031214-014803 (cit. on p. iii).

[17] P Gravesen, J Branebjerg, and O S Jensen. *Microfluidics-a review.* In: **Journal of micromechanics and microengineering** 3.4 (1993). DOI: 10.1088/0960-1317/3/4/002 (cit. on pp. iii, 113, 230).

[18] G Velve-Casquillas et al. *Microfluidic tools for cell biological research.* In: **Nano Today** 5.1 (2010), pp. 28–47. DOI: 10.1016/j.nantod.2009.12.001 (cit. on pp. iii, 113, 230).

[19] Y Sato and M Takinoue. *Creation of artificial cell-like structures promoted by microfluidics technologies.* In: **Micromachines** 10.4 (2019), p. 216. DOI: 10.3390/MI10040216 (cit. on pp. iii, 113, 230).

[20] F J Nédélec et al. *Self-organization of microtubules and motors.* In: **Nature** 389 (1997), pp. 305–308. DOI: doi:10.1038/38532 (cit. on pp. iii, 113).

[21] K Kinoshita et al. *Reconstitution of physiological microtubule dynamics using purified components.* In: **Science** 294.5545 (2001), pp. 1340–1343. DOI: 10.1126/science.1064629 (cit. on pp. iii, 113).

[22] A P Liu and D A Fletcher. *Biology under construction: In vitro reconstitution of cellular function.* In: **Nature Reviews Molecular Cell Biology** 10 (2009), pp. 644–650. DOI: 10.1038/nrm2746 (cit. on pp. iii, 113).

[23] M Dogterom and T Surrey. *Microtubule organization in vitro.* In: **Current Opinion in Cell Biology** 25.1 (2013), pp. 23–29. DOI: 10.1016/j.ceb.2012.12.002 (cit. on pp. iii, ix, 4, 7, 113).

[24] G M Whitesides and B Grzybowski. *Self-assembly at all scales.* In: **Science** 295.5564 (2002), pp. 2418–2421. DOI: 10.1126/science.1070821 (cit. on p. iv).

[25] S Zhang. *Fabrication of novel biomaterials through molecular self-assembly.* In: **Nature Biotechnology** 21 (2003), pp. 1171–1178. DOI: 10.1038/nbt874 (cit. on pp. iv, 117).

[26] S Whitelam and R L Jack. *The Statistical Mechanics of Dynamic Pathways to Self-Assembly.* In: **Annual Review of Physical Chemistry** 66.1 (2015), pp. 143–163. DOI: 10.1146/annurev-physchem-040214-121215 (cit. on pp. iv, 117).

[27] W M Jacobs and D Frenkel. *Self-Assembly of Structures with Addressable Complexity.* In: **Journal of the American Chemical Society** 138.8 (2016), pp. 2457–2467. DOI: 10.1021/jacs.5b11918 (cit. on pp. iv, xv, 117).

[28] Z Zeravcic, V N Manoharan, and M P Brenner. *Colloquium: Toward living matter with colloidal particles.* In: **Reviews of Modern Physics** 89.3 (2017), p. 031001. DOI: 10.1103/RevModPhys.89.031001 (cit. on pp. iv, 117, 119, 120, 230).

[29] A Fatica and D Tollervey. *Making ribosomes.* In: **Current Opinion in Cell Biology** 14.3 (2002), pp. 313–318. DOI: 10.1016/S0955-0674(02)00336-8 (cit. on pp. iv, xii, 117).

[30] D Kressler, E Hurt, and J Baßler. *Driving ribosome assembly.* In: **Biochimica et Biophysica Acta - Molecular Cell Research** 1803.6 (2010), pp. 673–683. DOI: 10.1016/j.bbamcr.2009.10.009 (cit. on pp. iv, xii, 117).

[31] H C Berg. *The Rotary Motor of Bacterial Flagella.* In: **Annual Review of Biochemistry** 72.1 (2003), pp. 19–54. DOI: 10.1146/annurev.biochem.72.121801.161737 (cit. on pp. iv, xii, 117).

[32] T Minamino and K Imada. *The bacterial flagellar motor and its structural diversity.* In: **Trends in Microbiology** 23.5 (2015), pp. 267–274. DOI: 10.1016/j.tim.2014.12.011 (cit. on pp. iv, xii, 117).

[33] D T Gillespie. *A general method for numerically simulating the stochastic time evolution of coupled chemical reactions.* In: **Journal of Computational Physics** 22.4 (1976), pp. 403–434. DOI: 10.1016/0021-9991(76)90041-3 (cit. on pp. iv, 126).

[34] L C Kapitein and C C Hoogenraad. *Which way to go? Cytoskeletal organization and polarized transport in neurons.* In: **Molecular and Cellular Neuroscience** 46.1 (2011), pp. 9–20. DOI: 10.1016/j.mcn.2010.08.015 (cit. on pp. iv, 3, 6).

[35] A B Kolomeisky. *Motor proteins and molecular motors.* CRC press, 2015, pp. 1–197. DOI: 10.1201/b18426 (cit. on pp. iv, ix, 3, 5).

[36] P M Hoffmann. *How molecular motors extract order from chaos (a key issues review).* In: **Reports on Progress in Physics** 79.3 (2016). DOI: 10.1088/0034-4885/79/3/032601 (cit. on pp. iv, 3).

[37] H Tokuo and M Ikebe. *Myosin X transports Mena/VASP to the tip of filopodia.* In: **Biochemical and Biophysical Research Communications** 319.1 (2004), pp. 214–220. DOI: 10.1016/j.bbrc.2004.04.167 (cit. on pp. iv, v).

[38] I A Belyantseva et al. *Myosin-XVa is required for tip localization of whirlin and differential elongation of hair-cell stereocilia.* In: **Nature Cell Biology** 7 (2005), pp. 148–156. DOI: 10.1038/ncb1219 (cit. on pp. iv, v, 6).

[39] R Nambiar, R E McConnell, and M J Tyska. *Myosin motor function: The ins and outs of actin-based membrane protrusions.* In: **Cellular and Molecular Life Sciences** 67.8 (2010), pp. 1239–1254. DOI: 10.1007/s00018-009-0254-5 (cit. on pp. iv, v, 6, 13).

[40] M L Kerber and R E Cheney. *Myosin-X: a MyTH-FERM myosin at the tips of filopodia.* In: **Journal of Cell Science** 124 (2011), pp. 3733–3741. DOI: 10.1242/jcs.023549 (cit. on pp. iv, v, 6).

[41] H W Lin, M E Schneider, and B Kachar. *When size matters: The dynamic regulation of stereocilia lengths.* In: **Current Opinion in Cell Biology** 17.1 (2005), pp. 55–61. DOI: 10.1016/j.ceb.2004.12.005 (cit. on pp. v, vii, 7, 8, 13).

[42] U Manor and B Kachar. *Dynamic length regulation of sensory stereocilia.* In: **Seminars in Cell and Developmental Biology** 19.6 (2008), pp. 502–510. DOI: 10.1016/j.semcdb.2008.07.006 (cit. on pp. v, vii, 5–8).

[43] P K Mattila and P Lappalainen. *Filopodia: molecular architecture and cellular functions*. In: **Nature Reviews Molecular Cell Biology** 9 (2008), pp. 446–454. DOI: 10.1038/nrm2406 (cit. on pp. v, 5–7).

[44] C T MacDonald, J H Gibbs, and A C Pipkin. *Kinetics of biopolymerization on nucleic acid templates*. In: **Biopolymers** 6 (1968), pp. 1–25. DOI: 10.1002/bip.1968.360060102 (cit. on pp. v, 8, 9).

[45] F Spitzer. *Interaction of Markov processes*. In: **Advances in Mathematics** 5.2 (1970), pp. 246–290. DOI: 10.1016/0001-8708(70)90034-4 (cit. on pp. v, 8, 9).

[46] T Chou, K Mallick, and R K Zia. *Non-equilibrium statistical mechanics: From a paradigmatic model to biological transport*. In: **Reports on Progress in Physics** 74.11 (2011). DOI: 10.1088/0034-4885/74/11/116601 (cit. on pp. v, 8, 9, 11).

[47] J Krug. *Boundary-Induced Phase Transitions in Driven Diffusive Systems*. In: **Physical Review Letters** 67.14 (1991), p. 1882. DOI: 10.1103/PhysRevLett.67.1882 (cit. on pp. v, 9–11).

[48] B Derrida, E Domany, and D Mukamel. *An exact solution of a one-dimensional asymmetric exclusion model with open boundaries*. In: **Journal of Statistical Physics** 69.3-4 (1992), pp. 667–687. DOI: 10.1007/BF01050430 (cit. on pp. v, 9–11).

[49] G Schütz and E Domany. *Phase transitions in an exactly soluble one-dimensional exclusion process*. In: **Journal of Statistical Physics** 72.1-2 (1993), pp. 277–296. DOI: 10.1007/BF01048050 (cit. on pp. v, 9–11).

[50] S A Janowsky and J L Lebowitz. *Finite-size effects and shock fluctuations in the asymmetric simple-exclusion process*. In: **Physical Review A** 45.2 (1992), p. 618. DOI: 10.1103/PhysRevA.45.618 (cit. on p. v).

[51] A B Kolomeisky et al. *Phase diagram of one-dimensional driven lattice gases with open boundaries*. In: **Journal of Physics A: Mathematical and General** 31.33 (1998), p. 6911. DOI: 10.1088/0305-4470/31/33/003 (cit. on pp. v, 9, 10, 18).

[52] L Santen and C Appert. *The Asymmetric Exclusion Process revisited: Fluctuations and Dynamics in the Domain Wall Picture*. In: **Journal of Statistical Physics** 106.1-2 (2002), pp. 187–199. DOI: 10.1023/A:1013176229983 (cit. on pp. v, 9).

[53] A Parmeggiani, T Franosch, and E Frey. *Phase Coexistence in Driven One-Dimensional Transport*. In: **Physical Review Letters** 90.8 (2003), p. 086601. DOI: 10.1103/PhysRevLett.90.086601 (cit. on pp. v, 10, 11, 15, 18).

[54] T Mignot and J W Shaevitz. *Active and passive mechanisms of intracellular transport and localization in bacteria*. In: **Current Opinion in Microbiology** 11.6 (2008), pp. 580–585. DOI: 10.1016/j.mib.2008.10.005 (cit. on p. vi).

[55] K Keren. *Cell motility: The integrating role of the plasma membrane*. In: **European Biophysics Journal** 40 (2011), p. 1013. DOI: 10.1007/s00249-011-0741-0 (cit. on p. vi).

[56] I Kaverina and A Straube. *Regulation of cell migration by dynamic microtubules*. In: **Seminars in Cell and Developmental Biology** 22.9 (2011), pp. 968–974. DOI: 10.1016/j.semcdb.2011.09.017 (cit. on p. vi).

[57] I Krämer. *Studies of totally asymmetric simple exclusion processes in different diffusive environments*. LMU Munich, Master thesis, 2015 (cit. on p. vi).

[58] ML Gupta et al. *Plus end-specific depolymerase activity of Kip3, a kinesin-8 protein, explains its role in positioning the yeast mitotic spindle.* In: **Nature Cell Biology** 8 (2006), pp. 913–923. DOI: 10.1038/ncb1457 (cit. on pp. vi, 6, 8, 41).

[59] V Varga et al. *Yeast kinesin-8 depolymerizes microtubules in a length-dependent manner.* In: **Nature Cell Biology** 8 (2006), pp. 957–962. DOI: 10.1038/ncb1462 (cit. on pp. vi, vii, 6, 8, 41).

[60] V Varga et al. *Kinesin-8 Motors Act Cooperatively to Mediate Length-Dependent Microtubule Depolymerization.* In: **Cell** 138.6 (2009), pp. 1174–1183. DOI: 10.1016/j.cell.2009.07.032 (cit. on pp. vi, vii, 8, 41).

[61] PM Grissom et al. *Kinesin-8 from Fission Yeast: A Heterodimeric, Plus-End–directed Motor that Can Couple Microtubule Depolymerization to Cargo Movement.* In: **Molecular Biology of the Cell** 20.3 (2009), pp. 963–972. DOI: 10.1091/mbc.E08-09-0979 (cit. on pp. vi, 8, 41).

[62] X Su, R Ohi, and D Pellman. *Move in for the kill: Motile microtubule regulators.* In: **Trends in Cell Biology** 22.11 (2012), pp. 567–575. DOI: 10.1016/j.tcb.2012.08.003 (cit. on pp. vi, vii, 8, 41).

[63] T Mitchison and M Kirschner. *Dynamic instability of microtubule growth.* In: **Nature** 312 (1984), pp. 237–242. DOI: 10.1038/312237a0 (cit. on pp. vi, viii, 4, 5, 7).

[64] J Howard and AA Hyman. *Growth, fluctuation and switching at microtubule plus ends.* In: **Nature Reviews Molecular Cell Biology** 10 (2009), pp. 569–574. DOI: 10.1038/nrm2713 (cit. on pp. vi, ix).

[65] JC Walter et al. *Surfing on Protein Waves: Proteophoresis as a Mechanism for Bacterial Genome Partitioning.* In: **Physical Review Letters** 119.2 (2017), p. 028101. DOI: 10.1103/PhysRevLett.119.028101 (cit. on pp. vi, viii, 46).

[66] S Bergeler and E Frey. *Regulation of Pom cluster dynamics in Myxococcus xanthus.* In: **PLOS Computational Biology** 14.8 (2018), e1006358. DOI: 10.1371/journal.pcbi.1006358 (cit. on pp. vi, viii, 46).

[67] MK Gardner, M Zanic, and J Howard. *Microtubule catastrophe and rescue.* In: **Current Opinion in Cell Biology** 25.1 (2013), pp. 14–22. DOI: 10.1016/j.ceb.2012.09.006 (cit. on pp. vi, viii, 4, 5, 7).

[68] B Bugyi and MF Carlier. *Control of Actin Filament Treadmilling in Cell Motility.* In: **Annual Review of Biophysics** 39.1 (2010), pp. 449–470. DOI: 10.1146/annurev-biophys-051309-103849 (cit. on pp. vi, vii, 5, 7).

[69] L Mohapatra et al. *Design Principles of Length Control of Cytoskeletal Structures.* In: **Annual Review of Biophysics** 45.1 (2016), pp. 85–116. DOI: 10.1146/annurev-biophys-070915-094206 (cit. on pp. vii, 7, 42).

[70] A Akhmanova and MO Steinmetz. *Tracking the ends: a dynamic protein network controls the fate of microtubule tips.* In: **Nature Reviews Molecular Cell Biology** 9 (2008), pp. 309–322. DOI: 10.1038/nrm2369 (cit. on p. vii).

[71] AE Carlsson. *Actin Dynamics: From Nanoscale to Microscale.* In: **Annual Review of Biophysics** 39.1 (2010), pp. 91–110. DOI: 10.1146/annurev.biophys.093008.131207 (cit. on pp. vii, 5, 7).

[72] HV Goodson and EM Jonasson. *Microtubules and Microtubule-Associated Proteins*. In: **Cold Spring Harbor Perspectives in Biology** 10.6 (2018), a022608. DOI: 10.1101/cshperspect.a022608 (cit. on pp. vii, 4, 5, 7).

[73] YHM Chan and WF Marshall. *How cells know the size of their organelles*. In: **Science** 337.6099 (2012), pp. 1186–1189. DOI: 10.1126/science.1223539 (cit. on pp. vii, 7).

[74] NW Goehring and AA Hyman. *Organelle growth control through limiting pools of cytoplasmic components*. In: **Current Biology** 22.9 (2012), R330–R339. DOI: 10.1016/j.cub.2012.03.046 (cit. on p. vii).

[75] WF Marshall. *Cell Geometry: How Cells Count and Measure Size*. In: **Annual Review of Biophysics** 45.1 (2016), pp. 49–64. DOI: 10.1146/annurev-biophys-062215-010905 (cit. on p. vii).

[76] N Sharma et al. *Soluble levels of cytosolic tubulin regulate ciliary length control*. In: **Molecular Biology of the Cell** 22.6 (2011), pp. 806–816. DOI: 10.1091/mbc.E10-03-0269 (cit. on p. vii).

[77] WF Marshall and JL Rosenbaum. *Intraflagellar transport balances continuous turnover of outer doublet microtubules: implications for flagellar length control*. In: **Journal of Cell Biology** 155.3 (2001), pp. 405–414. DOI: 10.1083/jcb.200106141 (cit. on pp. vii, 8).

[78] L Hao et al. *Intraflagellar transport delivers tubulin isotypes to sensory cilium middle and distal segments*. In: **Nature Cell Biology** 13 (2011), pp. 790–798. DOI: doi:10.1038/ncb2268 (cit. on pp. vii, 8).

[79] WF Marshall. *Subcellular size*. In: **Cold Spring Harbor Perspectives in Biology** 7.6 (2015), a019059. DOI: 10.1101/cshperspect.a019059 (cit. on pp. vii, 7).

[80] M Chesarone-Cataldo et al. *The Myosin Passenger Protein Smy1 Controls Actin Cable Structure and Dynamics by Acting as a Formin Damper*. In: **Developmental Cell** 21.2 (2011), pp. 217–230. DOI: 10.1016/j.devcel.2011.07.004 (cit. on pp. vii, 8).

[81] L Reese, A Melbinger, and E Frey. *Crowding of molecular motors determines microtubule depolymerization*. In: **Biophysical Journal** 101.9 (2011), pp. 2190–2200. DOI: 10.1016/j.bpj.2011.09.009 (cit. on pp. vii, 8, 12).

[82] A Melbinger, L Reese, and E Frey. *Microtubule length regulation by molecular motors*. In: **Physical Review Letters** 108.25 (2012), p. 258104. DOI: 10.1103/PhysRevLett.108.258104 (cit. on pp. vii, 8, 12, 42, 44).

[83] M Bojer. *Study of the totally asymmetric simple exclusion process on a length changing lane in a diffusive environment*. LMU Munich, Master thesis, 2016 (cit. on p. viii).

[84] AJ Hunt, F Gittes, and J Howard. *The force exerted by a single kinesin molecule against a viscous load*. In: **Biophysical Journal** 67.2 (1994), pp. 766–781. DOI: 10.1016/S0006-3495(94)80537-5 (cit. on pp. viii, 68).

[85] K Svoboda and SM Block. *Force and velocity measured for single kinesin molecules*. In: **Cell** 77.5 (1994), pp. 773–784. DOI: 10.1016/0092-8674(94)90060-4 (cit. on pp. viii, 68).

[86] K Visscher, MJ Schnitzer, and SM Block. *Single kinesin molecules studied with a molecular force clamp*. In: **Nature** 400 (1999), pp. 184–189. DOI: 10.1038/22146 (cit. on pp. viii, 6, 68).

[87] MT Valentine et al. *Individual dimers of the mitotic kinesin motor Eg5 step processively and support substantial loads in vitro.* In: **Nature Cell Biology** 8 (2006), pp. 470–476. DOI: 10.1038/ncb1394 (cit. on pp. viii, 68).

[88] S Fürthauer et al. *Self-straining of actively crosslinked microtubule networks.* In: **Nature Physics** 15 (2019), pp. 1295–1300. DOI: 10.1038/s41567-019-0642-1 (cit. on pp. ix–xi, 67, 70, 72, 73).

[89] KS Burbank, TJ Mitchison, and DS Fisher. *Slide-and-Cluster Models for Spindle Assembly.* In: **Current Biology** 17.16 (2007), pp. 1373–1383. DOI: 10.1016/j.cub.2007.07.058 (cit. on pp. ix, x, 3, 67, 73).

[90] G Yang et al. *Regional variation of microtubule flux reveals microtubule organization in the metaphase meiotic spindle.* In: **Journal of Cell Biology** 182.4 (2008), pp. 631–639. DOI: 10.1083/jcb.200801105 (cit. on pp. ix, x, 67, 73).

[91] J Brugués et al. *Nucleation and transport organize microtubules in metaphase spindles.* In: **Cell** 149.3 (2012), pp. 554–564. DOI: 10.1016/j.cell.2012.03.027 (cit. on pp. ix, x, 67, 73, 114).

[92] DA Fletcher and RD Mullins. *Cell mechanics and the cytoskeleton.* In: **Nature** 463 (2010), pp. 485–492. DOI: 10.1038/nature08908 (cit. on pp. ix, 3–6).

[93] TD Pollard and RD Goldman. *Overview of the cytoskeleton from an evolutionary perspective.* In: **Cold Spring Harbor Perspectives in Biology** 10.7 (2018), a030288. DOI: 10.1101/cshperspect.a030288 (cit. on pp. ix, 3–5).

[94] LC Kapitein et al. *The bipolar mitotic kinesin Eg5 moves on both microtubules that it crosslinks.* In: **Nature** 435 (2005), pp. 114–118. DOI: 10.1038/nature03503 (cit. on pp. ix, 6, 7, 67).

[95] RA Cross and A McAinsh. *Prime movers: The mechanochemistry of mitotic kinesins.* In: **Nature Reviews Molecular Cell Biology** 15 (2014), pp. 257–271. DOI: 10.1038/nrm3768 (cit. on pp. ix, 3, 7).

[96] K Kruse and F Jülicher. *Actively contracting bundles of polar filaments.* In: **Physical Review Letters** 85.8 (2000), p. 1778. DOI: 10.1103/PhysRevLett.85.1778 (cit. on pp. ix, x, 73).

[97] T Gao et al. *Multiscale polar theory of microtubule and motor-protein assemblies.* In: **Physical Review Letters** 114.4 (2015), p. 048101. DOI: 10.1103/PhysRevLett.114.048101 (cit. on pp. ix, x, 73).

[98] T Gao et al. *Multiscale modeling and simulation of microtubule-motor-protein assemblies.* In: **Physical Review E** 92.6 (2015), p. 062709. DOI: 10.1103/PhysRevE.92.062709 (cit. on pp. ix, x, 73).

[99] D Oriola, DJ Needleman, and J Brugués. *The Physics of the Metaphase Spindle.* In: **Annual Review of Biophysics** 47.1 (2018), pp. 655–673. DOI: 10.1146/annurev-biophys-060414-034107 (cit. on pp. ix, 3, 67).

[100] R Tan et al. *Cooperative Accumulation of Dynein-Dynactin at Microtubule Minus-Ends Drives Microtubule Network Reorganization.* In: **Developmental Cell** 44.2 (2018), 233–247.e4. DOI: 10.1016/j.devcel.2017.12.023 (cit. on p. ix).

[101] D T Miyamoto et al. *The kinesin Eg5 drives poleward microtubule flux in Xenopus laevis egg extract spindles.* In: **Journal of Cell Biology** 167.5 (2004), pp. 813–818. DOI: 10.1083/jcb.200407126 (cit. on pp. x, 67, 114).

[102] A Zlotnick et al. *A Theoretical Model Successfully Identifies Features of Hepatitis B Virus Capsid Assembly.* In: **Biochemistry** 38.44 (1999), pp. 14644–14652. DOI: 10.1021/bi991611a (cit. on pp. xi, xii, 117–119, 121).

[103] A Y Morozov, R F Bruinsma, and J Rudnick. *Assembly of viruses and the pseudo-law of mass action.* In: **Journal of Chemical Physics** 131.15 (2009), p. 155101. DOI: 10.1063/1.3212694 (cit. on pp. xi, xii, 117, 121).

[104] M F Hagan and O M Elrad. *Understanding the concentration dependence of viral capsid assembly kinetics - The origin of the lag time and identifying the critical nucleus size.* In: **Biophysical Journal** 98.6 (2010), pp. 1065–1074. DOI: 10.1016/j.bpj.2009.11.023 (cit. on pp. xi, xii, 117, 119, 121).

[105] Y Ke et al. *Three-Dimensional Structures Self-Assembled from DNA Bricks.* In: **Science** 338.6111 (2012), pp. 1177–1183. DOI: 10.1126/science.1227268 (cit. on pp. xi, xii, 117, 120, 121).

[106] B Wei, M Dai, and P Yin. *Complex shapes self–assembled from single–stranded DNA tiles.* In: **Nature** 485 (2012), pp. 623–626. DOI: 10.1038/nature11075 (cit. on pp. xi, xii, 117, 120, 121).

[107] A Reinhardt and D Frenkel. *Numerical evidence for nucleated self-assembly of DNA brick structures.* In: **Physical Review Letters** 112.23 (2014), p. 238103. DOI: 10.1103/PhysRevLett.112.238103 (cit. on pp. xi, xii, 117, 120, 121).

[108] W M Jacobs, A Reinhardt, and D Frenkel. *Rational design of self-assembly pathways for complex multicomponent structures.* In: **Proceedings of the National Academy of Sciences** 112.20 (2015), pp. 6313–6318. DOI: 10.1073/pnas.1502210112 (cit. on pp. xi, xii, 117, 121).

[109] A Murugan, J Zou, and M P Brenner. *Undesired usage and the robust self-assembly of heterogeneous structures.* In: **Nature Communications** 6 (2015), p. 6203. DOI: 10.1038/ncomms7203 (cit. on pp. xi, xii, xv, 117, 121, 178).

[110] A Zlotnick and S Mukhopadhyay. *Virus assembly, allostery and antivirals.* In: **Trends in Microbiology** 19.1 (2011), pp. 14–23. DOI: 10.1016/j.tim.2010.11.003 (cit. on pp. xi, xii, 117–119).

[111] M F Hagan. *Modeling Viral Capsid Assembly.* In: **Advances in Chemical Physics** 155 (2014), pp. 1–68. DOI: 10.1002/9781118755815.ch01 (cit. on pp. xi, xii, 117, 118).

[112] F C Simmel. *DNA-based assembly lines and nanofactories.* In: **Current Opinion in Biotechnology** 23.4 (2012), pp. 516–521. DOI: 10.1016/j.copbio.2011.12.024 (cit. on pp. xi, xiv, 117, 119, 120, 230).

[113] I Saaem and T H LaBean. *Overview of DNA origami for molecular self-assembly.* In: **Wiley Interdisciplinary Reviews: Nanomedicine and Nanobiotechnology** 5 (2013), pp. 150–162. DOI: 10.1002/wnan.1204 (cit. on pp. xi, xiv, 117, 119, 120, 230).

[114] P Wang et al. *The Beauty and Utility of DNA Origami.* In: **Chem** 2.3 (2017), pp. 359–382. DOI: 10.1016/j.chempr.2017.02.009 (cit. on pp. xi, xiv, 117, 119, 120, 230).

[115] L Cademartiri and K J Bishop. *Programmable self-assembly.* In: **Nature Materials** 14 (2015), pp. 2–9. DOI: 10.1038/nmat4184 (cit. on pp. xi, xv, 117, 119, 120, 230).

[116] S Whitelam. *Hierarchical assembly may be a way to make large information-rich structures.* In: **Soft Matter** 11 (2015), pp. 8225–8235. DOI: 10.1039/C5SM01375E (cit. on pp. xi, xv, 117, 121).

[117] M Kirschner and T Mitchison. *Beyond self-assembly: From microtubules to morphogenesis.* In: **Cell** 45.3 (1986), pp. 329–342. DOI: 10.1016/0092-8674(86)90318-1 (cit. on p. xii).

[118] E Nogales and H W Wang. *Structural intermediates in microtubule assembly and disassembly: How and why?* In: **Current Opinion in Cell Biology** 18.2 (2006), pp. 179–184. DOI: 10.1016/j.ceb.2006.02.009 (cit. on pp. xii, 4).

[119] J Roostalu and T Surrey. *Microtubule nucleation: Beyond the template.* In: **Nature Reviews Molecular Cell Biology** 18 (2017), pp. 702–710. DOI: 10.1038/nrm.2017.75 (cit. on p. xii).

[120] P Aldridge and K T Hughes. *Regulation of flagellar assembly.* In: **Current Opinion in Microbiology** 5.2 (2002), pp. 160–165. DOI: 10.1016/S1369-5274(02)00302-8 (cit. on p. xii).

[121] A Zlotnick. *To Build a Virus Capsid: An Equilibrium Model of the Self Assembly of Polyhedral Protein Complexes.* In: **Journal of Molecular Biology** 241.1 (1994), pp. 59–67. DOI: 10.1006/jmbi.1994.1473 (cit. on pp. xii, 117–119).

[122] C Chen, C C Kao, and B Dragnea. *Self-assembly of brome mosaic virus capsids: insights from shorter time-scale experiments.* In: **The Journal of Physical Chemistry A** 112.39 (2008), pp. 9405–9412. DOI: 10.1021/jp802498z (cit. on pp. xii, 118, 119, 124).

[123] M F Hagan, O M Elrad, and R L Jack. *Mechanisms of kinetic trapping in self-assembly and phase transformation.* In: **Journal of Chemical Physics** 135 (2011), p. 104115. DOI: 10.1063/1.3635775 (cit. on pp. xii, 117).

[124] D Endres and A Zlotnick. *Model-based analysis of assembly kinetics for virus capsids or other spherical polymers.* In: **Biophysical Journal** 83.2 (2002), pp. 1217–1230. DOI: 10.1016/S0006-3495(02)75245-4 (cit. on pp. xii, 117–119).

[125] M R D'Orsogna, Q Lei, and T Chou. *First assembly times and equilibration in stochastic coagulation-fragmentation.* In: **Journal of Chemical Physics** 143.1 (2015). DOI: 10.1063/1.4923002 (cit. on pp. xiii, 125).

[126] K F Wagenbauer, C Sigl, and H Dietz. *Gigadalton-scale shape-programmable DNA assemblies.* In: **Nature** 552 (2017), pp. 78–83. DOI: 10.1038/nature24651 (cit. on pp. xiv, 227).

[127] C G Evans and E Winfree. *Physical principles for DNA tile self-assembly.* In: **Chemical Society Reviews** 46.12 (2017), pp. 3808–3829. DOI: 10.1039/c6cs00745g (cit. on pp. xv, 117, 119, 230).

[128] A Ashkin. *Acceleration and Trapping of Particles by Radiation Pressure.* In: **Physical Review Letters** 24.4 (1970), p. 156. DOI: 10.1103/PhysRevLett.24.156 (cit. on p. 3).

[129] A Ashkin et al. *Observation of a single-beam gradient force optical trap for dielectric particles.* In: **Optics Letters** 11.5 (1986), pp. 288–290. DOI: 10.1364/ol.11.000288 (cit. on p. 3).

[130] J R Moffitt et al. *Recent Advances in Optical Tweezers.* In: **Annual Review of Biochemistry** 77.1 (2008), pp. 205–228. DOI: 10.1146/annurev.biochem.77.043007.090225 (cit. on p. 3).

[131] C Bradac. *Nanoscale Optical Trapping: A Review.* In: **Advanced Optical Materials** 6 (2018), p. 1800005. DOI: 10.1002/adom.201800005 (cit. on p. 3).

[132] W E Moerner and L Kador. *Optical detection and spectroscopy of single molecules in a solid.* In: **Physical Review Letters** 62.21 (1989), p. 2535. DOI: 10.1103/PhysRevLett.62.2535 (cit. on p. 3).

[133] S W Hell and J Wichmann. *Breaking the diffraction resolution limit by stimulated emission: stimulated-emission-depletion fluorescence microscopy.* In: **Optics Letters** 19.11 (1994), pp. 780–782. DOI: 10.1364/ol.19.000780 (cit. on p. 3).

[134] R M Dickson et al. *On/off blinking and switching behaviour of single molecules of green fluorescent protein.* In: **Nature** 388 (1997), pp. 355–358. DOI: 10.1038/41048 (cit. on p. 3).

[135] E Betzig. *Nobel Lecture: Single Molecules, Cells, and Super-Resolution Optics.* In: **Reviews of Modern Physics** 87.4 (2015), p. 1153. DOI: 10.1103/RevModPhys.87.1153 (cit. on p. 3).

[136] B O Leung and K C Chou. *Review of super-resolution fluorescence microscopy for biology.* In: **Applied Spectroscopy** 65.9 (2011), pp. 967–980. DOI: 10.1366/11-06398 (cit. on p. 3).

[137] A Pietraszewska-Bogiel and T W Gadella. *FRET microscopy: From principle to routine technology in cell biology.* In: **Journal of Microscopy** 241.2 (2011), pp. 111–118. DOI: 10.1111/j.1365-2818.2010.03437.x (cit. on p. 3).

[138] S Shashkova and M C Leake. *Single-molecule fluorescence microscopy review: Shedding new light on old problems.* In: **Bioscience Reports** 37.4 (2017), BSR20170031. DOI: 10.1042/BSR20170031 (cit. on p. 3).

[139] F Huber et al. *Cytoskeletal crosstalk: When three different personalities team up.* In: **Current Opinion in Cell Biology** 32 (2015), pp. 39–47. DOI: 10.1016/j.ceb.2014.10.005 (cit. on pp. 3–5).

[140] R Heald and A Khodjakov. *Thirty years of search and capture: The complex simplicity of mitotic spindle assembly.* In: **Journal of Cell Biology** 211.6 (2015), pp. 1103–1111. DOI: 10.1083/jcb.201510015 (cit. on pp. 3, 67).

[141] N Pavin and I M Tolić. *Self-Organization and Forces in the Mitotic Spindle.* In: **Annual Review of Biophysics** 45.1 (2016), pp. 279–298. DOI: 10.1146/annurev-biophys-062215-010934 (cit. on pp. 3, 67).

[142] S Petry. *Mechanisms of Mitotic Spindle Assembly.* In: **Annual Review of Biochemistry** 85.1 (2016), pp. 659–683. DOI: 10.1146/annurev-biochem-060815-014528 (cit. on pp. 3, 67).

[143] S L Prosser and L Pelletier. *Mitotic spindle assembly in animal cells: A fine balancing act.* In: **Nature Reviews Molecular Cell Biology** 18 (2017), pp. 187–201. DOI: 10.1038/nrm.2016.162 (cit. on pp. 3, 6, 67).

[144] J Howard. *Molecular motors: Structural adaptations to cellular functions.* In: **Nature** 389 (1997), pp. 561–567. DOI: 10.1038/39247 (cit. on pp. 3, 5, 6).

[145] R Heald et al. *Self-organization of microtubules into bipolar spindles around artificial chromosomes in Xenopus egg extracts.* In: **Nature** 382 (1996), pp. 420–425. DOI: 10.1038/382420a0 (cit. on pp. 3, 7).

[146] S Gadde and R Heald. *Mechanisms and molecules of the mitotic spindle.* In: **Current Biology** 14.18 (2004), R797–R805. DOI: 10.1016/j.cub.2004.09.021 (cit. on p. 3).

[147] H Lodish et al. *Intracellular ion environment and membrane electric potential.* In: **Molecular Cell Biology. 4th edition**. WH Freeman, 2000 (cit. on p. 4).

[148] A Desai and T J Mitchison. *Microtubule Polymerization Dynamics.* In: **Annual Review of Cell and Developmental Biology** 13.1 (1997), pp. 83–117. DOI: 10.1146/annurev.cellbio.13.1.83 (cit. on pp. 4, 7).

[149] J Howard and A A Hyman. *Dynamics and mechanics of the microtubule plus end.* In: **Nature** 422 (2003), pp. 753–758. DOI: doi:10.1038/nature01600 (cit. on pp. 4, 7).

[150] A Akhmanova and M O Steinmetz. *Control of microtubule organization and dynamics: Two ends in the limelight.* In: **Nature Reviews Molecular Cell Biology** 16 (2015), pp. 711–726. DOI: 10.1038/nrm4084 (cit. on pp. 4, 7).

[151] G M Cooper. *The Cell: A Molecular Approach. 2nd edition.* Sunderland (MA): Sinauer Associates, 2000 (cit. on pp. 5, 6).

[152] M L Gardel et al. *Elastic behavior of cross-linked and bundled actin networks.* In: **Science** 304.5675 (2004), pp. 1301–1305. DOI: 10.1126/science.1095087 (cit. on p. 5).

[153] C Revenu et al. *The co-workers of actin filaments: From cell structures to signals.* In: **Nature Reviews Molecular Cell Biology** 5 (2004), pp. 635–646. DOI: 10.1038/nrm1437 (cit. on pp. 5–7, 13).

[154] C Veigel and C F Schmidt. *Moving into the cell: Single-molecule studies of molecular motors in complex environments.* In: **Nature Reviews Molecular Cell Biology** 12 (2011), pp. 163–176. DOI: 10.1038/nrm3062 (cit. on pp. 5, 6).

[155] A B Kolomeisky. *Motor proteins and molecular motors: How to operate machines at the nanoscale.* In: **Journal of Physics Condensed Matter** 25 (2013), p. 463101. DOI: 10.1088/0953-8984/25/46/463101 (cit. on pp. 5, 6).

[156] J T Finer, R M Simmons, and J A Spudich. *Single myosin molecule mechanics: Piconewton forces and nanometre steps.* In: **Nature** 368 (1994), pp. 113–119. DOI: 10.1038/368113a0 (cit. on p. 6).

[157] R D Vale and R J Fletterick. *The design plan of kinesin motors.* In: **Annual Review of Cell and Developmental Biology** 13 (1997), pp. 745–77. DOI: 10.1146/annurev.cellbio.13.1.745 (cit. on p. 6).

[158] A J Roberts et al. *Functions and mechanics of dynein motor proteins.* In: **Nature Reviews Molecular Cell Biology** 14 (2013), pp. 713–726. DOI: 10.1038/nrm3667 (cit. on p. 6).

[159] J R Sellers. *Myosins: A diverse superfamily.* In: **Biochimica et Biophysica Acta - Molecular Cell Research** 1496.1 (2000), pp. 3–22. DOI: 10.1016/S0167-4889(00)00005-7 (cit. on p. 6).

[160] N Hirokawa et al. *Kinesin superfamily motor proteins and intracellular transport.* In: **Nature Reviews Molecular Cell Biology** 10 (2009), pp. 682–696. DOI: 10.1038/nrm2774 (cit. on p. 6).

[161] S S Brown. *Cooperation between microtubule- and actin-based motor proteins.* In: **Annual Review of Cell and Developmental Biology** 15.1 (1999), pp. 63–80. DOI: 10.1146/annurev.cellbio.15.1.63 (cit. on p. 6).

[162] K J Verhey and J W Hammond. *Traffic control: Regulation of kinesin motors.* In: **Nature Reviews Molecular Cell Biology** 10 (2009), pp. 765–777. DOI: 10.1038/nrm2782 (cit. on p. 6).

[163] C Appert-Rolland, M Ebbinghaus, and L Santen. *Intracellular transport driven by cytoskeletal motors: General mechanisms and defects.* In: **Physics Reports** 593 (2015), pp. 1–59. DOI: 10.1016/j.physrep.2015.07.001 (cit. on pp. 6, 11).

[164] R D Vale. *Myosin V motor proteins: Marching stepwise towards a mechanism.* In: **Journal of Cell Biology** 163.3 (2003), pp. 445–450. DOI: 10.1083/jcb.200308093 (cit. on p. 6).

[165] M A Hartman and J A Spudich. *The myosin superfamily at a glance.* In: **Journal of Cell Science** 125 (2012), pp. 1627–1632. DOI: 10.1242/jcs.094300 (cit. on p. 6).

[166] T Kambara, S Komaba, and M Ikebe. *Human myosin III is a motor having an extremely high affinity for actin.* In: **Journal of Biological Chemistry** 281.49 (2006), pp. 37291–37301. DOI: 10.1074/jbc.M603823200 (cit. on p. 6).

[167] F T Salles et al. *Myosin IIIa boosts elongation of stereocilia by transporting espin 1 to the plus ends of actin filaments.* In: **Nature Cell Biology** 11 (2009), pp. 443–450. DOI: 10.1038/ncb1851 (cit. on p. 6).

[168] J E Bird et al. *Chaperone-enhanced purification of unconventional myosin 15, a molecular motor specialized for stereocilia protein trafficking.* In: **Proceedings of the National Academy of Sciences** 111.34 (2014), pp. 12390–12395. DOI: 10.1073/pnas.1409459111 (cit. on p. 6).

[169] A Oladipo, A Cowan, and V Rodionov. *Microtubule Motor Ncd Induces Sliding of Microtubules In Vivo.* In: **Molecular biology of the cell** 18.9 (2007), pp. 3601–3606. DOI: 10.1091/mbc.e06-12-1085 (cit. on p. 7).

[170] G Fink et al. *The mitotic kinesin-14 Ncd drives directional microtubule-microtubule sliding.* In: **Nature Cell Biology** 11 (2009), pp. 717–723. DOI: 10.1038/ncb1877 (cit. on p. 7).

[171] T Surrey et al. *Physical Properties Determining Self-Organization of Motors and Microtubules.* In: **Science** 292.5519 (2001), pp. 1167–1172. DOI: 10.1126/science.1059758 (cit. on p. 7).

[172] J Howard and A A Hyman. *Microtubule polymerases and depolymerases.* In: **Current Opinion in Cell Biology** 19.1 (2007), pp. 31–35. DOI: 10.1016/j.ceb.2006.12.009 (cit. on p. 8).

[173] MR Mofrad. *Rheology of the Cytoskeleton*. In: **Annual Review of Fluid Mechanics** 41.1 (2009), pp. 433–453. DOI: 10.1146/annurev.fluid.010908.165236 (cit. on pp. 8, 12).

[174] FC MacKintosh and CF Schmidt. *Active cellular materials*. In: **Current Opinion in Cell Biology** 22.1 (2010), pp. 29–35. DOI: 10.1016/j.ceb.2010.01.002 (cit. on pp. 8, 12).

[175] MC Marchetti et al. *Hydrodynamics of soft active matter*. In: **Reviews of Modern Physics** 85.3 (2013), pp. 1143–1189. DOI: 10.1103/RevModPhys.85.1143 (cit. on pp. 8, 12).

[176] J Prost, F Jülicher, and JF Joanny. *Active gel physics*. In: **Nature Physics** 11 (2015), pp. 111–117. DOI: 10.1038/nphys3224 (cit. on pp. 8, 12).

[177] B Derrida et al. *Exact solution of a 1D asymmetric exclusion model using a matrix formulation*. In: **Journal of Physics A: Mathematical and General** 26 (1993), p. 1493. DOI: 10.1088/0305-4470/26/7/011 (cit. on pp. 9–11).

[178] RA Blythe and MR Evans. *Nonequilibrium steady states of matrix-product form: A solver's guide*. In: **Journal of Physics A: Mathematical and Theoretical** 40.46 (2007). DOI: 10.1088/1751-8113/40/46/R01 (cit. on p. 9).

[179] PL Krapivsky, S Redner, and E Ben-Naim. *A Kinetic View of Statistical Physics*. Cambridge University Press, 2010, pp. 103–133. DOI: 10.1017/CBO9780511780516.006 (cit. on p. 9).

[180] B Derrida, MR Evans, and K Mallick. *Exact diffusion constant of a one-dimensional asymmetric exclusion model with open boundaries*. In: **Journal of Statistical Physics** 79.5-6 (1995), pp. 833–874. DOI: 10.1007/BF02181206 (cit. on pp. 10, 18).

[181] R Lipowsky, S Klumpp, and TM Nieuwenhuizen. *Random Walks of Cytoskeletal Motors in Open and Closed Compartments*. In: **Physical Review Letters** 87.10 (2001), p. 108101. DOI: 10.1103/PhysRevLett.87.108101 (cit. on pp. 11, 12, 15).

[182] P Wilke, E Reithmann, and E Frey. *Two-Species Active Transport along Cylindrical Biofilaments is Limited by Emergent Topological Hindrance*. In: **Physical Review X** 8.3 (2018), p. 031063. DOI: 10.1103/PhysRevX.8.031063 (cit. on p. 11).

[183] MJI Müller, S Klumpp, and R Lipowsky. *Molecular motor traffic in a half-open tube*. In: **Journal of Physics Condensed Matter** 17.47 (2005). DOI: 10.1088/0953-8984/17/47/014 (cit. on p. 12).

[184] K Tsekouras and AB Kolomeisky. *Parallel coupling of symmetric and asymmetric exclusion processes*. In: **Journal of Physics A: Mathematical and Theoretical** 41.46 (2008). DOI: 10.1088/1751-8113/41/46/465001 (cit. on p. 12).

[185] J Tailleur, MR Evans, and Y Kafri. *Nonequilibrium phase transitions in the extraction of membrane tubes by molecular motors*. In: **Physical Review Letters** 102.11 (2009), p. 118109. DOI: 10.1103/PhysRevLett.102.118109 (cit. on p. 12).

[186] MR Evans et al. *Phase diagrams of two-lane driven diffusive systems*. In: **Journal of Statistical Mechanics: Theory and Experiment** 2011.6 (2011), P06009. DOI: 10.1088/1742-5468/2011/06/P06009 (cit. on p. 12).

[187] B Saha and S Mukherji. *Coupling driven exclusion and diffusion processes on parallel lanes: Boundary induced phase transitions and boundary layers*. In: **Journal of Statistical Mechanics: Theory and Experiment** 2013.9 (2013), P09004. DOI: 10.1088/1742-5468/2013/09/P09004 (cit. on p. 12).

[188] M R Evans and K E P Sugden. *An exclusion process for modelling fungal hyphal growth*. In: **Physica A: Statistical Mechanics and its Applications** 384.1 (2007), pp. 53–58. DOI: 10.1016/j.physa.2007.04.078 (cit. on p. 12).

[189] L E Hough et al. *Microtubule Depolymerization by the Kinesin-8 Motor Kip3p: A Mathematical Model*. In: **Biophysical Journal** 96.8 (2009), pp. 3050–3064. DOI: 10.1016/j.bpj.2009.01.017 (cit. on p. 12).

[190] M Schmitt and H Stark. *Modelling bacterial flagellar growth*. In: **Europhysics Letters** 96.2 (2011), p. 28001. DOI: 10.1209/0295-5075/96/28001 (cit. on p. 12).

[191] D Johann, C Erlenkämper, and K Kruse. *Length regulation of active biopolymers by molecular motors*. In: **Physical Review Letters** 108.25 (2012), p. 258103. DOI: 10.1103/PhysRevLett.108.258103 (cit. on p. 12).

[192] S Muhuri. *Scale-invariant density profiles of a dynamically extending TASEP*. In: **Europhysics Letters** 101 (2013), p. 38001. DOI: 10.1209/0295-5075/101/38001 (cit. on p. 12).

[193] D A Adams, B Schmittmann, and R K P Zia. *Far-from-equilibrium transport with constrained resources*. In: **Journal of Statistical Mechanics: Theory and Experiment** (2008), P06009. DOI: 10.1088/1742-5468/2008/06/P06009 (cit. on p. 12).

[194] L J Cook, R K P Zia, and B Schmittmann. *Competition between multiple totally asymmetric simple exclusion processes for a finite pool of resources*. In: **Physical Review E** 80.3 (2009), p. 031142. DOI: 10.1103/PhysRevE.80.031142 (cit. on p. 12).

[195] M Rank et al. *Limited Resources Induce Bistability in Microtubule Length Regulation*. In: **Physical Review Letters** 120.14 (2018), p. 148101. DOI: 10.1103/PhysRevLett.120.148101 (cit. on p. 12).

[196] J F Joanny and J Prost. *Active gels as a description of the actin-myosin cytoskeleton*. In: **HFSP Journal** 3.2 (2009), pp. 94–104. DOI: 10.2976/1.3054712 (cit. on p. 12).

[197] S Ramaswamy. *The Mechanics and Statistics of Active Matter*. In: **Annual Review of Condensed Matter Physics** 1.1 (2010), pp. 323–345. DOI: 10.1146/annurev-conmatphys-070909-104101 (cit. on p. 12).

[198] F Jülicher, S W Grill, and G Salbreux. *Hydrodynamic theory of active matter*. In: **Reports on Progress in Physics** 81.7 (2018), p. 076601. DOI: 10.1088/1361-6633/aab6bb (cit. on p. 12).

[199] K Kruse and F Jülicher. *Self-organization and mechanical properties of active filament bundles*. In: **Physical Review E** 67.5 (2003), p. 051913. DOI: 10.1103/PhysRevE.67.051913 (cit. on p. 12).

[200] A Ahmadi, T B Liverpool, and M C Marchetti. *Nematic and polar order in active filament solutions*. In: **Physical Review E** 72.6 (2005), p. 060901. DOI: 10.1103/PhysRevE.72.060901 (cit. on p. 12).

[201] IS Aranson and LS Tsimring. *Pattern formation of microtubules and motors: Inelastic interaction of polar rods.* In: **Physical Review E** 71.5 (2005), p. 050901. DOI: 10.1103/PhysRevE.71.050901 (cit. on p. 12).

[202] KE Sawin and TJ Mitchison. *Poleward microtubule flux in mitotic spindles assembled in vitro.* In: **Journal of Cell Biology** 112.5 (1991), pp. 941–954. DOI: 10.1083/jcb.112.5.941 (cit. on pp. 67, 114).

[203] P Maddox et al. *Poleward microtubule flux is a major component of spindle dynamics and anaphase A in mitotic Drosophila embryos.* In: **Current Biology** 12.19 (2002), pp. 1670–1674. DOI: 10.1016/S0960-9822(02)01183-1 (cit. on pp. 67, 114).

[204] M Uteng et al. *Poleward transport of Eg5 by dynein-dynactin in Xenopus laevis egg extract spindles.* In: **Journal of Cell Biology** 182.4 (2008), pp. 715–726. DOI: 10.1083/jcb.200801125 (cit. on pp. 67, 114).

[205] NP Ferenz, A Gable, and P Wadsworth. *Mitotic Functions of Kinesin-5.* In: **Seminars in Cell and Developmental Biology** 21.3 (2010), pp. 255–259. DOI: 10.1016/j.semcdb.2010.01.019 (cit. on pp. 67, 114).

[206] PE Prevelige, D Thomas, and J King. *Nucleation and growth phases in the polymerization of coat and scaffolding subunits into icosahedral procapsid shells.* In: **Biophysical Journal** 64.3 (1993), pp. 824–835. DOI: 10.1016/S0006-3495(93)81443-7 (cit. on pp. 117, 118, 124).

[207] JM Johnson et al. *Regulating self-assembly of spherical oligomers.* In: **Nano Letters** 5.4 (2005), pp. 765–770. DOI: 10.1021/nl050274q (cit. on p. 117).

[208] S Kler et al. *RNA encapsidation by SV40-derived nanoparticles follows a rapid two-state mechanism.* In: **Journal of the American Chemical Society** 134.21 (2012), pp. 8823–8830. DOI: 10.1021/ja2110703 (cit. on pp. 117, 118).

[209] R Schwartz et al. *Local rules simulation of the kinetics of virus capsid self-assembly.* In: **Biophysical Journal** 75.6 (1998), pp. 2626–2636. DOI: 10.1016/S0006-3495(98)77708-2 (cit. on pp. 117, 118).

[210] DC Rapaport, JE Johnson, and J Skolnick. *Supramolecular self-assembly: Molecular dynamics modeling of polyhedral shell formation.* In: **Computer Physics Communications** 121-122 (1999), pp. 231–235. DOI: 10.1016/S0010-4655(99)00319-7 (cit. on pp. 117, 118).

[211] MF Hagan and D Chandler. *Dynamic pathways for viral capsid assembly.* In: **Biophysical Journal** 91.1 (2006), pp. 42–54. DOI: 10.1529/biophysj.105.076851 (cit. on pp. 117, 118).

[212] HD Nguyen, VS Reddy, and CL Brooks. *Deciphering the kinetic mechanism of spontaneous self-assembly of icosahedral capsids.* In: **Nano Letters** 7.2 (2007), pp. 338–344. DOI: 10.1021/nl062449h (cit. on pp. 117, 118).

[213] DC Rapaport. *Role of reversibility in viral capsid growth: A paradigm for self-assembly.* In: **Physical Review Letters** 101.18 (2008), p. 186101. DOI: 10.1103/PhysRevLett.101.186101 (cit. on pp. 117, 118).

[214] JE Baschek, HCR Klein, and US Schwarz. *Stochastic dynamics of virus capsid formation: direct versus hierarchical self-assembly.* In: **BMC Biophysics** 5.22 (2012). DOI: 10.1186/2046-1682-5-22 (cit. on pp. 117, 118).

[215] TK Haxton and S Whitelam. *Do hierarchical structures assemble best via hierarchical pathways?* In: **Soft Matter** 9.29 (2013), pp. 6851–6861. DOI: 10.1039/c3sm27637f (cit. on pp. 117, 121).

[216] LO Hedges, RV Mannige, and S Whitelam. *Growth of equilibrium structures built from a large number of distinct component types.* In: **Soft Matter** 10.34 (2014), pp. 6404–6416. DOI: 10.1039/c4sm01021c (cit. on pp. 117, 121).

[217] VL Morton et al. *Insights into virus capsid assembly from non-covalent mass spectrometry.* In: **Mass Spectrometry Reviews** 27.6 (2008), pp. 575–595. DOI: 10.1002/mas.20176 (cit. on pp. 117, 118).

[218] JD Perlmutter and MF Hagan. *Mechanisms of Virus Assembly.* In: **Annual Review of Physical Chemistry** 66.1 (2015), pp. 217–239. DOI: 10.1146/annurev-physchem-040214-121637 (cit. on pp. 117, 118).

[219] MF Hagan and R Zandi. *Recent advances in coarse-grained modeling of virus assembly.* In: **Current Opinion in Virology** 18 (2016), pp. 36–43. DOI: 10.1016/j.coviro.2016.02.012 (cit. on pp. 117, 118).

[220] J Grant, RL Jack, and S Whitelam. *Analyzing mechanisms and microscopic reversibility of self-assembly.* In: **Journal of Chemical Physics** 135.21 (2011). DOI: 10.1063/1.3662140 (cit. on p. 117).

[221] GM Whitesides and M Boncheva. *Beyond molecules: Self-assembly of mesoscopic and macroscopic components.* In: **Proceedings of the National Academy of Sciences** 99.8 (2002), pp. 4769–4774. DOI: 10.1073/pnas.082065899 (cit. on p. 117).

[222] A Zlotnick. *Are weak protein-protein interactions the general rule in capsid assembly?* In: **Virology** 315.2 (2003), pp. 269–274. DOI: 10.1016/S0042-6822(03)00586-5 (cit. on pp. 117, 118).

[223] XS Chen et al. *Structure of small virus-like particles assembled from the L1 protein of human papillomavirus 16.* In: **Molecular Cell** 5.3 (2000), pp. 557–567. DOI: 10.1016/S1097-2765(00)80449-9 (cit. on p. 118).

[224] D Arslan et al. *Distant Mimivirus relative with a larger genome highlights the fundamental features of Megaviridae.* In: **Proceedings of the National Academy of Sciences** 108.42 (2011), pp. 17486–17491. DOI: 10.1073/pnas.1110889108 (cit. on p. 118).

[225] FHC Crick and JD Watson. *Structure of small viruses.* In: **Nature** 177 (1956), pp. 473–475. DOI: 10.1038/177473a0 (cit. on p. 118).

[226] DLD Caspar and A Klug. *Physical principles in the construction of regular viruses.* In: **Cold Spring Harbor Symposia on Quantitative Biology** 27 (1962), pp. 1–24. DOI: 10.1101/SQB.1962.027.001.005 (cit. on p. 118).

[227] P Ceres and A Zlotnick. *Weak protein-protein interactions are sufficient to drive assembly of hepatitis B virus capsids.* In: **Biochemistry** 41.39 (2002), pp. 11525–11531. DOI: 10.1021/bi0261645 (cit. on pp. 118, 119).

[228] A Ben-Shaul and WM Gelbart. *Statistical thermodynamics of amphiphile self-assembly: structure and phase transitions in micellar solutions.* In: **Micelles, Membranes, Microemulsions, and Monolayers**. Springer, 1994, pp. 1–104. DOI: 10.1007/978-1-4613-8389-5_1 (cit. on p. 119).

[229] RF Bruinsma et al. *Viral Self-Assembly as a Thermodynamic Process*. In: **Physical Review Letters** 90.24 (2003), p. 248101. DOI: 10.1103/PhysRevLett.90.248101 (cit. on p. 119).

[230] R Becker and W Döring. *Kinetische Behandlung der Keimbildung in übersättigten Dämpfen*. In: **Annalen der Physik** 416.8 (1935), pp. 719–752. DOI: 10.1002/andp.19354160806 (cit. on pp. 119, 124).

[231] GR Lazaro and MF Hagan. *Allosteric Control of Icosahedral Capsid Assembly*. In: **Journal of Physical Chemistry B** 120.26 (2016), pp. 6306–6318. DOI: 10.1021/acs.jpcb.6b02768 (cit. on pp. 119, 124).

[232] PWK Rothemund and ES Andersen. *The importance of being modular*. In: **Nature** 485 (2012), pp. 584–585. DOI: 10.1038/485584a (cit. on pp. 119, 120, 230).

[233] KV Gothelf. *LEGO-like DNA Structures*. In: **Science** 338.6111 (2012), pp. 1159–1161. DOI: 10.1126/science.1229960 (cit. on pp. 119, 120, 230).

[234] H Gu et al. *A Proximity-Based Programmable DNA Nanoscale Assembly Line*. In: **Nature** 465 (2010), pp. 202–205. DOI: 10.1038/nature09026 (cit. on p. 119).

[235] PC Nickels et al. *Molecular force spectroscopy with a DNA-origami – based nanoscopic force clamp*. In: **Science** 354.6310 (2016), pp. 305–307. DOI: 10.1126/science.aah5974 (cit. on p. 119).

[236] PWK Rothemund. *Folding DNA to create nanoscale shapes and patterns*. In: **Nature** 440 (2006), pp. 297–302. DOI: 10.1038/nature04586 (cit. on p. 120).

[237] NC Seeman. *Nucleic acid junctions and lattices*. In: **Journal of Theoretical Biology** 99.2 (1982), pp. 237–247. DOI: 10.1016/0022-5193(82)90002-9 (cit. on p. 120).

[238] F Zhang et al. *Complex wireframe DNA origami nanostructures with multi-arm junction vertices*. In: **Nature Nanotechnology** 10 (2015), pp. 779–784. DOI: 10.1038/nnano.2015.162 (cit. on p. 120).

[239] R Veneziano et al. *Designer nanoscale DNA assemblies programmed from the top down*. In: **Science** 352.6293 (2016), p. 1534. DOI: 10.1126/science.aaf4388 (cit. on p. 120).

[240] WM Shih, JD Quispe, and GF Joyce. *A 1.7-kilobase single-stranded DNA that folds into a nanoscale octahedron*. In: **Nature** 427 (2004), pp. 618–621. DOI: 10.1038/nature02307 (cit. on p. 120).

[241] SM Douglas et al. *Self-assembly of DNA into nanoscale three-dimensional shapes*. In: **Nature** 459 (2009), pp. 414–418. DOI: 10.1038/nature08016 (cit. on p. 120).

[242] ES Andersen et al. *Self-assembly of a nanoscale DNA box with a controllable lid*. In: **Nature** 459 (2009), pp. 73–76. DOI: 10.1038/nature07971 (cit. on p. 120).

[243] J Sharma et al. *Toward reliable gold nanoparticle patterning on self-assembled DNA nanoscaffold*. In: **Journal of the American Chemical Society** 130.25 (2008), pp. 7820–7821. DOI: 10.1021/ja802853r (cit. on p. 120).

[244] R Zandi et al. *Classical nucleation theory of virus capsids*. In: **Biophysical Journal** 90.6 (2006), pp. 1939–1948. DOI: 10.1529/biophysj.105.072975 (cit. on p. 124).

[245] RP Sear. *Nucleation: Theory and applications to protein solutions and colloidal suspensions*. In: **Journal of Physics Condensed Matter** 19.3 (2007), p. 033101. DOI: 10.1088/0953-8984/19/3/033101 (cit. on p. 124).

[246] C J Delebecque et al. *Organization of Intracellular Reactions with Rationally Designed RNA Assemblies*. In: **Science** 333.6041 (2011), pp. 470–474. DOI: 10.1126/science.1206938 (cit. on p. 227).

[247] J M Stewart and E Franco. *Self-assembly of large RNA structures: learning from DNA nanotechnology*. In: **DNA and RNA Nanotechnology** 2.1 (2015), pp. 23–35. DOI: 10.1515/rnan-2015-0002 (cit. on p. 227).

[248] F Praetorius et al. *Biotechnological mass production of DNA origami*. In: **Nature** 552 (2017), pp. 84–87. DOI: 10.1038/nature24650 (cit. on p. 227).

[249] M Li et al. *In vivo production of RNA nanostructures via programmed folding of single-stranded RNAs*. In: **Nature Communications** 9 (2018), p. 2196. DOI: 10.1038/s41467-018-04652-4 (cit. on p. 227).

Acknowledgment

If I have seen (a little) further, it is by standing on the shoulders of giants.
(Based freely on Isaac Newton)

There are many people who have contributed to this thesis in one way or another. A big thank you goes to all of them.

First of all, I would like to express my deepest gratitude to my supervisor Erwin Frey. I highly appreciate your continuous support throughout the last years and the freedom and trust you gave me from the very beginning to follow my scientific interests and to work on the diverse projects that kept me busy during my PhD. Thank you for all the time you put into these projects, for your positivity and for all the discussions we had about new ideas, putting our results into perspective or presenting them at conferences and meetings! In this context, I am also particularly grateful for the innumerable opportunities to attend conferences and summer schools, to meet and discuss with invited guests or even to invite them myself. I especially enjoyed the Boulder Summer School this year, which helped me to expand my horizon both scientifically as well as personally. This active participation in the scientific life would not have been possible without your support.

A special thanks also goes to the other members of my thesis advisory committee, Joachim Rädler and Ulrich Gerland. I have profited greatly from our discussions and your feedback and advice both in terms of the projects and with regard to career choices. In this regard, I also want to thank Joachim Krug for taking the time and effort to review my thesis.

I am very happy about the chance to be a part of the graduate school "Quantitative Biosciences Munich"(QBM) and I want to thank all the people that put so much effort into it, in particular Ulrike Gaul, Filiz Civril and Markus Hohle. Along similar lines, I am very grateful to Susanne Hennig, Claudia Leonhardt and Marilena Pinto for keeping up the spirit in the Center for NanoScience and the Munich Biophysics SFBs and for organizing the many seminars, workshops and retreats.

I am sure I would not have had half the fun during my PhD if the atmosphere in our group had not been as collaborative, open and supporting. A heartfelt thank you to all the current and previous members of the LMU Biophysics theory groups! In particular, I want to thank Marianne Bauer, Mareike Bojer, Florian Gartner, Patrick Wilke, Philipp Geiger, Michele Guerra, Frederik Träuble and Moritz Striebel, with whom I had the pleasure to work on various projects and to discuss not only science but anything loosely related to it. I very much enjoyed working with all of you and it was great to see so many different perspectives of science and approaches to solve problems - I definitely learned a lot. For all the helpful discussions and mutual scientific and personal support, I also want to thank my office mates Silke Bergeler, Emanuel Reithmann, David Brückner and (at least for a short time) Jonas Denk. For proof-reading parts of my thesis I want to thank Marianne Bauer, Silke Bergeler,

Mareike Bojer, Florian Gartner, Raphaela Geßele, Felix Kempf, Timo Krüger, Federica Mura, Emanuel Reithmann, Moritz Striebel, Manon Wigbers, Patrick Wilke, Laeschkir Würthner and my family. Finally, thank you very much to all of you that have not only been colleagues but have become good friends!

In this regard, I also want to warmly thank my friends since the first day of our physics journey, Julia Benedikter, Frauke Seeßelberg and Angela Burger, for the mutual help and encouragement throughout our studies. Thank you, Julia, for the (almost) weakly lunches and for the fact that we did not talk about physics but about everything else in life.

Thanks are also owed to all the people with whom I had a very good time organizing various events: Nico Coca-López and Ines Trübenbach for the time as CeNS student representatives, Alexandra Fink, Markus Kröss and Felix Zierhut for organizing "Science Rocks!" together, Silke Bergeler and Karsten Miermans for initiating the LS Frey Alumni meeting, Federica Mura for many (and in the end two successful) attempts to invite guests for the QBM lecture series, Stefano Ceolin, Victor Solis Mezarino, Madlin Schenk, Sophie Tritschler and Lina Wendeler for the QBM retreat in Venice, and David Brückner and Jonas Denk for the fun we had organizing Antholz!

There are also many people outside of physics who have been an important part of my life. I want to thank my close friends of the Stiftung and from Regensburg, the Kochrunde, the choir people and the Bouldercrew for the many things we experienced together, for making me enjoy life in Munich and for their encouragement. Similarly, I want to thank my family-in-law for their support, their interest in what I work on and the shared time.

A very special thanks goes to my parents, Beate Einsele-Krämer and Bernhard Krämer, and my brother, Robert Krämer. Thank you very much for always believing in me beyond what is reasonable, for trusting my choices and supporting my decisions. In particular, I would like to thank my mum for her love and steady support, my dad for his advice and encouragement and my brother for being an extremely good listener and for always knowing when to say what.

The place of honor is for my husband, Robert Graf. Thank you for your love and your understanding, for always being there for me, for making me laugh even in the most stressful situations and for your help and support in everything I do. I would not have made it without you.